ATMOSPHERIC ELECTRICITY

EDITED BY: Irina Alexandrovna Mironova, Martin Fullekrug,
Konstantinos Kourtidis and Evgeny Anatolievich Mareev

PUBLISHED IN: Frontiers in Earth Science

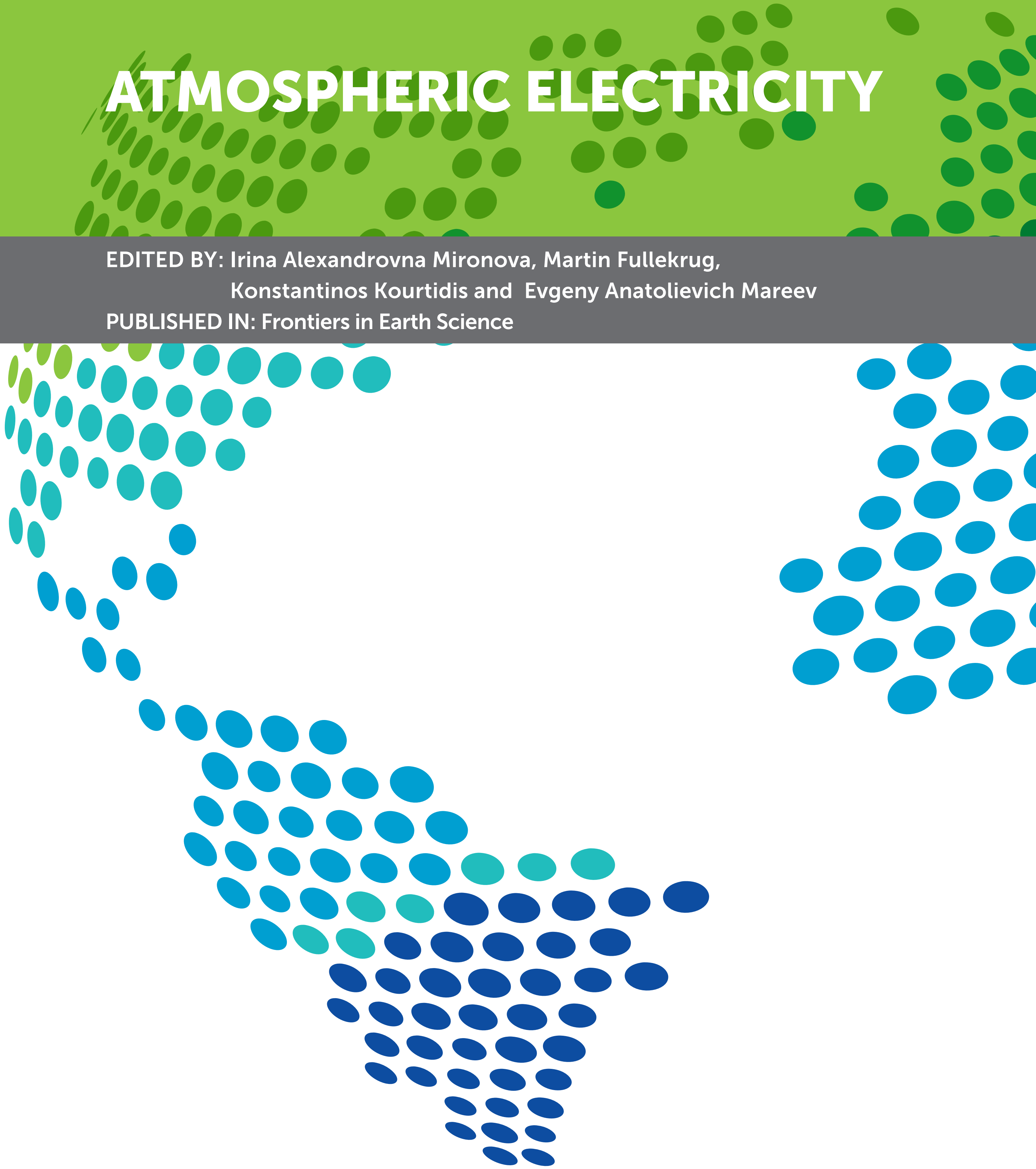

frontiers Research Topics

ISSN 1664-8714
ISBN 978-2-88974-605-7
DOI 10.3389/978-2-88974-605-7

About Frontiers

Frontiers is more than just an open-access publisher of scholarly articles: it is a pioneering approach to the world of academia, radically improving the way scholarly research is managed. The grand vision of Frontiers is a world where all people have an equal opportunity to seek, share and generate knowledge. Frontiers provides immediate and permanent online open access to all its publications, but this alone is not enough to realize our grand goals.

Frontiers Journal Series

The Frontiers Journal Series is a multi-tier and interdisciplinary set of open-access, online journals, promising a paradigm shift from the current review, selection and dissemination processes in academic publishing. All Frontiers journals are driven by researchers for researchers; therefore, they constitute a service to the scholarly community. At the same time, the Frontiers Journal Series operates on a revolutionary invention, the tiered publishing system, initially addressing specific communities of scholars, and gradually climbing up to broader public understanding, thus serving the interests of the lay society, too.

Dedication to Quality

Each Frontiers article is a landmark of the highest quality, thanks to genuinely collaborative interactions between authors and review editors, who include some of the world's best academicians. Research must be certified by peers before entering a stream of knowledge that may eventually reach the public - and shape society; therefore, Frontiers only applies the most rigorous and unbiased reviews.
Frontiers revolutionizes research publishing by freely delivering the most outstanding research, evaluated with no bias from both the academic and social point of view.
By applying the most advanced information technologies, Frontiers is catapulting scholarly publishing into a new generation.

What are Frontiers Research Topics?

Frontiers Research Topics are very popular trademarks of the Frontiers Journals Series: they are collections of at least ten articles, all centered on a particular subject. With their unique mix of varied contributions from Original Research to Review Articles, Frontiers Research Topics unify the most influential researchers, the latest key findings and historical advances in a hot research area! Find out more on how to host your own Frontiers Research Topic or contribute to one as an author by contacting the Frontiers Editorial Office: frontiersin.org/about/contact

ATMOSPHERIC ELECTRICITY

Topic Editors:
Irina Alexandrovna Mironova, Saint Petersburg State University, Russia
Martin Fullekrug, University of Bath, United Kingdom
Konstantinos Kourtidis, Democritus University of Thrace, Greece
Evgeny Anatolievich Mareev, Institute of Applied Physics (RAS), Russia

Citation: Mironova, I. A., Fullekrug, M., Kourtidis, K., Mareev, E. A., eds. (2022). Atmospheric Electricity. Lausanne: Frontiers Media SA.
doi: 10.3389/978-2-88974-605-7

Table of Contents

04 ***Editorial: Atmospheric Electricity***
Irina Mironova, Martin Füllekrug, Konstantinos Kourtidis and Evgeny Mareev

07 ***Electric Mode Excitation in the Atmosphere by Magnetospheric Impulses and ULF Waves***
V. A. Pilipenko, E. N. Fedorov, V. A. Martines-Bedenko and E. A. Bering

20 ***Measuring Global Signals in the Potential Gradient at High Latitude Sites***
José Tacza, Keri A. Nicoll, Edith L. Macotela, Marek Kubicki, Anna Odzimek and Jyrki Manninen

35 ***Locating Thunder Source Using a Large-Aperture Micro-Barometer Array***
Jan Rusz, Jaroslav Chum and Jiří Baše

45 ***Nature of Relationships Between Atmospheric Electricity Parameters at Ground Surface and Air Ionization on the Basis of Nuclear Accidents in Power Plants and Weapons Tests***
Marek Kubicki, Bogna Mysłek-Laurikainen and Anna Odzimek

59 ***Anthropogenic Noise and Its Footprint on ELF Schumann Resonance Recordings***
V. Tritakis, I. Contopoulos, C. Florios, G. Tatsis, V. Christofilakis, G. Baldoumas and C. Repapis

70 ***Evaluating the Response of Global Column Resistance to a Large Volcanic Eruption by an Aerosol-Coupled Chemistry Climate Model***
Yushan Xie, Ruyi Zhang, Zhipeng Zhu and Limin Zhou

84 ***Tree Canopies Influence Ground Level Atmospheric Electrical and Biogeochemical Variability***
Ellard R. Hunting, Sam J. England and Daniel Robert

92 ***Influence of Solar Wind on Secondary Cosmic Rays and Atmospheric Electricity***
Jaroslav Chum, Marek Kollárik, Ivana Kolmašová, Ronald Langer, Jan Rusz, Dana Saxonbergová and Igor Strhárský

107 ***Modeling of Spherical Dust Particle Charging due to Ion Attachment***
Sotirios A. Mallios, Georgios Papangelis, George Hloupis, Athanasios Papaioannou, Vasiliki Daskalopoulou and Vassilis Amiridis

129 ***Solar Cycle-Modulated Deformation of the Earth–Ionosphere Cavity***
Tamás Bozóki, Gabriella Sátori, Earle Williams, Irina Mironova, Péter Steinbach, Emma C. Bland, Alexander Koloskov, Yuri M. Yampolski, Oleg V. Budanov, Mariusz Neska, Ashwini K. Sinha, Rahul Rawat, Mitsuteru Sato, Ciaran D. Beggan, Sergio Toledo-Redondo, Yakun Liu and Robert Boldi

149 ***Experimental Validation of N_2 Emission Ratios in Altitude Profiles of Observed Sprites***
Cheng-Ling Kuo, Earle Williams, Toru Adachi, Kevin Ihaddadene, Sebastien Celestin, Yukihiro Takahashi, Rue-Ron Hsu, Harald U. Frey, Stephen B. Mende and Lou-Chuang Lee

frontiers
in Earth Science

EDITORIAL
published: 09 February 2022
doi: 10.3389/feart.2022.853584

Editorial: Atmospheric Electricity

Irina Mironova [1,2]*, *Martin Füllekrug* [3], *Konstantinos Kourtidis* [4] *and Evgeny Mareev* [5]

[1]Faculty of Physics, Saint Petersburg State University, Saint Petersburg, Russia, [2]National Research Nuclear University MEPhI, Moscow, Russia, [3]Deptment of Electronic and Electrical Engineering, University of Bath, Bath, United Kingdom, [4]Deptment of Environmental Engineering, Democritus University of Thrace, Xanthi, Greece, [5]Institute of Applied Physics, Russian Academy of Sciences, Nizhny Novgorod, Russia

Keywords: atmospheric electricity, global electric circuit, magnetosphere-ionosphere-atmosphere, Schumann resonances, aerosol and cloud microphysics

Editorial on the Research Topic

Atmospheric Electricity

Atmospheric electricity is related to a broad range of disciplines, including the global atmospheric electric circuit (GEC), energetic radiation and electrification of the atmosphere, aerosol and cloud microphysics, thunderstorms, lightning physics, high-energy processes, as well as relations to solar-terrestrial phenomena and the evolution of the Earth's climate and atmospheric chemistry. Studies in many areas of atmospheric electricity are rapidly advanced by ground-based, satellite and airborne measurements, laboratory investigations at various scales and chemistry-climate modelling.

Solar-terrestrial influences are explored in several papers. Chum et al. examined the influence of the solar wind on secondary cosmic rays and atmospheric electricity. A relationship between the heliospheric magnetic field, atmospheric electric field, lightning activity, and secondary cosmic rays is investigated with a focus on variations related to the solar rotation. It was found that fluctuations of lightning activity are in phase and in antiphase with the B_x and B_y components of the heliospheric/interplanetary magnetic field, respectively, in agreement with previous studies. On the other hand, the ~27-day solar rotation was not significant in the atmospheric electric field measured in Slovakia and Czechia and therefore, no significant influence of B_x and B_y on the atmospheric electric field was observed at these middle-latitude stations. Pilipenko et al. used GLOCAEM data and modeling to address the long-standing problem of the coupling between space weather disturbances and atmospheric electricity. The model predicts that the excitation rate of the E-mode by magnetospheric disturbances is low, such that only a weak E_z response with a magnitude of ~several V/m will be produced by ~100 nT geomagnetic disturbances. However, at heights ~30 km, the electric field of the E-mode becomes dominant. Bozóki et al. examine the solar cycle modulation of the Earth–Ionosphere Cavity resonator, which encloses electromagnetic radiation of lightning continuing current < 100 Hz, a phenomenon known as Schumann resonances. It is shown that to explain all observations, the effect of solar X-rays and energetic electron precipitation need to be considered, as they modify the quality factor of the cavity mainly over high latitudes.

Kuo et al. verified experimentally the ISUAL array photometer (AP) measured N_2 emission ratio 2P/1P and compared it with the theoretically predicted sprite emission ratio using numerical results on sprite streamers. AP-measured ratios in sprite halo events are consistent with predicted ratios for streamer head electric fields of 3.7 E_k and 4.6 E_k, where E_k is breakdown electric field. Most carrot sprite events initiated at altitudes 67.4 ± 7.6 km with smaller estimated electric fields 1~4 E_k. Below 60 km, AP-measured ratios fell below the predicted ratio ~1 E_k.

Disturbances to the atmospheric electric field due to large volcanic eruptions, nuclear accidents, nuclear weapons tests, and the presence of desert dust in the atmosphere is examined in three papers. Xie et al. use an aerosol coupled chemistry-climate model to develop a new global electric circuit model. Their results show that due to the Brewer-Dobson circulation, there are significant seasonal variations in the ion loss due to variations in the volcanic aerosol layer. In the winter hemisphere at

OPEN ACCESS

Edited and reviewed by:
Yuqing Wang,
University of Hawaii at Manoa,
United States

****Correspondence:***
Irina Mironova
i.a.mironova@spbu.ru

Specialty section:
This article was submitted to
Atmospheric Science,
a section of the journal
Frontiers in Earth Science

Received: *12 January 2022*
Accepted: *19 January 2022*
Published: *09 February 2022*

Citation:
Mironova I, Füllekrug M, Kourtidis K
and Mareev E (2022) Editorial:
Atmospheric Electricity.
Front. Earth Sci. 10:853584.
doi: 10.3389/feart.2022.853584

high latitudes, the column resistance will be larger than the column resistance in the summer hemisphere. With a volcanic aerosol layer in the decreasing phase of solar activity, the column resistance would be more sensitive to fluctuations of the electron flux of precipitating electrons from low to medium energies. Coupling this model with a global circuit sub-model including accurate ion pair production by relativistic electron precipitation could clarify the link between space weather and the troposphere. Kubicki et al. analyze atmospheric electricity parameters measured at the Geophysical Observatory in Świder, Poland, during major events that resulted in the release of a significant amount of artificial radioactive substances in the Earth's atmosphere. Namely, nuclear weapons testing 1958–1965, the Chernobyl disaster in 1986 and the Fukushima accident in 2011. Mallios et al. studied the attachment of ions to settling spherical dust particles iusing a 1D numerical model that estimates the acquired electrical charge on dust particles and calculates the electrical force that is applied to them. Using observed dust size distributions, the authors find that the particles acquire charge in the range of 1–1,000 elementary charges depending on their size and number density. The particles become mainly negatively charged, but under certain conditions particles $> 100\ \mu$m can be positive. The large-scale electric field can increase up to 20 times when compared to average fair-weather values. The results show that the electrical force is not enough to significantly influence the gravitational settling of the particles. This indicates that the process of ion attachment alone is not sufficient to modify particle dynamics and points to the need to include triboelectric effects and updrafts to fully represent the impact of electricity on particle dynamics in the model.

Hunting et al. assess theoretically how trees alter their surrounding electric fields and empirically compare the influence of trees on the dynamics of the atmospheric potential gradient, positive ions the ground level and electrochemical properties of the soil. It is shown that a substantial increase in atmospheric potential gradient only marginally affects the electric field under the tree canopy, and that soil electrochemical properties are tied to the temporal dynamics of positive ions near the ground level atmosphere. Trees reduce the temporal variability in both, ground level positive ion concentrations and soil redox potential. The results suggest that a tree can alter the temporal variability of the atmospheric electric field at the ground and soil electro-chemistry, and it is therefore possible that soil microorganisms, processes and electro-sensitive organisms are indirectly influenced by atmospheric electric fields.

Tacza et al. present potential gradient measurements from five remote stations at high latitudes in the Southern and Northern Hemisphere, to minimize the influence of local effects. They present a first description of new datasets from Halley, Antarctica, and Sodankylä, Finland, along with new criteria for the determination of fair-weather conditions at snow covered sites. It is shown that wind speeds as low as 3 m/s can loft snow particles, and that the fetch of the measurement site is an important factor in determining this threshold wind speed. The daily and seasonal analysis of the potential gradient in fair weather conditions shows an excellent agreement with the Carnegie curve of the global electric circuit. This demonstrates that high latitude sites, at which magnetic and solar influences are occasionally present, can also provide globally representative measurements for global electric circuit studies.

Rusz et al. use a large aperture array of microbarometers to calculate the source locations of infrasound emissions from lightning discharges by using the time delays between rapid changes of the electrostatic field and the arrival of the infrasound signals. For most of the analyzed cases, the calculated infrasound source location corresponds to the lightning location determined by the European lightning detection network EUCLID. The method allows for the calculation of the height of the infrasound source, which is typically found ~3–5 km. Tritakis et al. created artificial disturbances such as rifle firings, car engine operation, car radio, and apparatus shaking, near ELF recording stations to identify the impact of such radio frequency interference on the recordings of electromagnetic waves in the Schumann resonance band < 100 Hz. Such disturbances simulate anthropogenic noises from hunters, hikers and campers, which may occur near remote ELF recording stations. The work can assist the differentiation between artificial signals created from anthropogenic activity and natural signals attributed to geophysical phenomena.

AUTHOR CONTRIBUTIONS

IM conceptualized the idea of the Research Topic "*Atmospheric Electricity*." IM, MF, KK, and EM are contributors and editors of the Research Topic "*Atmospheric Electricity*." KK wrote the first draft of this editorial with editing and additional contributions from IM, MF, and EM. All authors listed have made a substantial, direct, and intellectual contribution to the work and approved it for publication.

FUNDING

IM's work in the SPbU "Ozone Layer and Upper Atmosphere Research Laboratory" was supported by the Ministry of Science and Higher Education of the Russian Federation under agreement contract no. 075-15-2021-583. The work of MF was sponsored by the Royal Society (UK) grant NMG/R1/180252 and the Natural Environment Research Council (UK) under grants NE/L012669/1 and NE/H024921/1. MF's project work has received funding from the European Union's Horizon 2020 research and innovation programme under the Marie Sklodowska-Curie grant agreement 722337.

ACKNOWLEDGMENTS

We thank authors of the papers published in the Research Topic "*Atmospheric Electricity*" for their valuable contributions and the referees for their important reviews. KK, IM, and EM acknowledge COST Action CA15211 "ELECTRONET". IM acknowledges Dr. Eugene Rozanov for his help with the organization of the Research Topic "*Atmospheric Electricity*." This Research Topic has been realized in collaboration with Dr. Svetlana Dementyeva. IM acknowledges the support from Roshan Patel of the "Frontiers in Earth Science" editorial office during the editorial process.

Conflict of Interest: The authors declare that the research was conducted in the absence of any commercial or financial relationships that could be construed as a potential conflict of interest.

frontiers
in Earth Science

ORIGINAL RESEARCH
published: 27 January 2021
doi: 10.3389/feart.2020.619227

Electric Mode Excitation in the Atmosphere by Magnetospheric Impulses and ULF Waves

V. A. Pilipenko[1,2]*, E. N. Fedorov[2], V. A. Martines-Bedenko[2] and E. A. Bering[3]

[1]Institute of Physics of the Earth, Moscow, Russia, [2]Space Research Institute, Moscow, Russia, [3]Department of Physics, University of Houston, Houstan, TX, United States

Variations of vertical atmospheric electric field E_z have been attributed mainly to meteorological processes. On the other hand, the theory of electromagnetic waves in the atmosphere, between the bottom ionosphere and earth's surface, predicts two modes, magnetic H (TE) and electric E (TH) modes, where the E-mode has a vertical electric field component, E_z. Past attempts to find signatures of ULF (periods from fractions to tens of minutes) disturbances in E_z gave contradictory results. Recently, study of ULF disturbances of atmospheric electric field became feasible thanks to project GLOCAEM, which united stations with 1 sec measurements of potential gradient. These data enable us to address the long-standing problem of the coupling between atmospheric electricity and space weather disturbances at ULF time scales. Also, we have reexamined results of earlier balloon-born electric field and ground magnetic field measurements in Antarctica. Transmission of storm sudden commencement (SSC) impulses to lower latitudes was often interpreted as excitation of the electric TH_0 mode, instantly propagating along the ionosphere–ground waveguide. According to this theoretical estimate, even a weak magnetic signature of the E-mode ~1 nT must be accompanied by a burst of E_z well exceeding the atmospheric potential gradient. We have examined simultaneous records of magnetometers and electric field-mills during >50 SSC events in 2007–2019 in search for signatures of E-mode. However, the observed E_z disturbance never exceeded background fluctuations ~10 V/m, much less than expected for the TH_0 mode. We constructed a model of the electromagnetic ULF response to an oscillating magnetospheric field-aligned current incident onto the realistic ionosphere and atmosphere. The model is based on numerical solution of the full-wave equations in the atmospheric-ionospheric collisional plasma, using parameters that were reconstructed using the IRI model. We have calculated the vertical and horizontal distributions of magnetic and electric fields of both H- and E-modes excited by magnetospheric field-aligned currents. The model predicts that the excitation rate of the E-mode by magnetospheric disturbances is low, so only a weak E_z response with a magnitude of ~several V/m will be produced by ~100 nT geomagnetic disturbance. However, at balloon heights (~30 km), electric field of the E-mode becomes dominating. Predicted amplitudes of horizontal electric field in the atmosphere induced by *Pc5* pulsations and travelling convection vortices, about tens of mV/m, are in good agreement with balloon electric field and ground magnetometer observations.

Keywords: atmosphere, ionosphere, ultra-low-frequency waves, magnetic and electric modes, balloon observations, ssc

Edited by:
*Irina Alexandrovna Mironova,
Saint Petersburg State University,
Russia*

Reviewed by:
*W. Jeffrey Hughes,
Boston University, United States
Kazue Takahashi,
Johns Hopkins University,
United States*

***Correspondence:**
*V. A. Pilipenko
space.soliton@gmail.com*

Specialty section:
*This article was submitted to
Atmospheric Science,
a section of the journal
Frontiers in Earth Science*

Received: *19 October 2020*
Accepted: *09 December 2020*
Published: *27 January 2021*

Citation:
*Pilipenko VA, Fedorov EN,
Martines-Bedenko VA and Bering EA
(2021) Electric Mode Excitation in the
Atmosphere by Magnetospheric
Impulses and ULF Waves.
Front. Earth Sci. 8:619227.
doi: 10.3389/feart.2020.619227*

INTRODUCTION: ARE THERE ULTRA-LOW-FREQUENCY SIGNATURES IN ATMOSPHERIC ELECTRIC FIELD?

The mutual fertilization of two geophysical disciplines—space physics and atmospheric electricity, has been rather low so far. This neglect is related to the fact that variations of the atmospheric electric field are commonly considered to be totally influenced by local meteorological processes. As a result, the magnetospheric community and atmospheric electricity community practically do not interact. In particular, in studies of waves and transients in the ultra-low-frequency (ULF) band (from mHz to Hz), the impact of magnetospheric disturbances on gradient of atmospheric potential (i.e., vertical electric field E_z) was commonly neglected, besides a few studies mentioned below.

Electromagnetic waves in the atmosphere, between the conductive layers of the bottom ionosphere and earth's surface, can be decomposed into the magnetic H-mode (TE or THM mode) and electric E-mode (TH or TEM mode). Each mode has a specific partial impedance characterizing its interaction with the earth's crust (Berdichevsky et al., 1971). The H-mode carries a vertical magnetic field disturbance, B_z, while the E-mode carries a vertical electric field disturbance, E_z. Upon modeling of magnetospheric MHD wave (Alfven (Hughes and Southwood, 1976) and fast compressional (Hamieri and Kivelson, 1991) modes) interaction with the ionosphere-atmosphere-ground system, the contribution of the E-mode is commonly neglected, so the ground response is believed to be produced by the H-mode only (Alperovich and Fedorov, 2007).

The E-modes are effectively excited in the ELF-VLF bands (e.g., Schumann resonances and sferics) by lightning electric discharges. Does the E-mode contribute also in the electromagnetic field of ULF waves? So far, there is no definitive answer to this question.

Apart from space physics applications, this problem is of key importance for magnetotelluric sounding (MTS) fundamentals. On the assumption that the incident ULF field is composed of a superposition of partial E- and H-modes, a new method of MTS, directional analysis, was developed by Chetaev (1970). This method is based on the premise that the spatial structure of ULF pulsations above a high-resistive crust does not meet the plane wave approximation and should be modeled as a horizontally propagating inhomogeneous plane wave with a complex wave vector (Dmitriev, 1970; Chetaev, 1985). According to this concept, the electric mode carrying a large vertical electric field/current in the air is a part of a primary wave. In this regard, verification of possible occurrences of E_z in the atmosphere in the ULF range is of fundamental importance for adequate MTS.

Attempts to detect ULF signatures in atmospheric E_z field have given contradictory results. Multicomponent magnetic and telluric observations provided seemingly promising results on the existence of the E-mode (Vinogradov, 1960; Savin et al., 1991). However, these studies used measurements of vertical telluric field in boreholes. Therefore, it is not clear whether the ULF signature in E_z was indeed caused by an incident partial E-mode, or by mode conversion owing to crust conductivity inhomogeneities. Direct measurements of the vertical electric field in the atmosphere seemingly indicated the possibility of the E-mode existence in the *Pc3* (Chetaev et al., 1975) and *Pc1* (Chetaev et al., 1977) frequency bands.

On the other hand, Anisimov et al. (1993) found no systematic pulsations in atmospheric E_z field coherent with geomagnetic *Pc3* pulsations at middle latitude. Rare events with quasiperiodic variations of E_z were possibly the result of advection by wind of spatially inhomogeneous aero electric structures. At high latitude, the coherence between E_z fluctuations and simultaneous geomagnetic pulsations was low, though they both sometimes demonstrated periodic variations in the same period range 5–30 min (Kleimenova et al., 1996).

The problem is further complicated by the sporadic occurrence on the ground of periodic long-lasting variations of E_z owing to small-scale meteorological processes in the ULF band. Upon the upward transmission, the near-surface electric field noise attenuates exponentially and becomes negligible at the typical balloon heights (~30 km). The electric field as observed by balloon platform is actually a local ohmic response to current, because a balloon is drifting with the wind, so space charge structures are not moving past balloon. Therefore, the balloon experiments are more promising than the ground observations for the study of magnetospheric effects in atmospheric electric field.

The ideal observational conditions in Antarctica (more than 30% days at the surface and >90% of the days at balloon altitude match the "fair weather" condition) enabled Bering et al. (1987) to address the long-standing problem of coupling between atmospheric electricity and space weather disturbances at ULF time scales using the coordinated balloon-born electric and ground magnetic observations. Several electric and magnetic field events were recorded during the 1985–86 Balloon Campaign at South Pole Station (Bering et al., 1988, Bering et al., 1990, Bering et al., 1995; Lin et al., 1995). However, no detailed theoretical analysis of these events was performed, so in *Simultaneous Geomagnetic and Ez Variations During Storm Sudden Commencement Events*, we will reexamine the results of the early balloon campaigns.

Another remaining controversy is related to the possibility of excitation of the electric TH_o mode (fundamental mode of the atmosphere–ground waveguide) by a magnetic storm sudden commencement (SSC). Kikuchi and Araki (1979) interpreted the propagation of SSC impulse from polar to low latitudes as "instantaneous" propagation of electromagnetic disturbance in TH_0 mode in the ionosphere-ground waveguide. This E-mode should carry a significant E_z disturbance, which can be detected by a sensor with a sufficient sampling rate (Yumoto et al., 1997). However, this predicted feature of SSC impulse was never validated.

In contrast to ubiquity of geomagnetic high-sampling observations, until recently there was no regular monitoring of the atmospheric electric field with a high time resolution. The previously mentioned results on occurrence of ULF pulsations in E_z field near the earth's surface were obtained from short-term observational campaigns, and these data were mostly lost completely, so the results cannot be verified. Recently, the study of short-period disturbances of the atmospheric electric field became feasible thanks to the project GLOCAEM (GLObal Coordination of Atmospheric Electricity Measurements), which united the high-resolution (up to 1 sec) measurements of potential gradient worldwide (Nicoll et al., 2019). The GloCAEM atmospheric electricity database for potential gradient measurements provided insights into a number of meteorological processes. Here, this database is used to examine the influence of geomagnetic disturbances on atmospheric electric field and to resolve a controversy about the possibility of the E-mode excitation by SSC. Also, we reexamine the results of coordinated balloon-born electric and ground magnetic observations in Antarctica.

To interpret the results of the SSC observations and earlier balloon experiments in Antarctica, we have developed a numerical model of electromagnetic ULF response to the incidence of oscillating magnetospheric field-aligned currents onto a realistic ionosphere–atmosphere system.

DATABASE OF GEOMAGNETIC AND ATMOSPHERIC MEASUREMENTS

To examine the impact of an interplanetary shock on the atmospheric electric field E_z as well, we used the list of observed SSC provided by International Index Service (http://isgi.unistra.fr and http://www.obsebre.es). The occurrence of IP shocks can also be seen in the plasma pressure p from the 1 min OMNI database (https://omniweb.gsfc.nasa.gov). We have examined all SSC events during the period 2007–2019.

As a source of information on disturbances of atmospheric electric field, we used the data provided by the project GloCAEM (GloCAEM.wordpress.com), which provides a portal to freely access potential gradient data from 17 sites worldwide. From available long-term 1 sec observations of atmospheric potential gradient (E_z), we have chosen data from the following sites:

- Reading (United Kingdom) 2011–2019, geographical coordinates 51.44°N, 0.94°W
- Hermon (Israel) 2015–2017, geographical coordinates 33°18′ N, 35°47′E
- CAS2 (Argentina) 2016–2019, geographical coordinates 31.80°S, 69.29°W

Available 1 sec data from some stations (e.g., Nycenk and Tripura) are low-quality, with too much interference, and have been omitted.

For magnetic field variations, we use the 1 min data from the INTERMAGNET array (https://intermagnet.github.io) from the following stations: near-equatorial stations MBO and AAE; midlatitude European stations ESK, LER, BFE, and CLF in the same region as atmospheric electricity sites. An SSC is a global phenomenon of a planetary scale, thus very close colocation of magnetometer and electric field sensor is not a crucial necessity. The map with location of selected stations is shown in **Figure 1**.

An ideal place for monitoring the fine characteristics of atmospheric electricity is the Antarctic plateau, because of the lack of anthropogenic influences, weak and stable winds, and lack of low-altitude clouds. A large database of 10 sec atmospheric E_z and J_z observations with high-sensitive field-mill and current collector has been collected at South Pole, Vostok, and Concordia stations (Byrne et al., 1991; Few et al., 1992; Burns at al., 1998). With the use of these data, relationships between variations of the atmospheric electricity and IMF parameters (Frank-Kamenetsky et al., 1999), and the ionospheric electric potential (Corney et al., 2003) were found. The Antarctic atmospheric electricity data are available via website (http://globalcircuit.phys.uh.edu). From available 10 sec magnetometer data from South Pole observatory and atmospheric electric field and current measurements during the period 1991–1993, we have analyzed 18 SSC events.

The balloon experimenters have stored their data and made them available online (https://uh.edu/research/spg/data.html). Payloads at an altitude of ~32 km carried 3-axis double probe electric field detectors and provided 15-s averaged 3-axis electric field data. We have re-analyzed the results of the 1985–86 Balloon Campaign at South Pole Station (Bering et al., 1987; Bering et al., 1995).

ESTIMATE OF E_Z PERTURBATIONS ACCOMPANYING STORM SUDDEN COMMENCEMENT EVENTS

Among a large variety of MHD disturbances in the near-earth environment, special attention has been paid to the study of SSC's caused by interaction of an interplanetary shock with the magnetosphere (Araki, 1977). The impulsive impact of a shock can bring a significant amount of energy and momentum into the magnetosphere in a very short time (Curto et al., 2007). Despite the seeming simplicity of such impact, the complexity of geomagnetic and plasma phenomena stimulated by an interplanetary shock turns out to be surprisingly large (Pilipenko et al., 2018). SSC transmission from high to low latitudes was often associated with the electric mode in the ionosphere–ground waveguide, instantly propagating along the earth's surface (Kikuchi and Araki, 1979). Among possible electric modes in the atmospheric waveguide, the fundamental TH_0 mode without a cutoff frequency is excited most effectively by a magnetospheric Alfven wave. Distinctive features of TH_0 mode are the propagation velocity just somewhat less than the light speed, and weak attenuation, which is due to the geometrical factor, not due to dissipation in the ionosphere (Kikuchi, 2014). Therefore, it seems that the TH_0 mode may contribute to geomagnetic response far from the MHD disturbance incident on the ionosphere (Kikuchi and Hashimoto, 2016). This notion about the TH_0 mode has been applied to interpret prompt SSC transmission from auroral to low latitudes (Kikuchi, 1986; Chi et al., 2001).

However, in the original papers on the TH_o mode, the excitation rate of this mode by magnetospheric sources was not considered. Simple scaling shows that a vertical current J_z

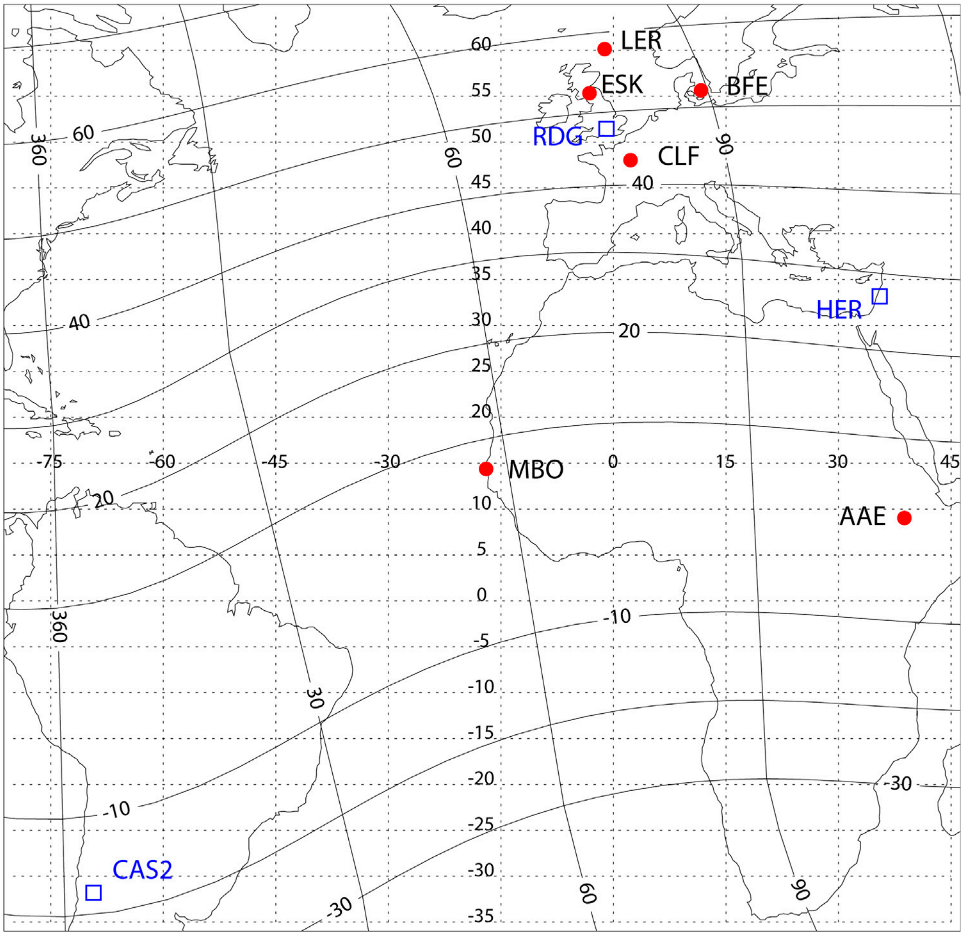

FIGURE 1 | The map with location of selected atmospheric electricity stations (blue empty squares) and magnetometers (red dots). Solid lines denote geomagnetic coordinates, and dotted lines correspond to geographic coordinates.

penetrating into the atmosphere resulting from the magnetospheric field-aligned current $J_Z^{(M)}$ with a transverse scale L is determined by the ratio between the resistance of the ionospheric E-layer (which is inversely proportional to the height-integrated Pedersen conductance Σ_P) and the resistance of the atmospheric column between the ground and height of the ionospheric conductive layer:

$$J_Z \big/ J_Z^{(M)} \simeq (L/L_*)^2. \tag{1}$$

In the atmosphere with exponential height-increasing conductivity $\sigma_A(z) = \sigma_0 \exp(z/\alpha)$ and negligible displacement current $\omega \ll \sigma_0/\varepsilon_0$ (that is for frequencies less than ~1 Hz), the parameter L_* is $L_* = \sqrt{\Sigma_P/(\sigma_0\alpha)}$. For typical values $\Sigma_P = 20$ S, $\Sigma_0 = 2*10^{-14}$ S/m, and $\alpha = 10$ km $L_* \sim 10^4$ km. This simple estimate shows that a somewhat significant part of the magnetospheric current would penetrate to the low-conductive atmosphere only for extremely large-scale disturbances. Thus, SSC seems to be a very promising source of E-mode excitation, because the scale of an SSC-associated source is the distance between the dawn and dusk ionospheric vortices, which is about several thousand km.

Let us estimate the expected magnitude of the vertical electric component E_z of the TH_0 mode. From the subsystem of Maxwell's equations for the E-mode, one can obtain the relationship between the components E_z and B_y of a wave propagating with the horizontal wave vector $k \equiv k_x$:

$$\frac{E_z}{B_y} \simeq \frac{kc}{k_0 \varepsilon_A}. \tag{2}$$

Here, the dielectric permittivity is $\varepsilon_A = 1 + i\sigma_A/\varepsilon_0\omega$, and $k_0 = \omega/c$ is the vacuum wave number. Assuming that $k \simeq R_E^{-1}$, **Eq. 2** yields in the case $\omega \ll \sigma_0/\varepsilon_0$:

$$\frac{E_z}{B_y} \simeq \frac{i}{\mu \sigma_0 R_E}. \tag{3}$$

From the relationship (**Eq. 3**), it follows that a TH_0 mode with magnetic component $B_y \sim 1$ nT in the atmosphere with $\sigma_0 = 10^{-13}$ S/m must be accompanied by a spike of atmospheric

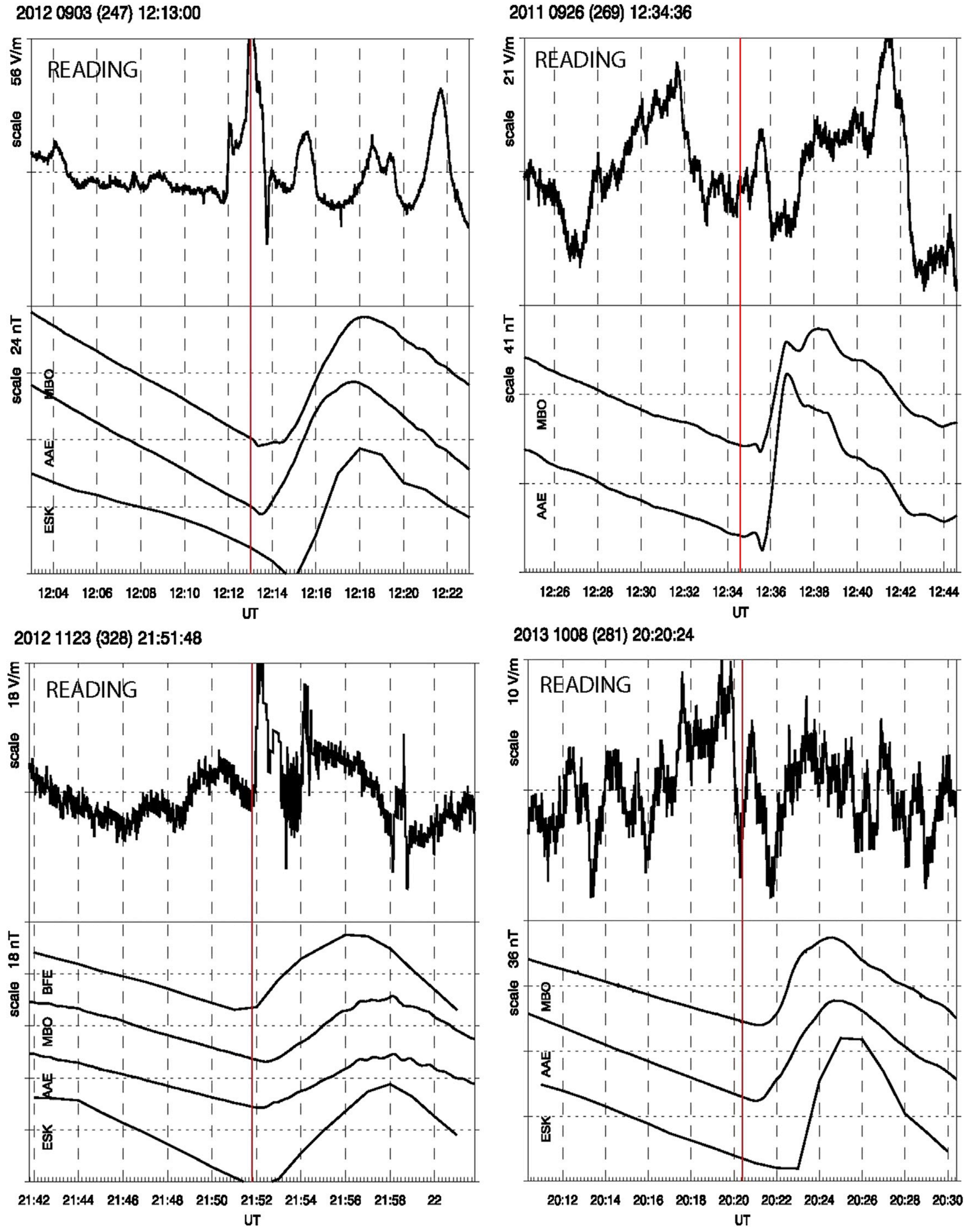

FIGURE 2 | Four events with seemingly bursts of E_z during SSC. Upper panels show variations of the atmospheric potential gradient, E_z, and bottom panel shows magnetograms (X component) from magnetometers in the same LT sector.

electric field E_z at the earth's surface with amplitude ~10^3 V/m. Thus, even a weak magnetic signature of the E-mode must be accompanied by a burst of E_z exceeding the atmospheric potential gradient. More rigorous treatment of the problem of magnetospheric field-aligned current interaction with the multilayered ionosphere-atmosphere-ground system will be provided in *Modeling of E-Mode Excitation by Magnetospheric FAC.*

SIMULTANEOUS GEOMAGNETIC AND E_Z VARIATIONS DURING STORM SUDDEN COMMENCEMENT EVENTS

We compare the above theoretical estimate with simultaneous observations of the atmospheric E_z field and geomagnetic variations (X-component). We have identified >50 events with simultaneous variations of E_z and ΔX. We examine the time intervals in the ±10 min vicinity of SSC events. The plots in **Figure 2** present examples, showing vertical electric field E_z (mV/m) from available stations and magnetic field ΔX (nT) component from selected stations. The data on the solar wind dynamic pressure has too many missing values for these events and are not shown. The moment of each SSC is marked by vertical lines in **Figure 2**.

In a majority of the events, no response of E_z on SSC was seen. The lack of E_z response imposes a limit on a possible amplitude of an expected electric mode—it is at least less than sensor sensitivity and background noise level. In none of >50 SSC events during 2007–2019 recorded by magnetometers and atmospheric electricity stations from the GLOCAEM array or Antarctica was a similar disturbance noticed.

However, in some events, a burst of E_z during an SSC can be seen. **Figure 2** presents several promising events. Let us exclude for a moment the possibility that the geomagnetic and E_z disturbances were just mere coincidences. In any case, the amplitudes of E_z disturbance occurring simultaneously with SSC do not exceed ~10 V/m. A similar negative result was obtained using E_z and J_z observations at the South Pole station (not shown). Therefore, SSC cannot be exciting or associated with the TH_0 mode.

MODELING OF E-MODE EXCITATION BY MAGNETOSPHERIC FAC

Basic features of electric field transmission from the ionosphere into the near-earth atmosphere in the DC approximation (when the time scale is larger than the relaxation time $\tau > \varepsilon_0/\sigma_0 \sim 20$ min) can be understood in a simple 1D model (Park, 1976). This model predicts that a potential difference Φ between the ionosphere and ground supports E_z varying with altitude z as follows:

$$E_z(z) = \Phi\Sigma_A/\sigma_A(z).$$

Here, Σ_A is the total conductance of the atmospheric column $\Sigma_A^{-1} = \int \sigma_A^{-1}(z)dz$. Typical values are $\Sigma_A \simeq 10^{-17}\,\mathrm{S/m^2}$, $\sigma_0 \sim 10^{-14}$ S/m, and $\Phi \sim 250$ kV. This relationship shows that a modification of the atmospheric conductivity profile $\sigma_A(z)$ by precipitation of high-energy solar particles (Kokorowski et al., 2006) or emanation of radioactive gas (Harrison et al., 2010) can modify $E_z(z)$ structure.

Penetration of nonsteady field, e.g., in the ULF band, is different and seldom studied. We have elaborated a model of the electromagnetic ULF response to an incidence of oscillating magnetospheric azimuthally symmetric FAC field-aligned current onto the realistic ionosphere and atmosphere. A similar multilayer model of the ionosphere-atmosphere-ground system has been used to examine the transmission of *Pc1* waves through the ionosphere to the ground (Fedorov et al., 2018). The geomagnetic field $\mathbf{B_0}$ at high latitudes may be assumed to be vertical. The problem is azimuthally symmetric, so a cylindrical coordinate system $\{z, \rho, \phi\}$ is used, with $\rho = 0$ in the axis of the current tube.

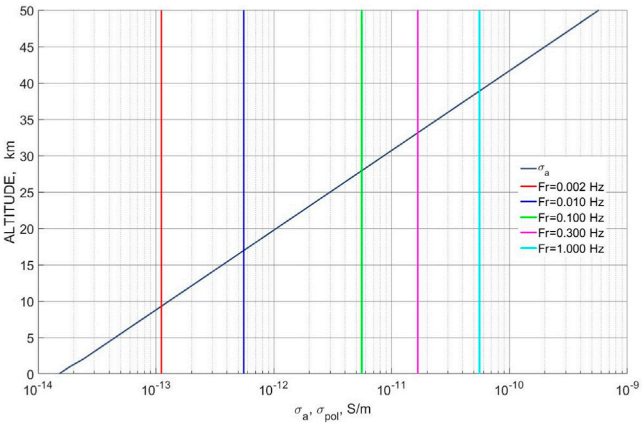

FIGURE 3 | The altitude dependence of the absolute magnitude of the atmospheric conductivity $|\sigma_A(z)|$ (black line). The magnitude of the displacement current $\varepsilon\varepsilon_0\omega$ for frequencies from 2 mHz to 1 Hz is denoted by vertical lines.

The model is based on a numerical solution of the full-wave equations in the realistic ionosphere. At the ground-atmosphere interface, the impedance boundary condition is imposed $E_\phi/B_\rho = E_\rho/B_\phi = Z_g/\mu$, where Z_g is the surface impedance. The ground conductivity is assumed to be $\sigma_g = 10^{-4}$ S/m. The parameters of the ionospheric collisional plasma were reconstructed using the IRI model (http://irimodel.org). The IRI parameters were chosen to correspond to day 2009, 06/21, 02 UT (premidnight) at auroral latitude (geographic latitude 56.5° and latitude 280.8°). According to the IRI model, the ionospheric conductances would be $\Sigma_P = 0.95$ S and $\Sigma_H = 1.40$ S.

The vertical profile of atmospheric conductivity is modeled by exponential dependence $\sigma_A(z) = \sigma_0 \exp(z/\alpha)$ that merges the IRI-predicted conductivity at z = 80 km. The choice of a more realistic conductivity profile will not change the results noticeably. The complex atmospheric conductivity that includes displacement current is given by $\sigma(z) = \sigma_A(z) - i\varepsilon\varepsilon_0\omega$ (where ε_0 is the vacuum permittivity). **Figure 3** shows the altitude dependence of the absolute magnitude of the complex conductivity (black line). The magnitude of the displacement current for frequencies from 2 mHz to 1 Hz is denoted by vertical lines. Evidently, at low altitudes, $\sigma(z)$ is determined by the displacement current, while at higher z, it is determined by the conductivity current. The height where $\omega\varepsilon_0\varepsilon = \sigma_A(z)$ is denoted $z = z^*(\omega)$.

We have calculated both the vertical and horizontal distributions of magnetic and electric field components, including the vertical electric field in the atmosphere. The 6-component electromagnetic field is excited by an incident Alfven wave (that is, oscillatory field-aligned current) with horizontal radius $R = 350$ km. The amplitudes of all field components are

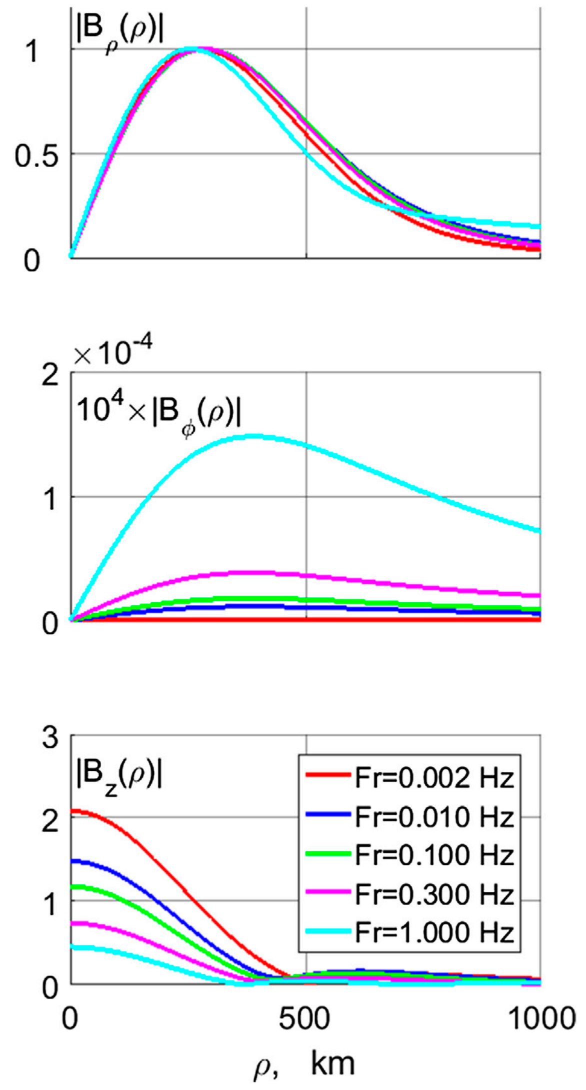

FIGURE 4 | The radial distribution of the magnetic component amplitudes (in nT), from top to bottom - B_ρ (ρ), B_ϕ (ρ), and B_z (ρ), on the ground for various frequencies.

normalized in such a way as to have the unit magnetic disturbance on the ground B_ρ (z = 0) = 1 nT for all frequencies in the region of spatial maximum $\rho = \rho_{\max}$. The magnetic mode in the atmosphere is excited by ionospheric Hall currents. These eddy currents produce a magnetic response in the atmosphere in the radial direction, that is, in the B_ρ component. The electric mode in the atmosphere is associated with vertical current. This current produces a magnetic disturbance in the azimuthal direction, that is, in the B_ϕ component. Thus, B_ρ and E_ϕ components are associated with H-mode, while B_ϕ and E_ρ components are associated with the E-mode.

The radial distribution of the amplitudes of the magnetic components on the ground for various frequencies is shown in **Figure 4**. The maximum of B_ρ (ρ) is reached at $\rho_{\max} = R/\sqrt{2} \simeq 280$ km (**Figure 4**, upper panel). The distribution of B_ϕ (ρ) component is rather similar (**Figure 4**, middle panel). This component is associated with the E-mode in the atmosphere, and it is about four orders of magnitude weaker than the radial component, associated with the H-mode. The occurrence of the vertical magnetic component B_z is due to inhomogeneity of an initial field, and its magnitude is determined by the ratio between the skin-depth and horizontal wave scale (Pilipenko et al., 1998). In contrast to horizontal components, the vertical component B_z(ρ) has spatial maximum beneath the current center ρ = 0 (**Figure 4**, bottom panel).

The radial distribution of the electric component amplitudes on the ground for various frequencies is shown in **Figure 5**. The electric field of the H-mode is revealed in the E_ϕ component, whereas the E-mode has E_ρ and E_z components. The distribution of horizontal electric components is similar to that of horizontal magnetic components (**Figure 5**, upper and middle panels). However, the vertical electric component E_z, associated with the E-mode, has maximum beneath the source at ρ = 0 (**Figure 5**, bottom panel). Amplitude of E_ρ component, ~3 10^{-5} mV/m, is about four orders of magnitude less than amplitude of E_ϕ component, ~0.2 mV/m. As expected for the

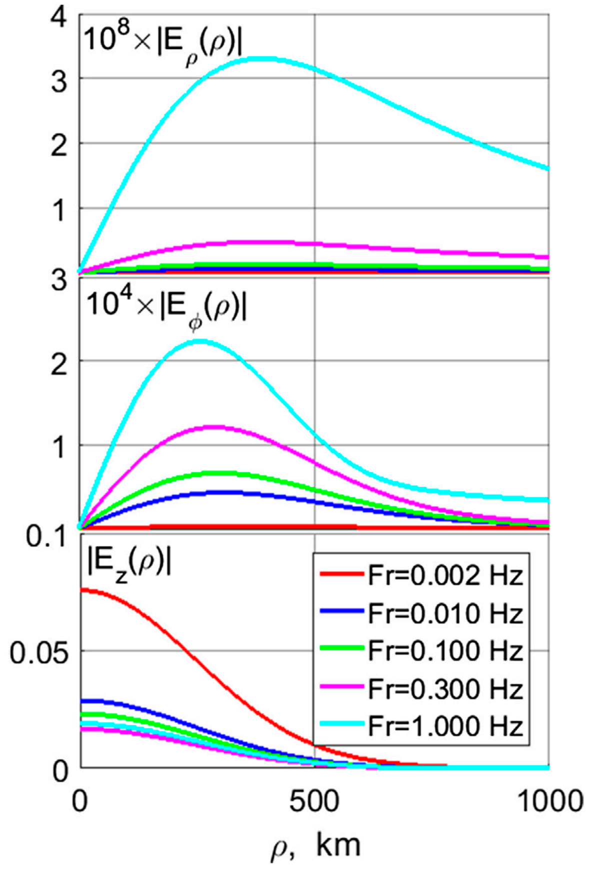

FIGURE 5 | The radial distribution on the ground of the electric component amplitudes, E_ρ (ρ), E_ϕ (ρ), and E_z (ρ) (in V/m), for various frequencies (shown in legend).

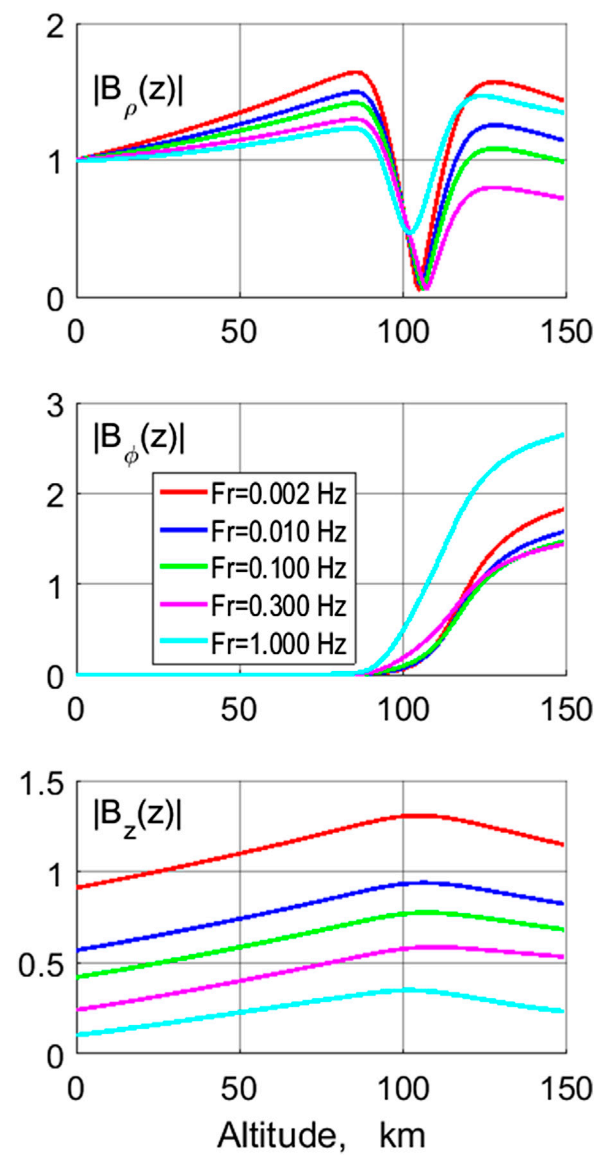

FIGURE 6 | The altitudinal profiles of the horizontal magnetic components (in nT) B_ρ (z), B_ϕ (z) at $\rho = \rho_{max}$ and the vertical component B_z (z) at $\rho = 0$.

electric field structure near the surface of a conductor, the normal to the surface electric field component E_z, ~80 mV/m is much larger than the transverse component.

The altitude profile of the horizontal magnetic components at the distance ρ_{max} is presented in **Figure 6**. The steep variation at z~90 km is related to a π/2 rotation of the polarization ellipse in the E-layer. The B_ρ component is nearly the same at all altitudes in the atmosphere. The B_ϕ component is many orders of magnitude less than the B_ρ component. The vertical magnetic component B_z is comparable in amplitude with the B_ρ component and just weakly increases with altitude.

The altitude profiles of the horizontal electric field components at ρ_{max} and vertical component E_z (z) at $\rho = 0$ are presented in **Figure 7**. The E_ϕ (z) component only weakly depends on altitude for low frequencies, but for higher frequencies, it grows with altitude up to the E-layer, as expected from Faraday's law $\partial_z E_\phi = i\omega B_\rho$. The altitude dependence of the E_ρ (z) component changes drastically at height $z = z^*$, where the Ohmic current equals the displacement current. This component is nearly constant in the more conductive upper atmosphere ($z > z^*$), but it drops in the less conductive lower atmosphere ($z < z^*$). For the vertical electric component, the modeling results can be understood, remembering that the altitude distribution of E_z (z) is proportional to the total complex conductivity Σ (z). The E_z perturbation at higher altitudes, $z > z^*$, decays exponentially $E_z(z) \propto \sigma_A(z)^{-1}$, whereas at lower altitudes, $z < z^*$, $E_z(z)$ is nearly constant. In the ionosphere (>80 km), the E_z component vanishes owing to the high field-aligned conductivity of the ionospheric plasma.

The relative magnitude of the atmospheric electric field disturbances owing to magnetospheric ULF variations may be seen in **Figure 8**. This figure compares the altitude structure of all three electric field components. At the ground, the horizontal components drop to very low magnitudes prescribed by the boundary impedance relationship. On the ground, the electric field of H-mode is dominating, $E_\rho << E_\phi$. However, because E_ρ increases fast until z ~ z*, at the balloon height (~30 km), the electric field of the E-mode becomes much larger, $E_\rho >> E_\phi$.

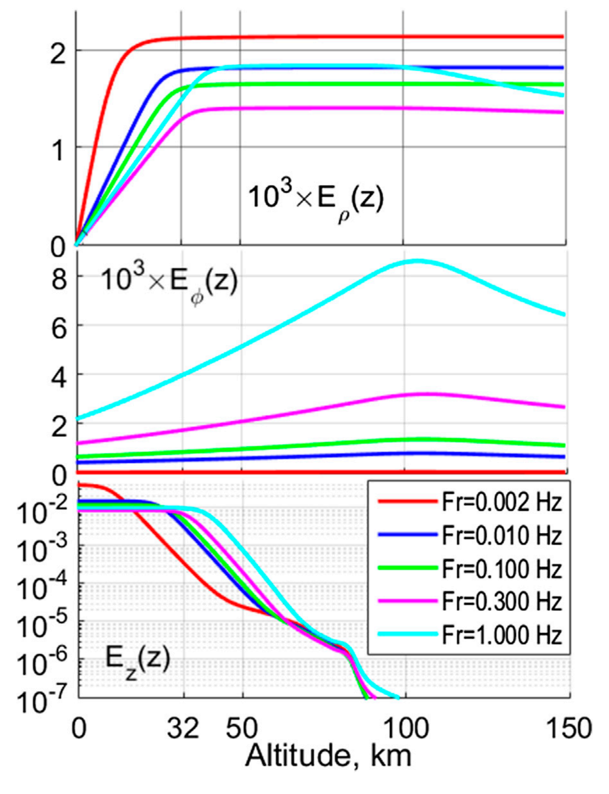

FIGURE 7 | The altitudinal profiles of the horizontal electric components E_ρ (z), E_ϕ (z) at $\rho = \rho_{max}$ and the vertical component E_z (z) at $\rho = 0$.

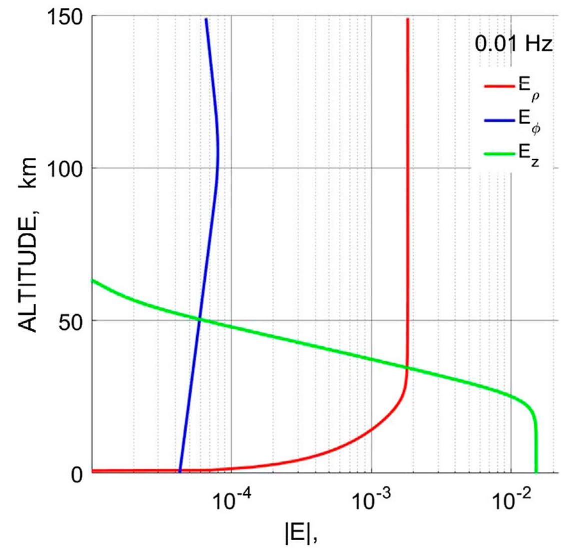

FIGURE 8 | The altitudinal structure of all three electric field components E_ρ (z), E_ϕ (z), and E_z (z) (in V/m).

This behavior can be comprehended from the following consideration. At the earth's surface, electric $\mathbf{E}^{(g)}$ and magnetic $\mathbf{B}^{(g)}$ components of the E-mode are about five orders of magnitude less than those of the H-mode. Magnetic components of both modes slowly vary with altitude: B_ϕ is practically constant till ~40 km and B_ρ increases about 1.5 times only till 80 km. The behavior of electric components is more complicated. From Faraday's law, it follows that the electric field of the H-mode varies with altitude as $E_\phi(z) \cong E_\phi^{(g)} - i\omega z B_\rho^{(g)} \approx E_\phi^{(g)}$. So, this electric field component is nearly constant throughout the atmosphere. The electric field of the E-mode strongly varies with altitude $E_\rho(z) \cong E_\rho^{(g)} - i(k^2/k_0)\, zcB_\phi^{(g)} \approx -i(k^2/k_0)\, zcB_\phi^{(g)}$. As a result, the ratio of electric fields of both modes varies with altitude as $\left|E_\rho(z)/E_\phi(z)\right| = (k^2 zc/k_0)\left|B_\phi^{(g)}/E_\phi^{(g)}\right|$. Therefore, starting from ground values $B_\phi^{(g)} = 1.1{*}10^{-6} nT$, $E_\phi^{(g)} = 2.5{*}10^{-6} V/m$, for $k = 10^{-3}$ 1/km, and $T = 500$ s, this ratio will grow linearly with altitude as $\left|E_\rho(z)/E_\phi(z)\right| = 3.2z$ (km). Thus, at balloon heights, electric field of the E-mode becomes much larger than that of the H-mode, whereas, on the other hand, the magnetic field of the E-mode (B_ϕ) is much less than that of the H-mode (B_ρ) in the entire atmosphere (up to the E-layer).

OBSERVATIONS OF E_Z PERTURBATIONS DURING TRAVELLING CONVECTION VORTICE AND *PC3-5* EVENTS IN ANTARCTICA

Responses of the atmospheric electric field associated with impulsive and wave magnetospheric disturbances were observed during the balloon campaigns. The reported events include travelling convection vortices (TCVs) and *Pc5* pulsations.

TCVs in the high latitude ionosphere are revealed on the ground as magnetic impulsive events with duration ~5–10 min. These localized daytime disturbances are thought to be responses to transients in the solar wind or magnetosheath. A survey of the campaign data looked for unipolar magnetic pulses above background in the vertical component B_Z on the ground and electric field perturbations ≥10 mV/m at balloon altitude (Lin et al., 1995). From total of 112 events found, electric field responses were observed for 90% of the events with the average E_z amplitude ~15 mV/m.

For example, the TCV event on January 3, 1986, was recorded by both the South Pole magnetometer and the balloon electric field sensor (Bering et al., 1990). This TCV was estimated to have a radius ~350 km and moved antisunward along the oval at a speed of ~4 km/s. The magnetometer observed a unipolar impulse in the magnetic vertical B_z component of ~80 nT and a bipolar impulse in the horizontal B_x component of ~100 nT. The accompanying atmospheric electric field pulse was less than 10 mV/m in the E_z component (at the noise level), and ~40 mV/m in the eastward E_y and ~25 mV/m in the poleward E_x components. In another event on Jan. 14, 1986, the TCV impulse amplitudes were ~20 nT in the horizontal magnetic and ~15 mV/m in the electric fields. The spike in the vertical E_z field reached ~40 mV/m.

As an example of *Pc5* pulsations, the event on July 9, 1975, may be presented (Maclennan et al., 1978). During this event coincident magnetic field, transverse electric field and electron precipitation fluctuations with 5 min period were measured around ~06 LT by ground magnetometer and balloon-borne double-probe and scintillation counter. The balloon reached a ceiling altitude of ~35 km. The experiment recorded magnetic variations with a peak-to-peak amplitude in the B_x component of ~6 nT and in the B_y component of ~8 nT, which were coherent with horizontal electric field variations with peak-to-peak amplitudes in the N-S component E_x of ~20 mV/m and in the E-W component E_y of ~15 mV/m.

Thus, the normalized transverse electric field response to TCV magnetic pulses is $E_\perp/B_\perp \sim (0.4–0.8)$ (mV/m)/nT and to *Pc5* waves is $E_\perp/B_\perp \sim 2.5$ (mV/m)/nT. The normalized response of vertical electric field to TCV magnetic pulses is $E_Z/B_\perp \sim 2$ (mV/m)/nT.

The expected model magnitude of an atmospheric electric field disturbance may be estimated from **Figure 5** for a 1 nT magnetic disturbance. The horizontal electric field disturbance at typical balloon altitude (32 km) is about 1.5 mV/m, depending on frequency. Thus, for a typical ground magnetic amplitude (20 nT), the balloon measurements should reveal an E perturbation of about 30 mV/m. This value is in a good agreement with the results of balloon observations discussed above (e.g., Bering et al., 1990). At the same time, the inductive electric field produced by the H-mode E_ϕ at balloon height would be ~1 mV/m only.

Amplitudes of the vertical and horizontal components become comparable at an altitude of ~30 km. For the ground magnetic disturbance with $B = 1$ nT and $f \sim 10$ mHz, the predicted vertical electric field disturbance is ~0.02 V/m. Thus, for intense ULF disturbances of the geomagnetic field ~100 nT, the disturbance of the ground level atmospheric field must be ~2 V/m. This value is small, and it can be detected by modern electric field sensors only under extremely quiet weather conditions.

APPARENT IMPEDANCES OF H- AND E-MODES

Simultaneous measurements of the wave electric and magnetic components gives one the possibility to determine the apparent wave impedance in order to obtain additional information about the wave mode. This method was applied by Pilipenko et al. (2012) to the radar-measured electric field and ground geomagnetic field of *Pc5* waves and by Bering et al. (1998) to the analysis of coordinated balloon-born electric and ground magnetometer measurements. More importantly, a preliminary knowledge of the atmosphere–ionosphere impedance gives one the possibility to estimate the wave electric field amplitude in the ionosphere from ground magnetometer observations.

Here, we first provide simple analytical estimates and then support them with numerical modeling. For the H-mode excited by a toroidal Alfvenic-type magnetospheric disturbance, the ratio between the dominant components of the electric field in the ionosphere, E_x, and ground magnetic response, B_x, follows from the thin ionosphere theory (Pilipenko et al., 2012):

$$\frac{E_x}{B_x} = \frac{1}{\mu \Sigma_H \sin I} \text{ or } \frac{E_x\,[\text{mV/m}]}{B_x\,[\text{nT}]} \simeq \frac{0.8}{\Sigma_H\,[\text{S}]}. \tag{4}$$

For the E-mode, the relationship between electric field in the ionosphere and ground magnetic disturbance was derived by Hughes, (1974). Here, we present a similar relationship for a wave infinite in the E-W direction ($k_y = 0$) and localized in N-S direction ($k \equiv k_x$). The ratio between the meridional electric field E_x and the azimuthal component of the magnetic field B_y on the ground is given by

$$\frac{E_x(z)}{B_y} = -i\frac{k^2c^2\alpha}{\omega}\ln\left(e^{-z/\alpha} + i\frac{\sigma_0}{\omega\varepsilon_0}\right). \tag{5}$$

This ratio is altitude-dependent and does not depend on the ionospheric conductivity. At altitudes $z > z_*$, the ratio coincides with the equation from Hughes, (1974) (transformed into SI units):

$$\frac{E_x(z)}{B_y} = -i\frac{k^2c^2\alpha}{\omega}\ln\left(-i\frac{\omega\varepsilon_0}{\sigma_0}\right). \tag{6}$$

Liu and Berkey, (1994) and Yizengaw et al. (2018) used the relationship between ionospheric electric field and magnetic field fluctuations from Hughes, (1974) to estimate the amplitude of the ionospheric electric field fluctuations driven by geomagnetic pulsations. However, the relationships they have used were incorrect choices. Moreover, it is wrong to model ULF pulsations as an E-mode.

The numerically calculated apparent impedances for both electric (E) and magnetic (H) modes (that is, the ratio E (z = 120 km)/B (z = 0) is shown in **Figure 9**. For the H-mode, the ratio E_ρ/B_ρ ~ 0.6 (mV/m)/nT. This value is very close to the theoretical estimate (4) for Σ_H~1.4 S. For the E-mode, the ratio E_ρ/B_ϕ is frequency dependent, slowly decreasing from ~10^2 (V/m)/nT at f ~ 3 mHz to ~10 (V/m)/nT at f ~ 1 Hz. Therefore, the E-mode impedance is at least four to five orders of magnitude larger that the impedance of the H-mode. Interpretation of ULF waves as E-mode would provide unrealistically high magnitudes of the wave electric field in the ionosphere.

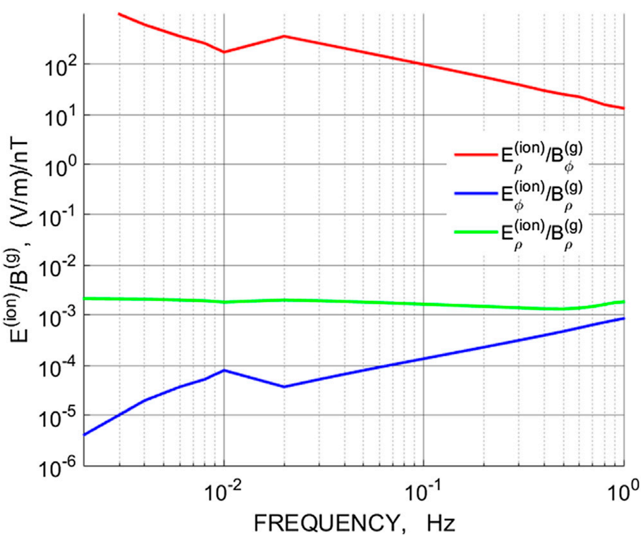

FIGURE 9 | The frequency dependence of the apparent impedances (that is *E* (f)/*B* (f) amplitude ratios) for magnetic and electric modes.

An attempt to compare *Pc1-3* pulsations using the South Pole search-coil magnetometer and balloon E-field data was made by Bering et al. (1998). While magnetic component was clearly observed as narrow-band emissions with power spectral densities (PSDs) $P_f^{(B)}$ ~ 0.1 $(\text{nT})^2$/Hz in *Pc1* band and ~9 $(\text{nT})^2$/Hz in *Pc3* band, the balloon-borne detector observed broadband emission without prominent features in the electric field spectra. During these events, the noise power spectral densities (PSDs) in the *Pc1* and *Pc3* bands were P_f ~ 2 10^3 and ~4 10^2 $(\text{mV/m})^2$/Hz, correspondingly. According to the modeling results, E/B ~ 2 (mV/m)/nT at f = 0.01–0.3 Hz (**Figure 7**), so at balloon heights, the PSD of the electric component could be $P_f^{(E)} = P_f^{(B)}(E/B)^2$ ~0.4 $(\text{mV/m})^2$/Hz in the *Pc1* band and ~30 $(\text{mV/m})^2$/Hz in *Pc3* band. Thus, the PSD of theoretically possible electric components of geomagnetic *Pc1* and *Pc3* pulsations was below the noise level.

DISCUSSION

The conclusion in *Estimate of E_z Perturbations Accompanying Storm Sudden Commencement Events* about the occurrence of large E_z in the ULF electric mode was made earlier in Zybin et al. (1974) from other considerations. The ULF field in the atmosphere can be locally approximated as an inhomogeneous plane wave with a horizontal wave vector **k**. In this approximation, the vertical component E_z in the field of *Pc3-5* pulsations must appear. The expected magnitude of E_z must be coupled with magnetic component magnitude as follows: $E_z = (k/\omega\varepsilon_o)B_\perp$. For the commonly observed horizonal velocity of *Pc3-5* pulsations $\omega/k \sim 20$ km/s, pulsations with a magnetic component amplitude $B_\perp = 1$ nT should be accompanied by disturbances of E_z ~60 V/m. To put it another way, the E_z component in the air can be estimated from the continuity of vertical current at the interface earth's crust—air $E_z^{(air)} = (\sigma_g/\omega\varepsilon_o)E_z^{(ground)}$. According to this estimate, the amplitude components of E_z in the air should be a few tens of V/m according to borehole observations of J_z for $\sigma_g \sim 10^{-4}$ S/m and ω~0.01 s^{-1}.

Our search for an E_z signature in disturbances from magnetospheric sources has given negative results. Even for the most promising source—large-scale intense SSC impulses, observations show that the excitation of the E-mode is negligible. Therefore, the assumption of the directional analysis (Chetaev et al., 1975; Chetaev et al., 1977; Chetaev, 1985) on the occurrence of the E-mode in the incident ULF wave field is not supported by observations. Nonetheless, the mathematical formalism developed in the frameworks of the directional analysis may be applied for MTS in the ELF band (e.g., Schumann resonance).

Our numerical modeling has resulted in a rather paradoxical conclusion. Excitation of the E-mode by magnetospheric sources is very weak, and this mode practically does not contribute into the ULF wave magnetic field. The E-mode contribution into the horizontal telluric field produced by ULF pulsations is also negligible. However, in the atmosphere, at the balloon heights, the electric field of this mode becomes dominant. Thus, an adequate interpretation of coordinated balloon-ground observations of *Pc5* waves and TCVs is possible only with account of multimode structure of ULF disturbance in the atmosphere comprising both H- and E-modes. The important aspect of this problem is the polarization structure of H- and E-modes (Nenovski, 1999). The pertinent theoretical modeling and comparison with data from coordinated balloon-ground observations will be considered elsewhere.

At the same time, periodic fluctuations of the atmospheric electric field E_z in the ULF range that are not associated with geomagnetic disturbances are quite common. These fluctuations may confuse and mislead a researcher upon a search of simultaneous geomagnetic and atmospheric electricity pulsations. Periodic fluctuations of the atmospheric potential gradient and vertical atmospheric current J_z in the range of *Pc4-5* frequencies were observed by Yerg and Johnson, (1974) and in the *Pc1* and *Pc3* bands by Anisimov et al. (1984). These fluctuations were not coherent with geomagnetic pulsations, so authors suggested that they may be caused by nonmagnetospheric sources, e.g., infrasound emissions from distant meteorological sources. *Pc5* pulsations of atmospheric electric field were observed near local midnight under very clear weather by balloon campaign (altitude ~32 km) (Liao et al., 1994). Both transverse and vertical electric field components of pulsations had amplitudes of 20–30 mV/m, but no similar signal was observed in magnetometer or riometer data. Narrow-band wave packets in the *Pc1* band in both horizontal and vertical components of the atmospheric electric field without a ground magnetic response were detected during the 1985–86 South Pole Balloon Campaign (Bering and Benbrook, 1995). The driving mechanisms of such "electrostatic" ULF pulsations are very speculative and have not been established.

The model implicitly assumes that a single cylindrical FAC is spread along the ionosphere out to infinity. In realistic magnetosphere–ionosphere disturbances, coupled incident and return FACs of opposite polarity are formed at various distances from each other, from about ten thousand km in SSC events to few hundred km in TCV or *Pc5* events. If the geometry of the magnetosphere–ionosphere current system is known, the modeled electromagnetic fields due to each isolated FAC are to be summed up.

We have considered a simple geometry with the plane ionosphere and ground and vertical geomagnetic field $\mathbf{B}_0$. This assumption is well justified for the consideration of local structure of electromagnetic disturbance at distances less than 10^3 km from an incident FAC. At larger distances upon propagation to low latitudes, additional factors become noticeable: ionosphere/ground curvature, inclination of geomagnetic field, and lateral inhomogeneity of ionospheric parameters. However, the magnetic field decreases with distance as $\sim r^{-2}$, so at large distances, the response would be too weak to observe. Probably, there is no need to advance theory to interpret very weak signatures at large distances from a source.

CONCLUSION

We have addressed the long-standing problem of coupling between atmospheric electricity and space weather disturbances at ULF time scales (from fractions minutes to tens of mins). The generation of ULF impulses and noises by atmospheric electric discharges is a more or less well-known aspect of the problem (see Pilipenko, 2012). The inverse aspect, the influence of magnetospheric magnetic disturbances on the atmospheric electric field is much less studied.

The GloCAEM atmospheric electricity field-mill measurements with 1 sec cadence have been used to examine the influence of geomagnetic SSC disturbances on atmospheric electricity. The predicted mechanism of SSC transmission by the electric-type TH_0 mode along the earth–ionosphere waveguide was not confirmed. Observations with field-mills and current collectors in Antarctica also have not found any signature of the E-mode accompanying SSC magnetic pulses. Therefore, the model of prompt transmission of disturbances from auroral latitudes to low latitudes by the atmospheric TH_0 mode is not supported by observations and should be rejected.

We have advanced the theory of ULF disturbance transmission though the ionosphere and atmosphere to the ground by considering the possible role of the electric mode. The constructed model of electromagnetic ULF response to an incidence of oscillating magnetospheric field-aligned current onto the realistic ionosphere is based on a numerical solution of the full-wave equations in the atmospheric-ionospheric collisional plasma whose parameters were reconstructed using the IRI model and a realistic vertical profile of atmospheric conductivity. The modeling strictly proved that excitation of the electric mode is weak and its contribution into the field of ULF waves on the ground is very small. In a most favorable situation, only a weak E_z disturbance with a magnitude of ~several V/m could be produced by a large-scale intense (~100 nT) geomagnetic disturbance. At the same time, the predicted amplitudes of electric field at balloon heights, ~few tens of mV/m, induced by *Pc5* pulsations and travelling convection vortices are in good agreement with coordinated balloon—ground magnetometer observations. Therefore, E-mode excitation by magnetospheric ULF disturbances cannot be completely ignored, because an adequate interpretation of balloon observations is possible only on the basis of a model comprising both H- and E-modes.

DATA AVAILABILITY STATEMENT

The datasets presented in this study can be found in online repositories. The names of the repository/repositories and accession number(s) can be found below: http://www.wdcb.ru/arctic_antarctic/antarctic_magn_3.ru.html.

AUTHOR CONTRIBUTIONS

VP performed theoretical analysis, EF did numerical modeling, VM-B analyzed data, and EB provided observational data.

FUNDING

This study was supported by the grants PLR-1744828 (VP) from the U.S. National Science Foundation and 20-05-00787 (EF, VM-B) from the Russian Fund for Basic Research. Details of the GloCAEM project are here https://drive.google.com/open?id=1l7VI98q4FfX5AoOEi5Y_kr-HL-58jp9E.

REFERENCES

Alperovich, L. S., and Fedorov, E. N. (2007). “Hydromagnetic waves in the magnetosphere and the ionosphere,”in *Astrophysics and space science library* (Berlin, Germany: Springer Science & Business Media), Vol. 353, 418.

Anisimov, S. V., Rusakov, N. N., and Troitskaya, V. A. (1984). Short-period variations of the vertical electric current in the air. *J. Geomagn. Geoelectr.* 36, 229–238. doi:10.5636/jgg.36.229

Anisimov, S. V., Kurneva, N. A., and Pilipenko, V. A. (1993). Input of electric mode into the field of *Pc3*-4 pulsations. *Geomagn. Aeron.* 33 (3), 35–41.

Araki, T. (1977). Global structure of geomagnetic sudden commencements, Planet. *Space Sci.* 25, 373–384. doi:10.1016/0032-0633(77)90053-8

Berdichevsky, M. N., Van’jan, L. L., and Dmitriev, V. I. (1971). Concerning the possibility to neglect vertical currents during magnetotelluric sounding. *Izv. AN SSSR, Fizika Zemli, N5*, 69–78.

Bering, E. A., and Benbrook, J. R. (1995). Intense 2.3-Hz electric field pulsations in the stratosphere at high auroral latitude. *J. Geophys. Res. Space Phys.* 100, 7791–7806. doi:10.1029/94JA02680

Bering, E. A., Benbrook, J. R., Howard, J. M., Oró, D. M., Stansbery, E. G., Theall, J. R., et al. (1987). The 1985-86 South Pole balloon campaign. *Memoirs of the National Institute of Polar Research* 48, 313–317.

Bering, E. A., Benbrook, J. R., Byrne, G. J., Liao, B., Theall, J. R., Lanzerotti, L. J., et al. (1988). Impulsive electric and magnetic field perturbations observed over South Pole: flux transfer events? *Geophys. Res. Lett.* 15, 1545–1548. doi:10.1029/GL015i013p01545

Bering, E. A., Lanzerotti, L. J., Benbrook, J. R., Lin, Z.-M., Maclennan, C. G., Wolfe, A., et al. (1990). Solar wind properties observed during high-latitude impulsive perturbation events. *Geophys. Res. Lett.* 17, 579–582. doi:10.1029/GL017i005p00579

Bering, E. A., Benbrook, J. R., Liao, B., Theall, J. R., Lanzerotti, L. J., and MacLennan, C. G. (1995). Balloon measurements above the South pole: study of the ionospheric transmission of ULF waves. *J. Geophys. Res.* 100, 7807–7820. doi:10.1029/94JA02810

Bering, E. A., Benbrook, J. R., Engebretson, M. J., and Arnoldy, R. L. (1998). Simultaneous electric and magnetic field observations of Pc1–2 and Pc3 pulsations. *J. Geophys. Res.: Space Physics* 103, 6741–6761. doi:10.1029/97JA03327

Burns, G. B., Frank-Kamenetsky, A. V., Troshichev, O. A., Bering, E. A., and Papitashvili, V. O. (1998). The geoelectric field: a link between the troposphere and the ionosphere. *Ann. Glaciol.* 27, 651–654. doi:10.3189/1998AoG27-1-651-654

Byrne, G. J., Bering, E. A., Few, A. A., and Morris, G. A. (1991). Measurements of atmospheric conduction currents and electric fields at the South pole. *Antarct. J. U. S.* 26, 291–294.

Chetaev, D. N. (1970). About structure of geomagnetic pulsation field and magnetotelluric soundings. *Solid Earth Phy.* 2, 52–56.

Chetaev, D. N. (1985). *Directional analysis of magnetotelluric observations.* Moscow: Nauka, 228.[in Russian]

Chetaev, D. N., Fedorov, E. N., Krylov, S. M., Lependin, V. P., Morghounov, V. A., Troitskaya, V. A., et al. (1975). On the vertical electric component of the geomagnetic pulsation field. *Planet. Space Sci.* 23, 311–314. doi:10.1016/0032-0633(75)90136-1

Chetaev, D. N., Chernysheva, S. P., Morghounov, V. A., Sheftel, V. A., and Zemliankin, G. A. (1977). On the pulsations of Ez(air) in the frequency range of *Pc1*. *Planet. Space Sci* 26, 507–508. doi:10.1016/0032-0633(78)90071-5

Chi, P. J., Russell, C. T., Raeder, J., Zesta, E., Yumoto, K., Kawano, H., et al. (2001). Propagation of the preliminary reverse impulse of sudden commencements to low latitudes. *J. Geophys. Res.* 106, 18857–18864. doi:10.1029/2001JA900071

Corney, R. G., Burns, G. B., Michael, K., Frank-Kamenetsky, A. V., Troshichev, O. A., Bering, E. A., et al. (2003). The influence of polar-cap convection on the geoelectric field at Vostok, Antarctica. *J. Atmos. Sol. Terr. Phys.* 65, 345–354. doi:10.1016/S1364-6826(02)00225-0

Curto, J. J., Araki, T., and Alberca, L. F. (2007). Evolution of the concept of Sudden storm commencements and their operative identification. *Earth Planets Space* 59, i–xii. doi:10.1186/BF03352059

Dmitriev, V. I. (1970). Impedance of a stratified media for an inhomogeneous plane wave. *Izv. AN SSSR. Fizika Zemli* N7, 63–69.

Fedorov, E. N., Pilipenko, V. A., Engebretson, M. J., and Hartinger, M. D. (2018). Transmission of a magnetospheric *Pc1* wave beam through the ionosphere to the ground. *J. Geophys. Res. B: Space Phys.* 123, 3965–3982. doi:10.1029/2018JA0253381–18

Few, A. A., Morris, G. A., Bering, E. A., Benbrook, J. R., Chadwick, R., and Byrne, G. J. (1992). Surface observations of global atmospheric electric phenomena at Amundsen-Scott South Pole Station. *Antarct. J. U. S.* 27, 307–309.

Frank-Kamenetsky, A. V., Burns, G. B., Troshichev, O. A., Papitashvili, V. O., Bering, E. A., III, and French, W. J. R. (1999). The geoelectric field at Vostok, Antarctica: it’s relation to the interplanetary magnetic field and the polar cap potential difference. *J. Atmos. Sol. Terr. Phys.* 61, 1347–1356. doi:10.1016/S1364-6826(99)00089-9

Hameiri, E., and Kivelson, M. G. (1991). Magnetospheric waves and the atmosphere-ionosphere layer. *J. Geophys. Res.* 96, 21125–21134.

Harrison, R. G., Aplin, K. L., and Rycroft, M. J. (2010). Atmospheric electricity coupling between earthquake regions and the ionosphere. *J. Atmos. Sol. Terr. Phys.* 72, 376–381. doi:10.1016/j.jastp.2009.12.004

Hughes, W. J., and Southwood, D. J. (1976). The screening of micropulsation signals by the atmosphere and ionosphere. *J. Geophys. Res.* 81, 3234–3240. doi:10.1029/JA081i019p03234

Hughes, W. J. (1974). The effect of the atmosphere and ionosphere on long period magnetospheric micropulsations. *Planet. Space Sci* 22, 1157–1172. doi:10.1016/0032-0633(74)90001-4

Kikuchi, T. (1986). Evidence of transmission of polar electric field to the low latitude at times of geomagnetic sudden commencement. *J. Geophys. Res.* 91, 3101–3105. doi:10.1029/JA091iA03p03101

Kikuchi, T. (2014). Transmission line model for the near-instantaneous transmission of the ionospheric electric field and currents to the equator. *J. Geophys. Res.* 119, 1131–1156. doi:10.1002/2013JA019515

Kikuchi, T., and Araki, T. (1979). Transient response of uniform ionosphere and preliminary reverse impulse of geomagnetic storm sudden commencement. *J. Atmos. Terr. Phys.* 41, 917–925. doi:10.1016/0021-9169(79)90093-X

Kikuchi, T., and Hashimoto, K. K. (2016). Transmission of the electric fields to the low latitude ionosphere in the magnetosphere-ionosphere current circuit. *Geoscience Letters* 3, 1–11. doi:10.1186/s40562-016-0035-6

Kleimenova, N. G., Nikiforova, N. N., Kozyreva, O. V., and Michnowsky, S. (1996). Long-period geomagnetic pulsations and fluctuations of the atmospheric electric field intensity at the polar cap latitudes. *Geomagn. Aeron.* 35 (N4), 469–477.

Kokorowski, M., Sample, J. G., Holzworth, R. H., Bering, E. A., Bale, S. D., Blake, J. B., et al. (2006). Rapid fluctuations of stratospheric electric field following a solar energetic particle event. *Geophys. Res. Lett.* 33, L20105. doi:10.1029/2006GL027718

Liao, B., Benbrook, J. R., Bering, E. A., Byrne, G. J., Theall, J. R., Lanzerotti, L. J., et al. (1994). Balloon observations of nightside Pc5 quasi-electrostatic waves above the South Pole. *J. Geophys. Res.: Space Physics* 99, 3879–3891. doi:10.1029/93JA02753

Lin, Z. M., Bering, E. A., Benbrook, J. R., Liao, B., Lanzerotti, L. J., Maclennan, C. G., et al. (1995). Statistical studies of impulsive events at high latitudes. *J. Geophys. Res.: Space Physics* 100, 7553–7566. doi:10.1029/94JA01655

Liu, J. Y., and Berkey, F. T. (1994). Phase relationships between total electron content variations, Doppler velocity oscillations and geomagnetic pulsations. *J. Geophys. Res.* 99, 17539–17545. doi:10.1029/94JA00869

Maclennan, C. G., Lanzerotti, L. J., Hasegawa, A., Bering, E. A., III, Benbrook, J. R., Sheldon, W. R., et al. (1978). On the relationship of ~3 mHz (Pc5) electric, magnetic, and particle variations. *Geophys. Res. Lett.* 5, 403–406. doi:10.1029/GL005i005p00403

Nenovski, P. (1999). Asymmetry in the electric and magnetic field polarization of geomagnetic pulsations. *J. Atmos. Sol. Terr. Phys.* 61, 1007–1015. doi:10.1016/S1364-6826(99)00048-6

Nicoll, K. A., Harrison, R. G., Barta, V., Bor, J., Brugge, R., et al. (2019). Towards a global network for atmospheric electric field monitoring. *J. Atmos. Sol. Terr. Phys.* 184, 18–29. doi:10.1016/j.jastp.2019.01.003

Park, C. G. (1976). Downward mapping of high-latitude ionospheric electric fields to the ground. *J. Geophys. Res.* 81, 168–174. doi:10.1029/JA081i001p00168

Pilipenko, V. A. (2012). Impulsive coupling between the atmosphere and ionosphere/magnetosphere. *Space Sci. Rev.* 168, 533–550. doi:10.1007/s11214-011-9859-8

Pilipenko, V., Vellante, M., Anisimov, S., De Lauretis, M., Fedorov, E., and Villante, U. (1998). Multi-component ground-based observation of ULF waves: goals and methods. *Ann. Geofisc.* 41, 63–77. doi:10.4401/ag-3794

Pilipenko, V., Belakhovsky, V., Kozlovsky, A., Fedorov, E., and Kauristie, K. (2012). Determination of the wave mode contribution into the ULF pulsations from combined radar and magnetometer data: method of apparent impedance. *J. Atmos. Sol. Terr. Phys.* 77, 85–95. doi:10.1016/j.jastp.2011.11.013

Pilipenko, V. A., Bravo, M., Romanova, N. V., Kozyreva, O. V., Samsonov, S. N., and Sakharov, Y. A. (2018). Geomagnetic and ionospheric responses to the interplanetary shock wave of March 17, 2015. *Izvestiya Phys. Solid Earth* 54 (N5), 721–740. doi:10.1134/S1069351318050129

Savin, M. G., Nikiforov, V. M., and Kharakhinov, V. M. (1991). About anomalies of vertical electric component of telluric field at Northern Sakhalin. *Izv. AN SSSR. Fizika Zemli* N2, 100–108.

Vinogradov, I. A. (1960). New experimental data on vertical component of short-period oscillations of telluric current field. *Geol. and Geophys.* B6, 100–105.

Yerg, D. G., and Johnson, K. R. (1974). Short-period fluctuations in the fair-weather electric field. *J. Geophys. Res.* 79, 2177–2184. doi:10.1029/JC079i015p02177

Yizengaw, E., Zesta, E., Moldwin, M. B., Magoun, M., Tripathi, N. K., Surussavadee, C., et al. (2018). ULF wave-associated density irregularities and scintillation at the equator. *Geophys. Res. Lett.* 45, 5290–5298. doi:10.1029/2018GL078163

Yumoto, K., Pilipenko, V., Fedorov, E., Kurneva, N., and De Lauretis, M. (1997). Magnetospheric ULF wave phenomena stimulated by SSC. *J. Geomagn. Geoelectr.* 49, 1179–1195. doi:10.5636/jgg.49.1179

Zybin, K. Yu., Krylov, S. M., Lependin, V. P., Morgunov, V. A., Troitskaya, V. A., and Chetaev, D. N. (1974). About vertical electric component of the geomagnetic pulsation field. *Doklady AN SSSR* 218 (4), 828–829.

Conflict of Interest: The authors declare that the research was conducted in the absence of any commercial or financial relationships that could be construed as a potential conflict of interest.

frontiers
in Earth Science

ORIGINAL RESEARCH
published: 29 January 2021
doi: 10.3389/feart.2020.614639

Measuring Global Signals in the Potential Gradient at High Latitude Sites

José Tacza[1,2]*, *Keri A. Nicoll*[3,4], *Edith L. Macotela*[5,6], *Marek Kubicki*[1], *Anna Odzimek*[1] and *Jyrki Manninen*[7]

[1]*Institute of Geophysics, Polish Academy of Sciences, Warsaw, Poland,* [2]*Center of Radio Astronomy and Astrophysics Mackenzie, Engineering School, Mackenzie Presbyterian University, Sao Paulo, Brazil,* [3]*Department of Meteorology, University of Reading, Reading, United Kingdom,* [4]*Department of Electronic and Electrical Engineering, University of Bath, Bath, United Kingdom,* [5]*Faculty of Mathematics and Natural Sciences, University of Rostock, Rostock, Germany,* [6]*Leibniz-Institute of Atmospheric Physics, University of Rostock, Kuhlungsborn, Germany,* [7]*Sodankyla Geophysical Observatory, University of Oulu, Sodankyla, Finland*

Previous research has shown that the study of the global electrical circuit can be relevant to climate change studies, and this can be done through measurements of the potential gradient near the surface in fair weather conditions. However, potential gradient measurements can be highly variable due to different local effects (e.g., pollution, convective processes). In order to try to minimize these effects, potential gradient measurements can be performed at remote locations where anthropogenic influences are small. In this work we present potential gradient measurements from five stations at high latitudes in the Southern and Northern Hemisphere. This is the first description of new datasets from Halley, Antarctica; and Sodankyla, Finland. The effect of the polar cap ionospheric potential can be significant at some polar stations and detailed analysis performed here demonstrates a negligible effect on the surface potential gradient at Halley and Sodankyla. New criteria for determination of fair weather conditions at snow covered sites is also reported, demonstrating that wind speeds as low as 3 m/s can loft snow particles, and that the fetch of the measurement site is an important factor in determining this threshold wind speed. Daily and seasonal analysis of the potential gradient in fair weather conditions shows great agreement with the “universal” Carnegie curve of the global electric circuit, particularly at Halley. This demonstrates that high latitude sites, at which the magnetic and solar influences can be present, can also provide globally representative measurement sites for study of the global electric circuit.

Keywords: potential gradient, carnegie curve, global electric circuit, polar cap potential, arctic, antarctica

Edited by:
Konstantinos Kourtidis,
Democritus University of Thrace, Greece

Reviewed by:
C. Panneerselvam,
Indian Institute of Geomagnetism (IIG), India
Yoav Yosef Yair,
Interdisciplinary Center Herzliya, Israel

Correspondence:
José Tacza
josect1986@gmail.com

Specialty section:
This article was submitted to Atmospheric Science, a section of the journal Frontiers in Earth Science

Received: *06 October 2020*
Accepted: *23 December 2020*
Published: *29 January 2021*

Citation:
Tacza J, Nicoll KA, Macotela EL, Kubicki M, Odzimek A and Manninen J (2020) Measuring Global Signals in the Potential Gradient at High Latitude Sites.
Front. Earth Sci. 8:614639.
doi: 10.3389/feart.2020.614639

INTRODUCTION

The global electric circuit (GEC) was proposed by Wilson (1921). In this circuit, the Earth is considered as a spherical capacitor where the conducting plates are the Earth’s surface and the electrosphere (see e.g., Haldoupis et al., 2017). Upward flowing electric currents move from the top of thunderstorms (and electrical shower clouds) to the highly conducting ionosphere, and flow back down again in fair weather regions, with a current density of ~2 pA/m^2. These currents flow freely through the Earth’s surface, closing the circuit (Rycroft et al., 2000; Rycroft et al., 2008). Analysis of the GEC behavior is important due to its relationship with several phenomena. In an extensive review, Williams and Mareev (2014) reported several works associated with the GEC, such as the role of lightning as a generator for the circuit, nuclear weapon test effects in the circuit, the impact of the tropical "El Nino Southern Oscillation" on the circuit, influence of aerosol and impact of a gamma ray flare, amongst others. Additionally, Rycroft et al. (2012) reported the influence of space weather on the GEC, arising from the influence of cosmic rays and energetic electrons precipitating from the magnetosphere to the lower atmosphere. Furthermore, the study of the GEC has been suggested as an indicator of global warming (Markson, 1986; Williams, 1992; Price, 1993; Williams, 2009) and its connections to clouds (Tinsley et al., 2007; Nicoll and Harrison, 2016).

The above-mentioned effects motivates the continuous monitoring of the GEC, and this can be indirectly performed through atmospheric electric field (or potential gradient, PG[1]) measurements in fair weather regions. In order to identify a global effect of the GEC on the PG measurements, a comparison can be made with the "universal" Carnegie curve, which is the average daily variation in PG in fair weather conditions[2] (Harrison, 2013; Tacza et al., 2020). It was obtained from the hourly average of PG measurements made over the world's ocean and represents the global daily contribution of the electrical activity in disturbed regions (Whipple, 1929; Peterson et al., 2017). However, PG measurements on the ground are highly variable due to different local factors, such as pollution (Harrison and Aplin, 2002; Silva et al., 2014), precipitation, convective processes in the planetary boundary layer (Anisimov et al., 2018), and changes in ionisation rate from the ambient radioactivity of the Earth's surface (Barbosa, 2020). Some of these local effects can be reduced by making PG measurements at high latitudes, where the measurement sites are far from large human populations, and the low surface temperatures, and lack of daylight conditions during certain months, inhibit daytime convection.

Early daily PG measurements performed at high latitudes (Arctic and Antarctic) contributed to the discovery of the diurnal universal variation of the potential gradient in universal Time, later adopted in the form of the Carnegie curve when it had been established (Odzimek, 2019). For example, Simpson (1905) performed PG measurements at Karasjok, Norway (69.1°N) and found a typical daily variation. The shape of this curve was very similar to the Carnegie curve but a proper comparison was not possible because at this time the Carnegie curve had not yet been discovered. Fisk and Fleming (1928) reported a good similarity with the Carnegie curve for PG measurements at Arctic stations located between 70° and 80°N. For PG measurements in the Antarctic, Park (1976a) reported a great similarity in the daily variation of PG for Vostok station (78°S) for the period March-November of 1974. In the same way, Cobb (1977) reported a great similarity with the Carnegie curve for air-earth current density and PG daily variation for the Amundsen-Scott station (90°S) for the period November 1972 through March 1974. Additionally, early comparison studies showed similarities between PG measurements performed in the Arctic and Antarctic. Simpson (1919) reported a great agreement in phase for PG daily values measured at Karasjok station (69.1°N, performed between 1903–1904) compared with Cape Evans station (77.6°S, performed between 1910–1913). In the same way, Kasemir (1972) found a very similar shape of the air-Earth current daily curve recorded in Thule, Greenland (78°N, performed between 1958 and 1959) compared with the PG daily curve recorded in Amundsen-Scott station (90°S, performed in 1964). He reported a great agreement in shape for both stations compared with the Carnegie curve but with a difference in the relative amplitude. More recently, in Antarctica, Burns et al. (2017) found a great agreement in the PG daily variation between Vostok and Concordia (75.1°S, 123°E) stations (distance between stations is 560 km).

PG measurements recorded at high latitudes must be approached with caution due to the fact that the ionosphere is not an equipotential in these regions. This occurs due to the additional influence of the interaction of the solar wind with the Earth's magnetic field, which generates a potential difference across the polar cap (Park, 1976b) and, therefore, influences PG measurement on the ground. There have been several models to describe this potential difference at high latitude (Hairston and Heelis, 1990; Papitashvili et al., 1994; Papitashvili et al., 1995; Weimer, 1995; Weimer, 2005). Tinsley et al. (1998) investigated the influence of the magnetosphere-ionosphere coupling processes on PG for the South Pole station using the Hairston-Heelis model and found a positive correlation for 27 days between 1982 through 1986. Frank-Kamenetsky et al. (1999) found a similar influence using the Papitashvili model for Vostok station for 115 days during 1979–1980. Corney et al. (2003) analyzed the effect of the cross-polar-cap potential difference above PG recorded at Vostok station using the models of Papitashvili and Weimer. The authors found a better representation using the Weimer model for 134 fair weather days during 1998. Furthermore, Burns et al. (2005) reported an excellent agreement in shape and the relative amplitude between the daily variation in PG recorded at Vostok station and the Carnegie curve after removing the polar-cap potential difference (using the Weimer model) for a five year interval (1998–2002).

In addition to the influence of the cross-polar-cap potential difference on PG measurements, the effect of local meteorological influences must also be taken into account. Measurements in the early 1990s by Burns et al. (1995) reported the influence of high wind speed and relative humidity on PG values at Davis station (68.6°S, 78°E). There was however good agreement between the Davis PG daily mean curve and the Carnegie curve, when the wind speed and the relative humidity were low (~3 m/s and 45%, respectively). Burns et al. (2012) found global signatures in the daily and seasonal variation in PG at Vostok when meteorological disturbances related to temperature and wind speed effects were removed. Furthermore, PG measurements were performed at Maitri station (70.76°S, 11.74°E), reported by Jeeva et al. (2016), who found that local katabatic winds could also produce substantial local effects on PG.

This paper presents the first detailed analysis of two new high latitude PG datasets, made in opposite hemispheres—Sodankyla

---

[1] Potential gradient = −Ez (where Ez is the vertical electric field).

[2] Fair weather conditions are those in which there is absence of hydrometeors, aerosol and haze, negligible cumuliform cloud and not extensive stratus cloud with cloud base below 1.5 km, and surface wind speed between 1 and 8 m/s (Harrison and Nicoll, 2018).

TABLE 1 | Details of the high latitude stations and instrumentation used to measure PG.

Site	Coordinates	Electric field mill	Height above surface (m)	Data duration	Site type	Range setting (V/m)	Measurement frequency (s)
Halley, Antarctica (HAL)	75°34′ S 25°30′ W MLAT 62.3°S	JCI 131	3	Feb 2015–Jan 2017	Ice sheet snow cover all year	±1,200	1
Sodankyla, Finland (SOD)	67° 22′ N 26° 38′ E MLAT 64.1°N	Campbell CS110	3	June 2017–present	Forest, snow cover from Oct to May	±20,000	1
Arctowski, Antarctica (ARC)	62° 09′ S 58° 25′ W MLAT 51°S	Rotating dipole field-mill Berlinski et al., (2007)	2	Jan 2014–Dec 2015	Snow cover from mid-March to Nov	±1,500	1
Hornsund, Norway (HOR)	77° N 15° 32′ E MLAT 74.0°N	Rotating dipole field-mill Berlinski et al., (2007)	2.5	Jan 2018–Dec 2019	Surroundings covered with rich vegetation tundra	±10,000	1
Vostok, Antarctica (VOS)	78° 30′ S 107° E MLAT 83.6°S	Rotating dipole field-mill Burns et al., (2017)	3	Jan 2006–Dec 2008	Snow cover all year	±2,500	10

in the Arctic, and Halley in the Antarctic. These new datasets are compared with existing datasets in high latitude regions to evaluate whether the sites are globally representative and suitable for studying the thunderstorm generator of the GEC. *High Latitude Datasets* describes the details of the datasets and their locations. *Summary of PG Data from New Sites and Fair Weather Definitions* presents a summary of the data from the new sites at Halley and Sodankyla. *Ionospheric Potential Contributions* evaluates the influence of the polar cap potential difference at each station. In *Diurnal Variations* and *Spectral Analysis*, a temporal and spectral analysis is performed for Halley and Sodankyla stations, respectively. *Global Electric Circuit Representation* analyses how globally representative each of the sites is, and *Conclusions* are presented in the last section.

HIGH LATITUDE DATASETS

This paper presents two new PG datasets made at high latitudes (Sodankyla, Finland; and Halley, Antarctica), and compares them with data from three other high latitude stations previously reported in the literature [Arctowski, Antarctica (Kubicki et al., 2016); Hornsund, Norway (Kubicki et al., 2016); Vostok, Antarctica (Burns et al., 2013)]. The PG data discussed here is all measured using electric field mills, mounted on cylindrical metal masts at 2–3 m above the surface. PG measurements were not calibrated for the form factor associated with the mounting of the field mill, thus, the PG values are relative, not absolute values. **Table 1** describes the electric field mill setup at each of the locations discussed, as well as the duration of each of the PG datasets (which range from 2006 to present). The surface cover of the sites varies from continuous snow cover at all times (Halley and Vostok), to the forest location of Sodankyla, where snow is only present for half of the year.

Figure 1A shows a map of the measurement sites discussed in this paper, demonstrating the high latitude nature of the locations. Examples of the electric field mill sensors used to make the PG measurements are shown in **Figures 1B,C** for Halley and Sodankyla stations, respectively.

Details of the various sites are now discussed, with a particular focus on Halley and Sodankyla, as these are not discussed elsewhere in the literature. The British Antarctic Survey Research station Halley VI (75°34′S, 25°30′W) is located on the Brunt Ice Shelf, in Antarctica, approximately 50 km from the coast. Halley is snow covered all year round, with a temperature range from −56° to +1°C, and annual snowfall of approximately 1.2 m. From January 2015 to January 2017 a JCI 131 electric field mill was installed on a 3 m mast approximately 1 km to the south west of the main station buildings. The only structure within 300 m of the field mill was a metal staging caboose (10 × 5 × 8 m high and 30 m from the field mill), which provided shelter for a logging PC and mains power infrastructure. The range of operation of the field mill was restricted to ±1200 V/m to focus on the fair weather range. A full array of meteorological sensors (including temperature, wind, RH, pressure, visibility, ceilometer, solar radiation) were operated at the main research base, ~1 km from the field mill.

The Sodankyla Geophysical Observatory (67° 22′N, 26° 38′E) is located in northern Finland, within the Arctic circle. The site is in a remote area within a forest, with the town of Sodankyla (population 9,000) being the only inhabited area at about 7 km from the observatory. The lack of human activity in the surrounding area means that sources of man-made pollution at Sodankyla are very low. Temperatures range from −32°C during winter (with snow cover from October to May) to +32°C in summer. A Campbell Scientific CS110 electric field mill was installed on a 3 m mast within a 50 m clearing in the forest from June 2017 to present. A full array of meteorological sensors (including temperature, wind, RH, pressure, visibility, ceilometer, solar radiation) are operated in the meteorological enclosure (near the sounding station), 350 m from the field mill.

A detailed description of site locations for Vostok, Hornsund and Arctowski stations are described in previous works, therefore we only provide a brief description here. Vostok station (78° 30′S,

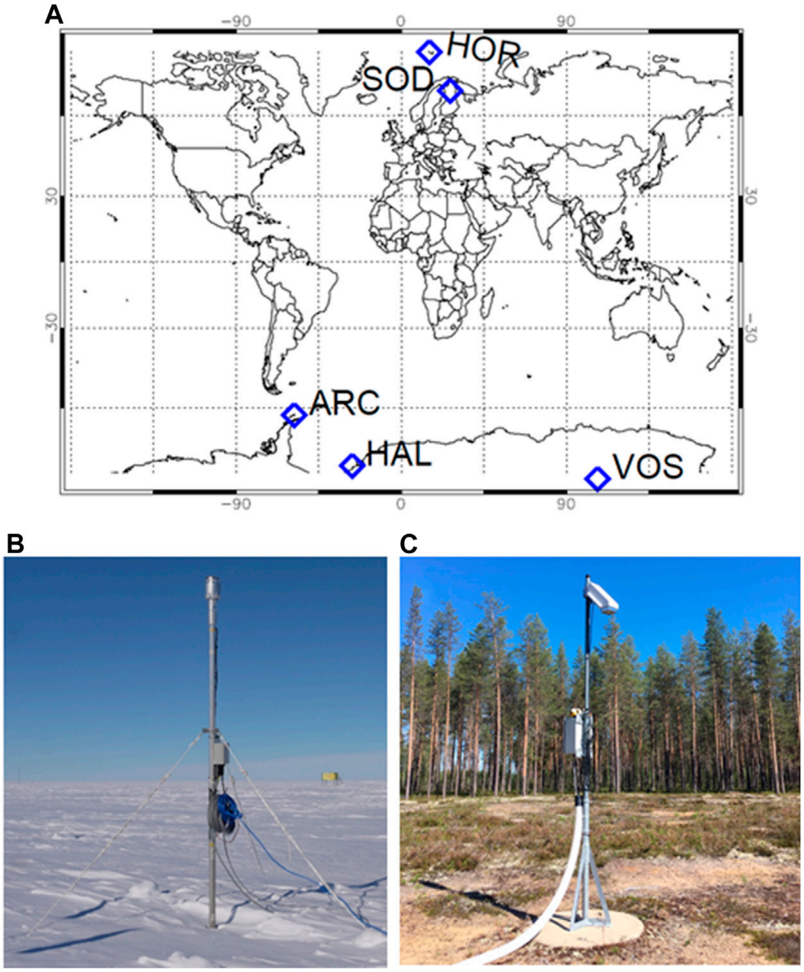

FIGURE 1 | (A) Map showing location of high latitude measurement sites described in the paper (denoted by blue diamonds). HOR, Hornsund, SOD, Sodankyla Geophysical Observatory, ARC, Arctowski, HAL, Halley, VOS, Vostok. Photo showing electric field mill at **(B)** Halley, and **(C)** Sodankyla.

107°E) is located on the Antarctic plateau, at a height of 3,489 m above sea level (Burns et al., 2005). Hornsund station (77°N, 15° 32′E) is located in the Svalbard archipelago in Norway. It is surrounded by tundra vegetation (Kubicki et al., 2016). Arctowski station (62° 09′S, 58° 25′W) is located in the Southern Shetland Islands, on King George Island. The weather conditions are modulated by the maritime climate zone of the Antarctic (Kubicki et al., 2016).

SUMMARY OF PG DATA FROM NEW SITES AND FAIR WEATHER DEFINITIONS

Figure 2 shows the time series of PG hourly measurements for Sodankyla (SOD, **Figure 2A**) and Halley (HAL, **Figure 2C**) stations. Additionally, the distribution of PG hourly values for both stations is shown in **Figures 2B,D** for Sodankyla and Halley, respectively. The median PG values are similar between the two sites (SOD = 69 V/m and HAL = 67 V/m), however, the PG variability is very different. This difference in variability is associated with the different meteorological conditions at each site. At Sodankyla, the highest variability is during spring and summer months, when liquid precipitation is common, causing large negative spikes in PG. During the winter, precipitation is mostly snowfall, which tends to produce mainly positive spikes in PG, hence the variability is smallest during these months. At Halley, the variability is quite different, with no obvious seasonal dependence. The extremely low temperatures at Halley all year round mean that there is very little (if any) liquid precipitation, only snowfall, hence the lack of negative spikes in PG at Halley. The few negative PG values here are likely related to blowing snow events. The source of the high variability in PG at Halley is mostly due to high wind speeds and freezing fog events.

In order to study GEC signals, it is first necessary to remove any unwanted local effects, such as from meteorological influences, so that only "fair weather" conditions are studied. Although publications exist in the literature regarding the typical definition of fair weather conditions, (e.g., Harrison and Nicoll,

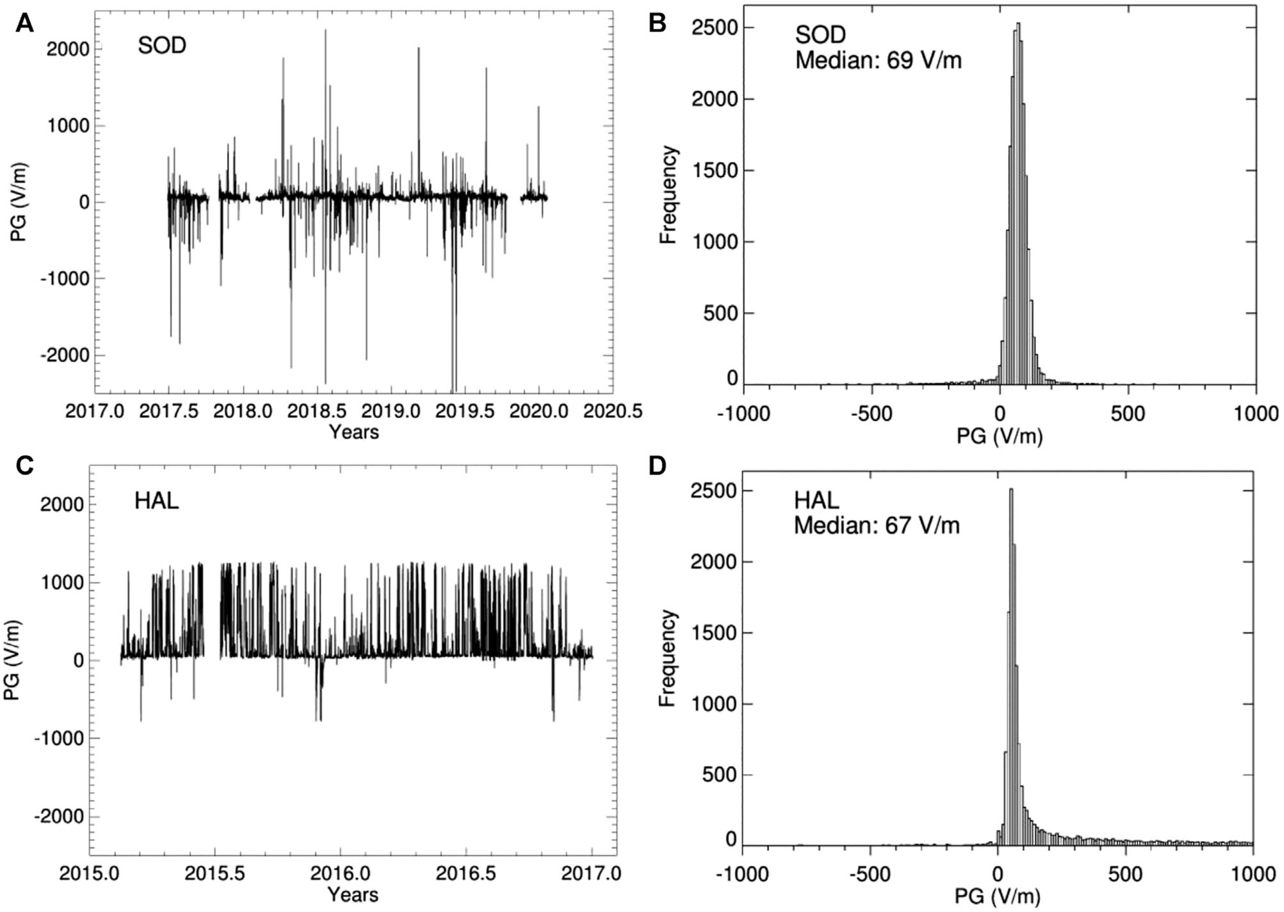

FIGURE 2 | Times series of PG for **(A)** Sodankyla, SOD, and **(C)** Halley, HAL, stations. PG histogram for **(B)** SOD and **(D)** HAL stations, for hourly mean values and plotted within a range of ±1000 V/m.

2018) these are generally only for measurement sites where suspended material (such as dust or snow) is unlikely. The criteria specified in Harrison and Nicoll (2018) for fair weather is as follows: absence of hydrometeors, aerosol and haze (with visibility >2 km), negligible cumuliform cloud and no extensive stratus cloud with cloud base below 1,500 m, and surface wind speed between 1 and 8 m/s. Here we briefly examine whether these visibility and wind speed definitions of fair weather are applicable to sites with considerable snow cover, which is typically the case at high latitude sites. Previous research (eg, Simpson, 1921; Currie and Pearce, 1949) has demonstrated that blowing snow particles can become highly charged, thought to be from tribolelectrification and contact charging. Observations have demonstrated that larger particles charge positively and smaller ones negatively (Latham and Stow, 1965), and the movement of these oppositely charged particles can give rise to large PGs of order kV/m.

It is generally accepted (as is the case for sand and dust), that there is a threshold value of wind speed above which snow particles become lifted (e.g., Bagnold, 1941). This is a function of how tightly bonded to the surface the snow particles are, and can depend on snow surface temperature, age of snow, length of duration of high wind speed before the wind event, and many other factors (Li and Pomeroy, 1997). The variability associated with defining a threshold wind speed for blowing snow is demonstrated by Burns et al. (1995) who observed an erratic relationship between PG and wind speed at Davis, Antarctica, where the threshold wind speed value varied between 2 and 14 m/s during individual blowing snow events, and was found to depend on near surface relative humidity (RH). Other values quoted in the literature include 6 m/s for Hornsund and Arctowski (Kubicki et al., 2016), and 10 m/s for Maitri (Panneerselvam et al., 2007). To examine the threshold wind speed for Halley, **Figure 3A** shows PG plotted against wind speed for 10 min average data for the entire duration of the dataset (31 months). A clear relationship exists between positive values of PG and wind speed for wind speeds above ~3 m/s, where the PG increases approximately linearly as wind speed increases. The PG is primarily positive until the wind speed reaches 5 m/s, when negative values also start to occur. At wind speeds lower than 3 m/s, the PG is typically <300 V/m, indicating mostly fair weather values. The cluster of large PG values at very low wind speeds (<1 m/s) is likely to be indicative of fog conditions. It should be noted that the maximum range of the field mill at

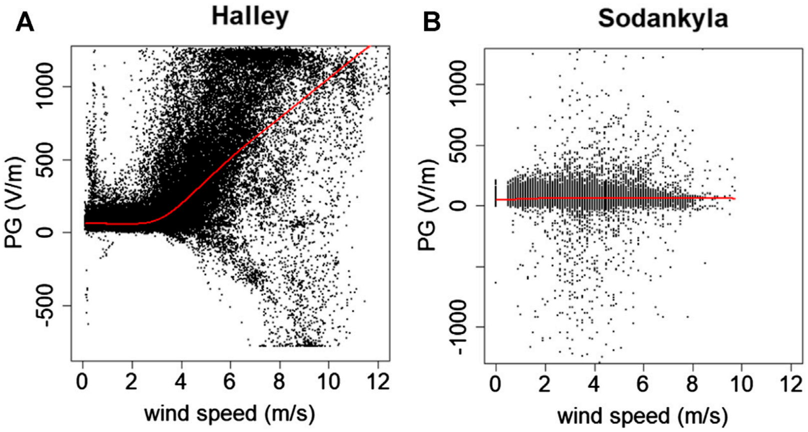

FIGURE 3 | Relationship between PG and wind speed at **(A)** Halley, for the entire duration of the data set, and at **(B)** Sodankyla when snow depth was >2 cm. Each point is a 10 min average value and the red line represents a lowess fit to the data.

Halley was only ± 1200 V/m, therefore it is very likely that much larger values of PG existed, but were not measured. **Figure 3B** shows a similar analysis for Sodankyla during months when snow was present on the ground (defined here as snow depth > 2 cm). Very different behavior is apparent, with no clear relationship between PG and wind speed, other than the PG values are mostly fair weather values at wind speeds <2 m/s. The difference in behavior between the two sites is likely related to the fetch of the sites (i.e., the distance upstream of a measurement site that is relatively uniform). At Sodankyla the fetch is small due to the forest location and presence of trees, limiting the transport of snow when it is lofted, whereas Halley is a completely open site, on a smooth, uniform ice sheet, with a long undisturbed fetch. We therefore conclude that the threshold wind speed for blowing snow electrification effects on PG is very much site dependent. At snow covered sites where there is a long fetch, blowing snow has a significant impact on PG, which is likely to start at wind speeds as low as ~3 m/s.

The second fair weather criterion which warrants detailed investigation at high latitude sites is visibility. PG is incredibly sensitive to the presence of aerosol particles or droplets in the air, which generally act to decrease the conductivity. Under conditions of constant vertical conduction current, this leads to an increase in PG, through Ohm's law. Visibility measurements provide a simple way to detect the presence of such particles by optical means, and can be made automatically using a transmissometer or present weather sensor. Harrison and Nicoll (2018) define fair weather as conditions of "no aerosol or haze, with visibility >2 km". The 2 km visibility comes from theoretical considerations (Harrison, 2012) which suggest that when aerosol particles are present in low concentration there are large visibilities and little effect on the ambient PG.

Figure 4A shows the relationship between PG and visibility measured at Halley for the entire dataset, which demonstrates that there are obvious clusters of data points in certain areas of the plot. **Figure 4B** demonstrates that the reason for the clustering in **Figure 4A**, is that the relationship between PG and visibility is highly dependent on the wind speed, where **Figure 4B** classifies the data according to low (<2 m/s, gray), medium (between 2 and 7 m/s, blue) and high (>7 m/s, red) wind speeds. From **Figure 4B**, the red points demonstrate that the highest wind speeds produce the lowest visibility values, and largest magnitude of PG values (including both positive and negative polarities), which are likely to be associated with blowing snow events and snow storms. Low wind speeds (gray points) tend to produce a narrow distribution of PG values, generally between 0–300 V/m (i.e., fair weather values), particularly for visibility >40 km, therefore a combination of wind speed and visibility measurements can assist in the determination of electrically quiescent conditions in snow covered environments. At Halley we therefore use the combination of wind speed <5 m/s (which is increased from the very strict threshold value of 3 m/s to allow more possible PG values), and visibility >40 km to define fair weather periods. The fair weather criteria implemented at each of the other high latitude sites discussed in this paper, as well as the number of fair weather days produced using these criteria is summarised in **Table 2**. At Sodankyla, the visibility is much more dependent on weather conditions rather than wind speed, so we use the more "traditional" fair weather criteria of cloud cover amount <3/8, wind speed 1 > 6 m/s, no rain precipitation, and visibility range >40 km. For Hornsund and Arctowski stations, fair weather days were chosen with low cloudiness (<4/8), no rain precipitation, drizzle, snow, hail, fog, and wind speed less than 6 m/s (as stated in Kubicki et al., 2016). On the other hand, for Vostok station, where the meteorological data is not easily available, we base our criteria for fair weather days only on the hourly PG variation, which should be between 0–300 V/m. For Hornsund, Arctowski and Vostok, a fair weather day consists of all 24 h PG values meeting the fair weather criteria; whilst for Halley and Sodankyla, at least 20 h must satisfy the criteria. The location of these high latitude sites also means that there is a possibility of unwanted solar effects on the fair weather PG days, therefore we exclude fair weather days where the geomagnetic Kp index was ≥5.

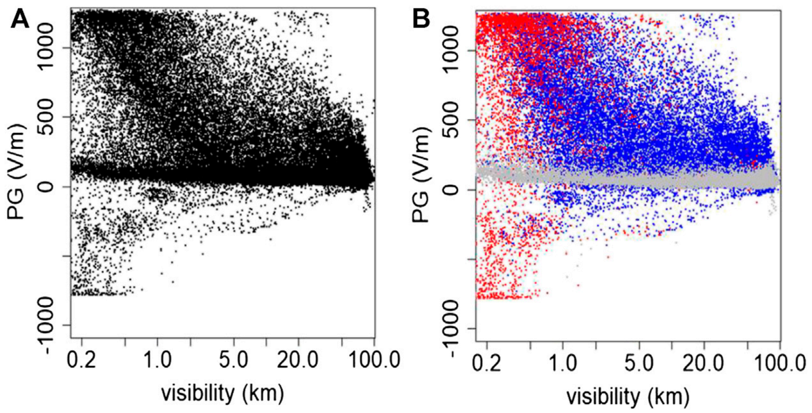

FIGURE 4 | (A) Relationship between PG and visibility at Halley **(B)** colored according to high wind speed conditions (red, wind speed >7 m/s), medium wind speed (blue, wind speed between 2 and 7 m/s), and low wind speed conditions (gray, wind speed <2 m/s). Each point is a 10 min average value.

TABLE 2 | Summary of criteria used to define fair weather conditions at each of the high latitude sites, and the total number of days on which fair weather was detected. Days on which the geomagnetic Kp index was ≥5 were excluded.

Location	Wind speed (m/s)	Cloud cover (oktas)	Visibility (km)	Precipitation	PG range (V/m)	Total number fair weather days (Kp < 5)	Dataset duration (months)
Halley	<5	NA	>30	NA	NA	83	24
Sodankyla	1 > 6	<3/8	>40	None	NA	116	32
Hornsund	<6	<4/8	No fog	None	NA	14	24
Arctowski	<6	<4/8	No fog	None	NA	11	24
Vostok	NA	NA	NA	NA	0–300	340	36

IONOSPHERIC POTENTIAL CONTRIBUTIONS

PG measurements performed at high latitudes (above 60° magnetic latitude) are influenced by the cross-polar-cap potential difference (Park, 1976b; Burns et al., 2012). When looking at diurnal variations in PG, this manifests itself as a superimposed signal on top of the expected Carnegie diurnal variation, and can be removed by careful analysis. From **Table 1**, all stations analyzed in this work are above 60° magnetic latitude (except Arctowski station), therefore, if GEC signals are to be considered, it is important to calculate the influence of the polar cap for each site. Following the results from Corney et al. (2003) and Burns et al. (2005), here we use the Weimer model to estimate the cross-polar-cap potential difference. The Weimer model derives the cross-polar-cap potential difference from the combination of the interplanetary magnetic field magnitude (B_z and B_y), solar wind velocity, proton number density and dipole tilt angle (Weimer, 1996; Weimer, 2005). **Figure 5** shows the potential difference above Vostok (VOS), Halley (HAL), Hornsund (HOR), and Sodankyla (SOD) stations calculated using the Weimer model (Weimer, 2019). The solid black line represents the mean daily variation and the points are the individual daily hours. The data period used was according to the availability of the PG data (eg, for Halley station the data period was between January 2015 and December 2016). **Figure 5** demonstrates that there is a significant effect of the cross-polar-cap potential difference above Vostok (MLAT: 83.6°S) and Hornsund (MLAT: 74°N) stations. There is a variation of 0 to −15 kV above Vostok station with a minimum peak at

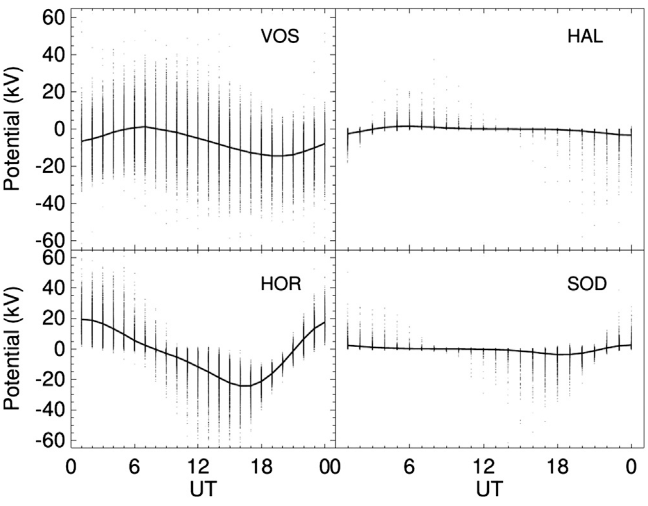

FIGURE 5 | Weimer model predictions of the high-latitude electric potentials for VOS (MLAT: 83.6°S; period: 2006–2008), HAL (MLAT: 62.3°S; period: 2015–2016), HOR (MLAT: 74.0°N; period: 2017–2019) and SOD (MLAT: 64.1°N; period: 2017–2019). The points are the individual hours and the solid line is the average value.

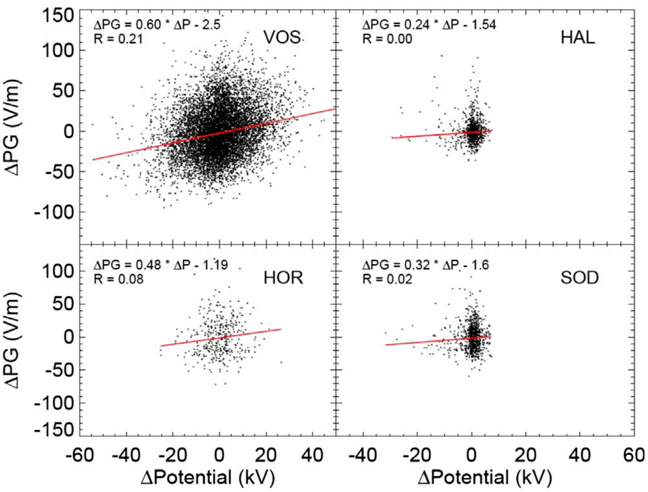

FIGURE 6 | Linear regression analysis of the variation from the mean of the vertical electrical field values and the Weimer model inferred cross polar cap potential difference above VOS, HAL, HOR, and SOD. Here, R indicates the Pearson correlation coefficient.

19–20 UT. This is in agreement with previous results (Corney et al., 2003; Burns et al., 2005). For Hornsund station, there is a mean daily variation of about ±20 kV where the maximum peak is about 23–02 UT and the minimum peak around 16–17 UT. For the lower magnetic latitude stations of Halley (MLAT: 62.3°S) and Sodankyla (MLAT: 64.1°N) stations, there is much less of an effect of the cross-polar cap potential. For Halley station there is a potential difference in the mean average of less than ±5 kV between 1–4 UT and between 20–24 UT. For the rest of the day, this value is almost zero. In the same way, for Sodankyla station a variation of less than ±5 kV is observed between 16–24 UT. For other hours the values are almost zero.

To examine what magnitude of effect the cross-polar-cap potential difference has on the measured PG values at the surface, the methodology described by Burns et al. (2005) is employed. First, the average diurnal variation must be removed from the PG, and ionospheric potential values separately. This is done as follows: $\Delta PG = PG(h) - PG_{mean}(h)$; and $\Delta Potential = Potential(h) - Potential_{mean}(h)$. PG (h) and Potential (h) are the hourly averaged PG and the potential difference, respectively, and $PG_{mean}(h)$ and $Potential_{mean}(h)$ are the monthly averages for each hour. For Hornsund station, the annual averages were used instead of the monthly averages, due to too few fair weather days to calculate the monthly averages (see **Table 2**). Following this process, linear regressions were calculated between ΔPG and ΔPotential to determine how closely linked the two variables were. For Vostok and Hornsund stations, all 24 hourly values were used. However, for Halley and Sodankyla stations we consider only 1–4 and 20–24 UT and 15–24 UT, respectively, since **Figure 5** indicates a relationship between ΔPG and ΔPotential for only those certain hours of the day. The results are shown in **Figure 6** for each station. The scatter in the plots could be associated with the hour to hour variability in the global electric circuit and/or movement of space charge influencing the surface electric conductivity (and therefore the ΔPG), which should not be correlated with the ionospheric potential (ΔPotential). Thus, we observe very low correlation coefficients. A similar effect is mentioned in more detail in Burns et al. (2005).

The ratios of ΔPG/ΔPotential for each of the sites are presented in **Table 3**, and range from 0.24 ± 0.13 V/m per kV for Halley, to 0.60 ± 0.03 V/m per kV for Vostok. Note that the ratio increases as the magnetic latitude of each station increases, as expected due to the influence of the interplanetary magnetic field and the solar wind (important parameters for the Weimer model) that is larger at higher magnetic latitudes. The above calculated ratios from **Figure 6** can now be applied to the expected variation in ΔPotential shown in **Figure 5**, to give final estimates of the effect of the cross-polar-cap potential on the surface PG at the various sites. Applying the maximum calculated variation in ΔPotential of ± 5 kV (from **Figure 5**) expected at Halley, produces only a very small variation in surface PG of 1.2 V/m. For a similar ΔPotential of ± 5 kV at Sodankyla, this produces a variation of 1.6 V/m. This is comparable to the error in the electric field mill measurements (which is typically ± 1 V/m), and therefore we conclude that on average, cross-polar-cap potential effects are negligible at Halley and Sodankyla. It is noted that the linear fit applied in **Figure 6** is not particularly valid for Halley or Sodankyla, but it is included here to demonstrate that there is little effect of ΔPotential on ΔPG. In contrast to the small effects observed at Halley and Sodankyla, for Hornsund and Vostok stations, a potential difference of ~20 kV should produce a variation of 9.6 and 12 V/m, respectively. These are an order of magnitude larger than those values at lower magnetic latitude stations and approximately 3% of the mean value of PG at Hornsund, and 6% at Vostok. Therefore cross-polar-cap potential effects should be taken into account when analyzing GEC signals at Hornsund and Vostok locations. It should be noted that the analysis performed here is only representative of the average magnetic field conditions. During periods of high magnetic activity there may well be noticeable effects of ΔPotential on the surface PG at Halley and Sodankyla, but this analysis of such effects is out with the scope of the present paper.

DIURNAL VARIATIONS

Once the effect of local meteorological influences and ionospheric potential changes has been taken into account it then becomes possible to examine global signals in surface PG data. **Figure 7** shows the mean diurnal variation in PG during fair weather at Halley and Sodankyla, separated according to season of the year. At both sites, the characteristic "Carnegie" curve, which represents the total global electrically active generators of the GEC, is apparent, with a minimum in the early morning hours (~03 UT), and maximum in the evening (~20 UT). At Sodankyla, **Figure 7A**, there is a second morning peak around 09 UT during the summer and autumn months. This is consistent with other sites [e g., Mitzpe Ramon, Israel (Yaniv et al., 2016); Reading, United Kingdom (Nicoll et al., 2019)], which display a second

TABLE 3 | Summary of effect of cross-polar-cap potential differences at various high latitude sites.

Location	Magnetic latitude (degrees)	Typical change in potential (ΔPotential) (kV)	Ratio of ΔPG/ΔPotential (V/m per kV)	Contribution to surface PG (V/m)
Halley	62.3 S	5	0.24 ± 0.13	1.2
Sodankyla	64.1 N	5	0.32 ± 0.16	1.6
Hornsund	74.0 N	20	0.48 ± 0.24	9.6
Vostok	83.6 S	20	0.60 ± 0.03	12.0

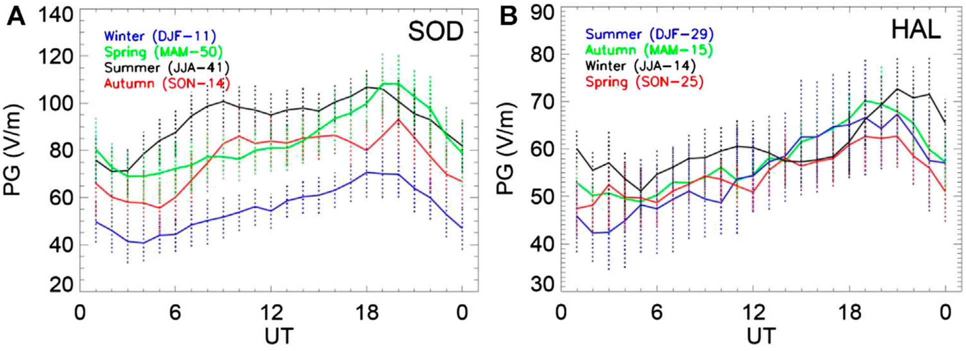

FIGURE 7 | Mean diurnal variation in PG for fair weather conditions as a function of season for **(A)** SOD and **(B)** HAL stations. The error bars are one standard deviation, and the legend gives the months as well as the number of points included for each season of the year.

morning peak during the convectively active months. The more quiescent meteorological conditions during the winter months (particularly during the polar night) results in a more regular diurnal variation in PG, and the disappearance of the morning maximum peak. At Halley, **Figure 7B**, there is no morning peak during any of the seasons.

At Halley, the average magnitude of the PG variation is similar during all seasons, but markedly lower at Sodankyla during the winter months compared to summer. This seasonal cycle in PG at Sodankyla can also be observed in the time series of PG measurements in **Figure 8A**. The winter minimum in PG at Sodankyla is likely to be a combination of two factors which can influence the near surface air conductivity, and thus the PG—a minimum in aerosol concentration, and maximum in radon concentration during the winter months. The existence of a seasonal cycle in aerosol at Sodankyla is evidenced by measurements of the columnar property of Aerosol Optical Depth (AOD). Although the AOD is very low at Sodankyla (typically <0.1 at 500 nm, meaning that this an effectively "clean" site), the AOD does minimize during the winter months, and maximize in the summer (Toledano et al., 2012). This seasonality is also observed in surface measurements of aerosol particle concentration from the relatively nearby site at Pallas, Finland, where in spring and summer the daily averages can exceed over 3,000 cm^{-3}, but in winter the daily averages decrease to 100 cm^{-3} (Hattaka et al., 2003). The higher aerosol concentrations in the summer months may act to decrease the conductivity, and increase the PG. At Halley, there is also a seasonal cycle in aerosol, which maximizes during the summer months, but even during this maximum period, aerosol concentrations are extremely low (121–179 cm^{-3} during the year 2015) (Lachlan-Cope et al., 2020), and therefore unlikely to have any noticeable effect on the conductivity and PG. The second factor contributing to lower PG values at Sodankyla in the winter months is the increased ionisation due to a seasonal variation in radon concentration. Radon emission depends on properties of the soil (such as temperature, moisture content), as well as meteorological variables controlling mixing processes in the boundary layer (e.g., Singh et al., 1988). Surface measurements of radon concentration from Pallas (Hattaka et al., 2003) demonstrate that radon emission maximizes in November and December, primarily due to stable boundary layer conditions. As the snow depth increases in late winter/early spring, this decreases the radon exhalation rate. The minimum in radon occurs during the summer months when convective mixing is active. We therefore conclude that the combination of low aerosol concentration, and increased ionisation from the high radon concentrations is therefore likely to reduce the PG at Sodankyla during the winter months. It therefore follows that, of the two new high latitude sites presented here, Halley provides more consistently globally representative PG data for GEC studies.

SPECTRAL ANALYSIS

In order to determine whether any regular short term oscillations are present in the new datasets from Halley and Sodankyla, spectral analysis methods are now employed. Wavelet analysis is one of the tools used to retrieve from a time series both the

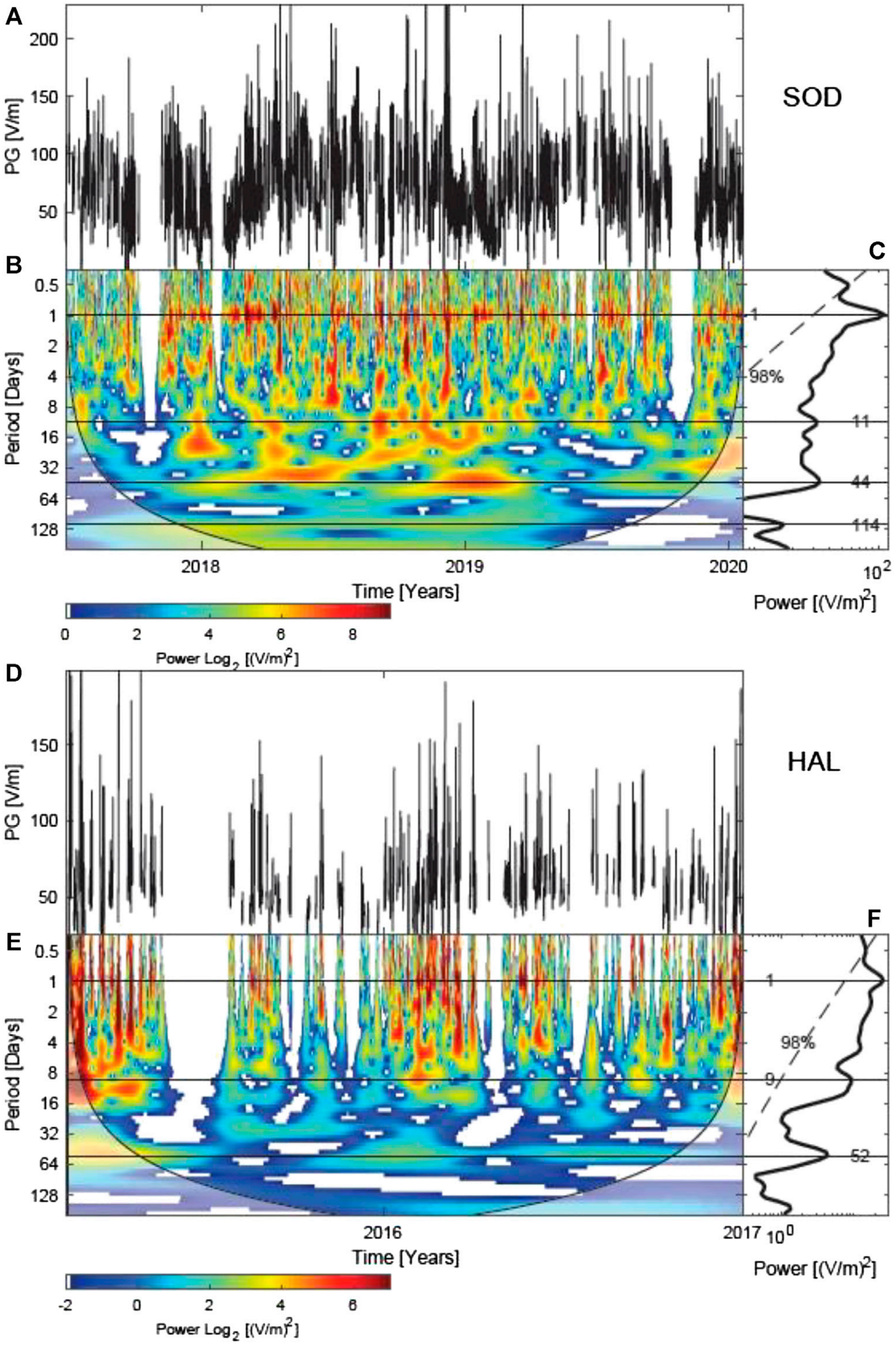

FIGURE 8 | Wavelet analysis for SOD and HAL stations. **(A,D)** Hourly average of the PG amplitude. Gaps are missing data. **(B,E)** Contours in the time–period domain of the real part of the wavelet power spectra of PG. The contour colors indicate the minimum and maximum magnitude, from blue to red, of the matches between the phases of the time series and the wavelet. The white shadowed lateral edges are values within the cone of influence. **(C,F)** The global wavelet power spectrum. The horizontal lines indicate the most significant oscillations and the dashed curve is the 98% confidence.

dominant modes and how those modes vary in time (Torrence and Compo, 1998). This study employs the continuous wavelet transform toolbox for MATLAB package (Grinsted et al., 2004), together with a Morlet mother function with frequency $w_0 = 6$ and a number of voices per power of two equal to 8. **Figure 8** shows the wavelet analysis for Sodankyla (A, B, C) and Halley (D, E, F) using PG hourly amplitudes for their entire dataset duration. **Figures 8A,D** show the time series, where data gaps correspond to periods of no power supply or when there are no fair weather days. To apply the wavelet analysis, constant time steps between samples is required. Such gaps were filled using the moving average of the original time series with a time window length of 3,072 h for both Sodankyla and Halley. This procedure minimizes the introduction of artifacts in the wavelet analysis (Macotela et al., 2019).

Figures 8B,E show the continuous wavelet power spectra corrected by their scales. This correction is employed to rectify the wavelet spectrum, which is biased in favor of larger periods (Liu et al., 2007). The contours represent the magnitude of the matches between the phases of the time series and the wavelet. The color bar indicates the amplitude of those contours that changes from blue to red. The black curves are the cone of influence. The values below this curve must be evaluated with caution. **Figures 8C,F** show the global wavelet power spectra for Sodankyla and Halley, respectively. The dashed line is their 98% confidence level for a white noise background level. Powers above this line are regarded as significant, whose maxima are indicated by horizontal lines.

Figure 8 shows that the significant oscillations are 1-, 9–11-, 44–52-, and 114-days oscillations. In this study we concentrate on the common periods found for Sodankyla and Halley. Thus, we disregard the 114-day period since it was only observed for Sodankyla, and the resolution at this timescale is low due to the short length of the datasets. The 1-day oscillation can be interpreted as the diurnal Carnegie oscillation and is the most significant oscillation in both time series (**Figures 8C,F**). This oscillation is much better observed in the periodogram for Sodankyla (**Figure 8B**), where it is clearest during the winter months. This observation is consistent with **Figure 7A**, which demonstrates that the strongest link with the single peak Carnegie curve is during the winter season.

In order to confirm our findings, we also performed the Lomb-Scargle periodogram, which allows the analysis of a time series with irregular time steps between samples. **Figure 9** shows the Lomb-Scargle periodogram of PG hourly values for Sodankyla (black dotted curve) and Halley (red continuous curve) with normalized power with respect to its value for the 1-day period. The 98% confidence levels are indicated by the red and black horizontal lines for Halley and Sodankyla, respectively. The most significant oscillations found by the wavelet analysis are also indicated by the blue and magenta vertical lines. The 0.5- and 1-day periods are significant in both time series in **Figure 9**, despite the 0.5 day period not being significant in the wavelet analysis at Halley. This 0.5-day periodicity in PG has been observed at other, more populated mid latitude sites (e.g., Silva et al., 2014), and is generally attributed to diurnal changes in boundary layer conditions, coupled with variations in local sources of pollution (such as traffic), which is more likely to be the case at Sodankyla than Halley.

The 1-day period is the well-known diurnal oscillation and its observation is expected. The 9–11 and 44–52-days oscillations are not well reported in the literature in PG, if at all. Bennett (2007) reports an 11-day periodicity in PG, air-Earth conduction current (Jc) and near surface conductivity at Reading, United Kingdom, from 14 months of data during 2006–2007, but does not conclude the origin of the periodicity. However, detailed spectral analysis of PG data from Argentina (Tacza et al., 2021) and Portugal (Silva et al., 2014), do not find evidence of these additional periodicities. To further test whether such periodicities are more common at high latitude sites, wavelet analysis was also performed on the PG data from Vostok station (figure not shown here), and 10- and 48-days oscillations were observed, as for Halley and Sodankyla.

It is likely that the sources of the 9–11- and 44–52-days oscillations are related to either local meteorological influences, or variations in ionisation rates [either from oscillations in radon concentration, or Galactic Cosmic Rays (GCRs)]. As there is effectively no radon emission at Halley (as the site location is on a ~1 km thick ice sheet), this is an unlikely explanation for the observed periodicities. We therefore investigate whether a relationship in the time-period domain exists between the PG and local meteorological measurements (for SOD), as indicated by Macotela et al. (2019). This involves employing the wavelet coherence and cross-wavelet transform. The wavelet coherence is used to measure the degree of local correlation of two series in the time-period domain, while the cross-wavelet transform is employed to find regions in the time-period domain where two time series show common power. The meteorological measurements used included temperature, relative humidity, horizontal visibility, wind direction, and wind speed. Results indicated that, as expected, horizontal visibility, wind direction and wind speed are related to the PG variability, but it is unclear what the source of such periodicities in meteorological phenomenon is. The remaining possibility which may explain the 9–11 days periodicity in PG is a solar influence. 9-day periodicities have been reported in a variety of solar parameters, including the Interplanetary Magnetic Field (IMF), solar wind speed, and also neutron monitors which detect the nucleonic component of Galactic Cosmic Rays (GCRs) (Singh et al., 2012). The 9-days oscillation is a harmonic of the 27-days solar rotation periodicity (Sabbah and Kudela, 2011). The existence of a 9-day periodicity in PG at Halley, Sodankyla and Vostok may therefore also demonstrate the suitability of high latitude sites for studying solar influences on the GEC, but further work on the source of this periodicity is required. This will be examined more closely in a further publication.

GLOBAL ELECTRIC CIRCUIT REPRESENTATION

Figure 10 shows the average diurnal variation in fair weather PG measured by the Carnegie research ship (plotted as a percentage of the mean) and the fair weather PG data from the five high

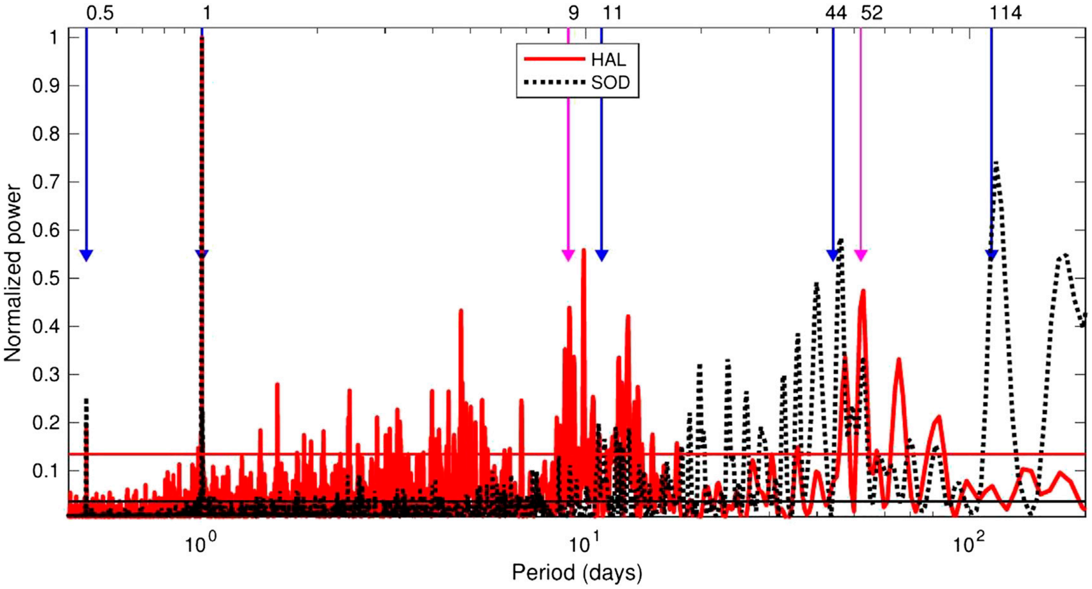

FIGURE 9 | Normalized Lomb-Scargle periodogram of PG hourly values for SOD (black dotted curve) and HAL (red continuous curve) stations. The black and red horizontal lines are the 98% significant levels, and the blue and magenta vertical lines are the significant oscillations found by the wavelet analysis for SOD and HAL, respectively. For the 0.5- and 1-day periods the blue and magenta curve are superposed.

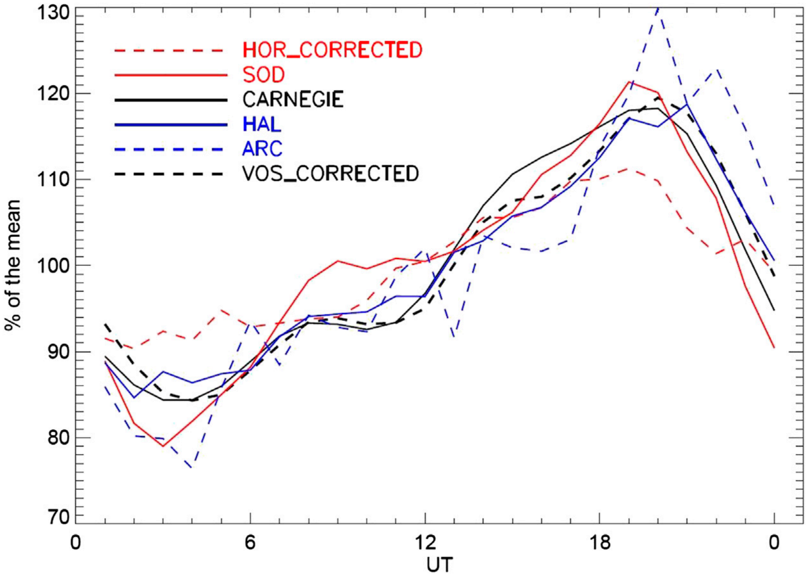

FIGURE 10 | Comparison of the PG annual daily variation, in fair weather conditions, between Sodankyla, SOD (red solid line), Hornsund, HOR (red dashed line), Halley, HAL (blue solid line), Arctowski, ARC (blue dashed line), Vostok, VOS (black dashed line) and the Carnegie curve, plotted as percent of the mean. The influence of the cross polar cap potential has been removed for Vostok and Hornsund stations in accordance with the methodology in *Ionospheric Potential Contributions*.

latitude sites discussed in this paper, in order to investigate their suitability for GEC analysis. According to the discussion in *Ionospheric Potential Contributions*, polar cap contributions to the ionospheric potential have been removed from the data at Vostok and Hornsund, but not from Sodankyla, Halley or Arctowski. **Figure 10** shows remarkably good agreement between the benchmark of the Carnegie data and most of the high latitude sites in terms of their percentage variations. At Hornsund the peak to peak variation is considerably smaller than at the other sites, but at Vostok (as reported by Burns et al., 2012) and Halley, it is almost identical to the Carnegie variation. This is in contrast to many mid latitude sites which often exhibit a much smaller variation around the time of the primary maximum, and also have secondary maxima related to local aerosol effects (e.g., Yaniv et al., 2016; Nicoll et al., 2019). The timing of the minima of the curves are all similar (to within an hour of 3 UT), with a slight difference in the timings of the maxima of the curves. At the two northern hemisphere sites of Sodankyla and Hornsund, the maxima is approximately 1 h earlier than the Carnegie maximum (at 20 UT), but similar at Vostok and Halley. This may be related to the geographical position of the sites in relation to the location of most of the thunderstorm generators, with the Antarctic sites being closest to the South American generator.

In terms of the suitability of the various high latitude sites for GEC studies, from those summarised here, the Antarctic sites of Vostok (as previously reported in the literature in various papers by Burns et al.), and Halley are sufficiently unaffected by aerosol sources, and possess a reasonably high proportion of fair weather days to be best suited to GEC research. The influence of the cross-polar-cap potential does affect the PG measurements at Vostok, however, and must be removed, unlike at Halley. The low number of fair weather days at Arctowski on the far northern tip of the Antarctic Peninsula, makes it difficult to assess the suitability of this site, hence further measurements are required. For the Arctic sites, Sodankyla provides a good proportion of fair weather days, but is still subject to local meteorological influences during the spring and summer months. Winter periods do, however, provide good agreement with the GEC oscillation. Finally, Hornsund, with its low number of fair weather days (max. 15–20% in year), and influence of the cross polar cap potential suggests that this is not the easiest of sites to obtain PG measurements for studying global thunderstorm activity, but GEC measurements are possible on individual days.

CONCLUSION

This paper presents the first analysis of PG data from two new high latitude sites at opposite ends of the Earth - Sodankyla in the Arctic, and Halley in the Antarctic. These new datasets are compared with other existing PG datasets from high latitudes in order to assess their suitability for Global Electric Circuit (GEC) measurements. Detailed analysis of meteorological data at Halley demonstrates the usefulness of visibility data for determination of fair weather conditions at snow covered sites, which is required to indicate globally representative data. A clear relationship between PG and wind speed at Halley is also demonstrated, which shows that snow can be lofted at wind speeds as low as 3 m/s, but also, for the first time, that the threshold wind speed for blowing snow effects on the PG is dependent on the fetch of the measurement site. Spectral analysis of the PG demonstrates 1 day, as well as 9–11 days and 44–52 day periodicities at both sites. Although the 1 day periodicity is expected, the others are less understood, and may be related to variations in local meteorological influences or solar parameters. The influence of cross-polar-cap variations in ionospheric potential is also investigated, and found to be negligible at the two new measurement sites. Comparison of the diurnal variations in PG data from Sodankyla and Halley, with the universal Carnegie curve of the GEC, shows good agreement in terms of the peak to peak oscillations, and timings of the minima and maxima of the curves. Sodankyla displays a secondary morning peak during the summer months, likely related to convective activity, but is in close agreement with the Carnegie GEC variation during the winter months. Comparison of the new data PG from Sodankyla and Halley with other existing high latitude PG datasets from Hornsund (Arctic), Arctowski (Antarctic), and Vostok (Antarctic), confirms the suitability of the continental Antarctic sites, in particular, for GEC measurements. Despite the difficulties associated with maintaining instrumentation in such harsh climatic conditions, the lack of aerosol contamination, and relatively high proportion of fair weather days means that of the high latitude stations studied here, Halley and Vostok provide the most suitable sites for GEC analysis.

DATA AVAILABILITY STATEMENT

Sodankyla PG data are available from KN (k.a.nicoll@reading.ac.uk) at the University of Reading on request. Halley PG data is available from the GloCAEM database hosted by CEDA: http://data.ceda.ac.uk/badc/glocaem/data/halley. Sodankyla meteorological data is available from the LITB database, of the Finnish Meteorological Institute (https://litdb.fmi.fi/). Vostok PG data is available from: Burns et al. (2013). Hornsund and Arctowski PG data are available on request from MK at Swider Geophysical Observatory (swider@igf.edu.pl). Weimer 2005 ionospheric electric potential model was provided by D. Weimer and is available at https://zenodo.org/record/2530324. Solar wind data were obtained from the National Space Science Data Center OMNIWeb database (https://omniweb.gsfc.nasa.gov/form/dx1.html).

AUTHOR CONTRIBUTIONS

JT and KN contributed to the study designing, data processing, data analysis, data interpreting, and manuscript writing. EM contributed to the spectral analysis and manuscript writing. MK, AO, and JM contributed to the data curation, data processing and data analysis. All authors contributed to the manuscript revision and approved the submitted version.

FUNDING

KN acknowledges an Independent Research Fellowship funded by the Natural Environment Research Council NERC (NE/L011514/1) and (NE/L011514/2). The Halley PG data was obtained in collaboration with the British Antarctic Survey (with thanks to David Maxfield and Mervyn Freeman) through a NERC Collaborative Gearing Scheme grant, and archived through the GloCAEM project (NERC International Opportunities Fund grant NE/N013689/1). Ilya Usoskin from the University of Oulu, Thomas Ulich and his technical team at Sodankyla Geophysical Observatory were instrumental in obtaining the Sodankyla PG measurements. JT acknowledges the Polish National Agency for

Academic Exchange for funding of the Ulam Program scholarship agreement no PPN/ULM/2019/1/00328/U/00001. Observations at Polish Polar Station Hornsund were supported by SPUB grants from Ministry of Science and Higher Education of Poland. The observations at Arctowski Antarctic station of the Institute of Biochemistry and Biophysics, Polish Academy of Sciences, have been financed by National Science Centre grant number NCN-2011/01/B/ST10/07118 (2011–2014) awarded to the Institute of Geophysics, Polish Academy of Sciences.

ACKNOWLEDGMENTS

JT thanks the Arctic Interactions research profile action of the University of Oulu for making possible his visit to the Sodankyla Geophysical Observatory. Work of MK and AO is financed by Institute of Geophysics, Polish Academy of Sciences, with a subsidy from Poland Ministry of Science and Higher Education (now Ministry of Education and Science). The authors thank the reviewers for their constructive comments and suggestions, which helped to improve the quality of the paper.

REFERENCES

Anisimov, S. V., Galichenko, S. V., Aphinogenov, K. V., and Prokhorchuk, A. A. (2018). Evaluation of the atmospheric boundary-layer electrical variability. *Boundary-Layer Meteorol.* 167 (2), 327–348.

Bagnold, R. A. (1941). Electrification of wind-blown sand: recent advances and key issues. *Eur. Phys. J. E Soft Matter.* 36 (12), 1–15. doi:10.1140/epje/i2013-13138-4

Barbosa, S. (2020). Ambient radioactivity and atmospheric electric field: a joint study in an urban environment. *J. Environ. Radioact.* 219, 106283. doi:10.1016/j.jenvrad.2020.106283

Bennett, A. (2007). Measurement of atmospheric electricity during different meteorological conditions. PhD thesis. Reading, UK: University of Reading.

Berlinski, J., Pankanin, G., and Kubicki, M. (2007). "Large scale monitoring of troposphere electric field," in Proceedings of the 13th International Conference on Atmospheric Electricity, Beijing, China, August 13–18, 2007 (Beijing: International Conference on Atmospheric Electricity), 124–126.

Burns, G. B., Hesse, M. H., Parcell, S. K., Malachowski, S., and Cole, K. D. (1995). The geoelectric field at Davis station, Antarctica. *J. Atmos. Sol. Terr. Phys.* 57 (14), 1783–1797. doi:10.1016/0021-9169(95)00098-m

Burns, G. B., Frank-Kamenetski, A. V., Troshichev, O. A., Bering, E. A., and Redell, B. D. (2005). Interannual consistency of bi-monthly differences in diurnal variations of the ground-level, vertical electric field. *J. Geophys. Res.* 110 (D10), 106. doi:10.1029/2004jd005469

Burns, G. B., Tinsley, B. A., Frank-Kamenetski, A. V., Troshichev, O. A., French, W. J. R., and Klekociuk, A. R. (2012). Monthly diurnal global atmospheric circuit estimates derived from Vostok electric field measurements adjusted for local meteorological and solar wind influences. *J. Atmos. Sci.* 69 (6), 2061–2082. doi:10.1175/jas-d-11-0212.1

Burns, G., Tinsley, B., Frank-Kamenetsky, A. V., Troshichev, O., and Bering, E. A. (2013). Vertical Electric Field—Vostok from 2006–2011. Canberra, ACT: Australian Antarctic Data Centre (Accessed September 7 2020). doi:10.4225/15/58880fc1a1fbd

Burns, G. B., Frank-Kamenetski, A. V., Tinsley, B. A., French, W. J. R., Grigioni, P., Camporeale, G., et al. (2017). Atmospheric global circuit variations from vostok and concordia electric field measurements. *J. Atmos. Sci.* 74 (3), 783–800. doi:10.1175/jas-d-16-0159.1

Cobb, W. E. (1977). "Atmospheric electric measurements at the south Pole," in *Electrical Processes in Atmospheres*. Editors H. Dolezalek and R. Reiter (Darmstadt, Germany: Steinkopf), 161–167.

Corney, R. C., Burns, G. B., Michael, K., Frank-Kamenetsky, A. V., Troshichev, O. A., Bering, E. A., et al. (2003). The influence of polar-cap convection on the geoelectric field at Vostok, Antarctica. *J. Atmos. Sol. Terr. Phys.* 65 (3), 345–354. doi:10.1016/s1364-6826(02)00225-0

Currie, B. W., and Pearce, D. C. (1949). Some qualitative results on the electrification of snow. *Can. J. Res.* 27 (1), 1–8. doi:10.1139/cjr49a-001

Fisk, H. W., and Fleming, J. A. (1928). The magnetic and electric observations of the maud expedition during 1918 to 1925. *Terr. Magnetism Atmos. Electr.* 33 (1), 37–43. doi:10.1029/te033i001p00037

Frank-Kamenetsky, A. V., Burns, G. B., Troshichev, O. A., Papitashvili, V. O., Bering, E. A., and French, W. J. R. (1999). The geoelectric field at Vostok, Antarctica: its relation to the interplanetary magnetic field and the cross polar cap potential difference. *J. Atmos. Sol. Terr. Phys.* 61 (18), 1347–1356. doi:10.1016/s1364-6826(99)00089-9

Grinsted, A., Moore, J. C., and Jevrejeva, S. (2004). Application of the cross wavelet transform and wavelet coherence to geophysical time series. *Nonlinear Process. Geophys.* 11 (5–6), 561–566. doi:10.5194/npg-11-561-2004

Hairston, M. R., and Heelis, R. A. (1990). Model of the high latitude ionospheric convection pattern during southward interplanetary magnetic field using DE-2 data. *J. Geophys. Res.* 95 (A3), 2333–2343. doi:10.1029/ja095ia03p02333

Haldoupis, C., Rycroft, M., Williams, E., and Price, C. (2017). Is the "earth-ionosphere capacitor" a valid component in the atmospheric electric circuit?. *J. Atmos. Sol. Terr. Phys.* 164, 127–131. doi:10.1016/j.jastp.2017.08.012

Harrison, R. G. (2012). Aerosol-induced correlation between visibility and atmospheric electricity. *J. Aerosol Sci.* 52, 121–126. doi:10.1016/j.jaerosci.2012.04.011

Harrison, R. G., and Aplin, K. L. (2002). Mid-nineteenth century smoke concentrations near London. *Atmos. Env.* 36, 4037–4043.

Harrison, R. G., and Nicoll, K. A. (2018). Fair weather criteria for atmospheric electricity measurements. *J. Atmos. Sol. Terr. Phys.* 179, 239–250. doi:10.1016/j.jastp.2018.07.008

Harrison, R. G. (2013). The Carnegie curve. *Surv. Geophys.* 34 (2), 209–232. doi:10.1007/s10712-012-9210-2

Hatakka, J., Aalto, T., Aaltonen, V., Aurela, M., Hakola, H., Komppula, M., et al. (2003). Overview of the atmospheric research activities and results at Pallas GAW station. *Boreal Environ. Res.* 8 (4), 365–384

Jeeva, K., Gurubaran, S., Williams, E. R., Kamra, A. K., Sinha, A. K., Guha, A., et al. (2016). Anomalous diurnal variation of atmospheric potential gradient and air-earth current density observed at Maitri, Antarctica. *J. Geophys. Res. Atmos.* 121 (21), 12593–12611. doi:10.1002/2016jd025043

Kasemir, H. W. (1972). Atmospheric electric measurements in the Arctic and the Antarctic. *Pure Appl. Geophys.* 100 (1), 70–80. doi:10.1007/bf00880228

Kubicki, M., Odzimek, A., and Neska, M. (2016). Relationship of ground-level aerosol concentration and atmospheric electric field at three observation sites in the Arctic, Antarctic and Europe. *Atmos. Res.* 178–179, 329–346. doi:10.1016/j.atmosres.2016.03.029

Lachlan-Cope, T., Beddows, D. C., Brough, N., Jones, A. E., Harrison, R. M., Lupi, A., et al. (2020). On the annual variability of Antarctic aerosol size distributions at Halley research station. *Atmos. Chem. Phys.* 20 (7), 4461–4476. doi:10.5194/acp-20-4461-2020

Latham, J., and Stow, C. D. (1965). The electrification of blowing snow. *J. Meteorol. Soc. Jpn.* 43 (1), 23–29.

Li, L., and Pomeroy, J. W. (1997). Probability of occurrence of blowing snow. *J. Geophys. Res. Space Phys.* 102 (D18), 21955–21964. doi:10.1029/97jd01522

Liu, Y., San Liang, X., and Weisberg, R. H. (2007). Rectification of the bias in the wavelet power spectrum. *J. Atmos. Ocean. Technol.* 24 (12), 2093–2102. doi:10.1175/2007jtecho511.1

Macotela, E. L., Clilverd, M., Manninen, J., Moffat-Griffin, T., Newnham, D. A., Raita, T., et al. (2019). D-region high-latitude forcing factors. *J. Geophys. Res. Space Phys.* 124 (1), 765–781. doi:10.1029/2018ja026049

Markson, R. (1986). Tropical convection, ionospheric potentials and global circuit variation. *Nature* 320 (6063), 588–594. doi:10.1038/320588a0

Nicoll, K. A., Harrison, R. G., Barta, V., Bor, J., Brugge, R., Chillingarian, A., et al. (2019). A global atmospheric electricity monitoring network for climate and geophysical research. *J. Atmos. Sol. Terr. Phys.* 184, 18–29. doi:10.1016/j.jastp.2019.01.003

Nicoll, K. A., and Harrison, R. G. (2016). Stratiform cloud electrification: comparison of theory with multiple in-cloud measurements. *Q. J. R. Meteorol. Soc.* 142 (700), 2679–2691. doi:10.1002/qj.2858

Odzimek, A. (2019). Polar regions in the global atmospheric electric circuit research, English translation of Obszary polarne w badaniach globalnego atmosferycznego obwodu elektrycznego Ziemi. *Przeglad Geofiz.* 64 (1–2), 35–72. doi:10.32045/PG-2019-002

Panneerselvam, C., Selvaraj, C., Jeeva, K., Nair, K. U., Anilkumar, C. P., and Gurubaran, S. (2007). Fairweather atmospheric electricity at Antarctica during local summer as observed from Indian station, Maitri. *J. Earth Syst. Sci.* 116 (3), 179–186. doi:10.1007/s12040-007-0018-2

Papitashvili, V. O., Belov, B. A., Faermark, D. S., Feldstein, Y. I., Golyshev, S. A., Gromova, L. I., et al. (1994). Electric potential patterns in the northern and southern polar regions parameterized by the interplanetary magnetic field. *J. Geophys. Res.* 99 (A7), 13251–13262. doi:10.1029/94ja00822

Papitashvili, V. O., Clauer, C. R., Levitin, A. R., and Belov, B. A. (1995). Relationship between the observed and modeled modulation of the dayside ionospheric convection by the IMF by component. *J. Geophys. Res.* 100 (A5), 7715–7722. doi:10.1029/94ja01344

Park, C. G. (1976a). Solar magnetic sector effects on the vertical atmospheric electric field at Vostok, Antarctica. *Geophys. Res. Lett.* 3 (8), 475–478. doi:10.1029/gl003i008p00475

Park, C. G. (1976b). Downward mapping of high-latitude ionospheric electric fields to the ground. *J. Geophys. Res.* 81 (1), 168–174. doi:10.1029/ja081i001p00168

Peterson, M., Deierling, W., Liu, C., Mach, D., and Kalb, C. (2017). A TRMM/GPM retrieval of the total generator current for the global electric circuit. *J. Geophys. Res.: Atmosphere.* 122 (18), 10025–10049. doi:10.1002/2016jd026336

Price, C. (1993). Global surface temperatures and the atmospheric electric circuit. *Geophys. Res. Lett.* 20 (13), 1363–1366. doi:10.1029/93gl01774

Rycroft, M. J., Israelsson, S., and Price, C. (2000). The global atmospheric electric circuit, solar activity and climate change. *J. Atmos. Sol. Terr. Phys.* 62 (17–18), 1563–1576. doi:10.1016/s1364-6826(00)00112-7

Rycroft, M. J., Harrison, R. G., Nicoll, K. A., and Mareev, E. A. (2008). An overview of Earth's global electric circuit and atmospheric conductivity. *Space Sci. Rev.* 137 (1–4), 83–105. doi:10.1007/s11214-008-9368-6

Rycroft, M. J., Nicoll, K. A., Aplin, K. L., and Harrison, R. G. (2012). Recent advances in global electric circuit between the space environment and the troposphere. *J. Atmos. Sol. Terr. Phys.* 90–91, 198–211. doi:10.1016/j.jastp.2012.03.015

Sabbah, I., and Kudela, K. (2011). Third harmonic of the 27 day periodicity of galactic cosmic rays: coupling with interplanetary parameters. *J. Geophys. Res. Space Phys.* 116 (A4), A04103. doi:10.1029/2010ja015922

Silva, H. G., Conceição, R., Melgão, M., Nicoll, K., Mendes, P. B., Tlemçani, M., et al. (2014). Atmospheric electric field measurements in urban environment and the pollutant aerosol weekly dependence. *Environ. Res. Lett.* 9, 114025.

Simpson, G. C. (1905). Atmospheric electricity in high latitudes. *Proc. R. Soc. A.* 76 (508), 61–97. doi:10.1098/rspa.1905.0014

Simpson, G. C. (1919). *British antarctic expedition, 1910–1913: Meteorology*. (Calcutta, India: Thacker, Spink and Co.), Vol. 1.

Simpson, G. C. (1921). "Atmospheric electricity," in *British antarctic exp. 1910–1913*. (London, United Kingdom: Har-rison and Sons), Vol. 1

Singh, M., Ramola, R. C., Singh, S., and Virk, H. S. (1988). The influence of meteorological parameters on soil gas radon. *J. Assoc. Explor. Geophys.* 9, 85–90.

Singh, Y. P., and Gautam, S. (2012). Temporal variations of short-and mid-term periodicities in solar wind parameters and cosmic ray intensity. *J. Atmos. Sol. Terr. Phys.* 89, 48–53. doi:10.1016/j.jastp.2012.07.011

Tacza, J., Raulin, J.-P., Macotela, E., Marun, A., Fernandez, G., Bertoni, F., et al. (2020). Local and global effects on the diurnal variation of the atmospheric electric field in South America by comparison with the carnegie curve. *Atmos. Res.* 240, 104938. doi:10.1016/j.atmosres.2020.104938

Tacza, J., Raulin, J.-P., Morales, C. A., Macotela, E., Marun, A., and Fernandez, G. (2021). Analysis of long-term potential gradient variations measured in the argentinian andes. *Atmos. Res.* 248, 105200. doi:10.1016/j.atmosres.2020.105200

Tinsley, B. A., Burns, G. B., and Zhou, L. (2007). The role of the global electric circuit in solar and internal forcing of clouds and climate. *Adv. Space Res.* 40 (7), 1126–1139. doi:10.1016/j.asr.2007.01.071

Tinsley, B. A., Liu, W., Rohrbaugh, R. P., and Kirkland, M. W. (1998). South pole electric field responses to overhead ionospheric convection. *J. Geophys. Res.* 103 (D20), 26137–26146. doi:10.1029/98jd02646

Toledano, C., Cachorro, V. E., Gausa, M., Stebel, K., Aaltonen, V., Berjón, A., et al. (2012). Overview of sun photometer measurements of aerosol properties in Scandinavia and Svalbard. *Atmos. Environ.* 52, 18–28. doi:10.1016/j.atmosenv.2011.10.022

Torrence, C., and Compo, G. (1998). A practical guide to wavelet analysis. *Bull. Am. Meteorol. Soc.* 79 (1), 61–78. doi:10.1175/1520-0477(1998)079<0061:apgtwa>2.0.co;2

Weimer, D. R. (1995). Models of high-latitude electric potentials derived with a least error fit of spherical harmonic coefficients. *J. Geophys. Res.* 100, 19595–19607.

Weimer, D. R. (1996). A flexible, IMF dependent model of high-latitude electric potentials having "space weather" applications. *Geophys. Res. Lett.* 23 (18), 2549–2552. doi:10.1029/96gl02255

Weimer, D. R. (2005). Improved ionospheric electrodynamic models and application to calculating Joule heating rates. *J. Geophys. Res.* 110 (A5), 306. doi:10.1029/2004ja010884

Weimer, D. R. (2019). Weimer 2005 ionospheric electric potential model for IDL (Version 2005). *J. Geophys. Res.* 110, A12307. doi:10.5281/zenodo.2530324

Whipple, F. J. W. (1929). On the association of the diurnal variation of electric potential gradient in fine weather with the distribution of thunderstorms over the globe. *Q. J. R. Meteorol. Soc.* 55 (229), 1–17. doi:10.1002/qj.49705522902

Williams, E., and Mareev, E. (2014). Recent progress on the global electric circuit. *Atmos. Res.* 135–136, 208–227. doi:10.1016/j.atmosres.2013.05.015

Williams, E. R. (1992). The Schumann resonance: a global tropical thermometer. *Science.* 256 (5960), 1184–1187. doi:10.1126/science.256.5060.1184

Williams, E. R. (2009). The global electric circuit: a review. *Atmos. Res.* 91 (2–4), 140–152. doi:10.1016/j.atmosres.2008.05.018

Wilson, C. T. R. (1921). Investigations on lightning discharges and on the electric field of thunderstorms. *Philos. Trans. Roy. Soc. London.* 221 (582–593), 73–115. doi:10.1098/rsta.1921.0003

Yaniv, R., Yair, Y., Price, C., and Katz, S. (2016). Local and global impacts on the fair-weather electric field in Israel. *Atmos. Res.* 172–173, 119–125. doi:10.1016/j.atmosres.2015.12.025

Conflict of Interest: The authors declare that the research was conducted in the absence of any commercial or financial relationships that could be construed as a potential conflict of interest.

frontiers
in Earth Science

ORIGINAL RESEARCH
published: 17 March 2021
doi: 10.3389/feart.2021.614820

Locating Thunder Source Using a Large-Aperture Micro-Barometer Array

Jan Rusz*, Jaroslav Chum and Jiří Baše

Institute of Atmospheric Physics, Czech Academy of Sciences (CAS), Prague, Czechia

Lightning generates sound waves across a wide range of frequencies, including infrasonic waves below 20 Hz. Source mechanism for these low frequency pulses is still area for debate. Infrasound pulses detected after rapid changes of electrostatic field during the thunderstorm activity were analyzed. The measurements were done by large aperture array of absolute microbarometers located in the Western part of the Czech Republic. Distances between four measuring sites are in the range of 4–10 km. The infrasound source position was calculated from time delays between the rapid change of electrostatic field and infrasound signal arrival to the individual microbarometers assuming propagation of spherical waves from the source. Only cases with a sufficient signal-to-noise ratio on all four microbarometers were analyzed. The variation of sound speed with height due to temperature height profile was taken into account. For most of the analyzed cases, the calculated infrasound source position corresponds to the lightning location determined by European lightning detection network (EUCLID). The calculated height of infrasound source is most often 3–5 km.

Keywords: infrasound, lightning, thunder, acoustic, spherical, waves

Edited by:
Martin Fullekrug,
University of Bath, United Kingdom

Reviewed by:
Graeme Marlton,
Met Office, United Kingdom
Thomas Farges,
Commissariat à l'Energie Atomique et aux Energies Alternatives (CEA), France

****Correspondence:***
Jan Rusz
rusz@ufa.cas.cz

Specialty section:
This article was submitted to Atmospheric Science, a section of the journal Frontiers in Earth Science

Received: *07 October 2020*
Accepted: *25 February 2021*
Published: *17 March 2021*

Citation:
Rusz J, Chum J and Baše J (2021) Locating Thunder Source Using a Large-Aperture Micro-Barometer Array. Front. Earth Sci. 9:614820. doi: 10.3389/feart.2021.614820

INTRODUCTION

Thunderstorms and lightning are known from the dawn of mankind. They represent an important natural hazard for human beings, animals and technological systems. Despite of that many physical mechanisms that occur during thunderstorms, such as lightning initiation, generation of X-ray and gamma emissions during thunderstorms etc. have been poorly understood and are a subject of intense research (Dwyer and Uman, 2014). One of the not fully explained phenomena is also the generation of acoustic pulses in the infrasound frequency range that are observed in addition to the audible thunderclap. According to recent works, the source of infrasound is fast adiabatic expansion of the hot lightning channel as it is generally accepted for audible frequency range (Few, 1969; Assink et al., 2008; Lacroix et al., 2019). Another mechanism could be the pressure change caused by ohmic air heating by currents flowing from the charged area into the lightning channel (Few, 1985). The third possible explanation might be an electrostatic pressure in the charged parts of the storm clouds. This possibility was originally suggested by Wilson (1920) and was later elaborated and discussed by Dessler (1973), Pasko (2009), and Chum et al. (2013). The infrasound pulse is generated, according to this hypothesis, after removal of electric charge to the lightning channel, which leads to a sudden change of pressure.

It should also be noted that it is not only lightning that generate infrasound in thunderstorms. Infrasound over wide frequency range is also generated via convective forces, vortex motion of air masses or turbulence inside the thunderclouds (Goerke and Woodward, 1966; Bedard, 2005; Akhalkatsi and Gogoberidze, 2009). These processes, together with local wind around microbarometers, enhance infrasound noise background and complicate detection of individual thunders. Thunderstorm-induced infrasound waves might experience a stratospheric refraction and can be detected by ground infrasound stations over distances of several hundreds of kilometers (Campus and Christie, 2010; Šindelářová et al., 2015), Moreover, continuous very low-frequency infrasound produced by large convective system can propagate to ionospheric heights and be detected remotely by radio sounding at altitudes around 200 km (Georges, 1973; Chum et al., 2018). On the other hand, a reliable detection and association of thunders to individual lightning is only possible at relatively small distances from lightning, on the order of several kilometers or few tens of kilometers (Fleagle, 1949).

Several authors reported that distinct infrasound pressure pulses that significantly exceeded the background noise originated from IC discharges (Holmes et al., 1971; Johnson et al., 2011; Chum et al., 2013; Arechiga et al., 2014). The previous studies that located lightning and thunderstorm activity from infrasound signals recorded by an array of infrasound/acoustic sensors used an assumption of plane acoustic waves. In other words, it was considered that infrasound thunder was generated at much larger distances than is the size of the array (Assink et al., 2008; Farges and Blanc, 2010; Chum et al., 2013; Arechiga et al., 2014; Lacroix et al., 2018 among others) and the direction of arrival was determined from phase (time) shifts between signals recorded by different sensors.

The aim of this study is to present an alternative approach. It is based on data obtained by large-scale (aperture) array formed by four infrasound sensors (microbarometers) located in the western part of the Czech Republic. The array is originally intended for detection of very long period infrasound and atmospheric gravity waves. It is shown in this study that it is also possible to use this array for location of sources of impulsive infrasound produced by lightning. As the size of the array (∼10 km) cannot be neglected with respect to the distances of nearby discharges, an assumption of spherical wave propagation from the source is used. The paper focuses on distinct pulses from nearby lightning and describes the method of calculation of the infrasound source location using spherical wave-fronts. Next, it presents the obtained results and discusses the uncertainties. It also uses data from collocated electrostatic field sensor and European lightning detection network (EUCLID) for detection of lightning and determination of its time, location, type and peak current, and for comparison with thunder source position obtained by the analysis of infrasound signals.

MATERIALS AND METHODS

Experiment

EUCLID

EUCLID provides information about the discharge location, time, peak current and its polarity. Intracloud (IC) and cloud-to-ground (CG) lightning are distinguished. It consists of about 164 sensors which detect the electromagnetic field generated by lightning at frequencies from 10 to 350 kHz. For the CG strokes, the location accuracy in the Czech Republic is about 100–200 m and detection efficiency is greater than 98% (Schulz et al., 2016). As for the IC discharges, the location accuracy is undefined because of their spatial extent. The accuracy is generally considered between 1 and 10 km, but strongly depends on spatial extent of the IC discharges. Detection efficiency for IC flashes was roughly estimated to be in the range from about 70 to 80% (Chum et al., 2013).

Large Aperture Array of Absolute Micro-Barometers (Western Bohemia Czech Infrasound)

The array is designed for detection of very long period infrasound and atmospheric gravity waves. Microbarometers are located in the Westernmost part of the Czech Republic. Measuring points use available facilities of small seismic stations operated by the Institute of Geophysics and form a tetragon with sides within the range of 4–10 km. The array configuration is shown in **Figure 1**. The geographical location and altitude for each site is given in **Table 1**. The sites are equipped with absolute microbarometers (Paroscientific, Inc.) with parts-per-billion resolution. Sampling frequency is 50 Hz and a GPS receiver is used for time stamping. The microbarometers are located in simple wooden huts that shield the sensors against winds. No additional spatial filtering for noise reduction by a system of branching hoses is used. The sensitivity of the sensors is sufficient to clearly record microbaroms, especially in winter when eastward stratospheric winds support propagation of microbarom signals from Atlantic Ocean (Landes et al., 2012).

Electrostatic Field Measurement

An electric field mill (Boltek, Electric Field Monitor EFM-100) is used to record vertical component E_z of atmospheric electrostatic field. More precisely, potential gradient, PG $= -E_z$ is measured and presented further. It means that positive values are measured for downward—pointing electric field. The device is located in Studenec (location 3 in **Figure 1**) near the microbarometer. It has response time of ∼0.1 s, the sampling rate of data is 25 Hz. The absolute values of electric field (PG) did not exceed several kV/m in Studenec during thunderstorms, which is different from measurements performed on high and sharp mounting peaks, where values reaching ∼100 kV/m were observed (Chum et al., 2020).

Data and Analysis Methods

Data from storms that occurred near the microbarometer array in spring and summer of 2018 were processed. Three thunderstorms that occurred on 23.5.2018, 24.5.2018, and 16.7.2018, with a moderate occurrence frequency of lightning were selected. The moderate frequency of lightning flashes is important for the unambiguous assignment of infrasound pulses to a particular flash.

Using EUCLID data together with electric field measurements, 175 flashes were detected at a distance of less than 30 km from the microbarometer array. For further processing, only 92

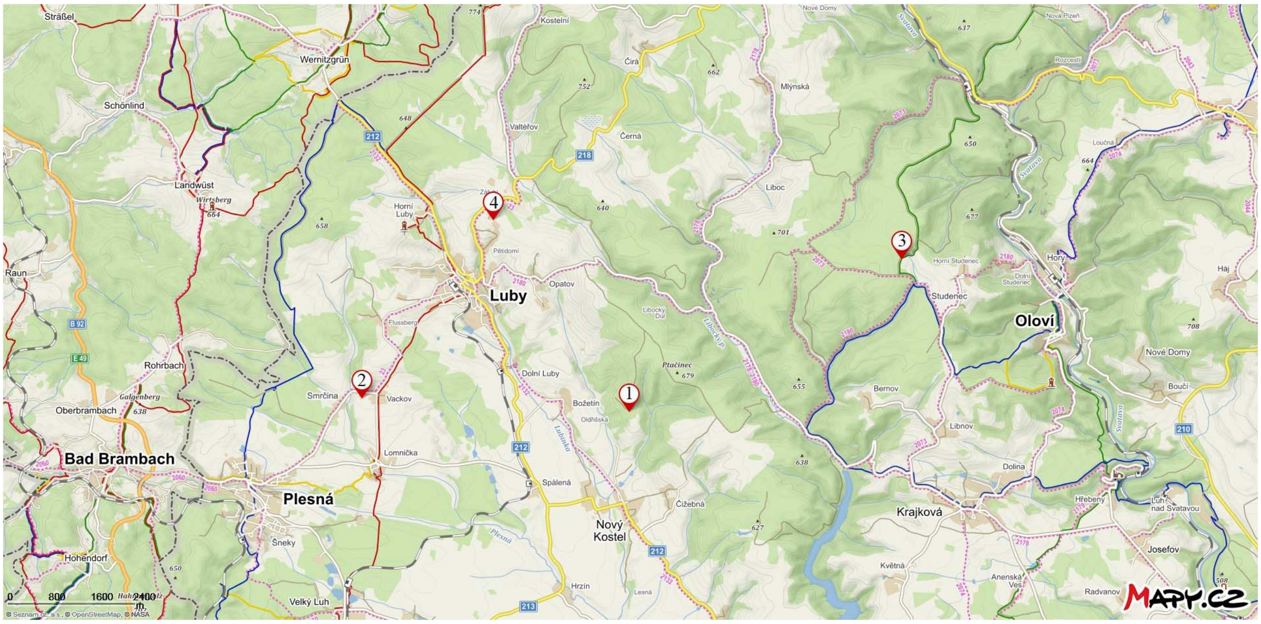

FIGURE 1 | Locations of microbarometers in Western Czechia.

cases with a sufficient signal-to-noise ratio on all four microbarometers were selected.

Identification of exact moments of lightning strokes is based on an analysis of the rapid, step-like changes of the electric field. In addition, the information about lightning locations by EUCLID within 30 km from EFM-100 is used for comparison.

Significant infrasound pulses were searched in the time interval of 70 s after each detected lightning flash. The time interval was set according to the experience with the evaluation of infrasound pulses. Choosing a longer interval would not provide any new results, pulses from a distance of more than 20 km were too weak and the assignment to a specific lightning was uncertain. Moreover, a step-like change of electric field is usually not observed for discharges occurring at larger distances. The event was only studied if the distinct signal was found on all four microbarometer records.

The infrasound source position was calculated from the time delays between the lightning and acoustic (infrasound) signal arrival to the individual microbarometers assuming propagation of spherical waves from the source. In the case of an ideal point source, the following system of equations is satisfied:

$$(x_n - x_0)^2 + (y_n - y_0)^2 + (z_n - z_0)^2 - (c_{avg\_n} \Delta t_n)^2 = 0 \qquad (1)$$

TABLE 1 | Coordinates and altitude of microbarometers.

	Location	Latitude	Longitude	Altitude
1	Nový Kostel (NKC)	50°13′56″	12°26′49″	564 m
2	Vackov (VAC)	50°14′ 04″	12°22′ 35″	530 m
3	Studenec (STC)	50°15′ 28″	12°31′ 06″	666 m
4	Luby (LBC)	50°15′ 52″	12°24′40″	638 m

where x_n, y_n, and z_n are Cartesian coordinates of the *n-th* array element (microbarometer), x_0, y_0, and z_0 are coordinates of the source, c_{avg_n} average speed of sound from the source to *n-th* sensor, and Δt_n are the measured time delays of the signal arrival to the *n-th* sensor. The relations (1) represent a set of four equations for three unknown coordinates x_0, y_0, and z_0 of the source that are solved by the weighted least square method described later.

Determining the Time Delay

The source of infrasound is actually a volume source rather than a point source. Also, the medium through which the signal propagates is inhomogeneous. Consequently, the infrasound thunder is usually observed as intense multiple pressure fluctuation rather than as an isolated pressure pulse. Examples of such pulses can be seen in **Figure 2**, indicated by colored ellipses. To find the exact time of arrival, a 2 Hz high-pass filter was first used to remove long—period fluctuations and noise background as much as possible. Then the signal variances of filtered signals over the time intervals of 0.2 s were calculated. We consider the maxima of these functions to be the times of signal arrival. The use of one specific time of each signal is limiting, leading to the determination of only single point source for each flash. However, the use of the entire pulse (longer pressure fluctuation) to reconstruct the spatial configuration of the infrasound source was not possible. Due to the large size of the microbarometer array, the infrasound signals propagating to the individual microbarometers are affected by different atmospheric conditions, are not well correlated at the microbarometer sites and cannot therefore be used to determine the source. **Figure 3** shows an example of the time evolution of the pressure variances with maxima marked by cross—symbols

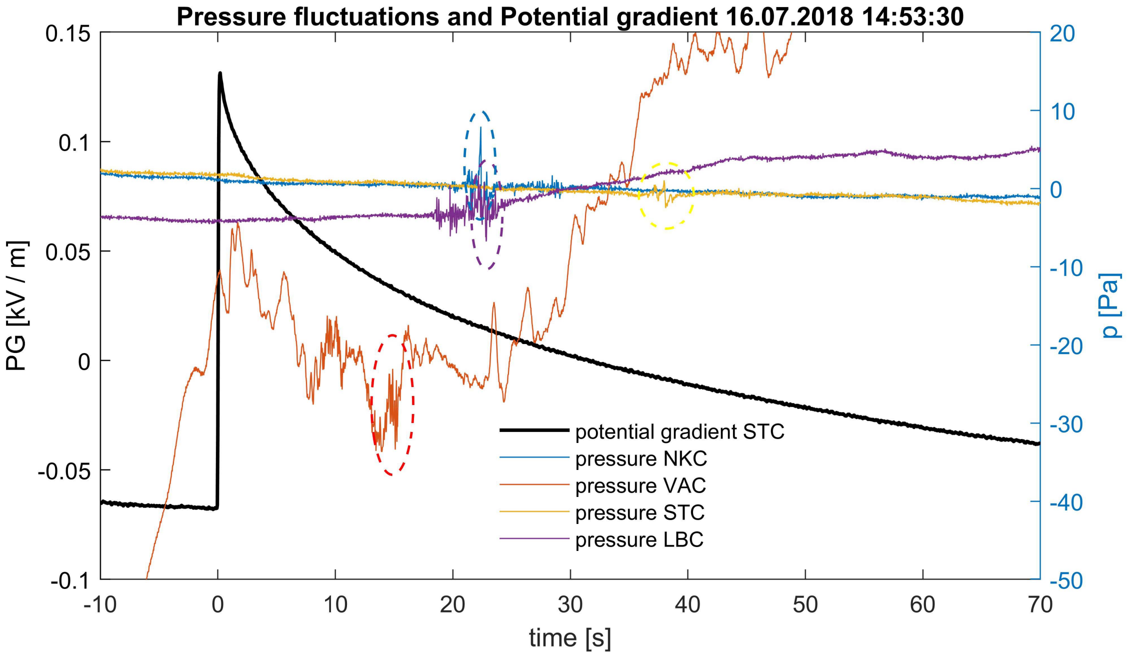

FIGURE 2 | Positive step—like change of potential gradient followed by little less clear oscillations on pressure curves.

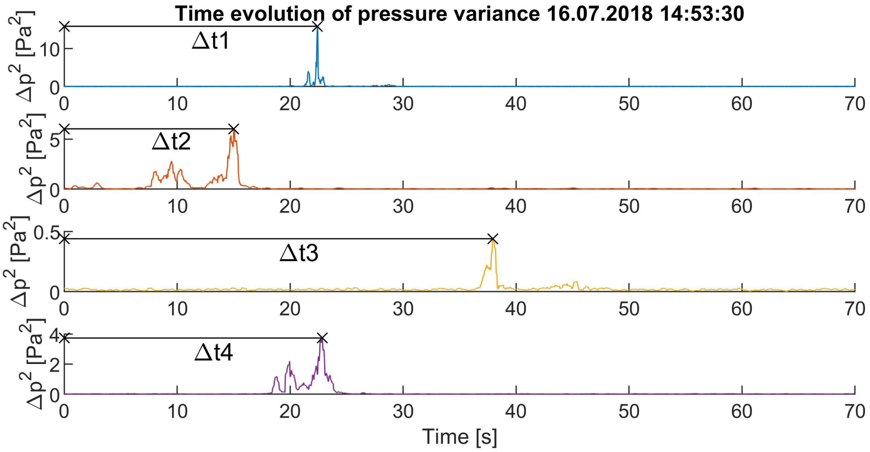

FIGURE 3 | Time evolution of HP-filtered pressure variations after the lightning stroke at 14:53:30.

for each microbarometer. Time zero in **Figure 3** corresponds to the time of lightning stroke at 14:53:30 UT.

The Speed of Sound

The calculation of the average sound velocity according to the source altitude was performed similarly as in Arechiga et al. (2014). We use an approximation of sound propagation along the straight line. We calculate speed of sound individually for each flash depending on its height and current temperature in the field area. The speed of sound depends mainly on the ambient temperature. For ideal gas, it is given by Eq. 2:

$$c = \sqrt{\gamma R T} \tag{2}$$

The speed of sound in real air is also affected by its humidity. Compared to the effect of temperature and wind, the effect of humidity is small and can be neglected in this calculation. The value of the heat capacity ratio γ for gas with for diatomic molecules is 1.4 and the specific gas constant R for dry air is $R = 287.058\ J\ kg^{-1}\ K^{-1}$. The variation of temperature with altitude z was modeled by a linear function with temperature lapse rate $k = -6.5\ K\ km^{-1}$.

$$T = T_3 + kz \tag{3}$$

The temperature T_3 for each lightning is obtained from the meteorological station collocated with EFM-100 (site 3 in **Figure 1**). The height z and the altitudes of the other measuring

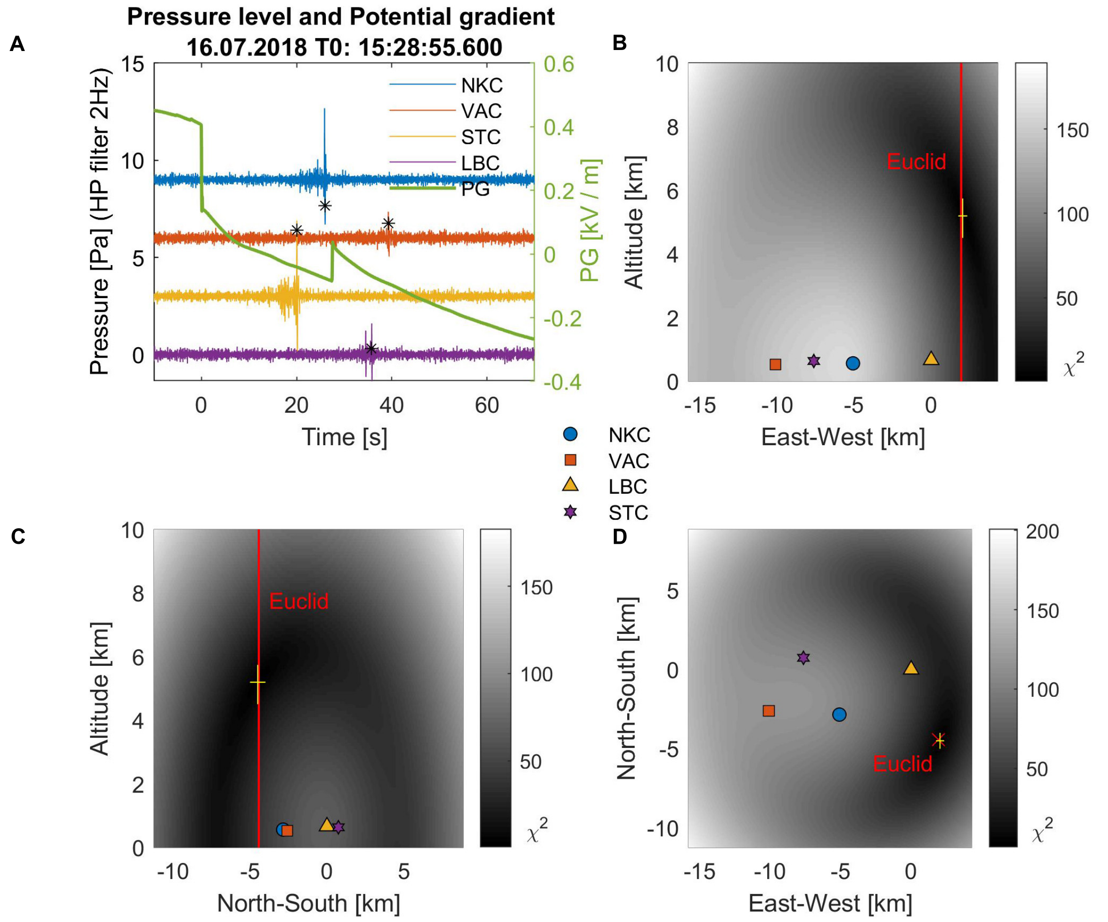

FIGURE 4 | (A) A rapid change in potential gradient followed by pressure fluctuations recorded by individual microbarometers. Pressure curves are high pass filtered and for clarity shifted from each other by 3Pa, **(B–D)** position of the infrasound source and lightning location in the three orthogonal planes. The position of the infrasound source (with a tolerance of σ) is indicated by a yellow cross. The position of the flash detected from the EUCLID is indicated by red cross on **(D)**. On **(B,C)** red lines are used, due to a missing altitude information. Background displays the $\chi^2(x, y)$ in Eq. 7.

stations are related to the altitude of the site 3. Assuming propagation along a straight line at elevation angle α for simplicity, the average speed of sound propagation from the source height z_0 to the height of n-*th* sensor z_n can be expressed as follows:

$$c_{avg\_n} = \frac{z_0 - z_n}{\Delta t_n \sin\alpha_n} \tag{4}$$

Using Eqs (2) and (3), the time of the straight-line propagation from the source to the n-*th* detector is expressed by the integral:

$$\Delta t_n = \int_{z_0}^{z_n} \frac{\frac{1}{\sin\alpha_n}dz}{\sqrt{\gamma R\left(T_3 + kz\right)}} = \frac{2}{\gamma R k \sin\alpha_n}\left(\sqrt{\gamma R\left(T_3 + kz_n\right)} - \sqrt{\gamma R\left(T_3 + kz_0\right)}\right) \tag{5}$$

After substituting into the Eq. 4:

$$c_{avg\_n} = \frac{z_0 - z_n}{\frac{2}{\gamma R k}\left(\sqrt{\gamma R\left(T_3 + kz_n\right)} - \sqrt{\gamma R\left(T_3 + kz_0\right)}\right)} \tag{6}$$

Therefore, in this approximation of propagation along the straight line, the average value of the sound speed is not dependent on the elevation angle α_n.

Finding the Solution

The weighted least squares method is used to solve the overdetermined set of Eq. 1 for the unknown coordinates x_0, y_0, and z_0. Specifically, the term χ^2_{min} defined in Eq. 7 is minimized.

$$\chi^2_{min} = \sum_{n=1}^{N} \frac{\left(x_n - x_0\right)^2 + \left(y_n - y_0\right)^2 + \left(z_n - z_0\right)^2 - \left(c_{avg\_n}\Delta t_n\right)^2}{\sigma_n^2} \tag{7}$$

Where χ^2_{min} is dimensionless goodness-of-fit parameter that corresponds to a chi-square distribution with one degree of freedom for correctly estimated weights $w_n^2 = 1/\sigma_n^2$. Note that the temperature dependence of sound speed on the source height enters in the solution—minimization of χ^2_{min} via c_{avg_n}, which is specified in Eq. 6.

Uncertainties Estimation

The uncertainties σ_n^2 are given by the uncertainties in determining speed of sound and of signal propagation time. We assume that the coordinates of the microbarometers $x_n,\ y_n,\ z_n$ are determined precisely. The uncertainty of determining time delay $\triangle t_n$ is based on infrasound thunder pulse width on the pressure variation (**Figure 3**). The width of the pulse is determined by the points where the variance of fast pressure variations drops to one half of its maximum. The correct assignment of the audio signals to the individual lightning bolts was ensured by selecting suitable sections of the storm with a relatively low frequency of lightning so that the assignment was unambiguous.

The accuracy of the sound speed is dependent on the knowledge of temperature and its altitude profile. Exact temperature measurement is only available at one location at the ground level. The highest recorded temperature change in the observed storms was 2°C. Thus, it is assumed that the maximum error in determining the temperature at different points on the ground should not exceed this value. The uncertainties in determining the average sound speeds c_{avg_n} are then obtained by substituting the expected temperatures for the temperatures changed by their maximum uncertainties into Eq. 6. The third parameter significantly affecting the uncertainty of the $c_{avg\_n}\triangle t_n$ product is the wind speed. It is again measured in one place only. The calculation (7) assumes zero wind speed. To estimate the uncertainty, we take the maximum speed value measured during the thunderstorm.

The total uncertainties used in Eq. 7 can be expressed as:

$$\sigma_\mathrm{n}^2 = \triangle \mathrm{t_n}^2\left(\partial c^2 + \partial v^2\right) + \partial\triangle \mathrm{t_n}^2 c_{avg\_n}^2 \tag{8}$$

Where $\partial\triangle \mathrm{t_n}$, ∂c, ∂v are uncertainties in determining time delays, speed of sound and wind speed. For the studied storms, values for ∂v were in range 2–5 m/s and ∂c was around 1.2 m/s for temperature uncertainty of 2°C.

Obviously, the closer is the source to the specific sensor, the smaller is the uncertainty as σ_n^2 increases with the propagation time $\triangle t_n$. Thus, the measurements obtained by microbarometers that are closer to the source have usually larger weights in Eq. 7.

The total error in determining the position of the infrasound thunder source is determined as follows. We add subsequently to the terms $\left(c_{avg\_n}\triangle t_n\right)^2$ in Eq. 7 the values of their uncertainties with positive or negative sign, $+\sigma_\mathrm{n}^2$, $-\sigma_\mathrm{n}^2$ or 0. Because we have four measuring sites, altogether $3^4 = 81$ different combinations to solve Eq. 7 are obtained. After solving them, we get 81 different source positions. We will then consider the largest positive and negative deviations of each component (x, y, z) from positions calculated for zero added to all $\left(c_{avg\_n}\triangle t_n\right)$ terms as the errors of the obtained source positions.

RESULTS

Data from three periods of storm activity on 23–24.5.2018 and 16.7.2018 were examined. In total, 92 lightning with complete data and sufficient data quality on all measuring channels were selected from a large number of flashes.

Three illustrative cases are described in detail further. The first example is a simple single-stroke IC flash detected southeast of the microbarometer array. The next two examples describe flashes composed of several return strokes. In the second case the flash was only composed of IC discharges, whereas in the third case both IC and CG return strokes were present in the multiple stroke discharge.

Example 1: Single Stroke Flash

The flash was observed during the storm activity on 16.7.2018 at 15:28:55.6, which can be seen as a rapid decrease of the potential gradient by about 0.25 kV in **Figure 4A**. EUCLID network detected one negative IC stroke with a peak current of −6.43 kA at 15:28:55.573. The location of the flash from the EUCLID network is marked by the red cross in **Figure 4D** and red lines in **Figures 4B,C**. Significant oscillations on the pressure curves with a maximum amplitude on the order of units of Pa are observed 20–40 s after the lightning flash. It is clearly visible that the intensity of the oscillations decreases with increasing time of arrival, i.e., with increasing distance from the lightning. Determination of the time of maximum oscillation is more reliable and accurate after applying the 2 Hz high pass filter (**Figure 4A**). The infrasound source position determined from the time delays of the infrasound signals is indicated by the yellow crosses in **Figures 4B–D**. The size of these crosses corresponds to the total positioning error. The determined horizontal position of the infrasound source corresponds well to the lightning location given by EUCLID.

Example 2: Multiple Stroke Flash

A multiple stroke discharge composed of five IC discharges was observed during the storm activity on 16.7.2018, recorded in **Figure 5A** as a sudden increase in potential gradient by about 0.2 kV at 14:53:30.04. EUCLID detected five IC discharges in the time interval 14:53:30.005–14:53:30.075. Their locations are indicated by red crosses and lines in **Figures 5B–D**. The strongest of the discharges (−11.01 kA) is highlighted by bold. The oscillations on the pressure curves last longer than in the previous case, they consist of several separate groups of oscillations. However, the maximum is still clearly visible. The position of the infrasound source, indicated by yellow crosses in **Figures 5B–D**, is again close to the locations of the individual discharges detected by EUCLID.

Example 3: Close Lightning Strike

A multiple flash was detected during the storm activity on 23.5.2018 at 14:29:39.4 is seen in **Figure 6A** as fast approximately 1.2 kV bidirectional change of potential gradient at this time. According to the EUCLID data, it consisted of three strokes. The strongest of them was CG discharge with the peak current of −34.14 kA. It was detected in close proximity to the measuring point 3 (**Figure 1**). The other two IC discharges were weaker and their distance from the measuring point was greater. **Figure 6A** show a sharp and distinct pressure variations at the measuring point 3 (marked yellow and with the STC code) observed about 2–3 s after the lightning flash. The maximum amplitude of this pulse exceeds 20 Pa, which is several times

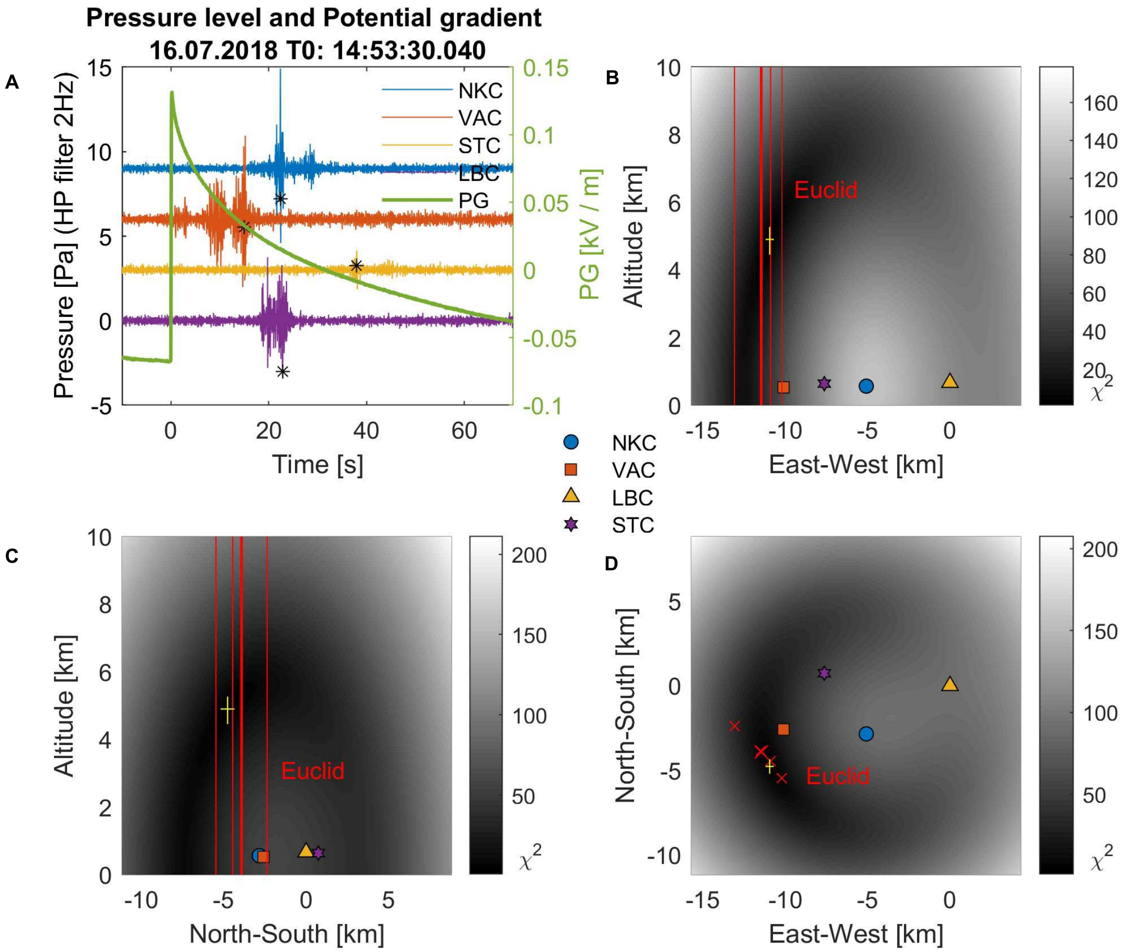

FIGURE 5 | An example of a multiple flash of five IC discharges. **(A)** A rapid change in potential gradient followed by pressure fluctuations recorded by individual microbarometers. Pressure curves are high pass filtered and for clarity shifted from each other by 3Pa, **(B–D)** position of the infrasound source and lightning location in the three orthogonal planes. The position of the flashes detected from the EUCLID are indicated by red. The strongest discharge is marked by bold. The position of the infrasound source (with a tolerance of σ) is indicated by a yellow cross. Colorful background displays the $\chi^2(x, y)$ in Eq. 7.

higher than the intensity of the oscillations measured by the other microbarometers. **Figures 6B–D** shows the position of the infrasound source near the measuring point 3, marked by yellow crosses. Again, the position of infrasound source is relatively close to the location of the strongest lightning discharge.

Statistical Results

Statistical investigation of altitudes of infrasound sources is presented. Since there were no pure CG flashes among the 92 processed flashes, we divide the events into two categories: pure IC flashes and mixed flashes, composed of both CG and IC discharges. **Figure 7A** shows the calculated altitudes of the infrasound sources and **Figure 7B** their uncertainties as a function of the distance from the center of the measuring array. It is clearly visible that the uncertainties increase with increasing distance from the array center. At a distance larger than 10 km from the center of the microbarometers, the detected altitudes are no longer reliable. The maximum distance of analyzed events did not exceed 17 km. The mean altitude and other basic statistical parameters are given in **Table 2**. Histogram presenting distribution of altitudes is shown in **Figure 8**. Red bars mark pure IC discharges whereas blue bars depict mixed flashes. As expected, the altitude range (variance) of pure IC discharges is less than that of the mixed ones.

TABLE 2 | Altitudes of the infrasound source.

	Mean (km)	Median (km)	Std. dev. (km)	Count
Mix	3.8	3.8	1.6	67
IC	4.3	4.5	1.3	25

DISCUSSION AND CONCLUSION

The infrasound source position was successfully calculated from the measured time delays between the lightning and acoustic signal arrival to the individual infrasound sensors of

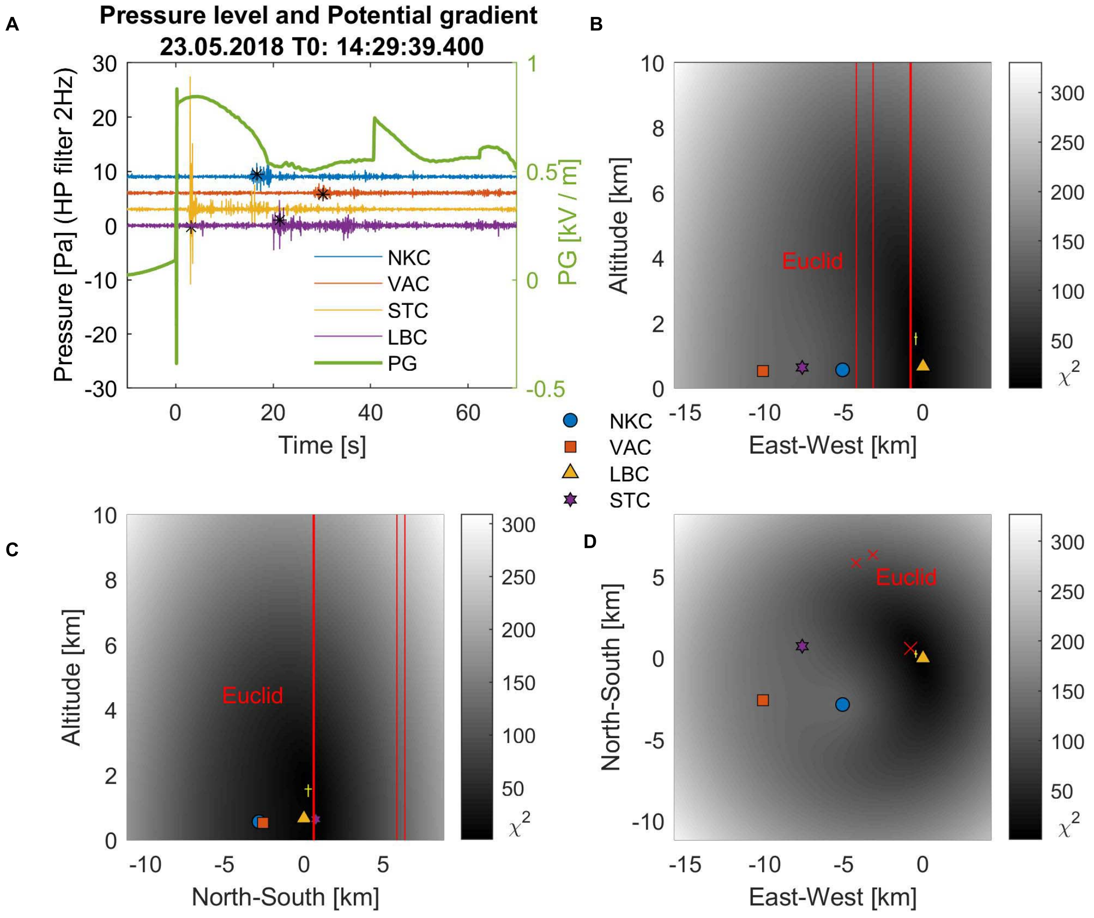

FIGURE 6 | (A) high passed filtered pressure fluctuations recorded by individual microbarometers follow quick bidirectional change in electrical potencial, **(B–D)** position of the infrasound source and lightning location in the three orthogonal planes. The calculated flash position indicated by a yellow cross is near to the STC measuring point, and comparatively close is also the strongest lightning stroke identified by the Euclid network (marked by bold red crosses and lines).

the large aperture microbarometer array assuming propagation of spherical waves from the source. The reliable detection of individual infrasound signals is only possible for thunderstorms with a low to moderate frequency of lightning. In the case of a time interval containing a number of multiple flashes, the infrasound signals are mixed or overlapped. Consequently, they cannot be properly detected and assigned to the causative lightning flash.

The weather conditions, especially temperature, wind speed and direction, and their altitude profiles could strongly affect the infrasound propagation. The infrasound signals propagating to the individual microbarometers might be affected by different atmospheric conditions. In some cases, the determination of the source position was not possible. More precisely, minimizing Eq. 7 did not lead to reasonably low χ^2_{min} values. The error caused by the weather conditions was greater than the estimated uncertainty according to Eq. 8 in these cases. Such events were not included in the results.

The requirement of sufficient signal to noise ratio of the lightning - induced infrasound signal on all four microbarometers and partly also the requirement that the lightning has to be detected both by EUCLID and electric field mill limited a maximum distance of lightning that could be analyzed. Thus, mostly lightning detected within a distance of 14 km from the center of the microbarometer array were analyzed. The farthest usable flash was detected at the distance of 17 km.

The uncertainties in determining the infrasound source positions in the horizontal plane are usually less than 1 km and the calculated positions of the infrasound sources correspond to the horizontal locations of the lightning flashes indicated by EUCLID for most of the selected cases.

The calculated uncertainties of the altitudes are more sensitive to the lightning distances from microbarometers. Up to the distances of about 5 km from the center of the array, the vertical uncertainties of the infrasound sources are comparable with the uncertainties in the horizontal plane. The vertical uncertainties, however, increase for larger distances. For distances larger than about 10 km, the calculated altitude is no longer reliable and/or informative. It should also be noted that the simplified assumption of the point infrasound source, on which the calculation is based, might not always be representative, especially

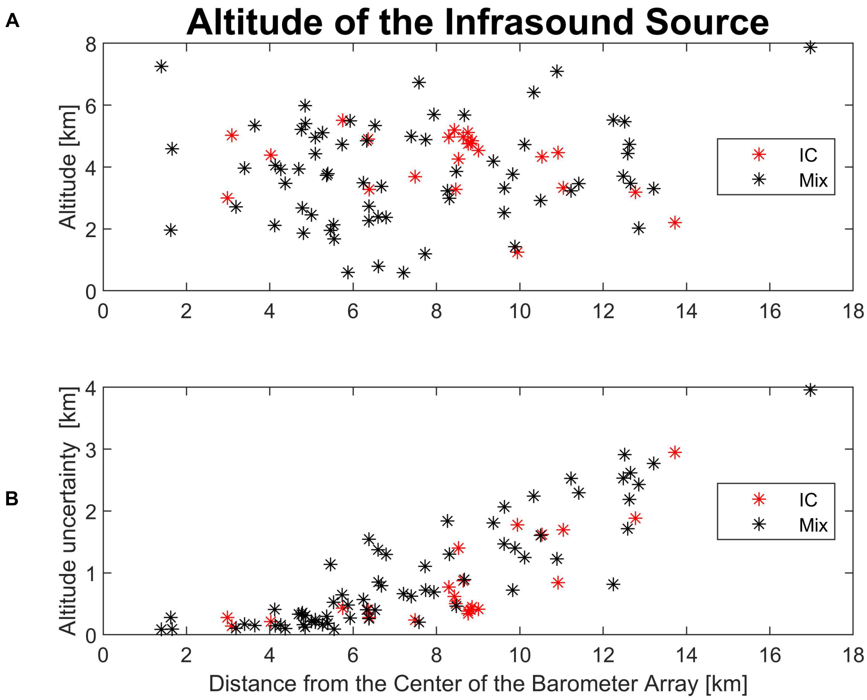

FIGURE 7 | (A) Calculated altitude of the of the infrasound source as a function of distance from the center of the microbarometer array. Purely IC discharges are colored in red. **(B)** Calculated altitude uncertainties as a function of distance from the center of the microbarometer array. Purely IC discharges are colored in red.

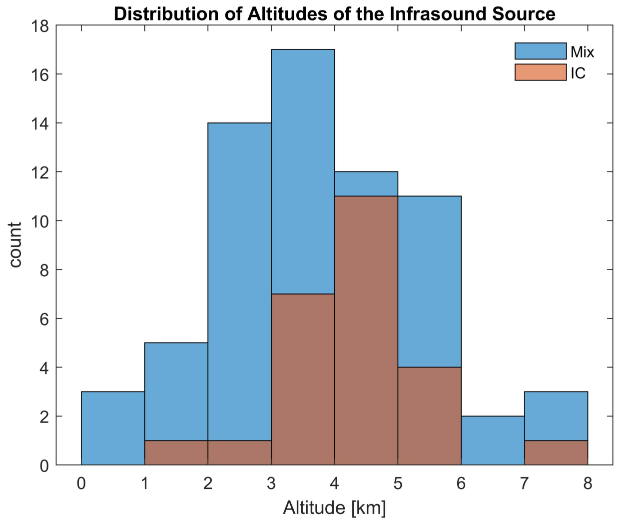

FIGURE 8 | Distribution of calculated altitudes of infrasound source. Purely IC discharges are colored in red.

for the multiple—stroke discharges. This simplification also contributes to the observed uncertainties.

The calculated altitudes of infrasound thunder sources are typically 2–6 km. The calculated altitudes of pure IC flashes are usually higher than those mixed IC + CG flashes. The usual altitude range of pure IC flashes (3–5 km) is also narrower than the range obtained for mixed flashes. There are no pure CG flashes among the analyzed cases. Based on the evaluated data, it can be hypothesized that the source of infrasound pulses are IC discharges in most cases or the upper parts of CG discharges. It should be, however, noted in this respect that the analysis was limited on the localization of the region (point) from which the highest infrasound power was generated to different directions because only time instants of the most distinct pressure fluctuations were used for the calculations of source positions. As mentioned previously, the pressure fluctuations at different microbarometer sites were not sufficiently correlated to imagine the whole lightning channel as was done by Lacroix et al. (2019) who used the small-scale array. Nevertheless, the localizations of the highest infrasound source power mostly to altitudes 3–5 km in this study are consistent with some previous studies that used small scale arrays and focused on the analysis of distinct short infrasound pulses (Chum et al., 2013; Arechiga et al., 2014). Note that the studies used different methods of analysis (plane wave versus spherical wave assumptions). We assume that several small-scale arrays distributed over the area of large-scale array would make it possible to investigate sources of infrasound thunders in more detail and complexity.

DATA AVAILABILITY STATEMENT

Electric field measurement data are available at http://datacenter.ufa.cas.cz/mlynky/?s=STC. Raw data from microbarographs and lightning data from the EUCLID network are available from the authors of the article at any time on request.

AUTHOR CONTRIBUTIONS

JC designed the study. JR performed analysis and data processing. JB was responsible for microbarometers and electric field measurement and data archiving. JC and JR wrote the manuscript. All authors read and approved the submitted version.

REFERENCES

Akhalkatsi, M., and Gogoberidze, G. (2009). Infrasound generation by tornadic supercell storms. *Q. J. R. Meteorol. Soc.* 135, 935–940. doi: 10.1002/qj.421

Arechiga, R., Stock, M., Thomas, R., Erives, H., Rison, W., Edens, H., et al. (2014). Location and analysis of acoustic infrasound pulses in lightning. *Geophys. Res. Lett.* 41, 4735–4744. doi: 10.1002/2014GL060375

Assink, J. D., Evers, L. G., Holleman, I., and Paulssen, H. (2008). Characterization of infrasound from lightning. *Geophys. Res. Lett.* 35, L15802. doi: 10.1029/2008GL034193

Bedard, A. J. (2005). Low-frequency atmospheric acoustic energy associated with vortices produced by thunderstorms. *Mon. Weather Rev.* 133, 241–263. doi: 10.1175/MWR-2851.1

Campus, P., and Christie, D. R. (2010). "Worldwide observations of infrasonic waves," in *Infrasound Monitoring for Atmospheric Studies*, eds A. Le Pichon, E. Blanc, and A. Hauchecorne (Dordrecht: Springer), 185–234. doi: 10.1007/978-1-4020-9508-5_6

Chum, J., Diendorfer, G., Šindelářová, T., Baše, J., and Hruška, F. (2013). Infrasound pulses from lightning and electrostatic field changes: observation and discussion. *J. Geophys. Res. Atmos.* 118, 653–610. doi: 10.1002/jgrd.50805

Chum, J., Langer, R., Baše, J., Kollárik, M., Strhárský, I., Diendorfer, G., et al. (2020). Significant enhancements of secondary cosmic rays and electric field at the high mountain peak of Lomnický Štít in High Tatras during thunderstorms. *Earth, Planets Space* 72:28. doi: 10.1186/s40623-020-01155-9

Chum, J., Liu, J.-Y., Podolská, K., and Šindelářová, T. (2018). Infrasound in the ionosphere from earthquakes and typhoons. *J. Atmos. Sol. Terr. Phys.* 171, 72–82. doi: 10.1016/j.jastp.2017.07.022

Dessler, A. J. (1973). Infrasonic thunder. *J. Geophys. Res.* 78, 1889–1896. doi: 10.1029/JC078i012p01889

Dwyer, J. R., and Uman, M. A. (2014). The physics of lightning. *Phys. Rep.* 534, 147–241.

Farges, T., and Blanc, E. (2010). Characteristics of infrasound from lightning and sprites near thunderstorm areas. *J. Geophys. Res.* 115:A00E31. doi: 10.1029/2009JA014700

Few, A. A. (1969). Power spectrum of thunder. *J. Geophys. Res.* 74, 6926–6934. doi: 10.1029/JC074i028p06926

Few, A. A. (1985). The production of lightning-associated infrasonic acoustic sources in thunderclouds. *J. Geophys. Res.* 90, 6175–6180. doi: 10.1029/JD090iD04p06175

Fleagle, R. G. (1949). The audibility of thunder. *J. Acoust. Soc. Am.* 21:411. doi: 10.1121/1.1906528

Georges, T. M. (1973). Infrasound from convective storms: examining the evidence. *Rev. Geophys. Space Phys.* 11, 571–594.

Goerke, V. H., and Woodward, M. W. (1966). Infrasonic observation of a severe weather system. *Mon.Weather Rev.* 94, 395–398.

Holmes, C. R., Brook, M., Krehbiel, P., and McCrory, R. (1971). On the power spectrum and mechanism of thunder. *J. Geophys. Res.* 76, 2106–2115. doi: 10.1029/JC076i009p02106

Johnson, J. B., Arechiga, R. O., Thomas, R. J., Edens, H. E., Anderson, J., and Johnson, R. (2011). Imaging thunder. *Geophys. Res. Lett.* 38, L19807. doi: 10.1029/2011GL049162

Lacroix, A., Coulouvrat, F., Marchiano, R., Farges, T., and Ripoll, J. F. (2019). Acoustical energy of return strokes: a comparison between a statistical model and measurements. *Geophys. Res. Lett.* 46, 11479–11489. doi: 10.1029/2019GL085369

Lacroix, A., Farges, T., Marchiano, R., and Coulouvrat, F. (2018). Acoustical measurement of natural lightning flashes: reconstructions and statistical analysis of energy spectra. *J. Geophys. Res. Atmos.* 123, 12,040–12,065. doi: 10.1029/2018JD028814

Landes, M., Ceranna, L., Le Pichon, A, and Matoza, R. S. (2012). Localization of microbarom sources using the IMS infrasound network. *J. Geophys. Res.* 117:D06102. doi: 10.1029/2011JD016684

Pasko, V. P. (2009). Mechanism of lightning-associated infrasonic pulses from thunderclouds. *J. Geophys. Res.* 114:D08205. doi: 10.1029/2008JD011145

Schulz, W., Diendorfer, G., Pedeboy, S., and Poelman, D. R. (2016). The European lightning location system EUCLID – Part 1: perfor-mance analysis and validation. *Nat. Hazards Earth Syst. Sci.* 16, 595–605.

Šindelářová, T., Chum, J., Skripniková, K., and Baše, J. (2015). Atmospheric infrasound observed during intense convective storms on 9-10 July 2011. *J. Atmos. Sol. Terr. Phys.* 122, 66–74. doi: 10.1016/j.jastp.2014.10.014

Wilson, C. T. R. (1920). Investigations on lightning discharges and on the electric field of thunderstorms. *Philos. Trans. R. Soc. A* 221, 73–115.

FUNDING

Support under the grant 18-01969S by the Czech Science Foundation was acknowledged.

ACKNOWLEDGMENTS

We are grateful to Gerhard Diendorfer at Austrian Electrotechnical Association (OVE—ALDIS), for providing data from the EUCLID network.

Conflict of Interest: The authors declare that the research was conducted in the absence of any commercial or financial relationships that could be construed as a potential conflict of interest.

frontiers
in Earth Science

ORIGINAL RESEARCH
published: 08 April 2021
doi: 10.3389/feart.2021.647913

Nature of Relationships Between Atmospheric Electricity Parameters at Ground Surface and Air Ionization on the Basis of Nuclear Accidents in Power Plants and Weapons Tests

Marek Kubicki, Bogna Mysłek-Laurikainen and Anna Odzimek*

Institute of Geophysics, Polish Academy of Sciences, Warsaw, Poland

Edited by:
Irina Alexandrovna Mironova,
Saint Petersburg State University,
Russia

Reviewed by:
Sergey Alexander Pulinets,
Space Research Institute (RAS),
Russia
Xuemeng Chen,
University of Tartu, Estonia

****Correspondence:***
Marek Kubicki
mkubicki@igf.edu.pl;
swider@igf.edu.pl

Specialty section:
This article was submitted to
Atmospheric Science,
a section of the journal
Frontiers in Earth Science

Received: *30 December 2020*
Accepted: *17 March 2021*
Published: *08 April 2021*

Citation:
Kubicki M, Mysłek-Laurikainen B and Odzimek A (2021) Nature of Relationships Between Atmospheric Electricity Parameters at Ground Surface and Air Ionization on the Basis of Nuclear Accidents in Power Plants and Weapons Tests. Front. Earth Sci. 9:647913. doi: 10.3389/feart.2021.647913

In this work we present an analysis of selected atmospheric electricity parameters, measured at the Geophysical Observatory in Świder (near Warsaw, Poland), in a review of the major events that resulted in the release of a significant amount of artificial radioactive substances in the Earth's atmosphere: the radioactive accident in Fukushima, Japan, beginning 12 March 2011, followed by the 9.0 earthquake and tsunami; Chernobyl disaster (27 April 1986); and nuclear weapons testing (1958–1965). The physical mechanisms of the impact of radioactive sources on the electrical parameters of the atmosphere are analyzed. The formation of free charge (small ions, represented by electric air conductivity) and bound-induced charges (measured vertical electric field and current) by radioactive aerosol and cloud nuclei were taken into account. The values of electric field E_Z, atmospheric air conductivity λ, and aerosol concentrations measured at a certain site depend on the time and space location of the released radioactive materials in relation to the measurement site and the meteorological situation. A frontal inflow of air masses containing radioactive substances may be noticeable at a large distance from the atmospheric electricity measuring site in fair weather conditions (Chernobyl disaster). Atmospheric precipitation plays a very important role in the transport of radioactive substances to the ground level (nuclear weapons testing). The relationship between the ionospheric potential V_i and the electric field near ground level E_Z resulting from the Global Electric Circuit (GEC) concept for the presence of a strongly ionized air layer in the lower stratosphere and the ground level was disturbed in nuclear weapons testing time. The aim of this work is a qualitative characterization of discussed events. Future modeling works are needed to investigate the dependence of quantitative GEC parameters in situations of global or regional high air ionization. For this purpose, available measurements of recorded atmospheric electricity parameters will be used.

Keywords: atmospheric electricity, nuclear accidents, nuclear weapons testing, radioactive air pollution, ionizing

INTRODUCTION

Most of the issues discussed while analyzing the electricity of the atmosphere in connection with air radioactivity can be divided into the following groups: (1) experiments with nuclear weapons carried out in the high atmosphere in the years 1950–1965, (2) incidents of failure of nuclear power plants, Chernobyl, Fukushima, and regular releases from nuclear fuel reprocessing plants, (3) natural radioactivity of the Earth's surface, resulting from the presence of radioactive elements in the rocks and the emanation of radon, thoron and progeny, and (4) cosmic radiation having a significant impact on ionization of air in the atmosphere (Williams and Mareev, 2014).

In the case of the first group, radioactive substances were accumulated in the stratosphere (e.g., Alvarado et al., 2014), being a source of radioactive radiation related to GEC. For the second type of events, radioactive substances were released in the bottom troposphere and transported by movements of the air masses in the planetary boundary layer; the range can be determined as regional or local. In this group, one can also distinguish re-suspended radioactive dust and gamma rays from the ground fallout (Pierce, 1972; Yamauchi et al., 2012; Yamauchi, 2012). The third group is the local specificity of the measurement area associated with the geological structure of the Earth's crust.

Based on measurements of atmospheric electricity, meteorology, and air pollution carried out at the Geophysical Observatory at Świder during the above-mentioned events, the mechanism of the influence of high radioactivity on the parameters of atmospheric electricity is assessed. It may result from the phenomenon of inducing a surface charge (bound) due to changes in the ionosphere charge (and potential) or free and bound charge generation through a radioactive cloud, or air mass that overcomes the measurement site.

The induced charge arises as a result of electrostatic induction. The bound charge is related to the effect of the polarization vector (e.g., Griffiths, 2017). It is the charge accumulated on the surface conductor or dielectric. Any charge that is not a result of polarization (e.g., small ions in the atmosphere) is a free charge.

The ionization source generates free charges, which are measured by the Gardien counter, located in the proximity of the source. Radioactive cloud and aerosol can be detected from a considerable distance based on changes in the electric field (e.g., field mill, radioactive collector) and current (e.g., Wilson plate) near the Earth's surface (Israel, 1973b). These sensors work by measuring the induced (bonded) charge on a measuring electrode. According to Gauss's law, free and bound charges are the source of the electric field (e.g., Griffiths, 2017). The ionizing phenomena in the ground-level air which contribute to the atmospheric electricity are mainly related to the presence of radioactive substances of natural and anthropogenic origins.

An important factor is also the atmospheric radioactive fallout (i.e., precipitations and dry depositions) causing the transport and descents of radioactive substances to the surface of the earth. During of the Chernobyl nuclear power plant accident, the parameters of the atmospheric electricity reacted with rapid and sudden changes only when the air mass transported the radioactive material over Poland. During many years of testing and using nuclear weapons, changes in the parameters of atmospheric electricity were recorded in the Świder Observatory.

In this discussion, one should also take into account the adaptation of the measurement technique, i.e., the selection of an appropriate sensor or the correct interpretation of the measured waveforms to assess the role of high radioactivity in the GEC.

The electric air conductivity is a product of the ion concentration (small, intermediate, and large), the ion mobility, and electric charge. The mobility of small ions is about three times that of large ions, hence (Chalmers, 1967) the small ions are mainly responsible for the conductivity in the air. Small ions are created by the ionization caused by the emanation of radioactive radon and thoron from the ground, and ionization by other radioactive elements in the air and by cosmic rays (Chamberline, 1991). The cosmic rays contain alpha particles (e.g., Mironova et al., 2015) that can be of great importance for the electric air conductivity.

The rate at which ions are produced at the Earth's surface is about 10 ion pairs of positive and negative in 1 cubic centimeter per 1 s (Israel, 1973a; Mysłek-Laurikainen et al., 2011).

Blicard (1965) reports that when there is no strong radiation, α-rays have the greatest influence on air ionization a few meters from the ground surface (α-4.4, β-0.03, γ-0.15 ion pairs $cm^{-1}s^{-1}$). Radioactive substances in the surface soil mainly emit the γ (3.2 ion pairs $cm^{-1}s^{-1}$) and β (0.3 ion pairs $cm^{-1}s^{-1}$) radiation. Gamma radiation plays a significant role in the radiation from the ground (Blicard, 1965).

In the steady state and with a constant aerosol concentration, an increase in air ionization, e.g., as a result of a nuclear accident, causes an increase in the number of small ions. An increase in the aerosol concentration at a constant ion production causes a decrease in the ion concentration. The electric conductivity of the air is responsible for the support of conduction currents flowing in the Earth's atmosphere. The conduction current density, electric air conductivity, and atmospheric electric field are related by Ohm's law. The air conductivity, electric current density, and electric field are the main parameters of atmospheric electricity (AE).

According to the ionization equation (Chalmers, 1967, pp. 104–107), the small ion concentration in the surface layer depends mostly on the ion production and aerosol concentration.

Radioactive aerosol has specific properties: it is highly electrically charged. The process of attachment of radioactive substances to aerosol particles depends mainly on aerosol size, radioactivity decay rates, and mean free path of radioactive species in the atmosphere, and the electric field affects the mobility of the ions produced. Air ionization is a result of β and α emission and the formation of radioactive aerosol (Reed et al., 1977; Clement and Harrison, 2000; Tripathi and Harrison, 2003). Gamma radiation is also produced during the beta and alpha decay of radioactive substances. Cosmic rays and natural and cosmogenic radionuclides are air ionizing factors due to gamma emission. Small ions, especially in the situation of artificial radioactivity, can be produced as a result of simultaneous radiation of different types.

The radioactive elements carried into the atmosphere are due to the numerous natural and anthropogenic phenomena. Natural are volcano eruption, radon and thoron exhalation from the ground, or radioactive dust particles coming as salt particles from the oceans or dust of radioactive rocks.

Since the discovery of radioactivity, the continuous increase of the number of pollution sources, like industrial use of radioactive materials or development of nuclear industry, fuel reprocessing, nuclear weapon tests in the air or underground explosions, and nuclear accidents (even if they have limited local range only) contribute to the registered electricity parameters.

The present study aims at explaining the role of artificial radioactivity in GEC using atmospheric electricity sensors and electrostatic analyzes. Simultaneous measurements of atmospheric electric parameters: electric field and air conductivity, radioactive fallout, precipitations, aerosol concentrations and meteorological parameters are presented. Variations of electric field and air conductivity in the presence of artificial ionization sources of various parameters are discussed. We proposed several scenarios of the atmosphere electric state, based on the relative locations of the ionization source.

Section "Instrumentation and Measurements" provides information on our instrumentations and measurement methods. Section "Analysis and Results" describes the electrical state of the atmosphere during global strong ionization incidents and analysis methods. Results are discussed and compiled in sections "Discussion" and "Conclusions."

INSTRUMENTATION AND MEASUREMENTS

Atmospheric electricity parameters have been measured at the Geophysical Observatory at Świder, located in central Poland (52.12 N, 21.24 E) since 1958 (Kubicki et al., 2007).

The atmospheric air conductivity (positive and negative) at the Świder Observatory has been measured at 1 m over the surface with a Gardien counter. The critical mobility of the counter is 1.5×10^{-4} $m^2V^{-1}s^{-1}$. The density of the air-Earth electric current was measured by Wilson antenna with a 0.5 m^2 metal plate. Electric field E_z has been measured by a radioactive collector and rotating dipole field mill at a height of 2 m. The radioactive collector (the activity of about 30 μCi) is placed on a metal rod seated in a heated insulator. The height of the collector above the ground is 2 m. The time constant is 7 s. Comprehensive meteorological observations are also carried out (Kubicki et al., 2016).

The time resolution of atmospheric electricity measurements is now 1 s. At the time of the weapons tests and the Chernobyl accident, continuous measurements were recorded on a paper tape. The condensation nuclei in size range from 5×10^{-9}m to 1×10^{-5}m have been measured with a photoelectric condensation nuclei counter at 6, 12, and 18 UT.

From 2011 at the Świder Observatory the aerosol concentrations in the particle range from 3 nm to 3 μm were measured by ultra-fine condensation counter.

The atmospheric fallout is collected into a steel container with a surface of 0.5 m^2. The time of depositions is 1 week. For dry depositions, a container is rinsed several times with distilled water, which then constitutes the measuring sample. The sample is vaporized and after the evaporation of water the damp remnant is transferred with the help of filter-paper and burned at a temperature not exceeding 500°C. To measure the global beta activity, the total ash mass is taken. Two Geiger-Müller (G-M) counters are used.

ANALYSIS AND RESULTS

Radon and Background Gamma Radiation in Świder Geophysical Observatory

The knowledge of the background radioactive radiation in the place where the electricity of the atmosphere is measured makes it possible to evaluate the global and regional effects.

Based on periodic measurements of the background of gamma and radon radiation, it can be stated that these values are small. The average value of radon concentration measured in May 2017 was 4.7 Bq m^{-3}. No diurnal variability was noticed. The lack of radon variability was supported by the fact that the electric air conductivity measurements showed a minimum in the evening hours. The influence of radon after the decay of the mixed layer would increase the electric air conductivity.

The gamma background radiation from soil and atmosphere is on the level of 2.7×10^{-6} R h^{-1} (1970–1972) (Michnowski et al., 1976; Peñsko et al., 1976). In general, the radon potential in central and northern Poland is very low. There are fine-grained sands, tills and clays in the region of the Świder Observatory. The additional soil permeability is very low (Złotoszewska-Niedziałek, 2012).

The gamma background radiation originates mainly from rocks and soil. Cosmic radiation for gamma rays adds to ionization rate about 2 ion pairs $cm^{-3}s^{-1}$ (Hoppel et al., 1986). Measurements in Świder Observatory do not indicate any significant correlation between gamma radiation dose rate and the electric field, air conductivity and concentrations of condensation nuclei (Peñsko et al., 1976). On the basis of 2 years of measurement of the background gamma radiation, a very low level was found. Short-term incidents of increased gamma radiation have been observed during heavy rain.

Relations between soil emitted γ-rays and the electric field have not been established by us, neither was it done in studies of Lopes et al. (2015) and Barbosa (2020).

Nuclear Weapons Testing

In the years 1958–1965, intensive tests on nuclear weapons were carried out at numerous places in the world. As a result, a significant portion of radioactive debris was injected into the upper troposphere and lower stratosphere. For many years this was a source of radioactivity with a changing intensity with time. The air layer at a height of 15–20 km was strongly ionized in the areas of nuclear weapons tests and a large area of the globe (Machta et al., 1962; Alvarado et al., 2014). One can distinguish two important physical mechanisms of transporting radioactive species to the surface of the earth; atmospheric turbulent mixing in the planetary boundary layer and radioactive fallout at ground level (wet and dry contaminations deposited at ground level). Horizontal transport of radioactive species in the stratosphere is due to jet streams. Depending on the latitude, radioactive contamination can reach thousands kilometers away from the source. The global circulation of the atmosphere causes that the highest concentration of aerosol in the lower stratosphere occurs in low latitudes, and the radioactive material falls into the air at the middle latitudes, i.e., above 30 degrees (Seinfeld and Pandis, 2016). Radioactive pollutants are transported in the stratosphere where jet streams occur. Therefore, the Świder Observatory, due to its geographical location (52 N°), can monitor these processes.

The exchange of air between the stratosphere and troposphere is a slow process. The temperature gradient causes the radioactive molecules to coagulate to aerosol particles. From the theory of coagulation, it follows that the radioactive aerosol has a size of 15–500 nm (Reed et al., 1977; Tripathi and Harrison, 2003). The attachment of radioactive particles to the aerosol of different size and structure is an important physical process that influenced the further transport of radioactive substances to the troposphere and their removal. About 50% of the radioactive products were attached to aerosol particles with a diameter of more than 100 nm (Reed et al., 1977; Grundel and Porstendorfer, 2004). The fallout of a radioactive aerosol from the stratosphere to the troposphere was seasonal, with a maximum in spring due to rainfall.

Figure 1 shows the long-term variations in yearly average of: electric field E_z or potential gradient PG = $-E_z$, electric air conductivity λ_+, radioactive fallout, aerosol (nuclei) concentrations, precipitation, and the number or thunderstorms. Long-term series of E_z measurements take into account the local measurement conditions related to the forest surroundings of the measurement site.

In the years 1958–1965/70, the field E_z was significantly lower (**Figure 1A**) compared to the long-term (1958–2000) average (216 Vm^{-1}). The annual changes of E_z were not that large (100–150 Vm^{-1}), with large changes in electric air conductivity (4–12 × 10^{-15} $\mathrm{Ohm}^{-1}\mathrm{m}^{-1}$) (**Figure 1B**).

Radioactive fallout (**Figure 1C**) caused an increase in ground layer ionization. The generation of ions (free charge) has enhanced electric air conductivity. The precipitation (**Figure 1E**) compared to the aerosol concentrations (**Figure 1D**) was the main transport factor of the radioactive debris from the stratosphere to the ground level. Huzita (1969), reported an increase in ion generation due to an increase in the dry radioactive fallout component, based on observations in Osaka during 1960–1962. The geology of the local measurement site is also important in the analysis of the relationship between artificial air ionization and electric air conductivity.

The electric field E_z in 1958–1968 did not represent changes in the ionosphere potential (Markson, 2007) due to the strong ionization at the ground level. The electric charge at the ionosphere should be demonstrated due to induction in E_z at ground level. From 1968 the fallout was small and almost constant. Electric air conductivity is approximately constant because the additional ionization source (fallout) has ceased. This caused a partial increase in E_z (1968–1978/80) but at the same time E_z response to Vi changes resulting from radioactive substances in the upper troposphere. The high level of air conductivity in the troposphere unlocked changes in the electric field E_z to induction through an electric charge and potential in the ionosphere. This appears to be a global effect, even if not supported by quantitative estimates.

Chernobyl Accident

On 1986 April 27 and 28 there was no cloud cover in the Świder Observatory. These were days with strong thermal convection. On the 26th of April 1986, a nuclear accident happened at about 01:23 UT in Chernobyl, Belarus, about 600 km from the Świder Observatory located in central Poland (52.12 N, 21.24 E).

On the next day, April 27, a sharp increase in the electric positive and negative conductivity was observed around 15 UT (**Figure 2**), and a maximum was reached at approximately 21 UT. During this period, the ground-level electric field significantly decreased and remained at a low level. The ratio of the positive to negative conductivity (**Figure 3**) was smaller than 1 (Warzecha, 1987). Similar effects have been observed in other locations over Europe (Israelsson and Knudsen, 1986; Sheftel et al., 1994). From April 27 to May 7 (**Table 1**) higher values of the electric air conductivity were observed at noon, due to convective exchange of the air and vertical transport of radioactive material from higher layers of the atmosphere to the ground. Due to the low wind speed and low dust concentration, the re-suspension of the radioactive material did not occur at that time. The mass of air contained very large amounts of radioactive elements: Cs-137, Cs-134, Sr-90, I-131, which emit β and γ radiation. This could be the reason for the change in the occurrence of a lower value of positive air conductivity as compared to the negative one, with their simultaneous increase (Sheftel et al., 1994). Such a situation has never been observed before. The increase in ionization causes a simultaneous increase in positive and negative air conductivity. Based on previous observations, the following changes in air conductivity can be distinguished. An increase in the aerosol concentration causes a simultaneous decrease in positive and negative air conductivity. During the occurrence of electrified clouds or precipitation, the changes in positive and negative air conductivity may have opposite directions.

During most of the days in May 1986, the variations of the electric field and air conductivity had large fluctuations in time and amplitude. Such a character of variations was absent before the accident. The average electric air conductivity in May 1986 was three times its normal May value (in 1981–1985), and the electric field in May 1986 was four times lower than the May average, and still three times lower than the average in August 1986 (Warzecha, 1991). These abnormal variations have been a result of the Chernobyl accident. The atmospheric electricity at Świder Observatory began returning to its pre-accident values in September 1986 (Kubicki et al., 2013).

The air mass containing radioactive substances passed over the measuring site around 19 UT (**Figure 2**). A simultaneous increase in the positive and negative electrical air conductivity indicates the presence of ionization sources. Free electric charges have been generated. The field dropped below 100 Vm^{-1}. At the time of the Chernobyl accident, the main factor affecting the atmospheric

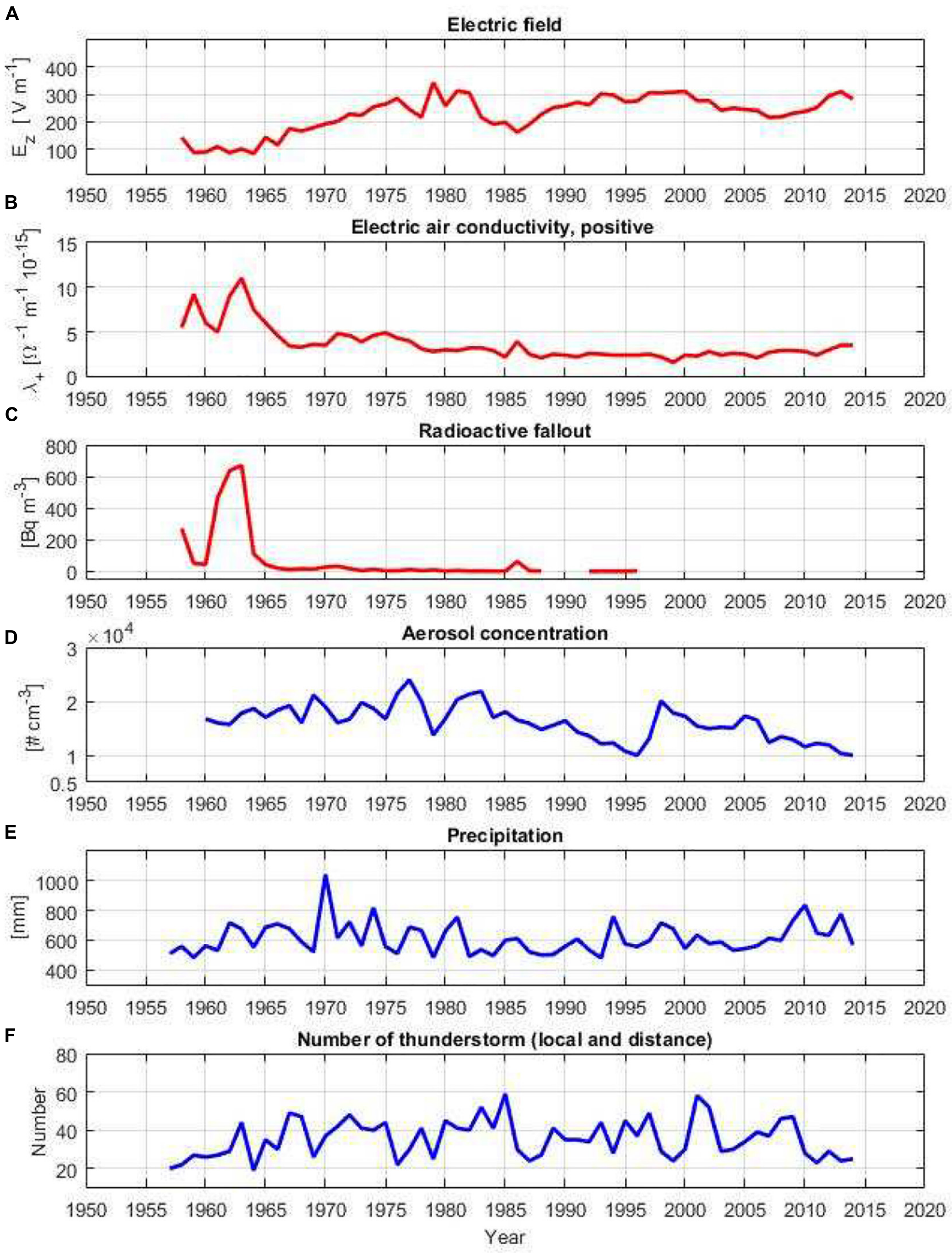

FIGURE 1 | Long term (1958–2014) variations: **(A)** electric field E_Z or potential gradient (PG = $-E_Z$), **(B)** electric air conductivity λ_+, **(C)** radioactive fallout, **(D)** aerosol concentrations, **(E)** precipitation, **(F)** number of thunderstorms. We use the convention that the downward directed, i.e., fair weather, atmospheric electric field is positive (*z*-axis is directed downward) (Krehbiel et al., 2014).

electricity is not the precipitation but the presence of a strong ionization source in dry contamination of air.

An interesting incident was the occurrence of the distant thunderstorm on April 30, when the ground surface ionization was very strong. Electric field registration showed the occurrence of lightning discharges. Low time recording resolution, appropriate for fair weather measurements (paper tape speed) did not allow for the analysis of the nature of the discharges and the electrical structure of the thundercloud to determine a possible influence of the high air conductivity of the surface layer. Nuclear lightning issues have been widely discussed, e.g., by Williams et al. (1988).

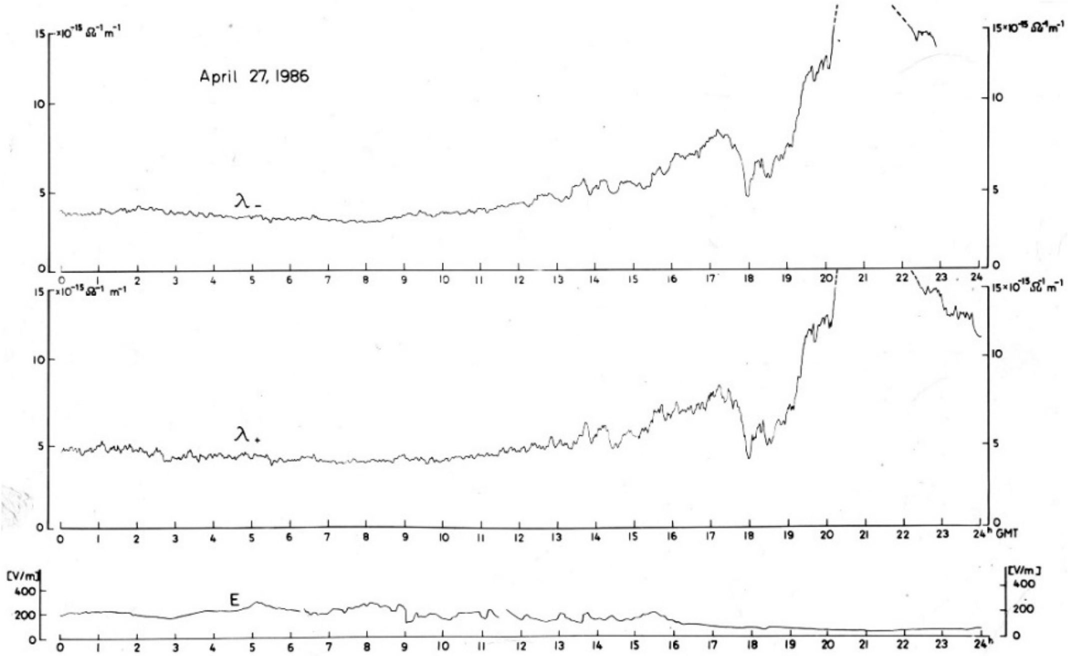

FIGURE 2 | Curves of the electric conductivity negative λ_- and positive λ_+ polarity and electric field strength E_z on April 27, 1986 (in UT). There was no precipitation, no low clouds. The convection in the boundary layer of the atmosphere vanishes about 19 UT. Adapted from Warzecha (1987).

Fukushima Accident

The nuclear accident in Fukushima, Japan, happened on 12 March 2011 as a result of damage by a 9.0 earthquake and tsunami (Newsletter on Atmospheric Electricity, 2011). **Figure 4** shows the trajectories of air masses that reached Poland on March 22 and 23. The Polish National Central Laboratory for Radiological Protection (CLOR)[1], informed that the radioactive material arrived over Poland on 23 March and the level of concentrations of some radioactive isotopes was insignificantly increasing until 1st April and then their level decreased rapidly. The detailed situation in Europe has been presented e.g., by Bossewa et al. (2012); Kirchner et al. (2012).

By the end of March, Fukushima radionuclides have been identified in various locations in the Northern Hemisphere, but they did not significantly affect the electrical parameters of the atmosphere measured in remote locations (Comprehensive Nuclear-Test-Ban Treaty Organization [CTBTO], 2011; Dragović et al., 2020). In Poland, the concentration of radionuclides was very low. I–131 was detected, its concentration being around several hundred μBq m^{-3}. The backward trajectories were calculated for heights of 0, 1, and 5 km (**Figure 4**) and 1.5, 2, 4 km (not presented). On this basis, it can be concluded that on March 22–23, air masses on an altitude of 4–5 km from the regions of Fukushima reached the Świder Observatory at an altitude of 1–4 km. The air mass came into the planetary boundary layer. At that time, the influence of radioactive contaminations on the atmospheric electricity was possible.

Indeed, significant effects of radiations on atmospheric electricity have been observed at Kakioka, Japan (Takeda et al., 2011; Dragović et al., 2020). A reliable estimate of such effects requires atmospheric electricity parameters observed during fair weather.

There were more than 10 fair weather days in March 2011 at the Świder Observatory, seven before the accident (1–4, 7, 9, 11) and seven after the accident (12, 21, 22, 23, 27, 30, and 31).

The fair weather conditions used in our analysis mean there is no rain, drizzle, snow, hail, fog, no local or distant thunderstorms, the lower cloudiness is less than 4/8 (8/8 is overcast), and when the wind velocity is less than 6 m/s, the electric field value was not negative (Kubicki et al., 2016). Additionally, fair weather days were selected in terms of eliminating the influence of aerosol. This criterion concerned: aerosol concentration ($<$20–25 × 10^3 particles cm^{-3}), electric field strength ($<$1,000 Vm^{-1}), analysis of simultaneous variability of electric field and air conductivity.

The daily averages of the field observed on all fair weather days in March 2011 are shown in **Figure 5**. The days with very low aerosol concentration were selected. The E_z data have been normalized (blue line) to the values of the daily average, to select artifacts caused by the Fukushima accident.

Diurnal variations of the electric field and the positive and negative air conductivity observed at Świder Observatory on fair weather days, 22nd and 23rd of March, when radioactive air masses reached Poland are shown in **Figures 6**, **7**.

Long-term average of positive conductivity of March is 2.44×10^{-15} $Ohm^{-1}m^{-1}$ (std, 0.97) and for April it is 3.16×10^{-15} $Ohm^{-1}m^{-1}$ (std, 1.39). In 2011, the air

---

[1] www.clor.waw.pl

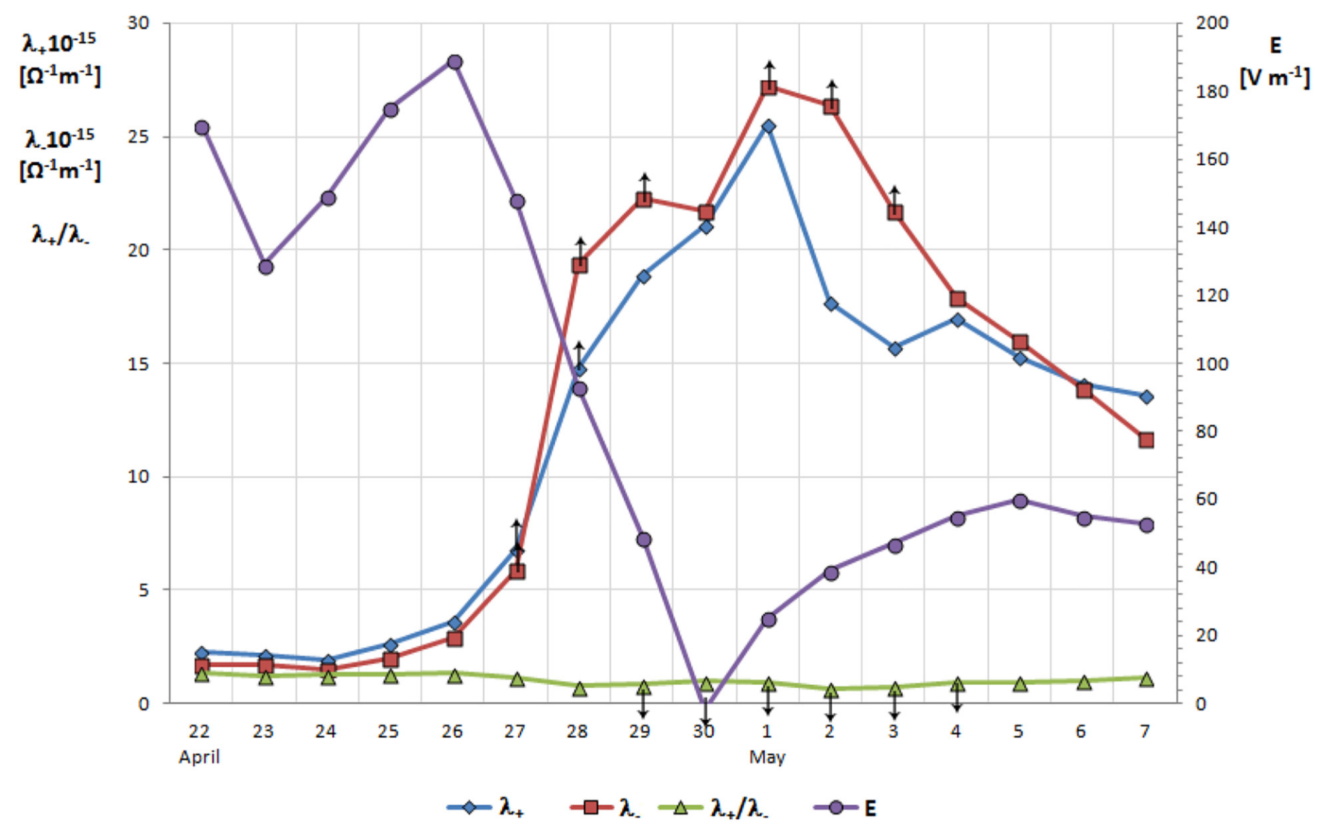

FIGURE 3 | Electric field E_z, positive λ_+ and negative λ_- air conductivity and ratio λ_+/λ_- from 22 April to 7 May 1986 measured in Świder Observatory. Daily average values are presented. The arrows indicate that the real value was greater than the presented value. It results from the adopted average method for measurement data processing in a situation where the course of the measured parameter was greater (for a time less than 20 min) than the range of the measuring instrument.

TABLE 1 | Daily values of electric parameters and meteorological observations from April 22 through May 7, 1986, at Świder Observatory: λ_+ – positive electric air conductivity, λ_- – negative electric air conductivity, E_z – electric field strength, N – number of concentration nuclei, D – air dust; S – cloudiness; C – type of clouds; Ws – wind speed; P – precipitation.

Date 1986	λ_+ 10^{-15} [ohm^{-1}m^{-1}]	λ_- 10^{-15} [ohm^{-1}m^{-1}]	E_z [V m^{-1}]	N 10^3 [cm^{-3}]	D [mg m^{-3}]	S [0–10]	C	Ws [ms^{-1}]	P [mm]
April 22	2.3	1.7	170	37.9	0.020	2.7	Ci	2.0	.
23	2.1	1.7	129	55.3	0.054	4.0	Ci	2.0	.
24	1.9	1.5	149	27.7	0.062	4.0	Ci, Cu	1.7	.
25	2.6	2.0	175	26.0	0.018	5.0	Cu, Ci, Ac	3.0	.
26	3.6	2.9	189	17.6	0.011	5.3	Ci	4.0	.
27	>6.8	>5.9	148	11.7	0.016	1.0	Ci, Cc	3.3	.
28	>14.8	>19.4	93	13.0	0.074	0.0	.	1.3	.
29	18.9	>22.3	49	10.6	0.037	1.7	Cu	2.0	.
30	21.1	21.7	<−2	11.9	0.008	4.0	Cu, Ac	1.7	0.0
May 1	25.5	>27.2	25	7.0	0.015	3.3	Cu, Ci	1.7	.
2	17.7	> 26.4	39	19.4	0.024	0.0	.	2.0	.
3	15.7	> 21.7	47	15.4	0.019	0.3	Cu	1.3	.
4	17.0	17.9	55	11.8	0.012	0.3	Ac, Ci	2.7	.
5	15.3	16.0	60	14.6	0.013	0.0	.	2.3	.
6	14.1	13.9	55	14.5	0.009	2.3	Cu, Ci	2.7	.
7	13.6	11.7	53	18.7	0.019	0.3	Ci	2.7	.

The dust D (PM, particulate matter, the mixture of solid particles and liquid droplets suspended in air) was measured by the reference method. The following cloud type classification was used: Cu, cumulus; Ac, altocumulus; Ci, cirrus; Cc, cirrocumulus.

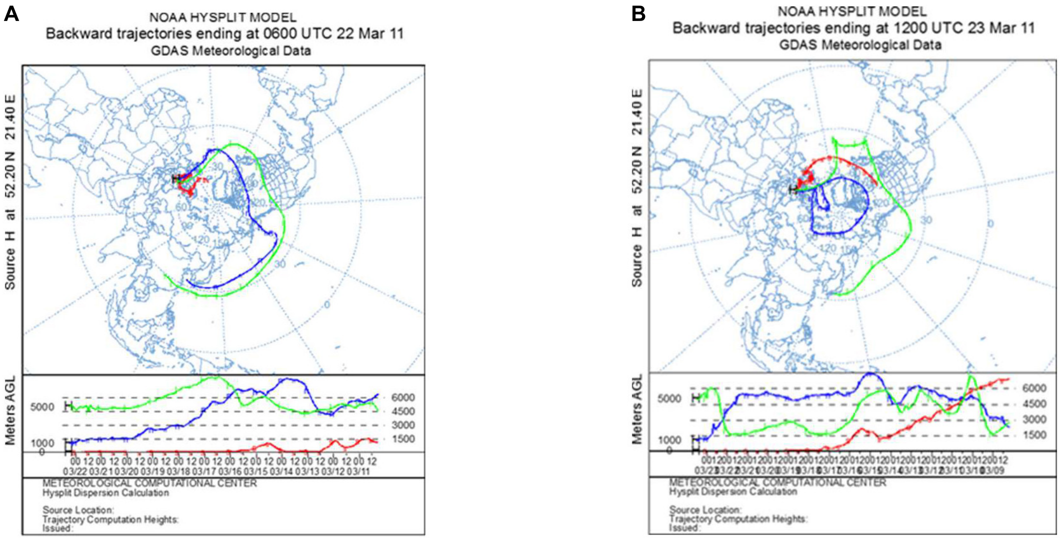

FIGURE 4 | Backward trajectory arrived at the Świder Observatory area on the **(A)** 22nd and **(B)** 23th of March (https://www.ready.noaa.gov/HYSPLIT.php).

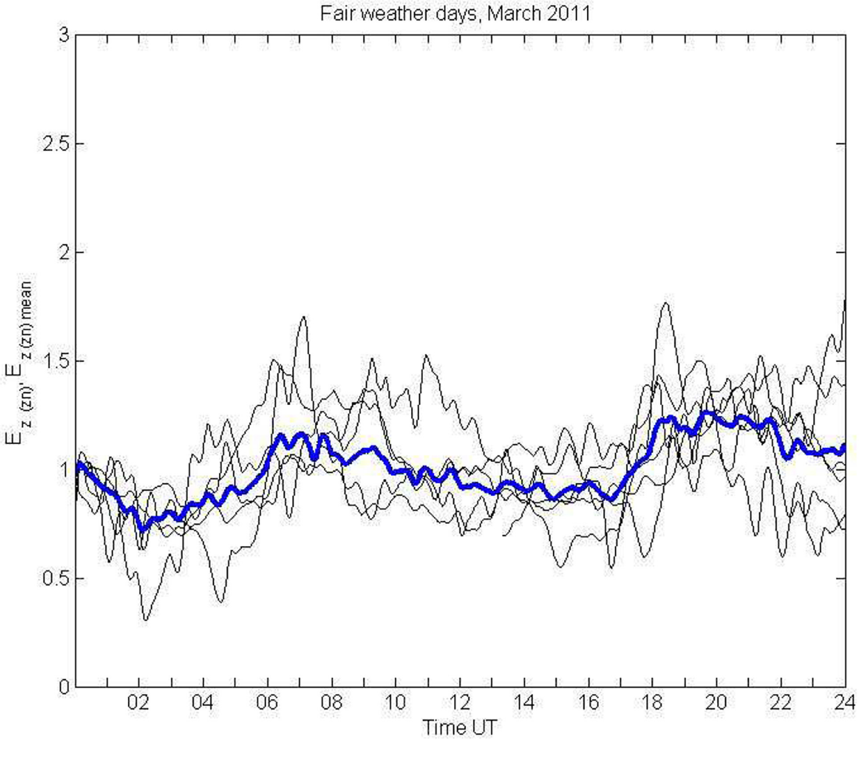

FIGURE 5 | Fair weather electric field E_z in March 2011. The daily averages of the field observed on all fair weather days in March 2011 (black lines). E_z normalized, mean-(blue line), represents norm, to compare with selected daily changes of E_z. The convention that the downward directed, i.e., fair weather, atmospheric electric field is positive was used (*z*-axis is directed downward).

conductivity averages for March and April were 1.79 and 2.5×10^{-15} $\mathrm{Ohm}^{-1}\mathrm{m}^{-1}$, respectively.

Long term average (1965–2000) of electric field of March is 300 Vm^{-1} (std, 85 Vm^{-1}), and for April it is 217 Vm^{-1} (std, 61 Vm^{-1}) (Kubicki et al., 2007). In 2011, the electric field averages for March and April were 320 and 231 Vm^{-1}, respectively. All monthly averages given above have been calculated for fair weather conditions.

On the basis of the presented values of positive electric air conductivity and electric field intensity it can be stated that the

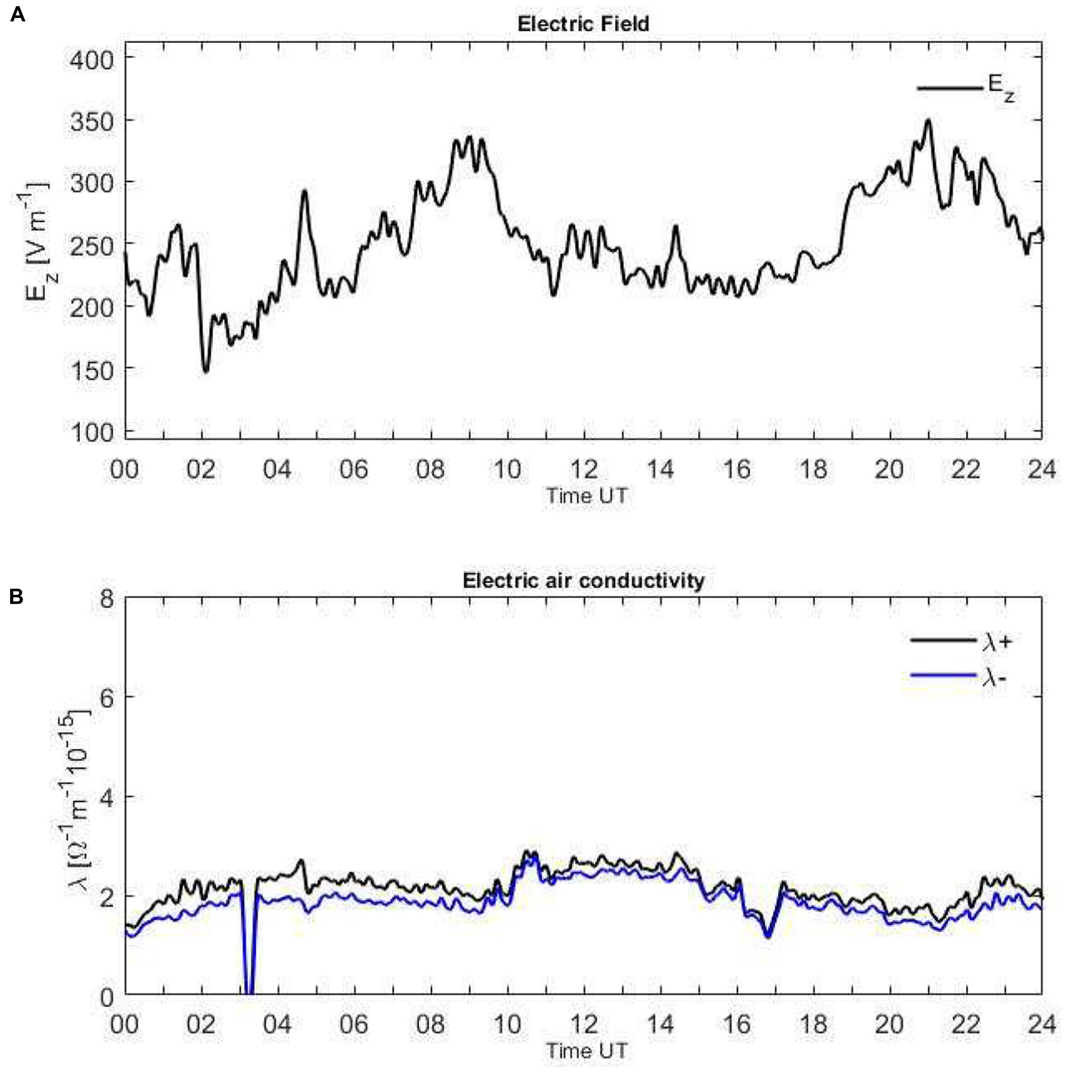

FIGURE 6 | Diurnal variation of the **(A)** electric field E_Z in fair weather and **(B)** positive λ+and negativeλ- conductivity measured at Świder Observatory on 22 March 2011. The decrease in the conductivity between 3 and 4 UT is due to instrument calibration. The 1-min values of E_z and air conductivity have been smoothed using a 15-min. high-pass Butterworth filter. Short rainfall (3 min) appeared at 3:09 UT, the average wind speed was 1.7 m s^{-1}, aerosol measured at 6, 12, and 18 UT was 8, 6, and 8 × 10^3 particles cm^{-3}.

Fukushima accident was not reflected in the monthly statistics recorded at the Świder Observatory. Diurnal variation of the electric field E_z and air conductivity were also not disturbed (**Figures 6**, **7**).

After the Chernobyl incident, the elevated monthly averages continued for 3 months and caused an increase in the annual average value in 1986 in comparison with the previous year, i.e., 1985 and the next year 1987 (**Figure 1**).

Based on the report of the Central Laboratory for Radiological Protection in Warsaw, it can be concluded that recorded concentrations of radioactive debris in Poland were tens of thousands times lower in Fukushima than in the Chernobyl accident (see text footnote 1).

The Fukushima accident did not affect the fair weather atmospheric electricity parameters measured at the ground surface at the Świder Observatory, despite the presence of a small concentration of radioactive substances.

DISCUSSION

Small positive and negative ions are the main factor determining the electrical conductivity of air. Alpha, beta, and gamma rays can produce ion-pairs. In situations of artificially increased radiation, radioactive electric charging of aerosols occurs (Clement and Harrison, 1992). Radioactive pollutants are ionizing the air primarily through beta and indirectly gamma decays. The most efficient radioactive sources that affect the electric air conductivity are radioactive elements that emit alpha radiation, e.g., Am-241 and Ra-226. Due to their size, energy and

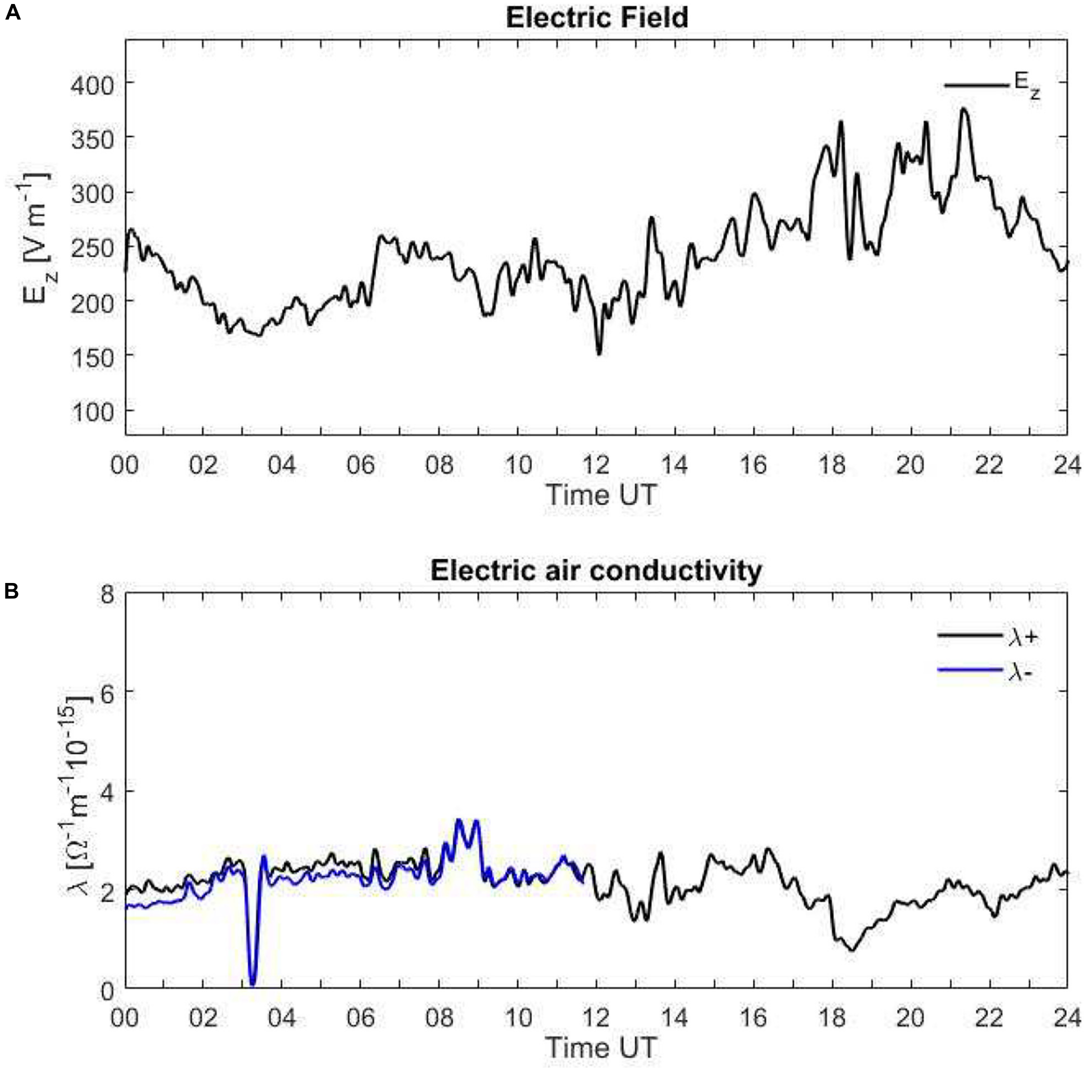

FIGURE 7 | Diurnal variation of the **(A)** electric field E_Z in fair weather and **(B)** positive $\lambda+$ and negative λ_- conductivity measured at Świder Observatory on 23 March 2011. The decrease in the conductivity between 3 and 4 UT is due to instrument calibration. The 1-min values of E_Z and air conductivity have been smoothed using a 15-min. high-pass Butterworth filter. There was no rainfall, the average wind speed was 2.0 m s^{-1}, aerosol concentration measured at 6, 12, and 18 UT was 8, 48, 29 × 10^3 particles cm^{-3}.

electric charge, the alpha particles can be considered an important source of air ionization (e.g., Seran et al., 2017). They induce a significant increase in the electrical conductivity of air but are unlikely to be a component of artificial radioactive releases.

Negative ions have higher mobility than positive ions (Gunn, 1954). The beta minus radiation that occurred during the Chernobyl incident could have caused a significant increase in the concentration of negative small ions compared to positive small ions. As a result, the negative electric air conductivity was greater than the positive air conductivity (**Figure 3**).

Charged aerosol through electrostatic interactions can influence microphysical processes in clouds and air (e.g., Clement and Harrison, 1995). The most important parameters that represent the cloud or radioactive aerosol are: particle concentrations and size, type of ionizing radiation, disintegration rate and height of the cloud base, particle properties and cloud lifetime. The charging mechanism of radioactive cloud or radioactive aerosol particles is very complicated (e.g., Greenfield, 1956; Reed et al., 1977; Clement and Harrison, 1995).

The presence of a radioactive cloud or aerosol is associated with the formation of a region of very high electric air conductivity in a less conductive atmosphere. However, the space charge of the radioactive cloud or air mass may be zero (Holzer, 1972; Greenfield, 1956), and the electric field and air conductivity changes in the lower atmosphere may also be insignificant (Harris, 1955). In a long time (several minutes), the electric charge is not accumulated in the radioactive cloud or air mass. There is also no separation of positive and negative electric charges. The electric dipole (negative charge on top) moment in the cloud is very small and occurs for a few minutes.

During this time perturbations of the air-Earth current may occur (Holzer, 1972).

Depending on the location of the ionizing radiation source in relation to the measuring sensors, several classes of the description of ionizing radiation impact on electric field, current and electric air conductivity measured at the earth's surface can be distinguished:

1. The ionization source is located at the atmospheric electricity measuring site or a short distance from it. The mechanism of interaction of radioactive substances is based on the direct ionization of the ground layer in which the sensors are located. Small ions are produced, radioactive particles attach to the aerosol particles, and a free electrical charge is created.

   The precipitation causes the radioactive substance to be transported to the ground surface, and locally significantly affects the parameters of the atmospheric electricity. This is presented on long-term courses in 1960–1967 (**Figure 1**).
2. The radiation source is initially located at a considerable distance from the measuring site. There is a cloud of radioactive aerosol moving with air masses. A space charge associated with a mass of cloud or an aerosol may cause a change in the electric field at ground level due to electrostatic induction (bound charge) in distant site measurements. This mechanism can be similar, e.g., to the changes in the electric field as a thunderstorm and electrified cloud [e.g., *cumulonimbus* (Cb), *nimbostratus* (Ns), *stratus* (St)] approaches. The influence of a radioactive source on the electric air conductivity is detected when small ions (free charge) reach the Gardien counter.

Based on the measurements on 27 April 1986 (Chernobyl accident), it can be concluded that the approaching radioactive aerosol had its signal in the course of the electric field from about 09 UT (**Figure 2**). The E_z fluctuations may indicate a change in the space charge of a moving air mass. Between 15 and 16 UT, the cloud already covered the measurement site at the Świder Observatory, E_z dropped significantly and remained at a low level for the next several hours. The appearance of the air mass has been well detected by E_z. Radioactive fallout (dry depositions) by mixing the atmosphere will increase the electric air conductivity in air column.

The electric field was very small and remained in this state even after the cloud had passed. Increasing ionization in the entire boundary layer of the atmosphere (e.g., 0–2,000 m) increases the electric air conductivity and significantly reduces the column resistance (unit resistance column of air). The resistance of the 2 km high air column is 60% of that of the earth-ionosphere air column (e.g., Chalmers, 1967). The ionized air layer reduced the electric field (was a short circuit).

Radioactive contaminations can affect the E_z distribution in fair weather areas. Around 17 UT, April 27 (**Figure 2**), there was a significant decrease followed by an increase in the electric air conductivity, probably caused by an increase in aerosol concentration (at 18 UT it was 20.4×10^3 particles cm^{-3}, while at 12 UT it was 9.8×10^3 particles cm^{-3}), the decline of vertical air mixing, and perhaps also a change in the wind direction from SSE to ESE. The aerosol in comparison with ionization as the main factor producing changes in the electrical air conductivity.

From 09 to 16 UT the relationship between E_z and λ it was not inversely proportional. A similar mechanism was described by Holzer (1972) during nuclear explosions.

3. The ionizing source is located very high, i.e., on the border of the troposphere and the stratosphere, in areas of high air conductivity. Also, this conductivity has been significantly increased by the presence of radioactive substances. This probably caused an increase in the electric charge and the potential V_i of the higher layers, i.e., the ionosphere. Markson (2007) shows that the increase of V_i was due to nuclear weapons testing. The V_i change did not manifest itself in the electric field E_z (**Figure 1A**) in an annual time scale. The main reason for the increase in V_i was the enhancement in global thunderstorm activity and an increase in the electric current between the top of the thunderstorm cloud and the ionosphere (Markson, 2007). Radioactive fallout increased the conductivity at the ground level, causing E_z to fall. The presence of two highly conductive air layers (separated by a layer of small conductivity) in the upper troposphere and surface layer may have caused the GEC to be not synchronized, i.e., global V_i and E_z in the Świder Observatory have not corresponded to each other. A detailed description of the presented dependencies would require the use of modeling for the establishment of a vertical air conductivity profile for nuclear weapons testing.

During movement of the contaminated air mass in the form of an aerosol or a cloud to the measuring site, the induced charge in the measuring sensor of the electric field or current density (field mill, Wilson antenna) will appear earlier than the ions (free charge) represented by the electric air conductivity and measured by a Gardien counter.

At the time of the Chernobyl accident, when the air mass of radioactive substances with advection transport reached the vicinity of the Świder Observatory, it caused a mild increase in electric air conductivity and a decrease in the electric field. There was no rain, and strong vertical turbulent exchange disappeared in the evening. Maximum values of conductivity were reached between 21 and 22 UT when the vertical turbulent air exchange vanishes. On this basis, it can be concluded that the radioactive aerosol has generated small ions in the entire planetary boundary layer. The forming stable boundary could additionally increase the concentration of small ions at the earth's surface. The ionization source was the homogeneous air mass with significant space dimensions; therefore, the electric field did not have a spike that had been described by Yamauchi et al. (2012).

The resultant electrical structure of the cloud with the radioactive material should not show any separation areas of electric charges. Analyzing the ionization mechanism for this case, it can be concluded that the electrification processes are intermittent and last very short compared to the disintegration rate (Greenfield, 1956). Based on measurements of the electric field near the ground, it is possible to detect the front of a radioactive cloud or aerosol air mass. If the air-Earth current measurements were carried out, one would expect bipolar pulses related to the time change in space charge radioactive cloud. The model of the radioactive cloud or aerosol with polarized electric charges (positive at the top, negative at the bottom) was proposed by Yamauchi et al. (2018) to analyze spikes in the course of an electric field during the Fukushima accident. During nuclear explosions, nuclear lightning can occur on the electric charge distribution in a strong electric field (Holzer, 1972; Williams et al., 1988). There may be a negative charge at the top of the thundercloud (Holzer, 1972), unlike the proposed model of Yamauchi et al. (2018).

When considering air ionization processes, the role of atmospheric aerosol should be taken into account. The condensation nuclei CN measured in the Świder Observatory include solid and liquid particles; gas form was not detected. The concentration nuclei during nuclear tests changed little in the years 1960–1965 and amounted to about 20×10^3 particles cm^{-3}. At the time of the Chernobyl accident, the concentration of condensation nuclei between April 25 and May 7 varied from 26 to 19×10^3 particles cm^{-3}. The effect of the aerosol on the electric field and air conductivity was not significant (**Figure 3**), as its concentration has not exceeded the critical value.

Radioactive substances attach to small aerosol particles, <500 nm (Tripathi and Harrison, 2003). Based on the measurements of the aerosol concentration, it can be concluded that there was no important increase in the number of condensation nuclei.

From 1986 April 27 to May 7 there was no precipitation, no low-level cloud, the wind was low, 1–3 ms^{-1}. The radioactivity contaminated aerosol was transported to the surface level in turbulent mixing. Particle re-suspension was rather absent, due to the low wind speed and the small dust concentration. On May1–3, the electric air conductivity was maximum ($15–27 \times 10^{-15}$ $Ohm^{-1}m^{-1}$) and E_z was very low, 25–47 Vm^{-1}. The aerosol concentration was 7–20×10^3 cm^{-3}. Ionization of the ground level would be much higher if atmospheric precipitation occurred. The ion effect on aerosol formation with nuclei is complicated for the high ionization conditions. Pulinets (2009) suggested that the ionization enhancement first increases ion concentrations but after several days it activates to increase small-size aerosol and decreases the electric air conductivity. This physical mechanism was not confirmed based on measurements carried out at the Świder Geophysical Observatory.

Enhanced conductivity in the upper troposphere and stratosphere as a result of a nuclear test, caused an increase of ionosphere potential, Vi. Markson (2007) reported the enhancement of ionosphere potential V_i by approximately 40% in the 1960–1965 period in nuclear weapons testing. The measured values of V_i have achieved maximum, 500 kV. By 1966, V_i has decreased to the value before nuclear testing and changed $+-10\%$ of the mean.

Markson (2007) suggested that the enhanced lightning activity due to increased ionization in the upper troposphere and stratosphere caused enhanced GEC source current between upper thundercloud and the ionosphere. Israelsson et al. (1987) has not reported an increased occurrence of lightning flashes in Sweden after the Chernobyl accident. The number of thunderstorms in the Świder Observatory in 1960–1967 is shown in **Figure 1F**. The maximum number of thunderstorms occurred in the same years (1962–1963) as the maximum of radioactive fallout. Finding a physical connection between the increased thunderstorm activity in 1963 and the radioactive fallout, would require additional studies on a monthly time scale, including comprehensive meteorological data.

The role of high ionization in the formation of atmospheric discharges was analyzed by Israelsson et al. (1987), and Williams et al. (1988). Indeed, the enhanced GEC source current could elevate the value of ionospheric potential and also enhance the lightning activity.

The global reach of the nuclear tests, Chernobyl, and Fukushima accident, is difficult to establish based on measurements in one location. However, it is possible to analyze the mechanism of the interaction of radioactive substances on the electrical state of the atmosphere. Nuclear testing could be considered a global phenomenon due to the location of the source of the radioactive substances in the stratosphere.

Related to natural ionization, the impact of these incidents may only be significant in some sites around the globe (e.g., Hoppel et al., 1986; Harrison et al., 2020).

It should also be noted that the interpretation of the parameters of atmospheric electricity based on direct measurements nearby a strong ionization source zone can be very difficult (e.g., accident in Fukushima, highly ionized air mass at the Świder Observatory). The application of Ohm's law may be limited due to the non-linear electrical properties of the atmosphere.

CONCLUSION

In the analysis of the mechanism of interaction of high radioactive contamination with the atmospheric electricity, parameters of the ionization source and its location in relation to the measuring site play an important role. The formation and charging of radioactive aerosols is an important issue for the presented studies. The properties of the aerosol at the measurement site may modify the level of air ionization and electricity.

The particles of the radioactive aerosol can have a significant electric charge. The beta and gamma radiation produced by radioactive substances generates most of the space charge in the form of small ions (free charge). The most effective transport of radioactive substances to the earth's surface is provided by atmospheric precipitation (wet component of radioactive fallout).

Relations between V_i and E_z for the conditions of occurrence of highly ionized layer at the ground level (due to radioactive fallout) and the border of the atmosphere and stratosphere (the case nuclear tests) require studies using models. Measurements of atmospheric electricity parameters E_z and λ are necessary and air-Earth current J_z is also useful to analyze the impact of air radioactivity during significant incidents (accident, nuclear tests, nuclear power failures, and release from fuel reprocessing plants), as these parameters allow a comprehensive electrostatic interpretation.

DATA AVAILABILITY STATEMENT

The raw data supporting the conclusions of this article will be made available by the authors, without undue reservation.

AUTHOR CONTRIBUTIONS

MK contributed to the data processing, data curation and data analysis, and manuscript writing. BM-L and AO contributed to the data analysis and manuscript writing. All authors equally cooperated in the research presented in this publication.

FUNDING

This work was financed by the Institute of Geophysics of the Polish Academy of Sciences with a subsidy from the Ministry of Education and Science, and supported by COST Actions CA15211, ELECTRONET. The HYSPLIT Model, Air Resources Laboratory NOAA, was gratefully acknowledged.

REFERENCES

Alvarado, J., Steinmann, P., Estier, S., Bochud, F., Haldimann, M., Froidevaux, P., et al. (2014). Anthropogenic radionuclides in atmospheric air over Switzerland during the last few decades. *Nat. Commun.* 5:3030.

Barbosa, S. (2020). Ambient radioactivity and atmospheric electricity field: a joint in an urban environment. *J. Environ. Radioact.* 219:106283. doi: 10.1016/j.jenvrad.2020.106283

Blicard, L. (1965). *Action of Radioactivity and Pollution Upon Parameters of Atmospheric Electricity, Problems of Atmospheric and Space Electricity*. Amsterdam: Elsevier.

Bossewa, P., Kirchner, G., De Cort, M., Vries, G., Nishev, A., and Felice, L. (2012). Radioactivity from Fukushima Dai-ichi in air over Europe; part 1: spatio-temporal analysis. *J. Environ. Radioact.* 114, 22–34. doi: 10.1016/j.jenvrad.2011.11.019

Chalmers, J. A. (1967). *Atmospheric Electricity*, 2nd Edn. New York: Pergamon Press.

Chamberline, AC. (1991). *Radioactive Aerosol*. New York: Cambridge University Press.

Clement, C. F., and Harrison, R. G. (1992). The charging of radioactive aerosols. *J. Aerosol Sci.* 23, 481–504. doi: 10.1016/0021-8502(92)90019-r

Clement, C. F., and Harrison, R. G. (1995). "Electrical behavior of radioactive aerosol in the environment," in *Proceedings of the IXth Annual Conference*, Norwich.

Clement, C. F., and Harrison, R. G. (2000). Enhanced localized charging of radioactive aerosols. *J. Aerosol Sci.* 3, 363–378. doi: 10.1016/s0021-8502(99)00064-6

Comprehensive Nuclear-Test-Ban Treaty Organization [CTBTO] (2011). *(Fukushima) Related Measurements by the CTBTO*.

Dragović, S., Yamauchi, M., Aoyama, M., Kajino, M., Petrović, J., Ćujić, M., et al. (2020). Synthesis of studies on significant atmospheric electrical effects of major nuclear accidents in Chernobyl and Fukushima. *Science Total Environ.* 733:139271. doi: 10.1016/j.scitotenv.2020.139271

Greenfield, S. M. (1956). Ionization of radioactive particles in the free air. *J. Geophys. Res.* 61, 27–33. doi: 10.1029/jz061i001p00027

Griffiths, D. J. (2017). *Introduction to Electrodynamics*. Cambridge: Cambridge University Press.

Grundel, M., and Porstendorfer, J. (2004). Differences between the activity size distributions of the different natural radionuclide aerosol in outdoor air. *Atmos. Environ.* 38, 3723–3728. doi: 10.1016/j.atmosenv.2004.01.043

Gunn, R. (1954). Diffusion charging of atmospheric droplets by ions, and the resulting combination coefficients. *J. Meteorol.* 11, 329–347.

Harris, D. L. (1955). Effects of radioactive debris from nuclear explosions on the electrical conductivity of the lower atmosphere. *J. Geophys. Res.* 60, 45–52. doi: 10.1029/jz060i001p00045

Harrison, R. G., Nicoll, K. A., Ambaum, M. H. O., Marlton, G. J., Aplin, K. L., and Lockwood, M. (2020). Precipitation modification by ionization. *Phys. Rev. Lett.* 124:198701.

Holzer, R. E. (1972). Atmospheric electrical effects of nuclear explosions. *J. Geophys. Res.* 77, 5845–5855. doi: 10.1029/jc077i030p05845

Hoppel, W. A., Anderson, R. V., and Willet, J. C. (1986). *Atmospheric Electricity in the Planetary Boundary Layer 1986, Studies in Geophysics, the Earth's Electrical Environment*. Washington, D. C: National Academy Press.

Huzita, A. (1969). "Effect of radioactivity fallout upon the electrical conductivity of the lower atmosphere," in *Planetary Electrodynamicseds* eds S. C. Coroniti and J. Hughes (New York: Gordon and Breach Science Publisher).

Israel, H. (1973a). *Atmospheric Electricity*, vol. I. Jerusalem: Israel Program for Scientific Translations.

Israel, H. (1973b). *Atmospheric Electricity*, Vol. II. Jerusalem: Israel Program for Scientific Translations.

Israelsson, S., and Knudsen, E. (1986). Effects of radioactive fallout from a nuclear power plant accident on electrical parameters. *J. Geophys. Res.* 91, 909–911.

Israelsson, S., Shutte, T., Pisler, E., and Lundquist, S. (1987). Increased occurrence of lightning flashes in Sweden during 1986. *J. Geophys. Res.* 92, 996–998.

Kirchner, G., Bossewa, P., and De Cort, M. (2012). Radioactivity from Fukushima Dai-ichi in air over Europe; part 2: what can it tellus about the accident? *J. Environ. Radioact.* 114, 35–40. doi: 10.1016/j.jenvrad.2011.12.016

Krehbiel, P., Mazur, V., and Rison, W. (2014). Standardizing the sign convention for atmospheric electric field measurements. *Newsletter Atmospheric Electricity* 25, 4–7.

Kubicki, M., Baranski, P., Odzimek, A., Michnowski, S., and Myslek-Laurikainen, B. (2013). Effects of the chernobyl and Fukushima nuclear accidents on atmospheric electricity parameters recorded at Polish observation stations. *Geophys. Res. Abstracts* 15:EGU2013-4715-1.

Kubicki, M., Michnowski, S., and Mysłek-Laurikainen, B. (2007). "Seasonal and daily variations of atmospheric electricity parameters registered at the geophysical observatory at Świder (Poland) during 1965–2000," in *Procedings of the 13th Conference on Atmospheric Electricity*, Beijing.

Kubicki, M., Odzimek, A., and Neska, M. (2016). Relationship of ground-level aerosol concentration and atmospheric electric field at three observation sites in the Arctic, Antarctic and Europe. *Atmos. Res.* 17, 329–346. doi: 10.1016/j.atmosres.2016.03.029

Lopes, F., Silva, H. G., Barias, S., and Barbosa, S. M. (2015). Preliminary results on soil-emitted gamma radiation and its relation with the local atmospheric electric field at Amieira (Portugal). *J. Phys. Confer. Ser.* 646:012215.

Machta, L., List, R. J., and Telegards, K. A. (1962). Survey of radioactivity fallout from Nuclear test. *J. Geophys. Res.* 67, 1389–1400.

Markson, R. (2007). The global circuit intensity: its measurement and variation over the last 50 years. *Bull. Am. Meteorol. Soc.* 88, 223–241. doi: 10.1175/bams-88-2-223

Michnowski, S., Peñsko, J., and Gwiazdowski, B. (1976). Some results on the measurements of radioactive, atmospheric electricity and meteorological parameters at the geophysical observatory at Publs. *Inst. Geophys. Pol. Acad. Sci.* 99, 53–63.

Mironova, I. A., Aplin, K. L., Arnold, F., Bazilevskaya, G. A., Harrison, R. G., and Krivolutsky, A. A. (2015). Energetic particle influence on the Earth's Atmosphere. *Space Sci. Rev.* 194, 1–96.

Mysłek-Laurikainen, B., Matul, M., Mikolajewski, S., Trzaskowska, H., and Kubicki, M. (2011). The airborne radioactivity and electrical properties of ground level air. *Nucleonika* 46, 195–197.

Newsletter on Atmospheric Electricity (2011). *Newsletter on Atmospheric Electricity*. Vol. 22 No 2 Nov 2011, pp 7–8.

Peñsko, J., Michnowski, S., Warzecha, and Gwiazdowski, B. (1976). Radioactivity, atmospheric electricity and meteorological elements measurements at Swider geophysical observatory. *Przegl. Geofiz.* 21, 281–286.

Pierce, E. T. (1972). Radioactive fall-out and secular effects in atmospheric electricity. *J. Geophys. Res.* 77, 482–487. doi: 10.1029/jc077i003p00482

Pulinets, S. A. (2009). Physical mechanism of the vertical electric field generation over active tectonic faults. *Adv. Space Res.* 44, 767–773. doi: 10.1016/j.asr.2009.04.038

Reed, L. D., Jordan, H., and Gieseke, J. A. (1977). Charging of radioactive aerosol. *J. Aerosol Sci.* 8, 457–463. doi: 10.1016/0021-8502(77)90038-6

Seinfeld, J. H., and Pandis, S. N. (2016). *Atmospheric Chemistry and Physics: From Air Pollution to Climate Change*. Hoboken, NJ: John Wiley & Sons, INC.

Seran, E., Godefroy, M., Pili, E., Michielsen, N., and Bondiguel, S. (2017). What we can learn from measurements of air electric conductivity in 222Rn-rich atmosphere, Earth and Space. *Sciences* 4, 91–106. doi: 10.1002/2016ea000241

Sheftel, V. M., Bandilet, O. I., Yaroshenko, A. N., Chernyshev, A. K., Few, A. A., and Geis, P. B. (1994). Space-time structure and reasons of global, regional, and local variations of atmospheric electricity. *J. Geophys. Res.* 99, 10797–10806. doi: 10.1029/93jd02857

Takeda, M., Yamauchi, M., Makino, M., and Owada, T. (2011). Initial effect of the Fukushima accident on atmospheric electricity. *Geophys. Res. Lett.* 38:L15811.

Tripathi, S. N., and Harrison, R. G. (2003). "Radioactive aerosols in the environment," in *Proceedings of the 12th International Conference on Atmospheric Electricity*, Versailles.

Warzecha, S. (1987). Results of atmospheric electricity measurements at Swider after the Chernobyl nuclear power plant accident. *Publs. Inst. Geophys. Poly. Acad. Sci.* 198, 137–151.

Warzecha, S. (1991). Long lasting radioactive contamination at Swider and its effect on the atmospheric electricity parameters after the Chernobyl nuclear power plant accident. *Publs. Inst. Geophys. Poly. Acad. Sci.* 238, 187–191.

Williams, E. R., and Mareev, E. (2014). Recent progress on the global electrical circuit. *Atmospheric Res.* 13, 208–227. doi: 10.1016/j.atmosres.2013.05.015

Williams, E. R., Cooke, C. M., and Wright, K. A. (1988). The role of electric space charge in nuclear lightning. *J. Geophys. Res.* 93, 1679–1688. doi: 10.1029/jd093id02p01679

Yamauchi, M. (2012). Secondary wind transport of radiative materials after the Fukushima accident. *Earth Planets Space* 64, e1–e4.

Yamauchi, M., Takeda, M., and Nagamachi, S. (2018). Effect of enhanced ionizing radiation on the cloud electricity after the Fukushima nuclear accident. *Earth Planets Space* 70:48.

Yamauchi, M., Takeda, M., Makino, M., Owada, T., and Miyagi, T. (2012). Settlement process of radioactive dust to the ground inferred from a the atmospheric electric field measurements. *Ann. Geophys.* 30, 49–56. doi: 10.5194/angeo-30-49-2012

Złotoszewska-Niedziałek, H. (2012). Structural uplift as geological barrier in the transport of pollution to the groundwater in the vicinity of the landfill site. English translation of Wypiętrzanie strukturalne jako bariera geologiczna dla migracji zanieczyszczeń wód podziemnych w rejonie składowiska odpadów. *Acta Sci. Pol. Architektura* 11, 49–56

Conflict of Interest: The authors declare that the research was conducted in the absence of any commercial or financial relationships that could be construed as a potential conflict of interest.

frontiers
in Earth Science

ORIGINAL RESEARCH
published: 10 June 2021
doi: 10.3389/feart.2021.646277

Anthropogenic Noise and Its Footprint on ELF Schumann Resonance Recordings

V. Tritakis[1,2]*, I. Contopoulos[1], C. Florios[1], G. Tatsis[3], V. Christofilakis[3], G. Baldoumas[3] and C. Repapis[1,2]

[1] Research Center for Astronomy and Applied Mathematics Academy of Athens, Athens, Greece, [2] Mariolopoulos-Kanaginis Foundation for Environmental Research, Athens, Greece, [3] Electronics-Telecommunications and Applications Lab, University of Ioannina, Ioannina, Greece

A set of various short artificial *disturbances from rifle firings, car engine operation, car radio, shakings of the apparatus, etc.*, were generated deliberately *near our ELF recording stations* in order to identify their footprint on the recordings of atmospheric electromagnetic radiation in the Schumann resonance (SR) band (from about 2–50 Hz). *Such disturbances simulate anthropogenic noises from hunters, hikers, campers, etc., which may occur in a remote-isolated ELF recording station.* We expect that our work will assist fellow scientists to differentiate between artificial signals created from anthropogenic activity and real signals attributable to geophysical phenomena.

Keywords: Schumann resonance, ELF, anthropogenic impacts, quality of data, track down of ELF noises

Edited by:
Konstantinos Kourtidis,
Democritus University of Thrace,
Greece

Reviewed by:
Tamás Bozóki,
Geodetic and Geophysical Institute
(MTA), Hungary
Janusz Mlynarczyk,
AGH University of Science
and Technology, Poland

****Correspondence:***
V. Tritakis
vassos44@gmail.com

Specialty section:
This article was submitted to
Atmospheric Science,
a section of the journal
Frontiers in Earth Science

Received: *25 December 2020*
Accepted: *24 February 2021*
Published: *10 June 2021*

Citation:
Tritakis V, Contopoulos I,
Florios C, Tatsis G, Christofilakis V,
Baldoumas G and Repapis C (2021)
Anthropogenic Noise and Its Footprint
on ELF Schumann Resonance
Recordings.
Front. Earth Sci. 9:646277.
doi: 10.3389/feart.2021.646277

INTRODUCTION

Schumann resonances (SRs) have gained great interest in the last 20 years. The reason is the recent identification of several correlations between SR activity and geophysical, even biological phenomena. For readers who are not familiar with SR, we briefly mention that these are extremely low frequency (ELF) atmospheric electromagnetic waves in the frequency band of 2–50 Hz. They are characterized by a set of spectral modes centered around 7.8, 14, 21, 28, and 35 Hz. SRs are quasi-stationary electromagnetic waves created in the spherical cavity between the earth's surface and the lower layers of the ionosphere. This spherical cavity is a natural waveguide that acts as an electromagnetic resonance cavity in the ELF band. The primary sources of SR are lightning discharges which emit electromagnetic radiation in a very wide range of frequencies. These signals are, in turn, amplified by the natural waveguide between the surface of the earth and the lower layers of the ionosphere, creating the resonances that were *studied theoretically* for the first time by the German physicist W. Schumann (1952) and *confirmed experimentally* by Balser and Wagner (1960, 1962).

Since the beginning of the 21st century, the important publications of Williams (1992, 2005) triggered a great shift in the interest of the scientific community toward the practical applications of SR. Williams reported how SR variations could be a sensitive measure of temperature fluctuations in the tropical atmosphere related to the lightning flash rate.

A strong correlation between SR intensity and the global surface temperature at latitude intervals that exceed ± 45° was also found by Sekiguchi et al. (2006). Concerning the local conditions in the greater geographic area of Greece, the work of Nastos et al. (2014) stands out.

They studied the *spatio*temporal analysis of lightning activity over Greece for 1 year using data from the Greek meteorological service. Furthermore, Proestakis et al. (2016) studied the association between lightning activity and aerosols in the Mediterranean region. Tatsis et al. (2016, 2020a) also *studied* SR correlations with local and global lightning centers.

Several other articles relating SR with earthquakes, biology, and other applied sciences have also appeared. An increase in SR

FIGURE 1 | North and South Observational Sites in Greece connected with a yellow line. *An extra site is also shown in Mount Penteli close to Athens where a set of tests were performed*.

FIGURE 2 | Photos of the North **(left)** and South **(middle)** SR installations. Also shown is the testing site on Mount Penteli *near suburb of Athens Drafi* **(right)**.

intensity was observed before the 2004 Mid-Niigata Prefecture earthquake and the 2007 Noto Hantou earthquake which was followed by a decrease after the occurrence of the earthquakes, implying a connection between SR and earthquake activity (Ohta et al., 2009). Extreme electromagnetic events (EEEs) that may be described as an increase *of* intensity in the frequency range around 20–25 Hz, as well as a shift of its peak frequency, have been detected before and after several medium-magnitude earthquakes in Northern Greece (Christofilakis et al., 2019; Florios et al., 2019, 2020). Similar results were observed during the 1999 Taiwan earthquake (Hayakawa et al., 2005, 2008; Xinyang et al., 2013).

Informative wide range reviews about this new branch of Seismo-electromagnetism have been published by Hayakawa and Molchanov (2007); Petraki et al. (2015), and Pulinets and Ouzounov (2016).

The main point of this article is to describe common incidental "noises" that may be introduced by anthropogenic activities in order to identify and exclude them from the raw recordings. For this reason, we performed tests during two different dates, in two

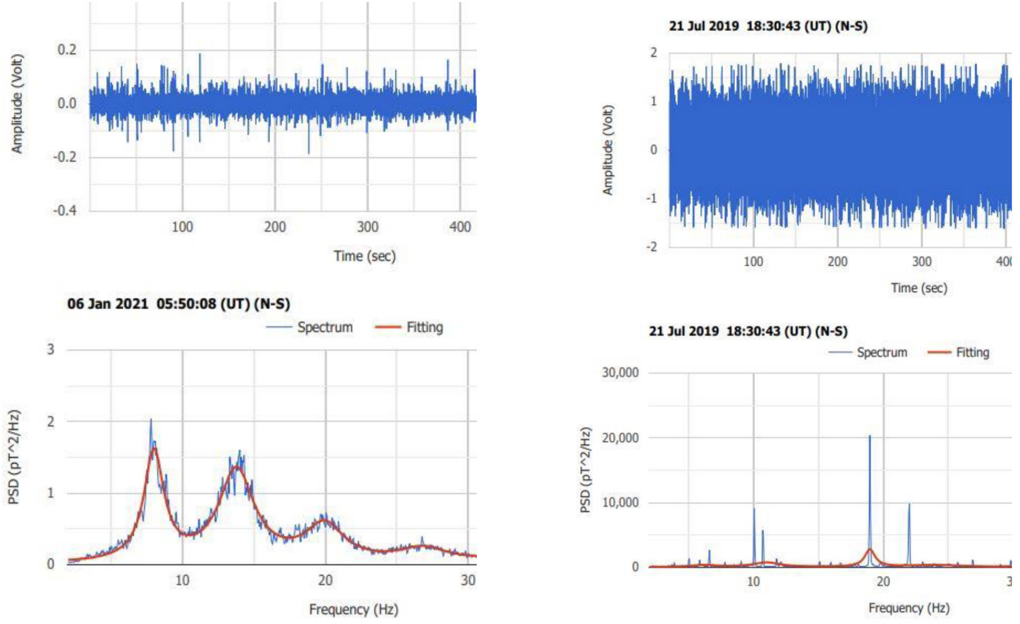

FIGURE 3 | Measurements recorded under quite different conditions. A "clean" typical SR spectrum received under ideal conditions **(left)**, and a spectrum received under improper conditions with strong electromagnetic interference in the ELF band **(right)**.

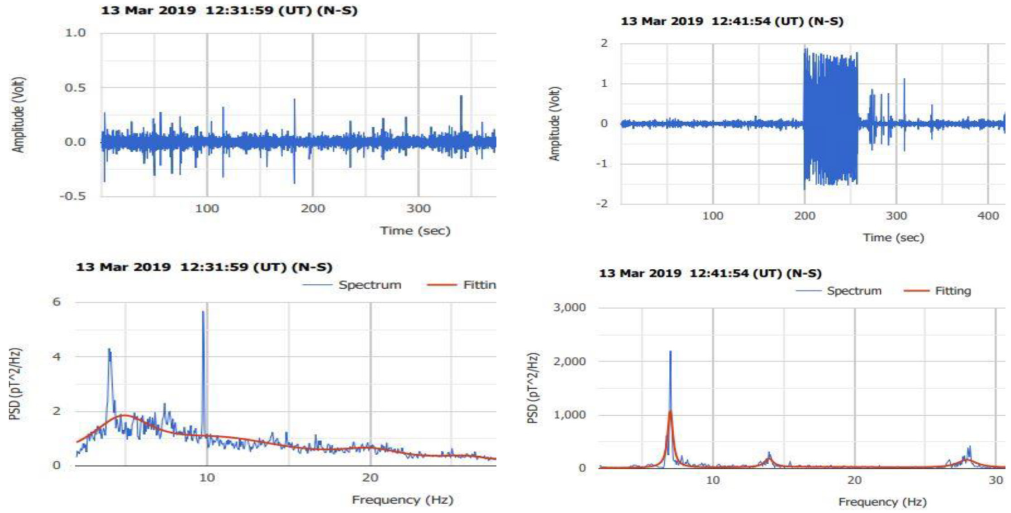

FIGURE 4 | Car engine footprint on the raw data **(right panel)**, and recording with the engine not running **(left panel)**.

different places, under different environmental conditions. We hope that our work will contribute to the diagnosis and rejection of incident ELF signals, thus assisting fellow scientists with the collection of reliable, good-quality SR data.

OBSERVATION SITES AND HARDWARE

There are two SR recording sites in Greece. The first one is located in the North close to the Greek-Albanian border (39° 54′ 49,8′′N/20° 35′ 26,1′′ E) [hereafter North Observational Site (NOS)] and the second one in the South on top of Mount Parnon (37° 13′18,33′′ N/22° 36′ 42,12′′E) [hereafter South Observational Site (SOS)] in the district of Laconia (**Figure 1**). The technical characteristics and details of the hardware operating at the two sites have been described in detail in previous publications (Tatsis et al., 2015, 2020b; Votis et al., 2018).

The NOS operates since 2016 in a small country-chapel and contains two coils orientated along the N-S and E-W directions, respectively. The SOS operates from the beginning of 2020 near the top of Mount Parnon in a shelter of the Greek Forest

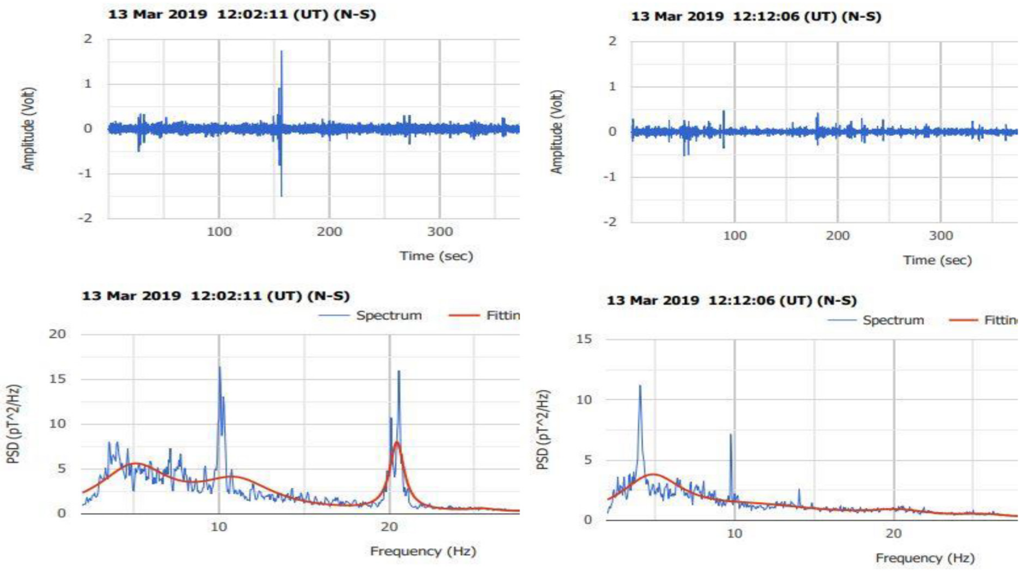

FIGURE 5 | Radio on **(left panel)** and radio off **(right panel)**.

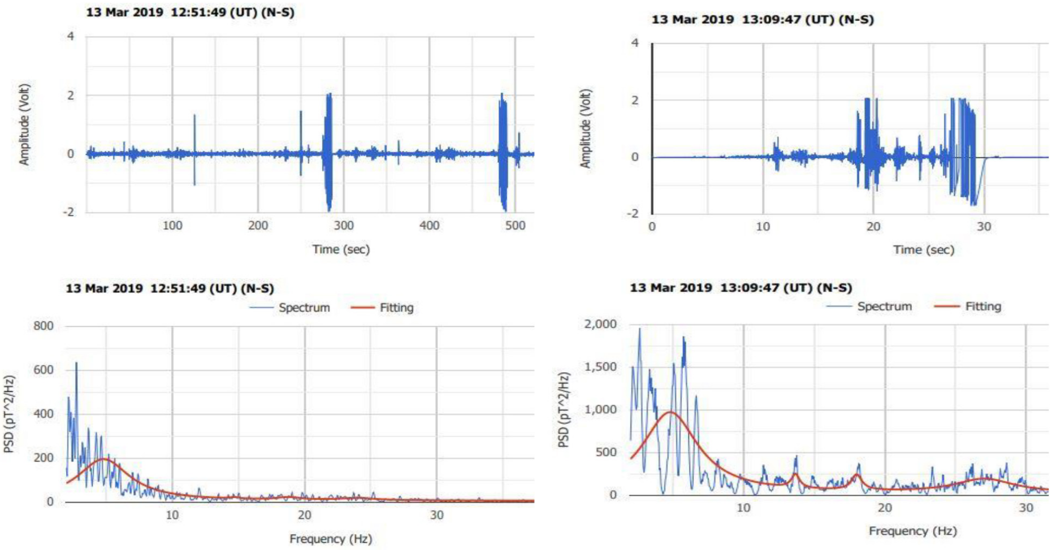

FIGURE 6 | Left panel: two vibrations of the coil by hand in the N-S and E-W directions (narrow stripes). **Right panel**: two additional intensive vibrations in clock and anti-clock directions by hand made 20 min later.

Services and contains, for the time being, only one N-S coil. The generation and recording of incidental "noises" were performed with one N-S coil in two places in two different time periods. The first test took place in an inhabited area outside Athens (Mount Penteli, near Drafi), and the second one in the SOS (**Figure 2**).

The components that were used during the tests were a single *60-cm long* coil with 80,000 turns of 0.24 mm *copper* wire and a logger for digitizing recordings and storing them in 10-min files on a simple SD card. In **Figure 3**, two 10-min files of measurements received under two quite different conditions are depicted. In the left panel, the observation was recorded in the SOS under ideal conditions in a pristine environment without electromagnetic interference (the closest electromagnetic source of disturbance is located 5 km away). The main four SR modes stand out very clearly, thus denoting a high-quality recording. The second observation (right panel) was recorded in a densely inhabited urban area where a very strong signal extending to the limits of the amplifier was received. The two measurements may be considered as reference observations denoting the quality extremes (best and worst) of SR measurements.

GENERATION AND RECORDING OF COMMON ANTHROPOGENIC NOISES

First Test in Drafi

The first systematic recording of various anthropogenic "noises" was performed on the 13th of March 2019 in an inhabited area of Mount Penteli near the suburb of Drafi outside Athens. The closest electric power line was 1 km *away* from the recording site. Descriptive samples of these recordings are shown below.

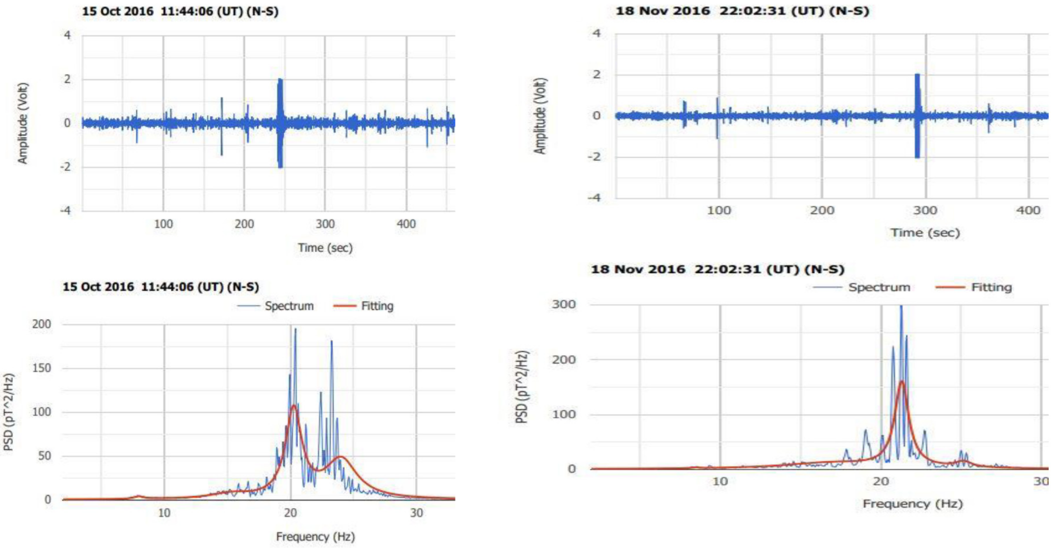

FIGURE 7 | Possible preseismic signals received a few hours before a medium size earthquake at Kalpaki (very close to the NOS site; **left panel**) and Kilkis (about 200 km away; **right panel**).

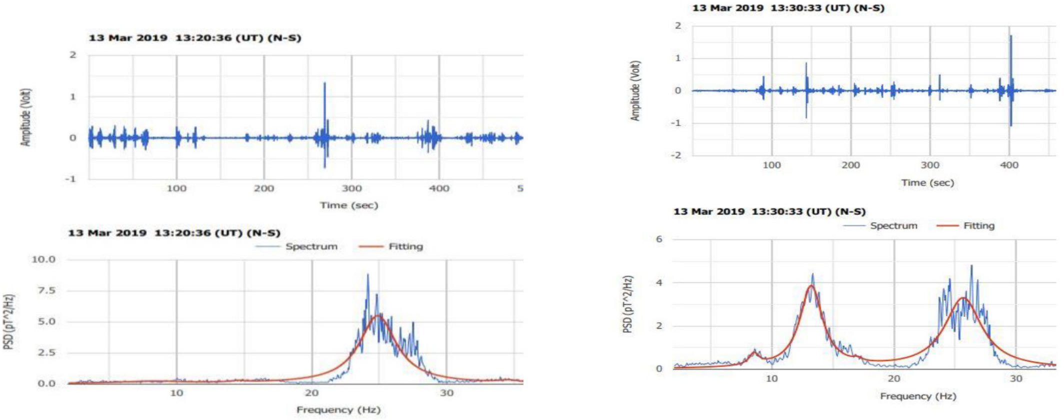

FIGURE 8 | Possible preseismic signal **(left)** and *signal due to* shooting by a two-barrel hunting rifle **(right)**.

In **Figure 4**, we present two successive 10-min recordings of the effect of turning on and off a car engine shown in the right panel. The engine was running *at* high RPMs for several seconds. The left panel corresponds to a "peaceful" recording in which, however, the SR modes do not appear. The main feature of the right panel is a wide strip of a very intense signal that yields a spectrum concentrated in a sharp peak around the first SR mode (lower panel).

In **Figure 5**, we present the effect of the operation of a car radio on the SR recording. A spike in the left panel indicates the turning on/off the radio.

In **Figure 6**, we show the effect of vibrating the coil by hand in two perpendicular directions, N-S and E-W (left panel) as well as in the clock and anti-clock direction (right panel). Two characteristic narrow stripes appear on the left panel, while stripes in the right panel are wider. These are very interesting recordings because similar stripes have been recorded before in relation to nearby seismic activity (see **Figure 7**). An important difference between **Figures 6**, **7** is that the stripes of **Figure 6** do not correspond to a particular spectrum with enhancement in the frequency range of 20–30 Hz like in **Figure 7**. This is a very important detail which allows us to separate preseismic recordings from simple coil vibrations due to other reasons.

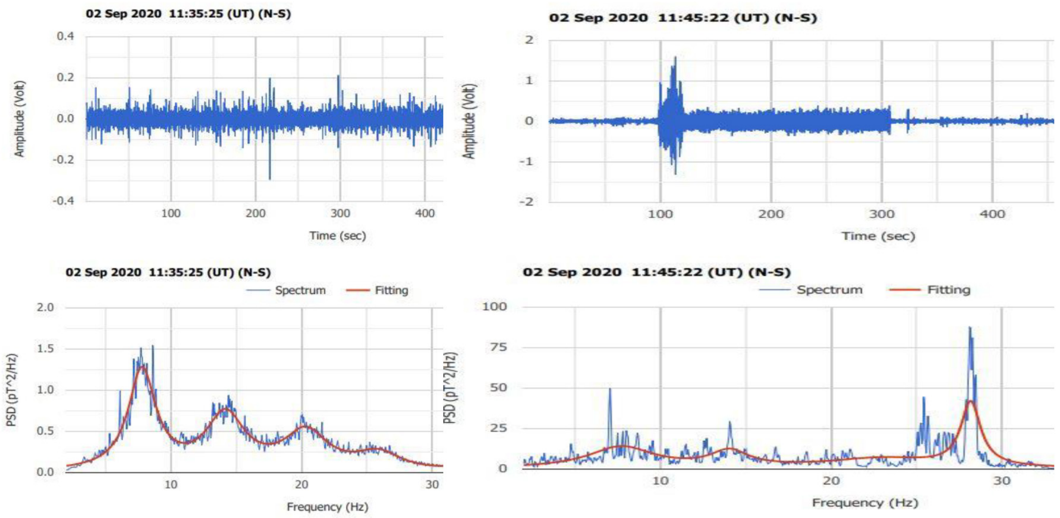

FIGURE 9 | Right panel: the peculiar features are due to a running car engine. **Left panel**: undisturbed SR spectrum 10 min before the car engine ignition.

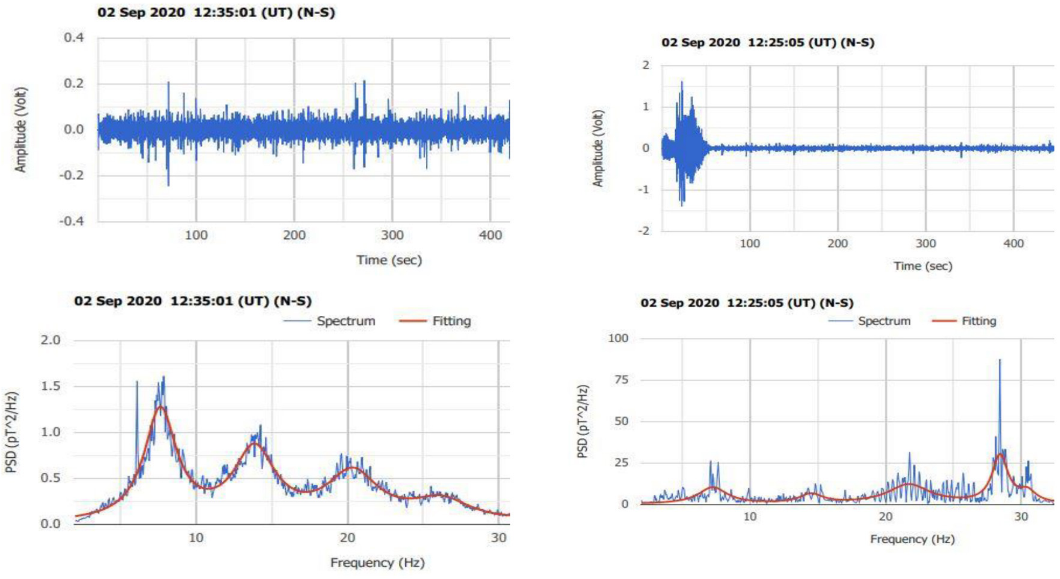

FIGURE 10 | Right panel: the effect of shooting with a hunting rifle. **Left panel**: undisturbed spectrum 10 min after shooting.

A synthetic but very interesting signal is presented is **Figure 8**. In the left panel, we see a clear enhancement of the spectrum in the frequency area 20–25 Hz range similar to those in **Figure 7**. This is the typical form of a possible preseismic signal identified in several cases (Christofilakis et al., 2019; Florios et al., 2019, 2020).

During the next 10 min, we fired a two barrel hunting rifle, as is evident *from* another enhancement in *the range* 10–20 Hz. It is very interesting that the first enhancement *in the range* 20–30 Hz stayed almost unchanged after firing. Six days later, a weak earthquake of magnitude 2.7 in the Richter scale occurred 6 km away from the place of observations. *This* was a serious candidate of preseismic recording in the raw SR data during the measurements shown in **Figure 8**.

In closing this section, we would like to note that a distance of only 1 km is not sufficient to avoid interference from electric power lines. The typical SR modes that appeared during the test performed in Drafi were very weak. This is an indication that SR observations must be performed in more isolated areas.

Second Test in the South Greek Site (SOS)

A second test was performed on the 2nd of September 2020 near the top of Mount Parnon where the measurement conditions are ideal. No electromagnetic source is present within at least 5 km around the site. In **Figure 9**, we present two successive recordings that correspond to a car engine *turning on and off*. In the left panel, a normal SR recording with four main modes around 7.8, 14, 21, and 28 Hz is evident. In the right panel, which is the next 10-min recording, the measurement was severely disturbed by the running car engine. The *turning on* and running of the car engine are obvious in the upper picture of the right panel.

In **Figure 10**, we demonstrate the consequence of firing a two-barrel hunting gun near the SR coil. The left panel of **Figure 10** is the undisturbed period immediately before the shooting. This is a normal recording where the four main modes are present. The next right panel is a disturbed recording after two successive shootings by the hunting gun. **Figures 9**, **10** represent very important tests because passing cars and hunters are very common around SR recording sites which are usually operating in isolated areas like forests and mountains.

In the left panel of **Figure 11**, we present a recording during which we hit the *metal* door and window of the observation site five times with the butt-end of our hunting gun. In the right panel, we present the successive undisturbed file recorded after knocking. We see the immediate recovery of the recording after the disturbance.

In **Figure 12**, we present very interesting details of **Figure 11**. This is a magnified snapshot of the left upper panel of **Figure 11**. It is very impressive how clearly all the action was recorded. At the beginning till the first 100 s, we see a set of five low intensity spikes. They represent the five knocks on the metallic door of the building from which the coil is located several meters away. Between 120 and 130 s, there is another set of five high intensity spikes which represent the five knocks on the *metal* window of the building exactly above the coil. The intensity difference in the two sets may be justified by the distance difference. The second set of knocks is bounded by short spikes that are due to our moving from one point to another around the site.

Interesting Signals Obtained in Extra Tests

Before closing the experimental part of this article, it is interesting to present two additional recordings that were obtained at times

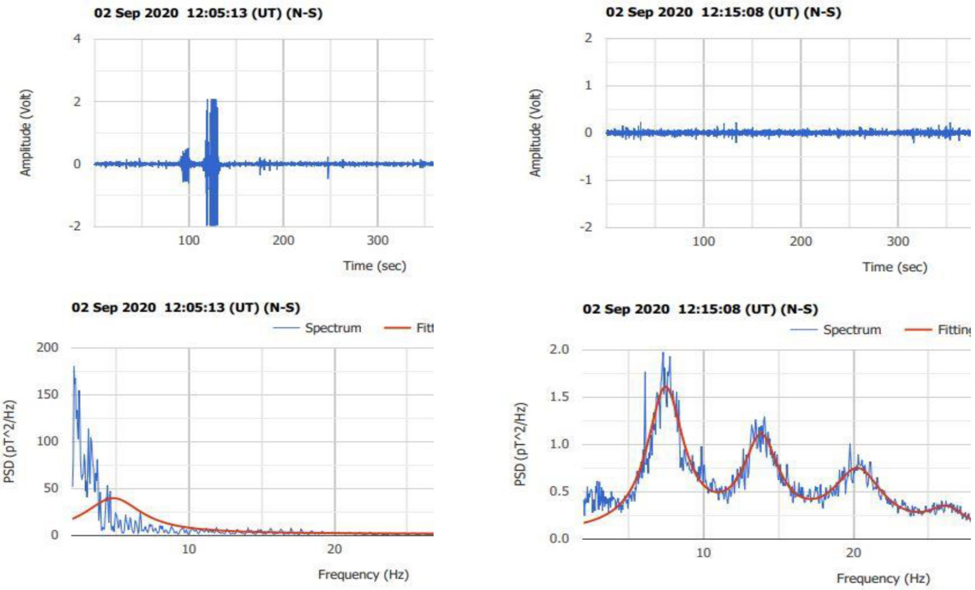

FIGURE 11 | Left panel: peculiar features due to five strong knocks on the door and five more on the window of the building in the south site. **Right panel**: spectrum recovery 10 min later.

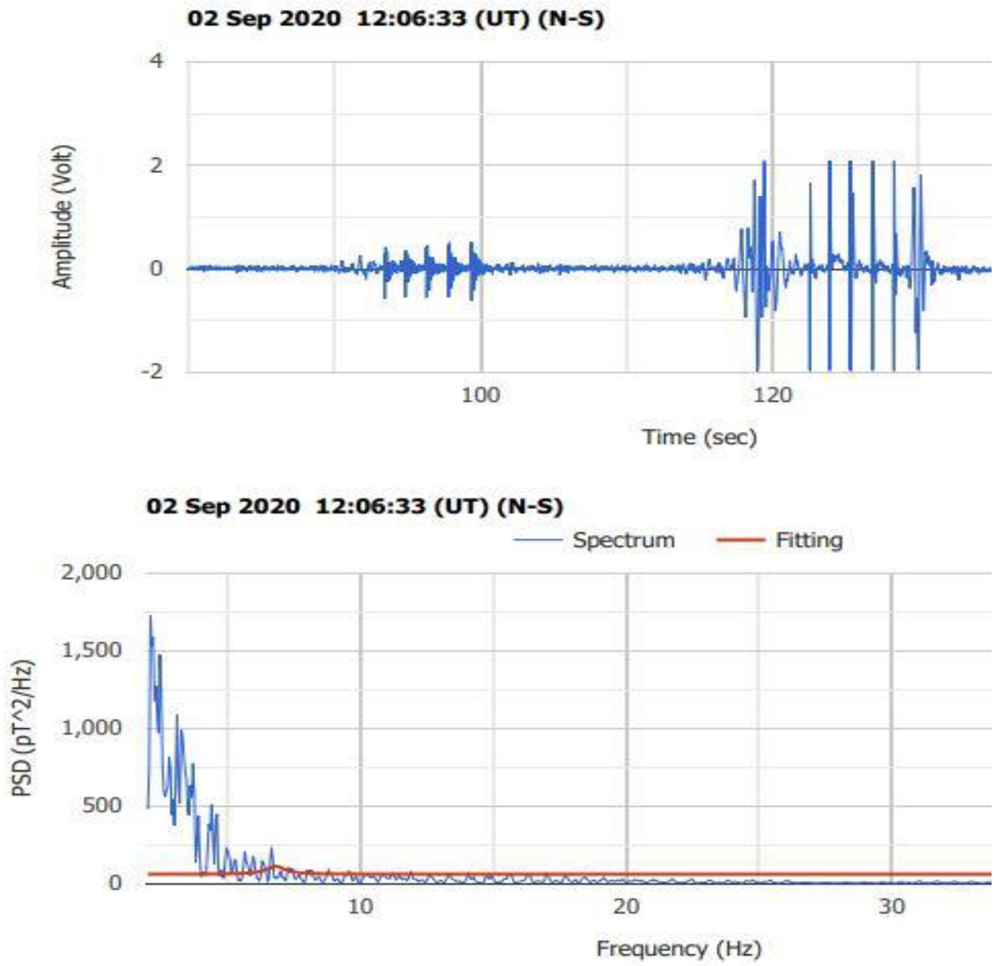

FIGURE 12 | Magnified snapshot of **Figure 11**. The short five knocks on the door and the five strong knocks on the window are evident.

different from the two main tests described above. They represent an example of how easy it is to misinterpret the recorded signals.

In **Figure 13**, we present two recordings collected in different times at a different place. The initial interpretation was that the signal had something to do with nearby operating machinery (pump or something similar). However, after additional indications, we realized that it was due to the fading of the energy supply of the logger. The batteries were almost exhausted, and this made the logger to *malfunction*.

In **Figure 14**, we present an additional case of coil vibration by hand similar to **Figure 6** because of the importance of these signals for the determination *of* preseismic activity. The lack of enhancements in the *frequency range of* 20–30 Hz is again evident.

DISCUSSION

The main benefit gained from the above tests is that the most important and at the same time the most difficult action is to select the proper location for the establishment of an SR observation site. We confirmed something already known, namely, that SR observation sites closer than 1–2 km away from urban areas are inadequate for the recording of good-quality data. In contrast, isolated sites as far away as possible from electromagnetic sources can provide very good quality data. However, two conflicting requirements arise from the above confirmation, which are hard to satisfy simultaneously. The first is that the station must be in a very isolated location as far as possible from anthropogenic activities, urban areas, transportation, and any electromagnetic source like electric power lines, antennas for mobile communication, windmill generators, etc. The above tests showed how sensitive SR signals are to all kinds of electrical and mechanical “noises.” The second requirement is safety. A station in an inhabited area without continuous safekeeping is an easy victim to people looking for valuable things or just metals sold by the kilo. The above conflicting requirements of isolation and safety introduce a series of risks which must be considered. One difficulty related to the isolation requirement is ease of access. A station located in

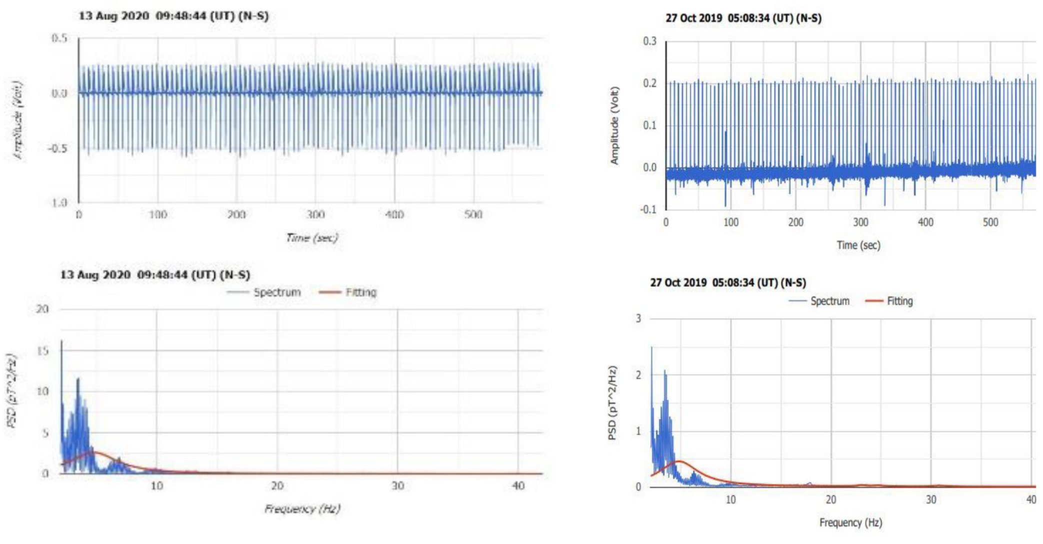

FIGURE 13 | Characteristic recordings when the logger's electrical supply is insufficient due to the exhaustion of batteries.

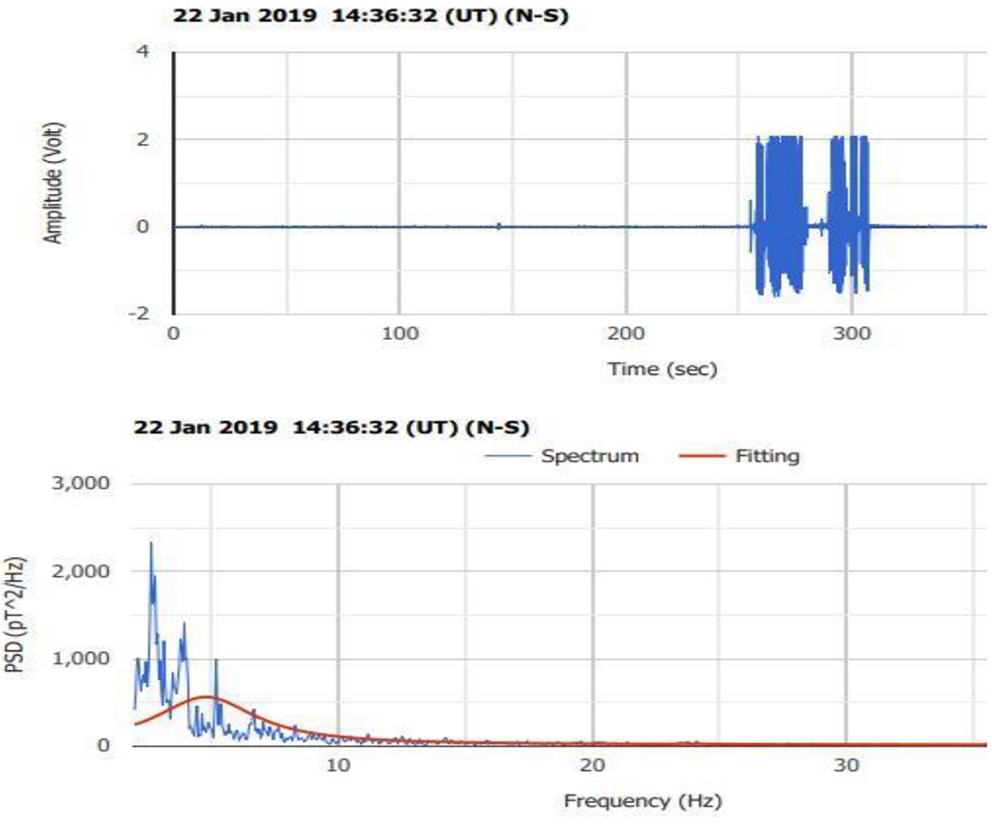

FIGURE 14 | Additional vibration by hand.

an isolated place under the above requirements has, in most cases, difficult access, requires driving for several hours on sometimes dangerous country roads on the sides of mountains, etc. Uninterrupted access to an SR station is necessary because the batteries that provide energy need replacement every 1–2 months, while data stored in memory cards must be collected. Unfortunately, wanton vandalism prohibits the installation of, e.g., exterior solar panels to recharge the batteries, or radio antennas to transmit data in real time. Even the most isolated stations are often accessible by farmers and their agriculture machinery, trucks, hunters, picnickers, pilgrims who visit a nearby country chapel, and other types of visitors and passers-by.

Consequently, it is very important for the data quality of a certain observational site to track down anthropogenic or other "noises" created by animals, strong winds, electric induction on metallic objects, etc.

CONCLUSION

The main conclusion from this work is that SR recordings are very sensitive to parasitic noise caused from anthropogenic activities. Experience on recognizing dummy signals is necessary to reject and remove them from the raw data time series. From this point of view, it is necessary, due to different local physical conditions among sites, to generate templates of common anthropogenic incidental "noises" in each observational site. Nowadays, there is an effort to construct coils with proper filters that would allow to obtain measurements close to urban areas. If successful, this would be a serious advantage that will remove the necessity of establishing isolated stations on mountains and other hard to access locations. For the moment, however, the further the site from anthropogenic activities, the better the quality of the recorded data. The comparison of measurements taken on top of Mount Parnon and in the suburbs of Athens makes clear how important distance from urban areas is for the quality of SR data recordings. A last but not least conclusion coming from the above tests is the confirmation that movements of the coils, by any reason, do not simulate preseismic signals like in **Figure 8** or signals described in previous publications (Christofilakis et al., 2019; Florios et al., 2019, 2020).

DATA AVAILABILITY STATEMENT

The raw data supporting the conclusions of this article will be made available by the authors, without undue reservation.

AUTHOR CONTRIBUTIONS

VT and CR made field experiments and data collection. IC and CF made the evaluation of data. GT, VC, and GB made hardware and software. All authors contributed to the article and approved the submitted version.

ACKNOWLEDGMENTS

We would like to thank the forest service of the Lakonia prefecture, in the town of Sparta, especially the director G. Zakkas and the forest personnel, K. Petrakos, K. Samartzis, N. Sourlis, and K. Tsagaroulis for their valuable contribution in the establishment and the service of our South Observation Site near the village of Vamvakou. We would also like to thank the residents and the ecclesiastical committee of the little town of Doliana in Northern Greece for offering the necessary accommodation needed for the establishment of our North Observation Site. Finally, we would like to address a warm thank you to the Mariolopoulos–Kanaginis Foundation for Environmental Research for its unending support of our activities.

REFERENCES

Balser, M., and Wagner, C. (1960). Observations of earth–ionosphere cavity resonances. *Nature* 188, 638–641. doi: 10.1038/188638a0

Balser, M., and Wagner, C. A. (1962). Diurnal power variations of the Earth-ionosphere cavity modes and their relationship to worldwide thunderstorm activity. *J. Geophys. Res.* 67, 619–625. doi: 10.1029/JZ067i002p00619

Christofilakis, V., Tatsis, G., Votis, G., Contopoulos, I., Repapis, C., and Tritakis, V. (2019). Significant ELF perturbations in the schumann resonance band before and during a shallow mid-magnitude seismic activity in the Greek area (Kalpaki). *J. Atmospheric Solar-Terrestrial Phys.* 182, 138–146. doi: 10.1016/j.jastp.2018.11.009

Florios, K., Contopoulos, I., Christofilakis, V., Tatsis, G., Chronopoulos, S., Repapis, C., et al. (2019). Pre-seismic electromagnetic perturbations in two earthquakes in northern greece. *Pure Appl. Geophys.* 177, 787–799. doi: 10.1007/s00024-019-02362-6

Florios, K., Contopoulos, I., Tatsis, G., Christofilakis, V., Chronopoulos, S., Repapis, C., et al. (2020). Possible earthquake forecasting in a narrow space-time-magnitude window. *Earth Sci. Inform.* 14, 349–364. doi: 10.1007/s12145-020-00535-9

Hayakawa, M., and Molchanov, O. A. (2007). eismo-Electromagnetics as a new field of Radiophysics: electromagnetic phenomena associated with earthquakes. *U.R.S.I. Radio Sci. Bull.* 320, 8–17.

Hayakawa, M., Nickolaenko, A. P., Sekiguchi, M., Yamashita, K., Ida, Y., and Yano, M. (2008). Anomalous ELF phenomena in the Schumann resonance band as observed at Moshiri (Japan) in possible association with an earthquake in Taiwan. *Nat. Hazards Earth Syst. Sci.* 8, 1309–1316. doi: 10.5194/nhess-8-1309-2008

Hayakawa, M., Ohta, K., Nickolaenko, A. P., and Ando, Y. (2005). Anomalous effect in Schumann resonance phenomena observed in Japan, possibly associated with the Chi-chi earthquake in Taiwan. *Annales Geophys.* 23, 1335–1346. doi: 10.5194/angeo-23-1335-2005

Nastos, P. T., Matsangouras, I. T., and Chronis, T. G. (2014). Spatio-temporal analysis of lightning activity over Greece — Preliminary results derived from the recent state precision lightning network. *Atmospheric Res.* 144, 207–217. doi: 10.1016/j.atmosres.2013.10.021

Ohta, K., Izutsu, J., and Hayakawa, M. (2009). Anomalous excitation of Schumann resonances and additional anomalous resonances before the 2004 Mid-Niigata prefecture earthquake and the 2007 Noto Hantou Earthquake. *Phys. Chem. Earth Parts A/B/C* 34, 441–448. doi: 10.1016/j.pce.2008.07.008

Petraki, E., Nikolopoulos, D., Nomicos, C., Stonham, J., Cantzos, D., Yannakopoulos, P., et al. (2015). Electromagnetic pre-earthquake precursors: mechanisms, data and models -a review. *Earth Sci. Climate Change* 6:1000250.

Proestakis, E., Kazadzis, S., Lagouvardos, K., Kotroni, V., and Kazantzidis, A. (2016). Lightning activity and aerosols in the Mediterranean region. *Atmospheric Res.* 170, 66–75. doi: 10.1016/j.atmosres.2015.11.010

Pulinets, S., and Ouzounov, D. (2016). "Earthquake precursors in atmosphere and ionosphere. A review and future prospects," in *Geophysical Research conference Abstracts, 18. 2016 EGU General Assembly*. (Vienna: Chapman University).

Schumann, W. O. (1952). On the free oscillations of a conducting sphere which is surrounded by an air layer and an ionosphere shell. *Z. Naturforschaftung* 7A, 149–154.

Sekiguchi, M., Hayakawa, M., Nickolaenko, A. P., and Hobara, Y. (2006). Evidence on a link between the intensity of Schumann resonance and global surface temperature. *Annales Geophys.* 24, 1809–1817. doi: 10.5194/angeo-24-1809-2006

Tatsis, G., Christofilakis, V., Chronopoulos, S. K., Kostarakis, P., Nistazakis, H. E., Repapis, C., et al. (2020b). Design and implementation of a test fixture for elf schumann resonance magnetic antenna receiver and magnetic permeability measurements. *Electronics* 9:171. doi: 10.3390/electronics9010171

Tatsis, G., Christofilakis, V., Chronopoulos, S. K., Baldoumas, G., Sakkas, A., Paschalidou, A. K., et al. (2020a). Study of the variations in the Schumann resonances parameters measured in a Southern Mediterranean environment. *Sci. Tot. Env.* 715:136926. doi: 10.1016/j.scitotenv.2020.136926

Tatsis, G., Votis, C., Christofilakis, V., Kostarakis, P., Tritakis, V., and Repapis, C. (2015). A prototype data acquisition and processing system for Schumann resonance measurements. *J. Atmospheric Solar-Terrestrial Phys.* 135, 152–160. doi: 10.1016/j.jastp.2015.11.001

Tatsis, G., Votis, C., Christofilakis, V., Kostarakis, P., Tritakis, V., Repapis, C., et al. (2016). Preliminary measurements of Schumann's Resonances (SR) in the Greek. *J. Eng. Sci. Technol. Rev.* 9, 61–64.

Votis, C. I., Tatsis, G., Christofilakis, V., Chronopoulos, S. K., Kostarakis, P., Tritakis, V., et al. (2018). A new portable ELF Schumann resonance receiver: design and detailed analysis of the antenna and the analog front-end. *J. Wireless Com. Netw.* 2018:155.

Williams, E. (1992). The schumann resonance: a global tropical thermometer. *Science* 256, 1184–1187. doi: 10.1126/science.256.5060.1184

Williams, E. (2005). Lightning, and climate: a review. *Atmospheric Res.* 76, 272–287. doi: 10.1016/j.atmosres.2004.11.014

Xinyang, O., Xuemin, Z., Nickolaenko, A. P., Hayakawa, M., Xuhui, S., and Yuanqin, M. (2013). Schumann resonance observation in China and anomalous disturbance possibly associated with Tohoku M9.0 earthquake. *Earth Sci.* 26, 137–145. doi: 10.1007/s11589-013-0009-0

Conflict of Interest: The authors declare that the research was conducted in the absence of any commercial or financial relationships that could be construed as a potential conflict of interest.

frontiers
in Earth Science

ORIGINAL RESEARCH
published: 16 June 2021
doi: 10.3389/feart.2021.673808

Evaluating the Response of Global Column Resistance to a Large Volcanic Eruption by an Aerosol-Coupled Chemistry Climate Model

Yushan Xie[1], **Ruyi Zhang**[1], **Zhipeng Zhu**[1] **and Limin Zhou**[1,2]*

[1]Key Laboratory of Geographic Information Science, Ministry of Education, East China Normal University, Shanghai, China, [2]Key Laboratory of Numerical Modeling for Atmospheric Science and Geophysical Fluid Dynamics, Institute of Atmospheric Physics, CAS, Beijing, China

Global electric circuits could be the key link between space weather and lower atmosphere climate. It has been suggested that the ultrafine erosol layer in the middle to upper stratosphere could greatly contribute to local column resistance and return current density. In previous work by Tinsley, Zhou, and Plemmons (Atmos. Res., 2006, 79 (3–4), 266–295), the artificial ultrafine layer was addressed and caused a significant symmetric effect on column resistance at high latitudes. In this work, we use an updated erosol coupled chemistry-climate model to establish a new global electric circuit model. The results show that the ultrafine aerosol layer exits the middle stratosphere, but due to the Brewer-Dobson circulation, there are significant seasonal variations in the ion loss due to variations in the ultrafine aerosol layer. In the winter hemisphere in the high latitude region, the column resistance will consequently be higher than that in the summer hemisphere. With an ultrafine aerosol layer in the decreasing phase of solar activity, the column resistance would be more sensitive to fluctuations in the low-energy electron precipitation (LEE) and middle-energy electron precipitation (MEE) particle fluxes.

Keywords: global electric circuit, ultrafine aerosol, column resistance, brewer-dobson circulation, solar activity

Edited by:
Irina Alexandrovna Mironova,
Saint Petersburg State University,
Russia

Reviewed by:
Arseniy Karagodin-Doyennel,
Physikalisch-Meteorologisches
Observatorium Davos, Switzerland
Ziniu Xiao,
Chinese Academy of Sciences (CAS),
China

***Correspondence:**
Limin Zhou
lmzhou@geo.ecnu.edu.cn

Specialty section:
This article was submitted to
Atmospheric Science,
a section of the journal
Frontiers in Earth Science

Received: *28 February 2021*
Accepted: *04 May 2021*
Published: *16 June 2021*

Citation:
Xie Y, Zhang R, Zhu Z and Zhou L (2021) Evaluating the Response of Global Column Resistance to a Large Volcanic Eruption by an Aerosol-Coupled Chemistry Climate Model. Front. Earth Sci. 9:673808. doi: 10.3389/feart.2021.673808

INTRODUCTION

The global atmospheric electric circuit could be important not only as a product of global thunderstorm activity (Bering et al., 1998) but also because it may cause climate change and weather itself via electrical effects on cloud microphysics, with external and internal drivers (Tinsley and Yu, 2004; Tinsley, 2008), which depend on the current density J_z flowing downwards from the ionosphere to the surface through clouds. This hypothesis has been reviewed in detail by Tinsley (2008).

The ionosphere forms a conducting shell, which is charged by highly electrified clouds, including thunderclouds in low latitude regions and air fronts at middle and high latitudes. The diurnal variations in the global upward current of approximately 1000 A create a diurnally varying ionospheric potential (Vi) that averages approximately 250 kV, which is essentially an equipotential out to approximately 50° geomagnetic latitudes. At any location away from the generators, the downward return current density (Jz) is 1–6 pA m-2, depending on the atmospheric resistance R of the column of the unit cross section there. The vertical column resistance R at any location is mainly determined by the altitude of the surface, the aerosol, the cloud and radioactive radon concentrations near the surface, and the flux of galactic cosmic rays (GCRs) at that latitude (Tinsley et al., 2006). The GCR flux creates ion pairs throughout the air column, increasing ion pairs cause the increase of conduct, leading to stronger Jz. There are two additional sources of ion pair production in the upper atmosphere: one is the relativistic electron flux and associated X-ray bremsstrahlung that penetrates down to approximately 30 km in sub-auroral latitudes (Tinsley, 1996; Frahm et al., 1997; Li et al., 2001a, b), and the other is solar energetic particle (SEP) events (Holzworth et al., 1987) that produce stratospheric ionization, excess positive charge, and occasionally a small amount of tropospheric ionization in the polar cap regions. We denote the stratospheric and tropospheric contributions to the column resistance at any location as S and T, respectively. Then Jz at that location is given by Ohm's Law: $Jz = Vi/(T + S)$. Therefore, any input that modulates Vi, T, or S will also modulate Jz. There are several quasi-static numerical models to evaluate the global distribution of column resistance, such as Hays and Roble (1979), Makino and Ogawa (1985—herein M085), Sapkota and Varshneya (1990—herein SV90), Tinsley et al. (2006—herein TZ06), Zhou and Tinlsey (2010—herein ZT09), and there are comprehensive models with the whole atmospheric dynamics and chemical components to calculate the column resistance to provide a full description of the response of the global air conductivity to internal drivers (tropospheric and stratospheric aerosols, radon gas concentrations, clouds) and external drivers (galactic cosmic rays, comet aerosols, clouds), such as Baumgaertner et al. (2013—herein BTNL 2013) and Lucas et al. (2015—herein LBT 2015).

It was proposed that the reduction in Jz due to the Forbush decrease in GCRs could be attributed to the latitudinal variations in the low atmospheric dynamics, represented by the vorticity area index (VAI), and the amplitude of the response was proportional to the amplitude of the Forbush decrease (Tinsley and Deen, 1991). Other studies claimed that the relationship between Jz and VAI was due to the internal variation of the thunderstorm (Hebert et al., 2012) or interplanetary magnetic field (IMF) (Wilcox et al., 1973; Lam and Tinsley, 2016; Zhou et al., 2018). Responses of cloud cover to heliospheric current sheet (HCS) crossings have been found by Kniveton et al. (2008) and to Forbush decreases by Veretenenko and Pudovkin (1997), and responses of global cloud cover to global Jz changes inferred from the electric field (Ez) measurements at Vostok have been found by Kniveton et al. (2008). On longer time scales, the relation between the relativistic electron flux and the pressure fluctuation in the winter ice island pressure center is important (Zhou et al., 2014). These responses between space weather and atmospheric parameters were more significant two or three years after large volcanic eruptions, such as the eruption of Mt. Aguge, Mt. El Chikon, and Mt. Pinatubo, which was proposed to be due to additional resistance by the ultrafine aerosol layer in the stratosphere (Tinsley and Yu, 2004; Zhou et al., 2014). It has been suggested that after a large volcanic eruption, the gaseous H_2SO_4 in the descending branch of the Brewer-Dobson circulation could be condensed by ion media nucleation and form large concentrations of ultrafine aerosols with radii of a few nanometers or tens of nanometers at mid-high latitudes, which could significantly increase the column resistance in the stratosphere.

The initial evaluation of this effect was performed by the global circuit model of TZ06 (Tinsley et al., 2006). In the TZ06 model, an ultrafine aerosol layer was modeled by Tinsley et al. (2006), where column resistance is mainly shown in situations with and without the estimated stratospheric ultrafine volcanic aerosol layer. The layer is located poleward of ±40° geographic latitudes, where the layer column resistance becomes the dominant part of the stratosphere and is calculated for the absence of ionization due to electron precipitation, such as relativistic electron flux. This ionization is considered to be present most of the time and to make the ultrafine layer a good conductor so that the column resistance in the stratosphere (S) is negligible with respect to that in the troposphere (T). It is only for periods of a few days when the slow solar wind at the HCS crosses the earth that the precipitating relativistic electron flux decreases by an order of magnitude; R increases and Jz decreases at higher latitudes during a few years following large explosive volcanic eruptions. The concentration and spatial distribution of stratospheric ultrafine aerosols in TZ06 are artificial and static with no temporal variation, which provides only a rough estimation of their effects. The improved comprehensive model of BTNL 2013, based on CESM1, where the sulfate aerosol process in the stratosphere is from English et al. (2011), includes all types of aerosols, including ultrafine aerosols due to ion media nucleation in the stratosphere, and provides a more realistic picture of the global circuit. However, the lack of heating as aerosol radiative feedback in English et al. (2011) causes a large bias in the aerosol burden between simulations and observations. The improved aerosol-chemistry-climate model SOCOL-AERv2 by Feinberg et al. (2019) can already provide a more accurate treatment of stratosphere aerosols for low and high volcanic periods with aerosol radiative heating, sedimentation schemes, and coagulation efficiency. The purpose of this work is to investigate the effect of the stratospheric aerosol layer on the column resistance with the comprehensive global electric circuit model, which is based on SOCOL-AERv2 coupled with the global electric model of TZ06, where ultrafine aerosols due to ion media nucleation are involved to more accurately evaluate the effect of ultrafine aerosols and the temporal variation in this effect. In addition, the effects of ionization due to galactic cosmic rays and high-energy electron precipitation are addressed.

DESCRIPTION OF THE MODEL

The chemistry-climate model (CCM) SOCOL (SOlar Climate Ozone Links) version three is a three-dimensional model developed by the research group at the Physical-Meteorological Observatory and World Radiation Center (PMOD/WRC) in collaboration with the Institute for Atmospheric and Climate Science, ETHZ Switzerland (Stenke et al., 2013). The effects of external drivers, such as galactic cosmic rays and solar protons, on the ozone layer and climate were investigated by the SOCOL model (Egorova et al., 2011; Mironova et al., 2021). A detailed description of the model can be found in Rozanov et al. (1999).

SOCOL is developed based on the Middle Atmosphere version of the European Center/Hamburg Model version 5 (MA-ECHAM5). MA-ECHAM5 (Roeckner et al., 2003) is the dynamical core of the model responsible for atmospheric physics and dynamics in SOCOL, with a hybrid sigma-pressure coordinate system spanning from the surface to 0.01 hPa. The horizontal spatial resolution of the model in this work is 3.75 × 3.75°. The model has 39 vertical levels from the surface to a height of approximately 80 km in a hybrid sigma-pressure coordinate system, and the vertical resolution decreases with altitude and is 2 km in the stratosphere. The dynamic frame in the model is solved with a semi-implicit time stepping scheme with a time resolution of 15 min. The advection of water vapor, cloud water, and trace constituents is calculated by a flux-based 25 mass-conserving and shape-preserving transport scheme (Lin and Rood, 1996). Full radiation calculations, chemistry, and transport calculations are performed every 2 h. The shortwave radiation scheme is based on the ECMWF model (Morcrette, 1991) with a modified parameterization for the water vapor continuum and corrected spectral Voigt line shape considering Doppler broadening at low pressure as well as with added aerosols, greenhouse gases, and clouds (Roeckner, 1995). The longwave radiation is based on the Rapid Radiative Transfer Model (RRTM) scheme (Mlawer et al., 1997).

The chemistry-transport module Model for the Evaluation of OZONe Trends (MEZON) (Egorova et al., 2003) shares the MA-ECHAM5 horizontal and vertical grids and treats 41 atmospheric species of hydrogen, oxygen, nitrogen, carbon, chlorine, and bromine groups treated with 140 gas-phase reactions, 46 photolysis reactions, and 16 heterogeneous reactions in/on liquid sulfate aerosols, water ice, and nitric acid trihydrate (NAT) (Stenke et al., 2013).

The ion pair production rate due to galactic cosmic rays is calculated by the CRAC (Cosmic Ray Atmospheric Cascade) model (Usoskin et al., 2010), which is based on a Monte Carlo simulation of the atmospheric cascade; in the troposphere and stratosphere, the accuracy is within 10% compared to the observation results. In the present work, we also add the ion pair due to low- and middle-energy electron precipitation (herein EEP, including LEE and MEE). The semi-empirical parameterization for LEE suggested by Funke et al. (2016) is involved, and the ionization rate due to MEE is based on Fang et al. (2010).

In the troposphere, 13 types of aerosols based on the GADS database and Hess et al. (1998) are involved, which is the same as the treatment in the TZ06 model. We use an analytical expression for the tropospheric aerosol size distribution given by Hess et al. (1998).

For the sulfate aerosol in the model, instead of the rough estimation that was used in TZ06, a detailed 2D sulfate aerosol model is coupled based on the updated size-resolved AER sulfate aerosol model, which was established in SOCOL by Sheng et al. (2015), Sukhodolov et al. (2018), and Feinberg et al. (2019). In this sulfate aerosol model, the particle distribution is resolved by 40 size bins spanning wet radii from 0.39 nm to 3.2 µm by volume doubling, which also provides the size distribution of the sulfate aerosol. In addition, the microphysical processes of homogeneous nucleation, condensation/evaporation, coagulation, and sedimentation, which were suggested by Sheng et al. (2015), are also included. In the upper stratosphere at altitudes over 30 km, the coagulation rate due to ion media nucleation is addressed in this new model, which is based on the INM model suggested by Yu and Turco (2001).

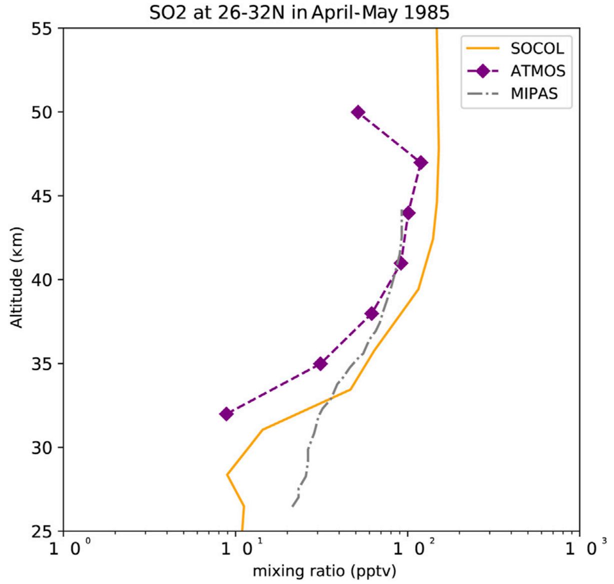

FIGURE 1 | Comparison of the SO2 mixing ratio at 26–32°N in april to May 1985 simulated by SOCOL-AER (orange solid line), from ATMOS observations (purple squares) and from MIPAS measurements (gray dashes).

The column resistance (R) varies with latitude and longitude, and with the upper boundary of 60 km in our model, R is given by

$$R = \int_{Zs}^{60} dz/\sigma(z) \tag{1}$$

where Zs is the elevation of the surface and σ(z) is air conductivity. The current density J_z throughout the column is then

$$J_z = V_i/R \tag{2}$$

where V_i is the overhead ionospheric potential. The most complex problem for this global circuit model is in evaluating σ(z) globally as a function of altitude, latitude, longitude, and time.

In this model, the first step is the evaluation of the ion pair production rate; the next step is the evaluation of the aerosol particle concentrations. Then, using the approximation that the concentrations of positive and negative ions in the air are equal, the ion pair concentration (n) is obtained by solving the equation

$$\frac{dN}{dt} = q - \alpha N^2 - \sum^{i} \beta_i S_i N \tag{3}$$

for the steady state condition where dN/dt = 0, where t is the time. Then, the conductivity is given by

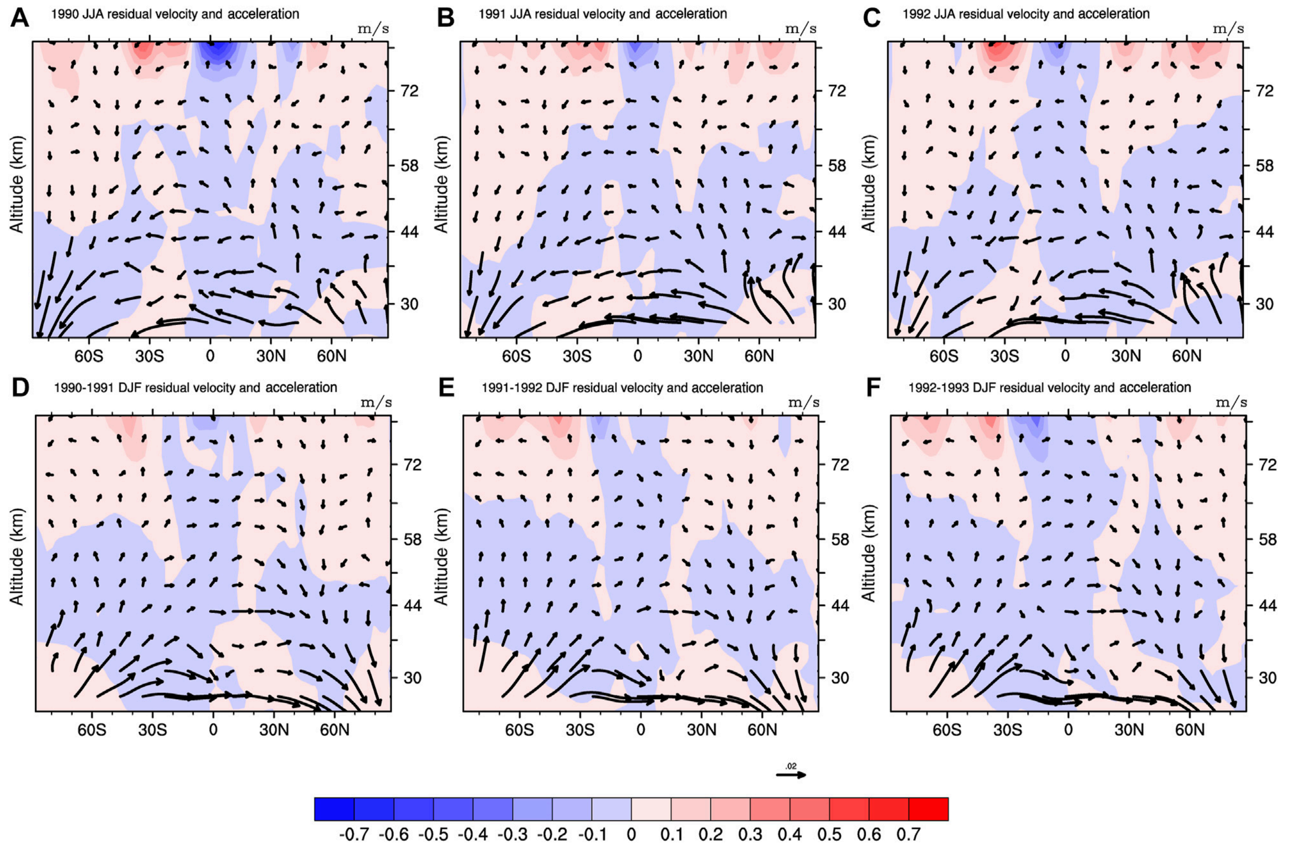

FIGURE 2 | The residual speed and acceleration in the summer (first row) and winter (second row) from 1990 to 1993. The colored diagram is acceleration, and the vector arrow is the composite of vertical wind and meridional wind ($v \times 4.899 \times 10^{-3}$).

$$\sigma = Ne(\mu 1 + \mu 2) \tag{4}$$

where e is the elementary charge, and $\mu 1$ and $\mu 2$ are the ion mobilities of the positive and negative ions.

We use a set of expressions for α that closely fit the results of Bates (1982). The expression for β_r as a function of aerosol particle radius, r, that we use is given by Hoppel (1985).

The present global electric circuit model calculates the atmospheric resistivity from the surface up to 60 km height with 335 bins. We took only 32 vertical bins below 60 km in the SOCOL-AERv2 model, all the outputs from the SOCOL-AERv2 model are linearly interpolated, and the sulfate gas concentration and sulfate aerosol surface area index (surface area density, SAD) are interpolated with the e power function.

RESULTS

Comparison of the SO_2 Mixing Ratio

Figure 1 compares the simulation results of the SO2 mixing ratio from SOCOL-AER at 26–32°N in April to May 1985 with MIPAS and ATMOS observed data (Höpfner et al., 2013; Rinsland et al., 1995). There are a number of similarities between the simulation results and satellite measurements. The estimated instrumental uncertainty of MIPAS is 5–10 pptv (Höpfner et al., 2013). Differences between observed data and simulation data below 45 km are less than 10°pptv. This result is similar to Sheng et al. (2015), who found that SOCOL-AER could successfully simulate aerosol features.

Brewer-Dobson Circulation Seasonal Variations

As shown in **Figure 2**, during 1990–1993, the Brewer-Dobson circulation exhibited significant seasonal variations. The top half of the figure shows circulation characteristics during summer; at nearly 30 km, the residual velocity at high latitudes decelerated in 1990 and 1992 but accelerated in 1991. The bottom half of **Figure 2** shows that near 30 km, the residual velocity at high latitudes accelerated the upper polar region during the 1990–1992 winter but decelerated in 1993.

Comparison of the Ion Production Rate by GCRs and EPP

Figures 3A–D show the ion pair production rate at standard temperature and pressure (STP) for particles with different energies during solar maxima and solar minima: 1) is for ion

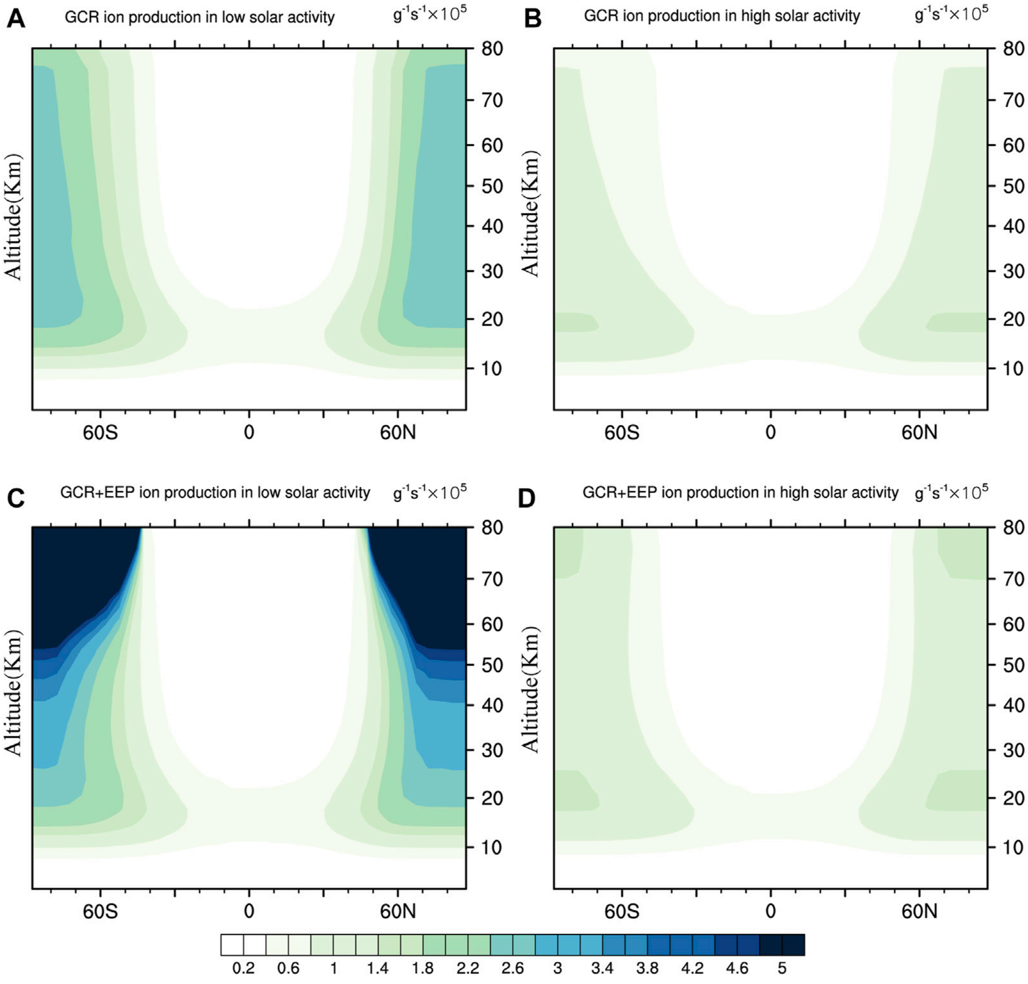

FIGURE 3 | The ion pair production rate due to GCRs and EEP. **(A)** shows the ion pair production rate due to GCRs during the solar minimum, **(B)** shows the ion pair production rate due to GCRs during the solar maximum, **(C)** shows the ion production rate due to GCRs + EEP during the solar minimum, and **(D)** shows the ion production rate due to GCRs + EEP during the solar maximum.

pair production rate due to GCRs during the solar minimum, 2) is for the ion pair production rate due to GCRs during the solar maximum, 3) is for the ion production rate due to GCRs + EEP during the solar minimum, and 4) is for the ion production rate due to GCRs + EEP during the solar maximum. This shows that the ion production rate during solar minima at an altitude of 60 km in the polar region due to ionization of GCRs and EEP could be twice that during solar maxima, and at 30 km, the ion production rate is enhanced by an additional 1.15 due to EEP. During solar maxima, the difference at an altitude of 60 km is less than 10%. Therefore, additional EEP ionization was significantly attributed to ion production above a height of 30 km in the polar region.

Sulfate Aerosol in the Middle Stratosphere

With the SOCOL-AERv2 model, a more accurate simulation of sulfate aerosol concentration was achieved. In general, there are two sulfate aerosol layers after a volcanic eruption: one is in the troposphere, and the other is in the low stratosphere layer, which is well known as the “Junge layer” (Junge and Manson, 1961). Yu and Turco (2001) and Tinsley (2005) suggested that there was a third layer in the middle to upper stratosphere due to ultrafine sulfate aerosols. Therefore, **Figure 4** shows the sulfate aerosol-related parameters in the middle to upper stratosphere. **Figure 4** shows the zonal mean SAD (panels a and b) and sulfate mass concentration (panels c and d) as a function of altitude above 23 km. **Figures 4A,C** show the results in December-January-February (DJF) 1992–1993 after the eruption of Mt. Pinatubo, and **Figures 4B,D** show the results in DJF 1990–1991 just before the eruption of Mt. Pinatubo. The results show that there is significant enhancement of SAD and sulfate mass concentration in the middle stratosphere after the eruption of Mt. Pinatubo compared with the results in DJF 1990–1991 before the eruption. The most interesting aspect of **Figures 4A,C** is that the maxima of SAD and sulfate mass concentration over the high latitudes of the Northern hemisphere are in the region of Brewer-Dobson circulation in the descending branch. In **Figures 2D,E** there is

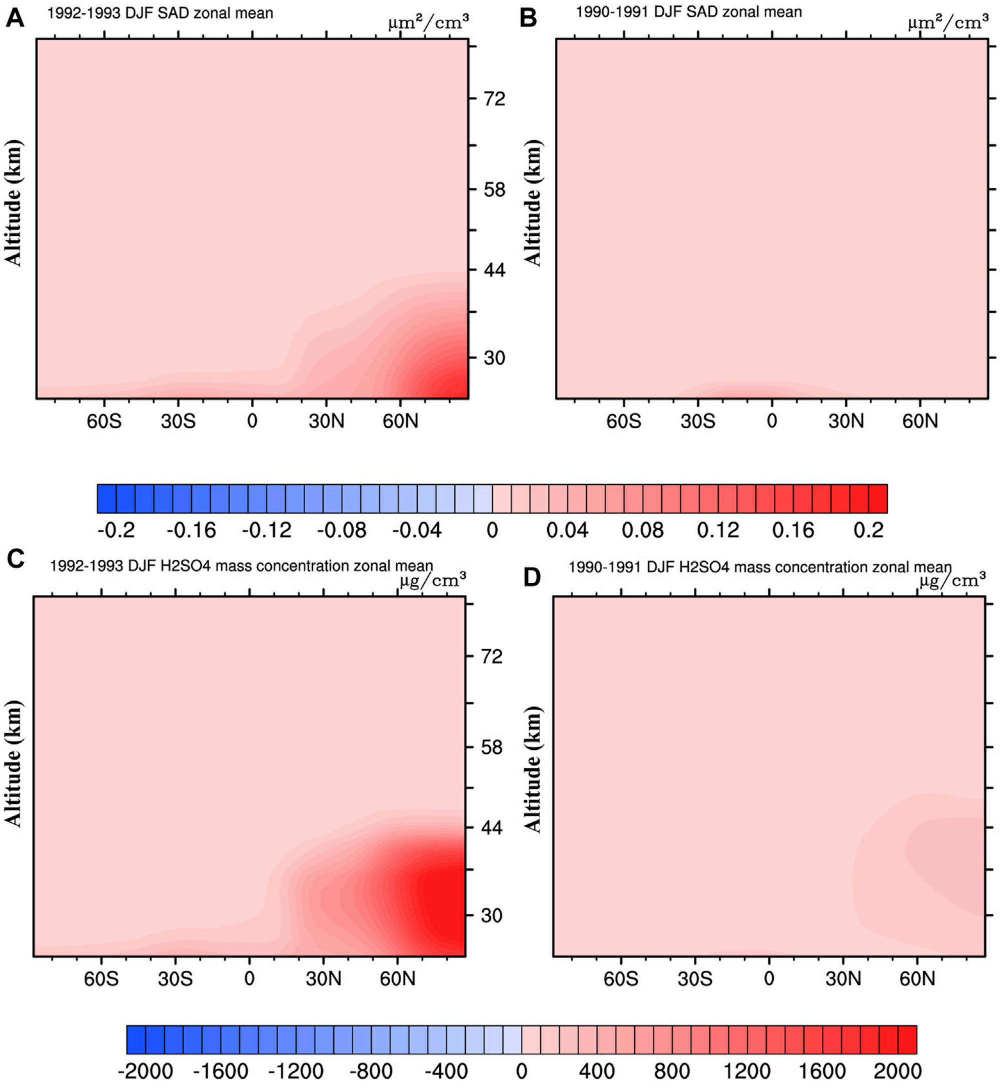

FIGURE 4 | The characteristics of sulfate aerosols in the middle and upper stratosphere (panels **(A)** and **(B)**) and sulfate mass concentration (panels **(C)** and **(D)**) as a function of altitude above 23 km.

a clear trend of residual velocity descent over the high latitudes of the Northern hemisphere at 30 km during the 1990–1992 winter. Compared to the estimation by Tinsley (2005) and Tinsley et al. (2006), the maximum SAD and sulfate mass concentrations are lower. They are centered at a height of approximately 30 km.

The Ion-Aerosol Attachment Efficiency

In the global electricity circuit model, ion loss due to ion-aerosol attachment is the main part of the whole ion loss. **Figure 5** shows the profile of the ion-aerosol attachment rate (β) in two different regions (Antarctic 1) and Indian Ocean 2)) under different volcanic eruptions. In these two plots, the gray lines are the results from the TZ06 model, the gray solid line is the value in DJF with high volcanic aerosol loading, and the gray dashed line is the value in DJF with low volcanic aerosol loading. The black solid line is for DJF in 1990–1991, the black dashed line is for DJF in 1991–1992, and the red solid line is for June-July-August (JJA) in 1991. The results show that the ultrafine aerosol layer appears in only the high latitude region, which is consistent with previous studies. The ion loss due to attachment to ultrafine aerosols at low volcanic activity in the new model is approximately 20 times larger than that in the TZ06 model. The maximum ion loss due to attachment to sulfate aerosols exists at a height of 35 km, which is consistent with the vertical distribution of sulfate aerosols in **Figure 4**. After the large volcanic eruption, β is enhanced by approximately 3–4 times due to seasonal variations, which is not addressed in TZ06, ZT09, or other models. The ion loss due to attachment to aerosols in the Junge layer is also increased by a factor of approximately 10 compared with the TZ06 model. Although aerosol in the Junge layer also exhibited a peak value in polar and tropical regions after volcanic

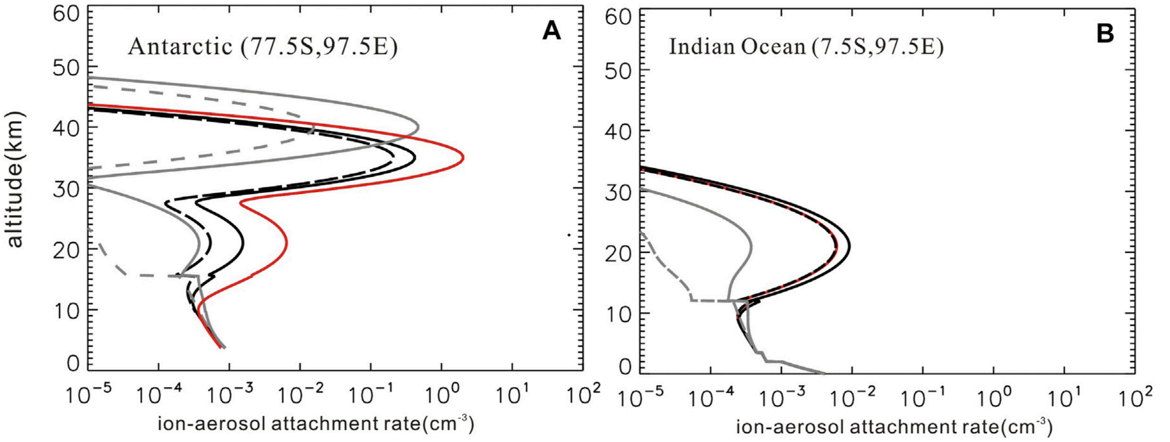

FIGURE 5 | "Vertical profile of the ion-aerosol attachment rate (β) in two different regions (Antarctic **(A)** and Indian Ocean **(B)**) under different volcanic eruptions. In these two plots, the gray lines are the results from the TZ06 model, the gray solid line is the value in DJF with high volcanic aerosol loading, and the gray dashed line is the value in DJF with low volcanic aerosol loading. The black solid line is for DJF in 1990–1991, the black dashed line is for DJF in 1991–1992, and the red solid line is for JJA in 1991.

eruption, it was only 100 times less than the effect due to surface aerosols and ultrafine aerosols.

Figure 6 shows the ion-aerosol attachment rate at a height of 35 km in JJA 1993 and DJF 1993–1994. In the high-latitude region, there is a significant seasonal fluctuation in β, and the maximum variation is over 10 times.

Profile of Resistivity

Figure 7 shows the vertical profiles of atmospheric resistivity in DJF in the 1) Antarctic and 2) Indian Ocean. The solid lines are for the 1990–1991 period, dotted lines are for the 1992–1993 period, and dashed lines are for the 1993–1994 period. In the high-latitude/Antarctic region, the effect of the Junge layer could not be detected, and ultrafine volcanic eruptions and resistivity at a 35 km height significantly contributed to the whole column resistance, especially after volcanic eruptions. The sulfate aerosol effect weakens with time. In the tropical Indian Ocean region, the peak resistivity was found at a height of 20 km, which is due to the Junge layer. However, the resistivity of the Junge layer is not large and does not significantly affect the whole column resistance value. It is apparent from **Figure 8B** that above the Indian Ocean air resistivity for the 1993–1994 period became almost the same as in pre-eruption time, a possible explanation for this might be that the effect and lifetime of ultrafine sulfate aerosols in the Junge layer was shorter than a year.

Global Distribution of Column Resistance

Figure 8 shows the gridded global column resistance in DJF: 1) 1990–1991, 2) 1991–1992, and 3) 1993–1994. In panel (a), a low column resistance appears in regions with high elevations or low geomagnetic latitudes, such as East Asia, where the column resistance is controlled by surface aerosols. After the eruption of Mt. Pinatubo, due to ultrafine aerosols, the column resistance at high latitudes significantly increases, and the maximum increase could be 2.8 times. In DJF, the greatest enhancement of column resistance exists in the Northern Hemisphere. Two years after the eruption, in panel (c), the effect of ultrafine aerosols declines.

Seasonal Effect

Figure 9 shows the percentage of column resistance enhancement between JJA 1993 and DJF 1993–1994. With simultaneous seasonal shifts in the column resistance, the column resistance at high latitudes undergoes large changes, and in the high latitudes of the winter hemisphere, the column resistance increases, while in the summer hemisphere, it decreases.

EEP Effect

Figures 10A–C show the percentage increases $((R_{GCR}—R_{GCR+EEP})/R_{GCR})\times100\%$, of the column resistances in DJF 1) 1990–1991, 2) 1991–1992, and 3) 1993–1994. In **Figure 10A** and **Figure 10B**, the maximum increase in the percentage of column resistance is less than 1.5%, and in **Figure 10C**, the maximum percentage is over 7.2% in both the northern and southern polar regions, which indicates that two years after the eruption of Mt. Pinatubo, there would be a significant effect due to the absence of EEP ionization on the column resistance. In 1990–1991 and 1991–1992, during the solar maxima, high solar activity prevented the energetic electrons from penetrating into the middle stratosphere. In 1993–1994, during the decreasing phase of solar activity, more energetic electrons reached the upper and even middle stratosphere. With ultrafine aerosols, the column resistance becomes sensitive to fluctuations in the energy particle flux.

DISCUSSION

Although the contribution of atmospheric resistivity from the sulfate aerosol layer in the lower stratosphere, called the Junge

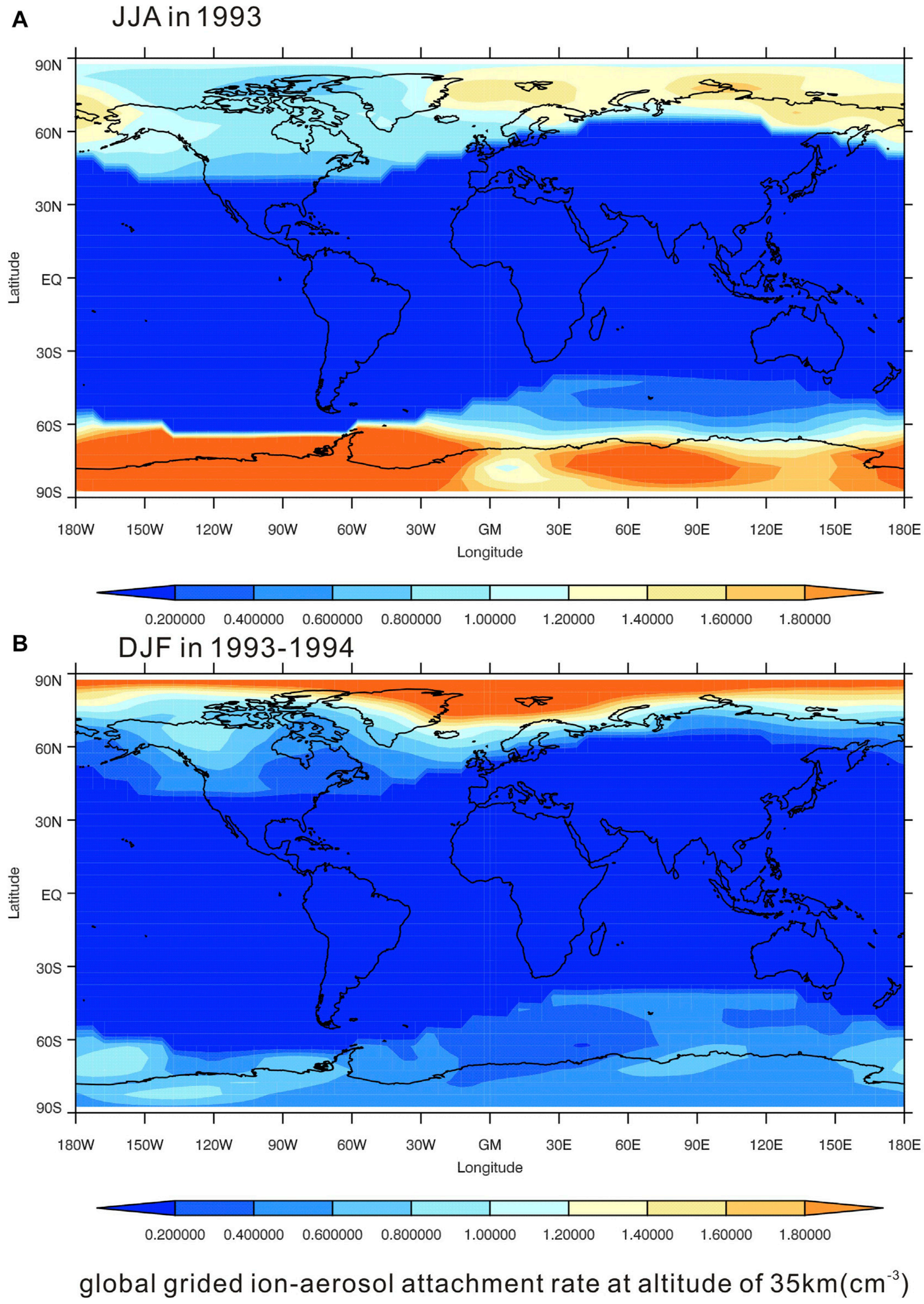

FIGURE 6 | Global ion-aerosol attachment rate at a height of 35 km, **(A)** for JJA in 1993 and **(A)** for DJF in 1993–1994.

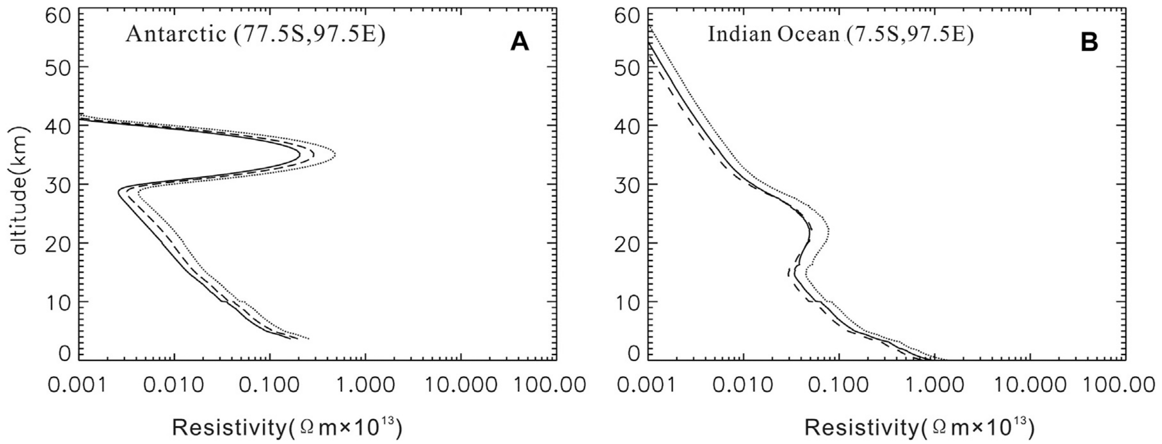

FIGURE 7 | Vertical profile of atmospheric resistivity in DJF in the **(A)** Antarctic and **(B)** Indian Ocean. The solid lines are for 1990–1991, dotted lines are for 1992–1993, and dashed lines are for 1993–1994.

layer, is larger in the present simulation than in the previous TZ06 model (Tinsley et al., 2006), the aerosols in the upper stratosphere still seem to have a main effect on the column resistance at high latitudes. The ultrafine aerosol layer has a significant effect on the column resistance after the volcanic eruption. Tinsley (2005) claimed that there was an ultrafine aerosol layer in the upper stratosphere formed by ion media nucleation, as suggested by Yu and Turco(2001), which could be consistent with the unexplained variability on all time scales in measured stratospheric conductivity (Tinsley, 2005; Bering et al., 2005), especially in the descending branch of the Brewer-Dobson circulation at high latitudes. In the GEC model of the TZ06 model, the artificial ultrafine aerosol layer centered at 40 km was modeled based on the numerical simulation by Yu and Turco (2001) for an H_2SO_4 mass concentration of 6.35×10^2 μg m^{-3}, which corresponds to a mass mixing ratio of 16 ppbm for the liquid droplets. In the TZ06 model, the sensitivity simulation showed that in the high volcanic eruption period, the column resistance in the high geomagnetic latitude region would be more sensitive to fluctuations in GCRs than in the low volcanic eruption period by a factor of two times due to the attribution of ultrafine aerosols and the high sensitivity of the polar region (Tinsley et al., 2006). Tinsley (2008) expected that the ultrafine aerosol concentration would have a maximum effect on the column resistance two years after a large volcanic eruption. However, in the present simulation, based on the chemical-climate model, the SAD in the ultrafine sulfate aerosol layer first appears in the descending branch of the Brewer-Dobson circulation at high latitudes soon after the eruption of Mt. Pinatubo, which significantly affects the regional column resistance. Different from previous models (TZ06, Tinsley et al., 2006), the column resistance response to volcanic eruptions shows a significant asymmetric structure in different hemispheres, and the column resistance in the high latitudes of the Northern Hemisphere has a larger response than that of the Southern Hemisphere. Two years after the volcanic eruption, the effect of ultrafine aerosols appears in only the North Atlantic region. This asymmetric structure might explain why more significant connections on day-to-day or annual time scales between space weather events and tropospheric responses, such as dynamic responses (Lam et al., 2014), cloud cover (Voiculescu et al., 2013) and cloud radiation (Frederick et al., 2019), appeared in the Northern Hemisphere than in the Southern Hemisphere.

It has been claimed that the Brewer-Dobson circulation is strengthened in the winter hemisphere (Butchart, 2014). Then, in the winter hemisphere, the transport rate of sulfate in the stratosphere is accelerated, and more ultrafine aerosols can be produced, which causes higher column resistance in the high latitude region of the winter hemisphere than in that of the summer hemisphere. In previous work, the main seasonal variation in the column resistance was mainly due to variations in the aerosol concentration in the troposphere due to changes in the boundary layer or emissions (Tinsley et al., 2006).

Many studies based on satellite observations and weather monitoring data have shown a significant connection between the fluctuations of space particles, such as GCRs, EEP, relativistic electron precipitation (REP), and the troposphere. The hypothesis suggested by Tinsley (2008) claimed that the return atmosphere current density (Jz) from the ionosphere to the land surface, which is partly controlled by atmospheric column resistance, could significantly affect the dynamic and thermal character in the troposphere through cloud electric microphysics, called the electri-scavenging or electri-anti-scavenging effect. The shorting out of the resistance of the ultrafine layer appears to be essentially when it occurs with REP, which produces bremsstrahlung X-rays that can dominate ion pair production in the middle stratosphere (Frahm et al., 1997). On the basis of SAMPEX measurements, this is likely to be most of the time at sub-auroral latitudes (Li et al., 2001a; Li et al., 2001b). However, for a few days around the times of HCS crossings, the REP decreases by up to an order of magnitude

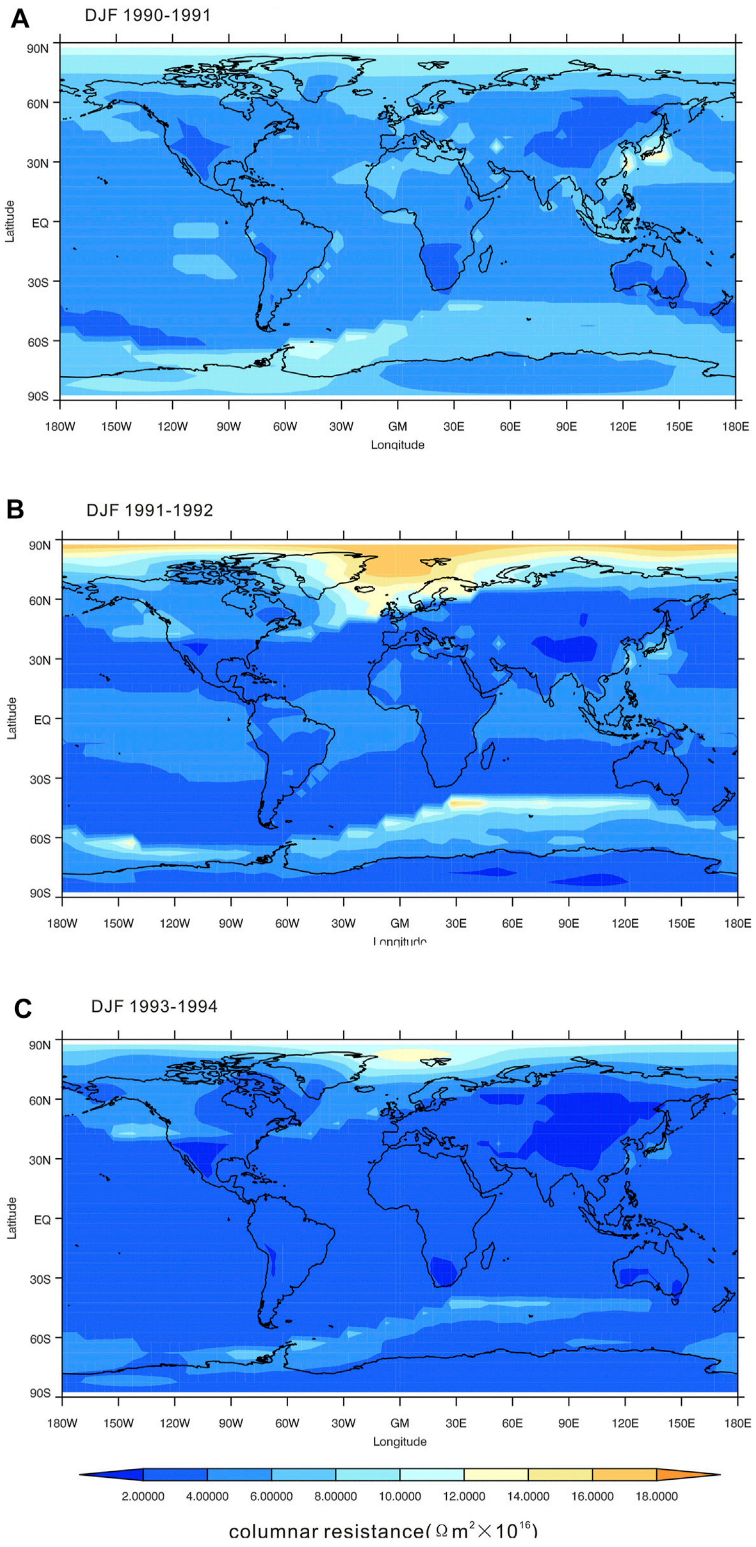

FIGURE 8 | The gridded global column resistance in DJF **(A)** 1990–1991, **(B)** 1991–1992, and **(C)** 1993–1994.

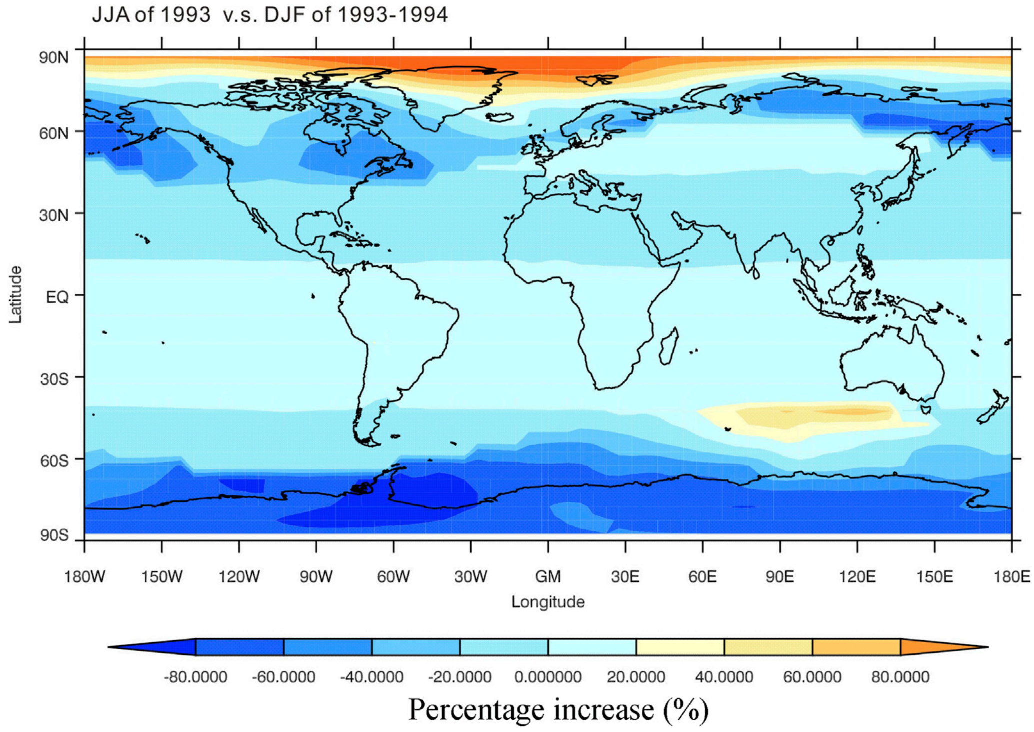

FIGURE 9 | The percentage increase in column resistance between JJA 1993 and DJF 1993–1994.

(Tinsley et al., 2000; Kirkland et al., 1996; Kniveton and Tinsley, 2004). Then, the column resistance in the sub-auroral region could increase to a high value, as calculated for the high volcanic aerosol situation, and Jz would decrease. This scenario for a decrease in Jz around the times of HCS crossings, when there is a high concentration of stratospheric aerosols, is in accordance with the sparse and noisy Jz observations for those times (Reiter, 1977; Fischer and Miihelisen, 1980; Tinsley et al., 1994). Because of the lack of a detailed model to simulate the global ion production rate due to REP, the effect of EEP is considered in the present model. The treatment of ultrafine aerosol concentrations and stratospheric ion mobility in the model confirms the essential contribution of ultrafine aerosols to column resistance. Even two years after a large volcanic eruption, the column resistance could still be sensitive to fluctuations in electron precipitation.

When the EEP effect was coupled with the seasonal effect, it could be predicted that the column resistance would be more sensitive to EEP changes in the winter hemisphere, which is consistent with most of the data analysis results.

Clouds seems to play an important role in local column resistance. The ZT09 model claimed that the variation in clouds caused less than 10% of the global atmospheric resistance, while the BTNL2013 model claimed that the effect of clouds was underestimated by the ZT09 model. Clouds are also a highly variable factor in atmospheric systems, in addition to total cloud coverage and cloud microphysics. While clouds are unstable and most cloud effects appear at low and middle latitudes, in high latitudes, ultrafine aerosols seem to be more important. Therefore, in the next step of the global circuit model, involving accurate clouds could be an important direction.

CONCLUSION

An updated global circuit model based on a chemistry-climate model (SOCOL-AERv2) with an accurate aerosol formation process is set up. The results provide a more accurate evaluation of the layer of ultrafine aerosols on global column resistance. The asymmetric distribution of ultrafine aerosols causes different responses of local column resistance to fluctuations in energetic particle precipitation. Column resistance in the high latitudes of the winter hemisphere would be more sensitive to energetic particle precipitation than that of the summer hemisphere. Since the EEP flux could contribute more relativistic electrons in the middle stratosphere, with the apparent ultrafine aerosol layer, the column resistance in the winter hemisphere would be more sensitive to fluctuations in the flux of REP. The whole atmosphere chemistry-climate model coupled with the global circuit sub-model including accurate ion pair production by REP could provide a clearer picture of the link between space weather and the troposphere.

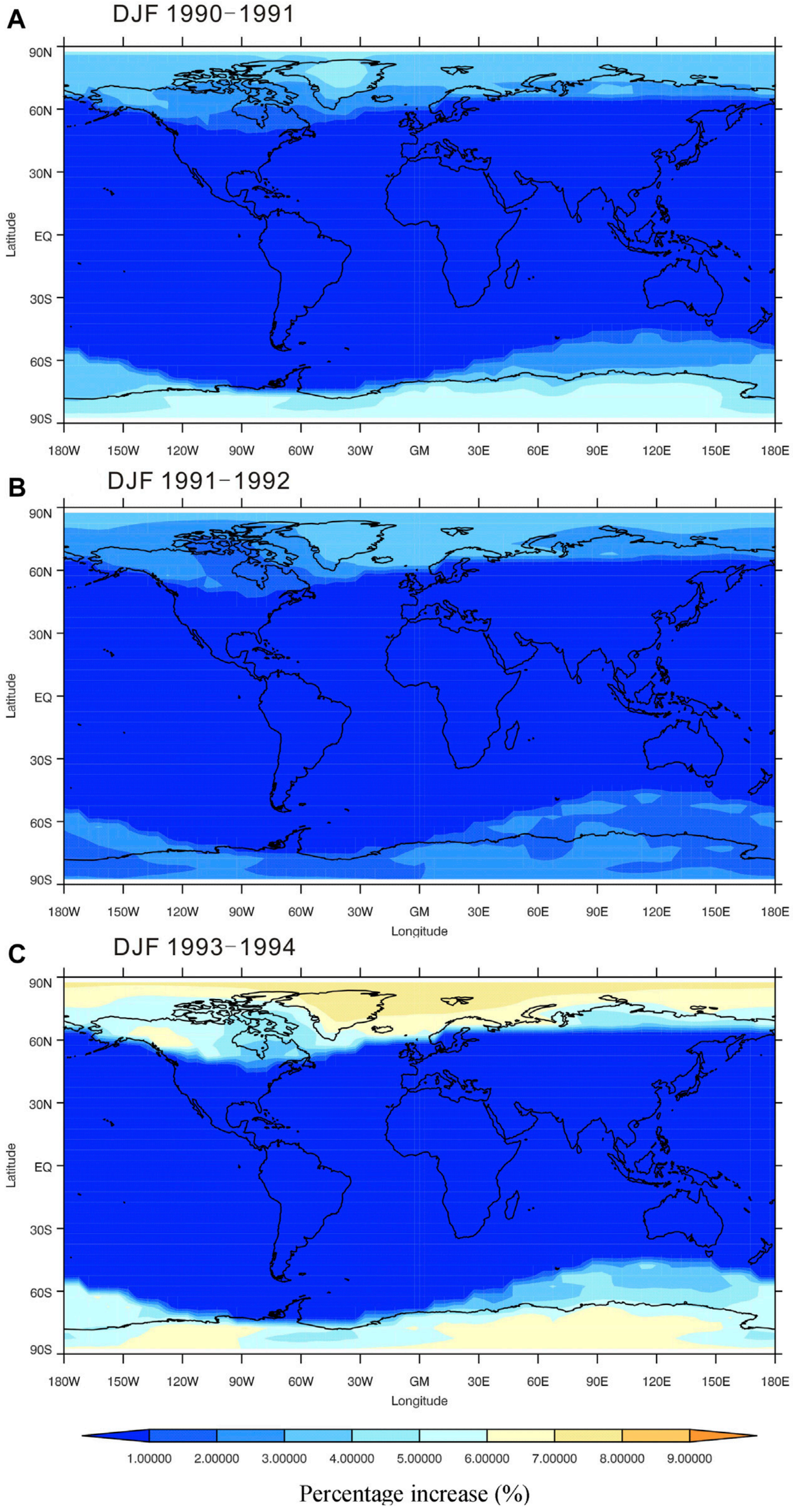

FIGURE 10 | The percentage increases $((R_{GCR}-R_{GCR+EEP})/R_{GCR})\times100\%$, of column resistance due to different external ionization sources in DJF **(A)** 1990–1991, **(B)** 1991–1992, and **(C)** 1993–1994.

DATA AVAILABILITY STATEMENT

The raw data supporting the conclusion of this article will be made available by the authors, without undue reservation.

AUTHOR CONTRIBUTIONS

LZ, designing the work for the publication and making the original GEC model, taking in charge of the whole work; YX, operating the updated global circuit model and finishing 80% writing work for the manuscript; RZ, operating the SOCOL_AER model and finishing 20% writing work of the manuscript; ZZ, operating the SOCOL_AER model.

FUNDING

This work was funded in part by the Strategic Priority Research Program of CAS (Grant No. XBD 41000000) and the National Science Foundation of China (41971020, 41905059).

REFERENCES

Bates, D. R. (1982). Recombination of Small Ions in the Troposphere and Lower Stratosphere. *Planet. Space Sci.* 30 (12), 1275–1282. doi:10.1016/0032-0633(82)90101-5

Baumgaertner, G. A. J., Thayer, J. P., Neely, R. R., and Lucas, G. (2013). Toward a Comprehensive Global Electric Circuit Model: Atmospheric Conductivity and its Variability in CESM1(WACCM) Model simulations. *J. Geophys. Res. Atmos.* 118 (16), 9221–9232. doi:10.1002/jgrd.50725

Bering, E. A., Benbrook, J. R., Holzworth, R. H., Byrne, G. J., and Gupta, S. P. (2005). Latitude Gradients in the Natural Variance in Stratospheric Conductivity Implications for Studies of Long-Term Changes. *Adv. Space Res.* 35 (8), 1385–1397. doi:10.1016/j.asr.2005.04.017

Bering, E. A., III, Few, A. A., and Benbrook, J. R. (1998). The Global Electric Circuit. *Phys. Today* 51 (10), 24–30. doi:10.1063/1.882422

Butchart, N. (2014). The Brewer-Dobson Circulation. *Rev. Geophys.* 52 (2), 157–184. doi:10.1002/2013rg000448

Egorova, T. A., Rozanov, E. V., Zubov, V. A., and Karol, I. L. (2003). Model for Investigating Ozone Trends (MEZON). *Izvestiya Atmos. Oceanic Phys.* 39 (3), 277–292.

Egorova, T., Rozanov, E., Ozolin, Y., Shapiro, A., Calisto, M., Peter, T., et al. (2011). The Atmospheric Effects of October 2003 Solar Proton Event Simulated with the Chemistry-Climate Model SOCOL Using Complete and Parameterized Ion Chemistry. *J. Atmos. Solar-Terrestrial Phys.* 73 (2), 356–365. doi:10.1016/j.jastp.2010.01.009

English, J. M., Toon, O. B., Mills, M. J., and Yu, F. (2011). Microphysical Simulations of New Particle Formation in the Upper Troposphere and Lower Stratosphere. *Atmos. Chem. Phys.* 11 (17), 9303–9322. doi:10.5194/acp-11-9303-2011

Fang, X., Randall, C. E., Lummerzheim, D., Wang, W., Lu, G., Solomon, S. C., et al. (2010). Parameterization of Monoenergetic Electron Impact Ionization. *Geophys. Res. Lett.* 37 (22), 1–5. doi:10.1029/2010gl045406

Feinberg, A., Sukhodolov, T., Luo, B.-P., Rozanov, E., Winkel, L. H. E., Peter, T., et al. (2019). Improved Tropospheric and Stratospheric Sulfur Cycle in the Aerosol-Chemistry-Climate Model SOCOL-AERv2. *Geosci. Model. Dev.* 12 (9), 3863–3887. doi:10.5194/gmd-12-3863-2019

Fischer, H. J., and Mühleisen, J. (1980). The Ionospheric Potential and the Solar Magnetic Sector Boundary Crossings. *Rep. Astron. Inst., Univ. Tübingen, Ravensburg, Germany.*

Frahm, R. A., Winningham, J. D., Sharber, J. R., Link, R., Crowley, G., Gaines, E. E., et al. (1997). The Diffuse aurora: A Significant Source of Ionization in the Middle Atmosphere. *J. Geophys. Res.* 102 (D23), 28203–28214. doi:10.1029/97jd02430

Frederick, J. E., Tinsley, B. A., and Zhou, L. (2019). Relationships between the Solar Wind Magnetic Field and Ground-Level Longwave Irradiance at High Northern Latitudes. *J. Atmos. Solar-Terrestrial Phys.* 193, 105063. doi:10.1016/j.jastp.2019.105063

Funke, B., López-Puertas, M., Stiller, G. P., Versick, S., and von Clarmann, T. (2016). A Semi-empirical Model for Mesospheric and Stratospheric NOy Produced by Energetic Particle Precipitation. *Atmos. Chem. Phys.* 16 (13), 8667–8693. doi:10.5194/acp-16-8667-2016

Hays, P. B., and Roble, R. G. (1979). A Quasi-Static Model of Global Atmospheric Electricity, 1. The Lower Atmosphere. *J. Geophys. Res.* 84 (A7), 3291–3305. doi:10.1029/ja084ia07p03291

Hebert, L., Tinsley, B. A., and Zhou, L. (2012). Global Electric Circuit Modulation of winter Cyclone Vorticity in the Northern High Latitudes. *Adv. Space Res.* 50 (6), 806–818. doi:10.1016/j.asr.2012.03.002

Hess, M., Koepke, P., and Schult, I. (1998). Optical Properties of Aerosols and Clouds: The Software Package OPAC. *Bull. Amer. Meteorol. Soc.* 79 (5), 831–844. doi:10.1175/1520-0477(1998)079<0831:opoaac>2.0.co;2

Holzworth, R. H., Norville, K. W., and Williamson, P. R. (1987). Solar Flare Perturbations in Stratospheric Current Systems. *Geophys. Res. Lett.* 14 (8), 852–855. doi:10.1029/gl014i008p00852

Höpfner, M., Glatthor, N., Grabowski, U., Kellmann, S., Kiefer, M., Linden, A., et al. (2013). Sulfur Dioxide (SO2) as Observed by MIPAS/Envisat: Temporal Development and Spatial Distribution at 15-45 Km Altitude. *Atmos. Chem. Phys.* 13 (20), 10405–10423. doi:10.5194/acp-13-10405-2013

Hoppel, W. A. (1985). Ion-Aerosol Attachment Coefficients, Ion Depletion, and the Charge Distribution on Aerosols. *J. Geophys. Res.*. 90 (D4), 5917–5923. doi:10.1029/JD090iD04p05917

Junge, C. E., and Manson, J. E. (1961). Stratospheric Aerosol Studies. *J. Geophys. Res.* 66 (7), 2163–2182. doi:10.1029/jz066i007p02163

Kirkland, M. W., Tinsley, B. A., and Hoeksema, J. T. (1996). Are Stratospheric Aerosols the Missing Link Between Tropospheric Vorticity and Earth Transits of the Heliospheric Current Sheet?. *J. Geophy. Res.: Atmosphe.* 101 (D23), 29689–29699. doi:10.1029/96JD01554

Kniveton, D. R., and Tinsley, B. A. (2004). Daily changes in global cloud cover and Earth transits of the heliospheric current sheet. *J. Geophys. Res.* 109, D11201. doi:10.1029/2003JD004232

Kniveton, D. R., Tinsley, B. A., Burns, G. B., Bering, E. A., and Troshichev, O. A. (2008). Variations in Global Cloud Cover and the Fair-Weather Vertical Electric Field. *J. Atmos. Solar-Terrestrial Phys.* 70 (13), 1633–1642. doi:10.1016/j.jastp.2008.07.001

Lam, M. M., Chisham, G., and Freeman, M. P. (2014). Solar Wind-Driven Geopotential Height Anomalies Originate in the Antarctic Lower Troposphere. *Geophys. Res. Lett.* 41 (18), 6509–6514. doi:10.1002/2014gl061421

Lam, M. M., and Tinsley, B. A. (2016). Solar Wind-Atmospheric Electricity-Cloud Microphysics Connections to Weather and Climate. *J. Atmos. Solar-Terrestrial Phys.* 149, 277–290. doi:10.1016/j.jastp.2015.10.019

Li, X., Baker, D. N., Kanekal, S. G., Looper, M., and Temerin, M. (2001a). Long Term Measurements of Radiation Belts by SAMPEX and Their Variations. *Geophys. Res. Lett.* 28 (20), 3827–3830. doi:10.1029/2001gl013586

Li, X., Temerin, M., Baker, D. N., Reeves, G. D., and Larson, D. (2001b). Quantitative Prediction of Radiation belt Electrons at Geostationary Orbit Based on Solar Wind Measurements. *Geophys. Res. Lett.* 28 (9), 1887–1890. doi:10.1029/2000gl012681

Lin, S.-J., and Rood, R. B. (1996). Multidimensional Flux-form Semi-lagrangian Transport Schemes. *Mon. Wea. Rev.* 124 (9), 2046–2070. doi:10.1175/1520-0493(1996)124<2046:mffslt>2.0.co;2

Lucas, G. M., Baumgaertner, A. J. G., and Thayer, J. P. (2015). A Global Electric Circuit Model within a Community Climate Model. *J. Geophys. Res. Atmos.* 120 (23), 12054–12066. doi:10.1002/2015jd023562

Makino, M., and Ogawa, T. (1985). Quantitative Estimation of Global Circuit. *J. Geophys. Res.* 90 (D4), 5961–5966. doi:10.1029/jd090id04p05961

Mironova, I., Karagodin-Doyennel, A., and Rozanov, E. (2021). The Effect of Forbush Decreases on the Polar-Night HOx Concentration Affecting Stratospheric Ozone. *Front. Earth Sci.* 8, 669. doi:10.3389/feart.2020.618583

Mlawer, E. J., Taubman, S. J., Brown, P. D., Iacono, M. J., and Clough, S. A. (1997). Radiative Transfer for Inhomogeneous Atmospheres: RRTM, a Validated Correlated-K Model for the Longwave. *J. Geophys. Res.* 102 (D14), 16663–16682. doi:10.1029/97jd00237

Morcrette, J. (1991). Evaluation of Model-generated Cloudiness: Satellite-observed and Model-generated Diurnal Variability of Brightness Temperature. *Monthly Weather Rev.* 119 (5), 1205–1224. doi:10.1175/1520-0493(1991)119<1205:EOMGCS>2.0.CO;2

Reiter, R. (1997). The Electric Potential of the Ionosphere as Controlled by the Solar Magnetic Sector Structure. Result of a Study Over the Period of a Solar Cycle. *J. Atmosph. Terrestrial Phys.* 39 (1), 95–99.

Rinsland, C. P., Gunson, M. R., Ko, M. K. W., Weisenstein, D. W., Zander, R., Abrams, M. C., et al. (1995). H2SO4photolysis: A Source of Sulfur Dioxide in the Upper Stratosphere. *Geophys. Res. Lett.* 22 (9), 1109–1112. doi:10.1029/95GL00917

Roeckner, E. (1995). Parameterization of clouds and radiation in climate models. United States. doi:10.2172/232602

Roeckner, E., Bäuml, G., Bonaventura, L., Brokopf, R., Esch, M., Giorgetta, M., et al. (2003). *The Atmospheric General Circulation Model ECHAM 5. PART I: Model Description*. Tech. Rep. 349 (Hamburg: Max-Planck-Institut für Meteorologie). Available at: http://www.mpimet.mpg.de/fileadmin/publikationen/Reports/max_scirep_349.pdf (Access July 9, 2019).

Rozanov, E. V., Zubov, V. A., Schlesinger, M. E., Yang, F., and Andronova, N. G. (1999). The UIUC Three-Dimensional Stratospheric Chemical Transport Model: Description and Evaluation of the Simulated Source Gases and Ozone. *J. Geophys. Res.* 104 (D9), 11755–11781. doi:10.1029/1999jd900138

Sapkota, B. K., and Varshneya, N. C. (1990). On the Global Atmospheric Electrical Circuit. *J. Atmos. Terrestrial Phys.* 52 (1), 1–20. doi:10.1016/0021-9169(90)90110-9

Sheng, J.-X., Weisenstein, D. K., Luo, B.-P., Rozanov, E., Stenke, A., Anet, J., et al. (2015). Global Atmospheric Sulfur Budget under Volcanically Quiescent Conditions: Aerosol-Chemistry-Climate Model Predictions and Validation. *J. Geophys. Res. Atmos.* 120 (1), 256–276. doi:10.1002/2014jd021985

Stenke, A., Schraner, M., Rozanov, E., Egorova, T., Luo, B., and Peter, T. (2013). The SOCOL Version 3.0 Chemistry-Climate Model: Description, Evaluation, and Implications from an Advanced Transport Algorithm. *Geosci. Model. Dev.* 6 (5), 1407–1427. doi:10.5194/gmd-6-1407-2013

Sukhodolov, T., Sheng, J.-X., Feinberg, A., Luo, B.-P., Peter, T., Revell, L., et al. (2018). Stratospheric Aerosol Evolution after Pinatubo Simulated with a Coupled Size-Resolved Aerosol-Chemistry-Climate Model, SOCOL-AERv1.0. *Geosci. Model. Dev.* 11 (7), 2633–2647. doi:10.5194/gmd-11-2633-2018

Tinsley, B. A. (1996). Correlations of Atmospheric Dynamics with Solar Wind-Induced Changes of Air-Earth Current Density into Cloud Tops. *J. Geophys. Res.* 101 (D23), 29701–29714. doi:10.1029/96jd01990

Tinsley, B. A., and Deen, G. W. (1991). Apparent Tropospheric Response to MeV-GeV Particle Flux Variations: A Connection via Electrofreezing of Supercooled Water in High-Level Clouds?. *J. Geophys. Res.* 96 (D12), 22283–22296. doi:10.1029/91jd02473

Tinsley, B. A. (2005). On the Variability of the Stratospheric Column Resistance in the Global Electric Circuit. *Atmosphe. Res.* 76 (1-4), 78–94. doi:10.1016/j.atmosres.2004.11.013

Tinsley, B. A. (2008). The Global Atmospheric Electric Circuit and its Effects on Cloud Microphysics. *Rep. Prog. Phys.* 71 (6), 066801. doi:10.1088/0034-4885/71/6/066801

Tinsley, B. A., Hoeksema, J. T., and Baker, D. N. (1994). Stratospheric Volcanic Aerosols and Changes in Air-Earth Current Density at Solar Wind Magnetic Sector Boundaries as Conditions for the Wilcox Tropospheric Vorticity Effect. *J. Geophys. Res.* 99 (D8), 16805–16813. doi:10.1029/94JD01207

Tinsley, B. A., and Yu, F. (2004). Atmospheric Ionization and Clouds as Links between Solar Activity and Climate. *Solar Variability Its Effects Clim., Geophys. Monogr. Ser.* 141, 321–339. doi:10.1029/141gm22

Tinsley, B. A., Zhou, L., and Plemmons, A. (2006). Changes in Scavenging of Particles by Droplets Due to Weak Electrification in Clouds. *Atmos. Res.* 79 (3-4), 266–295. doi:10.1016/j.atmosres.2005.06.004

Usoskin, I. G., Kovaltsov, G. A., and Mironova, I. A. (2010). Cosmic ray Induced Ionization Model CRAC:CRII: An Extension to the Upper Atmosphere. *J. Geophys. Res.* 115 (D10), 302. doi:10.1029/2009jd013142

Veretenenko, S. V., and Pudovkin, M. I. (1997). Effects of the Galactic Cosmic ray Variations on the Solar Radiation Input in the Lower Atmosphere. *J. Atmos. Solar-Terrestrial Phys.* 59 (14), 1739–1746. doi:10.1016/s1364-6826(96)00183-6

Voiculescu, M., Usoskin, I., and Condurache-Bota, S. (2013). Clouds Blown by the Solar Wind. *Environ. Res. Lett.* 8 (4), 045032. doi:10.1088/1748-9326/8/4/045032

Wilcox, J. M., Scherrer, P. H., Svalgaard, L., Roberts, W. O., and Olson, R. H. (1973). Solar Magnetic Sector Structure: Relation to Circulation of the Earth's Atmosphere. *Science (New York, N.Y.)* 180 (4082), 185–186. doi:10.1126/science.180.4082.185

Yu, F., and Turco, R. P. (2001). From Molecular Clusters to Nanoparticles: Role of Ambient Ionization in Tropospheric Aerosol Formation. *J. Geophys. Res.* 106 (D5), 4797–4814. doi:10.1029/2000jd900539

Zhou, L., and Tinsley, B. A. (2010). Global Circuit Model with Clouds. *J. Atmos. Sci.* 67 (4), 1143–1156. doi:10.1175/2009jas3208.1

Zhou, L., Tinsley, B., and Huang, J. (2014). Effects on winter Circulation of Short and Long Term Solar Wind Changes. *Adv. Space Res.* 54 (12), 2478–2490. doi:10.1016/j.asr.2013.09.017

Zhou, L., Tinsley, B., Wang, L., and Burns, G. (2018). The Zonal-Mean and Regional Tropospheric Pressure Responses to Changes in Ionospheric Potential. *J. Atmos. Solar-Terrestrial Phys.* 171, 111–118. doi:10.1016/j.jastp.2017.07.010

Conflict of Interest: The authors declare that the research was conducted in the absence of any commercial or financial relationships that could be construed as a potential conflict of interest.

frontiers
in Earth Science

BRIEF RESEARCH REPORT
published: 15 July 2021
doi: 10.3389/feart.2021.671870

Tree Canopies Influence Ground Level Atmospheric Electrical and Biogeochemical Variability

Ellard R. Hunting, Sam J. England and Daniel Robert**

School of Biological Sciences, University of Bristol, Bristol, United Kingdom

Static electric fields in the atmosphere are increasingly recognized as interacting with various organisms over several levels of biological organization. Recently, a link between atmospheric electrical variations and biogeochemical processes has been established in the context of open fields, yet biological structures like trees produce substantial alterations in atmospheric electric properties. Here, we assess whether these structural changes affect the dynamics of the electrical landscape and its relation to geochemical processes. To this end, we theoretically assess how trees alter their surrounding electric fields and empirically compare the temporal dynamics of atmospheric potential gradients, positive ions in the near-ground level atmosphere and soil electrochemical properties in an open field and under a tree. The developed model of electric fields around trees provides insight into the extent to which trees shield the underlying electric landscape, revealing that a substantial increase in atmospheric potential gradient only marginally affects the electric field under the canopy. We further show that soil electrochemical properties are tied to the temporal dynamics of positive ion in the near-ground level atmosphere, and that the presence of a tree reduces the temporal variability in both ground level positive ion concentrations and soil redox potential. This suggests that a tree can alter the temporal variability in atmospheric electricity and soil electro-chemistry, thereby likely indirectly influencing soil microorganisms and processes as well as electro-sensitive organisms that perceive and utilize atmospheric electric fields.

Keywords: atmospheric electricity, ions, wavelet variance, potential gradient, redox potential - Eh

Edited by:
Konstantinos Kourtidis,
Democritus University of Thrace,
Greece

Reviewed by:
Francesca Apollonio,
Sapienza University of Rome, Italy
Andrea Schievano,
University of Milan, Italy

****Correspondence:***
Ellard R. Hunting
e.r.hunting@bristol.ac.uk
Daniel Robert
d.robert@bristol.ac.uk

Specialty section:
This article was submitted to
Atmospheric Science,
a section of the journal
Frontiers in Earth Science

Received: *24 February 2021*
Accepted: *23 June 2021*
Published: *15 July 2021*

Citation:
Hunting ER, England SJ and Robert D (2021) Tree Canopies Influence Ground Level Atmospheric Electrical and Biogeochemical Variability. Front. Earth Sci. 9:671870. doi: 10.3389/feart.2021.671870

INTRODUCTION

The ground level atmosphere is host to various distributions of electrical charges and associated static electric fields (Rycroft et al., 2008) and it becomes increasingly apparent that electrostatic interactions form the basis of the electric ecology of various organisms over several levels of biological organization (e.g., molecules, cells, organisms, communities) (Clarke et al., 2013; Greggers et al., 2013; Morley and Robert, 2018; Hunting et al., 2021). Atmospheric charge distributions and electric fields are dynamic and can show variations over hours to seasons which are mainly driven by two sources. First, there is a build-up of mainly positive ions near the surface of the ground (Adkins, 1959; Crozier, 1965; Reiter, 1985) that results from a complex interplay of soil radon exhalation and decay, the charging of aerosols and atmospheric pollution (Kubicki et al., 2016). These largely elusive sources of charge result in hourly and daily variations in ground level (<2 m) atmospheric charges that are important at near surface layers of continental soils. Second, thunderstorm regions around the globe drive positive charges at higher altitudes (approx. 8–13 km) towards fair weather regions as

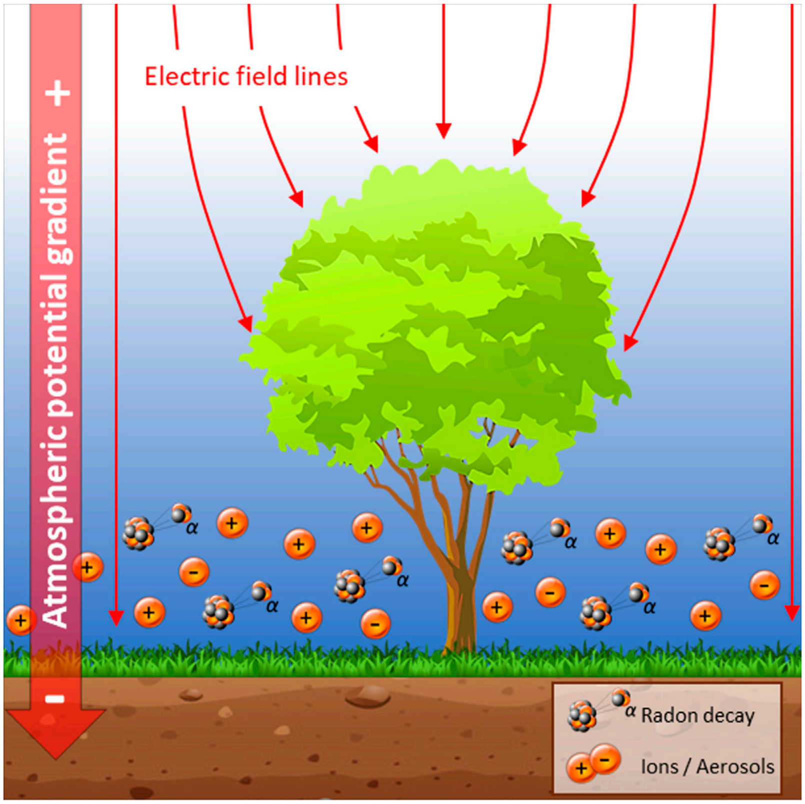

FIGURE 1 | Conceptual impression of the electric landscape around trees.

part of the global electric circuit (Wilson, 1903; Rycroft et al., 2008; Fdez-Arroyabe et al., 2021). This results in diel and seasonal variations in atmospheric potential gradients that, although sometimes measureable over continental soils, are far more prevalent in clean oceanic air. Consequently, atmospheric charge distributions and associated electrical fields and charge flow operate at local and global spatial scales and various temporal (hours to seasons) scales.

Atmospheric electric fields—as well as their dynamics—have recently been linked to biogeochemical processes below the Earth's surface by means of a charge separation between relatively negative charges in the Earth's interior and positive charge sources in the atmosphere (Hunting et al., 2019). Changes in atmospheric charges were observed to drive a subsurface migration of nutrients that are essential to microbial metabolism, thereby affecting efficiency and dynamics of microbial processes (Hunting et al., 2019). The conceptual and empirical foundation underlying the link between atmospheric electrical variations and biogeochemical processes has been established in the context of open fields (e.g., grasslands) and freshwater systems. However, both empirical data and mathematical models have shown that trees produce substantial alterations in the electric landscape, in particular the electric field strength in the surrounding air (Arnold et al., 1965; Borra et al., 1997; Bowker and Crenshaw 2007; Williams and Mareev, 2014; Clarke et al., 2017; Morley and Robert, 2018). In this, positive charges in the atmosphere draw a negative mirror charge to surfaces of trees with high curvatures (e.g., branches, needles) and thereby produce larger fields compared to surfaces that have a smaller degree of curvature or are flat (Feynman et al., 1964; Rowland et al., 2015; Clarke et al., 2017). Thus, as plants display some mobility in their surface electric charge carriers (electrons, charged molecules and ions), the electric field surrounding them will take up geometries that are influenced by the strength of atmospheric potential gradients as well as the plants' height and morphology. Likewise, large plants, such as trees, have been reported to contribute substantially to local variations in ground level atmospheric ions (e.g., Jayaratne et al., 2011) that are generated largely by transpiration. It thus becomes apparent that trees and their canopies present both an abiotic modifier as well as biogenic source of atmospheric electricity (See **Figure 1** for a conceptual and mathematical representation of electric fields and ions around trees).

In light of the largely uncharacterised and empirically elusive near-ground (0–2 m) electric landscape and its unsuspected roles in geochemical changes in both near-ground and subsurface environments, questions are thus arising whether structural changes within the landscape such as trees also affect the dynamics of atmospheric electricity and its relation to geochemical processes. Here, we theoretically assess how the structural and physical properties of trees are relevant in shaping their surrounding electric fields, and empirically compare the temporal dynamics of atmospheric potential gradients, positive ions in the near-ground level atmosphere and soil electrochemical properties in an open field and under a tree.

METHODS

Model of Atmospheric Electric Fields

Since modelling approaches with two-dimensional geometries published to date are potentially prone to exaggerating the electrical shielding effect of most structures, we modelled a three-dimensional geometry to assess the effect of a tree on local atmospheric electric fields. Modelling was performed using finite element analysis within COMSOL Multiphysics® v. 5.4 (COMSOL AB, Stockholm, Sweden) utilising the "Electric Currents" interface within the "AC/DC" module. The three-dimensional geometry consisted of a 300 m × 300 m x 300 m cube within which the model operated. The model ground level was occupied by a 300 m × 300 m x 2 m block of soil. At its centre, an approximate representation of a 30 m tall deciduous tree, with a 2 m wide trunk, and a canopy spanning roughly 30 m was positioned. This tree could be regarded as a model of an oak or an alder tree. The remainder of the geometry was assigned as air. The upper surface of this air column was given an electrical potential typical of a 300 m altitude in various meteorological conditions, representative of the atmospheric potential gradient (Wilson 1903; Bennett and Harrison 2007). The electrical ground was defined 2 m below the upper surface of the soil (a typical groundwater table depth). Meshing of this geometry was physics-controlled, set to "extremely fine" (**Supplementary Figure S1**). Electrical properties of all materials were obtained from measurements or estimates from primary literature. The electrical conductivity, σ, and relative permittivity, ε_r, were defined as: for soil, $\sigma = 0.05$ S/m, $\varepsilon_r = 15$ (Rhebergen et al., 2002; Brovelli and Cassiani, 2011); for living trees, $\sigma = 2 \times 10^{-4}$ S/m, $\varepsilon_r = 12$ (Suojanen et al., 2001; Gora and Yanoviak, 2015); and for air, $\sigma = 1 \times 10^{-14}$ S/m, $\varepsilon_r = 1$ (Hogg 1939; Higazi and Chalmers, 1966). Model outputs presented for this study were produced by plotting data from two-dimensional slices or one-dimensional cut lines through areas of interest within the three-dimensional geometry. An identical model, except with no tree present, was constructed as a reference. To test for the sensitivity of the results to parameter value selection, parametric sweeps were performed across a wide range of possible values for all of the included electrical material properties except for the relative permittivity of air as this is a well-known quantity that is unlikely to vary substantially.

Experimental Approach

Atmospheric Drivers of Soil Redox Potential

Soil redox potential was previously linked to ground level ion concentrations, yet it is necessary to assess whether local soil redox potential is potentially coupled to atmospheric potential gradients as well as other meteorological variables. Due to technical issues it was impossible to measure atmospheric potential gradients, atmospheric ions and other meteorological variables simultaneously in relation to soil redox potential. Two separate time-series where therefore measured to assess the relative importance of both atmospheric potential gradients and ions as a driver of soil redox potential. These time series measurements and subsequent experiments were performed at the University of Bristol, School of Veterinary Sciences, Langford United Kingdom, between October 2018 and February 2019, in which measurements took place during fair weather with occassional cloud cover (fair weather conditions as defined in Harrison and Nicoll, 2018).

The first time-series was recorded between 24-10-2018 and 31-10-2018 in open field conditions to assess whether local soil redox potential is potentially coupled to atmospheric potential gradients as well as other meteorological variables. To this end, the atmospheric potential gradients was continuously measured on site using a field mill (Boltek EFM 100 Field Mill) that consists of a horizontal electrode connected to an electrometer that is alternately exposed and shielded from the atmospheric electric field in which a charge is induced on the electrode that is proportional to the field. The field mill was positioned with its rotor facing up on top of a single vertical aluminium pole at 1.8 m above the top layer of the soil to assess variations in the atmospheric potential gradient above the first 2 m of the ground level atmosphere. Meteorological parameters where continuously measured on site using a Maximet (GMX501) weather station, and included temperature (°C), humidity (RH), air pressure (mB), solar radiation (W/m^2), windspeed (m/s) and precipitation (mm/min). Redox potentials (Eh) in soils were measured simultaneously every 20 min using a permanently installed platinum electrode at 10 cm depth connected to a Hypnos three data logger and corrected for a calomel reference electrode and measured pH. Details on the Eh monitoring devices and electrodes are described elsewhere (Vorenhout et al., 2011).

A second time-series was measured between 13-11-2018 and 17-11-2018 to assess the relation between soil redox potential and concentration of positive ions in the atmosphere just above (<0.2 m) the soil. This was simultaneously measured in an open field and next to the trunk of a grey alder (*Alnus incana*) in which the tree did not carry leaves and the top soil layer was covered with short (<10 cm) grass during the measurement period. Atmospheric cation concentrations were measured every second using two cylindrical capacitor-based ion-counters operating on the "Gerdien-tube" principle (Alpha-lab Inc., Salt Lake City, UT, United States), calibrated in open field conditions and recorded onto a PC using a National Instruments (Austin, Texas) DAQ system. Redox potentials (Eh) in soils were measured as described above.

Influence of Tree Canopy on Soil Redox Potential and Atmospheric Ions

Initial time-series measurements revealed that local soil redox potential was primarily governed by atmospheric cation concentrations (see results section for details). Therefore, to further quantify the influence of canopies on ground level variations of both redox potential and atmospheric ions, a

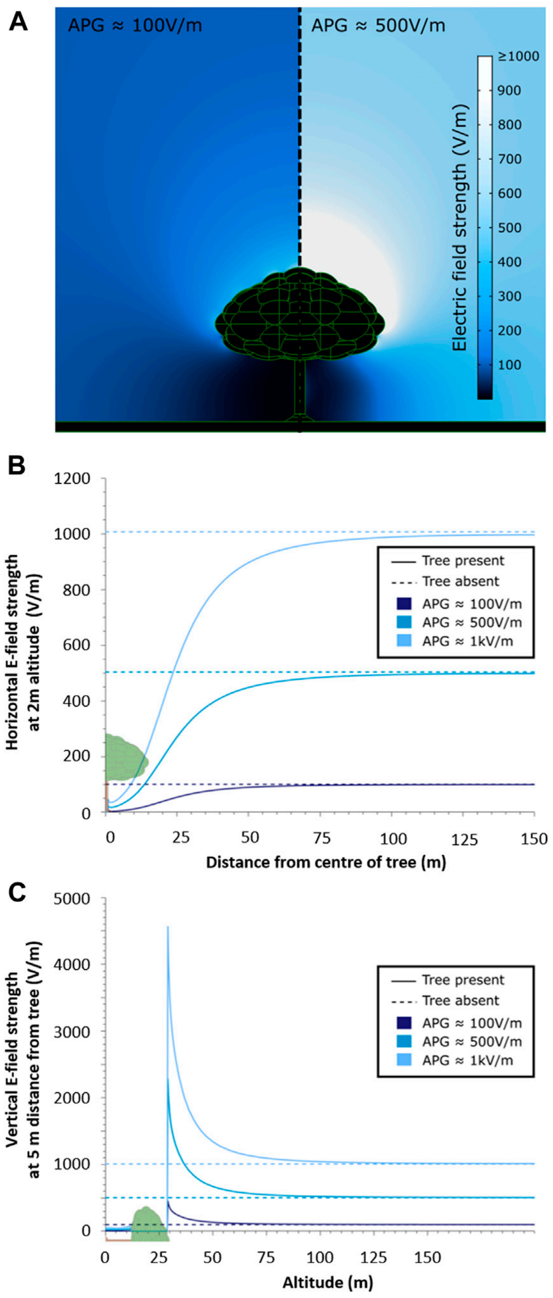

FIGURE 2 | Outputs from a three-dimensional finite element analysis model of the electric fields surrounding a tree stood in open ground, exposed to various vertical atmospheric potential gradients (APGs). **(A)** two-dimensional slice through the centre of the tree in two different APG strengths, 100 V/m **(left)** and 500 V/m **(right)**, showing the resultant electric landscape. **(B)** cutline horizontal transects taken through the model travelling from the centre of the tree outwards for 150 m, at an altitude of 2 m, for various APG strengths, exemplifying the electrical shielding effect of the tree both immediately underneath the tree and for large distances away from the canopy. Model outputs with a tree present (solid) are compared with identical models with no tree present (dashed) **(C)** cutline vertical transects taken through the model, travelling from the soil surface upwards for 200 m, 5 m horizontally from the centre of the tree, for various APG strengths, showing both the shielding effect beneath the canopy and the amplification of the APG above the tree. Again, model outputs with a tree present (solid) are compared with identical models with no tree present (dashed).

series of measurements in time were performed during the day in an open field and next to the trunk of a grey alder (*Alnus incana*) in February 2019. This focussed on the period between 10:00 am and 20:00 pm to avoid large influences of diel fluctuations typically observed in ground level atmospheric ion concentrations (e.g. Jayaratne et al., 2011). We used standardized soil microcosms to assure soils were comparable between both tree and open field conditions (i.e., sufficient water content, exclusion of ground water flow). To this end, 400 ml glass beakers were filled with a pre-wetted standardized soil mixture (quartz and turf, 3:1). Positive ground level atmospheric ions and soil redox potential were measured simultaneously in soil microcosms at 1 cm depth in which the microcosms were positioned at the base of a stand-alone tree and an open field, 5 m away from the margin of the canopy of the tree. This was repeated six times ($n = 6$) at six different fair weather days with freshly prepared microcosms. In this, soil redox potentials (Eh) were measured as described above, yet using two permanently installed gold-plated PCB electrodes (Vorenhout et al., 2011). Temporal variability of the measurements of the six individual days were subsequently assessed with a Wavelet transform spectral analysis in PAST (Hammer et al., 2001). This form of spectral analysis proved a valuable approach in evaluating spatial and temporal patterns in ecological research by creating a composite measure of temporal variance for each treatment or spatially separated samples over time (Bradshaw and Spies, 1992; Ibarra-Junquera et al., 2006; Escalante-Minakata et al., 2009). As applied here, we followed the procedures described in detail by Hunting et al. (2015). Amplitude of temporal variation were thus characterised, allowing the comparison between simultaneous or spatially separated measurements by quantifying the variance of the wavelet transform for each day and individual microcosms. Finally, differences between trees and open-field wavelet variances were assessed using a small sample-corrected Epps-Singleton test for equal distributions (Epps and Singleton, 1986).

RESULTS

Modelling using finite element analysis demonstrates that the presence of a tree has a marked impact on the surrounding electric field (**Figures 2A,B,C**). Beneath the tree, electric field strengths are reduced by more than an order of magnitude, supporting the hypothesis that trees act as electrical shields, greatly diminishing variability in electrical conditions beneath their canopies. A horizontal transect taken through the model (**Figure 2B**) shows that for a large tree in an open field, this shielding effect persists beyond the immediate vicinity of the tree, with the electric field strength continuing to be reduced in excess of 100 m away from the trunk in comparison to no tree being present. In contrast to this arboreal suppression of electric fields beneath the canopy, we conversely find that the electric field strength immediately above the tree is amplified above levels expected if no tree were present. Examining the vertical transect through the model, positioned 5 m away from the trunk

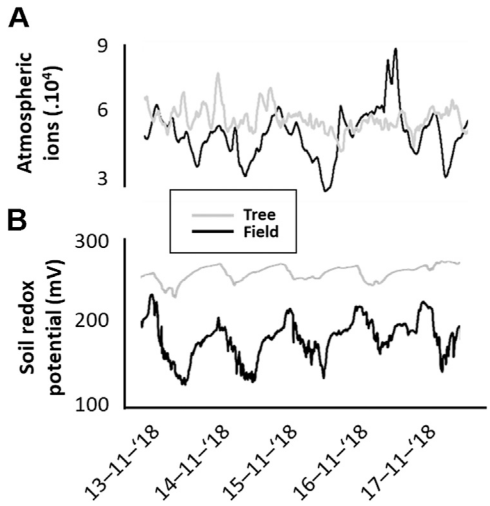

FIGURE 3 | Co-variability of positive atmospheric ions and soils redox potential as revealed by a time-series (13-11-2018 untill 17-11-2018) measurements of **(A)** concentration of positive ions in the atmosphere just above (<0.2 m) and **(B)** soil redox potential, Eh. This was simultaneously measured in an open field and next to the trunk of a grey alder (Alnus incana).

(**Figure 2C**), emphasises this effect, whereby significant amplification takes place near the treetop, persisting over significant distances, with some visible elevation of electric field strength even at 100 m above the tree canopy. Under a fair-weather atmospheric potential gradient of 100 V/m, or unstable conditions presenting 1 kV/m, the electric field in the immediate vicinity of the treetop can reach 450 V/m and 4.5 kV/m, respectively.

The results of the model were found to be insensitive to parameter value selection in most cases (**Supplementary Figure S3**), suggesting the results of this model hold for all realistic values of the included parameters. Specifically, within the wide-ranging but still potentially possible bounds tested, the permittivity of the soil and tree had no marked effect at all on the shielding ability of the tree. Likewise, within realistic ranges of air conductivity, the tree continues to act as an electrical shield. Some variation in the results is seen when the conductivity of the tree approaches that of the air. This is to be expected because it is largely the elevated conductivity of the tree, relative to the air, that allows it to act as an electrical shield. However, it is highly unlikely that a living tree would have a conductivity this low, and it can be seen that within a more realistic range of tree conductivities, the tree continues to be an effective electrical shield. Similarly, some increase in electric field strength is seen as the soil conductivity approaches that of air. This is again a very unlikely physical situation, but even at these extreme values, the tree continues to reduce the APG by an order of magnitude.

While differences is sampling frequencies prevented a statistical analysis of correlation between the measured variables, it becomes apparent that soil redox potential did not visibly co-vary with any of the measured atmospheric meteorological variables (**Supplementary Figure S1**). An increase in redox potential and subsequent emergence of a diel cycle coincided with a period of prolonged precipitation on the 27th of October, suggesting the soil was not necessarily saturated with water throughout the measurement period (e.g., Cusell et al., 2015). Diel cycles in soil redox potential between 29th and October 31, 2018 did not seem to be directly governed by changes in the atmospheric potential gradient.

The 5 days measurement period between 13th and November 17, 2018 suggests that ground-level positive atmospheric ions and soil redox potential in soil microcosms in the open field have distinct diel cycles (**Figures 3A,B**) that seem to co-vary. In contrast, near the trunk of a tree, soil redox potential revealed substantially (~80%) lower amplitude in diel variation, and ground-level positive atmospheric ions did not appear to have any diel rhythm (**Figures 3A,B**).

A representative example of the measured time-series similarly reveals that the moving averages of positive atmospheric ions and soils redox potential in soil microcosms covary during the day (**Figures 4A,B**). Comparison of Wavelet variances throughout the entire measurement period across the replicated time-series (**Figures 4C,D**) suggests that temporal variability was lower for both ground level atmospheric ion concentrations and soil redox potential near a tree compared to Wavelet variances in the open field (Epps-Singleton-derived error: $W^2 = 63.94$; $p < 0.001$ and $W^2 = 1{,}439.1$; $p < 0.001$, respectively).

DISCUSSION

The developed model of the electric fields around trees exemplifies the drastic influence of trees and other large plants on their electrical environment, even when only considering passive electrical interactions. Undoubtedly, an even more marked effect can be expected in tree lines or forests due to a cumulative effect of collections of plants and trees (see also Williams et al., 2005). Importantly, the extension of previous two-dimensional models on electrical shielding by trees (Clarke et al., 2017; Morley and Robert, 2018) into three dimensions corroborates the influence of vegetation on its local electrical environment. The presented three-dimensional model confirms that prior findings on the shielding ability of trees using a two-dimensional approach were qualitatively valid yet may not have been entirely numerically accurate. Previous studies demonstrated that tree canopies can alter atmospheric electric fields, almost nullifying them near the base of the tree trunk, while the reach of this shielding effect extended beyond the canopy cover by 5–20 m with increasing distance from the tree (Märcz and Harrison, 2003; Williams et al., 2005; Clarke et al., 2017; Morley and Robert, 2018). Our three-dimensional model confirms that the electric field strength is reduced to near zero beneath a tree canopy, and reveals that a substantial (5–10 fold) increase in atmospheric potential gradient only marginally affects electric fields under the canopy, articulating the extent to which a tree canopy shields its underlying electric landscape and distorts the atmospheric potential gradient beyond its own span. Remarkably, above the canopy the local electric field can be

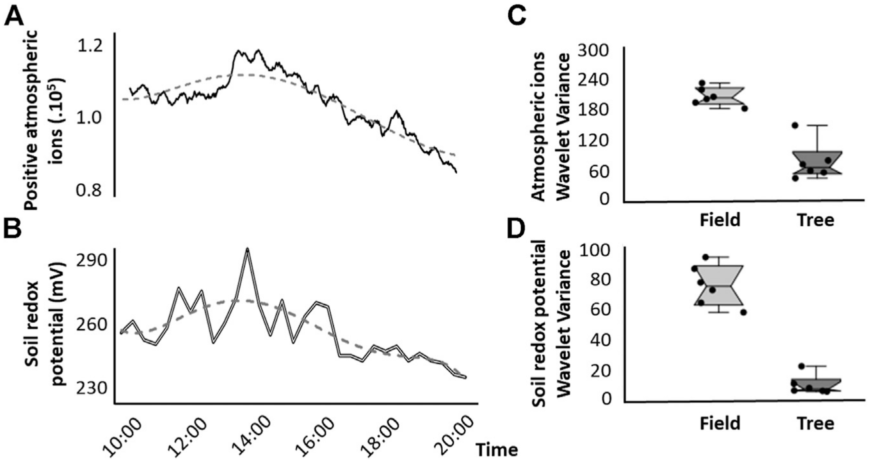

FIGURE 4 | Representative example of the measured time-series revealing co-variability of **(A)** positive atmospheric ions and **(B)** soils redox potential in soil microcosms, in which dashed line represents the hourly moving average. **(C,D)** Comparison of temporal variability across the replicated time-series for each day and individual microcosms for repeated measurements during fair weather days in February 2019. Temporal variability is expressed as Wavelet variances between near a tree and in an open field for **(C)** near ground-level atmospheric positive ions and **(D)** soil redox potential.

greatly enhanced, generating features in the electric landscape otherwise absent in open fields.

Local sources of atmospheric electricity in continental environments often remain ambiguous, relying on both globally driven atmospheric potential gradients and local sources of ionization (e.g., Wright et al., 2020). The absence of correlation between atmospheric potential gradients and other metereological parameters in our study strongly supports the notion that ground level atmospheric ion concentrations above soils are driven by local concentrations of atmospheric ions, charged aerosols and radionuclides (Kubicki et al., 2016). These ground level ion concentrations can be substantially higher around trees, observable especially in forests, compared to open fields due to transpiration of ions and radon by vegetation (e.g. Ling, et al., 2010; Jayaratne et al., 2011). Importantly, since transpiration is drastically reduced in winter, atmospheric ions between tree canopy cover and open fields are not expected to markedly differ in magnitude, suggesting that, in the present study, local sources of atmospheric ions such as soil radon exhalation and air pollution (e.g. fuel exhausts) made up the electric charges at near-ground level atmosphere in both open fields and near vegetation.

While several studies have focussed on how trees affect the local electric landscape, it remains largey unknown how trees, as large partially conductive and dielectric structures, affect the temporal dynamics of atmospheric potential gradients, and whether and how this affects multiscale chemical and biological processes. Using microcosms in fair weather conditions to exclude other major drivers of variability (e.g., shower clouds, soil water content), we observed clear differences in the dynamics between both ground level atmospheric ions and soil redox potential between the open field and below a tree canopy over a 5 days measuring period. Although clear diel cycles were visible in both ions and redox potential in open fields, diel cycles were not observed in atmospheric ions near the trunk of the tree. Soil redox potential was observed to have diel cycles, yet their magnitude was substantially lower (~10%) compared to open field conditions. A closer assessment of the temporal variability near a tree and the open field revealed that soil electrochemical properties are tied to temporal dynamics of positive ions in the near-ground level atmosphere, and that the presence of a tree reduced the temporal variability in both ground level positive ions concentrations and soil redox potential. This shows that, while ground level atmospheric ions were of primarily local origin, a tree can have a stabilizing effect on drivers of temporal variability. It is important to consider that various sources are known to contribute to ground-level electric variability, including windspeed, soil radon exhalation, tree transpiration and air-earth currents driven by atmospheric potential gradients (Jayaratne et al., 2011; Kubicki et al., 2016). Since our measurements were obtained in winter and near a single tree, it is unlikely that wind speed and tree transpiration were the source of variability. Likewise, soil radon exhalation is expected to add variability near trees provided tree soils are substantially more permeable compared to grasslands (Alaoui et al., 2011; Holthusen et al., 2018). Therefore, the most likely source of variability in this study is of atmospheric origin, in which a tree and its canopy appear to shield ground-level electric dynamics from atmospheric influences. This offers a plausible explanation to the frequently observed differences in the temporal characteristics of soil and sediment electrochemical signatures between open fields and near vegetation.

The observed interplay between vegetation, atmospheric electrical variations and soil redox potential is biologically relevant since redox potential is an important driver of bacterial community structure and metabolism in both soils and aquatic sediments (Newman and Banfield, 2002; Bertics and Ziebis, 2009; Hunting and van der Geest, 2011; Hunting et al., 2012), and oscillations in redox conditions are known to change microbial community composition (Pett-Ridge and Firestone, 2005) and promote bacterial metabolic processes (Aller, 1994). These changes in microbial metabolism can be attributed to the mobilization of microbial nutrients due to changes in the physico-chemical environment (Aller, 1994) as well as the migration of respiratory ions along electrochemical gradients and an electric field (Hunting et al., 2019). Bacteria themselves have been observed to occupy an apparent "redox niche" in which they actively migrate towards the most favourable electrochemical conditions (Bespalov et al., 1996) or actively control the redox conditions in their immediate surroundings by membrane bound and secreted redox mediators (Hunting and Kampfraath, 2013). The observed influence of local dynamics in atmospheric electricity governed by vegetation may thus affect microbial processes in soils and aquatic sediments in vegetated areas, and likely carries wider implications for electro-sensitive organisms (e.g., pollinators, ballooning spiders, and perhaps other arthropod species) that perceive and utilize atmospheric electric fields.

DATA AVAILABILITY STATEMENT

The raw data supporting the conclusion of this article will be made available by the authors, without undue reservation.

AUTHOR CONTRIBUTIONS

EH conceived the study and collected empirical data and performed statistical analyses. SE developed the model. EH drafted the manuscript. All authors contributed to study design and developing the manuscript.

FUNDING

EH received financial support from the Swiss National Science Foundation, SNF (CRSK-2 190855). DR is funded by the BBSRC (Grant BB/T003235/1) and the European Research Commission (ERC-ADG 743093), supporting EH and SE.

SUPPLEMENTARY MATERIAL

The Supplementary Material for this article can be found online at: https://www.frontiersin.org/articles/10.3389/feart.2021.671870/full#supplementary-material

Supplementary Figure 1 | Three-dimensional geometry of the tree used for finite element analysis.

Supplementary Figure 2 | Soil redox potential and meteorological parameters at the field site.

Supplementary Figure 3 | Sensitivity of model results to parametric sweeps across a wide range of possible values for all of the included electrical material properties, except relative permittivity of air.

REFERENCES

Adkins, C. J. (1959). The Small-Ion Concentration and Space Charge Near the Ground. *Q.J R. Met. Soc.* 85 (365), 237–252. doi:10.1002/qj.49708536506

Alaoui, A., Caduff, U., Gerke, H. H., and Weingartner, R. (2011). Preferential Flow Effects on Infiltration and Runoff in Grassland and forest Soils. *Vadose Zone J.* 10 (1), 367–377. doi:10.2136/vzj2010.0076

Aller, R. C. (1994). Bioturbation and Remineralization of Sedimentary Organic Matter: Effects of Redox Oscillation. *Chem. Geology.* 114 (3-4), 331–345. doi:10.1016/0009-2541(94)90062-0

Arnold, H. R., Pierce, E. T., and Whitson, A. L. (1965). The Effect of a Living Tree upon the Fair Weather Potential Gradient. *J. Atmos. Terrestrial Phys.* 27, 429–430. doi:10.1016/0021-9169(65)90045-0

Bennett, A. J., and Harrison, R. G. (2007). Atmospheric Electricity in Different Weather Conditions. *Weather* 62, 277–283. doi:10.1002/wea.97

Bertics, V. J., and Ziebis, W. (2009). Biodiversity of Benthic Microbial Communities in Bioturbated Coastal Sediments is Controlled by Geochemical Microniches. *ISME J.* 3, 1269–1285. doi:10.1038/ismej.2009.62

Bespalov, V. A., Zhulin, I. B., and Taylor, B. L. (1996). Behavioral Responses of *Escherichia coli* to Changes in Redox Potential. *Proc. Natl. Acad. Sci.* 93, 10084–10089. doi:10.1073/pnas.93.19.10084

Borra, J.-P., Roos, R. A., Renard, D., Lazar, H., Goldman, A., and Goldman, M. (1997). Electrical and Chemical Consequences of point Discharges in a forest during a Mist and a Thunderstorm. *J. Phys. D: Appl. Phys.* 30 (1), 84–93. doi:10.1088/0022-3727/30/1/011

Bowker, G. E., and Crenshaw, H. C. (2007). Electrostatic Forces in Wind-Pollination—Part 2: Simulations of Pollen Capture. *Atmos. Environ.* 41, 1596–1603. doi:10.1016/j.atmosenv.2006.10.048

Bradshaw, G. A., and Spies, T. A. (1992). Characterizing Canopy Gap Structure in Forests Using Wavelet Analysis. *J. Ecol.* 80, 205–215. doi:10.2307/2261007

Brovelli, A., and Cassiani, G. (2011). Combined Estimation of Effective Electrical Conductivity and Permittivity for Soil Monitoring. *Water Resour. Res.* 47, W08510. doi:10.1029/2011WR010487

Clarke, D., Morley, E., and Robert, D. (2017). The Bee, the Flower, and the Electric Field: Electric Ecology and Aerial Electroreception. *J. Comp. Physiol. A.* 203, 737–748. doi:10.1007/s00359-017-1176-6

Clarke, D., Whitney, H., Sutton, G., and Robert, D. (2013). Detection and Learning of floral Electric fields by Bumblebees. *Science*. 340, 66–69. doi:10.1126/science.1230883

Crozier, W. D. (1965). Atmospheric Electrical Profiles below Three Meters. *J. Geophys. Res.* 70 (12), 2785–2792. doi:10.1029/jz070i012p02785

Cusell, C., Mettrop, I. S., Loon, E. E. v., Lamers, L. P. M., Vorenhout, M., and Kooijman, A. M. (2015). Impacts of Short-Term Droughts and Inundations in Species-Rich Fens during Summer and winter: Large-Scale Field Manipulation Experiments. *Ecol. Eng.* 77, 127–138. doi:10.1016/j.ecoleng.2015.01.025

Epps, T. W., and Singleton, K. J. (1986). An Omnibus Test for the Two-Sample Problem Using the Empirical Characteristic Function. *J. Stat. Comput. Simulation*. 26, 177–203. doi:10.1080/00949658608810963

Escalante-Minakata, P., Ibarra-Junquera, V., Rosu, H. C., De León-Rodriquez, A., and González-García, R. (2009). Online monitoring of Mezcal Fermentation Based on Redox Potential Measurements. *Bioprocess Biosyst. Eng.* 32, 47–52. doi:10.1007/s00449-008-0219-3

Fdez-Arroyabe, P., Kourtidis, K., Haldoupis, C., Savoska, S., Matthews, J., Mir, L. M., et al. (2021). Glossary on Atmospheric Electricity and its Effects on Biology. *Int. J. Biometeorol.* 65 (1), 5–29. doi:10.1007/s00484-020-02013-9

Feynman, R. P., Leighton, R. B., and Sands, M. L. (1964). The Feynman Lectures on Physics: Electromagnetism and Matter (Vol. 2). Addison-Wesley Publishing Company.

Gora, E. M., and Yanoviak, S. P. (2015). Electrical Properties of Temperate forest Trees: a Review and Quantitative Comparison with Vines. *Can. J. For. Res.* 45 (3), 236–245. doi:10.1139/cjfr-2014-0380

Greggers, U., Koch, G., Schmidt, V., Dürr, A., Floriou-Servou, A., Piepenbrock, D., et al. (2013). Reception and Learning of Electric fields in Bees. *Proc. R. Soc. B.* 280 (1759), 20130528. doi:10.1098/rspb.2013.0528

Hammer, Ø., Harper, D. A., and Ryan, P. D. (2001). PAST: Paleontological Statistics Software Package for Education and Data Analysis. *Palaeontol. electronica*. 4 (1), 9, 2001 . Available at: http://palaeo-electronica.org/2001_1/past/issue1_01.htm

Harrison, R. G., and Nicoll, K. A. (2018). Fair Weather Criteria for Atmospheric Electricity Measurements. *J. Atmos. Solar-Terrestrial Phys.* 179, 239–250. doi:10.1016/j.jastp.2018.07.008

Higazi, K. A., and Chalmers, J. A. (1966). Measurements of Atmospheric Electrical Conductivity Near the Ground. *J. Atmos. Terrestrial Phys.* 28 (3), 327–330. doi:10.1016/0021-9169(66)90042-0

Hogg, A. R. (1939). The Conduction of Electricity in the Lowest Levels of the Atmosphere. *Memoires Commonw. Observatory*. 7, 1–24. Available at: http://adsabs.harvard.edu/pdf/1939MmMtS...7....1H

Holthusen, D., Brandt, A. A., Reichert, J. M., and Horn, R. (2018). Soil Porosity, Permeability and Static and Dynamic Strength Parameters under Native forest/grassland Compared to No-Tillage Cropping. *Soil Tillage Res.* 177, 113–124. doi:10.1016/j.still.2017.12.003

Hunting, E. R., Harrison, R. G., Bruder, A., van Bodegom, P. M., van der Geest, H. G., Kampfraath, A. A., et al. (2019). Atmospheric Electricity Influencing Biogeochemical Processes in Soils and Sediments. *Front. Physiol.* 10. doi:10.3389/fphys.2019.00378

Hunting, E. R., Matthews, J., de Arróyabe Hernáez, P. F., England, S. J., Kourtidis, K., Koh, K., et al. (2021). Challenges in Coupling Atmospheric Electricity with Biological Systems. *Int. J. Biometeorol.* 65 (1), 45–58. doi:10.1007/s00484-020-01960-7

Hunting, E. R., Vijver, M. G., van der Geest, H. G., Mulder, C., Kraak, M. H., Breure, A. M., et al. (2015). Resource Niche Overlap Promotes Stability of Bacterial Community Metabolism in Experimental Microcosms. *Front. Microbiol.* 6, 105. doi:10.3389/fmicb.2015.00105

Hunting, E. R., Whatley, M. H., van der Geest, H. G., Mulder, C., Kraak, M. H. S., Breure, A. M., et al. (2012). Invertebrate Footprints on Detritus Processing, Bacterial Community Structure, and Spatiotemporal Redox Profiles. *Freshw. Sci.* 31 (3), 724–732. doi:10.1899/11-134.1

Hunting, E. R., and Kampfraath, A. A. (2013). Contribution of Bacteria to Redox Potential (E H) Measurements in Sediments. *Int. J. Environ. Sci. Technol.* 10, 55–62. doi:10.1007/s13762-012-0080-4

Hunting, E. R., and Van der Geest, H. G. (2011). Predictability of Bacterial Activity and Denitrification in Aquatic Sediments with Continuous Measurements of Redox Potential. *Int. J. Environ. Sci. Technol* 8 (3), 553–560. doi:10.1007/bf03326241

Ibarra-Junquera, V., Escalante-Minakata, P., Murguía, J. S., and Rosu, H. C. (2006). Inferring Mixed-Culture Growth From Total Biomass Data in a Wavelet Approach. *Phys. A Stat. Mech. Appl.* 370, 777–792. doi:10.1016/j.physa.2006.03.015

Jayaratne, E. R., Ling, X., and Morawska, L. (2011). Role of Vegetation in Enhancing Radon Concentration and Ion Production in the Atmosphere. *Environ. Sci. Technol.* 45 (15), 6350–6355. doi:10.1021/es201152g

Kubicki, M., Odzimek, A., and Neska, M. (2016). Relationship of Ground-Level Aerosol Concentration and Atmospheric Electric Field at Three Observation Sites in the Arctic, Antarctic and Europe. *Atmos. Res.* 178-179, 329–346. doi:10.1016/j.atmosres.2016.03.029

Ling, X., Jayaratne, R., and Morawska, L. (2010). Air Ion Concentrations in Various Urban Outdoor Environments. *Atmos. Environ.* 44 (18), 2186–2193. doi:10.1016/j.atmosenv.2010.03.026

Märcz, F., and Harrison, R. G. (2003). Long-Term Changes in Atmospheric Electrical Parameters Observed at Nagycenk (Hungary) and the UK Observatories at Eskdalemuir and Kew. *Annales Geophysicae* 21, 2193–2200. doi:10.5194/angeo-21-2193-2003

Morley, E. L., and Robert, D. (2018). Electric Fields Elicit Ballooning in Spiders. *Curr. Biol.* 28, 2324–2330. doi:10.1016/j.cub.2018.05.057

Newman, D. K., and Banfield, J. F. (2002). Geomicrobiology: How Molecular-Scale Interactions Underpin Biogeochemical Systems. *Science*. 296, 1071–1077. doi:10.1126/science.1010716

Pett-Ridge, J., and Firestone, M. K. (2005). Redox Fluctuation Structures Microbial Communities in a Wet Tropical Soil. *Appl. Environ. Microbiol.* 71 (11), 6998–7007. doi:10.1128/aem.71.11.6998-7007.2005

Reiter, R. (1985). Fields, *Currents and Aerosols in the Lower Troposphere; published for the division of Atmospheric Sciences, National Science Foundation, Washington, D.C.* New Delhi: Amerind Publishing Co. Pvt. Ltd.

Rhebergen, J. B., Lensen, H. A., Schwering, P. B., Marin, G. R., and Hendrickx, J. M. (2002). "Soil Moisture Distribution Around Land Mines and the Effect on Relative Permittivity," in *Detection and Remediation Technologies for Mines and Minelike Targets VII* (Orlando, FL: International Society for Optics and Photonics), Vol. 4742, 269–280

Rowland, S. M., Schurch, R., Pattouras, M., and Li, Q. (2015). Application of FEA to Image-Based Models of Electrical Trees with Uniform Conductivity. *IEEE Trans. Dielect. Electr. Insul.* 22 (3), 1537–1546. doi:10.1109/tdei.2015.004922

Rycroft, M. J., Harrison, R. G., Nicoll, K. A., and Mareev, E. A. (2008). "An Overview of Earth's Global Electric Circuit and Atmospheric Conductivity," in *Planetary Atmospheric Electricity* (New York, NY: Springer), 83–105. doi:10.1007/978-0-387-87664-1_6

Suojanen, M., Lederle, C., Heim, R., Keikko, T., Kuusiluoma, S., and Korpinen, L. (2001). The Effect of Trees on Calculation of Electric fields Near 400 kV Transmission Lines. *WIT Trans. Model. Simulation*. 30, 935–944. doi:10.2495/CMEM010911

Vorenhout, M., van der Geest, H. G., and Hunting, E. R. (2011). An Improved Datalogger and Novel Probes for Continuous Redox Measurements in Wetlands. *Inter. J. Environ. Anal. Chem.* 91.7-8, 801–810. doi:10.1080/03067319.2010.535123

Williams, E., and Mareev, E. (2014). Recent Progress on the Global Electrical Circuit. *Atmos. Res.* 135-136, 208–227. doi:10.1016/j.atmosres.2013.05.015

Williams, E., Markson, R., and Heckman, S. (2005). Shielding Effects of Trees on the Measurement of the Earth's Electric Field: Implications for Secular Variations of the Global Electrical Circuit. *Geophys. Res. Lett.* 32, a–n. doi:10.1029/2005GL023717

Wilson, C. T. R. (1903). Atmospheric Electricity. *Nature*. 68, 102–104. doi:10.1038/068102d0

Wright, M. D., Matthews, J. C., Silva, H. G., Bacak, A., Percival, C., and Shallcross, D. E. (2020). The Relationship between Aerosol Concentration and Atmospheric Potential Gradient in Urban Environments. *Sci. Total Environ.* 716, 134959. doi:10.1016/j.scitotenv.2019.134959

Conflict of Interest: The authors declare that the research was conducted in the absence of any commercial or financial relationships that could be construed as a potential conflict of interest.

The handling editor declared a past co-authorship with one of the authors EH.

frontiers in Earth Science

ORIGINAL RESEARCH
published: 16 July 2021
doi: 10.3389/feart.2021.671801

Influence of Solar Wind on Secondary Cosmic Rays and Atmospheric Electricity

Jaroslav Chum[1]*, Marek Kollárik[2], Ivana Kolmašová[1,3], Ronald Langer[2], Jan Rusz[1], Dana Saxonbergová[1] and Igor Strhárský[2]

[1]Institute of Atmospheric Physics of the Czech Academy of Sciences, Prague, Czech Republic, [2]Institute of Experimental Physics, Slovak Academy of Sciences, Košice, Slovakia, [3]Faculty of Mathematics and Physics, Charles University, Prague, Czech Republic

A relationship between the heliospheric magnetic field, atmospheric electric field, lightning activity, and secondary cosmic rays measured on the high mount of Lomnický Štít (2,634 m a.s.l.), Slovakia, during the declining phase of the solar cycle 24 is investigated with a focus on variations related to solar rotation (about 27 days). The secondary cosmic rays are detected using a neutron monitor and the detector system SEVAN, which distinguishes between different particles and energies. Using spectral analysis, we found distinct ~27-day periodicities in variations of B_x and B_y components of the heliospheric magnetic field and in pressure-corrected measurements of secondary cosmic rays. The 27-day variations of secondary cosmic rays, on average, advanced and lagged the variations of B_x and B_y components by about 40° and −140°, respectively. Distinct 27-day periodicities were found both in the neutron monitor and the SEVAN upper and middle detector measurements. A nondominant periodicity of ~27 days was also found for lightning activity. A cross-spectral analysis between fluctuation of the lightning activity and fluctuation of the heliospheric magnetic field (HMF) showed that fluctuation of the lightning activity was in phase and in antiphase with B_x and B_y components of the HMF, respectively, which is in agreement with previous studies investigating the influence of solar activity on lightning. On the other hand, the ~27-day periodicity was not significant in the atmospheric electric field measured in Slovakia and Czechia. Therefore, no substantial influence of B_x and B_y on the atmospheric electric field was observed at these middle-latitude stations.

Keywords: cosmic rays, heliospheric magnetic field, solar wind, atmospheric electric field, lightning

Edited by:
Irina Alexandrovna Mironova,
Saint Petersburg State University,
Russia

Reviewed by:
Hripsime Mkrtchyan,
Alikhanyan National Laboratory,
Armenia
Mirela Voiculescu,
Dunarea de Jos University, Romania

***Correspondence:**
Jaroslav Chum
jachu@ufa.cas.cz

Specialty section:
This article was submitted to
Atmospheric Science,
a section of the journal
Frontiers in Earth Science

Received: *24 February 2021*
Accepted: *21 June 2021*
Published: *16 July 2021*

Citation:
Chum J, Kollárik M, Kolmašová I, Langer R, Rusz J, Saxonbergová D and Strhárský I (2021) Influence of Solar Wind on Secondary Cosmic Rays and Atmospheric Electricity. Front. Earth Sci. 9:671801. doi: 10.3389/feart.2021.671801

INTRODUCTION

It is well known that the heliospheric magnetic field (HMF) influences the intensity of cosmic rays (CRs) entering the Earth's atmosphere (Usoskin et al., 1998; Owens and Forsyth, 2013). Primary (galactic) cosmic rays consist of high-energy particles, mainly protons with energies of ~GeV and higher that interact with the Earth's atmosphere, creating a shower of different species of charged

---

Abbreviations: CR, cosmic rays; CSD, cross-spectral density; EFM, electric field mill; GSE, geocentric solar ecliptic (coordinate system); HCS, heliospheric current sheet; HMF, heliospheric magnetic field; LS, Lomnický Štít; NM, neutron monitor; PG, potential gradient; PSD, power spectral density; SCR, secondary cosmic rays; SW, solar wind; WWLLN, World Wide Lightning Location Network; WT, wavelet transform.

particles, neutrons, and gamma ray photons. These showers, also called secondary cosmic rays (SCRs), are usually measured using neutron monitors (NMs). The count rates measured using NMs depend not only on the intensity of CRs but also on the strength and orientation of the geomagnetic field and the altitude of the measuring site. Therefore, many NMs are located at high latitudes or high altitudes where the so-called cutoff rigidity is lower, which means that larger count rates are measured as particles with lower momentum can reach such sites (Shea and Smart, 2000; López-Comazzi and Blanco, 2020). It was found that the intensity of CRs is anticorrelated with solar activity, exhibiting about 11-year cycle variations (Usoskin et al., 1998). The lower the solar activity, the higher the intensity of CRs that is observed because more galactic CRs penetrate the heliosphere and reach the Earth. Voiculescu and Usoskin (2012) and Voiculescu et al. (2013) showed using statistical studies that solar activity and the HMF might impact cloud cover in specific regions on long timescales. Variations of CRs in the Earth's atmosphere are important from many aspects which are as follows: a possible link between climate and intensity of CRs *via* potential influence of CRs on cloud condensation nuclei (Kristjánsson et al., 2008; Kirkby 2008; Svensmark et al., 2009; Gray et al., 2010), the dominant role of CRs in the production rate of isotope ^{14}C used for dating (e.g., Gosse and Klein, 2015), modulation of doses received by humans and electronics on board aircrafts (Yang and Sheu, 2020), and possible influence on seed electrons for lightning initiation (Dwyer and Uman, 2014).

Periodicities or quasiperiodicities shorter than the 11-year period of the solar cycle were also identified in the CR intensity. For example, Kudela et al. (2002), Kudela et al. (2010), and Chowdhury and Kudela (2018) focused on periods longer than the solar rotation and studied Rieger-type fluctuations around ~154 days and quasiperiodicities around ~1.3, 1.7, and 2.25 years. The intensity of these periodicities usually varied during the solar cycle, and their origin is still under debate (Bazilevskaya et al., 2014). The Rieger-type fluctuations (~154 days) mainly occur around the solar maximum and were first investigated by Rieger et al. (1984). On the other hand, Saad Farid (2019) and López-Comazzi and Blanco (2020) also analyzed shorter periods such as the period of solar rotation (~27 days) and its harmonics (mainly ~13.5 days) besides the quasiperiodicities around 130 days and the Rieger-type fluctuations and quasiperiodicities in the range of 250–470 days.

The period of solar rotation (~27 days), which is the main focus of this study, arises from the tilt of the solar magnetic dipole with respect to the rotation axis, coronal-hole high-speed streams, and corotating interaction regions characterized by the interaction of fast and slow solar wind (Gosling and Pizzo, 1999; Grieder, 2001; López-Comazzi and Blanco, 2020). The much weaker fluctuations at the period of ~13.5 days might be just the second harmonics; however, the presence of the heliospheric current sheet (HCS) that separates oppositely oriented field lines of the HMF and occurs two times during the solar rotation (Owens and Forsyth, 2013) might also contribute to the observed fluctuations of SCRs at ~13.5 days. In an ideal Parker spiral (Parker, 1958), the polarity of the dawn–dusk component B_y and the sunward component B_x of the HMF changes from away from the Sun ($B_x < 0$ and $B_y > 0$) to toward the Sun ($B_x > 0$ and $B_y < 0$), exhibiting one cycle during one solar rotation; the geocentric solar ecliptic (GSE) coordinate system is considered here. Interestingly, a dependence of the atmospheric pressure and atmospheric electric field on the polarity of B_y was found in the polar regions, mainly in the winter Antarctic when the air was relatively isolated from the rest of the world (Mansurov et al., 1974; Burns et al., 2008; Lam and Tinsley, 2016). It is assumed that the pressure dependence on B_y results from an external electric field that is superposed at high latitudes on the internal electric field, which is maintained by thunderclouds in the atmospheric global electric circuit (Rycroft et al., 2000). The external electric field occurs because of the relative motion and the interaction of the solar wind (SW) with the Earth's magnetosphere, and its value in the SW sensed in the Earth frame (GSE coordinates) is given by the vector product $\boldsymbol{E} = -\boldsymbol{v} \times \boldsymbol{B}$, where $\boldsymbol{v}$ is the speed of the SW and $\boldsymbol{B}$ is the HMF, respectively. The component of the external electric field parallel with the Earth's axis is then $E_z = -(v_x B_y - v_y B_x) \approx -v_x B_y$ as $|v_x| >> |v_y|$. The relative fluctuations of B_y are much larger than the relative fluctuations of v_x; consequently, E_z is mainly controlled by B_y (Lam and Tinsley, 2016). The E_z component is directed along the Earth's axis and does not change during the Earth's rotation if B_y is constant (Lam and Tinsley, 2016). A dominant component of the external electric field perpendicular to the Earth's axis is the dawn–dusk component $E_y = -(v_z B_x - v_x B_z) \approx v_x B_z$ which exhibits 1-day periodicity due to the Earth's rotation. The E_z component, controlled by B_y, dominates in the polar regions. It maps along the Earth's magnetic field lines to the ionosphere and contributes to the total potential difference between the ionosphere and the Earth at high latitudes (Burns et al., 2008). The mechanism by which the atmospheric pressure is influenced by this external electric field is, however, unknown. It is hypothesized that an increase in the atmospheric vertical current that is associated with the increase in the potential difference between the ionosphere and the Earth's surface influences the cloud microphysics, especially at cloud boundaries. This might result in different growths of condensation nuclei and hence in different radiation properties (opaqueness) of clouds or release of latent heat (Nicoll and Harrison, 2009; Gray et al., 2010; Lam and Tinsley, 2016). No direct dependence of atmospheric pressure and the electric field on B_y has been observed at middle or low latitudes. Variations of the electric field associated with global thunderstorm activity, local weather, cloud electrification, and changes of air conductivity owing to fluctuations of aerosol concentration dominate here. However, several studies have discussed how lightning occurrence over Great Britain and Japan likely depends on the B_y polarity and the solar rotation period (Owens et al., 2014; Owens et al., 2015; Miyahara et al., 2018).

This study presents measurements of SCRs taken using an NM and the Space Environment Viewing and Analysis Network (SEVAN) located at the mountain peak of Lomnický Štít (LS) in the High Tatras, Slovakia, and their comparison with SW and HMF data and nearby measurements of the atmospheric electric field. The aim is to search for similarities in these data series, especially similarities related to the period of solar rotation, and to discuss a potential influence of the HMF and SCRs on atmospheric electricity.

MEASUREMENT SETUP

The near-Earth components of the SW velocity (v_x, v_y, and v_z) and the B_x, B_y, and B_z components of the HMF used in this study were downloaded from NASA/GSFC's Space Physics Data Facility's OMNIWeb service (https://omniweb.gsfc.nasa.gov/).

The SCRs are measured using two different types of detectors located on the peak of LS (49.195°N, 20.213°E) at the altitude of 2,634 m. The first is an NM installed on the top of LS in 1981. It is of the NM-64 type and consists of eight SNM-15 counting tubes with a length of 200 cm and a diameter of 15 cm, filled with BF_3 (Kudela and Langer, 2009). The NM at LS is a part of the global neutron monitor, which means that the data are included in the Neutron Monitor Database (NMDB). Cutoff rigidity of the NM at LS is 3.84 GV. The second is the SEVAN system, which has three separated plastic scintillators as detectors (Chilingarian et al., 2018). The upper and lower scintillators have the dimensions 100 × 100 × 5 cm and are separated from the middle scintillator by 4.5-cm-thick and 100 × 100 cm–wide lead absorbers. The middle detector is composed of five plastic slabs and has the dimensions 50 × 50 × 25 cm. The upper detector—channel 1—is mainly sensitive to low-energy charged particles, mainly electrons, and partly also to gamma rays (Chilingarian et al., 2018). The estimated energy threshold, considering the roof above the detector, is 7–8 MeV (Kudela et al., 2017). The middle scintillator—channel 2—mainly detects neutrons or high-energy gamma photons. It might be partly sensitive to electrons with energies of several tens of MeV. The lower detector—channel 3—registers high-energy charged particles, mainly muons with energies exceeding ~250 MeV. Besides the count rates in individual channels, different combinations of all three channels are also evaluated. Specific combinations can be used to identify the type of incident particles. For example, combinations [1,0,0], [0,1,0], and [1,1,1] mean that a particle was registered only in channel 1, only in channel 2, and in all channels simultaneously, respectively. The combination [1,0,0] is mainly used for detection of electrons or positrons (partly also photons) with energies around ~10 MeV. On the other hand, the combination [0,1,0] provides information about detection of neutrons, and the [1,1,1] combination provides information about the detection of high-energy (>250 MeV) charged particles, mainly muons (Chilingarian and Reymers, 2008; Chilingarian et al., 2021).

The electric field is measured on LS using an electric field mill EFM 100 sensor made by the Boltek company (Kudela et al., 2017). Relatively large values of the electric field are measured on the top of LS as it is a sharp, rocky mountain peak (Kudela et al., 2017; Chum et al., 2020). It should be noted that the mountain of LS represents a relatively conductive material, relative to the ambient air, and therefore locally enhances the intensity of the electric field. The EFM 100 at LS is in operation only during summer to prevent damage to its rotor due to the frequent ice coverage in winter. Therefore, the data of the electric field measured in Czechia at the stations of Panská Ves (50.527°N, 14.568°E, altitude 318 m) and Studenec (50.258°N, 12.518°E, altitude 666 m) are also provided for completeness and comparison. These stations are the closest available stations providing electric field data at a similar latitude and are part of a global atmospheric electricity monitoring network (Nicoll et al., 2019). More precisely, the electric field data are given as potential gradient (PG), which means that positive values correspond to the downward pointing electric field (electrons are accelerated upward). All the EFM 100 sensors used are installed in inverted positions to minimize precipitation noise.

To evaluate lightning activity, we used data provided by the World Wide Lightning Location Network (WWLLN), which operates about 70 sensors in the frequency range from 3 to 30 kHz (Rodger at al., 2004). Localization of individual discharges is based on the detection of sferics, impulsive signals radiated by lightning and propagating in a waveguide formed by the Earth's surface and the bottom of the ionosphere. The WWLLN provides the exact times and locations of the detected lightning together with their estimated energy, energy error, and number of the stations used for the estimation of the relevant locations and energies. In this study, we used lightning detections which occurred between latitudes 48° and 51°N and longitudes 11° and 23°E. This region roughly covers the area of Czechia and Slovakia. The detection efficiency of the WWLLN did not change during the analyzed period.

METHODS

To investigate the influence of the SW and the HMF on SCRs and the atmospheric electric field, we search for similar fluctuations in the HMF, SW, SCRs, and atmospheric electric field by performing spectral analysis, namely, Fourier transform and wavelet transform (WT). Because various quantities have different absolute values and units, it is useful to work with normalized unitless quantities. All the quantities are therefore normalized by applying **Eq 1** before performing the spectral analysis as follows:

$$a_{norm} = \frac{a - mean(a)}{\sigma_a}, \tag{1}$$

where a is the analyzed quantity (components of SW velocity, components of the HMF, counts measured by the NM and the SEVAN, and the PG), and σ_a is the standard deviation of the distribution of the quantity a. The normalization allows for an easy comparison of fluctuations and the spectral content of various quantities.

All the data are available with 1-min resolution. It is necessary to consider that the data might contain outliers. For example, enhancements of SCRs related to the large atmospheric electric field were observed during thunderstorms (Kudela et al., 2017; Chum et al., 2020). The extreme values are therefore first removed from the 1-min data before the application of **Eq 1**. The extreme values or outliers were removed following the approach taken by

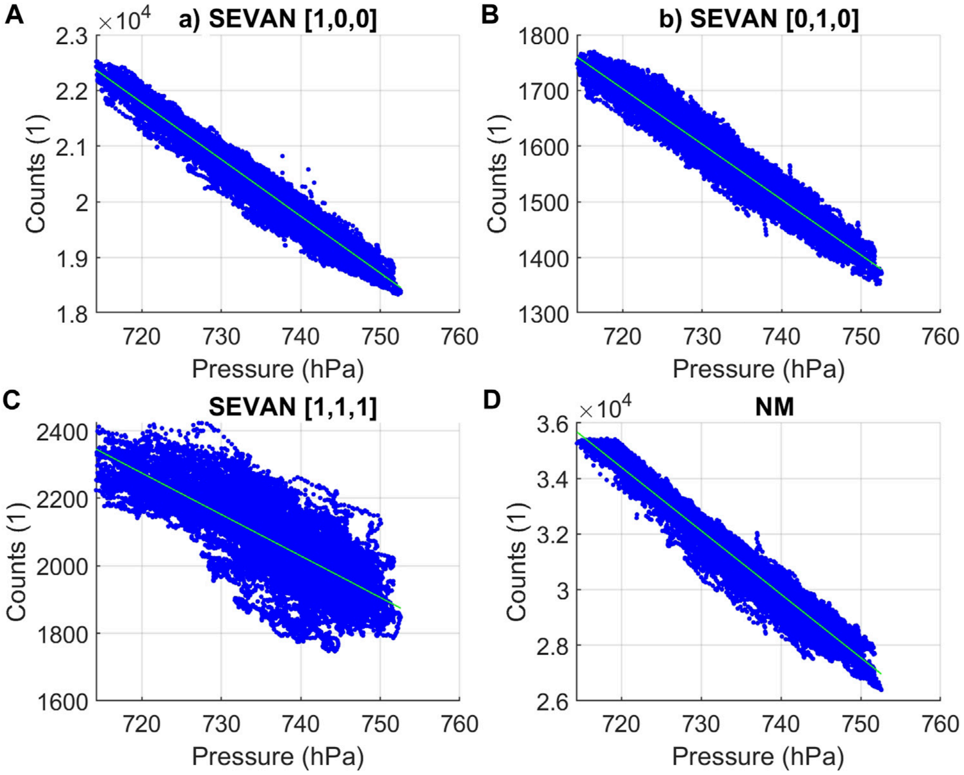

FIGURE 1 | Scatterplots between measured counts (2-h mean values of 1-min data) and atmospheric pressure on LS. Green lines indicate linear regressions. **(A)** SEVAN [1,0,0] combination, **(B)** SEVAN [0,1,0] combination, **(C)** SEVAN [1,1,1] combination, and **(D)** NM.

López-Comazzi and Blanco (2020). It means that all the values lying outside the range [Q_1-1.5(Q_3-Q_1), Q_3+1.5(Q_3-Q_1)] were considered outliers, where Q_1 and Q_3 are the first quartile and the third quartile, respectively. The extreme values were removed for all the data, except the lightning counts in the considered area (48–51°N, 11–23°E). To reduce data volume and to speed up the data processing, we computed 2-h mean values from the original 1-min data. It should be noted that we are interested in fluctuations in the order of days. As the 2-h mean values act as a low-pass filter with a cutoff period of 2 h, the 2-h mean values were calculated with a 1-h step to fulfill the sampling theorem (sampling frequency should be at least twice the highest frequency in the signal). The mean values were only calculated if more than 50% of the data were available in the given 2-h intervals. Otherwise, the values were substituted by linear interpolation before the spectral analysis.

It should also be noted that only a rough proxy for fair-weather electric field data is obtained by removing extreme values from PG data using the method mentioned in the previous paragraph. The PG data might be influenced by the presence of moderately charged clouds, fog, or aerosols that significantly change the air conductivity and hence the PG. However, this approach can be justified as we are interested in the spectral content of the PG signal, rather than in absolute values. It is necessary to have as few data gaps as possible for spectral analysis. The main aim is to search for periodicities related to solar rotation, and it is unlikely that periodicities of fog or aerosol concentrations would follow the periodicities of solar rotation. Moreover, we found that we obtained a similar Carnegie curve for the Panská Ves station to that obtained in the study by Nicoll et al. (2019), who used another, stricter proxy for fair-weather data.

We chose the period from 2016 to 2019 for the study as for this period, all the data of interest are available for most of the time.

The measured values of SCRs depend on atmospheric pressure, as is documented in **Figure 1A–D**, which shows scatterplots between the counts recorded in SEVAN channel 1 ([1,0,0] combination), channel 2 ([0,1,0] combination), combination [1,1,1], and in the NM. To remove the pressure influence on the measured values of SCRs, the counts were first corrected on pressure using the linear relationships displayed in the individual plots in **Figure 1** by green lines. Actually, the relationship between the counts and atmospheric pressure is expected to be exponential. However, the scatterplots indicate that linear correction does not introduce a substantial error in the observed range of pressure variations. Obviously, the counts for combination [1,1,1] (**Figure 1C**) exhibit the most complicated fluctuations and pressure correction is the least effective. The residual counts, obtained by subtracting the linear regression curves (green lines) from the measured counts, are used for spectral analysis after their normalization using **Eq 1**.

In addition to Fourier and wavelet transform, cross-spectral analysis is performed for the quantities that exhibit similar

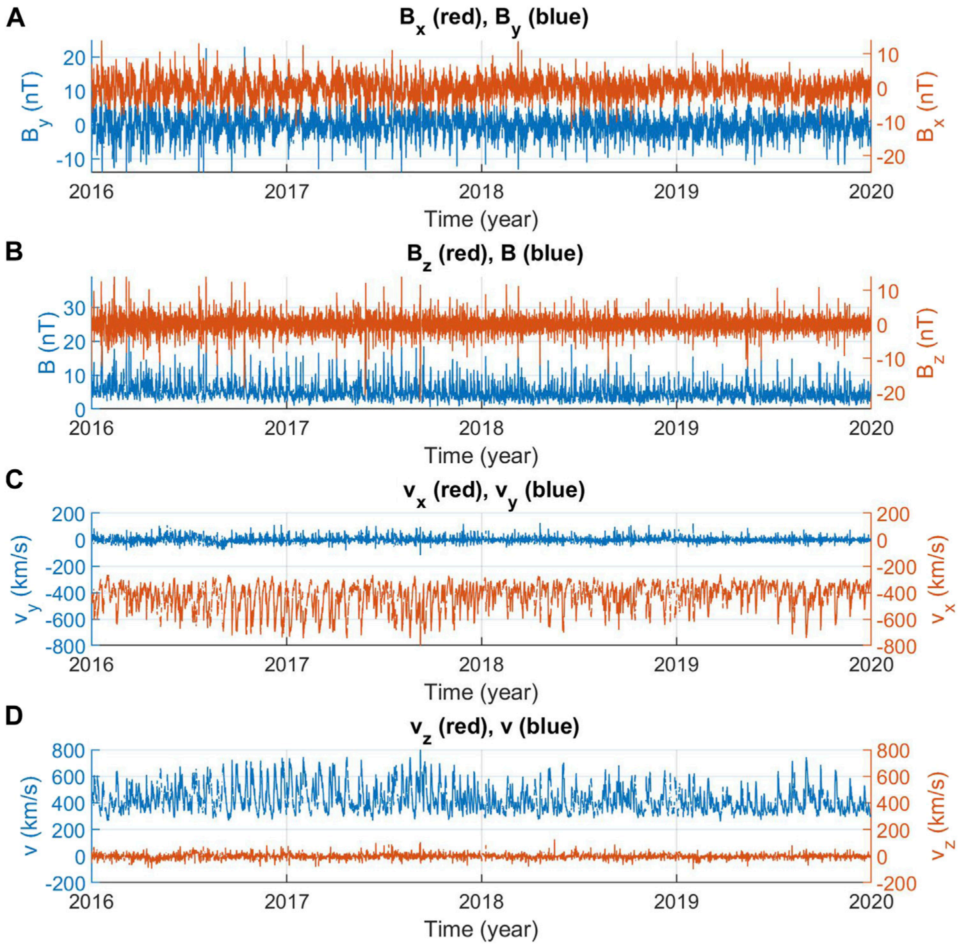

FIGURE 2 | Components of the HMF **(A, B)** and components of SW velocity **(C, D)** in GSE coordinates.

spectra, namely, a distinct peak around the period of solar rotation. The cross-spectra make it possible to investigate a phase relation between quantities of interest. For example, cross-spectral densities (CSDs) for normalized pressure-corrected NM counts N_{NM} and the normalized B_x component of the HMF are calculated using relation **Eq. 2** as follows:

$$CSD(\omega) = N_{NM}(\omega) \cdot B_x^*(\omega) = |N_{NM}(\omega)| \cdot |B_x(\omega)| \cdot e^{i[\varphi_{NM}(\omega) - \varphi_{Bx}(\omega)]}, \quad (2)$$

where $N_{NM}(\omega)$ is the Fourier transform of the normalized residual NM counts, $B_x^*(\omega)$ is the complex conjugate of the Fourier transform of the normalized B_x component of the HMF, and i^2 = -1. The phase shift $\phi(\omega)$ between the two signals at a given frequency is then obtained as follows:

$$\phi(\omega) = \varphi_{NM}(\omega) - \varphi_{Bx}(\omega). \quad (3)$$

The NM counts advance the B_x variations for positive $\phi(\omega)$ and *vice versa*.

RESULTS

Heliospheric Parameters and Cosmic Rays

Figure 2A,B shows the components of the HMF, together with its absolute value B, and the components of SW velocity (**Figure 2C,D**), including its absolute value v, for the years 2016–2019 in GSE coordinates. The B_x and B_y components have similar amplitudes and are mostly anticorrelated, which is an expected situation for the Parker spiral (Owens and Forsyth, 2013). The dominant component of the SW velocity is the v_x component (**Figures 2C, D**). The mean value of v_x in the GSE coordinates calculated over the displayed period of time is –425 km/s. The negative sign means that the SW velocity is directed from the Sun to the Earth. **Figure 3** shows the power spectral densities (PSDs) of the normalized components of the HMF and SW velocity (normalized quantities of those displayed in **Figure 2**). The PSDs are displayed as a function of the period, rather than of the frequency. Only periods up to 40 days are presented. **Figure 3A** shows that the PSDs of B_x and B_y have a distinct peak around the period of 27.5 days. Both peaks have similar values, and the peak for B_x (red) is only slightly larger than

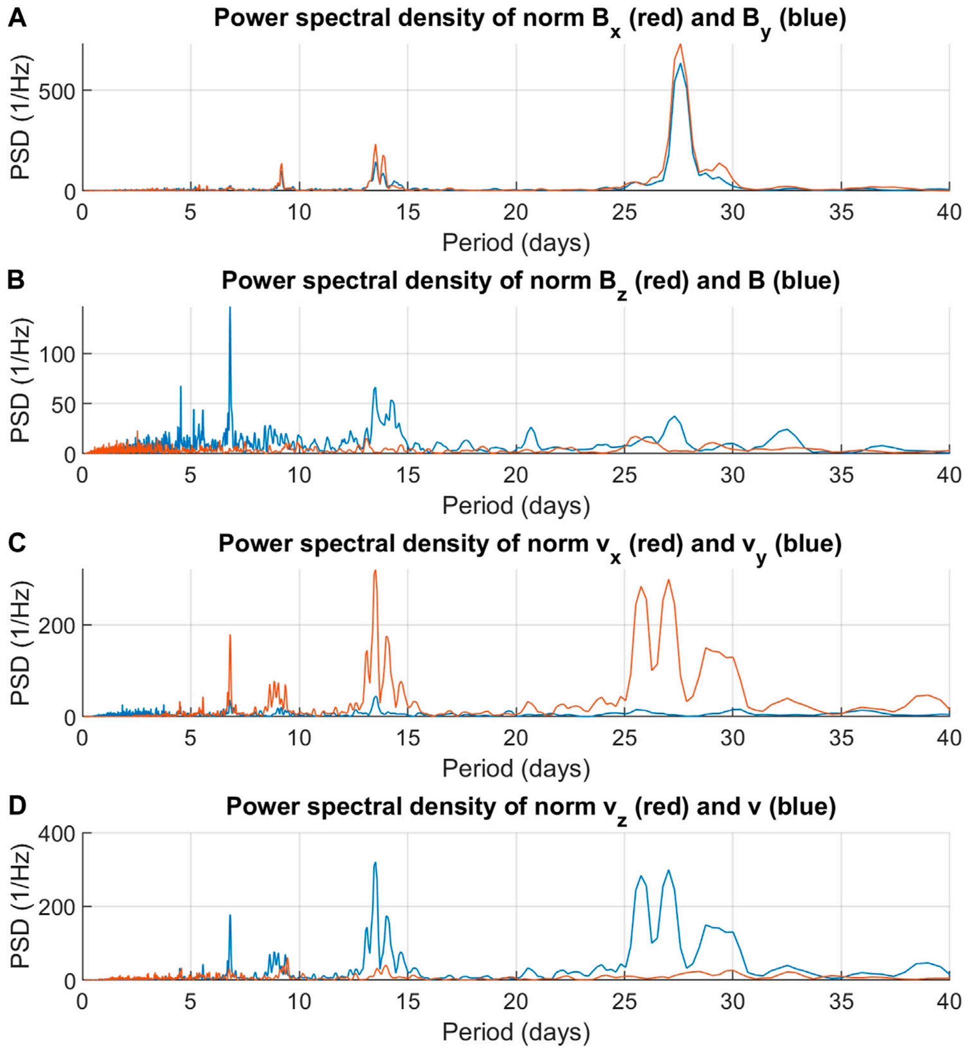

FIGURE 3 | Power spectral densities (PSD) of normalized components of the HMF **(A, B)** and velocity of SW **(C, D)**.

that for B_y (blue). **Figure 3B** demonstrates that no significant peak around the period of solar rotation (~27 days) was observed for the B_z component. **Figure 3C** shows that the PSD of the v_x component of SW velocity has two distinct peaks associated with solar rotation, namely, at the periods of 25.7 and 27 days. A likely explanation for these two peaks is a differential rotation of the Sun (Owens and Forsyth, 2013). SW originating from coronal holes around the solar pole exhibits a period of around 25 days, whereas SW arriving from the equatorial regions of the Sun is characterized by a period of around 27 days. Obviously, the periodicity of v_x propagates into the periodicity of the absolute value of SW velocity v (**Figure 3D**).

Figure 4 shows time fluctuations of the normalized pressure-corrected counts recorded in SEVAN channel 1 ([1,0,0] combination), channel 2 ([0,1,0] combination), combination [1,1,1], and in the NM. To ensure homogeneity of the data, only counts from June 10, 2016 to April 15, 2019 are used for the analysis. Before this selected interval, changes in the acquisition electronics of the SEVAN were made. After this interval, many data gaps and discontinuities in SEVAN data occurred. **Figure 5** presents the PSD of the normalized counts that are displayed in **Figure 4**. The PSD of SEVAN [1,0,0] and [0,1,0] combinations and the PSD of NM counts exhibit remarkable peaks at the period of solar rotation, around 27 days. However, no such distinct peak was observed for the SEVAN [1,1,1] combination (**Figure 5C**) that detects high-energy charged particles (muons). A likely explanation for that is that the HMF and SW are not able to sufficiently modulate the CR particles of high energies that are responsible for muon production because of the large gyro-radii of high-energy particles. There is a relatively good similarity between the spectra obtained for the B_x and B_y components of the HMF and the PSD obtained for the SEVAN [0,1,0] combination and NM counts. Both these detectors are mainly sensitive to neutral particles, the SEVAN [0,1,0] combination being also partly sensitive to high-energy gamma rays. A partial similarity with the PSD of B_x and B_y is also observed for the

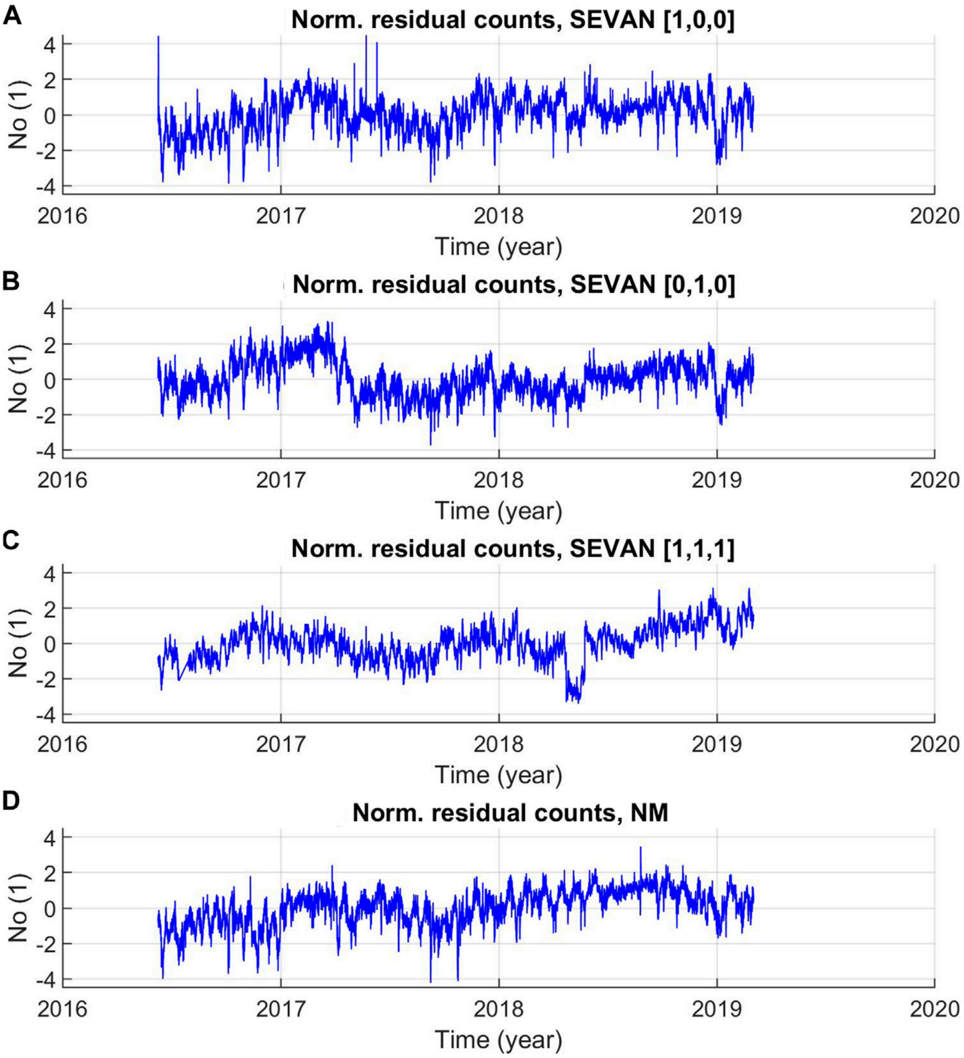

FIGURE 4 | Normalized pressure-corrected counts observed using the SEVAN **(A, B, C)** and an NM **(D)** on LS.

SEVAN [1,0,0] combination, sensitive to low-energy charged particles (approximately above 7 MeV), electrons and positrons. A partial detection of gamma rays cannot be excluded.

It is useful to investigate the time evolution of the spectra. **Figure 6A–F** presents the wavelet transform of the normalized B_x, v_x, and normalized counts recorded using the SEVAN [1,0,0], [0,1,0], and [1,1,1] combinations and the NM, respectively. The peak around the period of ~27 days in the WT of B_x is most distinct in 2016 and in the beginning of 2017, which corresponds to the declining phase of the solar cycle 24. A second harmonic, ~13.5 days, is also clearly visible in the WT of B_x. The time evolution of the second harmonic, however, does not follow the intensity observed at the period of ~27 days. An almost identical result was obtained for the WT of B_y (not shown). Periods of ~27 and ~13.5 days can also be clearly identified in the WT of normalized v_x. Intensities observed at the periods of ~27 and ~13.5 days are comparable, which can also be seen in the PSD displayed in **Figure 3C**. It should be noted that a frequency resolution of the WT is not sufficient to distinguish the periods of 25.7 and ~27 days observed in **Figure 3C**. **Figures 6C, D, F** show that the fluctuations of SCRs measured using the SEVAN [1,0,0] and [0,1,0] combinations and the NM exhibit relatively broad peaks around the period of ~27 days. These peaks are more or less randomly distributed during the analyzed period of time. Intervals with relatively high intensities (distinct peaks) are followed by intervals with lower intensities. Therefore, it is likely that the fluctuations of SCRs are also modulated by other mechanisms besides the HMF and SW velocity. The exact origin of these mechanisms is unknown. We note that the counts were corrected to the local ambient pressure. However, we cannot exclude that a pressure or temperature profile in the atmosphere above the SEVAN and the NM could modulate the recorded counts (Riádigos et al., 2020). A potential influence of some other, unconsidered parameters of the solar and geomagnetic activity and of the atmospheric state can also not be excluded.

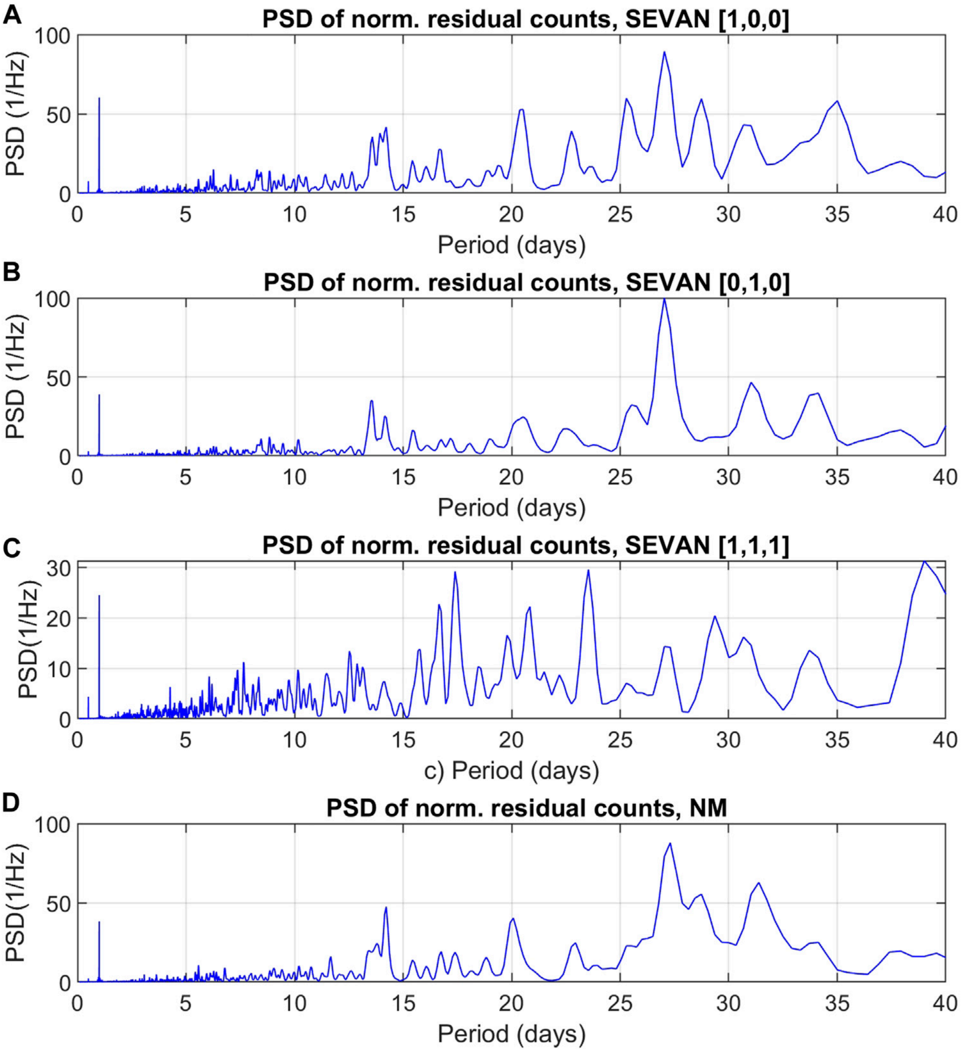

FIGURE 5 | Power spectral densities (PSD) of normalized pressure-corrected counts measured using the SEVAN **(A, B, C)** and an NM **(D)** on LS.

Atmospheric Electric Field

Figure 7 presents the normalized PG recorded at Studenec, Panská Ves, and LS. As mentioned in the Introduction, measurements on LS were not performed in winter to prevent damage from icing on the rotor of the EFM 100 sensor. It can be noticed that a higher PG was usually observed in winter than in summer. Large concentrations of aerosols and/or fogs during winter inversions is a likely reason for the relatively large PG in winter. A seasonal dependence of the PG also makes it difficult to analyze a potential influence of the B_y polarity on the PG using anything other than spectral methods. **Figure 8** shows the PSD of the normalized PG that is displayed in **Figure 7**. **Figure 8** demonstrates that no significant peak around the period of solar equatorial rotation (~27 days) was observed in the PG data. Therefore, unlike the studies in polar regions (Burns et al., 2008; Lam and Tinsley, 2016), no influence of the B_y polarity on the PG was observed at the considered middle-latitude stations. However, a local, nondominant peak at the period of around ~25.7 days corresponding to solar rotation at high solar latitudes was found in the PSD for all three stations. It should be remembered that a peak at this period was also observed in the PSD of v_x. However, the spectra of v_x and the PG do not exhibit similarities at other periods.

The PSD of PG data measured in Panská Ves and Studenec also exhibits sharp peaks at the periods of ~0.5 and 1 day. It means that the Carnegie curve has two peaks (Nicoll et al., 2019). Interestingly, the PSD of PG data recorded in Panská Ves (partly also in Studenec) has a peak at the period of 7 days. It could possibly indicate a weekend reduction of industrial aerosol concentrations (Silva et al., 2014) as Panská Ves lies the closest to urban areas of all these three stations. A detailed analysis of this phenomenon is outside the scope of the present study.

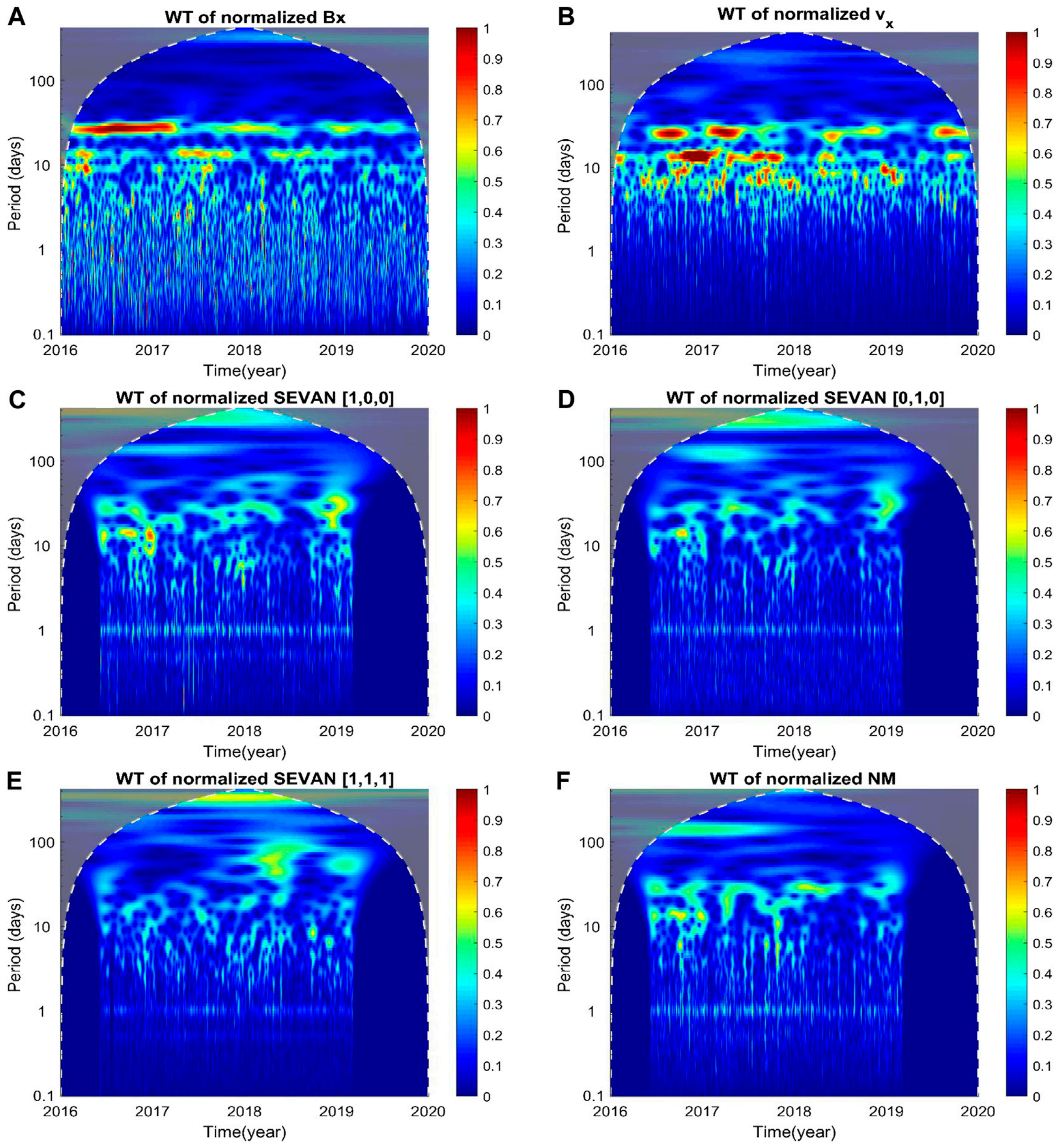

FIGURE 6 | Wavelet transform of **(A)** B_x component of the HMF, **(B)** v_x component of SW velocity, and **(C–F)** normalized pressure-corrected counts measured using SEVAN combinations [1,0,0], [0,1,0], and [1,1,1] and the NM, respectively, on LS.

Phase Relations and Lightning Activity

As we have found a relatively good correspondence between the power spectral density peaks at the period of ~27 days for B_x and B_y and for the SCR counts corresponding to the low-energy charged particles and neutrons measured using the SEVAN [1,0,0] and [0,1,0] combinations, respectively, and for the NM counts (compare **Figure 3A** with **Figures 5A, B, D**), it is useful to investigate phase relations (time delays) between these variables around the period of ~27 days. **Figure 9** presents the CSD of the normalized B_x and NM counts, calculated according to **Eq 2**. Only data from the time interval from June 10, 2016 to April 15, 2019 were used to analyze the same period of time for both data series. **Figures 9A, B** show the absolute value and the phase of the CSD, respectively. The phase difference between the NM and B_x counts fluctuates around 40° at the period of ~27 days, which clearly dominates in the cross-spectrum. In other words, the count variations observed using the NM advance the variations of the near-Earth B_x component of the HMF at the period of ~27 days by approximately 3 days. Very similar results were obtained for cross-spectral analyses of the SEVAN [1,0,0] and [0,1,0] combinations and B_x (not shown). Calculating the cross-spectrum of B_x and B_y, it is easy to verify that the phase difference between B_x and B_y is very close to 180°. Consequently, the count variations recorded using the NM and the SEVAN [1,0,0] and

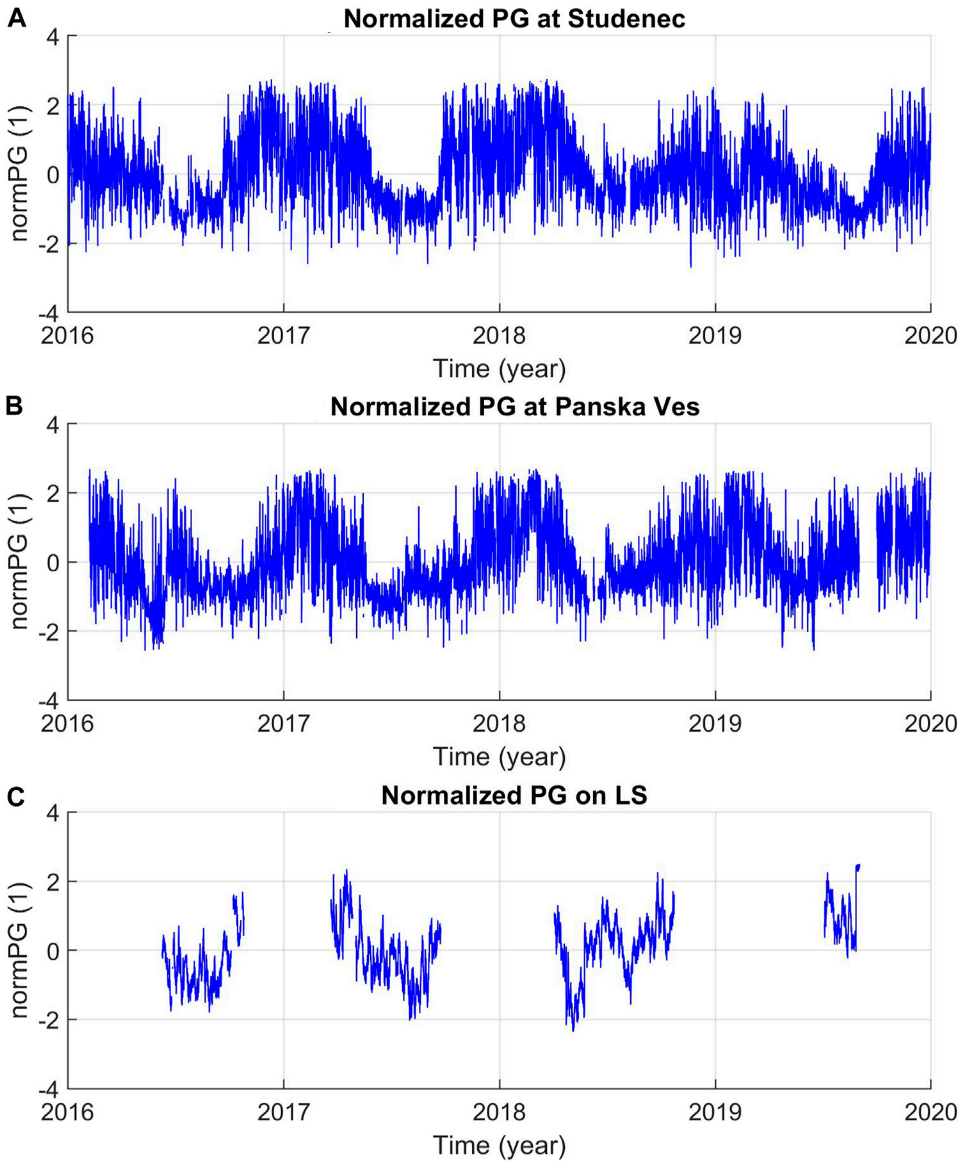

FIGURE 7 | Normalized PG (proxy for fair weather) at Studenec **(A)**, Panska Ves **(B)**, and LS **(C)**.

[0,1,0] combinations lag the variations of B_y. The phase difference is around −140° and exhibits a frequency dependence, as is demonstrated in **Figures 9C–H**, which show the absolute values and phase differences of the CSD for the NM–B_y, SEVAN [1,0,0]–B_y, and SEVAN [0,1,0]–B_y data series. Asterisks in the individual plots of **Figure 9** mark the maximum of the absolute values of the CSD and values larger than ½ of this maximum, including the corresponding phase differences. The phase differences change around the maxima; nevertheless, they are relatively stable for the frequencies (periods) of interest, marked by the asterisks, unlike the values of phase differences outside the maxima.

It is useful to remember that it is assumed that SCRs might play an important role in lightning initiation by providing seed energetic electrons and the ionization necessary for breakdown processes (e.g., Dwyer and Uman, 2014). Recently, Shao et al. (2020) performed a detailed radio frequency interferometry of the fast positive breakdown process that started a normal intracloud lightning and concluded that the breakdown process was ignited by a cosmic ray shower. Thus, there is a possibility that the discovered ~27-day modulation of SCRs that is primarily caused by the ~27-day periodicity in the HMF and solar wind, which influences the primary CRs entering the Earth's atmosphere, could also modulate lightning occurrence. Indeed, some previous statistical studies indicate that the polarity of B_y and corotating interaction regions that often embed the HCS modulate lightning activity in middle latitudes (Owens et al., 2014; Owens et al., 2015; Miyahara

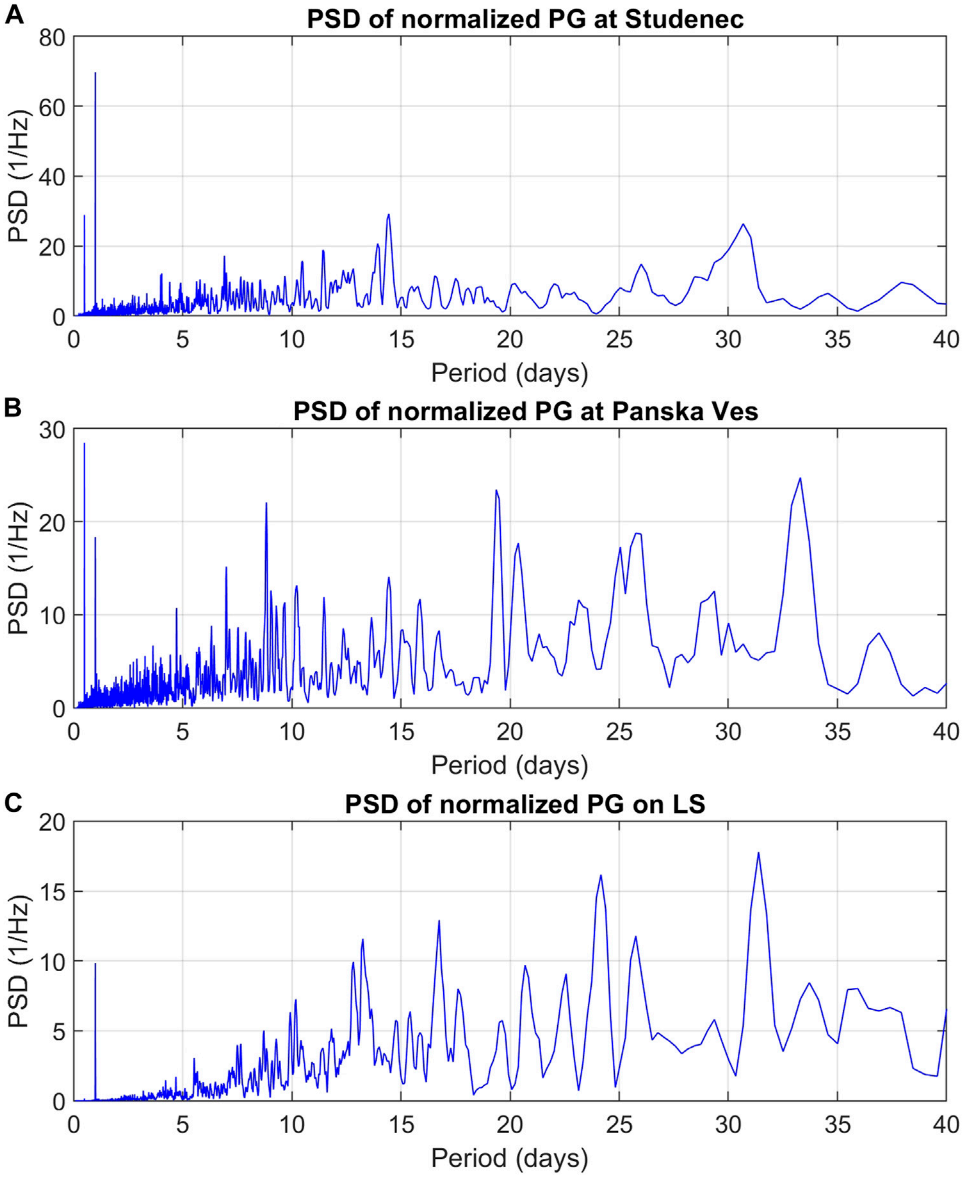

FIGURE 8 | Power spectral densities (PSD) of the normalized PG (proxy for fair weather) measured at Studenec **(A)**, Panská Ves **(B)** and on LS **(C)**.

et al., 2018). It should be noted that the polarity of B_y (B_x) reverses in the HCS.

On the other hand, the high electric field in thunderclouds might also be responsible for enhancements of SCRs. Such enhancements were also observed on Lomnický Štít (Kudela et al., 2017; Chum et al., 2020). In these cases, however, the seed energetic electrons generated by cosmic rays were likely multiplied in the process called relativistic runaway electron avalanche (RREA) suggested by Gurevich et al. (1992). Thunderstorm ground enhancements (TGEs) of SCRs were usually observed only in SEVAN channel 1, except one extreme event, for which the TGE was also reliably detected using the NM and the SEVAN [0,1,0] combination, which indicated a possibility of photonuclear reactions in the atmosphere and/or the material surrounding the detectors (Chum et al., 2020). It should be remembered in this respect that the significant enhancements of SCRs due to high electric fields—the several minutes–long TGEs—represented outliers in our dataset and were removed from the analysis, as was described in the section "Methods." Therefore, the observed ~27-day periodicity of SCRs is modulated by the HMF/SW and not by thunderstorms.

We investigated the periodicity of lightning activity in the area with the coordinates 48–51°N, 11–23°E, covering roughly Czechia and Slovakia. **Figure 10A** presents the number of lightnings recorded by the WWLLN in subsequent 1-h intervals for the period 2016–2019. Obviously, the lightning counts are high in the summer seasons. The seasonal variability produces a spectral

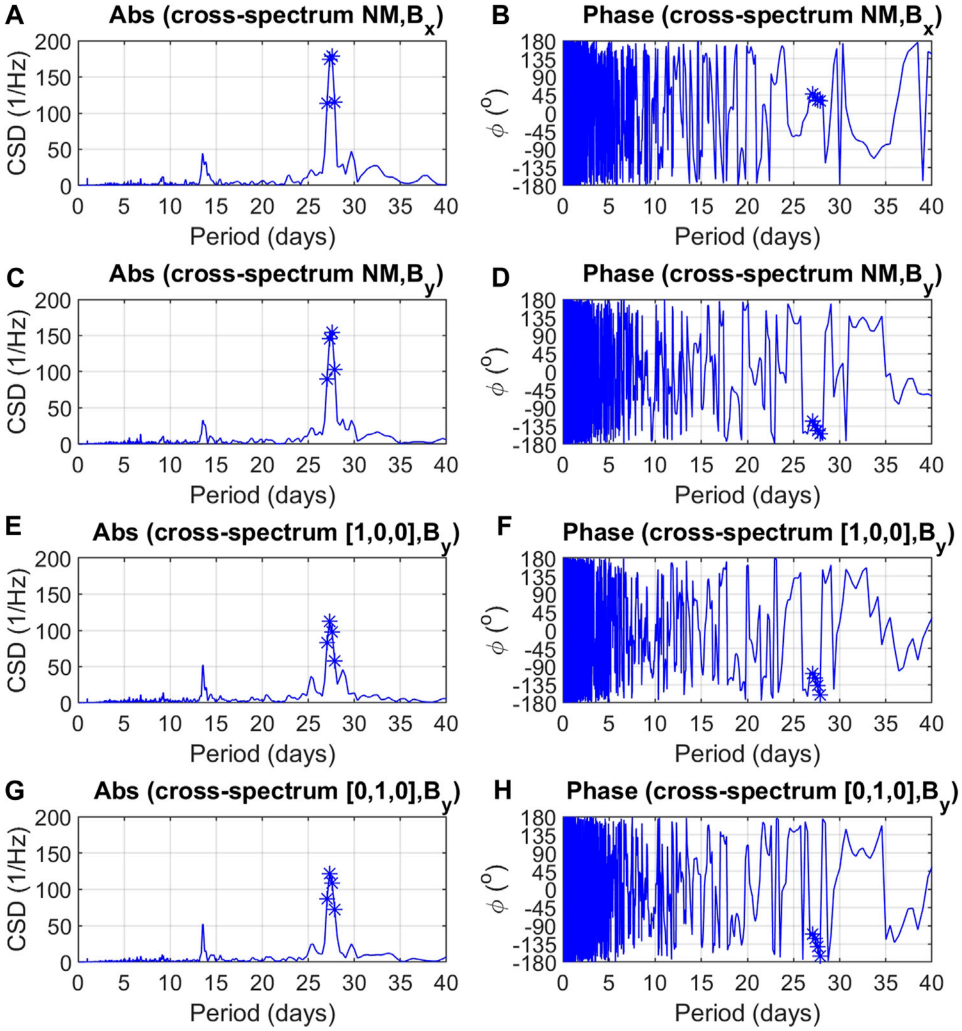

FIGURE 9 | Cross-spectral densities (absolute values and phase differences) of **(A, B)** normalized pressure-corrected NM counts and Bx, **(C, D)** normalized pressure-corrected NM counts and B_y, **(E, F)** normalized pressure-corrected SEVAN [1,0,0] counts and B_y, and **(G, H)** normalized pressure-corrected SEVAN [0,1,0] counts and B_y. Asterisks mark the peak of absolute values of CSD, including its flanks, and the corresponding phase difference.

peak around the period of one year and partly around lower harmonics (~half, ~third, ~quarter, and ~fifth of the year). The spectral peaks related to the seasonal variability are therefore sufficiently far from the period of ~27 days on the frequency (period) axis. To calculate the spectra, lightning counts were first normalized using the method described in the section "Methods." **Figure 10B** shows the PSD of normalized lightning counts. The most distinct and sharp spectral peak is observed for the period of 1 day (**Figure 10B**) as the lightning activity usually peaked between 14–15 UT over Czechia and Slovakia in the analyzed period. Besides the dominant peak at the 1-day period, several relatively flat peaks of similar amplitudes also occurred. One of these flat peaks is at the period of ~27 days. **Figures 10C, D** display results of cross-spectral analysis between the lightning counts and B_y; specifically, the absolute values of CSD and phase differences are shown, respectively. The distinct peak at the period of ~27 days of absolute values of the CSD is mainly caused by the high power spectral density of B_y at this period. Asterisks in the individual plots of **Figure 9** mark the maximum of the absolute values of the CSD at the period of ~27 days and values larger than ½ of this maximum, including the corresponding phase differences. It should be noted that the phase difference around the maximum is relatively stable. The observed phase difference is about 180°, which indicates that a probability of lightning occurrence is in antiphase with B_y. In other words, the probability of lightning occurrence decreases for $B_y > 0$ and increases for $B_y < 0$. Consequently, it is in phase with B_x (not shown) as fluctuations of B_x and B_y are anticorrelated at the period of ~27 days. It should be emphasized that the dependence of lightning activity on the values/polarity of B_x and B_y is only weak as the spectral peak at ~27 days in the spectrum of lightning counts (**Figure 10B**) is not dominant. Nevertheless, this finding is an interesting result which is in agreement with the previous statistical study performed by

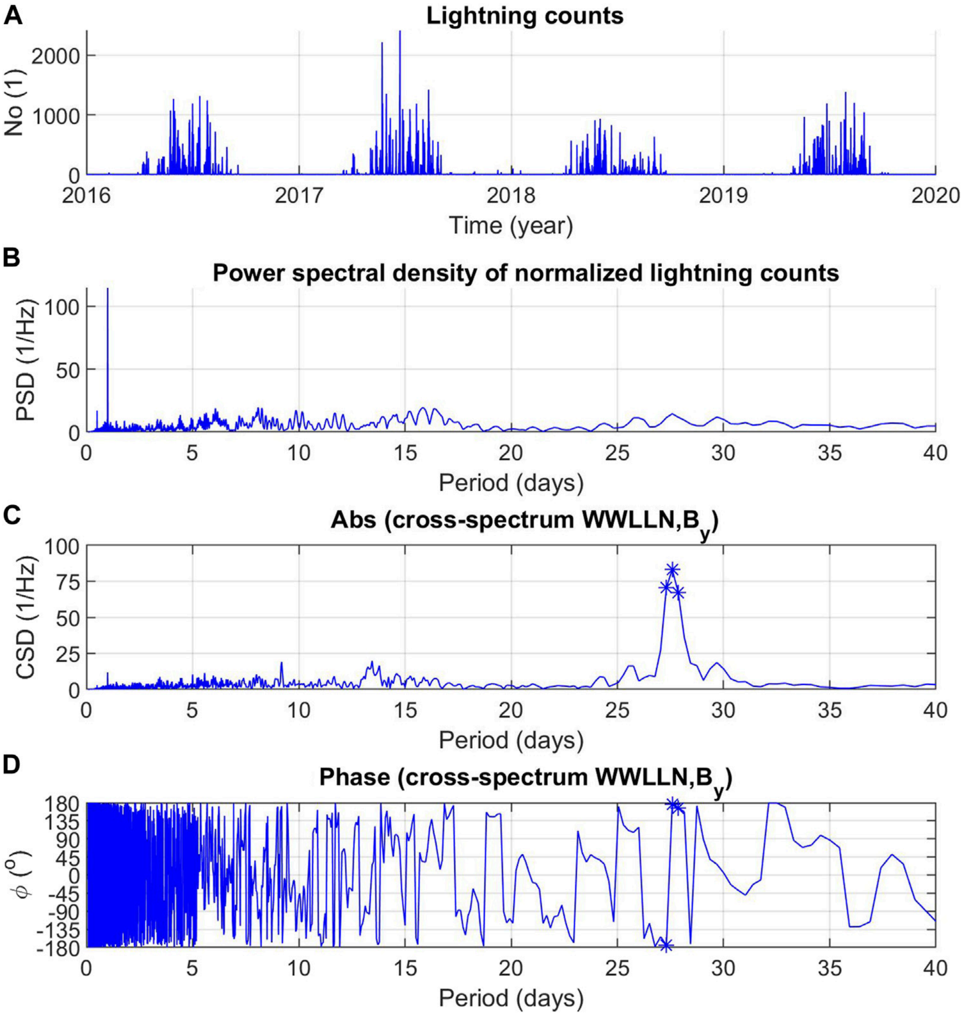

FIGURE 10 | Analysis of lightning activity. **(A)** Lightning counts over Czechia and Slovakia. **(B)** Power spectral density (PSD) of normalized lightning counts. **(C, D)** Cross-spectral densities (absolute values and phase differences) of normalized lightning counts and *By*. Asterisks mark the peak of absolute values of CSD, including its flanks, and the corresponding phase difference.

Owens et al. (2014), who showed that the lightning occurrence over the UK was modulated by the polarity of the HMF and found that the lightning occurrence was lower for the orientation of the HMF away from the Sun ($B_x < 0$ and $B_y > 0$) than it was for the orientation toward the Sun ($B_x > 0$ and $B_y < 0$).

CONCLUSION

Effects of the HMF on SCRs and on atmospheric electricity at middle latitudes were studied by using measurements of SCRs in Slovakia (LS), the electric field in Slovakia (LS) and Czechia (Panská Ves and Studenec), and lightning activity in Czechia and Slovakia. By analyzing the spectra of the near-Earth HMF, velocities of SW, atmospheric electric field, and SCRs measured using the NM and SEVAN detectors located on the mount of Lomnický Štít, Slovakia, it was found that the variations with the period of solar rotation (~27 days) and its second harmonic (~13.5 days) are well expressed both in the HMF and SW and in SCR data. Especially, count variations registered by the NM and by the SEVAN low-energy and neutron channels ([1,0,0] and [0,1,0] combinations, respectively) exhibit distinct peaks at the period of ~27 days. We also investigated the phase difference between the B_x and B_y components of the HMF and the variations of the NM and SEVAN counts and found that the variations of NM and SEVAN [1,0,0] and [0,1,0] data advance, on average, the fluctuations of the B_x component of the HMF by roughly 40°, which corresponds to about a 3-day time-shift at the period of 27 days. As B_x and B_y are practically in the antiphase as predicted by Parker (1958), the variations of NM, SEVAN [1,0,0], and SEVAN [0,1,0] data lag the fluctuations of the B_y component of the HMF by roughly –140°.

No reliable signatures of the ~27-day periodicity were found in the electric field (PG) measurements in Czechia and Slovakia. Therefore, we conclude that the B_y component of the HMF does not influence the PG measured at these middle-latitude stations.

This differs from the observation at polar stations, mainly stations in the winter Antarctic, where the fair-weather PG substantially depended on the B_y polarity (Mansurov et al., 1974; Burns et al., 2008). On the other hand, minor signatures of ~25.7-day periodicities were found in the analyzed PG observations. Such a periodicity was also observed in the SW velocity. Because of the large differences between the PG and SW spectra, it is difficult to reliably determine whether the 25.7-day periodicity in PG data is induced by SW, as it is likely a random coincidence. Our observations show that variations of the PG measured in Czechia and Slovakia are likely fully controlled by processes in the troposphere.

The lightning activity in Slovakia and Czechia and its periodicity were investigated using data from the WWLLN. We observed a minor peak of the lightning activity at the period of solar rotation of about 27 days. The fluctuation of lightning counts at this period was in phase with the B_x component of the HMF and was in antiphase with the B_y component. In other words, lightning was more probable for the orientation of the HMF toward the Sun ($B_x > 0$ and $B_y < 0$) than for the orientation away from the Sun ($B_x < 0$ and $B_y > 0$). It should be noted that this effect is weak and that the lightning activity is mainly controlled by processes in the troposphere. A similar relation was also observed for the lightning occurrence in the UK by Owens et al. (2014), who used, however, a statistical approach in their study. The fact that similar results were obtained using different methods and for different regions enhances the credibility of these findings.

A more detailed investigation of the phase differences between the measured SCR, lightning occurrence, and B_y (B_x) for different phases of the solar cycle, together with investigation of other characteristics of solar activity, and analysis of the physical mechanisms leading to the observed relations is a potential subject for future study.

DATA AVAILABILITY STATEMENT

The datasets presented in this study can be found in online repositories. The names of the repository/repositories and accession number(s) can be found below: the SW and HMF data can be found at NASA/GSFC's Space Physics Data Facility's OMNIWeb (https://omniweb.gsfc.nasa.gov/). The SEVAN and NM data and PG data from Lomnický Štít can be downloaded from http://data.space.saske.sk/status/ (access is provided by R. Langer, langer@saske.sk, on request). PG data from Czechia are available at https://www.ufa.cas.cz/en/institute-structure/department-of-ionosphere-and-aeronomy/measurements-operated-by-department-of-ionosphere-and-aeronomy/.

AUTHOR CONTRIBUTIONS

JC designed and wrote the manuscript and performed most of the analysis. MK, RL, and IS are responsible for and provided the SCR data. IK provided the lightning counts from the WWLLN. DS helped with solar wind data. JR helped with the wavelet transform. All authors read and approved the submitted version.

FUNDING

Support under the grants SAV-18-04 and SAV-21-01 by the Czech Academy of Sciences is acknowledged. IK also acknowledges the support under the project 20-09671S of the Czech Science Foundation.

ACKNOWLEDGMENTS

We are grateful to Jiří Baše for maintaining the electric field measurements. JC also acknowledges valuable discussions with Keri Nicoll that preceded this study.

REFERENCES

Bazilevskaya, G., Broomhall, A.-M., Elsworth, Y., and Nakariakov, V. M. (2014). A Combined Analysis of the Observational Aspects of the Quasi-Biennial Oscillation in Solar Magnetic Activity. *Space Sci. Rev.* 186, 359–386. doi:10.1007/s11214-014-0068-0

Burns, G. B., Tinsley, B. A., French, W. J. R., Troshichev, O. A., and Frank-Kamenetsky, A. V. (2008). Atmospheric Circuit Influences on Ground-Level Pressure in the Antarctic and Arctic. *J. Geophys. Res.* 113, D15112. doi:10.1029/2007JD009618

Chilingarian, A., Babayan, V., Karapetyan, T., Mailyan, B., Sargsyan, B., and Zazyan, M. (2018). The SEVAN Worldwide Network of Particle Detectors: 10 Years of Operation. *Adv. Space Res.* 61, 2680–2696. doi:10.1016/j.asr.2018.02.030

Chilingarian, A., Hovsepyan, G., Karapetyan, G., and Zazyan, M. (2021). Stopping Muon Effect and Estimation of Intracloud Electric Field. *Astroparticle Phys.* 124, 102505. doi:10.1016/j.astropartphys.2020.102505

Chilingarian, A., and Reymers, A. (2008). Investigations of the Response of Hybrid Particle Detectors for the Space Environmental Viewing and Analysis Network (SEVAN). *Ann. Geophys.* 26, 249–257. Available at: www.ann-geophys.net/26/249/2008/. doi:10.5194/angeo-26-249-2008

Chowdhury, P., and Kudela, K. (2018). Quasi-periodicities in Cosmic Rays and Time Lag with the Solar Activity at a Middle Latitude Neutron Monitor: 1982-2017. *Astrophys. Space Sci.* 363, 250. doi:10.1007/s10509-018-3467-y

Chum, J., Langer, R., Baše, J., Kollárik, M., Strhárský, I., Diendorfer, G., et al. (2020). Significant Enhancements of Secondary Cosmic Rays and Electric Field at the High Mountain Peak of Lomnický Štít in High Tatras during Thunderstorms. *Earth Planets Space* 72, 28. doi:10.1186/s40623-020-01155-9

Dwyer, J. R., and Uman, M. A. (2014). The Physics of Lightning. *Phys. Rep.* 534 (4), 147–241. doi:10.1016/j.physrep.2013.09.004

Gosling, J. T., and Pizzo, V. J. (1999). Formation and Evolution of Corotating Interaction Regions and Their Three Dimensional Structure. *Space Sci. Rev.* 89, 21–52. doi:10.1023/A:100529171190010.1007/978-94-017-1179-1_3

Gosse, J., and Klein, J. (2015). "Terrestrial Cosmogenic Nuclide Dating," in *Encyclopedia of Scientific Dating Methods*. Editors W. J. Rink and J. W. Thompson (New York: Springer), 29, 799–813. doi:10.1007/978-94-007-6304-3_148

Gray, L. J., Beer, J., Geller, M., Haigh, D. J., Lockwood, M., Matthes, K., et al. (2010). Solar Influences on Climate. *Rev. Geophys.* 48, RG4001. doi:10.1029/2009RG000282

Grieder, P. (2001). *Cosmic Rays at Earth*, 1. Amsterdam: Elsevier.

Gurevich, A. V., Milikh, G. M., and Roussel-Dupre, R. A. (1992). Runaway Electron Mechanism of Air Breakdown and Preconditioning during a Thunderstorm. *Phys. Lett. A* 165 (5-6), 463–468. doi:10.1016/0375-9601(92)90348-P

Kirkby, J. (2008). Cosmic Rays and Climate. *Surv. Geophys.* 28, 333–375. doi:10.1007/s10712-008-9030-610.1007/s10712-008-9030-6

Kristjánsson, J. E., Stjern, C. W., Stordal, F., Fjæraa, A. M., Myhre, G., and Jónasson, K. (2008). Cosmic Rays, Cloud Condensation Nuclei and Clouds - a Reassessment Using MODIS Data. *Atmos. Chem. Phys.* 8 (24), 7373–7387. doi:10.5194/acp-8-7373-2008

Kudela, K., Chum, J., Kollárik, M., Langer, R., Strhárský, I., and Baše, J. (2017). Correlations between Secondary Cosmic Ray Rates and Strong Electric Fields at Lomnický Štít. *J. Geophys. Res. Atmos.* 122, 700–710. doi:10.1002/2016JD026439

Kudela, K., and Langer, R. (2009). Cosmic ray Measurements in High Tatra Mountains: 1957-2007. *Adv. Space Res.* 44 (10), 1166–1172. doi:10.1016/j.asr.2008.11.028

Kudela, K., Mavromichalaki, H., Papaioannou, A., and Gerontidou, M. (2010). On Mid-term Periodicities in Cosmic Rays. *Sol. Phys.* 266, 173–180. doi:10.1007/s11207-010-9598-0

Kudela, K., Rybák, J., Antalová, A., and Storini, M. (2002). Time Evolution of Low-Frequency Periodicities in Cosmic ray Intensity. *Solar Phys.* 205, 165–175. doi:10.1023/A:1013869322693

Lam, M. M., and Tinsley, B. A. (2016). Solar Wind-Atmospheric Electricity-Cloud Microphysics Connections to Weather and Climate. *J. Atmos. Solar-Terrestrial Phys.* 149, 277–290. doi:10.1016/j.jastp.2015.10.019

López-Comazzi, A., and Blanco, J. J. (2020). Short-Term Periodicities Observed in Neutron Monitor Counting Rates. *Sol. Phys.* 295, 81. doi:10.1007/s11207-020-01649-5

Mansurov, S. M., Mansurova, L. G., Mansurov, G. S., Mikhnevich, V. V., and Visotsky, A. M. (1974). North–south Asymmetryofgeomagneticandtroposphericevents. *J.Atmos.Terr.Phys.* 36 (1), 1957–1962. doi:10.1016/0021-9169(74)90182-2

Miyahara, H., Kataoka, R., Mikami, T., Zaiki, M., Hirano, J., Yoshimura, M., et al. (2018). Solar Rotational Cycle in Lightning Activity in Japan during the 18-19th Centuries. *Ann. Geophys.* 36, 633–640. doi:10.5194/angeo-36-633-2018

Nicoll, K. A., Harrison, R. G., Barta, V., Bor, J., Brugge, R., Chillingarian, A., et al. (2019). A Global Atmospheric Electricity Monitoring Network for Climate and Geophysical Research. *J. Atmos. Solar-Terrestrial Phys.* 184, 18–29. doi:10.1016/j.jastp.2019.01.003

Nicoll, K. A., and Harrison, R. G. (2009). Vertical Current Flow through Extensive Layer Clouds. *J. Atmos. Solar-Terrestrial Phys.* 71 (12), 2040–2046. doi:10.1016/j.jastp.2009.09.011

Owens, M. J., and Forsyth, R. J. (2013). The Heliospheric Magnetic Field. *Living Rev. Solar Phys.* 10, 5. doi:10.12942/lrsp-2013-5

Owens, M. J., Scott, C. J., Bennett, A. J., Thomas, S. R., Lockwood, M., Harrison, R. G., et al. (2015). Lightning as a Space-Weather hazard: UK Thunderstorm Activity Modulated by the Passage of the Heliospheric Current Sheet. *Geophys. Res. Lett.* 42, 9624–9632. doi:10.1002/2015GL066802

Owens, M. J., Scott, C. J., Lockwood, M., Barnard, L., Harrison, R. G., Nicoll, K., et al. (2014). Modulation of UK Lightning by Heliospheric Magnetic Field Polarity. *Environ. Res. Lett.* 9 (11), 115009. doi:10.1088/1748-9326/9/11/115009

Parker, E. N. (1958). Dynamics of the Interplanetary Gas and Magnetic Fields. *ApJ* 128, 664–676. doi:10.1086/146579

Riádigos, I., García-Castro, D., González-Díaz, D., and Pérez-Muñuzuri, V. (2020). Atmospheric Temperature Effect in Secondary Cosmic Rays Observed with a 2 M 2 Ground-Based tRPC Detector. *Earth Space Sci.* 7, e2020EA001131. doi:10.1029/2020EA001131

Rieger, E., Share, G. H., Forrest, D. J., Kanbach, G., Reppin, C., and Chupp, E. L. (1984). A 154-day Periodicity in the Occurrence of Hard Solar Flares? *Nature* 312, 623–625. doi:10.1038/312623a0

Rodger, C. J., Brundell, J. B., Dowden, R. L., and Thomson, N. R. (2004). Location Accuracy of Long Distance VLF Lightning Locationnetwork. *Ann. Geophys.* 22 (3), 747–758. doi:10.5194/angeo-22-747-2004

Rycroft, M. J., Israelsson, S., and Price, C. (2000). The Global Atmospheric Electric Circuit, Solar Activity and Climate Change. *J. Atmos. Solar-Terrestrial Phys.* 62, 1563–1576. doi:10.1016/S1364-6826(00)00112-7

Saad Farid, A. I. (2019). High Frequency Spectral Features of Galactic Cosmic Rays at Different Rigidities during the Ascending and Maximum Phases of the Solar Cycle 24. *Astrophys Space Sci.* 364, 57. doi:10.1007/s10509-019-3544-x

Shao, X. M., Ho, C., Bowers, G., Blaine, W., and Dingus, B. (2020). Lightning Interferometry Uncertainty, Beam Steering Interferometry, and Evidence of Lightning Being Ignited by a Cosmic ray Shower. *J. Geophys. Res. Atmos.* 125, e2019JD032273. doi:10.1029/2019JD032273

Shea, M. A., and Smart, D. F. (2000). Fifty Years of Cosmic Radiation Data. *Space Sci. Rev.* 93, 229–262. doi:10.1023/A:1026500713452

Silva, H. G., Conceição, R., Melgão, M., Nicoll, K., Mendes, P. B., Tlemçani, M., et al. (2014). Atmospheric Electric Field Measurements in Urban Environment and the Pollutant Aerosol Weekly Dependence. *Environ. Res. Lett.* 9 (11), 114025. doi:10.1088/1748-9326/9/11/114025

Svensmark, H., Bondo, T., and Svensmark, J. (2009). Cosmic ray Decreases Affect Atmospheric Aerosols and Clouds. *Geophys. Res. Lett.* 36, L15101. doi:10.1029/2009GL038429

Usoskin, I. G., Kananen, H., Mursula, K., Tanskanen, P., and Kovaltsov, G. A. (1998). Correlative Study of Solar Activity and Cosmic ray Intensity. *J. Geophys. Res.* 103 (A5), 9567–9574. doi:10.1029/97JA03782

Voiculescu, M., Usoskin, I., and Condurache-Bota, S. (2013). Clouds Blown by the Solar Wind. *Environ. Res. Lett.* 8, 045032. doi:10.1088/1748-9326/8/4/045032

Voiculescu, M., and Usoskin, I. (2012). Persistent Solar Signatures in Cloud Cover: Spatial and Temporal Analysis. *Environ. Res. Lett.* 7, 044004. doi:10.1088/1748-9326/7/4/044004

Yang, Z.-Y., and Sheu, R.-J. (2020). An In-Depth Analysis of Aviation Route Doses for the Longest Distance Flight from Taiwan. *Radiat. Phys. Chem.* 168, 108548. doi:10.1016/j.radphyschem.2019.108548

Conflict of Interest: The authors declare that the research was conducted in the absence of any commercial or financial relationships that could be construed as a potential conflict of interest.

frontiers in Earth Science

ORIGINAL RESEARCH
published: 05 August 2021
doi: 10.3389/feart.2021.709890

Modeling of Spherical Dust Particle Charging due to Ion Attachment

Sotirios A. Mallios[1]*, Georgios Papangelis[1], George Hloupis[2], Athanasios Papaioannou[1], Vasiliki Daskalopoulou[1,3] and Vassilis Amiridis[1]

[1]National Observatory of Athens (IAASARS), Athens, Greece, [2]Department of Surveying and GeoInformatics Engineering, Faculty of Engineering, University of West Attica, Athens, Greece, [3]Department of Physics, Faculty of Astrophysics and Space Physics, University of Crete, Heraklion, Greece

The attachment of positive and negative ions to settling spherical dust particles is studied. A novel 1D numerical model has been developed to parameterize the charging process in the presence of a large-scale electric field. The model is able to self-consistently calculate the modification of atmospheric ion densities in the presence of the dust particles, and the consequent alteration of the atmospheric electrical conductivity and the large-scale electric field. Moreover, the model estimates the acquired electrical charge on the dust particles and calculates the electrical force that is applied on them. Using observed dust size distributions, we find that the particles can acquire electrical charge in the range of 1–1,000 elementary charges depending on their size and number density. The particles become mainly negatively charged, but under specific conditions giant mode particles (larger than 50 μm radius) can be positive. Moreover, the large-scale electric field can increase up to 20 times as much as the fair weather value. However, our approach shows that the resultant electrical force is not enough to significantly influence their gravitational settling, as the ratio between the electrical force magnitude and the gravity magnitude does not exceed the value of 0.01. This indicates that the process of ion attachment alone is not sufficient to create strong electrical effects for the modification of particle dynamics. Therefore, other processes, such as the triboelectric effect and updrafts, must be included in the model to fully represent the impact of electricity on particle dynamics.

Keywords: dust particle electrification, dust particle charging, ion attachment, dust particle settling, dust particle transport, atmospheric electricity

Edited by:
Konstantinos Kourtidis,
Democritus University of Thrace,
Greece

Reviewed by:
Yoav Yosef Yair,
Interdisciplinary Center Herzliya, Israel
James Matthews,
University of Bristol, United Kingdom

***Correspondence:**
Sotirios A. Mallios
smallios@noa.gr

Specialty section:
This article was submitted to
Atmospheric Science,
a section of the journal
Frontiers in Earth Science

Received: 14 May 2021
Accepted: 20 July 2021
Published: 05 August 2021

Citation:
Mallios SA, Papangelis G, Hloupis G,
Papaioannou A, Daskalopoulou V and
Amiridis V (2021) Modeling of Spherical
Dust Particle Charging due to
Ion Attachment.
Front. Earth Sci. 9:709890.
doi: 10.3389/feart.2021.709890

1 INTRODUCTION

Mineral dust plays an important role in the Earth's atmosphere, and in the Earth System in total. It significantly impacts radiation (Li et al., 2004), as dust particles absorb shortwave and long-wave radiations, potentially causing a net atmospheric warming (Kok et al., 2017). Moreover, mineral dust interacts with liquid or ice clouds, modifying their optical properties and lifetimes (DeMott et al., 2003), and affecting the precipitation processes (Creamean et al., 2013). Finally, the lifetime of the mineral dust particles affects the deposition fluxes over land and ocean (van der Does et al., 2018). Once dust particles are deposited at the surface, they provide micro nutrients to the ocean or to land ecosystems (e.g., Jickells et al., 2005).

All aforementioned processes are strongly affected by the dust Particle Size Distribution (PSD). The dust PSD changes rapidly after emission since the preferential gravitational settling quickly removes the larger particles. However, Earth System Models and transport models fail to properly simulate dust deposition. There have been comparisons of model simulation against measurements, that show a consistent overestimation of large particle removal (e.g., Ginoux et al., 2001; Colarco et al., 2002). On the other hand, dust model inter-comparison by Huneeus et al. (2011) found that, the model estimates of deposition vary over a large range, yet mainly underestimating the observations. Adebiyi and Kok (2020) showed that the mass of coarse dust (Diameter ≥5 μm) in the atmosphere is about four times greater than the simulated in current climate models, resulting in greater total dust mass load. This signifies the importance of proper modeling of the mineral dust deposition.

The conclusion that climate models underestimate the coarse mode dust in the atmosphere, is consistent with observations. Denjean et al. (2016) showed that the effective diameter of the Saharan dust coarse mode does not vary with dust age over the Mediterranean for transport times between 1.5 and 7 days. This conclusion has been drawn by consolidating high-quality aircraft measurements of dust PSDs performed during the last years in the framework of few large-scale experimental campaigns (Ryder et al., 2013a; Ryder et al., 2013b; Ryder et al., 2018; Ryder et al., 2019). Weinzierl et al. (2017) presented results of aircraft and ground-based measurements during the SALTRACE campaign in the tropical Atlantic in 2013/2014. Particles with sizes in the range of 10–30 μm were detected over Barbados, during a Langrangian flight sequence from Cape Verde, far beyond the Stokes gravitational settling expectations. Similar conclusions were also validated by deposition of giant particles (size greater than 75 μm), as depicted by samplers mounted on moored dust-collecting surface buoys, located in the Atlantic Ocean at 2,400 and 3,500 km from the west African coast (van der Does et al., 2018). These collected dust particles were mostly well-rounded quartz particles up to 450 μm in polar diameter, with what appeared to be high aspect ratios. Moreover, Goudie and Middleton (2001) reported that particles larger than 62.5 μm are commonly carried from Sahara to the British Isles.

van der Does et al. (2018) discussed four potential different mechanisms that could facilitate long-range transport of large/giant particles. These mechanisms are: 1) strong winds causing fast horizontal transport, 2) strong turbulence keeping particles in suspension for longer time (Garcia-Carreras et al., 2015), 3) electrical forces that balance the gravitational force (Nicoll et al., 2010; Renard et al., 2018; Toth et al., 2020), and 4) the presence of thunderstorms or tropical cyclones that can create strong uplifts. Additionally, the particle shape and orientation can also influence the dust particle transport time (Huang et al., 2020; Mallios et al., 2020; Mallios et al., 2021b). Specifically, Mallios et al. (2020, 2021b) showed that simulating dust particles as prolate spheroids, they can remain much longer in the atmosphere than their spherical counterparts, and that the particle vertical orientation can increase the residual time in the atmosphere significantly, compared to the horizontal one. Vertical orientation becomes possible in the presence of external large scale electric fields of strength in the order of 10^4 V/m (two orders of magnitude greater than the fair weather electric field values) (Mallios et al., 2021a).

The field of Atmospheric Electricity research can provide insights on the electrical processes and their contribution to the transport of dust plumes. The Earth's atmosphere is a conducting medium, attributed to the presence of ions, created by ionization by galactic cosmic rays radiation. Ions attach to dust particles through the processes of ionic diffusion and Coulomb interaction (Gunn, 1954; Klett, 1971) and the polarization due to the presence of an external electric field (Gunn, 1956; Klett, 1971), leading to their subsequent charging (Zhou and Tinsley, 2007; Zhou and Tinsley, 2012). This large scale electric field is created by the potential difference between the lower part of the ionosphere and the Earth's surface (Rycroft et al., 2008), and is modified by the ion density reduction caused by the ion attachment process, which leads to the electrical conductivity reduction and the atmospheric columnar resistance enhancement (Zhou and Tinsley, 2007; Baumgaertner et al., 2014). Moreover, the dust particles can be also charged during collisions, a mechanism known as triboelectric process (Kamra, 1972; Eden and Vonnegut, 1973), that results in large particle being predominantly positively charged and small particles negatively (e.g. Zhao et al., 2002; Lacks et al., 2008; Shinbrot and Herrmann, 2008; Merrison, 2012). This size preferential polarity acquisition in combination with updrafts or shape induced gravitational sorting (Yang et al., 2013; Mallios et al., 2020; Mallios et al., 2021b), can create charge separation that further enhances the electric field magnitude, similarly to processes that take place in thunderstorms (e.g., Chiu, 1978; Helsdon et al., 2002; Williams and Yair, 2006, and references therein).

Motivated by the studies of dust particle electrification and charging, we focus on dust charging due to ion attachment process and we develop an 1D numerical model for the of spherical dust particle settling in the presence of a large scale electric field. The model is able to calculate self consistently the modification of the atmospheric ion densities in the presence of the dust particles, and the consequent alteration of the atmospheric electrical conductivity and the large scale electric field. Moreover, it is able to evaluate the acquired electrical charge on the dust particles, and thus to calculate the electrical force that is applied on them. Finally, the effect of the electrical force on the gravitational settling and the terminal velocity is quantified.

In **Section 2**, the mathematical formulation of the model is presented and explained. In **Section 3**, results of the model under different conditions are presented and discussed. Finally, in **Section 4** the results of this work are summarized.

2 MATERIALS AND METHODS

2.1 System Dynamics

The bottom (z = 0 km, Earth's surface) and the top (z = 40 km) boundaries are assumed to be perfect conductors of electricity. Although the lower part of the ionosphere is typically at ~70–80 km (e.g., Rycroft et al., 2008), the perfectly conducting boundary can be placed at 40 km (for simulation purposes), since the electric field at this altitude is mainly vertical, regardless of the electrical activity at altitudes below 12 km (Pasko et al., 1997).

TABLE 1 | Physical constant values.

Symbol	Name	Value	Unit
R^*	Specific gas constant for dry air	287.058	J/(kg K)
K	Boltzmann constant	1.381×10^{-23}	$m^2kg/(s^2K)$
T_0	Reference temperature	288.15	K
P_0	Reference pressure	1,013.25	hPa
S	Sutherland's constant	120	K
q_e	Elementary charge	1.602×10^{-19}	C
ε_0	Vacuum permittivity	8.854×10^{-12}	F/m
μ_0^+	Positive ion mobility at reference conditions	1.4×10^{-4}	$m^2/(V\ s)$
μ_0^-	Negative ion mobility at reference conditions	1.9×10^{-4}	$m^2/(V\ s)$
η_0	Viscosity at reference temperature	1.789×10^{-5}	Pa s
G	Gravitational acceleration	9.80665	m/s^2
ϱ_p	Mass density of dust particle	2,600	kg/m^3

Increasing the upper boundary altitude to 50 km, the relative difference between the results in the area of interest (up to 12 km altitude) is less than 1%. The electrical potential at the bottom boundary is set equal to 0 V, while at the top boundary is set to 250 kV, which can be seen as the average potential along the ionosphere (Rycroft et al., 2000).

In the region under investigation, the ion conductivity is dominant over the electron conductivity, as electron number density exceeds the bipolar ion number densities at altitudes above ~60 km (Pasko et al., 1997). Therefore, the particle types that are considered in the presented formalism are the atmospheric small ions, and the dust particles in terms of atmospheric aerosol content.

As a first approximation in order to highlight the possible physical mechanisms, we neglect the wind speed, and we consider the atmosphere to be stagnant, which denotes to the particle velocity with respect to the air being the same with the particle velocity with respect to an observer at the ground, $\vec{v}_\mathrm{p}$.

The continuity equation for positive and negative small ion number densities, $n^\pm$, is:

$$\frac{dn^\pm}{dt} = -\vec{\nabla}\cdot\left[\pm n^\pm \mu^\pm \vec{E} - D^\pm_{\mathrm{ion}}\vec{\nabla}n^\pm\right] + q - a n^+ n^- - n^\pm \sum_i \beta_i^\pm , \tag{1}$$

where $\mu^\pm$ are the positive and negative small ion electrical mobilities, $\vec{E}$ is the large scale electric field, $D^\pm_{\mathrm{ion}}$ are the positive and negative small ion diffusion coefficients, q is the ion pair production rate, a is the ion-ion recombination rate, and $\beta_i^\pm$ are the positive and negative ion attachment rates to dust particles with radius r_i. The first two terms in brackets are the flux of small ions due to their motion in response to the large scale electric field, and the ionic diffusion. The third term describes the production rate of positive and negative ions, while the last two terms express the ion losses due to recombination, and attachment to dust particles.

The current continuity equation for the charge transport of dust particles with radius r_i is:

$$\frac{d\rho_{\mathrm{p},i}}{dt} = -\vec{\nabla}\cdot\left[\rho_{\mathrm{p},i}\vec{v}_{\mathrm{p},i} - D_{\mathrm{p},i}\vec{\nabla}\rho_{\mathrm{p},i}\right] + q_\mathrm{e}\left(\beta_i^+ n^+ - \beta_i^- n^-\right), \tag{2}$$

where $\rho_{\mathrm{p},i}$ is the dust particle charge density, $\vec{v}_{\mathrm{p},i}$ is the dust particle velocity, $D_{\mathrm{p},i}$ is the dust particle diffusion coefficient, and q_e is the elementary charge. We note that all physical constants appearing in the manuscript, are listed in **Table 1**. The first two terms in brackets are the charge flux due to the dust particles advection/settling (advection is a valid term for the 3D case where horizontal components of velocity exist, while the settling happens in the 1D case, where the particles fall in the vertical direction), and the diffusion. The third term describes the gain of charge due to the ion attachment.

The continuity equation for the transport of number densities, $N_{\mathrm{p},i}$, that correspond to dust particles with radius r_i, is:

$$\frac{dN_{\mathrm{p},i}}{dt} = -\vec{\nabla}\cdot\left[N_{\mathrm{p},i}\vec{v}_{\mathrm{p},i} - D_{\mathrm{p},i}\vec{\nabla}N_{\mathrm{p},i}\right], \tag{3}$$

where the terms in brackets are the dust particle flux due to the advection/settling and the diffusion.

Eqs. 2, **3** have the same particle velocities, and the same particle diffusion coefficients, since they refer to different properties of the same particle. The particle charge density and the particle number density are related through the expression $\rho_{\mathrm{p},i} = q_{\mathrm{p},i}N_{\mathrm{p},i}$, with $q_{\mathrm{p},i}$ being the particle net charge. These three quantities vary over time, but different equations govern their variation. The linkages between their temporal and spatial variations, are the common velocity and diffusion coefficient.

Finally, the large scale electric field, $\vec{E}$, is calculated from the total charge density, ρ_{tot}, from the Gauss law:

$$\vec{\nabla}\cdot\vec{E} = \frac{\rho_{\mathrm{tot}}}{\varepsilon_0} = \frac{\sum_i \rho_{\mathrm{p},i} + q_\mathrm{e}\left(n^+ - n^-\right)}{\varepsilon_0}. \tag{4}$$

Although **Eqs. 1–4** are generic, in this work we shall focus on the 1D case, in the vertical direction along the altitude. Applicability of the model can be easily extended to other types of aerosols that can be simulated by spherical shapes and act as good conductors of electricity.

Substituting $\vec{E}$ in **Eq. 4** with $-\vec{\nabla}\Phi$, the Poisson equation is derived, which is solved using a Full Multigrid Algorithm (FMG) (Press et al., 1992, p. 877). The advection terms in **Eqs. 1–3** are discretized as an average between the second order Upstream Nonoscillatory (UNO2) advection scheme (Li, 2008) and the third order Quadratic Upstream Interpolation for Convective Kinematics with Estimated Upstream Terms (QUICKEST) method (Leonard, 1979). This approach reduces the artificial

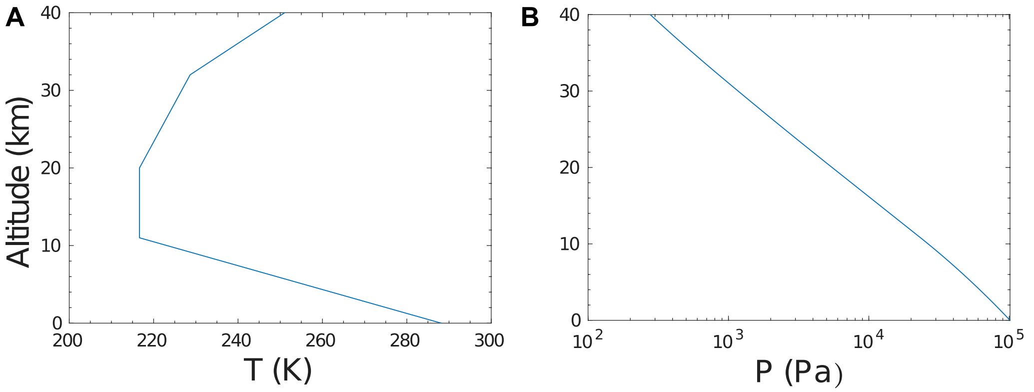

FIGURE 1 | Vertical distribution of the meteorological parameters in SATP: **(A)** temperature T, and **(B)** pressure P.

numerical diffusion significantly, without using computationally demanding flux limiters or flux corrected transport (FTC) schemes. The diffusion terms in **Eqs. 1–3** are discretized as a second order central difference scheme.

The simulation domain is divided in 2049 mesh points, and increasing further their number by a factor of two leads to a relative difference less than 5% between the results. The results obtained with the aforementioned approach and the given mesh points, are very close (relative difference less than 2%) to the results obtained with a first order upwind scheme (Press et al., 1992, p. 834) with 8,192 mesh points. This shows that the used scheme is indeed less diffusive than a first order upwind scheme under the same conditions, and also that the averaging of two schemes can be a valid procedure. After all, the principle of a weighted average between a stable but diffusive low order scheme with an unstable but less diffusive higher order scheme is the core of the FTC schemes (Zalesak, 1979). The FMG algorithm ensures fast convergence of the Poisson equation solution, when the number of mesh points becomes very large (as in our case) (Press et al., 1992, p. 871).

2.2 Meteorological Conditions

The U.S. Standard Atmosphere 1976 (NOAA/NASA/USAF, 1976) is considered as the standard static atmospheric model, and the vertical distributions of pressure, P, and temperature, T, are constant over time (**Figure 1**). The air mass density, ϱ_{air}, at a given altitude can be calculated from pressure and temperature, provided that the atmosphere is an ideal gas:

$$\varrho_{air} = \frac{P}{R^{\star}\mathrm{T}}, \tag{5}$$

where $R^{\star}$ is the specific gas constant for dry air.

2.3 Ionization Rate

There are three mechanisms that create the atmospheric ions (Tinsley and Zhou, 2006, and references therein): 1) ionization by natural radioactivity originating in the ground, including direct α, β, and γ radiation from the surface layers and dust aerosol, and radiation from radioactive gases (principally 222 Rn but also 220 Rn) and daughter products that are carried up into the troposphere by vertical convection. 2) In the troposphere the dominant ionization mechanism is the flux of galactic cosmic rays (GCR). This does not apply in polar and subpolar regions, where the ionization due to solar energetic particles is important (Mishev, 2013). 3) In the stratosphere there are additional ion pair sources such as the flux of relativistic electrons (of a few MeV energy) precipitated from the radiation belts and peaking at subauroral latitudes, and the solar energetic particle events (mainly protons) in the polar and subpolar regions (Mishev, 2013).

In the current study the ionization rate as formulated by Tinsley and Zhou (2006) is adopted with two simplifications. The first is to neglect the natural radioactivity effect originating in the ground. This leads to a cruder but smoother vertical profile of the ion densities and the electrical conductivity along the altitude. Moreover, such a choice eliminates the variation of the ionization rate between continental and marine areas (as we show in **Section 2.10**), and thus the only dependence that is left is on the geomagnetic latitude. This leads to an approximation of the ionization rate which is more suitable for highlighting the mechanism of the particle-ions interactions, which is the focus of the work, and interpreting the obtained results.

The second simplification is the creation of a generic temporal ionization rate profile, by averaging the solar minimum and solar maximum profiles given in the aforementioned work, leading to a profile independent of the solar cycle. This resulting empirical profile, although admittedly simple, is suitable since it serves as the baseline approach for the investigation of the ionization rate distribution effects on the ion density and, consequently, the atmospheric electrical conductivity distribution. Indeed, for in depth analysis more detailed profiles would be a better representation, regarding e.g. the annual variation, however, this goes beyond the scope of the paper at hand.

The mathematical formalism for the ionization rate, q, is listed in **Table 2**. The quantities q_i and z_i that depend on the geomagnetic latitude, and are used in the formulas, are plotted in **Figure 2**.

2.4 Recombination Rate

The ion-ion recombination rate, a, is derived by fitting the values of Bates (1982).

TABLE 2 | Interpolation formulas and their scale heights for ionization rates, q.

Altitude range (km)	q (pairs/(m^3 s))	Scale height (km)
$z < z_a$	$q_a \exp[(z - z_a)/s_s]$	$s_s = z_a/\ln(q_a/q_s)$
$z_a \leq z < z_b$	$q_b \exp[(z - z_b)/s_a]$	$s_a = (z_b - z_a)/\ln(q_b/q_a)$
$z_b \leq z < z_c$	$q_c \exp[(z - z_c)/s_b]$	$s_b = (z_c - z_b)/\ln(q_c/q_b)$
$z_c \leq z < z_m$	$q_m \exp\left[-((z - z_m)/s_c)^2\right]$	$s_c = (z_m - z_c)/[\ln(q_m/q_c)]^{1/2}$
$z_m \leq z$	$q_d + (q_m - q_d)\exp\left[-((z - z_m)/s_c)^2\right]$	—

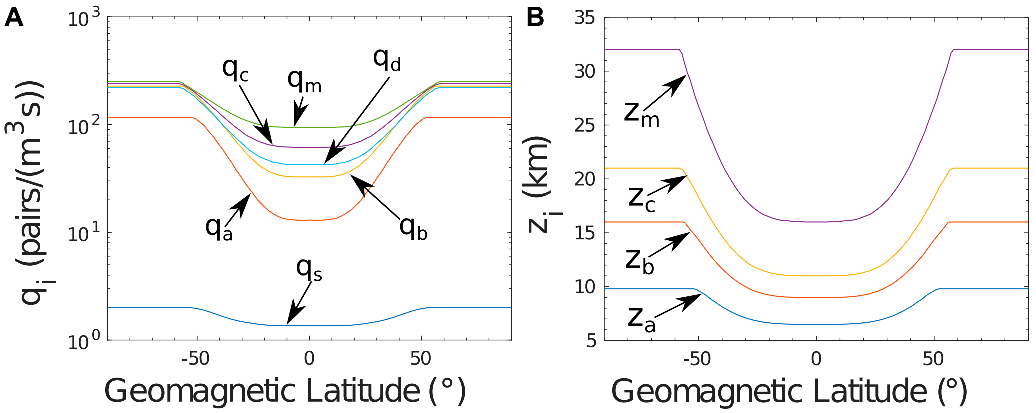

FIGURE 2 | Quantities used in the interpolation formulas for the ionization rate calculation, as functions of the geomagnetic latitude: **(A)** q, and **(B)** z_i.

$$a = \begin{cases} 1.6667 \times 10^{-12} & ,[M] \geq 0.32 \\ (8.5407058 \times 10^{-2} + 8.0752966[M] - 9.8086851[M]^2) \times 10^{-12} & ,[M] < 0.32 \end{cases}, \tag{6}$$

where $[M]$ is the concentration of air molecules in units of 2.69×10^{19} cm^{-3}.

In the case of US Standard Atmosphere, $[M]$ in units of m^{-3} can be calculated as:

$$[M] = \frac{P}{kT}, \tag{7}$$

where P is the pressure, k is the Boltzmann constant, and T is the temperature.

2.5 Ionic Electrical Mobilities

The ion electrical mobilities $\mu^{\pm}$ are scaled along the altitude as (Zhou and Tinsley, 2007):

$$\mu^{\pm} = \mu_0^{\pm} \frac{P_0}{P} \left(\frac{T}{T_0}\right)^{1.5} \frac{T_0 + S}{T + S}, \tag{8}$$

where $\mu_0^{\pm}$ is the electrical mobility of positive and negative ions at reference pressure, P_0, and reference temperature, T_0, and S is the Sutherland's constant. In the present work, $\mu_0^{\pm}$ are adopted by Bricard (1965), and are listed in **Table 1**.

2.6 Diffusion Coefficients

The positive and negative small ion diffusion coefficient, $D_{\text{ion}}^{\pm}$, is given by the Einstein's relation:

$$D_{\text{ion}}^{\pm} = \frac{\mu^{\pm} kT}{q_e}. \tag{9}$$

The diffusion coefficient for dust particles of radius r_i, $D_{p,i}$, is given by the Einstein's relation:

$$D_{p,i} = \mu_{m,i} kT = \frac{C_c}{6\pi\eta r_i} kT, \tag{10}$$

where $\mu_{m,i}$ is the mechanical mobility, given by the Cunningham-Knudsen-Weber-Millikan equation (e.g., Tammet, 1995), η is the air dynamic viscosity, and C_c is the slip correction factor.

The dynamic viscosity, η, is scaled along the altitude according to Sutherland's model (e.g., Zhou and Tinsley, 2007, and references therein):

$$\eta = \eta_0 \left(\frac{T}{T_0}\right)^{1.5} \frac{T_0 + S}{T + S}, \tag{11}$$

where η_0 is the viscosity at reference temperature T_0.

The slip correction factor is adopted by Davies (1945) as:

$$C_c = 1 + \frac{l}{r_i}\left[1.257 + 0.4 \exp\left(\frac{-1.1 r_i}{l}\right)\right], \tag{12}$$

where l is the mean free path in air that is given by the expression (Jennings, 1988):

$$l = \sqrt{\frac{\pi}{8}} \frac{\eta}{0.4987445} \frac{1}{\sqrt{\varrho_{\text{air}} P}}. \tag{13}$$

2.7 Particle Velocity

The magnitude of the velocity, $v_{p,i}$, of a particle with radius r_i at any time point is calculated by solving the Newton's second law of motion:

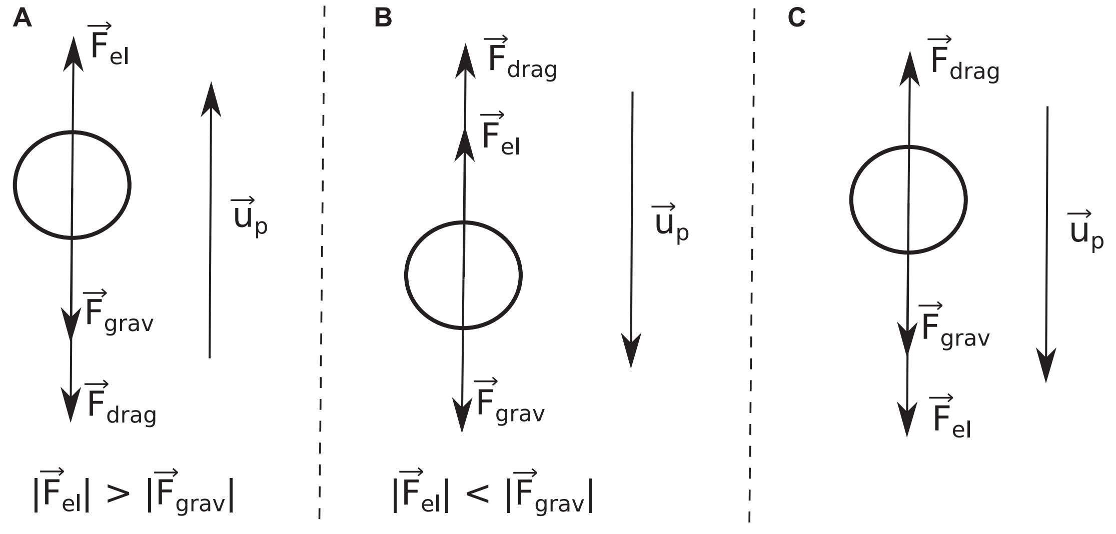

FIGURE 3 | Motion of charged sphere in homogeneous electric and gravitational fields: **(A)** upward motion, **(B)** and **(C)** downward motion.

$$m_{\mathrm{p},i}\frac{d\vec{v}_{\mathrm{p},i}}{dt}=\sum\vec{F}=\vec{F}_{\mathrm{el}}+\vec{F}_{\mathrm{grav}}+\vec{F}_{\mathrm{drag}}, \tag{14}$$

where $m_{\mathrm{p},i}$ is the particle mass, $\vec{F}_{\mathrm{el}}$ is the electric force that acts upon the particle, $\vec{F}_{\mathrm{grav}}$ is the gravity force, and $\vec{F}_{\mathrm{drag}}$ is the drag force.

In 1D case, and assuming the positive direction to be upwards, **Eq. 14** becomes:

$$m_{\mathrm{p},i}\frac{dv_{\mathrm{p},i}}{dt}=\begin{cases} q_{\mathrm{p},i}E-m_{\mathrm{p},i}g-F_{\mathrm{drag}}, & q_{\mathrm{p},i}E\geq m_{\mathrm{p},i}g \\ q_{\mathrm{p},i}E-m_{\mathrm{p},i}g+F_{\mathrm{drag}}, & q_{\mathrm{p},i}E< m_{\mathrm{p},i}g \end{cases}. \tag{15}$$

with $m_{\mathrm{p},i}$ being the particle mass:

$$m_{\mathrm{p},i}=\varrho_{\mathrm{p}}V_{\mathrm{p},i}=\varrho_{\mathrm{p}}\frac{4}{3}\pi r_i^3, \tag{16}$$

and ϱ_{p} being the mass density of a dust particle.

When the electric force, $q_{\mathrm{p},i}E$, is positive (negative charge in a downward pointing electric field, or positive charge in an upward pointing electric field) and greater than gravity, $m_{\mathrm{p},i}$, the particle moves upwards (positive velocity or acceleration) and the drag force is negative pointing downwards in the same direction as gravity (**Figure 3A**). When the electric force is positive but less than gravity, the particle moves downwards (negative velocity or acceleration) and the drag force points upwards (**Figure 3B**). Finally, in the case of negative electric force (negative charge in an upward pointing electric field, or positive charge in a downward pointing electric field), the particle moves downwards, and the drag force points upwards (**Figure 3C**).

The magnitude of the drag force is:

$$F_{\mathrm{drag}}=\frac{1}{2}\frac{C_{\mathrm{d}}}{C_{\mathrm{c}}}A_{\mathrm{p},i}\varrho_{\mathrm{air}}v_{\mathrm{p},i}^2=\frac{C_{\mathrm{d}}\pi r_{\mathrm{p},i}^2\varrho_{\mathrm{air}}v_{\mathrm{p},i}^2}{2C_{\mathrm{c}}}, \tag{17}$$

where $A_{\mathrm{p},i}$ is the projected area of the assumed spherical dust particle, and C_{d} is the drag coefficient, adopted by Clift and Gauvin (1971):

$$C_{\mathrm{d}}=\frac{12}{Re}\left(1+0.2415\mathrm{Re}^{0.687}\right)+\frac{0.42}{1+\frac{19019}{Re^{1.16}}}, \tag{18}$$

with Re being the Reynolds number, defined as:

$$\mathrm{Re}=\frac{\varrho_{\mathrm{air}}r_{\mathrm{p},i}v_{\mathrm{p,\,i}}}{\eta}. \tag{19}$$

It is noted that in both **Eqs. 17**, **19** the magnitude of the particle velocity $v_{\mathrm{p},i}$ is used. According to the definition of the Reynolds number and the drag force, the magnitude of the particle velocity with respect to the air is needed. Since in our analysis we neglect the effects of the wind, and therefore the wind speed is set to zero, the velocity of the particle with respect to an observer at the ground, $v_{\mathrm{p},i}$, is the same as the velocity of the particle with respect to the air.

The choice of **Eq. 18** as an expression for the drag coefficient comes from the fact that it is valid for Reynolds numbers up to 10^5, allowing the study of very large particles. Moreover, it is within 6% of experimental measurements (Clift et al., 2005). Additionally, it has been shown by Mallios et al. (2020) that, **Eq. 18** compared to the drag coefficient derived by Proudman and Pearson (1957), which is the most accurate analytical expression for Re < 0.1, gives a relative error less than 2%. Finally, it is noted that since the slip correction factor, C_{c}, has been introduced for the correction of the Stokes law (and therefore it is valid only in the Stokes region), it appears in **Eq. 17** only in the case of Re < 0.1 (Mallios et al., 2020).

Finally, in order us to avoid very small time steps for the solution of **Eq. 15**, that will lead to large simulation times, we apply the following procedure for the calculation of the particle velocity, $v_{\mathrm{p},i}$. The time step of the simulation is calculated based on the processes of **Eqs. 1–3**. **Eq. 15** is discretized as:

$$v_{\mathrm{p},i}^{t+dt}=v_{\mathrm{p},i}^{t}+\frac{dt}{m_{\mathrm{p},i}}\begin{cases} q_{\mathrm{p},i}E-m_{\mathrm{p},i}g-F_{\mathrm{drag}}, & q_{\mathrm{p},i}E\geq m_{\mathrm{p},i}g \\ q_{\mathrm{p},i}E-m_{\mathrm{p},i}g+F_{\mathrm{drag}}, & q_{\mathrm{p},i}E< m_{\mathrm{p},i}g \end{cases}, \tag{20}$$

where F_{drag} is calculated using the velocity at time point t, $v_{\mathrm{p},i}^t$.

If $|F_{\mathrm{drag}}| > |q_{\mathrm{p},i}E - m_{\mathrm{p},i}g|$, it means that in the period of dt the particle has reached its terminal velocity. In this case the velocity is calculated by solving the equation:

$$|F_{\mathrm{drag}}| = |q_{\mathrm{p},i}E - m_{\mathrm{p},i}g|, \tag{21}$$

using the Brent's method (Press et al., 1992, p. 359).

In the case that $|F_{\mathrm{drag}}| \leq |q_{\mathrm{p},i}E - m_{\mathrm{p},i}g|$, the terminal velocity has not been reached, and **Eq. 20** is solved.

2.8 Ion Attachment Rates

For the quantification of ion attachment to dust particles, the particles are assumed perfect electrical conductors (Fuks, 1958, p. 81).

2.8.1 Continuum Regime

The formulation of the attachment rates that is adopted in this work, is valid in the continuum regime. This means that the ionic mean free path, $l_{\mathrm{ion}}^{\pm}$, is smaller than the particle radius, r_i. Defining the particle diffusion Knudsen number, $Kn_{\mathrm{D}}^{\pm}$, as (Dahneke, 1983):

$$Kn_{\mathrm{D}}^{\pm} = \frac{l_{\mathrm{ion}}^{\pm}}{r_i} = \frac{2D_{\mathrm{ion}}^{\pm}}{<v>^{\pm} r_i} = \frac{2D_{\mathrm{ion}}^{\pm}}{r_i}\sqrt{\frac{\pi m^{\pm}}{8kT}}, \tag{22}$$

where $< v >^{\pm}$ is the average thermal velocity, and $m^{\pm}$ is the mass of positive and negative ions respectively, the continuum regime is defined for $Kn_{\mathrm{D}} < 1$.

The ionic mass, $m^{\pm}$, can be correlated with the ion electrical mobility, $\mu_0^{\pm}$, at reference pressure, P_0, and reference temperature, T_0. The only available data set covering the mass range up to 2,122 amu has been derived by Kilpatric (1971), in measurements of molecular ion mobility in nitrogen, at a pressure of 1,013.25 hPa and temperature of 473 K. Meyerott et al. (1980) reproduced the results of Kilpatric (1971) as the most complete data for big cluster ions. Tammet (1995) based on the dataset of Kilpatric (1971) derived an ion mass–reduced mobility correlation at temperature equal to 273 K, and pressure equal to 1,013.25 hPa. Scaling the data set of Kilpatric (1971) to reference temperature, T_0, and reference pressure, P_0, the following ion mass–reduced mobility correlations are derived by numerical fitting the data points:

$$m^{+} = 2.386 \times 10^{-37} \left(\mu_0^{+}\right)^{-513.526\mu_0^{+} - 3.113}, \tag{23}$$

$$m^{-} = 4.176 \times 10^{-28} \left(\mu_0^{-}\right)^{1309.138\mu_0^{-} - 0.976}, \tag{24}$$

where $m^{\pm}$ are given in kg. It is noted that the mean absolute error of **Eq. 23** is 6.8%, and of **Eq. 24** is 6.3% (both less than 10%). Although these errors are larger than the mean absolute error of the expression derived by Tammet (1995), which does not exceed the value of 2%, they are much simpler to use and can be seen as a very good compromise between simplicity and accuracy.

Using the adopted values of $\mu_0^{\pm}$ by Bricard (1965) in **Eqs. 23** and **24**, we get $m^{+} = 4.486 \times 10^{-25\ \mathrm{kg}}$, and $m^{-} = 2.124 \times 10^{-25\ \mathrm{kg}}$. Substituting these values to **Eq. 22**, it is found that, the continuum regime condition is satisfied for $r_i \geq 0.2$ μm up to altitude equal to 12 km, which is the typical limit between the upper troposphere—lower stratosphere. In the case of altitudes up to 20 km, where the lower edge of the stratosphere near the equator can be, the continuum regime condition is satisfied for $r_i \geq 1.2$ μm.

2.8.2 Physical Mechanisms

According to the field–diffusion theory, two major mechanisms act simultaneously for the ion attachment to particles. The first is the diffusion to the particle surface, and the second is the conduction in the electric field (Helsdon et al., 2002). The electric field is the superposition of the external large scale electric field, the induced dipole electric field, and the electric field due to charges on the particle (Lawless, 1996). In the presence of bipolar ion, particle charge approaches a steady-state level as charging time increases (Fjeld and McFarland, 1989). Gauntt et al. (1984) showed that neither the diffusion nor the field approximation alone evaluate correctly the steady state particle charge in the case of $\frac{q_{\mathrm{e}} r_i |\vec{E}|}{kT} > 1$, but the superposition of the two mechanisms, while not rigorous, yields reasonably accurate results (Gauntt et al., 1984). Hence, this method is suggested as a practical means for calculating charge acquired under bipolar charging conditions, and is adopted in the present work, since to the best of our knowledge up to now, no rigorous analytical solution of field diffusion theory equations for stationary or moving particles have been put forth.

2.8.3 Stationary Particles

In the case of stationary particles, the diffusion approximation is obtained by neglecting the effect of the external electric field on the particle and on the ion transport, while retaining the effect of the particle charge (Fjeld and McFarland, 1989). The total rate per unit volume of positive and negative ion loss due to their attachment to dust particles of radius r_i, and number density $N_{\mathrm{p},i}$ is (Gunn, 1954):

$$\frac{dn^{\pm}}{dt} = 4\pi r_i D_{\mathrm{ion}}^{\pm} \frac{\pm \Phi_{\mathrm{s}}}{\exp(\pm \Phi_{\mathrm{s}}) - 1} N_{\mathrm{p},i} n^{\pm}, \tag{25}$$

$$\Phi_{\mathrm{s}} = \frac{q_{\mathrm{p},i} q_{\mathrm{e}}}{4\pi\varepsilon_0 r_i kT}. \tag{26}$$

Φ_{s} is called self potential and indicates the influence of the particle charge to the diffusion current that flows to the particle. When $\Phi_{\mathrm{s}} < 1$, the thermal energy of the ions, kT/q_{e}, is larger than the electric potential energy of the particle due to its charge. This means that ion diffusion dominates and the ion mobilities are the important factors that determine the type and the number of the ions that attach to the particle. When $\Phi_{\mathrm{s}} > 1$, the surface electric field magnitude of the particle is larger than the ion thermal energy, and the ion drift in the presence of the particle surface electric field dominates. In the limit that $\Phi_{\mathrm{s}} \ll 1$, **Eq. 25** becomes:

$$\frac{dn^{\pm}}{dt} = 4\pi r_i D_{\mathrm{ion}}^{\pm} N_{\mathrm{p},i} n^{\pm}, \tag{27}$$

The field approximation is obtained by neglecting diffusion, and calculating the charging rate from the transport of ions along the electric field lines to the surface of the particle (Fjeld and McFarland, 1989). The electrical forces due to the images of the ions with respect to the conducting particles have been neglected, because as has been shown by Marlow and Brock (1975), their effect is not important in the continuum regime. The total rate per unit volume of positive and negative ion loss due to their attachment to dust particles of radius r_i, and number density $N_{\mathrm{p},i}$ is (Gunn, 1956):

$$\frac{dn^+}{dt} = \begin{cases} 0 & , q_{\mathrm{p},i} \geq q_{\mathrm{F}} \\ -\dfrac{N_{\mathrm{p},i}\mu^+ q_{\mathrm{p},i}}{\varepsilon_0} n^+ & , q_{\mathrm{p},i} \leq -q_{\mathrm{F}} \\ N_{\mathrm{p},i}\mu^+ \left|\vec{E}\right| 3\pi r_i^2 \left[1 - \left(\dfrac{q_{\mathrm{p},i}}{q_{\mathrm{F}}}\right)\right]^2 n^+ & , q_{\mathrm{F}} > q_{\mathrm{p},i} > -q_{\mathrm{F}} \end{cases}, \tag{28}$$

$$\frac{dn^-}{dt} = \begin{cases} \dfrac{N_{\mathrm{p},i}\mu^- q_{\mathrm{p},i}}{\varepsilon_0} n^- & , q_{\mathrm{p},i} \geq q_{\mathrm{F}} \\ 0 & , q_{\mathrm{p},i} \leq -q_{\mathrm{F}} \\ N_{\mathrm{p},i}\mu^- \left|\vec{E}\right| 3\pi r_i^2 \left[1 + \left(\dfrac{q_{\mathrm{p},i}}{q_{\mathrm{F}}}\right)\right]^2 n^- & , q_{\mathrm{F}} > q_{\mathrm{p},i} > -q_{\mathrm{F}} \end{cases}, \tag{29}$$

where $q_{\mathrm{F}} = 12\pi\varepsilon_0\left|\vec{E}\right| r_i^2$ is the limiting charge value for which the particle is considered to be totally positive or negatively charged.

Several approaches have been proposed in the past for the superposition of these two mechanisms, both in theoretical and model simulation basis. Several theoretical expressions that combine the mechanisms or that numerically solve the field-diffusion problem have been proposed in the past (Klett, 1971; Smith and McDonald, 1975; Liu and Kapadia, 1978; Fjeld et al., 1983; Wang, 1983; Fjeld and McFarland, 1989; Lawless, 1996). Unfortunately, these expressions cannot be easily expanded to other cases such as moving particles, or different shapes, because they contain parts of approximate solutions that restrict the generalization. Moreover, some of them have convergence difficulties, or are valid in cases and conditions that are not commonly used (Lawless, 1996). On the other hand, a simple superposition of **Eq. 27** with **Eqs. 28**, **29** (Chiu, 1978) or **Eq. 25** with **Eqs. 28**, **29** (Helsdon et al., 2002), although not rigorous, offers the flexibility of generalization, because each individual charging mechanism has been studied extensively on a broad spectrum of applications.

The disadvantage of the superposition used by Chiu (1978) is that, in the case that $\left|q_{\mathrm{p},i}\right| \geq q_{\mathrm{F}}$, where the particle is not polarized, and therefore mainly the diffusion and the electric field created by the particle charge influence the attachment process, the expression does not give the **Eq. 25**. On the other hand, the superposition used by Helsdon et al. (2002) has the disadvantage of accounting for the electrical effect due to the particle net charge twice (both in diffusion and conduction mechanisms). In order to tackle these issues we propose the following superposition:

$$\frac{dn^+}{dt} = \begin{cases} 4\pi r_i D_{\mathrm{ion}}^+ \dfrac{\Phi_{\mathrm{s}}}{\exp\left(\Phi_{\mathrm{s}}\right) - 1} N_{\mathrm{p},i} n^+ & , \left|q_{\mathrm{p},i}\right| \geq q_{\mathrm{F}} \\ \left(4\pi r_i D_{\mathrm{ion}}^+ + \mu^+ \left|\vec{E}\right| 3\pi r_i^2 \left[1 - \left(\dfrac{q_{\mathrm{p},i}}{q_{\mathrm{F}}}\right)\right]^2\right) N_{\mathrm{p},i} n^+ & , \left|q_{\mathrm{p},i}\right| < q_{\mathrm{F}} \end{cases}, \tag{30}$$

$$\frac{dn^-}{dt} = \begin{cases} 4\pi r_i D_{\mathrm{ion}}^- \dfrac{-\Phi_{\mathrm{s}}}{\exp\left(-\Phi_{\mathrm{s}}\right) - 1} N_{\mathrm{p},i} n^- & , \left|q_{\mathrm{p},i}\right| \geq q_{\mathrm{F}} \\ \left(4\pi r_i D_{\mathrm{ion}}^- + \mu^- \left|\vec{E}\right| 3\pi r_i^2 \left[1 + \left(\dfrac{q_{\mathrm{p},i}}{q_{\mathrm{F}}}\right)\right]^2\right) N_{\mathrm{p},i} n^- & , \left|q_{\mathrm{p},i}\right| < q_{\mathrm{F}} \end{cases}, \tag{31}$$

Eqs. 30, **31** in the case that the particle is not polarized give the solution of the diffusion approximation, and in the case that the particle is polarized lead to the superposition used by Chiu (1978). Moreover, the effect of the electric field due to the particle net charge is not counted twice as in superposition by Helsdon et al. (2002).

Long and Yao (2010) presented an evaluation of nine different particle charging models based on existing experimental results. One of the conclusions was that the field-diffusion combined model developed by Lawless (1996) should be the first choice relatively for numerical models of the particle dynamics. Since this model is shown to be the most preferable in terms of the theoretical consideration, accuracy and computational time, we use it as a reference for comparison with our proposed superposition (**Eqs. 30**, **31**). The results are shown in **Figure 4**, where the attachment rates for positive ions, β^+, are plotted as a function of particle charge, for different values of external electric field (the same conclusions are derived for the negative ions attachment rates). In **Eqs. 25**, **27–31** as attachment rate, $\beta^\pm$ (with units $1/s$), the expression in the right hand side that is multiplied with the appropriate ion number density, $n^\pm$, is defined (leading to an expression of the form $\frac{dn^\pm}{dt} = \beta^\pm n^\pm$).

Figure 4A shows the relative difference as a function of normalized particle charge, for different particle radii, in the presence of external electric field with magnitude 10^2 V/m. For $r_i = 0.2$ μm the mean relative difference in the studied range of the particle charge is 0.12 %. For $r_i = 2$ μm it is 1.08 %, for $r_i = 20$ μm it is 8.09 %, and for $r_i = 200$ μm it is 9.02 %.

The maximum particle charge is chosen to be 1,000 elementary charges, which is in the same order of magnitude with the charge derived from the charge density measured by Kamra (1972), and assuming particle density equal to 10^8 particles/m^3, which is the annual mean of the lower limit of aerosol concentration over oceans (Tinsley and Zhou, 2006). The specific measurement was conducted over dust devils, which is an extreme phenomenon compared to the regular dust transport (in such conditions Nicoll et al. (2010) measured three orders of magnitude lower charge density) and the particle density is at the lower limit of particle densities observed in detached dust layers. For larger particle densities, keeping the charge density the same, the individual particle charge decreases. Therefore, the 1,000 elementary charges per particle can be used as an upper limit for the particle charge.

Figure 4B shows the mean relative difference for a range of particle charges −1,000 to 1,000 elementary charges, as a function of particle radius, in the presence of external field with various magnitudes. The mean relative difference does not exceed the value of 50 % for a range of electric field magnitudes from 0 to 10^5 V/m. Therefore, the proposed superposition of **Eqs. 30**, **31** can be considered as physically

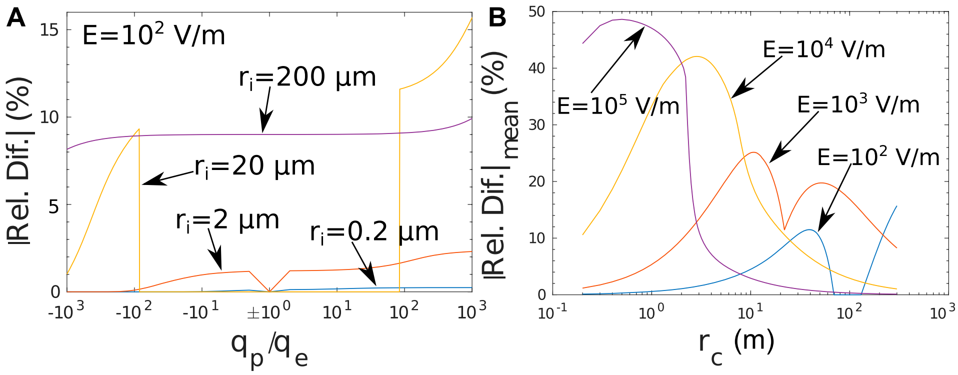

FIGURE 4 | Comparison between **Eq. 30** and formulation by Lawless (1996): **(A)** Relative difference as a function of normalized particle charge, for different particle radii, in the presence of external electric field with magnitude 10^2 V/m, and **(B)** mean relative difference for a range of particle charges −1,000 to 1,000 elementary charges, as a function of particle radius, in the presence of external field with various magnitudes.

reasonable, and although they are not strict analytical solutions of the ion transport equation that describes the ion attachment process, they can be used in numerical models to describe adequately the effects of the ion attachment to particles.

The maximum electric field magnitude in **Figure 4B** is chosen to be in the order of magnitude of observed electric field values right before a lightning flash (e.g., Marshall et al., 2005; Stolzenburg et al., 2007). Regarding dust layers transported for days in the Earth's atmosphere, away from the emission source, no case of lightning discharge has been reported, indicating that, in these cases, the value of 10^5 V/m is unlikely to be reached or exceeded. Thus, it can be used as an upper limit of the electric field magnitude. On the other hand, in cases of dust storms or dust devils that occur on Earth (or other planets, e.g., Mars) and in the vicinity of the emission source, the value of 10^5 V/m (or the equivalent electric field threshold on that planet) can be reached. This can happen due to the intense electrification caused by the triboelectric effect, which is the dominant electrification mechanism during the emission of dust particles in the atmosphere, and the large scale charge separation caused by the strong updrafts (Krauss et al., 2003). A short review on the electrification of dust storms and on the resultant electric field strengths has been made by Riousset et al. (2020). When the electric field threshold is reached, or exceeded, a discharge occurs, leading to a decrease of the electric field magnitude. Therefore, 10^5 V/m acts again as an upper limit of the electric field magnitude.

2.8.4 Moving Particles

Eqs. 30, 31 can be easily transformed in the case of moving particles. According to Gunn (1954), the diffusion approximation for moving particles leads to the following expression for the total rate per unit volume of positive and negative ion loss:

$$\frac{dn^{\pm}}{dt} = 4\pi r_i D^{\pm}_{\text{ion}} A^{\pm}_{\text{v}} \frac{\pm\hat{\Phi}^{\pm}_{\text{s}}}{\exp\left(\pm\hat{\Phi}^{\pm}_{\text{s}}\right) - 1} N_{\text{p},i} n^{\pm}, \tag{32}$$

$$\hat{\Phi}^{\pm}_{\text{s}} = \frac{q_{\text{p},i} q_{\text{e}}}{4\pi\varepsilon_0 r_i kT A^{\pm}_{\text{v}}}, \tag{33}$$

$$A^{\pm}_{\text{v}} = 1 + F\sqrt{\frac{r_i |\vec{v}|_{\text{p},i}}{2\pi D^{\pm}_{\text{ion}}}}, \tag{34}$$

where the term $A^{\pm}_{\text{v}}$ represents the ventilation effect on the ion attachment process.

The coefficient F is an experimentally derived coefficient to match the theoretical results with actual measurements. It depends on the detailed air flow over the spherical particle, and can be described as a fitting function of the Reynolds number, Re, based on measurements by Kinzer and Gunn (1951) as:

$$F = \begin{cases} 10^{(7.446\text{Re}-4.619)} & ,\text{Re} \le 0.5 \\ 0.079\text{Re}^3 - 0.899\text{Re}^2 + 3.156\text{Re} - 1.289 & ,0.5 < \text{Re} \le 5 \\ 2.218\text{Re}^{-0.169} & ,5 < \text{Re} \le 423 \\ 5.165\times10^{-7}\text{Re}^2 - 2.828\times10^{-4}\text{Re} + 0.882 & ,\text{Re} > 423 \end{cases} \tag{35}$$

The field approximation for moving particles has been studied by Whipple and Chalmers (1944), based on the theory of charge acquisition by particles falling through a region containing ions proposed by Wilson (1929). The total rate per unit volume of positive and negative ion loss is:

$$\frac{dn^{+}}{dt} = \begin{cases} 0 & ,q_{\text{p},i} \ge q_{\text{F}} \\ -\frac{N_{\text{p},i}\mu^{+}q_{\text{p},i}}{\varepsilon_0} n^{+} & ,q_{\text{p},i} \le -q_{\text{F}} \\ 0 & ,q_{\text{F}} > q_{\text{p},i} > 0, \vec{v}_{\text{p},i} \uparrow\uparrow \vec{E}, |\vec{v}|_{\text{p},i} > \mu^{+}|\vec{E}| \\ -\frac{N_{\text{p},i}\mu^{+}q_{\text{p},i}}{\varepsilon_0} n^{+} & ,0 > q_{\text{p},i} > -q_{\text{F}}, \vec{v}_{\text{p},i} \uparrow\uparrow \vec{E}, |\vec{v}|_{\text{p},i} > \mu^{+}|\vec{E}|, \\ N_{\text{p},i}\mu^{+}\left|\vec{E}\right| 3\pi r_i^2 \left[1 - \left(\frac{q_{\text{p},i}}{q_{\text{F}}}\right)\right]^2 n^{+} & ,\vec{v}_{\text{p},i} \uparrow\uparrow \vec{E}, |\vec{v}|_{\text{p},i} < \mu^{+}|\vec{E}| \\ N_{\text{p},i}\mu^{+}\left|\vec{E}\right| 3\pi r_i^2 \left[1 - \left(\frac{q_{\text{p},i}}{q_{\text{F}}}\right)\right]^2 n^{+} & ,q_{\text{F}} > q_{\text{p},i} > -q_{\text{F}}, \vec{v}_{\text{p},i} \uparrow\downarrow \vec{E} \end{cases} \tag{36}$$

where $\vec{v}_{\mathrm{p},i}\uparrow\uparrow\vec{E}$ means that the velocity vector and the electric field vector are in the same direction (the particle moves in the same direction as the electric field lines), while $\vec{v}_{\mathrm{p},i}\uparrow\downarrow\vec{E}$ means that the velocity vector and the electric field vector are in opposite directions (the particle moves in the opposite direction from the electric field lines).

$$\frac{dn^-}{dt}=\begin{cases}\dfrac{N_{\mathrm{p},i}\mu^- q_{\mathrm{p},i}}{\varepsilon_0}n^- & ,q_{\mathrm{p},i}\geq q_{\mathrm{F}}\\ 0 & ,q_{\mathrm{p},i}\leq -q_{\mathrm{F}}\\ \dfrac{N_{\mathrm{p},i}\mu^- q_{\mathrm{p},i}}{\varepsilon_0}n^- & ,q_{\mathrm{F}}>q_{\mathrm{p},i}>0,\ \vec{v}_{\mathrm{p},i}\uparrow\downarrow\vec{E},\ |\vec{v}|_{\mathrm{p},i}>\mu^-|\vec{E}|\\ 0 & ,0>q_{\mathrm{p},i}>-q_{\mathrm{F}},\ \vec{v}_{\mathrm{p},i}\uparrow\downarrow\vec{E},\ |\vec{v}|_{\mathrm{p},i}>\mu^-|\vec{E}|\\ N_{\mathrm{p},i}\mu^-|\vec{E}|3\pi r_i^2\left[1+\left(\dfrac{q_{\mathrm{p},i}}{q_{\mathrm{F}}}\right)\right]^2 n^- & ,\vec{v}_{\mathrm{p},i}\uparrow\downarrow\vec{E},\ |\vec{v}|_{\mathrm{p},i}<\mu^-|\vec{E}|\\ N_{\mathrm{p},i}\mu^-|\vec{E}|3\pi r_i^2\left[1+\left(\dfrac{q_{\mathrm{p},i}}{q_{\mathrm{F}}}\right)\right]^2 n^- & ,q_{\mathrm{F}}>q_{\mathrm{p},i}>-q_{\mathrm{F}},\ \vec{v}_{\mathrm{p},i}\uparrow\uparrow\vec{E}\end{cases},\tag{37}$$

Although **Eqs 36, 37** have been derived under the stream-line flow assumption, it has been discussed by Whipple and Chalmers (1944) that the provided formalism is appropriate even in turbulent environments. As a matter of fact, Gott (1936) gives experimental evidence to show that turbulence does not affect the general validity of Wilson's theory.

A superposition similar to **Eqs 30**, **31** leads to the following expression for the combined diffusion-field theory approximation in the case of moving spherical particles:

$$\frac{dn^+}{dt}=\begin{cases}4\pi r_i D^+_{\mathrm{ion}}A^+_{\mathrm{v}}\dfrac{\hat{\Phi}^+_{\mathrm{s}}}{\exp\left(\hat{\Phi}^+_{\mathrm{s}}\right)-1}N_{\mathrm{p},i}n^+ & ,|q_{\mathrm{p},i}|\geq q_{\mathrm{F}}\\ 4\pi r_i D^+_{\mathrm{ion}}A^+_{\mathrm{v}}N_{\mathrm{p},i}n^+ & ,q_{\mathrm{F}}>q_{\mathrm{p},i}>0,\ \vec{v}_{\mathrm{p},i}\uparrow\uparrow\vec{E},\ |\vec{v}|_{\mathrm{p},i}>\mu^+|\vec{E}|\\ \left(4\pi r_i D^+_{\mathrm{ion}}A^+_{\mathrm{v}}-\dfrac{\mu^+ q_{\mathrm{p},i}}{\varepsilon_0}\right)N_{\mathrm{p},i}n^+ & ,0>q_{\mathrm{p},i}>-q_{\mathrm{F}},\ \vec{v}_{\mathrm{p},i}\uparrow\uparrow\vec{E},\ |\vec{v}|_{\mathrm{p},i}>\mu^+|\vec{E}|\\ \left(4\pi r_i D^+_{\mathrm{ion}}A^+_{\mathrm{v}}+\mu^+|\vec{E}|3\pi r_i^2\left[1-\left(\dfrac{q_{\mathrm{p},i}}{q_{\mathrm{F}}}\right)\right]^2\right)N_{\mathrm{p},i}n^+ & ,\vec{v}_{\mathrm{p},i}\uparrow\uparrow\vec{E},\ |\vec{v}|_{\mathrm{p},i}<\mu^+|\vec{E}|\\ \left(4\pi r_i D^+_{\mathrm{ion}}A^+_{\mathrm{v}}+\mu^+|\vec{E}|3\pi r_i^2\left[1-\left(\dfrac{q_{\mathrm{p},i}}{q_{\mathrm{F}}}\right)\right]^2\right)N_{\mathrm{p},i}n^+ & ,q_{\mathrm{F}}>q_{\mathrm{p},i}>-q_{\mathrm{F}},\ \vec{v}_{\mathrm{p},i}\uparrow\downarrow\vec{E}\end{cases},\tag{38}$$

$$\frac{dn^-}{dt}=\begin{cases}4\pi r_i D^-_{\mathrm{ion}}A^-_{\mathrm{v}}\dfrac{-\hat{\Phi}^-_{\mathrm{s}}}{\exp\left(-\hat{\Phi}^-_{\mathrm{s}}\right)-1}N_{\mathrm{p},i}n^- & ,|q_{\mathrm{p},i}|\geq q_{\mathrm{F}}\\ \left(4\pi r_i D^-_{\mathrm{ion}}A^-_{\mathrm{v}}+\dfrac{\mu^- q_{\mathrm{p},i}}{\varepsilon_0}\right)N_{\mathrm{p},i}n^- & ,q_{\mathrm{F}}>q_{\mathrm{p},i}>0,\ \vec{v}_{\mathrm{p},i}\uparrow\downarrow\vec{E},\ |\vec{v}|_{\mathrm{p},i}>\mu^-|\vec{E}|\\ 4\pi r_i D^-_{\mathrm{ion}}A^-_{\mathrm{v}}N_{\mathrm{p},i}n^- & ,0>q_{\mathrm{p},i}>-q_{\mathrm{F}},\ \vec{v}_{\mathrm{p},i}\uparrow\downarrow\vec{E},\ |\vec{v}|_{\mathrm{p},i}>\mu^-|\vec{E}|\\ \left(4\pi r_i D^-_{\mathrm{ion}}A^-_{\mathrm{v}}+\mu^-|\vec{E}|3\pi r_i^2\left[1+\left(\dfrac{q_{\mathrm{p},i}}{q_{\mathrm{F}}}\right)\right]^2\right)N_{\mathrm{p},i}n^- & ,\vec{v}_{\mathrm{p},i}\uparrow\downarrow\vec{E},\ |\vec{v}|_{\mathrm{p},i}<\mu^-|\vec{E}|\\ \left(4\pi r_i D^-_{\mathrm{ion}}A^-_{\mathrm{v}}+\mu^-|\vec{E}|3\pi r_i^2\left[1+\left(\dfrac{q_{\mathrm{p},i}}{q_{\mathrm{F}}}\right)\right]^2\right)N_{\mathrm{p},i}n^- & ,q_{\mathrm{F}}>q_{\mathrm{p},i}>-q_{\mathrm{F}},\ \vec{v}_{\mathrm{p},i}\uparrow\uparrow\vec{E}\end{cases}\tag{39}$$

2.9 Dust Particle Number Density Distribution

Several aircraft campaigns over recent years have attempted to measure the properties of Saharan mineral dust. Ryder et al. (2018) and Weinzierl et al. (2017) provide lists of the major aircraft campaigns with a focus on *in-situ* dust measurements. In the current work, we use the mean size distribution between altitudes of 1–6 km at STP, measured by Ryder et al. (2013b) during the Fennec 2011 aircraft campaign at Mauritania and Mali, since they represent measurements very close to the dust particle emission sources (**Figure 5A**).

2.9.1 Size Bins Apportionment

The PSD discretization is of high importance for the correctness of the results. The number of bins, along with the size of each bin, must ensure that the initial measured distribution is properly introduced to the model without significant loss of information, deformation, or non convergence of the final results.

The adopted size distribution is discretized using 19 bins, listed in **Table 3**. **Figure 5B** provides the representation of the discretized number density distribution from Fennec, using the aforementioned binning, along with 5, 10, 20 equilateral bins, respectively. **Figure 5C** shows a comparison between the measured distribution, with the reconstructed ones from the different types of binning. It becomes apparent that as the number of the equilateral bins increases, the initial distribution is better approximated. Nevertheless, a significantly large number of bins is required for the proper approximation of the whole range of the distribution (judging from the slow convergence at the small particles, more than 40). On the other hand, the adopted binning of the current work approximates very well a wider range of the initial distribution using a fairly small number of bins (19 bins). Furthermore, **Figure 5D** illustrates the relative difference between the reconstructed distributions and the initial one. As the number of bins increases and their length becomes much smaller than the mean radius of each bin, the relative difference with the original distribution decreases.

For the current work binning, the agreement becomes ~1% for the narrow bins, while for the larger bins the relative difference increases to values comparable to other types of binning. Moreover, the relative difference is better distributed in a wider range of particle radii. Therefore, it is proven that the adopted binning leads to a better introduction of the initial distribution to the model, especially the bins that have length less than 1% of the mean radius (even numbered bins). In the Results section, we demonstrate that the electrical properties, calculated using the adopted binning, are the convergence limits of the values obtained by increasing the number of equilateral bins.

2.9.2 Spatial Particle Number Density Distribution

The dust particles are introduced in the simulation domain using two different spatial distributions. The first one is a rectangular distribution of the form (**Figure 5E**):

$$N^I_{\mathrm{p},i}=\frac{1}{2}N_{0,i}\left(\frac{273.2}{T}\right)\left(\frac{P}{101320}\right)\times\begin{cases}\left[1-\tanh\left(\dfrac{z-h^I_i-\dfrac{d^I_i}{2}}{b_z}\right)\right] & ,z\geq h_i\\ \left[1-\tanh\left(\dfrac{-d^I_i}{2b_z}\right)\right] & ,z<h_i\end{cases},\tag{40}$$

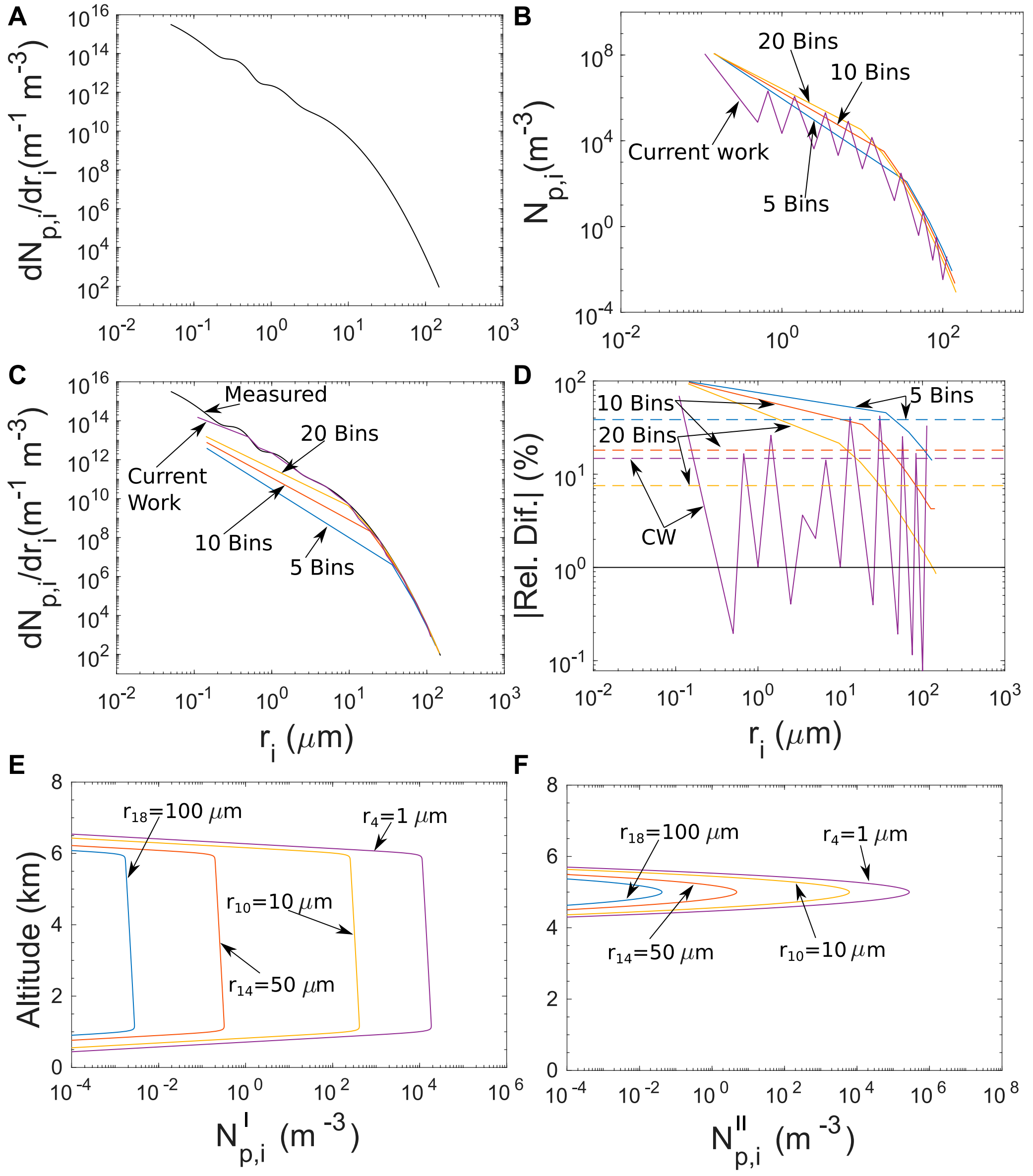

FIGURE 5 | Particle number density distributions: **(A)** measured mean normalized number density distribution by Ryder et al. (2013b), **(B)** number density distribution for different binnings, **(C)** reconstructed normalized number density distributions, **(D)** relative difference between the reconstructed normalized number density distributions and the measured one, with dashed lines being the average values, **(E)** $N^{I}_{p,i}$ and **(F)** $N^{II}_{p,i}$.

where $h_i^I = 3$ km is the altitude of the distribution center, $d_i^I = 2{,}500$ m is the distribution depth, and $b_z = 3d_z$ is a smoothing factor regarding the number of mesh points that will sample the boundary of the distribution (in our case 3). The two terms right before the bracket convert the number density $N_{0,i}$ from STP to the model ambient temperature and pressure conditions at a given altitude, z.

The second is a Gaussian distribution, mathematically expressed as (**Figure 5F**):

$$N^{II}_{\mathrm{p},i} = 12.6536 N_{0,i} \exp\left[-4\log(2)\frac{z-h_i^{II}}{\left(d_i^{II}\right)^2}\right], \qquad (41)$$

where $h^{II} = 5{,}000$ m is the altitude of the distribution center, and $d_i^{II} = 250$ m is the distribution depth, defined as the distance between the altitudes that the number density is reduced to half of its maximum value (full width at half maximum of a Gaussian distribution). The factor 12.6536 ensures that the integral of $N^{II}_{\mathrm{p},i}$ along the altitude gives the same result as the integral of $N^{I}_{\mathrm{p},i}$ along the altitude. This means that both distributions lead to the same surface particle density, and consequently to the same total number of particles.

The number density distribution $N^{I}_{\mathrm{p},i}$ is similar with the one measured by Ryder et al. (2013a), while the distribution $N^{II}_{\mathrm{p},i}$ denotes a study case where the particles are more concentrated, with higher number density, leading to different electrical properties.

TABLE 3 | Discretization bins of the size distribution.

i	Bin$_i$ start (μm)	Bin$_i$ end (μm)	r_i (μm)	$N_{0,i}$ (m^{-3})
1	0.05	0.49754	0.11009	1.129286×10^8
2	0.49754	0.5025	0.5	7.29383×10^4
3	0.5025	0.9952	0.67089	2.088442×10^6
4	0.9952	1.005	1	2.196567×10^4
5	1.005	2.4877	1.4363	1.176378×10^6
6	2.4877	2.5125	2.5	4.171284×10^3
7	2.5125	4.976	3.4757	2.029122×10^5
8	4.976	5.025	5	2.045581×10^3
9	5.025	9.952	6.6764	8.080773×10^4
10	9.952	10.05	10	4.882423×10^2
11	10.05	24.878	13.132	1.42718×10^4
12	24.878	25.125	25	1.6105×10^1
13	25.125	49.756	30.175	3.065036×10^2
14	49.756	50.25	50	3.805×10^1
15	50.25	74.635	57.013	5.401142
16	74.635	75.375	75	2.673747×10^{-2}
17	75.375	99.514	83.132	3.160056×10^{-1}
18	99.514	100.5	100	3.303402×10^{-3}
19	100.5	150	112.55	3.96402×10^{-2}

2.10 Initial Fair Weather Electrical Conditions

At $t = 0$ s all the dust particle bins are placed in the simulation domain, under fair weather conditions and are left to evolve under the influence of gravity, the electrical and drag forces. The initial fair weather electrical conditions are obtained by solving **Eqs 1**, **4** in the absence of dust particles, until steady state is reached. By doing that, the ambient fair weather ion densities, $n^{\pm}_{\mathrm{fw}}$, electrical conductivity, $\sigma_{\mathrm{fw}} = q_{\mathrm{e}}\left(n^{+}_{\mathrm{fw}}\mu^{+} + n^{-}_{\mathrm{fw}}\mu^{-}\right)$, total charge, $q_{\mathrm{tot,fw}} = q_{\mathrm{e}}\left(n^{+}_{\mathrm{fw}} - n^{-}_{\mathrm{fw}}\right)$, and electric field magnitude, $E_{\mathrm{z,\ fw}}$, are derived.

Since the ionization rate, q, which is the source of atmospheric ions, depends on the geomagnetic latitude, and therefore the latitude and longitude, three different locations have been chosen for the calculation of the fair weather electrical conditions, and the study of their spatial variation. These are: 1) Mauritania (MR, 24.316°, −10.962°), 2) Cape Verde (CV, 16°, −24°), and 3) Barbados (BB, 13.167°, −59.33°). The three locations have been chosen because they belong to the route of the transatlantic transport of Saharan dust from Africa to Caribbean (Weinzierl et al., 2017; van der Does et al., 2018).

Figure 6 shows a comparison between the initial fair weather electrical conditions of the aforementioned locations. **Figures 6A**,**B** show that the ionization rate in Cape Verde and in Barbados is practically the same, with the relative difference being less than 1%, leading to the same fair weather electrical conditions.

On the other hand the ionization rate in Mauritania is higher, and can reach a maximum relative difference value of 40% compared with the ionization rate in Cape Verde. Regardless this significant difference in the ionization rates, the relative differences in the fair weather ion densities (**Figures 6C,D**) and the fair weather total charge densities (**Figures 6E,F**) do not exceed the value of 20%. At this point we note that the small difference between the positive and negative ion densities allows only one field to be graphed in **Figure 6C**. In the case of the fair weather electric field, the relative difference is even smaller, and does not exceed the value of 10% (**Figures 6G,H**). Therefore, the ionization rate dependence, solely, on the geomagnetic latitude does not create significant variations of the initial fair weather electrical conditions along the transatlantic transport of the dust particles. This means that, for the given simplistic ionization rate formulation it does not make a difference on the choice of the reference location between Mauritania and Barbados. In the simulation results presented in the current work, the fair weather electrical conditions of Mauritania are used as initial electrical conditions, because this location is closer to the measured dust particle size distribution that is used in the model. At this point we want to emphasize that, in reality there are additional spatial and temporal variation of the ionization rate that for the sake of simplicity have been omitted, which will lead to larger fair weather conditions differences along the transatlantic passage than the ones presented here, and their impact on the electrical evolution of the dust particles are planned to be studied in future work using a higher dimension model.

3 RESULTS-DISCUSSION

3.1 Particle Charging and Electrical Force

Figure 7 shows the time dynamics of the electrical properties of Bin$_{18}$ (particles with radius, $r = 100$ μm), as well as the ambient conductivity and the large scale electric field magnitude. The ambient conductivity, σ, decreases, because the atmospheric ions attach to the total number of particles regardless their size, leading to a reduction of the ionic densities (**Figure 7A**). The conductivity reduction within the dust layer results in an increase of the columnar resistance, and a decrease in the conduction current at the ground (Baumgaertner et al., 2014). Since the conductivity at the ground does not change from the fair weather value, the electric field magnitude, depicted in **Figure 7B**, decreases to reflect the reduction in the conduction current (Daskalopoulou et al., 2021). On the other hand, as the system evolves towards the steady state, the conduction current $J_{\mathrm{z}} = \sigma E_{\mathrm{z}}$ tends to become constant along the altitude, and therefore when the conductivity decreases the electric field magnitude increases (**Figure 7B**).

At time $t_4 = 2{,}668$ s, more than 70% of the Bin$_{18}$ particles have vanished (**Figure 7C**). As these particles fall to the ground their charge density increases since more ions attach to them (**Figure 7D**). Especially in the region below the main dust layer (below 1 km), where the ion density increases to the fair weather values, the falling dust particles encounter a larger pool of ions available for attachment than the one within the layer. This consequently leads to an increase of the particle charge (**Figure 7E**). The dust particles are charged negatively, since more negative ions attach to them than positive ones, due to their higher mobilities. To be more precise, the ion attachment process depends both on the ion mobilities and the ion densities (**Eqs 30**, **31**, **38**, **39**). If the mobility ratio, $\frac{\mu^-}{\mu^+}$ is larger than the ion density ratio, $\frac{n^+}{n^-}$, the ion mobilities influence the attachment process, otherwise, the ion densities do that. In our case, the

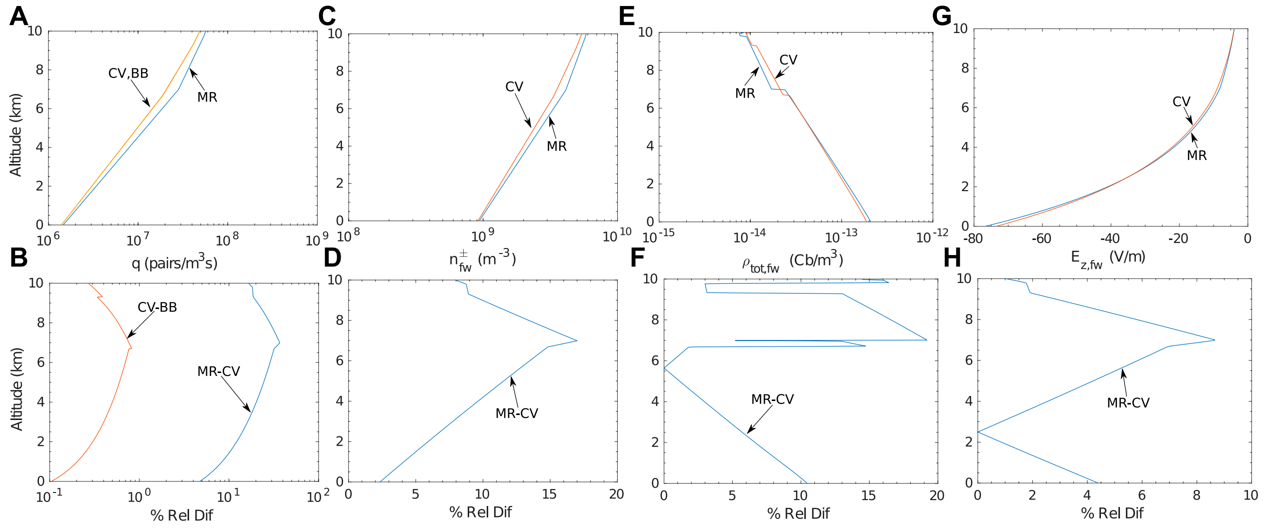

FIGURE 6 | Initial fair weather conditions in Mauritania (MR), Cape Verde (CV), and Barbados (BB): **(A)** ionization rates, **(B)** Relative difference between ionization rates, **(C)** fair weather ion densities, **(D)** relative difference between fair weather ion densities, **(E)** fair weather total charge densities, **(F)** relative difference between fair weather total charge densities, **(G)** fair weather electric field magnitudes, **(H)** relative difference between fair weather electric field magnitudes.

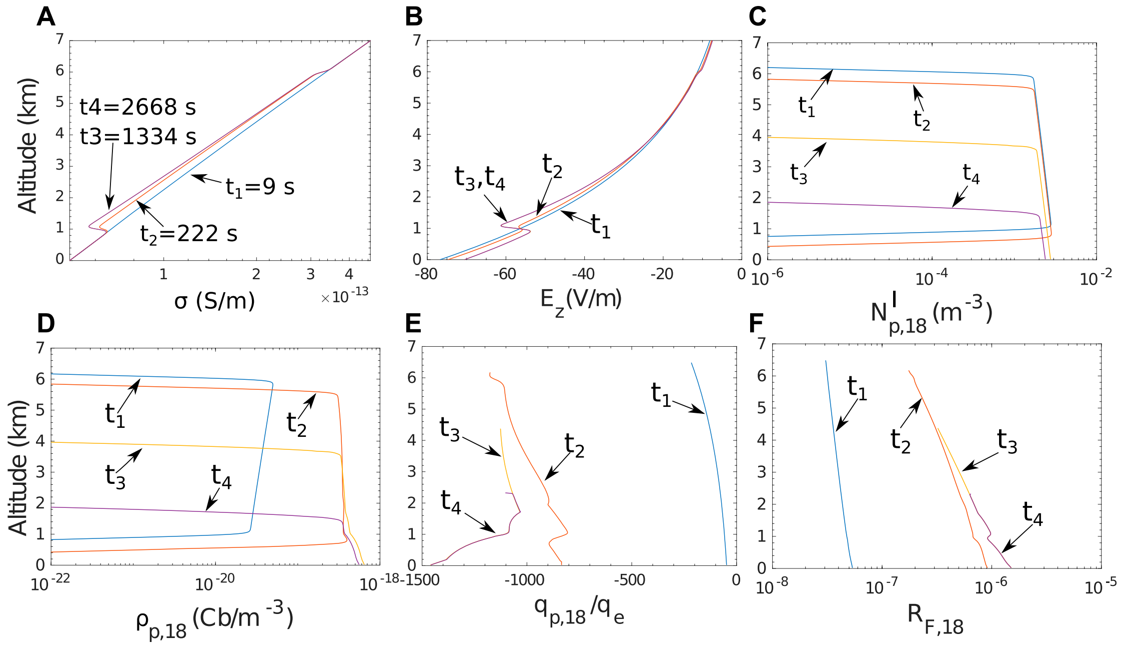

FIGURE 7 | Time dynamics of electrical properties of Bin18 ($r = 100\ \mu m$): **(A)** Atmospheric conductivity, **(B)** large scale electric field magnitude, **(C)** particle number density, **(D)** particle charge density, **(E)** number of elementary charges per particle, **(F)** ratio between the electrical force and the gravity.

ion mobility ratio is equal to 1.357, while the fair weather ion density ratio ranges between the values 1.0014 and 1, depending on the altitude, and thus the ion mobilities characterize, initially, the type of ions that attach to particles. As the negative ion density decreases faster than the positive ion density, the ion density rate increases up to the value where it becomes equal to the mobility ratio. Further increase of the ion density ratio, leads the positive ions to attach faster to the particle than the negative, resulting a reduction of the particle negative net charge, or even the charging of the particle with positive charge. In the case presented in **Figure 7**, the ion density ratio does not become larger than the mobility ratio, and all the particles of all bins have negative net charge.

Regardless of the charge and the large scale electric field magnitude, the electrical force that is acted upon the particles is negligible compared to gravity. As it can be seen in **Figure 7F**, the ratio between the electrical force and the gravity, $R_{F,18}$ is less than 2×10^{-6}.

For a better representation of the bin particles dynamics, and so as to efficiently display the electrical properties of the other bins as well, we define the following average quantities. The average particle charge of a bin, $<q_{\mathrm{p},i}>$, at every time step is:

$$<q_{\mathrm{p},i}> = \frac{\int_{z_{\min,i}}^{z_{\max,i}} q_{\mathrm{p},i} N_{\mathrm{p},i} dz}{\int_{z_{\min,i}}^{z_{\max,i}} N_{\mathrm{p},i} dz}, \tag{42}$$

where $z_{\max,i}$, and $z_{\min,i}$, are the maximum and the minimum altitudes of the particle distribution that belongs to Bin i, respectively.

The average electrical force magnitude of a bin, $<F_{\mathrm{el},i}>$, at every time step is:

$$<F_{\mathrm{el},i}> = \frac{\int_{z_{\min,i}}^{z_{\max,i}} F_{\mathrm{el},i} N_{\mathrm{p},i} dz}{\int_{z_{\min,i}}^{z_{\max,i}} N_{\mathrm{p},i} dz}. \tag{43}$$

The average velocity magnitude of a bin, $<v_{\mathrm{p},i}>$, at every time step is:

$$<v_{\mathrm{p},i}> = \frac{\int_{z_{\min,i}}^{z_{\max,i}} v_{\mathrm{p},i} N_{\mathrm{p},i} dz}{\int_{z_{\min,i}}^{z_{\max,i}} N_{\mathrm{p},i} dz}. \tag{44}$$

The average altitude of a bin, $<z_{\mathrm{p},i}>$, at every time step is:

$$<z_{\mathrm{p},i}> = \frac{\int_{z_{\min,i}}^{z_{\max,i}} z_{\mathrm{p},i} N_{\mathrm{p},i} dz}{\int_{z_{\min,i}}^{z_{\max,i}} N_{\mathrm{p},i} dz}. \tag{45}$$

The usefulness of the defined average quantities can be described as follows. At $t = 0$ s, all the particle bins are placed at the same altitude in the simulation domain, and they form the dust layer. Since each bin consists of particles with different sizes, it moves with different velocity. As time progresses, each bin starts being detached from the dust layer and moves towards the ground. At each time step depending on the velocity, each bin is located at different average altitude, $< z_{\mathrm{p},i} >$, in the presence of different electric field magnitude, E_z. During their motion, the particle bins are not deformed, because the magnitude of the forces acted on them is not sufficient to cause any deformation (e.g., **Figure 7C**). This results that when the bins are at the same average altitude, the same average electric field is present, and the only quantities that are different are the average charge, the average electrical force magnitude, and the average velocity. By plotting these properties as a function of the average altitude, we can compare them under the same conditions, and their differences are only due to the particle bin size, and the bin number density.

Figures 8A,B show the time evolution of the conductivity and electric field magnitude ratios with respect to their fair weather values, at different altitudes. As the conductivity decreases with respect to the fair weather value, the electric field magnitude increases, with two exceptions. The first one is at z = 6 km, which is close to the upper boundary of the layer. As layer boundary we define the region where the dust particle number density gradually decreases to values at least two orders of magnitude less than the values inside the layer (in the case of the layer upper boundary), or the region where the dust particle number density gradually increases to the maximum values inside the layer (in the case of the layer lower boundary). In this region as the conductivity increases to the initial fair weather values, the electric field decreases. Similar behavior has been derived by Zhou and Tinsley (2007), and by Harrison et al. (2020) in layer clouds. This has to do with the reduction of the current density due to the increase of the columnar resistance caused by the conductivity reduction inside the layer (Rycroft et al., 2008). As the system approaches the steady state, the current density along the altitude tends to become constant (which is the steady state condition inside conductors (see e.g. Landau and Lifshitz, 1963, p. 86)). Since the potential difference between the boundaries of the simulation domain is constant, the increase of the columnar resistance caused by the conductivity reduction in the layer, leads to a decrease of the current density. In the regions where the conductivity remains the same to the initial fair weather values, decrease of the current density results in a decrease of the electric field. Consequently, in the upper boundary of the dust layer, as the conductivity increases to fair weather values, the electric field decreases with respect to its fair weather value to reflect the decrease of the current density.

The second is at the ground (z = 0 km), where initially the electric field decreases, but as time progresses and several bins arrive at the ground it increases. The initial decrease of the electric field, right after the placement of the dust layer, seems to contradict measurements and observations that show significant increase when dust is present (e.g. Katz et al., 2018; Zhang and Zhou, 2020).This can be explained, first of all, by the fact that the 1d model is not appropriate for the study of effects upon the arrival of the dust layer, since it assumes an infinite symmetrical horizontal extent of the layer. The particles are placed instantaneously above a location, and are left to move vertically according to the forces acting upon them. Effects caused by the horizontal transport of the layer that can create horizontal electrical currents that eventually close to the ground enhancing the fair weather electric field (due to the electrical structure of the layer or the horizontal wind) require 2d or 3d modeling for a more detailed study. Especially the presence of horizontal winds, that are responsible for the dust particle transport, can alter the fair weather electric field by modifying the electrical structure of the atmosphere, as has been shown by Anisimov et al. (2001). As a matter of fact, the differences between the measurements, presented by Katz et al. (2018), during day and night at Wise Observatory and Mt. Hermon are attributed, among other factors, to the effect of the winds at the lower layer.

While the dust particles are aloft, and in the absence of any charge separation within, the electric field at the ground decreases as a consequence of the increase of the columnar resistance as has been shown by Harrison et al. (2020) and Daskalopoulou et al. (2021). As dust particles approach the ground and the electrical conductivity decreases, because the dust particle number density increases, the electric field increases. The increase is not large because the calculation is terminated when 99.9% of particles with radius 5 μm vanish from the domain (hence smaller particles remain more than 5 days in the atmosphere, having terminal velocities in the order of a few cm per hour, and their settling is so

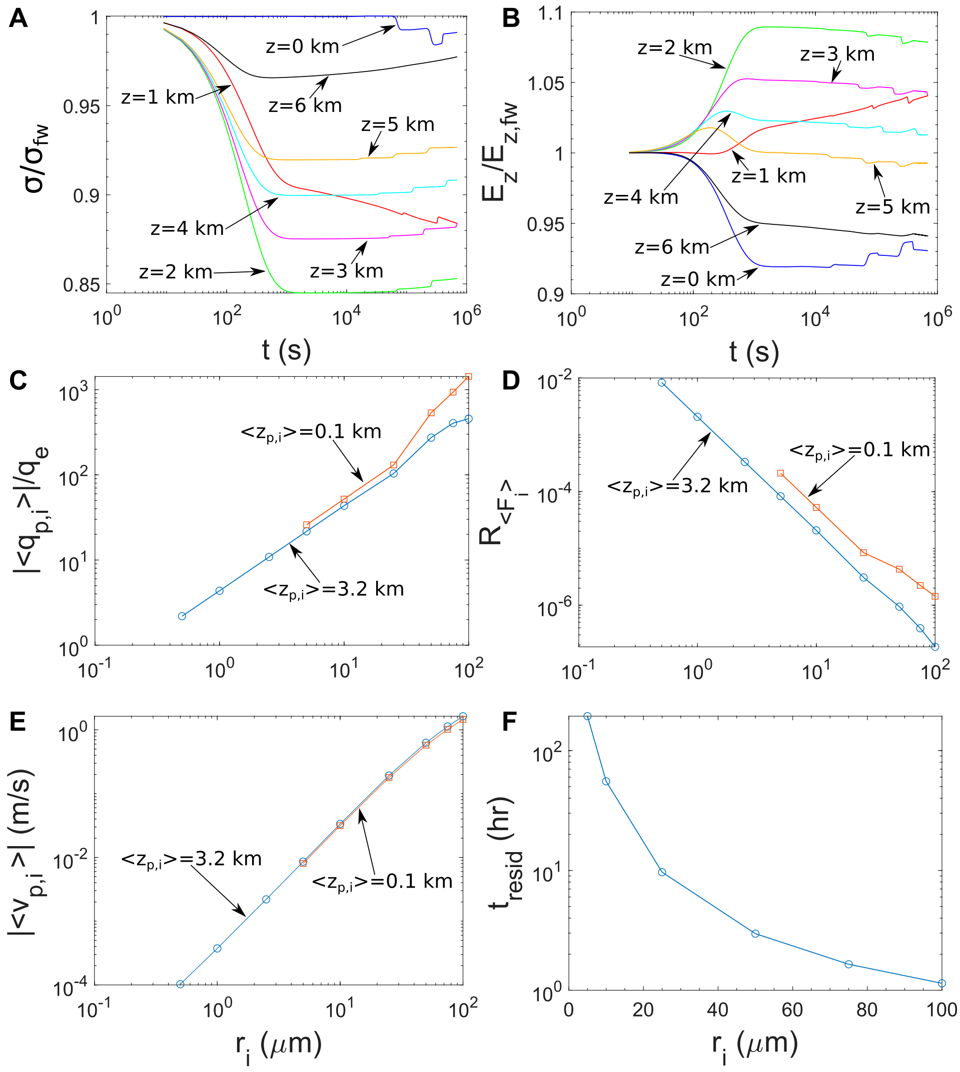

FIGURE 8 | Characteristics of particles distributed along the altitude according to $N^{l}_{p,i}$: **(A)** Conductivity reduction with respect to the fair weather value at different altitudes over time, **(B)** electric field magnitude modification with respect to the fair weather value at different altitudes over time, **(C)** average number of elementary charges per particle as a function of particle radius for different average bin distribution altitudes, **(D)** ratio between average electrical force magnitude and gravity magnitude as a function of particle radius for different average bin distribution altitudes, **(E)** average particle velocity as a function of particle radius for different average bin distribution altitudes, **(F)** residual time of particles in the atmosphere until **99.9%** of their concentration is lost.

slow that we choose not to include it in the current study, for the sake of saving simulation time). Small particles (that are the majority of the dust particle population) are still in the domain and above the ground. In the case of Katz et al. (2018) and Zhang and Zhou (2020) the measuring instruments (field mills) are well within the dust layer that reaches the ground. The increase of the electric field inside the layer and when it is already present has been reported by the measurements and agrees with our findings. Differences in the electric field polarities can exist as a consequence of multiple factors that are neglected in the current model, such as wind or other electrification mechanisms, which are planned to be studied in future work. Finally, we note that, although the conductivity decreases by a factor up to 0.85, the electric field enhancement factor is no greater than 1.08.

Figure 8C shows the relation between the number of elementary charges per particle and the particle size, at different altitudes. As the particle size decreases, particle charge decreases also as it is highly depended on particle size. Additionally, smaller particles have greater number densities than the large ones, and the attached ions tend to be divided on more particles leading to a decrease of the attached number of ions per particle (particle competition described by Gunn (1954)). Moreover, the charge of the larger particles increases as they travel within the atmosphere, as the attachment process depends on the particle velocity and the generated flow pattern, described

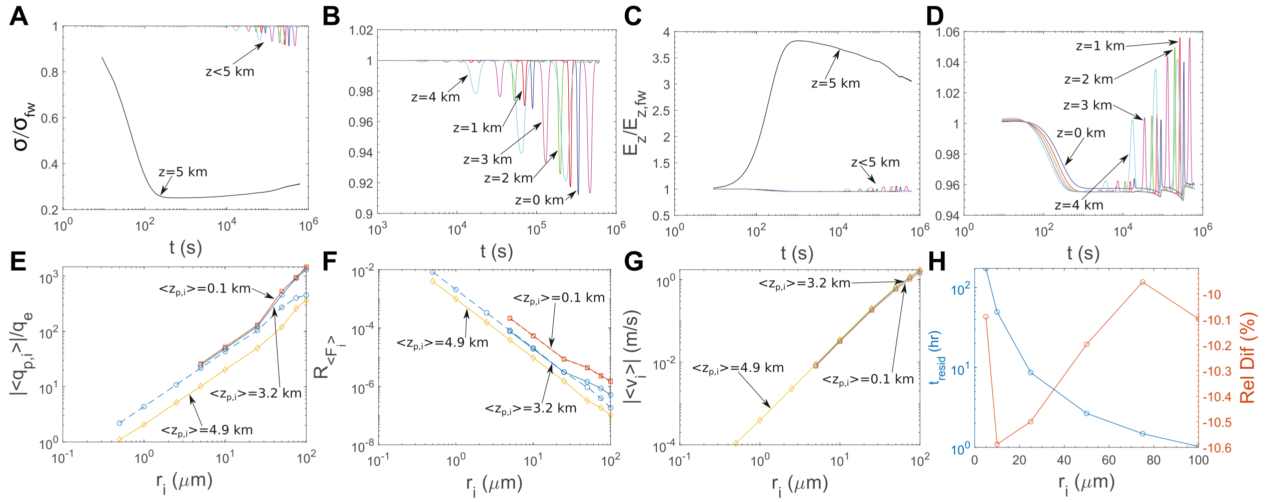

FIGURE 9 | Characteristics of particles distributed along the altitude according to $N^{II}_{p,i}$: **(A)** Conductivity reduction with respect to the fair weather value at different altitudes over time, **(B)** magnification of panel (A) in the region $z < 5$ km, **(C)** electric field magnitude modification with respect to the fair weather value at different altitudes over time, **(D)** magnification of panel **(C)** in the region $z < 5$ km, **(E)** average number of elementary charges per particle as a function of particle radius for different average bin distribution altitudes, **(F)** ratio between average electrical force magnitude and gravity magnitude as a function of particle radius for different average bin distribution altitudes, **(G)** average particle velocity as a function of particle radius for different average bin distribution altitudes, **(H)** residual time of particles in the atmosphere until 99.9% of their concentration is lost, and relative difference with the results of $N^{I}_{p,i}$. In panels (E)–(G) with dashed line of the same color and marker are the same results in the case of $N^{I}_{p,i}$ for comparison.

by the Reynolds number. The larger the particle velocity the larger the difference between the particle charge at different altitudes.

Figure 8D illustrates the dependence of the ratio between the electrical force and gravity, on the particle size. As the particle size decreases both electrical force and gravity decrease (the first one because the particle charge decreases, and the second due to the size reduction). The gravitational force reduction is larger than the particle charge reduction, and the force ratio increases, but does not overcome a value of 0.01. Additionally, as large particles settle, the force ratio increases due to the subsequent increase of the particle charge with velocity, which leads to an increase of the electrical force.

The velocity of the particles is a result mainly of the gravity and the drag forces. It does not charge significantly over the altitude and decreases as the particle size decreases (**Figure 8E**). The residual time in the atmosphere, until 99.9% of the particle concentration of each size falls to the ground, spans in the range between 1 h, for particles with radius 100 μm, up to ~ 120 h (5 days) with particles of radius equal to 5 μm (**Figure 8F**) The later results are consistent with the calculations presented by Mallios et al. (2020, 2021b).

3.2 Dependence on the Layer Depth

In this case the electrical properties of the distribution $N^{II}_{p,i}$ are examined. **Figures 8D–9A** show the time evolution of the conductivity (**Figures 9A,B**) and electric field magnitude (**Figures 9C,D**) ratios with respect to their fair weather values at different altitudes. The number density in this case is almost one order of magnitude higher than the $N^{I}_{p,i}$, and the conductivity reduction inside the layer is reduced by a factor of ~0.25, almost 3 times lower than the previous case. The electric field magnitude is increased similarly by a factor of 3.5. In the region outside the layer, the conductivity reduction/electric field enhancement at each altitude depends on the number density of each bin located at that altitude at any given time point (**Figures 9B,D**).

The higher number density in the distribution leads to a more significant particle competition for ions. This leads to lower charge per particle than in the previous case when the particles are inside the layer. This can be seen clearly in **Figure 9E** where the number of elementary charges for particles that are located at average altitude equal to 4.9 km (in the center of the layer), is lower than in the previous case (dashed blue line in **Figure 9E**). As the particles keep falling the velocity influences the attachment process and increases the particle charge up until an average altitude of 3.2 km, where the particle charge remains constant for each size, regardless of the altitude.

Similar remarks hold for the case of the ratio between the electrical force and the gravity (**Figure 9F**). The velocity does not vary significantly over the altitude (**Figure 9G**), and since the electrical force is still insignificant compared to gravity, the particle velocity is the same as the previous case. The difference in the spatial distribution leads to a difference in the residual time that individual particles remain in the atmosphere by 10% (**Figure 9H**).

3.3 Dependence on the Particle Number Density

In order to demonstrate the charging mechanism dependence on the particle number density, we increase $N^{I}_{p,i}$ by a factor of 10, leading the number density to become comparable to the fair

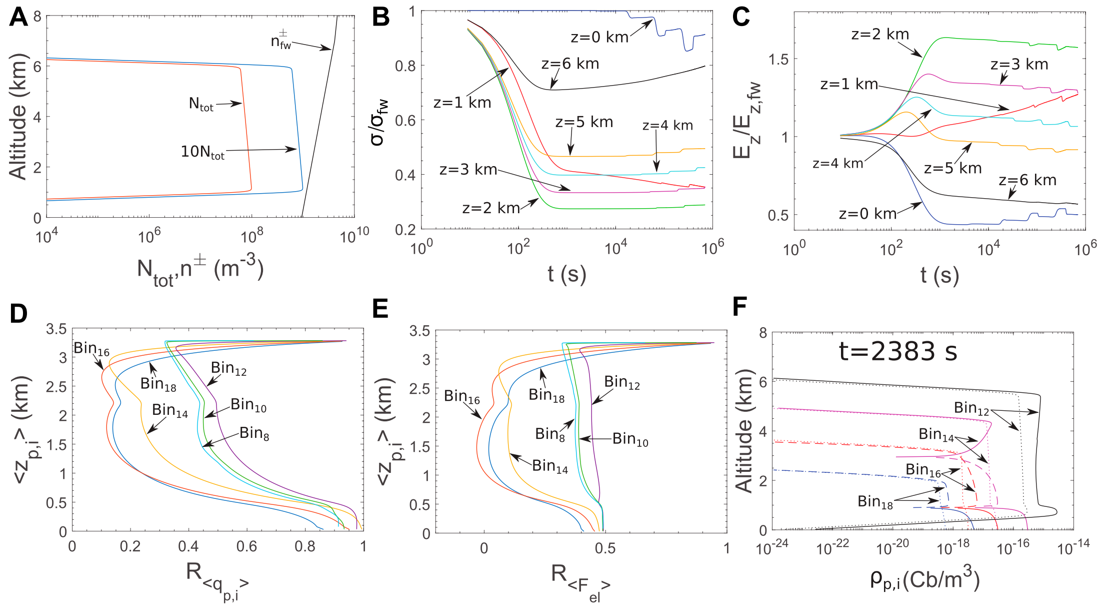

FIGURE 10 | Comparison between the case of $N^I_{p,i}$ and the case of $10N^I_{p,i}$: **(A)** Total particle number density compared to the ambient fair weather ion density, **(B)** conductivity reduction with respect to the fair weather value at different altitudes over time for $10N^I_{p,i}$, **(C)** electric field magnitude modification with respect to the fair weather value at different altitudes over time for $10N^I_{p,i}$, **(D)** average particle charge ratio between $N^I_{p,i}$ and $10N^I_{p,i}$, for several bins, **(E)** average electrical force ratio between $N^I_{p,i}$ and $10N^I_{p,i}$, for several bins, **(F)** snapshot of particle charge density distribution for some bins in the case of $10N^I_{p,i}$. With solid lines are the negative values, with dashed lines are the positive values and with dotted lines are the values of the charge density distributions in the case of $N^I_{p,i}$ (which are all negative).

weather ion density (**Figure 10A**). This increase is not unrealistic, as it represents the maximum measured values by Ryder et al. (2013b) during the Fennec 2011 campaign. Such an increase of the ion density leads to a conductivity reduction by a factor up to ~0.3 (**Figure 10B**) inside the layer, and an electric field magnitude enhancement by a factor of 1.7 (**Figure 10C**). The particle competition in this case reduces the average particle charge by a factor up to 0.1–0.2 in the case of particles with radius larger than 50 μm, and up to 0.4 for the rest sizes (**Figure 10D**), compared to the case of **Figure 8**. Similar reduction is observed in the case of the electrical force (**Figure 10E**).

Another interesting point that is revealed by **Figure 10E**, that for some bins the electrical force changes polarity and becomes positive. This means that the particles are charged positively. In **Figure 10F**, where a snapshot of the charge density dynamics is depicted, it is clear that the charge polarity in the case of particles with radius larger than 50 μm changes to positive values (Bin_{14}–Bin_{18}). This happens for the following reason. Since the ion attachment rate is proportional to the particle number density (**Eqs 30**, **31**, **38**, **39**), the negative ions attach more to bins with smaller radii (that have several order of magnitude more particles than bins with larger radii). In the case of the distribution with $N^I_{p,i}$, as the particles move to lower altitudes, since the particle density is much less than the ambient ion density, the ions replenish from the ionization process and there are always enough negative ions to attach to particles (the ratio of ion densities is less than the mobility ratio, see **Section 3.1**). In the case $10N^I_{p,i}$ case the particle density is comparable to the ambient ion density, and therefore the negative ions do not have time to replenish. Given that most negative ions attach to small particles, the ratio of ion densities becomes larger than the mobilitiy ratio for larger particles, and they can become positively charged. Consequently, ion attachment alone is capable to charge positively large particles and negatively small ones, as was previously stated only for the triboelectric effect (e.g., Zhao et al., 2002; Lacks et al., 2008; Shinbrot and Herrmann, 2008; Merrison, 2012).

Similar conclusions were derived by Yair and Levin (1989) based on the ion attachment to aerosols formulation by Hoppel and Frick (1986). They studied polydisperse spherical conducting aerosols with radii up to 0.5 μm and found that for small aerosol concentrations, particles were charged mostly negatively, but that an increase in aerosol concentrations lead to differential charging, resulting in opposite charging of the small (mostly negative) and the large (mostly positive) particles. This effect was enhanced for size distributions which had a significant component of large particles. Their results showed dependency only on the particle concentration, as opposed to the current work findings, that show dependency on the particle concentrations with respect to the atmospheric ion concentrations. The latter distinction is attributed to the difference in the scale of the problem under examination. In the present study, the particle sizes are larger than the ionic mean free path and therefore the ionic diffusion is expected to influence the attachment process. In the case of Yair and Levin (1989) the aerosol sizes are comparable, or smaller, than the ionic mean free path and the processes of three body trapping and image capture are dominant. In general, it becomes clear that regardless the scale of the problem, the ion attachment to

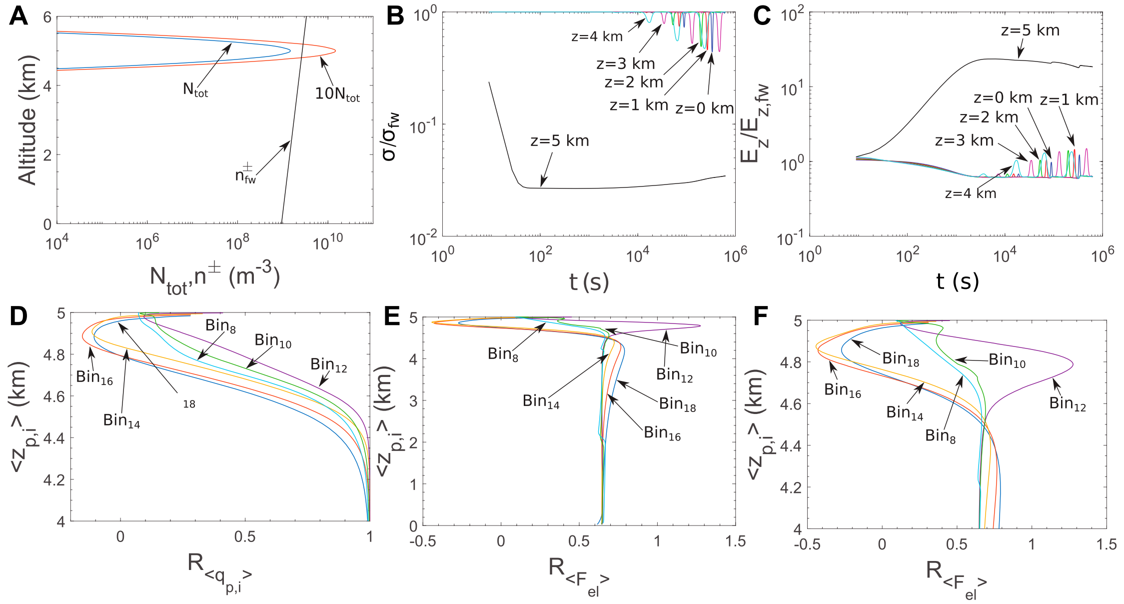

FIGURE 11 | Comparison between the case of $N^{II}_{p,i}$ and the case of $10N^{II}_{p,i}$: **(A)** Total particle number density compared to the ambient fair weather ion density, **(B)** conductivity reduction with respect to the fair weather value at different altitudes over time for $10N^{II}_{p,i}$, **(C)** electric field magnitude modification with respect to the fair weather value at different altitudes over time for $10N^{II}_{p,i}$, **(D)** average particle charge ratio between $N^{II}_{p,i}$ and $10N^{II}_{p,i}$, for several bins, **(E)** average electrical force ratio between $N^{II}_{p,i}$ and $10N^{II}_{p,i}$, for several bins, **(F)** magnification of panel (E) for average altitude range between 4 and 5 km.

particles can lead to different polarities of the particle charges in case of different particle sizes.

Figure 11 shows the case of the densely packed $N^{II}_{p,i}$ particle distribution, enhanced by a factor of 10. In the specific case, the particle number density becomes larger than the fair weather ion densities (**Figure 11A**). The conductivity inside the layer reduces by a factor up to ~0.03 (**Figure 11B**), while the electric field is enhanced by a factor up to ~20 with respect to the fair weather values (**Figure 11C**) The change of charge polarity in the case of large particles is more apparent in this case **Figures 11D–F**.

From the results of **Figures 10**, **11** we deduce that, the increase of the dust particle density favors the increase of the ambient large scale electric field, but does not favor the charging process of the dust particles, because their net charge decreases. Overall, the increase of the dust particle density acts against the effects of the electrical force, because the reduction of the particle charge is more prominent than the increase of the electric field, and the electrical force ultimately decreases. This indicates that the ion attachment process (acting on the enhancement of the ambient electric field) combined with a second charging process, such as the triboelectric effect (acting on the enhancement of the particle charge), might create a sufficient electrical force that in turn influences the settling of the dust particles. We plan on investigating this further on future work.

3.4 Validation of the Particle Size Distribution Discretization

Figure 12 illustrates the results regarding the comparison of different types of binning. **Figure 12A** shows the number of elementary charges per particle as a function of the particle radius. As the number of equilateral bins increases, the results converge to the results calculated by the current work binning. This becomes more clear in **Figures 12C,E**, where initial size range is split in sub ranges 10–150 μm, and 0.1–10 μm, respectively. The same conclusions are derived in the case of the ratio between the electrical force magnitude and the gravity magnitude (**Figures 2**, **12B,D,F**).

4 CONCLUSION

Ion attachment to dust particles is one of the major charging mechanisms during their gravitational settling within the atmospheric column. It can, therefore, lead to an enhancement of the ambient fair weather electric field, due to the ion density and, consequently, the atmospheric electrical conductivity reduction. This is the first consistent attempt, to our knowledge, to analytically represent the phenomena by integrating a measured size distribution of spherical dust particles, in the 1D model that incorporates the calculation of new attachment rates of non stationary spherical particles.

We have shown that ion attachment is capable of charging dust particles, with radius between 1 −100 μm, with a net charge that ranges between 1 −1,000 elementary charges depending on the dust particle number density. The particle velocity enhances the acquired particle net charge, but converges to a steady state value as the particle is traveling in the fair weather atmosphere away from the initial dust

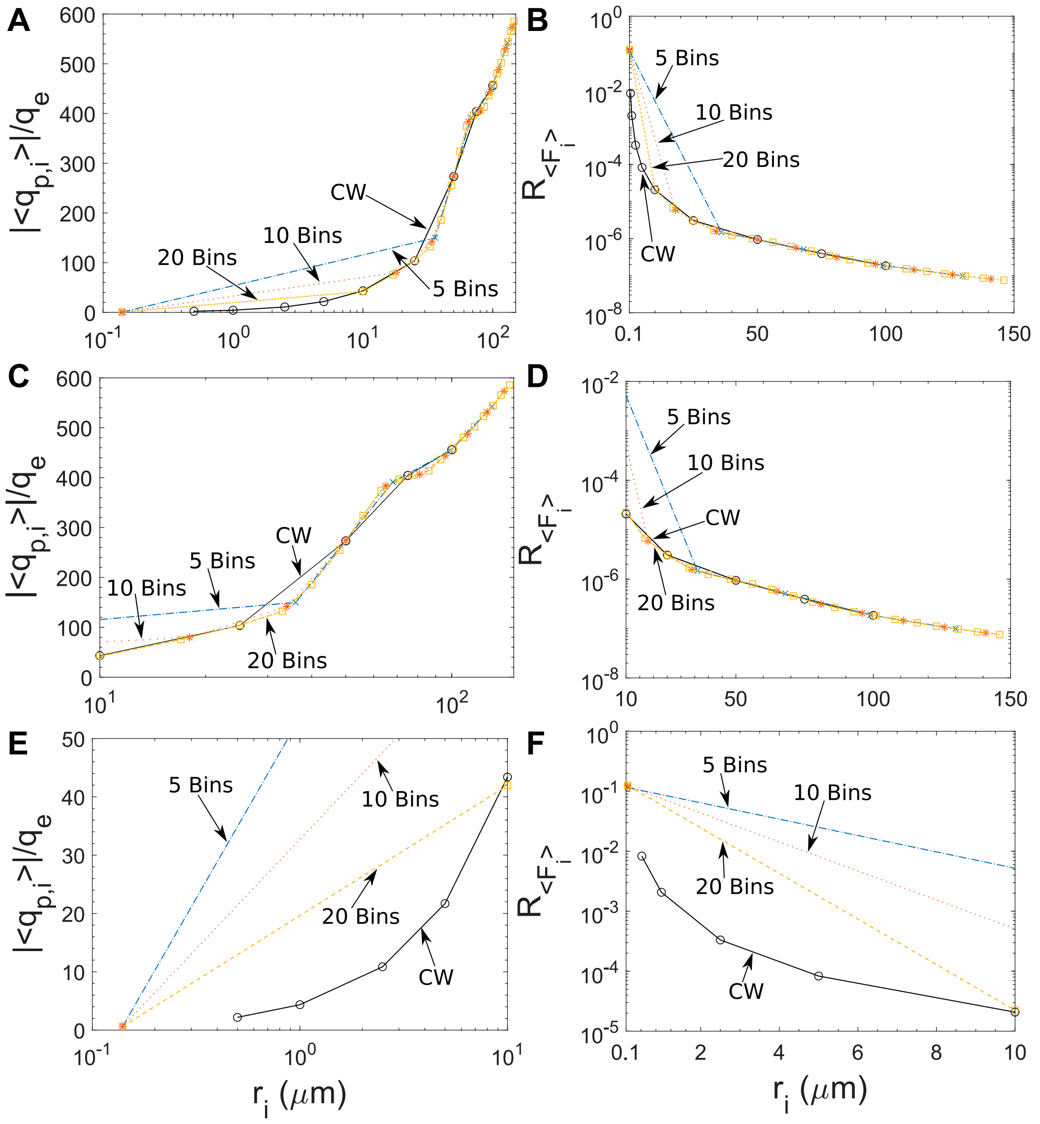

FIGURE 12 | Study on the proper discretization of the size distribution: **(A)** Number of elementary charges per particle as a function of particle radius for different types of binnings, **(B)** ratio between the electrical force magnitude and the gravity magnitude as a function of particle radius for different types of binnings, **(C,D)** magnification of panels (A) and (B) for particle radius in the range of 10 – 150 μm, **(E,F)** magnification of panels (A) and (B) for particle radius in the range of 0.1 – 10 μm.

layer. The influence of the total number density on the particle charging process appears stronger than its influence on the electric field enhancement. If the number density is very close or becomes even larger than the ambient ion density, large particles can be charged positively while within the initial dust layer. This is attributed to the lack of negative ions, which tend to attach to small particles, that have number densities several orders of magnitude greater than the larger ones. A similar charging behavior was found in atmospheric aerosols with sizes smaller than 0.5 μm in radius, by Yair and Levin (1989). The dust layer depth is expected to influence both the net particle charge and the ambient electric field enhancement, but overall, the electrical force applied to the particles remains the same. The magnitude of the electrical force is found to be, at best, two orders of magnitude lesser than gravity, which leads to no significant influence to the particle dynamics, for particles with radius in the range 1–100 μm. Nonetheless, other processes must be combined with the ion attachment, such as the triboelectric effect or the updrafts, for a better quantification of the electrical force possible influence on the particle gravitational settling. In parallel to this work, sophisticated profiling measurements with novel atmospheric electricity sensors are launched in planned experiments within the D-TECT project, in order to further evaluate our model. These steps will be concluded in future work.

DATA AVAILABILITY STATEMENT

Publicly available datasets were analyzed in this study. This data can be found here: http://www.met.reading.ac.uk/~jp902366/research/fennec/data.php.

AUTHOR CONTRIBUTIONS

SM conceptualized the model formalism, developed the model and wrote the paper. GP assisted in the model development and contributed in the paper writing. AP and GH directed the preparation of the paper, supervised the study and provided scientific consultation regarding the model results interpretation. VD prepared the particle size distribution discretization, the particle number density distributions along the altitude, and contributed in the paper writing. VA co-supervised the study, and provided scientific consultation regarding the mathematical formalism of the particle number density distribution and the particle size distribution discretization.

FUNDING

SM, GP, GH, and AP are funded by the project: "Modeling and Measuring Electrical Properties of Desert Dust Layers–Medimnos" (MIS 5049929) under the call for proposals "Researcher support with emphasis on new researchers" (EDBM103). The project is co-financed by Greece and the European Union (European Social Fund- ESF) by the Operational Programme Human Resources Development, Education and Lifelong Learning 2014–2020. VD would like to acknowledge funding by Greece and the European Union (European Social Fund-ESF) through the Operational Programme "Human Resources Development, Education and Lifelong Learning" in the context of the project "Strengthening Human Resources Research Potential *via* Doctorate Research" (MIS-5000432), implemented by the State Scholarships Foundation (IKY). VA acknowledges funding by the project "D-TECT" (Grant Agreement 725698) funded by the European Research Council (ERC) under the European Union's Horizon 2020 research and innovation programme.

REFERENCES

Adebiyi, A. A., and Kok, J. F. (2020). Climate Models Miss Most of the Coarse Dust in the Atmosphere. *Sci. Adv.* 6, eaaz9507. doi:10.1126/sciadv.aaz9507

Anisimov, S. V., Mareev, E. A., Shikhova, N. M., and Dmitriev, E. M. (2001). Mechanisms for the Formation of Electric-Field Pulsation Spectra in the Near-Surface Atmosphere. *Radiophys. Quan. Electron.* 44, 520–532. doi:10.1023/a:1017905732496

Bates, D. R. (1982). Recombination of Small Ions in the Troposphere and Lower Stratosphere. *Planet. Space Sci.* 30, 1275–1282. doi:10.1016/0032-0633(82)90101-5

Baumgaertner, A. J. G., Lucas, G. M., Thayer, J. P., and Mallios, S. A. (2014). On the Role of Clouds in the Fair Weather Part of the Global Electric Circuit. *Atmos. Chem. Phys.* 14, 8599–8610. doi:10.5194/acp-14-8599-2014

Bricard, J. (1965). "Action of Radioactivity and of Pollution upon Parameters of Atmospheric Electricity," in *Problems of Atmospheric and Space Electricity*. Editor S. C. Coroniti, 82–117.

Chiu, C.-S. (1978). Numerical Study of Cloud Electrification in an Axisymmetric, Time-dependent Cloud Model. *J. Geophys. Res.* 83, 5025–5049. doi:10.1029/jc083ic10p05025

Clift, R., and Gauvin, W. H. (1971). Motion of Entrained Particles in Gas Streams. *Can. J. Chem. Eng.* 49, 439–448. doi:10.1002/cjce.5450490403

Clift, R., Grace, J. R., and Weber, M. E. (2005). *Bubbles, Drops, and Particles*. Dover Publications.

Colarco, P. R., Toon, O. B., Torres, O., and Rasch, P. J. (2002). Determining the UV Imaginary index of Refraction of Saharan Dust Particles from Total Ozone Mapping Spectrometer Data Using a Three-Dimensional Model of Dust Transport. *J. Geophys. Res.* 107. doi:10.1029/2001jd000903

Creamean, J. M., Suski, K. J., Rosenfeld, D., Cazorla, A., DeMott, P. J., Sullivan, R. C., et al. (2013). Dust and Biological Aerosols from the Sahara and Asia Influence Precipitation in the Western U.S. *Science* 339, 1572–1578. doi:10.1126/science.1227279

Dahneke, B. (1983). "Simple Kinetic Theory of Brownian Diffusion in Vapors and Aerosols," in *Theory of Dispersed Multiphase Flow*. Editor R. E. Meyer (Academic Press), 97–133. doi:10.1016/B978-0-12-493120-6.50011-8

Daskalopoulou, V., Mallios, S. A., Ulanowski, Z., Hloupis, G., Gialitaki, A., Tsikoudi, I., et al. (2021). The Electrical Activity of Saharan Dust as Perceived from Surface Electric Field Observations. *Atmos. Chem. Phys.* 21, 927–949. doi:10.5194/acp-21-927-2021

Davies, C. N. (1945). Definitive Equations for the Fluid Resistance of Spheres. *Proc. Phys. Soc.* 57, 259–270. doi:10.1088/0959-5309/57/4/301

DeMott, P. J., Sassen, K., Poellot, M. R., Baumgardner, D., Rogers, D. C., Brooks, S. D., et al. (2003). African Dust Aerosols as Atmospheric Ice Nuclei. *Geophys. Res. Lett.* 30. doi:10.1029/2003GL017410

Denjean, C., Cassola, F., Mazzino, A., Triquet, S., Chevaillier, S., Grand, N., et al. (2016). Size Distribution and Optical Properties of mineral Dust Aerosols Transported in the Western Mediterranean. *Atmos. Chem. Phys.* 16, 1081–1104. doi:10.5194/acp-16-1081-2016

Eden, H. F., and Vonnegut, B. (1973). Electrical Breakdown Caused by Dust Motion in Low-Pressure Atmospheres: Considerations for Mars. *Science* 180, 962–963. doi:10.1126/science.180.4089.962

Fjeld, R. A., Gauntt, R. O., and McFarland, A. R. (1983). Continuum Field-Diffusion Theory for Bipolar Charging of Aerosols. *J. Aerosol Sci.* 14, 541–556. doi:10.1016/0021-8502(83)90010-1

Fjeld, R. A., and McFarland, A. R. (1989). Evaluation of Select Approximations for Calculating Particle Charging Rates in the Continuum Regime. *Aerosol Sci. Technol.* 10, 535–549. doi:10.1080/02786828908959293

Fuks, N. A. (1958). *The Mechanics of Aerosols*. Maryland: Technical Information Division, Directorate of Technical Services, U.S. Army Chemical Warfare Laboratories.

Garcia-Carreras, L., Parker, D. J., Marsham, J. H., Rosenberg, P. D., Brooks, I. M., Lock, A. P., et al. (2015). The Turbulent Structure and Diurnal Growth of the Saharan Atmospheric Boundary Layer. *J. Atmos. Sci.* 72, 693–713. doi:10.1175/JAS-D-13-0384.1

Gauntt, R. O., Fjeld, R. A., and Mcfarland, A. R. (1984). Bipolar Charging of Near-Micrometer Sized Aerosol. *IEEE Trans. Ind. Applicat.* IA-20, 1636–1641. doi:10.1109/tia.1984.4504653

Ginoux, P., Chin, M., Tegen, I., Prospero, J. M., Holben, B., Dubovik, O., et al. (2001). Sources and Distributions of Dust Aerosols Simulated with the GOCART Model. *J. Geophys. Res.* 106, 20255–20273. doi:10.1029/2000JD000053

Gott, J. P. (1936). Movements of Electrically Charged Cloud Particles. *Math. Proc. Camb. Phil. Soc.* 32, 486–492. doi:10.1017/S0305004100019198

Goudie, A. S., and Middleton, N. J. (2001). Saharan Dust Storms: Nature and Consequences. *Earth-Science Rev.* 56, 179–204. doi:10.1016/S0012-8252(01)00067-8

Gunn, R. (1954). Diffusion Charging of Atmospheric Droplets by Ions, and the Resulting Combination Coefficients. *J. Meteorol.* 11, 339–347. doi:10.1175/1520-0469(1954)011<0339:DCOADB>2.0.CO;2

Gunn, R. (1956). The Hyperelectrification of Raindrops by Atmospheric Electric fields. *J. Meteorol.* 13, 283–288. doi:10.1175/1520-0469(1956)013<0283:THORBA>2.0.CO;2

Harrison, R. G., Nicoll, K. A., Mareev, E., Slyunyaev, N., and Rycroft, M. J. (2020). Extensive Layer Clouds in the Global Electric Circuit: Their Effects on Vertical Charge Distribution and Storage. *Proc. R. Soc. A.* 476, 20190758. doi:10.1098/rspa.2019.0758

Helsdon, J. H., Jr., Gattaleeradapan, S., Farley, R. D., and Waits, C. C. (2002). An Examination of the Convective Charging Hypothesis: Charge Structure, Electric fields, and Maxwell Currents. *J. Geophys. Res.* 107. doi:10.1029/2001JD001495

Hoppel, W. A., and Frick, G. M. (1986). Ion-Aerosol Attachment Coefficients and the Steady-State Charge Distribution on Aerosols in a Bipolar Ion Environment. *Aerosol Sci. Technol.* 5, 1–21. doi:10.1080/02786828608959073

Huang, Y., Kok, J. F., Kandler, K., Lindqvist, H., Nousiainen, T., Sakai, T., et al. (2020). Climate Models and Remote Sensing Retrievals Neglect Substantial Desert Dust Asphericity. *Geophys. Res. Lett.* 47, 1–11. doi:10.1029/2019GL086592

Huneeus, N., Schulz, M., Balkanski, Y., Griesfeller, J., Prospero, J., Kinne, S., et al. (2011). Global Dust Model Intercomparison in AeroCom Phase I. *Atmos. Chem. Phys.* 11, 7781–7816. doi:10.5194/acp-11-7781-2011

Jennings, S. G. (1988). The Mean Free Path in Air. *J. Aerosol Sci.* 19, 159–166. doi:10.1016/0021-8502(88)90219-4

Jickells, T. D., An, Z. S., Andersen, K. K., Baker, A. R., Bergametti, G., Brooks, N., et al. (2005). Global Iron Connections between Desert Dust, Ocean Biogeochemistry, and Climate. *Science* 308, 67–71. doi:10.1126/science.1105959

Kamra, A. K. (1972). Measurements of the Electrical Properties of Dust Storms. *J. Geophys. Res.* 77, 5856–5869. doi:10.1029/JC077i030p05856

Katz, S., Yair, Y., Price, C., Yaniv, R., Silber, I., Lynn, B., et al. (2018). Electrical Properties of the 8-12th September, 2015 Massive Dust Outbreak over the Levant. *Atmos. Res.* 201, 218–225. doi:10.1016/j.atmosres.2017.11.004

Kilpatric, W. D. (1971). An Experimental Mass-Mobility Relation for Ions in Air at Atmospheric Pressure. *Proc. 19th Annu. Conf. Mass. Spectrosc.* 19, 320–325.

Kinzer, G. D., and Gunn, R. (1951). The Evaporation, Temperature and thermal Relaxation-Time of Freely Falling Waterdrops. *J. Meteorol.* 8, 71–83. doi:10.1175/1520-0469(1951)008<0071:tetatr>2.0.CO;2

Klett, J. D. (1971). Ion Transport to Cloud Droplets by Diffusion and Conduction, and the Resulting Droplet Charge Distribution. *J. Atmos. Sci.* 28, 78–85. doi:10.1175/1520-0469(1971)028<0078:ittcdb>2.0.co;2

Kok, J. F., Ridley, D. A., Zhou, Q., Miller, R. L., Zhao, C., Heald, C. L., et al. (2017). Smaller Desert Dust Cooling Effect Estimated from Analysis of Dust Size and Abundance. *Nat. Geosci* 10, 274–278. doi:10.1038/ngeo2912

Krauss, C. E., Hor nyi, M., and Robertson, S. (2003). Experimental Evidence for Electrostatic Discharging of Dust Near the Surface of Mars. *New J. Phys.* 5, 70. doi:10.1088/1367-2630/5/1/370

Lacks, D. J., Duff, N., and Kumar, S. K. (2008). Nonequilibrium Accumulation of Surface Species and Triboelectric Charging in Single Component Particulate Systems. *Phys. Rev. Lett.* 100. doi:10.1103/PhysRevLett.100.188305

Landau, L. D., and Lifshitz, E. M. (1963). *Electrodynamics of Continuous Media*, Vol. 8. Pergamon Press.

Lawless, P. A. (1996). Particle Charging Bounds, Symmetry Relations, and an Analytic Charging Rate Model for the Continuum Regime. *J. Aerosol Sci.* 27, 191–215. doi:10.1016/0021-8502(95)00541-2

Leonard, B. P. (1979). A Stable and Accurate Convective Modelling Procedure Based on Quadratic Upstream Interpolation. *Comput. Methods Appl. Mech. Eng.* 19, 59–98. doi:10.1016/0045-7825(79)90034-3

Li, F., Vogelmann, A. M., and Ramanathan, V. (2004). Saharan Dust Aerosol Radiative Forcing Measured from Space. *J. Clim.* 17, 2558–2571. doi:10.1175/1520-0442(2004)017<2558:sdarfm>2.0.co;2

Li, J.-G. (2008). Upstream Nonoscillatory Advection Schemes. *Mon. Weather Rev.* 136, 4709–4729. doi:10.1175/2008MWR2451.1

Liu, B. Y. H., and Kapadia, A. (1978). Combined Field and Diffusion Charging of Aerosol Particles in the Continuum Regime. *J. Aerosol Sci.* 9, 227–242. doi:10.1016/0021-8502(78)90045-9

Long, Z., and Yao, Q. (2010). Evaluation of Various Particle Charging Models for Simulating Particle Dynamics in Electrostatic Precipitators. *J. Aerosol Sci.* 41, 702–718. doi:10.1016/j.jaerosci.2010.04.005

Mallios, S. A., Daskalopoulou, V., and Amiridis, V. (2021a). Orientation of Non Spherical Prolate Dust Particles Moving Vertically in the Earth's Atmosphere. *J. Aerosol Sci.* 151, 105657. doi:10.1016/j.jaerosci.2020.105657

Mallios, S. A., Drakaki, E., and Amiridis, V. (2021b). Corrigendum to "Effects of Dust Particle Sphericity and Orientation on Their Gravitational Settling in the Earth's Atmosphere" [Journal of Aerosol Science 150 (2020) 105634]. *J. Aerosol Sci.* 153, 105736. doi:10.1016/j.jaerosci.2020.105736

Mallios, S. A., Drakaki, E., and Amiridis, V. (2020). Effects of Dust Particle Sphericity and Orientation on Their Gravitational Settling in the Earth's Atmosphere. *J. Aerosol Sci.* 150, 105634. doi:10.1016/j.jaerosci.2020.105634

Marlow, W. H., and Brock, J. R. (1975). Unipolar Charging of Small Aerosol Particles. *J. Colloid Interf. Sci.* 50, 32–38. doi:10.1016/0021-9797(75)90250-7

Marshall, T. C., Stolzenburg, M., Maggio, C. R., Coleman, L. M., Krehbiel, P. R., Hamlin, T., et al. (2005). Observed Electric fields Associated with Lightning Initiation. *Geophys. Res. Lett.* 32. doi:10.1029/2004gl021802

Merrison, J. P. (2012). Sand Transport, Erosion and Granular Electrification. *Aeolian Res.* 4, 1–16. doi:10.1016/j.aeolia.2011.12.003

Meyerott, R. E., Reagan, J. B., and Joiner, R. G. (1980). The Mobility and Concentration of Ions and the Ionic Conductivity in the Lower Stratosphere. *J. Geophys. Res.* 85, 1273–1278. doi:10.1029/JA085iA03p01273

Mishev, A. (2013). Short- and Medium-Term Induced Ionization in the Earth Atmosphere by Galactic and Solar Cosmic Rays. *Int. J. Atmos. Sci.* 2013, 1–9. doi:10.1155/2013/184508

Nicoll, K. A., Harrison, R. G., and Ulanowski, Z. (2010). Observations of Saharan Dust Layer Electrification. *Environ. Res. Lett.* 6, 014001. doi:10.1088/1748-9326/6/1/014001

NOAA/NASA/USAF (1976). *U.S Standard Atmosphere 1976*. Washington, DC, United States: Tech. Rep. NASA-TM-X-74335, NOAA-S/T-76-1562.

Pasko, V. P., Inan, U. S., Bell, T. F., and Taranenko, Y. N. (1997). Sprites Produced by Quasi-Electrostatic Heating and Ionization in the Lower Ionosphere. *J. Geophys. Res.* 102, 4529–4561. doi:10.1029/96JA03528

Press, W. H., Teukolsky, S. A., Vetterling, W. T., and Flannery, B. P. (1992). "Numerical Recipes in C," in *The Art of Scientific Computing*. 2nd Ed. (USA: Cambridge University Press).

Proudman, I., and Pearson, J. R. A. (1957). Expansions at Small Reynolds Numbers for the Flow Past a Sphere and a Circular cylinder. *J. Fluid Mech.* 2. doi:10.1017/s0022112057000105

Renard, J.-B., Dulac, F., Durand, P., Bourgeois, Q., Denjean, C., Vignelles, D., et al. (2018). *In Situ* measurements of Desert Dust Particles above the Western Mediterranean Sea with the Balloon-Borne Light Optical Aerosol Counter/sizer (LOAC) during the ChArMEx Campaign of Summer 2013. *Atmos. Chem. Phys.* 18, 3677–3699. doi:10.5194/acp-18-3677-2018

Riousset, J. A., Nag, A., and Palotai, C. (2020). Scaling of Conventional Breakdown Threshold: Impact for Predictions of Lightning and TLEs on Earth, Venus, and Mars. *Icarus* 338, 113506. doi:10.1016/j.icarus.2019.113506

Rycroft, M. J., Harrison, R. G., Nicoll, K. A., and Mareev, E. A. (2008). An Overview of Earth's Global Electric Circuit and Atmospheric Conductivity. *Space Sci. Rev.* 137, 83–105. doi:10.1007/s11214-008-9368-6

Rycroft, M. J., Israelsson, S., and Price, C. (2000). The Global Atmospheric Electric Circuit, Solar Activity and Climate Change. *J. Atmos. Solar-Terrestrial Phys.* 62, 1563–1576. doi:10.1016/S1364-6826(00)00112-7

Ryder, C. L., Highwood, E. J., Lai, T. M., Sodemann, H., and Marsham, J. H. (2013a). Impact of Atmospheric Transport on the Evolution of Microphysical and Optical Properties of Saharan Dust. *Geophys. Res. Lett.* 40, 2433–2438. doi:10.1002/grl.50482

Ryder, C. L., Highwood, E. J., Rosenberg, P. D., Trembath, J., Brooke, J. K., Bart, M., et al. (2013b). Optical Properties of Saharan Dust Aerosol and Contribution from the Coarse Mode as Measured during the Fennec 2011 Aircraft Campaign. *Atmos. Chem. Phys.* 13, 303–325. doi:10.5194/acp-13-303-2013

Ryder, C. L., Highwood, E. J., Walser, A., Seibert, P., Philipp, A., and Weinzierl, B. (2019). Coarse and Giant Particles Are Ubiquitous in Saharan Dust export Regions and Are Radiatively Significant over the Sahara. *Atmos. Chem. Phys.* 19, 15353–15376. doi:10.5194/acp-19-15353-2019

Ryder, C. L., Marenco, F., Brooke, J. K., Estelles, V., Cotton, R., Formenti, P., et al. (2018). Coarse-mode mineral Dust Size Distributions, Composition and Optical Properties from AER-D Aircraft Measurements over the Tropical

Eastern Atlantic. *Atmos. Chem. Phys.* 18, 17225–17257. doi:10.5194/acp-18-17225-2018

Shinbrot, T., and Herrmann, H. J. (2008). Static in Motion. *Nature* 451, 773–774. doi:10.1038/451773a

Smith, W. B., and McDonald, J. R. (1975). Calculation of the Charging Rate of fine Particles by Unipolar Ions. *J. Air Pollut. Control. Assoc.* 25, 168–172. doi:10.1080/00022470.1975.10470068

Stolzenburg, M., Marshall, T. C., Rust, W. D., Bruning, E., MacGorman, D. R., and Hamlin, T. (2007). Electric Field Values Observed Near Lightning Flash Initiations. *Geophys. Res. Lett.* 34. doi:10.1029/2006GL028777

Tammet, H. (1995). Size and Mobility of Nanometer Particles, Clusters and Ions. *J. Aerosol Sci.* 26, 459–475. doi:10.1016/0021-8502(94)00121-e

Tinsley, B. A., and Zhou, L. (2006). Initial Results of a Global Circuit Model with Variable Stratospheric and Tropospheric Aerosols. *J. Geophys. Res.* 111. doi:10.1029/2005jd006988

Toth, J. R., III, Rajupet, S., Squire, H., Volbers, B., Zhou, J., Xie, L., et al. (2020). Electrostatic Forces Alter Particle Size Distributions in Atmospheric Dust. *Atmos. Chem. Phys.* 20, 3181–3190. doi:10.5194/acp-20-3181-2020

van der Does, M., Knippertz, P., Zschenderlein, P., Giles Harrison, R., and Stuut, J.-B. W. (2018). The Mysterious Long-Range Transport of Giant mineral Dust Particles. *Sci. Adv.* 4, eaau2768. doi:10.1126/sciadv.aau2768

Wang, P.-K. (1983). Collection of Aerosol Particles by a Conducting Sphere in an External Electric Field-Continuum Regime Approximation. *J. Colloid Interf. Sci.* 94, 301–318. doi:10.1016/0021-9797(83)90268-0

Weinzierl, B., Ansmann, A., Prospero, J. M., Althausen, D., Benker, N., Chouza, F., et al. (2017). The Saharan Aerosol Long-Range Transport and Aerosol-Cloud-Interaction Experiment: Overview and Selected Highlights. *B. Am. Meteorol. Soc.* 98, 1427–1451. doi:10.1175/BAMS-D-15-00142.1

Whipple, F. J. W., and Chalmers, J. A. (1944). On Wilson's Theory of the Collection of Charge by Falling Drops. *Q.J R. Met. Soc.* 70, 103–119. doi:10.1002/qj.49707030402

Williams, E., and Yair, Y. (2006). "The Microphysical and Electrical Properties of Sprite-Producing Thunderstorms," in *Sprites, Elves and Intense Lightning Discharges*. Editors M. Füllekrug, E. A. Mareev, and M. J. Rycroft (Springer Netherlands), 57–83. doi:10.1007/1-4020-4629-4\text{_}3

Wilson, C. T. R. (1929). Some Thundercloud Problems. *J. Franklin Inst.* 208, 1–12. doi:10.1016/s0016-0032(29)90935-2

Yair, Y., and Levin, Z. (1989). Charging of Polydispersed Aerosol Particles by Attachment of Atmospheric Ions. *J. Geophys. Res.* 94, 13085–13091. doi:10.1029/jd094id11p13085

Yang, W., Marshak, A., Kostinski, A. B., and Várnai, T. (2013). Shape-induced Gravitational Sorting of Saharan Dust during Transatlantic Voyage: Evidence from CALIOP Lidar Depolarization Measurements. *Geophys. Res. Lett.* 40, 3281–3286. doi:10.1002/grl.50603

Zalesak, S. T. (1979). Fully Multidimensional Flux-Corrected Transport Algorithms for Fluids. *J. Comput. Phys.* 31, 335–362. doi:10.1016/0021-9991(79)90051-2

Zhang, H., and Zhou, Y. H. (2020). Reconstructing the Electrical Structure of Dust Storms from Locally Observed Electric Field Data. *Nat. Commun.* 11, 5072. doi:10.1038/s41467-020-18759-0

Zhao, H., Castle, G. S. P., and Inculet, I. I. (2002). The Measurement of Bipolar Charge in Polydisperse Powders Using a Vertical Array of Faraday Pail Sensors. *J. Electrostatics* 55, 261–278. doi:10.1016/S0304-3886(01)00209-1

Zhou, L., and Tinsley, B. A. (2007). Production of Space Charge at the Boundaries of Layer Clouds. *J. Geophys. Res.* 112. doi:10.1029/2006JD007998

Zhou, L., and Tinsley, B. A. (2012). Time Dependent Charging of Layer Clouds in the Global Electric Circuit. *Adv. Space Res.* 50, 828–842. doi:10.1016/j.asr.2011.12.018

Conflict of Interest: The authors declare that the research was conducted in the absence of any commercial or financial relationships that could be construed as a potential conflict of interest.

frontiers in Earth Science

ORIGINAL RESEARCH
published: 26 August 2021
doi: 10.3389/feart.2021.689127

Solar Cycle-Modulated Deformation of the Earth–Ionosphere Cavity

Tamás Bozóki[1,2]*, *Gabriella Sátori*[1], *Earle Williams*[3], *Irina Mironova*[4], *Péter Steinbach*[5,6], *Emma C. Bland*[7], *Alexander Koloskov*[8,9], *Yuri M. Yampolski*[8], *Oleg V. Budanov*[8], *Mariusz Neska*[10], *Ashwini K. Sinha*[11], *Rahul Rawat*[11], *Mitsuteru Sato*[12], *Ciaran D. Beggan*[13], *Sergio Toledo-Redondo*[14], *Yakun Liu*[3] and *Robert Boldi*[15]

[1]*Institute of Earth Physics and Space Science (ELKH EPSS), Sopron, Hungary,* [2]*Doctoral School of Environmental Sciences, University of Szeged, Szeged, Hungary,* [3]*Parsons Laboratory, Massachusetts Institute of Technology, Cambridge, MA, United States,* [4]*Earth's Physics Department, St. Petersburg State University, St. Petersburg, Russia,* [5]*Department of Geophysics and Space Science, Eötvös Loránd University, Budapest, Hungary,* [6]*ELKH-ELTE Research Group for Geology, Geophysics and Space Science, Budapest, Hungary,* [7]*Department of Arctic Geophysics, University Centre in Svalbard, Longyearbyen, Norway,* [8]*Institute of Radio Astronomy, National Academy of Sciences of Ukraine, Kharkiv, Ukraine,* [9]*State Institution National Antarctic Scientific Center of Ukraine, Kyiv, Ukraine,* [10]*Institute of Geophysics, Polish Academy of Sciences, Warsaw, Poland,* [11]*Indian Institute of Geomagnetism, Navi Mumbai, India,* [12]*Faculty of Science, Hokkaido University, Sapporo, Japan,* [13]*British Geological Survey, Edinburgh, United Kingdom,* [14]*Department of Electromagnetism and Electronics, University of Murcia, Murcia, Spain,* [15]*College of Natural and Health Sciences, Zayed University, Dubai, United Arab Emirates*

Edited by:
Konstantinos Kourtidis,
Democritus University of Thrace,
Greece

Reviewed by:
Rosane Rodrigues Chaves,
Federal University of Rio Grande do Norte, Brazil
Alexander Nickolaenko,
National Academy of Sciences of Ukraine, Ukraine
Marni Pazos,
National Autonomous University of Mexico, Mexico
V. Tritakis,
Academy of Athens, Greece

***Correspondence:**
Tamás Bozóki
bozoki.tamas@epss.hu

Specialty section:
This article was submitted to Atmospheric Science, a section of the journal Frontiers in Earth Science

Received: *31 March 2021*
Accepted: *10 August 2021*
Published: *26 August 2021*

Citation:
Bozóki T, Sátori G, Williams E, Mironova I, Steinbach P, Bland EC, Koloskov A, Yampolski YM, Budanov OV, Neska M, Sinha AK, Rawat R, Sato M, Beggan CD, Toledo-Redondo S, Liu Y and Boldi R (2021) Solar Cycle-Modulated Deformation of the Earth–Ionosphere Cavity. Front. Earth Sci. 9:689127. doi: 10.3389/feart.2021.689127

The Earth–ionosphere cavity resonator is occupied primarily by the electromagnetic radiation of lightning below 100 Hz. The phenomenon is known as Schumann resonances (SR). SR intensity is an excellent indicator of lightning activity and its distribution on global scales. However, long-term measurements from high latitude SR stations revealed a pronounced in-phase solar cycle modulation of SR intensity seemingly contradicting optical observations of lightning from satellite, which do not show any significant solar cycle variation in the intensity and spatial distribution of lightning activity on the global scale. The solar cycle-modulated local deformation of the Earth–ionosphere cavity by the ionization of energetic electron precipitation (EEP) has been suggested as a possible phenomenon that may account for the observed long-term modulation of SR intensity. Precipitating electrons in the energy range of 1–300 keV can affect the Earth–ionosphere cavity resonator in the altitude range of about 70–110 km and modify the SR intensities. However, until now there was no direct evidence documented in the literature supporting this suggestion. In this paper we present long-term SR intensity records from eight stations, each equipped with a pair of induction coil magnetometers: five high latitude ($|\text{lat}| > 60^\circ$), two mid-high latitude ($50^\circ < |\text{lat}| < 60^\circ$) and one low latitude ($|\text{lat}| < 30^\circ$). These long-term, ground-based SR intensity records are compared on the annual and interannual timescales with the fluxes of precipitating 30–300 keV medium energy electrons provided by the POES NOAA-15 satellite and on the daily timescale with electron precipitation events identified using a SuperDARN radar in Antarctica. The long-term variation of the Earth–ionosphere waveguide's effective height, as inferred from its cutoff frequency, is independently analyzed based on spectra recorded by the DEMETER satellite. It is shown that to account for all our observations one needs to consider both the effect of solar X-rays and EEP which modify the quality factor of the cavity and deform it dominantly over low- and high latitudes, respectively. Our results suggest that SR measurements should be considered as an alternative tool for collecting information about and thus monitoring changes in the ionization state of the lower ionosphere associated with EEP.

Keywords: Schumann resonance, earth-ionosphere cavity, energetic electron precipitation, solar cycle, solar X-rays, DEMETER, extremely low frequency, Q-factor

INTRODUCTION

The Earth's surface and the lower ionosphere together form an electromagnetic cavity resonator with resonance frequencies in the extremely low frequency (ELF, 3 Hz–3 kHz) band at ~8, ~14, ~20, ~26 Hz etc.. These resonances are named after Schumann (1952) who described them theoretically in 1952, 8 years before full frequency spectra were actually observed by Balser and Wagner (1960). Schumann resonances (SR) are excited primarily by lightning-radiated electromagnetic waves and the approximate number of 30–100 lightning strokes per second worldwide (Christian et al., 2003) maintains the resonance field quasi-continuously. It follows that SR are excellent indicators of lightning activity and distribution on global scales (see e.g., Williams et al., 2021). The possible connection between atmospheric electricity (including SR) and biological systems is another topic with substantial scientific interest (e.g., Elhalel et al., 2019; Fdez-Arroyabe et al., 2020; Price et al., 2021; Savoska et al., 2021; Sukhov et al., 2021). Until the end of the 1980's SR measurements were sparse and due to the restricted computational and data storage capacities long-term continuous recording was not really feasible at that time. In the early 90s' owing to the rapid development of large computational capacities and motivated by a fundamental Science article (Williams, 1992) many SR stations started to operate on a continuous basis worldwide (e.g., Sátori et al., 1996; Price and Melnikov, 2004; Neska et al., 2007; Ondrášková et al., 2007; Bór et al., 2020) which gave a new impetus for SR-related research.

Much published material has appeared describing the standard (recurrent) daily and seasonal variations of SR spectral parameters (modal frequency, intensity and sharpness of maxima) at different stations (e.g., Sátori, 1996; Nickolaenko and Hayakawa, 2002; Price and Melnikov, 2004; Roldugin et al., 2004a; Ondrášková et al., 2007; Yatsevich et al., 2008; Toledo-Redondo et al., 2010; Zhou et al., 2013; Nickolaenko and Hayakawa, 2014; Fornieles-Callejón et al., 2015; Manu et al., 2015; Musur and Beggan, 2019; Tatsis et al., 2020). These standard variations in SR are mainly the consequence of the daily and seasonal variations of global lightning activity which fundamentally affect the observed SR spectral parameters (Sátori, 1996). On the other hand, standard variations in SR are also connected to the effect of the day-night terminator, i.e., to changes in the shape of the Earth–ionosphere cavity (Melnikov et al., 2004; Sátori et al., 2007; Prácser et al., 2021). SR measurements demonstrated that the characteristic variations of global lightning activity are highly recurrent on a day-to-day and year-to-year basis (see e.g., Sátori, 1996). The latter was confirmed by optical observations of lightning from space as well (Williams et al., 2000; Christian et al., 2003).

Occasional variations in SR have also been documented, which are partly connected to transient extra-terrestrial phenomena that can modify the shape of the Earth–ionosphere cavity and thereby to "untune" its resonance frequencies. It is important to note that as a consequence of any change in the shape of the Earth–ionosphere cavity all the resonance frequencies shift in the same direction at all stations on Earth, but whether they increase or decrease depends on the actual modification of the conductivity profile in the upper atmosphere (Zhou and Qiao, 2015; Sátori et al., 2016; Kudintseva et al., 2018). Solar X-ray bursts (Roldugin et al., 2004b; Sátori et al., 2005; Dyrda et al., 2015; Sátori et al., 2016; Shvets et al., 2017) and solar proton events (Schlegel and Füllekrug, 1999; Roldugin et al., 2003; Singh et al., 2014) are known to cause such changes in frequencies (of both signs). In contrast, occasional variations in SR intensity with extra-terrestrial origin have been associated only with solar proton events so far (Schlegel and Füllekrug, 1999; Roldugin et al., 2003), and recently, indication for periods with increased SR intensity during geomagnetic storms was demonstrated as well (Salinas et al., 2016; Pazos et al., 2019). We note that variations in SR were also reported connected to seismic activity (e.g., Christofilakis et al., 2019; Galuk et al., 2019; Florios et al., 2020; Hayakawa et al., 2020).

SR measurements have also revealed the long-term solar cycle modulation of SR frequencies (e.g., Kulak et al., 2003a; Kulak et al., 2003b; Sátori et al., 2005; Ondrášková et al., 2011; Nickolaenko et al., 2015; Musur and Beggan, 2019; Koloskov et al., 2020) which has been attributed to the more than two orders of magnitude difference in solar X-ray flux between the minimum and maximum of solar activity (Sátori et al., 2005; Williams and Sátori, 2007). This effect is inherently non-uniform as only the sunlit portion of the lower ionosphere is affected by X-rays (and EUV radiation). It is to be noted that the long-term modulation of SR frequencies can be observed at all SR stations around the globe just as in the case of transient extra-terrestrial phenomena (X-ray bursts, solar proton events) discussed above.

In 2015 long-term SR intensity records from the Ukrainian Antarctic station "Akademik Vernadsky" were published which clearly showed a pronounced solar cycle modulation (up to 60%) of SR intensity (Nickolaenko et al., 2015), just as in an earlier paper by Füllekrug et al. (2002) using data from the Antarctic station Arrival Heights. Recently, Koloskov et al. (2020) reported that SR intensity records at the Vernadsky station are still in phase with the solar cycle and that a new SR station began operation at Svalbard in the Arctic in 2013 that also shows the solar cycle modulation of SR intensity. The origin of this effect is a challenging question as satellite observations do not show a solar cycle variation in the intensity and distribution of lightning activity (which is recognized as the primary origin of SR

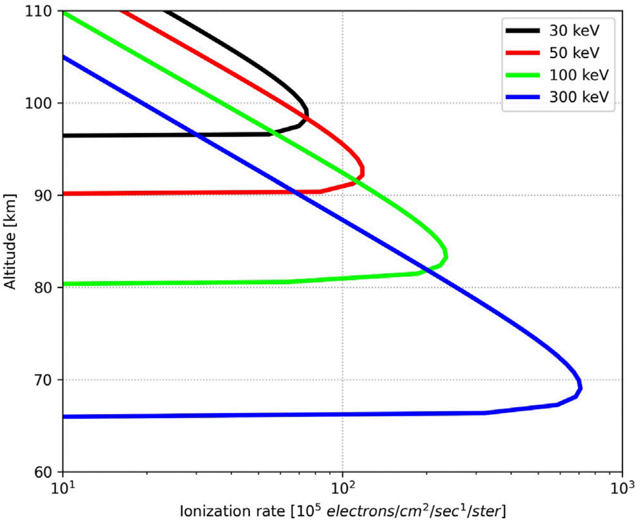

FIGURE 1 | Ionization rates versus altitude for monoenergetic electron flux based on the models described in Artamonov et al., 2017 and Mironova et al., 2019a.

intensity variations) (Christian et al., 2003; Williams et al., 2014; Williams, 2016). Furthermore, as highlighted above, there is little clear evidence reported in the literature so far regarding the direct influence of extra-terrestrial processes on SR intensity over shorter timescales which could form the basis of the longer-term modulation from the solar cycle. In studies by Williams et al. (2014) and Sátori et al. (2016) the authors argued that energetic electron precipitation (EEP) may account for the observed interannual SR intensity modulation by affecting the ionospheric height locally over the observer. As for the physical basis the authors suggested (following Sentman and Fraser, 1991) that the energy flux through the waveguide, parallel with the Earth's surface, must be conserved and when the local height is reduced by EEP, the magnetic field and attendant intensity must increase locally (a scenario illustrated in **Figure 9**). However, until now no direct evidence has been presented in the literature supporting the suggested EEP-effect on SR either on the solar-cycle or on shorter timescales.

Energetic particles are trapped in the magnetosphere in radiation belts (RBs). They are heated to relativistic energies (from several tens of keV up to the order of MeV) by various wave particle interactions (WPI), field line reconnection processes and large-scale electric fields (see e.g., Baker et al., 2018). Particle acceleration, as well as losses from pitch angle scattering into the atmosphere, can be intensified during geomagnetic storm periods in space weather events (Reeves et al., 2003). The characteristic timescale of single precipitation loss events reflects the duration of the causative source mechanism, and generally falls in the sub-second to hours range.

The expected effect of electron precipitation on SR depends in part on the characteristic penetration depth of the electrons into the atmosphere (Sátori et al., 2016) and the main factor determining the penetration depth of precipitating electrons is their energy (Rees, 1989), as illustrated in **Figure 1**. Model calculations (Artamonov et al., 2017; Mironova et al., 2019a) show that the upper ("magnetic") boundary of the Earth–ionosphere cavity resonator (near 90–110 km) (Sátori et al., 2005; 2016) is strongly affected by precipitating electrons in the 1–30 keV energy range. However, EISCAT incoherent scatter radar measurements show that the electron density can increase dramatically down to ~70 km during strongly ionizing EEP events (Belova et al., 2005; Miyoshi et al., 2015). This observation suggests that electrons in the energy range of 30–300 keV can influence the upper ("magnetic") boundary of the Earth–ionosphere cavity resonator as well (**Figure 1**). It is important to note that **Figure 1** illustrates only necessary conditions that energetic electrons will lower the local ionospheric height. Sufficient conditions involve the orders-of-magnitude increase in ionizing flux of energetic electrons, as discussed earlier for X-radiation (Williams and Satori, 2007).

The paper by Toledo-Redondo et al. (2012) is a pioneering work on long-term quasi-global variations in the night-time height of the Earth–ionosphere cavity. Based on the extraction of the waveguide cutoff frequency in DEMETER satellite observations, the authors showed that the effective height of the waveguide was anti-correlated with the solar activity between 2006 and 2009.

A collection of simultaneously recording ELF stations is needed to characterize the deformation of the Earth–ionosphere cavity. In this paper our first objective is to extend the published set of long-term SR intensity records by presenting new results from the high latitude (|lat| > 60°) stations: Hornsund (Svalbard), Syowa (Antarctica) and Maitri (Antarctica), from the mid-high latitude (50° < |lat| < 60°) stations: Eskdalemuir (United Kingdom) and Belsk (Poland), and from the low latitude (|lat| < 30°) station: Shillong (India), as well as an extended set of measurements from the high latitude Ukranian stations in the Arctic (Sousy) and Antarctic (Vernadsky). SR observations are compared with long-term fluxes of precipitating 30–300 keV electrons provided by the National Oceanic and Atmospheric Administration (NOAA) Polar Operational Environmental Satellites (POES) and with electron precipitation events identified in Super Dual Auroral Radar Network (SuperDARN) measurements in Antarctica (Bland et al., 2019). An extended set of the global waveguide's effective height, as observed in the survey electric field ELF-VLF spectra recorded by the French DEMETER satellite (Toledo-Redondo et al., 2012), is also presented and analyzed.

DATA AND METHODS

SR Data

In this paper we present long-term induction coil measurements from eight different SR stations which observe the variation of the horizontal magnetic field in the lowest part of the ELF band and analyze monthly average magnetic intensities of the first SR mode. **Figure 2** shows the location of the SR stations as well as the great circle paths (GCPs) of the wave propagation directions in which the coils are most sensitive. A common

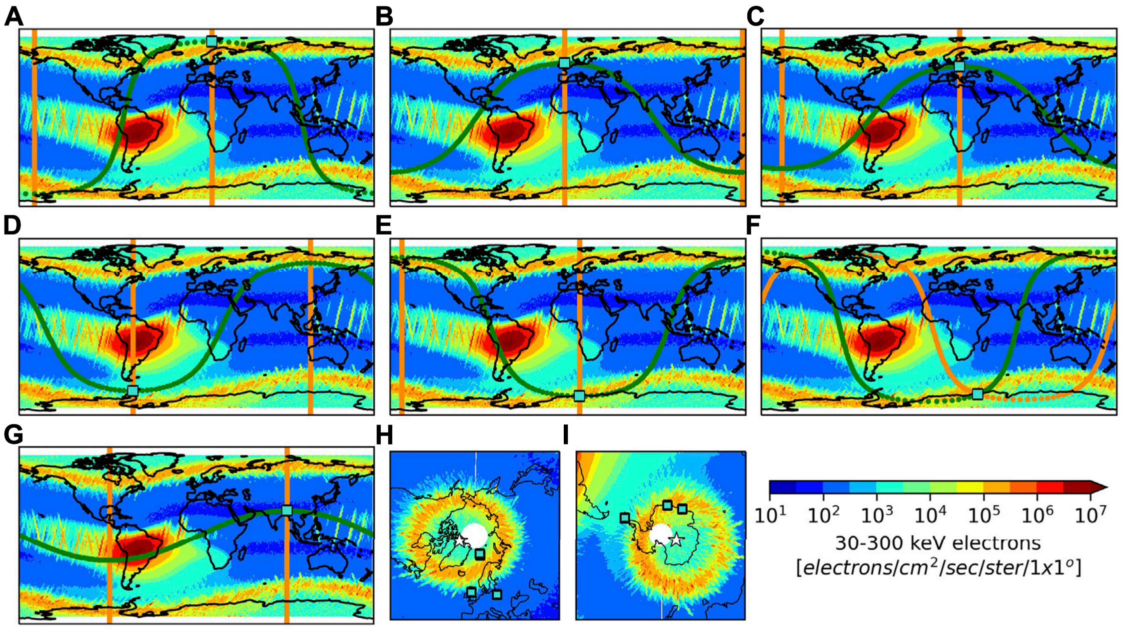

FIGURE 2 | The location of the **(A)** Hornsund (HRN)/Sousy (SOU), **(B)** Eskdalemuir (ESK), **(C)** Belsk (BEL), **(D)** Vernadsky (VRN), **(E)** Maitri (MAI), **(F)** Syowa (SYO) and **(G)** Shillong (SHI) SR stations (turquoise squares) and the wave propagation directions (great circle paths) for which the coils are the most sensitive (H_{NS} = green, H_{EW} = orange). Note that at the SYO station the coils are oriented along the geomagnetic north-south and east-west directions. The background world maps show the distribution of precipitated 30–300 keV electrons in 1 × 1 degree spatial resolution in 2005 (yielding the highest precipitation fluxes in the time interval investigated in this study) provided by the NOAA-15 satellite. The polar views (|lat| > 40°) of the Northern **(H)** and Southern **(I)** Hemispheres together with the location of the high- and mid-high latitude SR stations and the geomagnetic poles (white stars).

map is shown for the Hornsund and Sousy stations in **Figure 2** as these two stations are in close proximity (within 150 km, both at Svalbard) compared to the wavelength of ELF waves (of the order of 10 Mm). Induction coils are usually aligned with the local geographical meridian and perpendicular to it, except at the Syowa station where they are oriented along the geomagnetic north-south and east-west directions (**Figure 2F**).

The Institute of Geophysics of the Polish Academy of Sciences established SR measurements at the Polish Polar Station Hornsund at Svalbard (HRN; 77.0°N, 15.6°E; L = 14.0; **Figure 2A**) and at the Central Geophysical Observatory in Belsk, Poland (BEL; 51.8°N, 20.8°E; L = 2.2; **Figure 2C**) in 2004 and 2005, respectively (Neska et al., 2007; Neska et al., 2019). From the HRN station measured data were processed from September 2004 to October 2020. The main data gaps within this time period are: 06/2006-11/2007, 07-11/2008, 03/2009, 09/2009, 07-08/2011, 09/2015-03/2016 and 01-09/2017 (H_{EW}). From the BEL station the fully processed April 2005–December 2012 time period contains the following data gaps: 06/2005, 08/2005, 04-05/2006 and 01-02/2007. Since the entire dataset had been reprocessed for the present study we describe the applied data processing technique in detail.

Raw time series measurements were bandpass-filtered and 10-min estimates of average power spectral density (PSD) with a frequency resolution of ~0.2 Hz were generated by applying Welch's method (Welch, 1967). Welch's method estimates the PSD by dividing the data into overlapping segments, determining the PSD of each segment and averaging them. In order to minimize the aliasing effect of regional lightning activity and exceptionally intense lightning strokes generating Q-bursts (Guha et al., 2017) the PSD of data segments containing spikes greater than 40 pT in absolute value were omitted before averaging. From the obtained 10-min average PSD the intensity of the first SR mode was determined by means of the weighted average method (Nickolaenko et al., 2015). The peak frequency of the first mode (f_1) was calculated from the discrete PSD as:

$$f_1 = \frac{\sum_{6.5\,Hz}^{9.5\,Hz} f_k\, PSD_k}{\sum_{6.5\,Hz}^{9.5\,Hz} PSD_k}, \tag{1}$$

and the PSD of the nearest frequency value to this peak frequency was assigned as the intensity of the first SR mode.

SR measurements can easily be affected (contaminated) by different local noise processes (with natural and artificial origin), such as local lightning, wind, human activity, etc. (see e.g., Tatsis et al., 2021; Tritakis et al., 2021). In order to further improve the quality of the results a manual data sanitization step has been carried out before calculating the monthly averaged intensities. Our method relies on the evidence that the daily variation of SR intensity is usually highly similar within a month (Sátori, 1996). Therefore the intensity of the first SR mode was plotted as a function of UT time for all the days within the processed month and days with unusual daily intensity variation were excluded when calculating the monthly average.

SR measurements are carried out by the British Geological Survey at Eskdalemuir Observatory (ESK; 55.3°N, 3.2°W; L = 2.7; **Figure 2B**) near the Scottish Borders of the United Kingdom since September 2012 (Beggan and Musur, 2018; Musur and Beggan, 2019). For the present study processed data are available from June 2012 to December 2020 with a few gaps in the record. Details about the station and data processing can be found in Musur and Beggan (2019).

The Institute of Radio Astronomy (IRA) of the National Academy of Sciences of Ukraine established observations at two high latitude SR stations in the Arctic and in the Antarctic, respectively. The Arctic station is located at the Sousy facility of the Tromso Geophysical Observatory (the Arctic University of Norway, UiT) at Svalbard (SOU; 78.1°N, 16.0°E; L = 16.1; **Figure 2A**) and began operation in September 2013 while the Antarctic station is located in the Western Antarctic at the Ukrainian station "Akademik Vernadsky" (VRN; 65.25°S, 64.25°W; L = 2.6; **Figure 2D**) and began operation in March 2002. From the SOU station data are available from September 2013 to August 2020 with data gaps in 04/2014, 05/2014, 07/2016 while from the VRN station data are available from March 2002 to April 2020 with one long gap between 09/2009 and 03/2010. For more information about the stations and data processing we refer to the paper of Koloskov et al. (2020). Here we note only that data segments with distorted SR spectra were removed from the VRN and SOU databases before averaging. From the VRN station an extended dataset of the spectral intensity at 11 Hz (between the first and second resonance peaks) is also presented (Koloskov et al., 2020). Later in this study we show that a substantial portion of long-term SR intensity variations are related to changes in the quality factor (Q-factor) of the Earth–ionosphere cavity, which characterizes the rate of energy dissipation at a given resonance mode (Madden and Thompson, 1965; Kulak et al., 2003a). The investigation of spectral intensity between the first and second resonance peaks (near 11 Hz) is motivated by this observation as it is expected to have only a minor dependence on the Q-factor of the cavity. We note that recording at the frequency of about 11 Hz was originally proposed and implemented by Fraser-Smith et al. (1991a), Fraser-Smith et al. (1991b).

The Indian Antarctic station Maitri (MAI; 70.8°S, 11.7°E; L = 5.0; **Figure 2E**) is located in the Eastern Antarctic and SR data from the station are available from March 2010 to December 2019 with data gaps in 04/2018, 11-12/2018 (H_{EW}) and 11/2019. It is important to note that at the Maitri station the magnetic coils were oriented initially along the geomagnetic north-south and east-west directions. However, by the end of 2012 they were reoriented along the geographic main directions. In order to work with a homogeneous dataset and to be consistent with the other SR stations, SR intensity values from Maitri are shown only from January 2013 in the present study. For more information about the station we refer to the paper by Manu et al. (2015). Low latitude SR measurements are available from the Shillong station (SHI; 25.92°N, 91.88°E; L = 1.15; **Figure 2G**) in India (Rawat et al., 2012) from January 2008 to December 2016 with data gaps in 07/2008, 05/2014 and 01-04/2015. Raw SR measurements from SHI were processed with the same technique as described for the HRN and BEL stations.

The induction coil magnetometers at the Japanese permanent research station Syowa (SYO; 69.0°S, 39.6°E; L = 6.3; **Figure 2F**) were set up in February 2000 and processed data are available for the present study from January 2006 to December 2015 with data gaps in 03/2008, 07/2008, 06-07/2014 and 06-08/2015. At the SYO station the coils are aligned with the geomagnetic north-south and east-west directions (D = −48.5° in the year of installation). For more information about the station we refer to the paper by Sato and Fukunishi (2005). For the SYO data the same manual data sanitization process as for the HRN and BEL data has been applied.

EEP Observations

Satellite Measurements

The flux of precipitating E > 30 keV, >100 keV, >300 keV electrons is provided by the T0 telescope of the Medium Energy Proton and Electron Detector (MEPED) instrument (as part of the Space Environment Monitor 2 instrument package) onboard the NOAA-15 satellite (Rodger et al., 2010). Electrons that are detected by the T0 telescope (pointing outward along the local zenith) on the quasi-polar (98.70°), Sun-synchronous, low earth orbit (LEO) (~807 km) of the NOAA-15 satellite are in the atmospheric loss cone and will enter the atmosphere (Rodger et al., 2010). However, it is to be noted that the T0 telescope detects particles only near the center of the atmospheric loss cone and therefore underestimates the total flux of precipitating electrons (Rodger et al., 2010; van de Kamp et al., 2016; Mironova et al., 2019b).

To demonstrate the typical geographical configuration of the propagation paths (great circle paths) corresponding to the different SR stations and the electron precipitation-affected areas the distribution of precipitated 30–300 keV electrons (as a sum of the measured flux in the three corresponding channels of the T0 telescope) in 1 × 1 degree spatial resolution in 2005 (yielding the highest precipitation fluxes in the time interval investigated in this study) are displayed in the background in the subplots of **Figure 2**. As can be seen on the maps three main areas are affected primarily by electron precipitation: two high latitude, zonally continuous stripes in the Northern and Southern Hemispheres which we will refer to hereafter as precipitation belts, and the South Atlantic Magnetic Anomaly in South America. Five of the investigated SR stations (HRN, SOU, VRN, MAI, SYO) lie very close (within 1 Mm and << the wavelength of the ELF waves) to at least one of these areas. Furthermore, some propagation paths cross the South Atlantic Magnetic Anomaly. The great circle path corresponding to the H_{NS} component at the SHI station needs to be highlighted as well which does not cross the precipitation belts at all. Furthermore, the South Atlantic Magnetic Anomaly is also very far from this measuring site. Therefore, we do not expect EEP-related local SR intensity changes in this H_{NS} component.

SuperDARN Measurements

A list of EEP events derived from the Syowa East SuperDARN radar was used to identify individual EEP-related anomalies in our SR records in June 2011. Although SuperDARN radars are designed primarily for detecting plasma structures in the E and F region ionospheres (Greenwald et al., 1995; Chisham et al., 2007), they can also be used to estimate HF radio wave attenuation in the ionospheric D region using an approach similar to riometry (Bland et al., 2018). In this study we use the EEP event list for the Syowa East SuperDARN radar described in Bland et al. (2019). This radar is located in Antarctica at 69.00°S, 39.58°E (geographic), so all of the June 2011 events were observed under night-time/twilight conditions.

Sunspot Number and AE Index

The traditional sunspot number is used to characterize the magnitude and length of the solar cycles and to identify the year(s) of the maximum and minimum solar activities. The auroral electrojet (AE) index is a measure of geomagnetic activity in the auroral zone (Davis and Sugiura, 1966) and is often applied as an indicator for EEP activity (e.g., Lam et al., 2010). These datasets are available from the OMNIWeb database (https://omniweb.gsfc.nasa.gov/form/dx1.html).

X-Ray Observations

The 0.1–0.8 nm X-ray measurements of the Space Environment Monitor (SEM) instrument onboard the GOES 10 and 15 satellites is used to characterize solar radiation-related changes in the Earth–ionosphere cavity (Sátori et al., 2005; Sátori et al., 2016). Monthly average flux values were determined from the 1-min and 5-min resolution datafiles available from NOAA's corresponding database (https://satdat.ngdc.noaa.gov/sem/goes/data/avg/).

Satellite-Based Observations of Waveguide Cutoff

Long-term variation of the upper boundary region of the Earth–ionosphere cavity resonator is also investigated in this study by using satellite-based wave recordings. The lower ionosphere forms the highly variable reflecting upper surface of the Earth–ionosphere waveguide (EIWG). Since far from the source, lightning impulses propagate in a guided manner, the effective height of the EIWG (reflecting altitudes) can be observed as suppressions in wave field strength at higher ELF, lower VLF frequencies around the cutoffs of distinct wave modes (see modeling details in Cummer, 2000; Ferencz et al., 2007). This effect is best recognized in case of the 1st guided mode at approximately 1.6 kHz, exhibiting often a lower intensity band in the spectrum of single impulses as well as in time averaged dynamic power spectra of the cavity background field (Toledo-Redondo et al., 2012).

Due to the excitation of the lower ionosphere by waves in the EIWG with the above described character, the wide-band ELF-VLF wave records of LEO satellites also exhibit this specific spectral pattern. The electric field data of the French DEMETER satellite (Berthelier et al., 2006) with a polar LEO orbit has been utilized here to determine guided cutoffs, and thus to follow the change of the cavity's shape during approximately a quarter solar cycle period. Six years of night-time ELF-VLF spectra (whole years of 2005–2010) recorded at topside altitudes (660–710 km) between 65° geomagnetic latitudes have been analyzed. This uniquely rich, continuous ELF-VLF wave database is composed of power spectrum values under 20 kHz with 19.53 Hz resolution in frequencies and 2.048 s resolution in time (survey mode). Occurrences of wave power minima around the supposed cutoffs and their parameters (minimum frequency, sharpness, reliability factor) has been determined in consecutive spectrum vectors by applying a quadratic fit in the 1.4–1.95 kHz frequency range. The settings of the identifying algorithm have been fine-tuned by using a training set of several hundred of half orbits selected randomly from the whole recording base. In order to suppress noise and still maintain good spatial and temporal resolution, an averaged spectrum of eleven consecutive measurements was found optimal as input data. This step reliably finds the minima (if present) and yields approximately 1.5° spatial resolution in latitude. The effective height corresponding to the cutoff frequency is then determined by applying the condition for the transverse resonance (see e.g., Bliokh et al., 1977) of the waveguide (Toledo-Redondo et al., 2012):

$$h_{eff} = \frac{3 \cdot 10^8}{2 \cdot f_{cutoff}}. \qquad (2)$$

We present annual averages of the effective height for different latitudinal domains. Raw data consisting of satellite coordinates, times at the mid positions of the averaged recording set and the parameters of the identified effect were stored for later analysis. The investigated domains consist of various geomagnetic latitudes: low- ($|\mathrm{mlat}| < 20°$), mid- ($20° \le |\mathrm{mlat}| < 50°$) and mid-high ($50° \le |\mathrm{mlat}| \le 65°$). Data points corresponding to the South Atlantic Magnetic Anomaly (defined as $-50° \le |\mathrm{lat}| \le 0°$ and $-90° \le \mathrm{lon} \le 40°$) were excluded when calculating the yearly averages.

RESULTS

Results Based on SR Measurements

Multi-station Schumann resonance observations are used in this study to investigate long-term variations in SR intensity, selected year-to-year variations, and short-term variations attributable to single EEP events that affect both magnetic hemispheres. These topics are addressed in three separate sections below.

Long-Term Variations

Figure 3 displays the collection of SR intensity records available for the present study in the time window spanning about one and a half solar cycles between 2002 and 2020 (solar cycles 23 and 24) together with selected indicators of the solar and geomagnetic activity and of EEP. Subplot **Figure 3A** shows the monthly average values of the sunspot number, the AE index and the X-ray flux. The EEP flux of 30–300 keV electrons in daily (black) and monthly (red) time resolution are shown in **Figure 3B**. The EEP flux in daily time resolution is included to demonstrate its highly variable nature. The precipitation fluxes can vary by 3 orders of magnitude within a few days during geomagnetic

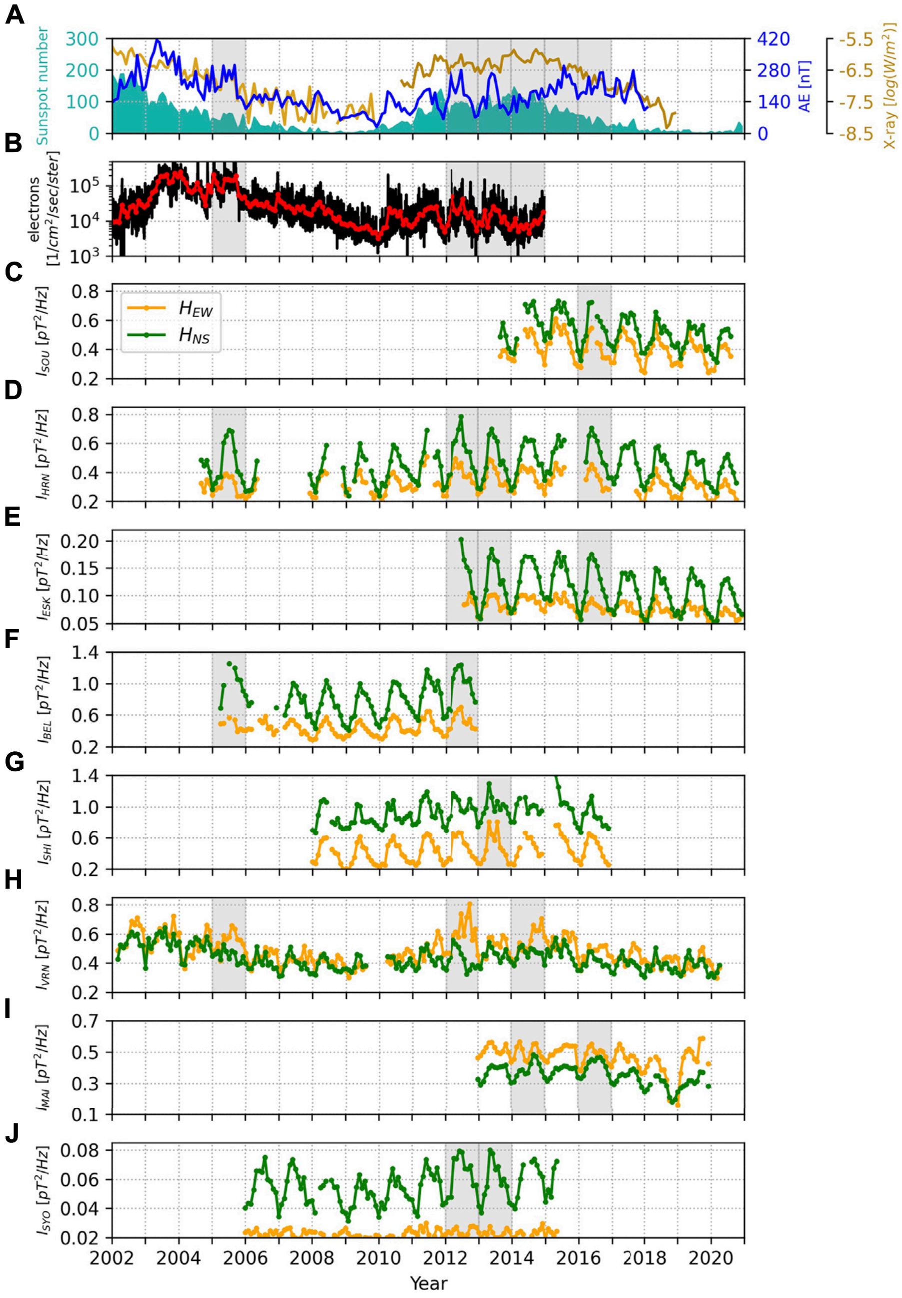

FIGURE 3 | (A) Monthly average values of the sunspot number (turquoise), the AE index (blue) and the X-ray flux (GOES-10: gold, GOES-15: dark gold), **(B)** 30–300 keV electron precipitation fluxes in daily (black) and monthly (red) time resolution as well as the long-term records of the first SR mode's intensity in monthly time resolution at the **(C)** Sousy (SOU), **(D)** Hornsund (HRN), **(E)** Eskdalemuir (ESK), **(F)** Belsk (BEL), **(G)** Shillong (SHI), **(H)** Vernadsky (VRN), **(I)** Maitri (MAI) and **(J)** Syowa (SYO) SR stations. Gray background highlights years with exceptional SR intensities.

storms (Clilverd et al., 2010). The long-term records of the first SR mode's intensity in the H_{EW} and H_{NS} magnetic field components are shown in monthly time resolution from the Sousy (SOU), Hornsund (HRN), Eskdalemuir (ESK), Belsk (BEL), Shillong (SHI), Vernadsky (VRN), Maitri (MAI) and Syowa (SYO) stations in **Figures 3C–J**. From the different stations SR data are available in the time windows described earlier in Section *Data and Methods*.

As can be seen in **Figure 3A**, the X-ray flux follows the time variation of the sunspot number in contrast to the AE index which has a distinct phase delay with respect to the solar maxima after 2002 and 2014/2015, and also shows extraordinary behavior in 2012 and in 2013 preceding the last solar cycle maximum in 2014. A good correlation is evident between the time series of the AE index and the 30–300 keV EEP fluxes as shown in **Figures 3A,B**. We note that a moderate annual variation is present in both

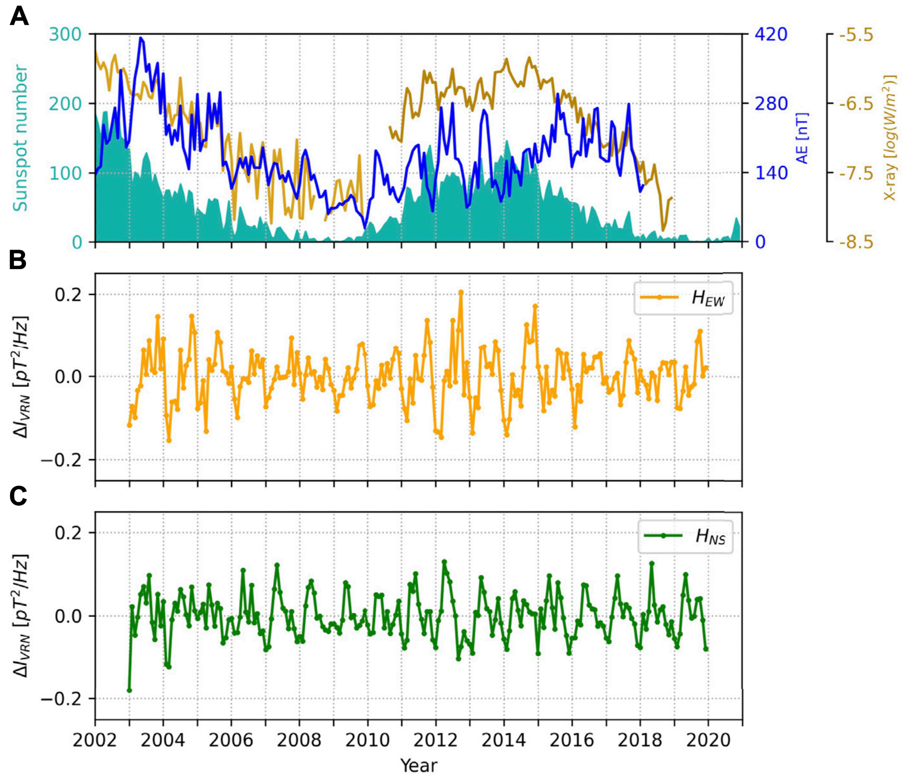

FIGURE 4 | (A) Monthly average values of the sunspot number (turquoise), the AE index (blue) and the X-ray flux (GOES-10: gold, GOES-15: dark gold) as well as the residual monthly average SR intensities for the **(B)** H_{EW} and **(C)** H_{NS} components at the Vernadsky (VRN) station (see the main text for more details).

parameters with Northern Hemisphere (NH) summer maxima as noted in earlier works (e.g., Suvorova, 2017; Lockwood et al., 2020).

The SR intensity records in **Figures 3C–J** show a complex behavior. On one hand a seasonal variation is present in the data with the highest intensity values usually observed in NH summer months. This general behavior is in accordance with the NH summer annual maxima in the magnitude of global lightning activity (Sátori, 1996; Christian et al., 2003). We also note the presence of semi-annual variations (with spring and autumn peaks) at some SR stations (Sátori and Zieger, 1996). The absolute level of SR intensity may show up to an order of magnitude difference station-by-station. We attribute this observation primarily to the different source-observer geometries but it could also hint to problems with the absolute calibration of the stations. Calibration issues are the most likely explanation for the eye-catching differences between the SR intensity records of the SOU and HRN stations which should be almost the same based on the close proximity of the stations.

On the other hand, the solar cycle modulation is evident at all SR stations and is in phase with the solar cycle (as indicated by the sunspot number). The solar cycle modulation of SR intensity is usually more pronounced in one of the magnetic field components: in the H_{EW} component at the VRN and SHI stations and in the H_{NS} component at the SOU, HRN, ESK, BEL, MAI and SYO stations. Years with exceptionally high SR intensities in these field components (in comparison with neighboring years) are highlighted with grey background in **Figures 3C–J**: 2016 at the SOU; 2005, 2012, 2013 and 2016 at the HRN; 2012, 2013 and 2016 at the ESK; 2005 and 2012 at the BEL; 2013 at the SHI; 2005, 2012 and 2014 at the VRN; 2014 and 2016 at the MAI and 2012 and 2013 at the SYO stations. These exceptional years in SR intensity, which can be found in the declining phase of the solar cycles (2005, 2015, 2016) or in the vicinity of the solar cycle maxima (2012, 2013, 2014), are in agreement with enhanced levels of EEP as indicated by the AE index and the 30–300 keV EEP fluxes. As the solar cycle modulation of SR intensity is clearly present at the two mid-high latitude stations (ESK and BEL) and at the one low latitude (SHI) station as well, the effect is not confined to high latitudes.

The magnitude of the annual variation in SR intensity tends to follow the solar cycle as well. This behavior is in keeping with the suggestion of the solar cycle modification of cavity height. Higher magnitudes can be identified in the years near the solar maxima and smaller ones near the solar minimum (see **Figures 3C–J**). This observation had been noted earlier for the total horizontal magnetic field by Koloskov et al. (2020). To take a closer look at this phenomenon we have removed the yearly averages from the VRN records for each (H_{NS}, H_{EW}) field component and plotted the residuals (ΔI) in **Figure 4**. The solar cycle modulation of the annual SR intensity variation is different for the two field

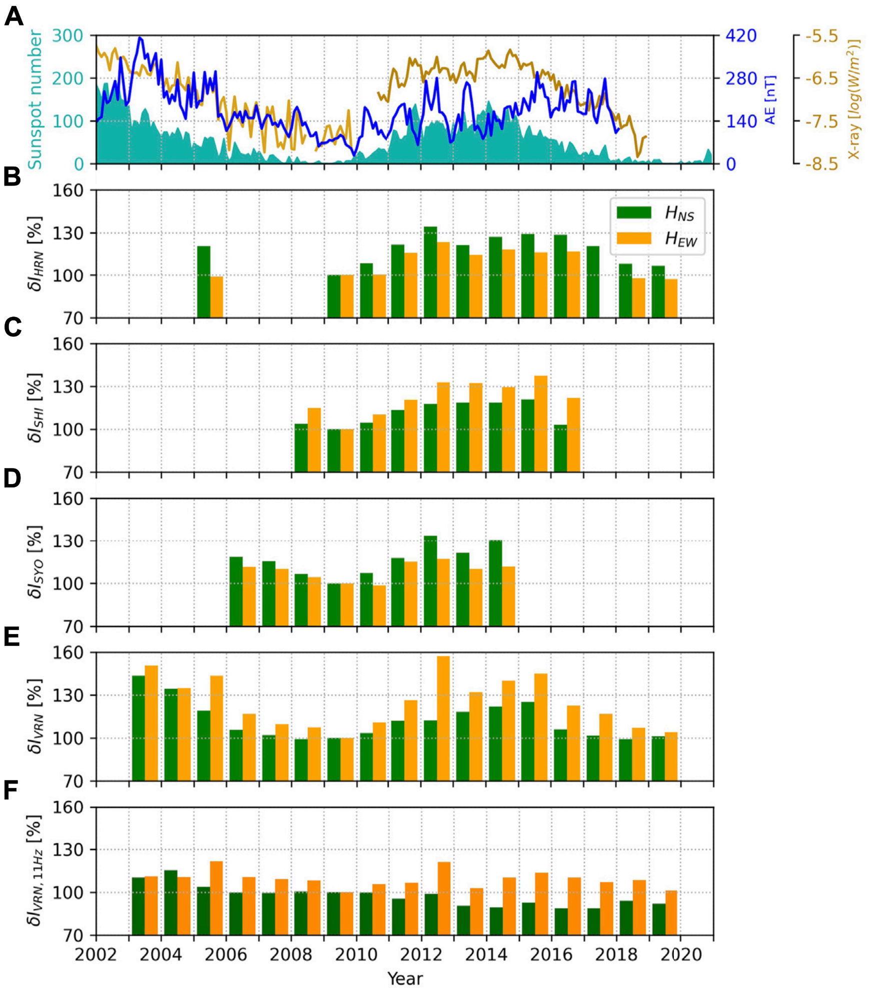

FIGURE 5 | (A) Monthly average values of the sunspot number (turquoise), the AE index (blue) and the X-ray flux (GOES-10: gold, GOES-15: dark gold) as well as the normalized yearly averages of the first SR mode's intensity at the **(B)** HRN, **(C)** SHI, **(D)** SYO and **(E)** VRN stations and **(F)** of the intensity at 11 Hz at the VRN station.

components at the VRN station. It is clearly more pronounced in the H_{EW} component for the one and a half solar cycle between 2002 and 2020. At the VRN station the H_{EW} component also shows the stronger modulation in its overall level (as compared to the H_{NS} component) (see **Figure 3H**). The magnitude of the annual variation in the H_{EW} component is the largest in 2012, second largest in 2014 and third largest in 2002. The smallest magnitude appears near the solar minimum in 2008. The solar cycle modulation of the H_{NS} component is considerably smaller. Nevertheless, the minimum in the magnitude of the annual variation near the solar minimum in 2008/2009 and the maximum near 2012 is clearly visible in the H_{NS} component as well.

In order to quantify the solar cycle modulation of SR intensity we derived yearly averages and normalized them with the intensity values corresponding to the solar minimum year 2009 (δI) for the four SR stations exhibiting the longest records: HRN, SHI, VRN and SYO (**Figure 5**). It follows that the 100% corresponds to the year 2009 for each component of each station in the figure. When calculating the yearly averages some missing values were determined with interpolation using the SR intensity values of the neighboring months (in case of 1 missing month) or based on the same months measured in the neighboring years (in case of >1 adjacent missing months). If neither of these two approaches was feasible for any year, that year was omitted. The long-term records of spectral intensity at 11 Hz are also displayed for each (H_{NS}, H_{EW}) field component from the VRN station in the same format.

As we stated earlier in this section, solar radiation-related changes in the Earth–ionosphere cavity are expected to follow the solar cycle (as indicated by the sunspot number) while EEP-related changes are expected to deviate from that cycle and to show a common behavior with the AE index. Next we investigate the normalized yearly average intensities displayed in **Figure 5** in this aspect. The relative SR intensity values corresponding to the first resonance mode generally follow the different phases of the solar cycle. However, this statement is rather true for the field component exhibiting smaller long-term variability (H_{EW} at

TABLE 1 | Normalized yearly averages of the first SR mode's intensity for the years 2005, 2009, 2012 and 2015.

Station	Component	2005 (%)	2009 (sol.min) (%)	2012 (%)	2015 (sol.max.) (%)
HRN	H_{EW}	100	100	125	115
HRN	H_{NS}	120	100	135	130
SHI	H_{EW}	—	100	135	140
SHI	H_{NS}	—	100	120	120
SYO	H_{EW}	—	100	120	—
SYO	H_{NS}	—	100	135	—
VRN	H_{EW}	145	100	160	145
VRN	H_{NS}	120	100	110	125

TABLE 2 | Normalized yearly averages of ELF intensity of 11 Hz at VRN for the years 2005, 2009, 2012, 2015.

Station	Component	2005 (%)	2009 (sol.min) (%)	2012 (%)	2015 (sol.max.) (%)
VRN (11 Hz)	H_{EW}	120	100	120	115
VRN (11 Hz)	H_{NS}	105	100	100	90

HRN and SYO, H_{NS} at SHI and VRN) while in the more variable field component (H_{NS} at HRN and SYO, H_{EW} at SHI and VRN) the largest intensity enhancements are present in years of AE extremities like in 2005, 2012 and 2015. In these years, intensity enhancements of ~20–35% can be observed at the HRN, SHI and SYO stations while at the VRN station (showing the largest variation in intensity) the enhancements are as high as 40–60% (**Table 1**). We also note that the long-term record of the VRN station mirrors the magnitude difference between solar cycle 23 and 24, i.e. higher intensity values correspond to previous one. The year of 2012 yields the highest relative SR intensity values at all four SR stations. Regarding the relative SR intensity values corresponding to 11 Hz at VRN the H_{EW} component shows enhanced values (~20%) in the years of AE extremities (2005 and 2012) (**Table 2**) while the H_{NS} component exhibits a general decreasing trend throughout the investigated time period. The origin of this decreasing trend in the data is not clear at the moment.

Year-to-Year Comparisons

As confirmed by **Figure 5**, it is not always the solar cycle maximum that yields the highest SR intensity values. This observation is in accordance with electron precipitation fluxes presented in **Figure 3B**. In **Figure 6** we present the electron precipitation conditions for the Northern and Southern polar regions in the solar minimum year 2009, the solar maxima years 2002 and 2014 as well as in selected years with exceptionally high SR intensity values: 2005 and 2012, based on NOAA-15 electron precipitation fluxes. In general, the yearly averaged flux values go up and down together in all regions affected by EEP in the selected years. The year 2005 is in the declining phase of the 23rd solar cycle while 2012 is close to the last solar maximum year of 2014. Electron precipitation is clearly the weakest in the solar minimum year of 2009 as expected. However, only a small (less than one order of magnitude) increase is noticeable from 2009 to the solar maximum year of 2014. The solar maximum year of 2002 yields larger fluxes than the solar maximum year of 2014 (around one order of magnitude larger compared to the solar minimum year of 2009). On the other hand, a remarkable increase of electron precipitation flux is identifiable in the selected years 2005 and 2012 yielding exceptionally high SR intensity values as well. The enhancement is around two orders of magnitude in 2005 as compared to the solar minimum year of 2009. This robust change in EEP flux is of the same order of magnitude as the variation of solar X-rays on the solar cycle timescale (**Figure 5A**) (Sátori et al., 2005; Williams and Sátori, 2007).

Short-Term Variations Synchronous in Two Hemispheres

The well-organized motions of energetic electrons along the magnetic field lines suggest that EEP events and their associated cavity deformation may often be quasi-synchronous in the Northern and Southern Hemispheres. **Figure 7** shows SR intensity records for two selected days from June 2011 (14 June and 23 June) together with independently identified EEP events based on Syowa East SuperDARN radar measurements from the event collection of Bland et al. (2019). To identify non-standard (not lightning-related) variations in the diurnal SR intensity records, quiet day diurnal SR intensity curves were determined for each field component of each station for June 2011. Quiet days were selected based on the AE index as days with AE values smaller than 400 nT. **Figure 7** contains the average diurnal variation of these quiet days and in addition the corresponding standard deviations. In order to investigate whether EEP events are able to modify the global Q-factor of the Earth–ionosphere cavity resonator we applied the Lorentzian fitting technique (see e.g., Mushtak and Williams, 2002) on SR spectra from the Hornsund station. In **Figure 7** the extracted Q-factors are displayed in the same format as the SR intensity records.

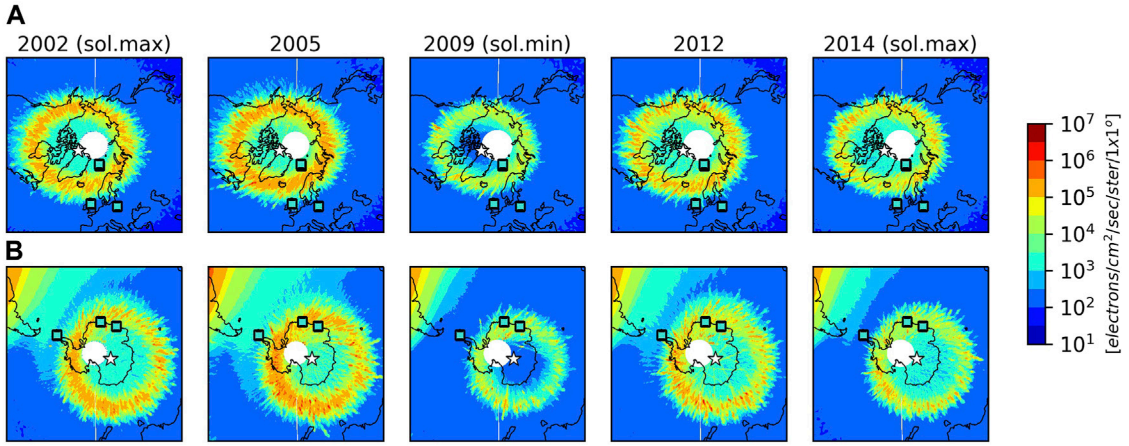

FIGURE 6 | The distribution of precipitated 30–300 keV electrons for the Northern **(A)** and Southern **(B)** polar regions for the years 2002, 2005, 2009, 2012 and 2014, together with the location of the high and mid-high latitude SR stations and the geomagnetic poles (white stars).

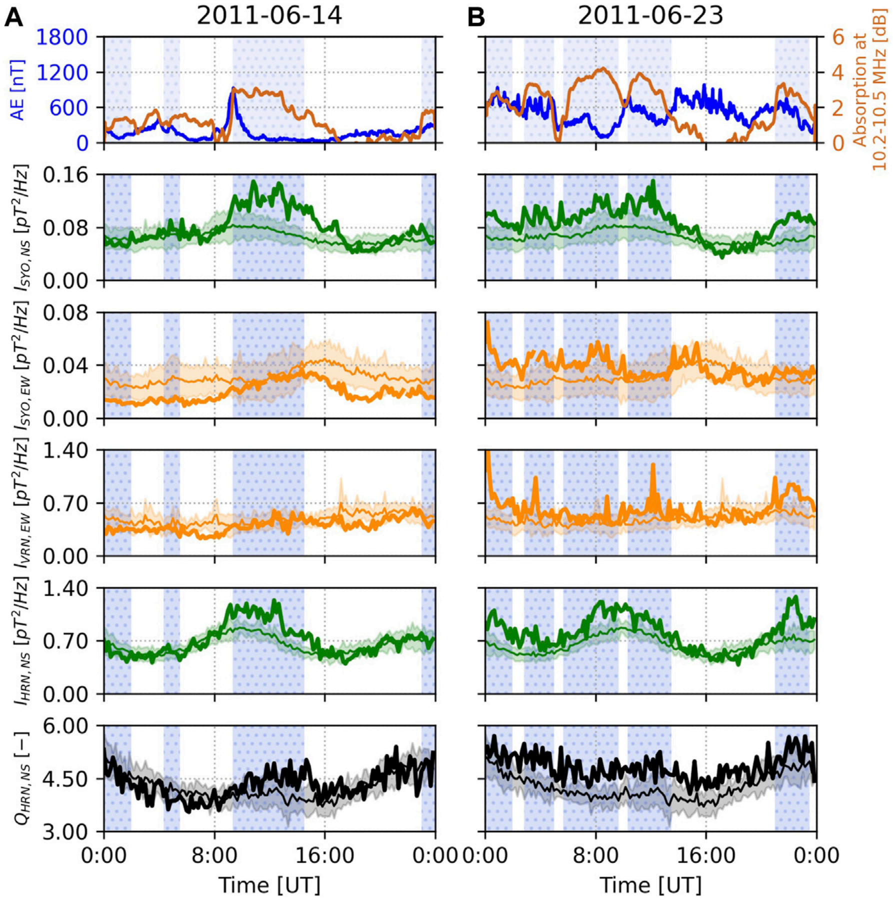

FIGURE 7 | Comparison of EEP events (with respective time intervals shaded and dotted) identified in Syowa East SuperDARN radar measurements by Bland et al. (2019) and SR intensity records (H_{EW}: orange, H_{NS}: green) for June 14, 2011 **(A)** and June 23, 2011 **(B)**. The top row shows the time variation of the AE index (blue) and the radio wave absorption values in the D-region (red) at 10.2–10.5 MHz as inferred from the radar measurements. SR intensity records from the SYO, VRN and HRN stations for the selected days (thick curves) are displayed together with the average diurnal variation of quiet days (thin curves in same color) and the corresponding standard deviations (same color shaded area) (see the main text for more details). The last row of the figure shows Q-factor records from the HRN station that tend to be enhanced during EEP events.

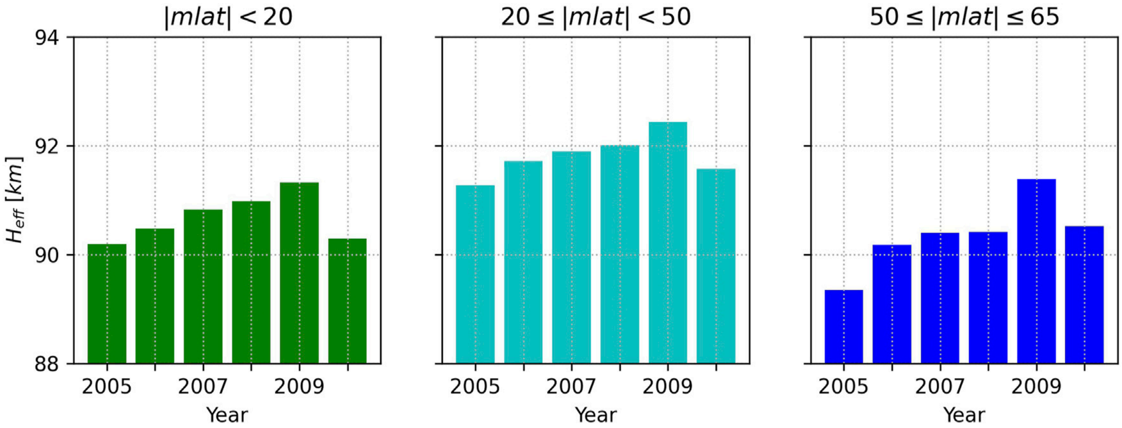

FIGURE 8 | Yearly averages of the Earth–ionosphere waveguide's effective height based on DEMETER observations. A similar solar cycle modulation is evident in each of three latitude ranges.

On June 14, 2011 the strongest EEP event within the day can be observed between 09:20 and 14:30 UT at Syowa with radio wave absorption values greater than 2 dB (**Figure 7A**). The event starts with a substantial increase of the AE index. SR intensity clearly increases during the event not only in the H_{NS} component at Syowa (so near the radar) but in the Northern Hemisphere under daytime conditions at the Hornsund (HRN) station as well where increased Q-factor values (by ~10–30%) can be observed during the event. The relative increase of SR intensity is as large as 50–100% at Syowa during this event. On June 23, 2011 several strong (absorption >3 dB) EEP events occured between 00:00 and 13:00 UT and one other event can be observed between 21:00 and 23:30 UT. The imprint of these events can be identified in both field components at SYO, in the H_{NS} component at HRN (with increased Q-factor values by ~10–30%) as well as in the H_{EW} component at Vernadsky (VRN), even though the VRN station lies in a considerably different longitudinal sector than Syowa. This documented synchronous behavior provides evidence for the large spatial extents of the EEP events (~4 h magnetic local time extent).

Results Based on DEMETER Measurements

The effective height of the Earth–ionosphere waveguide as inferred from DEMETER satellite measurements of the waveguide cutoff frequency at night-time (see Section *Satellite-Based Observations of Waveguide Cutoff* for details) can be regarded as a quantity providing an independent view on the deformation of the Earth–ionosphere waveguide. **Figure 8** shows the yearly average values of the effective height from 2005 to 2010 corresponding to low-, mid- and mid-high geomagnetic latitudes.

In general, the Earth–ionosphere waveguide height seems to be the lowest at mid-high latitudes while it is the highest at midlatitudes with average height values of 90.4 and 91.8 km, respectively. The effective height is also smaller at low latitudes (90.7 km) as compared to midlatitudes (91.8 km). Regarding the long-term trend in the data, the solar cycle variation is evident in all the investigated domains. **Table 3** summarizes the relative height differences between 2005 and the solar minimum year of 2009 for low-, mid- and mid-high geomagnetic latitudes. The relative height difference is the greatest at mid-high latitudes (which represent the highest observed latitudes in this case) (2.2%) and the smallest at low latitudes (1.2%).

TABLE 3 | Relative differences in the waveguide's effective height between 2005 and the solar minimum year of 2009 for low-, mid- and mid-high geomagnetic latitudes.

|mlat| < 20°	20° ≤ |mlat| < 50°	50° ≤ |mlat| ≤ 65°
1.2%	1.3%	2.2%

DISCUSSION

In this section, we suggest a general interpretation for the results obtained, before attempting to estimate the height changes of the Earth–ionosphere cavity associated with EEP. Finally, we describe the most important characteristics of our SR- and DEMETER-based results.

Solar X-Rays and EEP: The Two Main Effects to be Considered

In order to interpret correctly the obtained results it is first important to state that although SR intensity variations are generally connected with changes in the distribution and/or intensity of global lightning activity, satellite observations of lightning activity do not show any significant solar cycle variation on the global scale (Christian et al., 2003; Williams et al., 2014). This is in line with the observation that the total

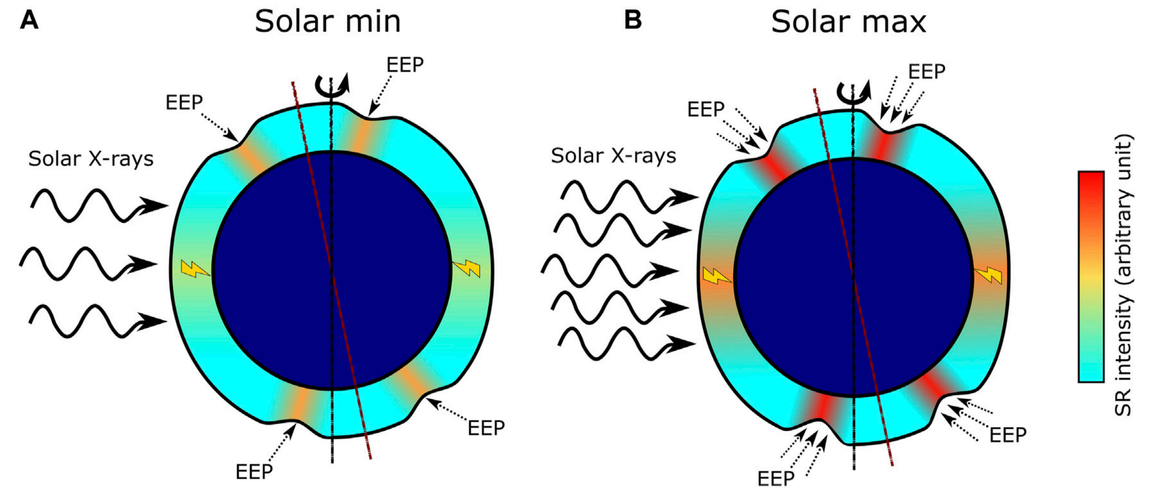

FIGURE 9 | Illustration of the deformation of the Earth–ionosphere cavity at solar minimum **(A)** and solar maximum **(B)**. At solar maximum X-rays and EEP reduce the cavity height more significantly (dominantly over low- and high latitudes, respectively) which results in enhanced SR intensity values beneath the deformed regions.

energy output from the Sun varies on the order of 0.1% throughout the solar cycle (Fröhlich and Lean, 1998). Therefore, the solar cycle modulation of SR intensity needs to be accounted for by long-term changes in the Earth–ionosphere cavity, i.e., by changes in the propagation conditions of ELF waves. As the solar cycle variations in Galactic Cosmic Rays (GCR) is considered to have only a negligible effect (<1%) on the intensity SR (Sátori et al., 2005) hereafter we discuss the possible effects related to the Sun.

Two fundamental mechanisms can be distinguished for the Sun-related impact on the near-Earth environment: one based on photons and the other on charged particles. The majority of solar photons arrive in the Earth's equatorial zone while charged particles precipitate in the upper atmosphere in the high latitude precipitation belts and in the South Atlantic Magnetic Anomaly (**Figure 2**). The long-term behavior of these two effects is markedly different on the solar cycle timescale. While the flux of solar photons generally follows the solar cycle, the precipitation of charged particles does not (Asikainen and Ruopsa, 2016) (**Figure 3**). We documented both of these behaviors in long-term SR intensity records of different field components at different stations (**Figure 5**). Therefore, we suggest that a combined effect of photons and charged particles needs to be considered to account for all our SR-based observations (as illustrated in **Figure 9**).

The long-term solar cycle modulation of the Earth–ionosphere cavity by solar X-rays had been first documented by Sátori et al. (2005) based on long-term SR frequency records. Both SR frequencies and Q-factors observed at different stations exhibited maxima during the two solar maxima in 1992 and 2002 and minima in 1996. The observed variations were interpreted on the basis of a uniform cavity and the presence of two characteristic ionospheric layers (Greifinger and Greifinger, 1978; Mushtak and Williams, 2002). The height and scale height of the lower (electric) layer were considered to be invariant over the solar cycle while for the upper (magnetic) layer the authors inferred a height decrease of 4.7 km and a scale height decrease from 6.9 to 4.2 km for the first SR mode from solar maximum to solar minimum. These changes result in an increase of the resonator's Q-factor by 12–15% (Sátori et al., 2005). The intensity of a damped simple harmonic oscillator is known to be proportional to the square of its Q-factor (Feynman et al., 1963), in agreement with the theoretical description of SR (Nelson, 1967, Eqs 2–24; Williams et al., 2006). It follows that a 12–15% change in the Q-factor of the Earth–ionosphere cavity can result in a 25–30% increase of the first SR mode's intensity. This estimate is in agreement with the relative SR intensity values corresponding to the H_{NS} component at the SHI and VRN stations (**Figure 5**). As the Q-factor is a general property of the Earth–ionosphere cavity this effect should contribute to the long-term SR intensity variation at all SR stations around the globe.

The phenomenon involving charged particles deposited into the atmosphere through various heliophysical and geomagnetic processes is called energetic particle precipitation (EPP). EPP covers a wide variety of charged particles but protons and electrons are the two main constituents to be considered with significantly high fluxes (Mironova et al., 2015). As it has been stated in earlier works (Williams et al., 2014; Sátori et al., 2016) proton events are too sporadic in time to yield the observed persistent long-term modulation of SR intensity. Therefore, we consider the precipitation of electrons hereafter which is usually referred to as energetic electron precipitation (EEP).

The expected effect of EEP on SR strongly depends on the characteristic penetration depth of the electrons into the atmosphere. SR are primarily responsive to two specific altitude regions where the ionospheric dissipation is predominant (Sátori et al., 2016). These are usually referred to as the electric (capacitive) and magnetic (inductive) heights (Madden and Thompson, 1965; Greifinger and Greifinger, 1978) to be found at around 50–60 km and 90–110 km altitudes, respectively (Mushtak and Williams, 2002; Greifinger

TABLE 4 | Observed SR intensity variations at the VRN station in the H_{EW} field component and the predicted contributions of global Q-factor- and local ionospheric height changes.

	Observed (%)	Q-factor related (%)	Height change related (%)
First SR mode	40–60	25–30	15–30
11 Hz	20–25	~0	20–25

et al., 2007; Kulak and Mlynarczyk, 2013). The main factor determining the penetration depth of precipitating electrons is their energy (**Figure 1**). Model calculations show that the magnetic height can be affected by electrons in the 1–30 keV energy range while the electric height only by electrons with energy above 300 keV (Rees, 1989; Sátori et al., 2016; Artamonov et al., 2017; Mironova et al., 2019a). However, EISCAT incoherent scatter radar measurements show that in connection with EEP the isopycnic surfaces of electron density can occasionally descend by some tens of kilometers in the high latitude D- and E-region (Belova et al., 2005; Miyoshi et al., 2015). To account for such a large decrease in the SR magnetic height the effect of 30–300 keV electrons needs to be considered as well. Generally, it is true that the lower the energy of electrons the higher the precipitated flux and the more continuous the precipitation in time (Lam et al., 2010). Therefore, to account for the long-term modulation of SR intensity, electrons in the 1–300 keV energy range (affecting the magnetic height of SR) are the best candidates. This energy range covers both auroral and radiation belt electrons (Mironova et al., 2015). EEP is expected to affect the height of the Earth–ionosphere cavity and the measured magnetic field locally where precipitation occurs consistent with the conservation of energy flux (Sentman and Fraser, 1991; Williams et al., 2014; Sátori et al., 2016). A permanent local decrease in the magnetic height is expected to modulate the amplitudes of all natural variations in SR intensity on all timescales as shown for the magnitudes of the annual variation in **Figure 4**.

We also showed that EEP events are able to modify the Q-factor of the Earth–ionosphere cavity (**Figure 7**) which is in line with our observation that they can affect both hemispheres as well as large longitudinal regions. This effect may result in globally observable changes in SR intensity but this aspect needs to be investigated further in the future. It is possible that the long-term 12–15% change in the Q-factor of the Earth–ionosphere cavity documented by Sátori et al. (2005) may involve EEP-related changes as well.

Two important pieces of evidence were shown in this paper for an EEP-related deformation of the Earth–ionosphere cavity. First, exceptional increases of SR intensities were documented in certain years, as in 2005 and 2012 (**Figure 5**), which are not solar maximum years, but are characterized by enhanced electron fluxes (**Figure 6**). Based on satellite observations Asikainen and Ruopsa (2016) reported on enhanced electron precipitation at >30 and >100 keV fluxes related to Coronal Mass Ejections (CMEs) in 2005 and 2012 which is in agreement with our findings. Second, direct observation of EEP-related SR intensity enhancements were presented at widely separated SR stations on two selected days in June 2011 (**Figure 7**).

Estimating the Long-Term Ionospheric Height Changes Associated With EEP

In this section we estimate the long-term average ionospheric height changes associated with EEP for the H_{EW} component at the VRN station yielding the highest intensity variation on the solar cycle timescale (40–60%) (**Table 4**). If we accept that 25–30% of the observed SR intensity enhancement is attributable to a global change of the cavity's Q-factor (independently of whether this change is related solely to X-rays or to EEP as well) the remaining 15–30% in years with the largest enhancement can be considered to be related to the local waveguide deformation caused by EEP.

We estimate the EEP-related height changes of the waveguide from the intensity at 11 Hz (the first minimum between the first and second resonance peaks) which can be considered to be mostly unaffected by the Q-factor of the cavity. Greifinger et al. (2005) have made predictions for changes in the SR amplitude as a function of the ionospheric height above the source and above the observer in the form of symbolic equations. According to these equations the measured magnetic intensity at a given frequency is proportional to the reciprocal value of the squared local magnetic height. It follows that the 20–25% intensity enhancements documented at 11 Hz in 2005 and 2012 (which are in a good agreement with the resonance mode-based estimation of 15–30%) correspond to an average magnetic height decrease of ~10% at VRN.

This average decrease in the magnetic height is considerably smaller than the decrease of isopycnic surfaces during an EEP event as observed by the EISCAT radar, with enhanced ionization down to ~70 km (e.g., Miyoshi et al., 2015). Although EEP events are very common especially near solar maximum and can result in SR intensity enhancements in order of 50–100% (as shown in **Figure 7**), they are not permanent and each event is often confined to a limited longitudinal range (Clilverd et al., 2007; Bland et al., 2021). Therefore, the smaller percentage average increase of SR intensity and the inferred decrease in the magnetic height is reasonable on the interannual timescale.

Interpretation of SR-Based Results

As can be seen in **Figure 5** and **Table 1** the solar cycle modulation of SR intensity can be different station-to-station depending on the station location and on the wave propagation path corresponding to the measured field component. A deformation in the Earth–ionosphere cavity is expected to affect SR intensity locally where the deformation occurs, whereas a change in its Q-factor is expected to affect SR intensity (I) globally, for all propagation paths that cross the affected area(s). As we stated earlier, we aimed to describe these effects by two simple formulas:

$$I \sim Q^2 \tag{3}$$

and

$$I \sim \left(1/H_m^2\right) \tag{4}$$

where Q and H_m denote the Q-factor of the cavity and its local magnetic height, respectively. The solar cycle modulation of the H_{NS} field component at the SHI and VRN stations can be well described by the X-ray-related global variation of the cavity's Q-factor and the H_{EW} field component at the VRN station by the combined effect of the Q-factor variation and an EEP-related height decrease of ~10%.

At different SR stations the wave propagation directions corresponding to the perpendicular magnetic coils are differently affected by EEP. It seems to be generally true that the longer the propagation path crosses the precipitation-affected area(s) the larger the solar cycle modulation of SR intensity. It is usually the H_{NS} coil, sensitive to the east-west propagation direction, which yields propagation paths with greater extents beneath the precipitation belt. This is the case for the high latitude SOU, HRN, MAI and SYO stations (see **Figures 2A,E,F**) where the solar cycle modulation is indeed larger in the H_{NS} component as compared to the H_{EW} component (**Figures 3**, **5**). The H_{NS} coil is also more responsive at the two mid-high latitude SR stations ESK and BEL in spite the fact that the GCPs corresponding to the H_{NS} component at these two stations do not cross the northern precipitation belt according to **Figures 2B,C**. This result may indicate that the precipitation belts are more extended towards lower latitudes as shown by the POES data. Towards lower latitudes the flux of precipitating 30–300 keV electrons decreases and POES is known to underestimate flux values below ~10^4–10^5 electrons/cm^2/sec/ster (van de Kamp et al., 2016; van de Kamp et al., 2018).

The magnetic height of SR is affected by electrons with energies lower than 30 keV (the lowest channel of POES satellites) and these electrons may form wider precipitation belts. At the VRN and SHI stations the SR response is more pronounced in the H_{EW} coil, sensitive to the north-south propagation direction. At SHI the H_{EW} is the one field component with a GCP crossing the precipitation belts (**Figure 2G**) while at VRN the propagation path corresponding to the H_{EW} component meets not only the southern precipitation belt but the South Atlantic Magnetic Anomaly as well (**Figure 2B**). Besides the dominant response of the H_{EW} component as compared to the H_{NS} component this fact may account for the observation that the H_{EW} component at the VRN station yields the highest response among all the investigated records. Another factor that should be important for this observation is that the longitudinal sector including America is shown to be affected by harder electron precipitation spectrum than the other parts of the globe which can be attributed to the tilted-offset dipole magnetic field of Earth (Clilverd et al., 2007). We note that 2012 shows the highest relative SR intensity values at the HRN and VRN stations (**Figure 5**; **Table 1**) despite the observation that POES measurements show larger EEP fluxes in 2005 as compared to 2012 (**Figure 6**). We can explain this observation by the fact that in 2012 both X-rays and EEP show enhanced values while 2005 is in the declining phase of the solar cycle characterized by a lower X-ray flux (**Figures 3A,B**).

As we noted earlier in Section *Results* EEP is known to have seasonal dependence (Clilverd et al., 2007; Suvorova, 2017; Bland et al., 2019), i.e., June/July maxima in its occurrence rate can be identified in both hemispheres. We note that rocket measurements at polar stations also showed maximum electron density in June/July at the 80 km height of the ionospheric D-region in both hemispheres (Danilov and Vanina, 1999). We suggest that this seasonal dependence may contribute to the observed modulation of the magnitude of the annual SR intensity variation (**Figure 4**).

Interpretation of DEMETER-Based Results

DEMETER observations showed that the effective height of the Earth–ionosphere waveguide is generally the highest at mid geomagnetic latitudes, lower at low geomagnetic latitudes and the very lowest at the highest observed geomagnetic latitudes (in proximity to the precipitation belts) (**Table 3**) which is in a general agreement with our SR-based findings that the Earth–ionosphere cavity is deformed by solar X-rays (dominantly over lower latitudes) and by EEP (dominantly over higher latitudes) (as illustrated in **Figure 9**). The deformation effect of EEP has a larger variability on the solar cycle timescale which results in a larger height reduction at higher latitudes as shown by the effective heights. This finding is in keeping with the high latitude location of the precipitation belts. Although the documented 2.2% height decrease between 2005 and 2009 corresponding to mid-high latitudes is considerably smaller than the ~10% value inferred for the VRN station, one needs to keep in mind that 1) DEMETER data are restricted to geomagnetic latitudes lower than 65°, 2) the South Atlantic Magnetic Anomaly (which is in close vicinity to VRN) is excluded from the dataset, 3) electromagnetic waves with higher ELF, lower VLF frequencies are responsive at different altitude regions than the magnetic height of SR and 4) this is an integrated value for all longitudes while the longitudinal sector including America is shown to be affected by harder electron precipitation.

It is to be noted as well that the inferred effective height values were measured exclusively on the nightside by DEMETER at 22:30 LT where solar X-rays are absent. We can explain this seeming contradiction by assuming that lightning impulses may propagate in the dayside hemisphere of the EIWG before escaping the waveguide on the nightside (but close to the local sunset).

CONCLUSIONS

In the present study long-term records of the first SR magnetic mode intensity from eight different stations were compared with the fluxes of precipitating medium energy electrons and with independently identified EEP events to confirm that the long-term solar cycle modulation of SR intensity (documented originally at high latitude stations) is caused by the EEP-related local deformation of the Earth–ionosphere cavity. Although our results generally confirmed the presence of EEP-related deformations in the Earth–ionosphere cavity, we also found that the EEP-effect alone cannot account for all our SR-based observations and that the combined effect of solar X-rays and EEP needs to be considered. We have identified four distinct factors that can play important role in shaping long-term SR intensity records: 1) X-ray related deformations of the cavity, 2) X-ray related changes in the Q-factor of the cavity, 3) EEP-related deformations of the cavity and 4) EEP-related changes in the Q-factor of the cavity. The exact interplay of these factors depends on the location of the SR station and the orientation of the magnetic coils, i.e., on the wave propagation path corresponding to the actual measurement. The deformation of the cavity is expected to affect SR intensity locally beneath the deformed area(s) whereas Q-factor variations are expected to introduce globally observable changes in SR intensity.

In connection to EEP we showed that there is a very good phase agreement between certain SR intensity records and the long-term variation of 30–300 keV EEP fluxes as provided by the POES NOAA-15 satellite which is most conspicuous in years not exactly coincident with the solar maximum, as in for example 2005 and 2012 when both the EEP flux and SR intensity showed exceptional values. We documented SR intensity and Q-factor enhancements connected to individual EEP events on the daily timescale in June 2011 by comparing the corresponding records with EEP events independently identified by Bland et al. (2019) in the measurements of the Syowa East SuperDARN radar. We showed that the effect of certain EEP events can be identified in SR intensity records from both the Southern and Northern Hemispheres (under different sunlit conditions), from different longitudinal sectors and the EEP-related relative enhancement of SR intensity can attain values as high as 50–100%. The solar cycle modulation of the magnitude of the annual SR intensity variation was demonstrated and efforts were made to quantify the ionospheric height changes associated with EEP. It has been shown that near the Antarctic station Vernadsky (yielding the largest long-term SR intensity variation) the upper (magnetic) characteristic height of the Earth–ionosphere cavity resonator decreased by ~10% in the most conspicuous years of EEP activity.

This paper is the first one to show that the solar cycle variation of SR intensity is consistently observable all around the globe and gives a qualitative explanation for this observation. Quantitative conclusions were made as well based on simple SR intensity—cavity height, SR intensity—Q-factor relations, which describe the identified effects reasonably well. To achieve a more detailed interpretation of our observation-based results it is necessary to apply a full model of the SR. We hope that our work will motivate and assist such works in the future.

The effective height of the Earth–ionosphere waveguide as inferred from DEMETER measurements provided an independent view on the long-term deformation of the Earth–ionosphere cavity. We showed that the largest height of the cavity can be found at mid (geomagnetic) latitudes while the waveguide is depressed at low and high (geomagnetic) latitudes which is in a general agreement with our general conclusion that the Earth–ionosphere cavity is deformed by solar X-rays dominantly over lower latitudes and by EEP dominantly over higher latitudes. It has also been demonstrated that effective height of the waveguide varies on the solar cycle timescale at all (geomagnetic) latitudes and this effect is stronger at high (geomagnetic) latitudes where energetic electrons can enter along magnetic field lines.

We suggest that SR measurements may be suitable to collect information and thus to monitor changes in the lower ionosphere associated with EEP which would be highly valuable for investigating space weather processes and their impact on atmospheric chemistry (see e.g., Mironova et al., 2015; Duderstadt et al., 2021). Such measurements could yield quasi-continuous information on EEP in a global sense in contrast to the space and time limitations of satellite and radar observations.

Finally, the value of high latitude stations for SR-based research should be emphasized. Due to their remote locations, these SR stations have usually much lower cultural noise contamination than stations at low- and mid-latitudes. And because they are also remote from thunderstorm activity they are not subjected to the interference caused by nearby lightning. These two properties make high latitude stations highly valuable for SR-connected research aims, such as the reconstruction of global lightning activity (see e.g., Bozóki et al., 2019; Prácser et al., 2019) by inversion methods. However, because of the extra-terrestrial effects on the SR cavity at higher latitude as documented in this work, it is of vital importance to realize all possible masking effects when analyzing these data-sets in connection with lightning-related climate research.

DATA AVAILABILITY STATEMENT

The raw data supporting the conclusion of this article will be made available by the authors, without undue reservation.

AUTHOR CONTRIBUTIONS

TB, GS, and EW led the interpretation of results and the writing of the manuscript. TB processed the SR data and prepared the figures. IM processed the POES data and contributed to the interpretation of EEP-related results. PS and ST-R processed the DEMETER data and contributed to the interpretation of DEMETER-based results. EB provided information on individual EEP events and contributed to the interpretation of the EEP-related results. AK, YY, and OB provided SR data from the Vernadsky and Sousy stations and contributed to the interpretation of SR-related results. MN provided SR data from the Hornsund and Belsk stations. AS and RR provided SR data from the Maitri and Shillong stations. MS provided SR data from the Syowa station. CB provided SR data from the Eskdalemuir station. YL collected and organized long-term SR records in the MIT SuperCloud database. RB applied the Lorentzian fitting technique on SR data.

FUNDING

The work of TB and GS was supported by the COST Action CA15211 and by the National Research, Development, and Innovation Office, Hungary-NKFIH, K115836. The contribution to this work by EW and YL has been supported by both the Grainger Foundation and by the US National Science Foundation (Grant # 6942679). The work of the Ukrainian team (AK, YY, and OB) was partially supported by MES of Ukraine projects 0121U112293 and NAS of Ukraine projects 0121U108110 and 0121U108635. EB is supported by the Research Council of Norway (grant #287427). IM work on processing, interpreting results of EEP data was supported by a grant from the Russian Science Foundation (Project RSF No. 20-67-46016). The database of POES data was prepared by IM in the frame of the SPBU “Ozone Layer and Upper Atmosphere Research Laboratory” supported by the Ministry of Science and Higher Education of the Russian Federation under agreement 075-15- 2021-583.

ACKNOWLEDGMENTS

We are very grateful to Chris Hall, scientific leader of Tromso Geophysical Observatory, and to the staff of TGO for the support of the Ukrainian ELF magnetometer-unit operating at Svalbard as well as to the National Antarctic Scientific Center of Ukraine providing SR measurements at the Ukrainian Antarctic station “Akademik Vernadsky.” Kornél Kapás’ kind assistance is acknowledged in revisiting theoretical considerations in P. H. Nelson’s thesis.

REFERENCES

Artamonov, A., Mironova, I., Kovaltsov, G., Mishev, A., Plotnikov, E., and Konstantinova, N. (2017). Calculation of Atmospheric Ionization Induced by Electrons with Non-Vertical Precipitation: Updated Model CRAC-EPII. *Adv. Space Res.* 59 (9), 2295–2300. doi:10.1016/j.asr.2017.02.019

Asikainen, T., and Ruopsa, M. (2016). Solar Wind Drivers of Energetic Electron Precipitation. *J. Geophys. Res. Space Phys.* 121 (3), 2209–2225. doi:10.1002/2015JA022215

Baker, D. N., Erickson, P. J., Fennell, J. F., Foster, J. C., Jaynes, A. N., and Verronen, P. T. (2018). Space Weather Effects in the Earth’s Radiation Belts. *Space Sci. Rev.* 214, 17. doi:10.1007/s11214-017-0452-7

Balser, M., and Wagner, C. A. (1960). Observations of Earth-Ionosphere Cavity Resonances. *Nature* 188, 638–641. doi:10.1038/188638a0

Beggan, C. D., and Musur, M. (2018). Observation of Ionospheric Alfvén Resonances at 1-30 Hz and Their Superposition with the Schumann Resonances. *J. Geophys. Res. Space Phys.* 123 (5), 4202–4214. doi:10.1029/2018JA025264

Belova, E., Kirkwood, S., Ekeberg, J., Osepian, A., Häggström, I., Nilsson, H., et al. (2005). The Dynamical Background of Polar Mesosphere Winter Echoes from Simultaneous EISCAT and ESRAD Observations. *Ann. Geophys.* 23 (4), 1239–1247. doi:10.5194/angeo-23-1239-2005

Berthelier, J. J., Godefroy, M., Leblanc, F., Malingre, M., Menvielle, M., Lagoutte, D., et al. (2006). ICE, the Electric Field Experiment on DEMETER. *Planet. Space Sci.* 54 (5), 456–471. doi:10.1016/j.pss.2005.10.016

Bland, E. C., Heino, E., Kosch, M. J., and Partamies, N. (2018). SuperDARN Radar-Derived HF Radio Attenuation During the September 2017 Solar Proton Events. *Space Weather* 16 (10), 1455–1469. doi:10.1029/2018SW001916

Bland, E. C., Partamies, N., Heino, E., Yukimatu, A. S., and Miyaoka, H. (2019). Energetic Electron Precipitation Occurrence Rates Determined Using the Syowa East SuperDARN Radar. *J. Geophys. Res. Space Phys.* 124, 6253–6265. doi:10.1029/2018JA026437

Bland, E., Tesema, F., and Partamies, N. (2021). D-region Impact Area of Energetic Electron Precipitation During Pulsating Aurora. *Ann. Geophys.* 39, 135–149. doi:10.5194/angeo-39-135-2021

Bliokh, P. V., Galyuk, Y. P., Hünninen, E. M., Nikolaenko, A. P., and Rabinovich, L. M. (1977). Resonance Effects in the Earth-Ionosphere Cavity. *Radiophys Quan. Electron* 20, 339–345. doi:10.1007/BF01033918

Bór, J., Sátori, G., Barta, V., Szabóné-André, K., Szendrői, J., Wesztergom, V., et al. (2020). Measurements of Atmospheric Electricity in the Széchenyi István Geophysical Observatory, Hungary. *Hist. Geo Space Sci.* 11 (1), 53–70. doi:10.5194/hgss-11-53-2020

Bozóki, T., Prácser, E., Sátori, G., Dálya, G., Kapás, K., and Takátsy, J. (2019). Modeling Schumann Resonances with Schupy. *J. Atmos. Solar-Terrestrial Phys.* 196, 105144. doi:10.1016/j.jastp.2019.105144

Chisham, G., Lester, M., Milan, S. E., Freeman, M. P., Bristow, W. A., Grocott, A., et al. (2007). A Decade of the Super Dual Auroral Radar Network (SuperDARN): Scientific Achievements, New Techniques and Future Directions. *Surv. Geophys.* 28, 33–109. doi:10.1007/s10712-007-9017-8

Christian, H. J., Blakeslee, R. J., Boccippio, D. J., Boeck, W. L., Buechler, D. E., Driscoll, K. T., et al. (2003). Global Frequency and Distribution of Lightning as Observed from Space by the Optical Transient Detector. *J. Geophys. Res.* 108, D1. doi:10.1029/2002JD002347

Christofilakis, V., Tatsis, G., Votis, C., Contopoulos, I., Repapis, C., and Tritakis, V. (2019). Significant ELF Perturbations in the Schumann Resonance Band Before and During a Shallow Mid-magnitude Seismic Activity in the Greek Area (Kalpaki). *J. Atmos. Solar-Terrestrial Phys.* 182, 138–146. doi:10.1016/j.jastp.2018.11.009

Clilverd, M. A., Meredith, N. P., Horne, R. B., Glauert, S. A., Anderson, R. R., Thomson, N. R., et al. (2007). Longitudinal and Seasonal Variations in Plasmaspheric Electron Density: Implications for Electron Precipitation. *J. Geophys. Res.* 112, A11. doi:10.1029/2007JA012416

Clilverd, M. A., Rodger, C. J., Gamble, R. J., Ulich, T., Raita, T., Seppälä, A., et al. (2010). Ground-based Estimates of Outer Radiation belt Energetic Electron Precipitation Fluxes into the Atmosphere. *J. Geophys. Res.* 115, A12. doi:10.1029/2010JA015638

Cummer, S. A. (2000). Modeling Electromagnetic Propagation in the Earth-Ionosphere Waveguide. *IEEE Trans. Antennas Propagat.* 48, 1420–1429. doi:10.1109/8.898776

Danilov, A. D., and Vanina, L. B. (1999). Comparison of the Polar D-Region Behavior in the Arctic and Antarctic. *Adv. Space Res.* 24 (12), 1655–1664. doi:10.1016/S0273-1177(99)00333-6

Davis, T. N., and Sugiura, M. (1966). Auroral Electrojet Activity indexAEand its Universal Time Variations. *J. Geophys. Res.* 71 (3), 785–801. doi:10.1029/JZ071i003p00785

Duderstadt, K. A., Huang, C. L., Spence, H. E., Smith, S., Blake, J. B., Crew, A. B., et al. (2021). Estimating the Impacts of Radiation Belt Electrons on Atmospheric Chemistry Using FIREBIRD II and Van Allen Probes Observations. *Geophys. Res. Atmos.* 126, e2020JD033098. doi:10.1029/2020JD033098

Dyrda, M., Kulak, A., Mlynarczyk, J., and Ostrowski, M. (2015). Novel Analysis of a Sudden Ionospheric Disturbance Using Schumann Resonance Measurements. *J. Geophys. Res. Space Phys.* 120 (3), 2255–2262. doi:10.1002/2014JA020854

Elhalel, G., Price, C., Fixler, D., and Shainberg, A. (2019). Cardioprotection from Stress Conditions by Weak Magnetic Fields in the Schumann Resonance Band. *Sci. Rep.* 9, 1645. doi:10.1038/s41598-018-36341-z

Fdez-Arroyabe, P., Fornieles-Callejón, J., Santurtún, A., Szangolies, L., and Donner, R. V. (2020). Schumann Resonance and Cardiovascular Hospital Admission in the Area of Granada, Spain: An Event Coincidence Analysis Approach. *Sci. Total Environ.* 705, 135813. doi:10.1016/j.scitotenv.2019.135813

Ferencz, O. E., Ferencz, C., Steinbach, P., Lichtenberger, J., Hamar, D., Parrot, M., et al. (2007). The Effect of Subionospheric Propagation on Whistlers Recorded by the DEMETER Satellite - Observation and Modelling. *Ann. Geophys.* 25, 1103–1112. doi:10.5194/angeo-25-1103-2007

Feynman, R. P., Leighton, R. B., and Sands, M. L. (1963). *The Feynman Lectures on Physics*, 1. Reading, Mass: Addison-Wesley Pub. Co.

Florios, K., Contopoulos, I., Christofilakis, V., Tatsis, G., Chronopoulos, S., Repapis, C., et al. (2020). Pre-seismic Electromagnetic Perturbations in Two Earthquakes in Northern Greece. *Pure Appl. Geophys.* 177, 787–799. doi:10.1007/s00024-019-02362-6

Fornieles-Callejón, J., Salinas, A., Toledo-Redondo, S., Portí, J., Méndez, A., Navarro, E. A., et al. (2015). Extremely Low Frequency Band Station for Natural Electromagnetic Noise Measurement. *Radio Sci.* 50 (3), 191–201. doi:10.1002/2014RS005567

Fraser-Smith, A. C., McGill, P. R., Bernardi, A., Helliwell, R. A., and Ladd, M. E. (1991a). "Global Measurements of Low-Frequency Radio Noise," in *Environmental and Space Electromagnetics*. Editor H. Kikuchi (Tokyo): Springer).

Fraser-Smith, A. C., Ogawa, T., McGill, P. R., Bernardi, A., Ladd, M. E., and Helliwell, R. A. (1991b). "Measurements of ELF/VLF Radio Noise in Japan," in *Environmental and Space Electromagnetics*. Editor H. Kikuchi (Tokyo): Springer). doi:10.1007/978-4-431-68162-5_20

Fröhlich, C., and Lean, J. (1998). The Sun's Total Irradiance: Cycles, Trends and Related Climate Change Uncertainties since 1976. *Geophys. Res. Lett.* 25 (23), 4377–4380. doi:10.1029/1998GL900157

Füllekrug, M., Fraser-Smith, A. C., and Schlegel, K. (2002). Global Ionospheric D-Layer Height Monitoring. *Europhys. Lett.* 59, 626–632. doi:10.1209/epl/i2002-00150-y

Galuk, Y. P., Kudintseva, I. G., Nickolaenko, A. P., and Hayakawa, M. (2019). Scattering of ELF Radio Waves by a Localized Non-uniformity in the Lower Ionosphere. *J. Atmos. Solar-Terrestrial Phys.* 194, 105093. doi:10.1016/j.jastp.2019.105093

Greenwald, R. A., Baker, K. B., Dudeney, J. R., Pinnock, M., Jones, T. B., Thomas, E. C., et al. (1995). DARN/SuperDARN. *Space Sci. Rev.* 71, 761–796. doi:10.1007/BF00751350

Greifinger, C., and Greifinger, P. (1978). Approximate Method for Determining ELF Eigenvalues in the Earth-Ionosphere Waveguide. *Radio Sci.* 13 (5), 831–837. doi:10.1029/RS013i005p00831

Greifinger, P., Mushtak, V., and Williams, E. (2005). "The Lower Characteristic ELF Altitude of the Earth–Ionosphere Waveguide: Schumann Resonance Observations and Aeronomical Estimates," in IEEE 6th International Symposium on Electromagnetic Compatibility and Electromagnetic Ecology, St. Petersburg, Russia, 21-24 June 2005 (IEEE), 250–254. doi:10.1109/EMCECO.2005.1513116

Greifinger, P. S., Mushtak, V. C., and Williams, E. R. (2007). On Modeling the Lower Characteristic ELF Altitude from Aeronomical Data. *Radio Sci.* 42, 2. doi:10.1029/2006RS003500

Guha, A., Williams, E., Boldi, R., Sátori, G., Nagy, T., Bór, J., et al. (2017). Aliasing of the Schumann Resonance Background Signal by Sprite-Associated Q-Bursts. *J. Atmos. Solar-Terrestrial Phys.* 165-166, 25–37. doi:10.1016/j.jastp.2017.11.003

Hayakawa, M., Nickolaenko, A. P., Galuk, Y. P., and Kudintseva, I. G. (2020). Scattering of Extremely Low Frequency Electromagnetic Waves by a Localized Seismogenic Ionospheric Perturbation: Observation and Interpretation. *Radio Sci.* 55, 12. doi:10.1029/2020RS007130

Koloskov, A. V., Nickolaenko, A. P., Yampolsky, Y. M., Yu, C., Budanov, O. V., and Budanov, O. V. (2020). Variations of Global Thunderstorm Activity Derived from the Long-Term Schumann Resonance Monitoring in the Antarctic and in the Arctic. *J. Atmos. Solar-Terrestrial Phys.* 201, 105231. doi:10.1016/j.jastp.2020.105231

Kudintseva, I. G., Galuk, Y. P., Nickolaenko, A. P., and Hayakawa, M. (2018). Modifications of Middle Atmosphere Conductivity During Sudden Ionospheric Disturbances Deduced from Changes of Schumann Resonance Peak Frequencies. *Radio Sci.* 53 (5), 670–682. doi:10.1029/2018RS006554

Kulak, A., Kubisz, J., Michalec, A., Zięba, S., and Nieckarz, Z. (2003b). Solar Variations in Extremely Low Frequency Propagation Parameters: 2. Observations of Schumann Resonances and Computation of the ELF Attenuation Parameter. *J. Geophys. Res.* 108, A7. doi:10.1029/2002JA009305

Kulak, A., and Mlynarczyk, J. (2013). ELF Propagation Parameters for the Ground-Ionosphere Waveguide with Finite Ground Conductivity. *IEEE Trans. Antennas Propagat.* 61 (4), 2269–2275. doi:10.1109/TAP.2012.2227445

Kulak, A., Zięba, S., Micek, S., and Nieckarz, Z. (2003a). Solar Variations in Extremely Low Frequency Propagation Parameters: 1. A Two-Dimensional Telegraph Equation (TDTE) Model of ELF Propagation and Fundamental Parameters of Schumann Resonances. *J. Geophys. Res.* 108, A7. doi:10.1029/2002JA009304

Lam, M. M., Horne, R. B., Meredith, N. P., Glauert, S. A., Moffat-Griffin, T., and Green, J. C. (2010). Origin of Energetic Electron Precipitation >30 keV into the Atmosphere. *J. Geophys. Res.* 115, A4. doi:10.1029/2009JA014619

Lockwood, M., Owens, M. J., Barnard, L. A., Haines, C., Scott, C. J., McWilliams, K. A., et al. (2020). Semi-Annual, Annual and Universal Time Variations in the Magnetosphere and in Geomagnetic Activity: 1. Geomagnetic Data. *J. Space Weather Space Clim.* 10, 23. doi:10.1051/swsc/2020023

Madden, T., and Thompson, W. (1965). Low-Frequency Electromagnetic Oscillations of the Earth-Ionosphere Cavity. *Rev. Geophys.* 3 (2), 211–254. doi:10.1029/RG003i002p00211

Manu, S., Rawat, R., Sinha, A. K., Gurubaran, S., and Jeeva, K. (2015). Schumann Resonances Observed at Maitri, Antarctica: Diurnal Variation and its Interpretation in Terms of Global Thunderstorm Activity. *Curr. Sci.* 109 (4), 784–790.

Melnikov, A., Price, C., Sátori, G., and Füllekrug, M. (2004). Influence of Solar Terminator Passages on Schumann Resonance Parameters. *J. Atmos. Solar-Terrestrial Phys.* 66 (13-14), 1187–1194. doi:10.1016/j.jastp.2004.05.014

Mironova, I. A., Aplin, K. L., Arnold, F., Bazilevskaya, G. A., Harrison, R. G., Krivolutsky, A. A., et al. (2015). Energetic Particle Influence on the Earth's Atmosphere. *Space Sci. Rev.* 194, 1–96. doi:10.1007/s11214-015-0185-4

Mironova, I., Artamonov, A. A., Bazilevskaya, G. A., Rozanov, E. V., Kovaltsov, G. A., Makhmutov, V. S., et al. (2019b). Ionization of the Polar Atmosphere by Energetic Electron Precipitation Retrieved from Balloon Measurements. *Geophys. Res. Lett.* 46, 990–996. doi:10.1029/2018GL079421

Mironova, I., Bazilevskaya, G., Kovaltsov, G. A. A., Artamonov, A., Rozanov, E., Mishev, A., et al. (2019a). Spectra of High Energy Electron Precipitation and Atmospheric Ionization Rates Retrieval from Balloon Measurements. *Sci. Total Environ.* 693, 133242. doi:10.1016/j.scitotenv.2019.07.048

Miyoshi, Y., Oyama, S., Saito, S., Kurita, S., Fujiwara, H., Kataoka, R., et al. (2015). Energetic Electron Precipitation Associated with Pulsating Aurora: EISCAT and Van Allen Probe Observations. *J. Geophys. Res. Space Phys.* 120 (4), 2754–2766. doi:10.1002/2014JA020690

Mushtak, V. C., and Williams, E. R. (2002). ELF Propagation Parameters for Uniform Models of the Earth-ionosphere Waveguide. *J. Atmos. Sol. Terr. Phys.* 64 (18), 1989–2001. doi:10.1016/S1364-6826(02)00222-5

Musur, M. A., and Beggan, C. D. (2019). Seasonal and Solar Cycle Variation of Schumann Resonance Intensity and Frequency at Eskdalemuir Observatory, UK. *Sun and Geosphere* 14, 1. doi:10.31401/SunGeo.2019.01.11

Nelson, P. H. (1967). Ionospheric Perturbations and Schumann Resonance Data. PhD thesis. Project NR-371-401 (Cambridge Mass: Geophysics Lab. MIT).

Neska, M., Czubak, P., and Reda, J. (2019). Schumann Resonance Monitoring in Hornsund (Spitsbergen) and Suwałki (Poland). *Publs. Inst. Geophys. P.A.S.* 425, 41–45. doi:10.25171/InstGeoph_PAS_Publs-2019-008

Neska, M., Sátori, G., Szendroi, J., Marianiuk, J., Nowozynski, K., and Tomczyk, S. (2007). Schumann Resonance Observation in Polish Polar Station at Spitsbergen and Central Geophysical Observatory in Belsk. *Publs. Inst. Geophys. Pol. Acad. Sc. C* 99, 398.

Nickolaenko, A., and Hayakawa, M. (2014). *Schumann Resonance for Tyros*. Tokyo: Springer. doi:10.1007/978-4-431-54358-9

Nickolaenko, A. P., and Hayakawa, M. (2002). *Resonances in the Earth–Ionosphere Cavity*. Amsterdam: Springer Netherlands.

Nickolaenko, A. P., Koloskov, A. V., Hayakawa, M., Yampolski, Yu. M., Budanov, O. V., and Korepanov, V. E. (2015). 11-Year Solar Cycle in Schumann Resonance Data as Observed in Antarctica. *Sun and Geosphere* 10 (1), 39–50.

Ondrášková, A., Kostecký, P., Ševčík, S., and Rosenberg, L. (2007). Long-Term Observations of Schumann Resonances at Modra Observatory. *Radio Sci.* 42, 2. doi:10.1029/2006RS003478

Ondrášková, A., Ševčík, S., and Kostecký, P. (2011). Decrease of Schumann Resonance Frequencies and Changes in the Effective Lightning Areas Toward the Solar Cycle Minimum of 2008-2009. *J. Atmos. Solar-Terrestrial Phys.* 73 (4), 534–543. doi:10.1016/j.jastp.2010.11.013

Pazos, M., Mendoza, B., Sierra, P., Andrade, E., Rodríguez, D., Mendoza, V., et al. (2019). Analysis of the Effects of Geomagnetic Storms in the Schumann Resonance Station Data in Mexico. *J. Atmos. Solar-Terrestrial Phys.* 193, 105091. doi:10.1016/j.jastp.2019.105091

Prácser, E., Bozóki, T., Sátori, G., Takátsy, J., Williams, E., and Guha, A. (2021). Two Approaches for Modeling ELF Wave Propagation in the Earth-Ionosphere Cavity with Day-Night Asymmetry. *IEEE Trans. Antennas Propagat.* 69, 4093–4099. doi:10.1109/TAP.2020.3044669

Prácser, E., Bozóki, T., Sátori, G., Williams, E., Guha, A., and Yu, H. (2019). Reconstruction of Global Lightning Activity Based on Schumann Resonance Measurements: Model Description and Synthetic Tests. *Radio Sci.* 54 (3), 254–267. doi:10.1029/2018RS006772

Price, C., and Melnikov, A. (2004). Diurnal, Seasonal and Inter-Annual Variations in the Schumann Resonance Parameters. *J. Atmos. Solar-Terrestrial Phys.* 66 (13-14), 1179–1185. doi:10.1016/j.jastp.2004.05.004

Price, C., Williams, E., Elhalel, G., and Sentman, D. (2021). Natural ELF Fields in the Atmosphere and in Living Organisms. *Int. J. Biometeorol.* 65, 85–92. doi:10.1007/s00484-020-01864-6

Rawat, R., Singh, A. K., Pathan, B. M., Sinha, A. K., Jeeva, K., Labde, S., et al. (2012). *Diurnal and Seasonal Characteristics of Schumann Resonance*. Mysore, India: 39th COSPAR Scientific Assembly.

Rees, M. H. (1989). *Physics and Chemistry of the Upper Atmosphere*. Cambridge: Cambridge University Press.

Reeves, G. D., McAdams, K. L., Friedel, R. H. W., and O'Brien, T. P. (2003). Acceleration and Loss of Relativistic Electrons During Geomagnetic Storms. *Geophys. Res. Lett.* 30, 10. doi:10.1029/2002GL016513

Rodger, C. J., Clilverd, M. A., Green, J. C., and Lam, M. M. (2010). Use of POES SEM-2 Observations to Examine Radiation Belt Dynamics and Energetic Electron Precipitation into the Atmosphere. *J. Geophys. Res.* 115, A4. doi:10.1029/2008JA014023

Roldugin, V. C., Maltsev, Y. P., Vasiljev, A. N., Schokotov, A. Y., and Belyajev, G. G. (2004a). Diurnal Variations of Schumann Resonance Frequency in NS and EW Magnetic Components. *J. Geophys. Res.* 109, A8. doi:10.1029/2004JA010487

Roldugin, V. C., Maltsev, Y. P., Vasiljev, A. N., Schokotov, A. Y., and Belyajev, G. G. (2004b). Schumann Resonance Frequency Increase during Solar X-ray Bursts. *J. Geophys. Res.* 109, A1. doi:10.1029/2003JA010019

Roldugin, V. C., Maltsev, Y. P., Vasiljev, A. N., Shvets, A. V., and Nikolaenko, A. P. (2003). Changes of Schumann Resonance Parameters During the Solar Proton Event of 14 July 2000. *J. Geophys. Res.* 108, A3. doi:10.1029/2002JA009495

Salinas, A., Toledo-Redondo, S., Navarro, E. A., Fornieles-Callejón, J., and Portí, J. A. (2016). Solar Storm Effects During Saint Patrick's Days in 2013 and 2015 on the Schumann Resonances Measured by the ELF Station at Sierra Nevada (Spain). *J. Geophys. Res. Space Phys.* 121 (12), 234. doi:10.1002/2016JA023253

Sato, M., and Fukunishi, H. (2005). New Evidence for a Link Between Lightning Activity and Tropical Upper Cloud Coverage. *Geophys. Res. Lett.* 32, 12. doi:10.1029/2005GL022865

Sátori, G. (1996). Monitoring Schumann Resonances-11. Daily and Seasonal Frequency Variations. *J. Atmos. Terrestrial Phys.* 58 (13), 1483–1488. doi:10.1016/0021-9169(95)00146-8

Sátori, G., Neska, M., Williams, E., and Szendrői, J. (2007). Signatures of the Day-Night Asymmetry of the Earth-Ionosphere Cavity in High Time Resolution Schumann Resonance Records. *Radio Sci.* 42, 2. doi:10.1029/2006RS003483

Sátori, G., Szendröi, J., and Verö, J. (1996). Monitoring Schumann Resonances-I. Methodology. *J. Atmos. Terrestrial Phys.* 58 (13), 1475–1481. doi:10.1016/0021-9169(95)00145-X

Sátori, G., Williams, E., and Mushtak, V. (2005). Response of the Earth-Ionosphere Cavity Resonator to the 11-year Solar Cycle in X-Radiation. *J. Atmos. Solar-Terrestrial Phys.* 67 (6), 553–562. doi:10.1016/j.jastp.2004.12.006

Sátori, G., Williams, E., Price, C., Boldi, R., Koloskov, A., Yampolski, Y., et al. (2016). Effects of Energetic Solar Emissions on the Earth-Ionosphere Cavity of Schumann Resonances. *Surv. Geophys.* 37, 757–789. doi:10.1007/s10712-016-9369-z

Sátori, G., and Zieger, B. (1996). Spectral Characteristics of Schumann Resonances Observed in Central Europe. *J. Geophys. Res.* 101, 29663–29669. doi:10.1029/96JD00549

Savoska, S., Fdez-Arroyabe, P., Cifra, M., Kourtidis, K., Rozanov, E., Nicoll, K., et al. (2021). Toward the Creation of an Ontology for the Coupling of Atmospheric Electricity with Biological Systems. *Int. J. Biometeorol.* 65, 31–44. doi:10.1007/s00484-020-02051-3

Schlegel, K., and Füllekrug, M. (1999). Schumann Resonance Parameter Changes during High-Energy Particle Precipitation. *J. Geophys. Res.* 104, 10111–10118. doi:10.1029/1999JA900056

Schumann, W. O. (1952). Über die strahlungslosen Eigenschwingungen einer leitenden Kugel, die von einer Luftschicht und einer Ionosphärenhülle umgeben ist. *Z. Naturfirschung* 7 (2), 149–154. doi:10.1515/zna-1952-0202

Sentman, D. D., and Fraser, B. J. (1991). Simultaneous Observations of Schumann Resonances in California and Australia: Evidence for Intensity Modulation by the Local Height of theDregion. *J. Geophys. Res.* 96 (15), 15973–15984. doi:10.1029/91JA01085

Shvets, A. V., Nickolaenko, A. P., and Chebrov, V. N. (2017). Effect of Solar Flares on the Schumann-Resonance Frequences. *Radiophys Quan. El* 60, 186–199. doi:10.1007/s11141-017-9789-8

Singh, B., Tyagi, R., Hobara, Y., and Hayakawa, M. (2014). X-Rays and Solar Proton Event Induced Changes in the First Mode Schumann Resonance Frequency Observed at a Low Latitude Station Agra, India. *J. Atmos. Solar-Terrestrial Phys.* 113, 1–9. doi:10.1016/j.jastp.2014.02.010

Sukhov, V., Sukhova, E., Sinitsyna, Y., Gromova, E., Mshenskaya, N., Ryabkova, A., et al. (2021). Influence of Magnetic Field with Schumann Resonance Frequencies on Photosynthetic Light Reactions in Wheat and Pea. *Cells* 10 (1), 149. doi:10.3390/cells10010149

Suvorova, A. V. (2017). Flux Enhancements of > 30 keV Electrons at Low Drift Shells L. *J. Geophys. Res. Space Phys.* 122 (12), 274. doi:10.1002/2017JA024556

Tatsis, G., Christofilakis, V., Chronopoulos, S. K., Baldoumas, G., Sakkas, A., Paschalidou, A. K., et al. (2020). Study of the Variations in the Schumann Resonances Parameters Measured in a Southern Mediterranean Environment. *Sci. Total Environ.* 715, 136926. doi:10.1016/j.scitotenv.2020.136926

Tatsis, G., Sakkas, A., Christofilakis, V., Baldoumas, G., Chronopoulos, S. K., Paschalidou, A. K., et al. (2021). Correlation of Local Lightning Activity with Extra Low Frequency Detector for Schumann Resonance Measurements. *Sci. Total Environ.* 787, 147671. doi:10.1016/j.scitotenv.2021.147671

Toledo-Redondo, S., Parrot, M., and Salinas, A. (2012). Variation of the First Cut-Off Frequency of the Earth-Ionosphere Waveguide Observed by DEMETER. *J. Geophys. Res.* 117, A4. doi:10.1029/2011JA017400

Toledo-Redondo, S., Salinas, A., Portí, J., Morente, J. A., Fornieles, J., Méndez, A., et al. (2010). Study of Schumann Resonances Based on Magnetotelluric Records from the Western Mediterranean and Antarctica. *J. Geophys. Res.* 115, D22. doi:10.1029/2010JD014316

Tritakis, V., Contopoulos, I., Florios, C., Tatsis, G., Christofilakis, V., Baldoumas, G., et al. (2021). Anthropogenic Noise and its Footprint on ELF Schumann Resonance Recordings. *Front. Earth Sci.* 9. doi:10.3389/feart.2021.646277

van de Kamp, M., Rodger, C. J., Seppälä, A., Clilverd, M. A., and Verronen, P. T. (2018). An Updated Model Providing Long-Term Data Sets of Energetic Electron Precipitation, Including Zonal Dependence. *J. Geophys. Res. Atmos.* 123 (17), 9891–9915. doi:10.1029/2017JD028253

van de Kamp, M., Seppälä, A., Clilverd, M. A., Rodger, C. J., Verronen, P. T., and Whittaker, I. C. (2016). A Model Providing Long-Term Data Sets of Energetic Electron Precipitation during Geomagnetic Storms. *J. Geophys. Res. Atmos.* 121 (12), 520. doi:10.1002/2015JD024212

Welch, P. (1967). The Use of Fast Fourier Transform for the Estimation of Power Spectra: A Method Based on Time Averaging over Short, Modified Periodograms. *IEEE Trans. Audio Electroacoust.* 15 (2), 70–73. doi:10.1109/TAU.1967.1161901

Williams, E., Bozóki, T., Sátori, G., Price, C., Steinbach, P., Guha, A., et al. (2021). Evolution of Global Lightning in the Transition from Cold to Warm Phase Preceding Two Super El Niño Events. *Geophys. Res. Atmos.* 126, 3. doi:10.1029/2020JD033526

Williams, E. (2016). Comments on: "11-year Cycle in Schumann Resonance Data as Observed in Antarctica". *Sun and Geosphere* 11 (1), 75–76.

Williams, E., Guha, A., Boldi, R., Satori, G., Koloskov, A., and Yampolski, Y. (2014). "Global Circuit Response to the 11-Year Solar Cycle: Changes in Source or in Medium?," in XV International Conference on Atmospheric Electricity, Norman, Oklahoma, USA, 15-20 June 2014.

Williams, E. R., Mushtak, V. C., and Nickolaenko, A. P. (2006). Distinguishing Ionospheric Models Using Schumann Resonance Spectra. *J. Geophys. Res.* 111 (D16). doi:10.1029/2005JD006944

Williams, E. R., Rothkin, K., Stevenson, D., and Boccippio, D. (2000). Global Lightning Variations Caused by Changes in Thunderstorm Flash Rate and by Changes in the Number of Thunderstorms. *J. Appl. Meteorol. Climatol. (TRMM Spec. Issue)* 39 (12), 2223–2230. doi:10.1175/1520-0450(2001)040<2223:GLVCBC>2.0.CO;2

Williams, E. R., and Sátori, G. (2007). Solar Radiation-Induced Changes in Ionospheric Height and the Schumann Resonance Waveguide on Different Timescales. *Radio Sci.* 42, 2. doi:10.1029/2006RS003494

Williams, E. R. (1992). The Schumann Resonance: A Global Tropical Thermometer. *Science* 256 (5060), 1184–1187. doi:10.1126/science.256.5060.1184

Yatsevich, E. I., Nickolaenko, A. P., and Pechonaya, O. B. (2008). Diurnal and Seasonal Variations in the Intensities and Peak Frequencies of the First Three Schumann-Resonance Modes. *Radiophys Quan. El* 51, 528–538. doi:10.1007/s11141-008-9056-0

Zhou, H., and Qiao, X. (2015). Studies of the Variations of the First Schumann Resonance Frequency During the Solar Flare on 7 March 2012. *J. Geophys. Res. Atmos.* 120 (10), 4600–4612. doi:10.1002/2014JD022696

Zhou, H., Yu, H., Cao, B., and Qiao, X. (2013). Diurnal and Seasonal Variations in the Schumann Resonance Parameters Observed at Chinese Observatories. *J. Atmos. Solar-Terrestrial Phys.* 98, 86–96. doi:10.1016/j.jastp.2013.03.021

Conflict of Interest: The authors declare that the research was conducted in the absence of any commercial or financial relationships that could be construed as a potential conflict of interest.

The handling editor is currently organizing a Research Topic with one of the authors IM.

ORIGINAL RESEARCH
published: 16 November 2021
doi: 10.3389/feart.2021.687989

Experimental Validation of N_2 Emission Ratios in Altitude Profiles of Observed Sprites

Cheng-Ling Kuo[1,2]*, **Earle Williams**[3], **Toru Adachi**[4,5], **Kevin Ihaddadene**[6], **Sebastien Celestin**[7], **Yukihiro Takahashi**[8], **Rue-Ron Hsu**[9], **Harald U. Frey**[10], **Stephen B. Mende**[10] and **Lou-Chuang Lee**[1,11]

[1]Department of Space Science and Engineering, National Central University, Taoyuan, Taiwan, [2]Center for Astronautical Physics and Engineering, National Central University, Taoyuan, Taiwan, [3]Massachusetts Institute of Technology, Cambridge, MA, United States, [4]Waseda Institute for Advanced Study, Waseda University, Tokyo, Japan, [5]Meteorological Research Institute, Tsukuba, Japan, [6]Department of Physics and Space Science Center, University of New Hampshire, Durham, NC, United States, [7]LPC2E, University of Orleans, CNRS, Orleans, France, [8]Department of Cosmosciences, Hokkaido University, Sapporo, Japan, [9]Department of Physics, National Cheng Kung University, Tainan, Taiwan, [10]Space Sciences Laboratory, University of California, Berkeley, Berkeley, CA, United States, [11]Institute of Earth Sciences, Academia Sinica, Taipei, Taiwan

Edited by:
Irina Alexandrovna Mironova,
Saint Petersburg State University,
Russia

Reviewed by:
Matthew McHarg,
United States Air Force Academy,
United States
Evgeny Anatolievich Mareev,
Institute of Applied Physics (RAS),
Russia
Dongshuai Li,
Institute of Astrophysics of Andalusia
(IAA), Spain

***Correspondence:**
Cheng-Ling Kuo
clkuo@jupiter.ss.ncu.edu.tw

Specialty section:
This article was submitted to
Atmospheric Science,
a section of the journal
Frontiers in Earth Science

Received: 30 March 2021
Accepted: 26 October 2021
Published: 16 November 2021

Citation:
Kuo C-L Williams E, Adachi T,
Ihaddadene K, Celestin S,
Takahashi Y,
Hsu R-R Frey HU, Mende SB and
Lee L-C (2021) Experimental Validation
of N_2 Emission Ratios in Altitude
Profiles of Observed Sprites.
Front. Earth Sci. 9:687989.
doi: 10.3389/feart.2021.687989

Recent efforts to compare the sprite ratios with theoretical results have not been successfully resolved due to a lack of theoretical results for sprite streamers in varying altitudes. Advances in the predicted emission ratios of sprite streamers with a simple analytic equation have opened up the possibility for direct comparisons of theoretical results with sprite observations. The study analyzed the blue-to-red ratios measured by the ISUAL array photometer with the analytical expression for the sprite emission ratio derived from the modeling of downward sprite streamers. Our statistical studies compared sprite halos and carrot sprites where the sprite halos showed fair agreement with the predicted ratios from the sprite streamer simulation. But carrot sprites had lower emission ratios. Their estimated electric field has a lower bound of greater than 0.4 times the conventional breakdown electric field (E_k). It was consistent with the results of remote electromagnetic field measurements for short delayed or big/bright sprites. An unexpectedly lower ratio in carrot sprites occurred since sprite beads or glow in carrot sprites may exist and contribute additional red emission.

Keywords: transient luminous event, sprite, sprite halo, carrot sprites, ISUAL

INTRODUCTION

A spectrophotometric diagnostic of sprites is of interest because the measured emission ratios indicate their characteristic energy and ionization degree in their discharge phenomena (Armstrong et al., 1998, 2000; Morrill et al., 2002). Previous spectral observations demonstrated two major visual emission bands: N_2 second positive band (2P, $C^3\Pi_u - B^3\Pi_g$) for blue emission, and N_2 first positive band (1P, $B^3\Pi_g – A^3\Sigma_u^+$) for red emission (Mende et al., 1995; Green et al., 1996; Hampton et al., 1996). One of the minor blue emission bands is the $N_2{}^+$ first negative band (1N) for ionization associated emission (Armstrong et al., 1998, 2000; Morrill et al., 2002; Kanmae et al., 2010a, 2010b; Stenbaek-Nielsen et al., 2020). Observational techniques for sprite emission ratios have made significant progress using spectrophotometers (Armstrong et al., 1998; 2000), array photometers (Miyasato et al., 2002; 2003), optical spectra at 10,000 fps (Kanmae et al., 2010a, 2010b; Stenbaek-Nielsen et al., 2020) in ground campaigns, airplane campaigns (Morrill et al., 2002), and satellite measurements (Kuo et al., 2005; Mende et al., 2005; Adachi et al., 2006; Liu et al., 2006; Adachi et al.,

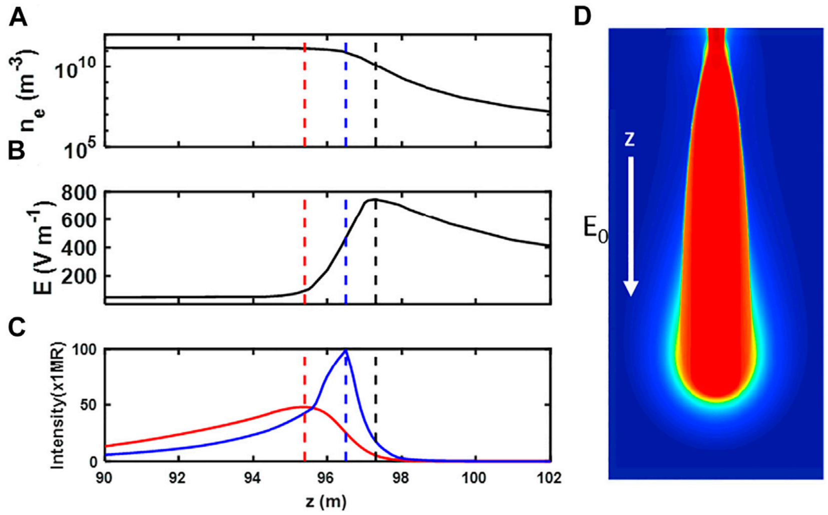

FIGURE 1 | The inhomogeneous spatial distribution of electron density (n_e), electric field (E), and their 1P and 2P emission intensity in a sprite streamer. Here we show the computer simulation of a sprite streamer at time of 0.27 ms where the axial profiles of **(A)** electron density, **(B)** electric field and **(C)** N_2 1P and 2P intensity are plotted along the propagating direction (z) with the ambient field $12 \times \frac{N}{N_0}$ kV cm^{-1} (~0.4 E_k), and at the altitude 70 km. The vertical red, blue and black dashed lines indicate the peaks of N_2 1P, 2P emission and the electric field, respectively. A time lag between their peaks should be considered in sprite emission ratios. Panel **(D)** show the 2D cross section of the contour plot of positive streamer electron density of a streamer with positive streamer where electric field is downward (Ihaddadene and Celestin, 2017).

2008; Kuo et al., 2008; Kuo et al., 2009). The investigation of the electrical discharge phenomena using remote sensing observation will help us study the impact of plasma chemistry and energy deposition by sprites in the middle atmosphere (Gordillo-Vázquez and Pérez-Invernón, 2021).

The sprite emission ratio of N_2 2P to 1P can indicate the gained energy of accelerated electrons and the applied electric field in the streamer process and stands as a proxy for the electron energy leading to the emissions (Stenbaek-Nielsen et al., 2020). However, an inconsistent interpretation of sprite emission has appeared from past to now. Previous studies show sub-electric breakdown results (<1 E_k) in their observation (Morrill et al., 2002; Miyasato et al., 2003) where E_k is the electric field required for conventional breakdown. But their interpretation cannot reflect the high electric field (3–5 E_k) at a streamer head with a high emission rate. The estimated peak electric field in a streamer head provides insight into the sprite inception and the later development of sprite streamers from their initiation locations to lower altitude. The sprite emission estimation for a non-uniform streamer (Celestin and Pasko, 2010) complicates the electric field's optical diagnostic method.

The analysis by Celestin and Pasko (2010) may explain why the electric field is estimated in the range of 1–2 E_k by Adachi et al. (2006). The emission ratios (2P/1N) reported by Kuo et al. (2005, 2009) indicated that the peak electric field of ~3 E_k in sprites and ~3.4–5.5 E_k in gigantic jets. These derived E-field values were underestimated for a peak electric field greater than 5 E_k in a sprite streamer simulation (Liu et al., 2006). Recently, *Ihaddadene* and *Celestin* (2017) developed analytic expressions from a streamer simulation to interpret the observed emission ratios

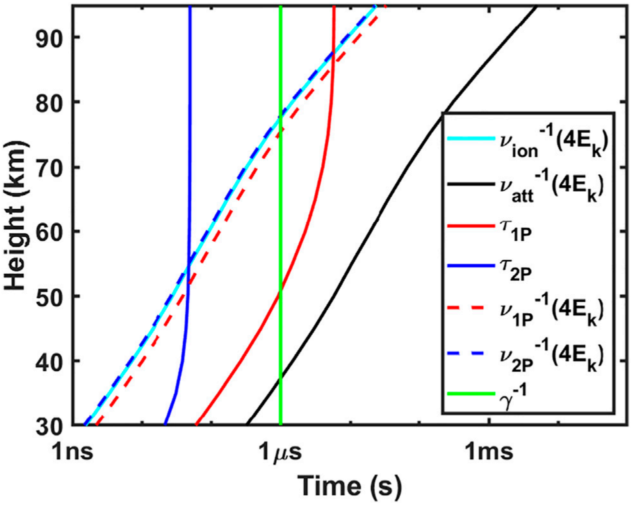

FIGURE 2 | The characteristic time coefficient for calculating sprite emissions are compared in units of seconds at different altitudes. The characteristic time scales versus altitude where these time coefficients represent the ionization rate (cyan solid line) ν_{ion}^{-1}, the excitation rate ν_{1P}^{-1} for N_2 $B^3\Pi_g$ state (red dashed line) at 4 E_k, the excitation rate ν_{2P}^{-1} for $C^3\Pi_u$ state (blue dashed line) at 4 E_k, the lifetime τ_{1P} of N_2 1P (red solid line), and the lifetime τ_{2P} of 2P band (blue solid line) emissions. The lifetimes of the N_2 1P and 2P bands tend to be shorter due to the higher quenching rates (i.e., de-excitation processes) with increased neutral density at lower altitudes. The characteristic time for electron attachment rate ν_{att}^{-1} at 4 E_k (black solid line) indicates the lifetime of streamer body where accumulated electrons at the streamer body are dissipated away after impact ionization by high electric field at the streamer head. The characteristic time (γ^{-1} for the green line) for the growth rate γ in a sprite streamer is almost constant.

at various altitudes. But they still lack spectroscopic data analysis to validate their sprite emission calculation at 50–90 km.

The interpretation of measured sprite emission at a sprite altitude of 50–90 km based on streamer modeling is still challenged (Celestin and Pasko, 2010). The neutral density varies exponentially with altitude. The transmittances for 2P and 1P emissions are sensitive to their observation path, as shown in **Eq. 1**. For sprite emission calculation in **Eq. 2**, their associated time coefficients depend on altitude. Besides, a sprite streamer's characteristic spatial and temporal scale decreases exponentially with ambient neutral density at heights from 70 to 30 km. For example, the spatial scale of a sprite streamer varies from tens of meters at an altitude of 70 km to tens of centimeters at an altitude of 30 km (Pasko et al., 1998; Liu and Pasko, 2004). **Figure 1** shows a streamer simulation at an altitude of 70 km. The non-uniform spatial distribution of their emission intensity at1P and 2P makes it impossible to easily estimate their sprite emission ratios, where the red and blue curves in **Figure 1C** indicate the 1P and 2P intensities along the streamer propagation direction. In **Figure 2**, the characteristic time coefficients in **Eq. 2** vary with altitude. Even for a single streamer, the inhomogeneous emission intensity makes it difficult to estimate their emission ratios. We should consider the observation detection limits on their temporal and spatial scales and the synthesis effects of their spatial and temporal resolution on the emission measurement.

To approach this issue, we revisited similar analyses of the emission ratio by Adachi et al. (2006) based on analytic expressions from a streamer simulation (Ihaddadene and Celestin, 2017). Unlike ground and airplane campaigns, satellite measurement allow for a better transmittance, especially in the shorter wavelength range (e.g., the blue emission). The higher detected intensity in the blue emission may avoid underestimation of total blue emission when considering their transmittance. This study utilized the ISUAL dataset involving sprite blue and red emission onboard the FORMOSAT-2 satellite in *The ISUAL array photometer*. *Analytical expressions for sprite emission ratios* derived the analytical expressions for sprite emission ratios in an altitude profile of 50–90 km. After analyzing measured emission ratios, we validated an analytic expression for a streamer emission to interpret the observed emission ratios at various altitudes in *Data Analyses*. In the *Summary*, we summarized our results.

THE ISUAL ARRAY PHOTOMETER

The ISUAL payload on the FORMOSAT-2 satellite consists of an ICCD imager, a six-channel spectrophotometer (SP), and a dual-band array photometer (AP). The ISUAL AP contains blue (370–450 nm) and red (530–650 nm) bands of multiple-anode photometers at a sampling rate of 20 kHz. Each group of the AP has 16 vertically-stacked photomultiplier tubes (PMTs) with a combined field of view (FOV) of 22 deg (H) x 3.6 deg (V) (Chern et al., 2003; Mende et al., 2005; Frey et al., 2016). The ISUAL AP, imager, and SP are co-aligned at the centers of their respective FOVs.

FORMOSAT-2 is a Sun-synchronous satellite with 14 revisiting orbits per day. The ISUAL payload surveys transient luminous events (TLEs) and other luminescent emissions in the upper atmosphere globally with a side-looking view from an orbital altitude of 891 km. Wu et al. (2017) estimated a mean pointing error of 0.05° using star calibration with 1,296 stars from 2004 to 2014. The average pointing accuracy of ISUAL corresponds to a vertical resolution of 3.0 km at the maximum observation distance (3,500 km). Each AP channel has a half-height of 5.7–7.0 km for a distance of 2,900–3,500 km. Using satellite information recorded for TLE events, we can determine the altitude and location of the events based on the assumption that a bright center of a lightning-illuminated cloud has 10 ± 5 km (Kuo et al., 2008). Later, we constrained the uncertainty as a maximum value of the AP half height, considering the ISUAL pointing accuracy and the cloud height error after finally checking the top altitude of sprites at 90 km with an uncertainty of less than the AP half-height. The details of the uncertainty assessment on height are considered in *Uncertainty in sprite emission ratios*.

The AP band emission percentages $B_k(h)$ for N_2 1P and 2P band emission were used to convert the AP-measured brightness with blue and red filters into the specified total band emissions (2P and 1P, respectively). This was done while considering the atmospheric transmittance and instrument calibrations, including the filter wavelength range, lens transmittance, and detector response function (Frey et al., 2016). The percentage of the total band emission in an ISUAL AP is defined as the band percentage $B_k(h)$, which is also a function of the altitude h and can be expressed as:

$$B_k(h) = \frac{\int I_k(h,\lambda)T(h,\lambda)R(\lambda)d\lambda}{\int I_k(h,\ \lambda)d\lambda} \tag{1}$$

where $I_k(h,\lambda)$ is the intensity of emission lines in the specified band emission (N_2 1P and 2P band emission) at an altitude h, which varies with the wavelength λ. $T(\lambda,h)$ is the atmospheric transmittance, and $R(\lambda)$ is the AP response function (Frey et al., 2016).

We selected sprite events in the first 7 years (2005–2011) of satellite operation to avoid later-stage degradation in the AP sensitivities. Later, we used the band percentage $B_k(h)$ to retrieve the AP-measured total emissions of the N_2 2P and 1P bands. For $I_k(\lambda)$, we considered the N_2 1P and 2P spectrum with a vibrational distribution function obtained by Gordillo-Vázquez et al. (2012), where the vibrational distribution is obtained from halos and sprites at 85 km and from sprites alone at 75 km. The significant changes are the unknown percentage of vibrational number $v = 0$ for the N_2 1P spectrum. The uncertainty in the band percentage is typically ±15%. For the worst case, the error of the ratio is as high as 30%. We neglected the N_2^+ 1N emission in the AP-measured blue emission. For an ambient electric field $<2E_k$, the contribution of N_2^+ 1N emission to N_2 2P is less than 2% according to similar calculations performed in *Analytical Expressions for Sprite Emission Ratios*.

ANALYTICAL EXPRESSIONS FOR SPRITE EMISSION RATIOS

A measurement of the N_2 emission band ratio in sprites (e.g., 2P/1P or 1N/2P) is one of the most common remote optical diagnostic methods used to explore the physical conditions of complex sprite phenomena (Armstrong, 1998, 2000; Morrill et al., 2002; Miyasato et al., 2003; Kuo et al., 2005; Adachi et al., 2006; Adachi et al., 2008; Kuo et al., 2008; Kuo et al., 2009; Stenbaek-Nielsen et al., 2020). Sprite streamers associated with the first positive (1P), second positive (2P), and first negative (1N) band emission of N_2 can be analyzed using the analytical expressions for emission ratios in sprite streamer simulations (Celestin and Pasko, 2010; Pérez-Invernón et al., 2018). Here, we present the simplest expression for the sprite emission Ratio 1 (r_{CB}) adopted in previous studies (Morrill et al., 2002; Miyasato et al., 2003; Kuo et al., 2005; Mende et al., 2005; Adachi et al., 2006; Adachi et al., 2008; Kuo et al., 2008; Kuo et al., 2009) in *The Spatially Localized Instantaneous Emission Ratio*. In *The spatially and temporally integrated ratio*, we modified the simplest expression by using an integral form for Ratio 2 (R_{CB}) by considering the spatially and temporally integrated effects of the observations on the sprite emissions. Finally, we propose a complete presentation of Ratio 3 (R^*_{CB}) considering the expansion of sprite streamers in *The Spatially and Temporally Integrated Effect and the Experimental Growth of Streamer Expansion*.

The Spatially Localized Instantaneous Emission Ratio

Following the calculation of streamer emissions (Pasko et al., 1997; Pasko et al., 1998; Barrington-Leigh and Inan, 1999; Liu et al., 2006; Celestin and Pasko, 2010; Ihaddadene and Celestin, 2017), the number density of the specified k-th excited state n_k is calculated using the population and depopulation equation:

$$\frac{\partial n_k}{\partial t} = \nu_k n_e - n_k\left(A_k + q^k_{N_2} n_{N_2} + q^k_{O_2} n_{O_2}\right) + \sum\nolimits_m n_m A_m \qquad (2)$$

where ν_k is the excitation rate (s^{-1}), which depends on the applied electric field (Moss et al., 2006) with consideration of the cascade terms $\sum_m n_m A_m$, such as the cascading term n_C for the N_2 1P ($B^3\Pi_g$–$A^3\Sigma_u^+$) band emission. The number density of the specified k-th excited state spontaneously emits photons at a rate of the Einstein coefficient A_k, and τ_k is the lifetime defined by $\tau_k = (A_k + q^k_{N_2} n_{N_2} + q^k_{O_2} n_{O_2})^{-1}$. The quenching coefficients $q^k_{N_2}$ and $q^k_{O_2}$ are de-excitation rates by the ambient neutral density (n_{N_2} or n_{O_2}). The lifetime τ_k of the k-th excited state is a function of height where larger neutral density at lower altitudes would decrease the lifetimes. If a maximum value of n_k is reached ($\frac{\partial n_k}{\partial t} = 0$), the spatially localized instantaneous emission ratio $r_{k'k}$ is represented by (Celestin and Pasko, 2010),

$$r_{k'k} = \frac{n_{k'} A_{k'}}{n_k A_k} = \frac{\nu_{k'} A_{k'} \tau_{k'}}{\nu_k A_k \tau_k}, \qquad (3)$$

where k' -th and k-th excited states are emission bands of interest. In this study, the Ratio 1 is chosen as the ratio r_{CB} of the N_2 2P ($C^3\Pi_u - B^3\Pi_g$) to N_2 1P ($B^3\Pi_g - A^3\Sigma_u^+$) band emission, which is given by:

$$r_{CB} = \frac{n_C A_C}{n_B A_B} = \frac{\nu_C n_e \tau_C A_C}{(\nu_B n_e \tau_B + n_C A_C \tau_B) A_B} = \frac{\nu_C A_C \tau_C}{\nu_B A_B \tau_B}\left(1 + \frac{\nu_C \tau_C A_C}{\nu_B}\right)^{-1} \qquad (4)$$

where the cascading term $(1 + \frac{\nu_C \tau_C A_C}{\nu_B})^{-1}$ is considered as the cascading from the $C^3\Pi_u$ state into the $B^3\Pi_g$ state; τ_B and τ_C indicate the lifetime of their corresponding excited state $C^3\Pi_u$ and $B^3\Pi_g$, respectively. The number densities of the excited state $n_B = \nu_B n_e \tau_B + n_C A_C \tau_B$ and $n_C = \nu_C n_e \tau_C$ are obtained from **Eq. 2** if a steady-state at its peak value is reached ($\frac{\partial n_k}{\partial t} = 0$). In **Eq. 2**, the number density n_k of specified emission band is increased at the excitation rate ν_k, which is proportional to the applied electric field. For a maximum electric field, the n_k takes a time lag to reach its maximum value of specified band emission intensity.

Figure 1 illustrates a simulation result of the sprite streamer (Ihaddadene and Celestin, 2017). The panels (a), (b), and (c) of **Figure 1** show the axial profiles of electron density, electric field and N_2 1P/2P intensity along the propagating z-direction at a time of 0.27 ms and at an altitude of 70 km. For N_2 1P/2P emission peaks (red/blue dashed line in **Figure 1B**), there exists a time lag between an emission peak and an electric field peak (black dashed line). Hence, Ratio 1 (r_{CB}) in **Eq. 4** is applied only for the ideal case. However, the optical diagnostic of sprites could not be spatially localized at a streamer head region and at an instantaneous time without considering time delays between their emission peaks. We should consider the temporally and spatially integrated effects compared with observation results. In the next section, we discuss further the temporally and spatially integrated impact on the Ratio 1 r_{CB}.

The Spatially and Temporally Integrated Ratio

Due to the AP detection limits both on spatial resolution (~12 km at a distance 3,000 km) and temporal scale (50 μs), the spatially localized instantaneous emission ratio $\boldsymbol{r_{CB}}$ should be considered as the time-integrated and spatial-integrated measurement by the AP. That means that **Eq. 3** is spatially and temporally integrated. The spatially and temporally integrated ratio $\boldsymbol{R_{k'k}}$ (noted by Ratio 2 hereafter) is:

$$R_{k'k} = \iint r_{k'k}\,dt\,dV = \frac{A_{k'} \iint \left(\frac{\partial n_{k'}}{\partial t}\right) dt\,dV}{A_k \iint \left(\frac{\partial n_k}{\partial t}\right) dt\,dV} \qquad (5a)$$

$$= \frac{A_{k'} \tau_{k'} \iint \nu_{k'} n_e\,dt\,dV}{A_k \tau_k \iint \nu_k n_e\,dt\,dV} = \frac{A_{k'} \tau_{k'} \nu_{k'} N^*_{e,k'}}{A_k \tau_k \nu_k N^*_{e,k}} \qquad (5b)$$

where $N^*_{e,k}$ is the correction term for spatially and temporally integrating the electron density in the streamer region, and is expressed by $\iint (\frac{\partial n_k}{\partial t}) dt\,dV \equiv \tau_k \nu_k N^*_{e,k}$ where $N^*_{e,k}$ is defined by $\nu_k N^*_{e,k} \equiv \iint \nu_k n_e\,dt\,dV$ (Ihaddadene and Celestin, 2017) and in which the maximum contribution to the integration is at peak time of $n_k(t)$. Considering the cascading from the $C^3\Pi_u$ state into the $B^3\Pi_g$ state, we reformulated the Ratio 2 (R_{CB}), which is expressed by

$$R_{CB} = \frac{A_C \tau_C \nu_C}{A_B \tau_B \nu_B} \left(\frac{N^*_{e,C}}{N^*_{e,B}} \right) \left[1 + \left(\frac{N^*_{e,C}}{N^*_{e,B}} \right) \frac{A_C \tau_C \nu_C}{\nu_B} \right]^{-1} \tag{6}$$

where the cascading term is derived in a similar way in the **Eq. 4** except for the addition of the term $(\frac{N^*_{e,C}}{N^*_{e,B}})$.

In **Eqs. 5a** we can realize that $\frac{\partial n_k}{\partial t}$ and $\frac{\partial n_{k'}}{\partial t}$ can be replaced with the right hand side of **Eq. 2** where n_k is the $B^3\Pi_g$ state and $n_{k'}$ is the $C^3\Pi_u$ state for the considered N_2 2P and 1P emission band, respectively. The first term $\nu_k n_e$ of **Eq. 2** indicates the electron impact excitation where the excitation rate ν_k means the excitation rate for N_2 1P and 2P and the electron number density $n_e(t) = n_{e0} e^{\int_0^t} \nu_i(E) dt \approx n_{e0} e^{\nu_i(E_h)t}$ under the approximation of constant exponential growth rate $\nu_i(E_h)$ through the rapidly increasing electron density from the streamer head region to the streamer body region (Babaeva and Naidis, 1997; Liu et al., 2004).

Since the lifetime τ_B is greater than the lifetime τ_C, the peak time of $n_B(t)$ is delayed longer than the peak time of $n_C(t)$, also shown in **Figure 1C**. We should consider the time delayed effect of integrating the exponentially increased electron density in the definition form of $\nu_k N^*_{e,k} = \iint \nu_k n_e dt dV$ where the electron density $n_e(t)$ in the streamer head exponentially increases over time and can be approximated by $n_e(t) \approx n_{e0} e^{\nu_i(E_h)t}$ with $0 \leq t \leq \tau_h$ where τ_h denotes the time scale of n_e from the ambient electron density n_{e0} to the streamer body electron density n_{eb}. After its peak time, the number density $n_B(t)$ relaxes over time with a characteristic time scale of the previously defined lifetime τ_B.

In the **Eq. 3** for Ratio 1 $r_{k'k}$ we assumed the electron number density can be canceled simultaneously at the same peak $n_k(t)$ time as $\frac{\partial n_k}{\partial t} = 0$. For Ratio 2 ($R_{k'k}$) in Eq. 5, the correction for the higher value of temporal integrating n_e in N_2 1P as compared with 2P was considered by the spatially and temporally integrated term $N^*_{e,k}$ (Tables 5, 6 in Ihaddadene and Celestin, 2017). The simulation shows the peak time of $n_B(t)$ with longer lifetime τ_B delay at a time scale of <1 μs. The required propagation time of the streamer head region is defined by τ_h. For a typical streamer with a velocity $5 \times 10^6 \sim 1 \times 10^7$ m/s at an altitude of 70 km (Liu and Pasko, 2004), the $\tau_h = 1 \sim 2$ μs, corresponding to its streamer radius with ~10 m. With the coefficients with $\tau_h = 1.5$ μs and $\nu_i(5E_k) = 6 \times 10^6$ s^{-1}, the electron density drastically increased by $e^{\nu_i(E_h)\tau_h} \approx 10^4$ in front of the streamer and back to the streamer body. A time delay of peak value $n_B(t)$ after $n_C(t)$ will increase the electron density $n_e(t)$ in the integration term of $\nu_k N^*_{e,k}$ at the peak time of $n_B(t)$. Therefore, we expected that $(\frac{N^*_{e,C}}{N^*_{e,B}}) < 1$ for higher integrated values $N^*_{e,B}$ than $N^*_{e,C}$.

Figure 1C clearly shows the unsynchronized issue in the calculation of Ratio 1 $r_{k'k}$ in **Eq. 3**. The smaller propagation distance (z) at the location of the N_2 1P peak value (red) compared to the N_2 2P peak intensity (blue dashed line) reveals the postponed time of the N_2 1P peak intensity in comparison with N_2 2P peak intensity, i.e., approximated to be the time of peak values for the excited state density $n_B(t)$ than that for $n_C(t)$. When the postponed time of the N_2 1P peak intensity is attained, it corresponds to the higher value of electron density, shown in the red dashed line in **Figure 1A**.

In addition, Liu et al. (2009) compared their sprite streamer simulations with a high-speed video recording with 50 μs resolution. During the initial stage of development, the sprite streamer accelerates its speed while the brightness of the streamer head increases exponentially due to the expansion of the streamer head radius in a concise time of 1 ms. Therefore, we should consider the exponential growth rate of the streamer head brightness at the sprite initial expansion stage, i.e., the left-hand side $\frac{\partial n_k}{\partial t}$ term cannot be neglected in our ratio calculation.

The Spatially and Temporally Integrated Effect and the Exponential Growth of Streamer Expansion

For the typical exponential growth of the streamer expansion stage at altitudes of 50–90 km, the time scale is about 1 μs; i.e., the exponential growth rate is 10^6 s^{-1} (Liu et al., 2009; Kosar et al., 2012). Corresponding to streamer head expansion, the time scale of 1 μs for the exponential growth rate is much shorter than the AP time resolution of 50 μs. **Figure 2** shows the 1 μs for the exponential growth rate at the green vertical line while the lifetimes of N_2 1P (τ_{1P}) and 2P (τ_{2P}) are compared. The emission band with a lifetime exceeding 1 μs should be carefully addressed, especially for 1P at an altitude of >50 km. Therefore, the exponential growth of the streamer expansion stage should be considered, with $\frac{\partial n_k}{\partial t} = \gamma n_k$, where the exponential growth rate γ is considered in the streamer simulation of *Ihaddadene and Celestin* (2017). After substitution with the left-hand-side of **Eq. 1**, the measured emission ratios $R^*_{k'k}$ of the k' -th to k -th band is modified by the following:

$$R^*_{k'k} = \frac{A_{k'} N_{k'}}{A_k N_k} = \frac{A_{k'} \tau_{k'} \nu_{k'} N^*_{e,k} (1 + \tau_k \gamma)}{A_k \tau_k \nu_k N^*_{e,k} (1 + \tau_{k'} \gamma)} \tag{7}$$

where k' and k are $C^3\Pi_u$ and $B^3\Pi_g$, and their corresponding effective spatially and temporally integrated excited state number densities are $N^*_{e,C}$ and $N^*_{e,B}$, respectively.

If the growth rate satisfies $\gamma \ll \tau_k^{-1}$ and $\gamma \ll \tau_{k'}^{-1}$ without considering cascading terms, **Eq. 7** is approximated as Eq. 5 at an altitude <50 km ($\tau_B \sim 1$ μs and $\tau_C \sim 47$ ns), also shown by red and blue lines in **Figure 2**. It is noted that the lifetime τ_k is decreased by higher neutral density at a lower altitude. Considering the cascading from the $C^3\Pi_u$ state to the $B^3\Pi_g$ state and the spatially and temporally integrated excited state $N_B = \frac{\tau_B \nu_B N^*_{e,B}}{1+\gamma\tau_B} [1 + \frac{A_C \tau_C \nu_C}{\nu_B (1+\gamma\tau_C)} \frac{N^*_{e,C}}{N^*_{e,B}}]$, the spatially and temporally integrated emission ratios with consideration of the exponential growth of streamer expansion (Ratio 3 R^*_{CB}) become:

$$R^*_{CB} = \frac{A_C \tau_C \nu_C}{A_B \tau_B \nu_B} \left(\frac{N^*_{e,C}}{N^*_{e,B}} \right) \left(\frac{1 + \tau_B \gamma}{1 + \tau_C \gamma} \right) \left[1 + \left(\frac{N^*_{e,C}}{N^*_{e,B}} \right) \frac{A_C \tau_C \nu_C}{\nu_B (1 + \tau_C \gamma)} \right]^{-1} \tag{8}$$

where the first factor $F_1 \equiv (\frac{N^*_{e,C}}{N^*_{e,B}})$ is estimated to be about 0.7 (0.57) for streamer head electric fields 3.7 E_k (4.6 E_k) under ambient electric fields of 0.4 E_k (0.9 E_k) at AP measured altitudes of 50–90 km. The first factor F_1 reflects the correction for the spatially and temporally integrated effect on the streamer head where the electric field in the streamer head is dominant over its peak field magnitude in comparison with the altitude changes (Tables 8, 9 in Ihaddadene and Celestin, 2017). The second factor $F_2 \equiv (\frac{1+\tau_B\gamma}{1+\tau_C\gamma})$ is responsible for the exponential growth of sprite streamers and is sensitive to altitude. The γ value is obtained from the simulation work of *Ihaddadene and Celestin* (2017). The lifetime (τ_B and τ_C) in *The Spatially Localized Instantaneous Emission Ratio* are highly quenched by the increasing neutral density at lower altitude. Therefore, we should carefully estimate the effects using F_2 on the brightness ratios in varying altitude conditions. The third factor $F_3 \equiv [1 + (\frac{N^*_{e,C}}{N^*_{e,B}}) \frac{A_C\tau_C\nu_C}{\nu_B(1+\tau_C\gamma)}]^{-1}$ is the cascading effect term, which is considered by the spatially and temporally integrated effect and the exponential growth of the streamer expansion. Next, in *Data Analyses*, we compare the AP-measured emission ratios of sprite events with Ratio 1 r_{CB} in **Eq. 4**, Ratio 2 R_{CB} in **Eq. 6**, and Ratio 3 R^*_{CB} in **Eq. 8**.

These height-dependent emission values of Ratio 1 (r_{CB}), Ratio 2 (R_{CB}), and Ratio 3 (R^*_{CB}) are shown by the red dotted, dashed, and solid curves for a peak electric field of 0.9–4.6 E_k, and blue ones for 0.4–3.7 E_k in the altitude profiles of **Figures 6–10**, respectively. The predicted emission ratios are approximately constant above altitudes of the quenching height ~67 km for N_2 1P (Kuo et al., 2008) with less quenching effect. Due to the increased quenching rate by ambient molecules below the 1P quenching altitude, the decreasing intensity of 1P emission could cause greater values of predicted emission ratios. In *Data analyses*, we analyzed ISUAL AP data, compared with predicted emission ratios of Ratio 1 (r_{CB}), Ratio 2 (R_{CB}), and Ratio 3 (R^*_{CB}), and validated further the analytic expressions from a streamer simulation (Ihaddadene and Celestin, 2017).

DATA ANALYSES

Adachi et al. (2008) analyzed the ISUAL AP data and estimated the electric field in sprite events. They confirmed the estimated electric field 0.8–3.2 ± 0.42 E_k in sprite streamer regions at altitudes <75 km. A wide distribution of estimated electric fields from the AP-measured emission ratios needs to be clarified. What kind of process was involved in sprites associated with a lower electric field? In *Uncertainty in Sprite Emission Ratios*, we discuss the strategies to limit the measurement uncertainty of sprite emission ratios for our selected sprite events. After comparing sprite images, we found that most carrot sprite events have lower sprite emission ratios than sprite halo events. In *Comparison with Morphology of Recorded Sprites Observed at 5000 fps*, we associated the streamer processes in ISUAL-observed sprite halo and carrot events with detailed image sequences from a high-speed camera at the Lulin Observatory in Taiwan in 2018. *Two Distinct Types of Observed Sprites Determined by the Inception Altitudes: Sprite Halo Event and the Carrot Sprite Event* presents the altitude profiles of sprite ratios for two typical cases: sprite halo and carrot sprite events, respectively. In *The Statistical Analysis of AP-measured Emission Ratios*, we compared the statistical data on emission ratios with predicted emission ratios, and validated the analytic expressions from a streamer simulation (Ihaddadene and Celestin, 2017). In *The Effects of AP-measured Ratios for a Pre-Existing Sprite on a Later-Occurring Sprite*, we discussed the pre-ionization effects on sprite emissions.

Uncertainty in Sprite Emission Ratios

We attributed uncertainties in sprite emission measurements to the following: 1) band percentage uncertainties, 2) altitude errors, 3) lightning contamination. In contrast with previous studies using estimated electric field results (Kuo et al., 2005; Adachi et al., 2006; Adachi et al., 2008; Kuo et al., 2008; Kuo et al., 2009), we presented the emission ratio of the total intensity of the 2P to 1P band in the data points of **Figures 6–11**. The measured emission ratio should be independent of their observed instrument (spectrophotometer, array photometer, or intensified imager) if their relative instrument detection efficiency for 2P/1P emissions is well calibrated. However, that also causes an error of the band percentage $B_k(h)$ calculation introduced into a total specified band emission.

As mentioned in the discussion of altitude errors in *The ISUAL array photometer*, some of these errors from different calculations could be accumulated. After checks on the ISUAL recorded images, the altitude errors would be controlled within ±5 km based on a top altitude of 90 km for triangularly measured sprites (Sentman et al., 1995; Wescott et al., 2001). Besides, we selected sprite events with the distance of 2,900–3,500 km, where few errors in the $B_k(h)$ would be introduced. The uncertainty in the band percentage can be limited to ±10%. However, as mentioned in *The ISUAL array photometer*, the unknown percentage of the 1P spectrum with vibrational number $\nu = 0$ would contribute as much as 30% to the error.

Most sprite events were reported with substantial blue lightning contamination (Adachi et al., 2008) due to the short delay time <0.1 ms between the parent lightning and sprite events. We chose sprite events for which lightning signals can be separated from sprite emissions. If a time delay between lightning and sprite emission is longer than >0.1 ms, the AP vertical channel can separate the lower-altitude lightning emission from the higher-altitude sprite emission. For our considered sprite events in **Table 1**, the AP-measured blue/red emission peak occurred at least 0.1 ms after the time of recorded lightning SP5 at 777.4 nm, and no simultaneous lightning was contaminating other AP channels.

Comparison With Morphology of Recorded Sprites Observed at 5,000 fps

Figure 3 helps us to study the features for the specific streamer processes using the AP-measured sprite emission ratio. We identify the sprite streamer processes with four major processes: 1) sprite streamer inception, 2) upper branches of

TABLE 1 | The event list for two sprite categories (sprite halo and carrot sprite events) and their inception altitudes and emission times.

Trigger time (UT)	Type[a]	Inception altitudes (km)	Emission time (ms)
Oct 3, 2005 14:43:37.240	SH	88.5 ± 6.3	0.6
Sep 4, 2006 15:05:30.844	SH	80.5 ± 6.0	1.4
Apr 29, 2007 06:38:30.728	SH	86.5 ± 6.2	0.7
Aug 24, 2007 16:57:01.582	SH	81.5 ± 6.3	0.9
Mar 26, 2005 21:37:06.144	CS	71.9 ± 6.8	3.5
Jul 30, 2005 04:39:42.742	CS	72.4 ± 5.7	3.4
Jul 17, 2007 11:38:13.200	CS	75.3 ± 6.1	3.2
Sep 28, 2009 04:25:56.262	CS	59.2 ± 7.0	2.5
Jul 11, 2010 04:36:16.235	CS	68.8 ± 6.8	3.0
Sep 1, 2011 04:42:58.161	CS	56.7 ± 7.0	2.4

[a] *Sprite type is determined by their inception altitudes and by their distinguished halo emission where SH and CS denote sprite halo event and carrot sprite, respectively.*

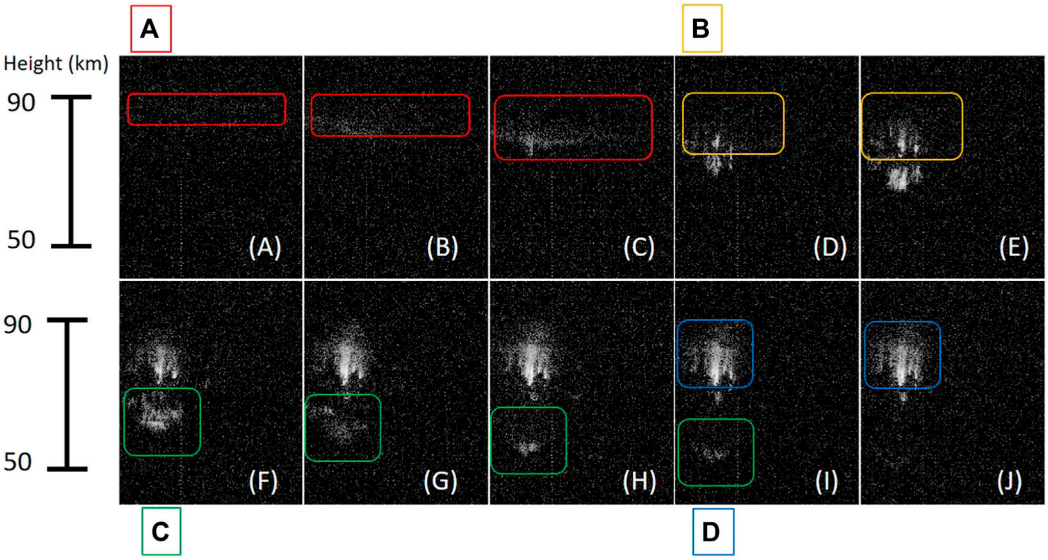

FIGURE 3 | Although AP lacks sufficient spatial resolution to point out their development stages, we used typical sprite events in the 2018 Taiwan campaign and extracted the major dynamic features of sprite development. These features of sprite developing stages help us to analyze the AP-measured emission ratio for the ISUAL-recorded sprites events in times and in altitudes, also corresponding to **Figures 4 (A–D)**.

bi-directional streamers with negative polarity, 3) downward propagating streamers with positive polarity, and 4) reigniting of upward streamer in the sprite cluster region. **Figure 4** also illustrates the stages 1–4 of streamer processes for sprites. In the development stage (1), **Figures 3A–C**, **4A** pinpoint the occurrence of steamer inception near the downward edge of the sprite halo. The bi-directional streamers fully developed into upper and lower branches in the stage (2) in **Figures 3D,E**, **4B**. The streamer heads in their lower branches propagated downward with extra brightness, shown in **Figures 3F–H**, **4C**. The sprite body's emission was continuously recorded in several later frames of the images in **Figures 3I,J**, **4D**. Next, we will analyze their AP-measured emission ratio based on the time and the height of ISUAL-recorded sprite events. The morphology of a typical sprite event recorded at 5,000 fps helps us imagine the successive image frames and identify the stages 1–4 for recorded sprites since the ISUAL payload lacks the detailed dynamics in their recorded sprites.

Two Distinct Types of Observed Sprites Determined by Their Inception Altitudes: Sprite Halo Event and the Carrot Sprite Event

Sprites involve streamer heads emerging from the downward leading edge of a halo or plasma inhomogeneity and branching into both downward streamers and upward-propagating streamers simultaneously (Stanley et al., 1999; Stenbaek-Nielsen et al., 2000; Moudry et al., 2003; Marshall and Inan, 2005; Cummer et al., 2006; McHarg et al., 2007; Stenbaek-Nielsen et al., 2013). Numerical studies compared sprite halo and carrot sprites (Qin et al., 2011). The short-delayed halo sprites were possibly produced by a–CG (Cloud-to-Ground lightning with negative polarity) with an impulsive lightning current and without continuing current, while long-delayed carrot sprites were triggered by + CG (Cloud-to-Ground lightning with positive polarity) due to a long-lasting high field region for a

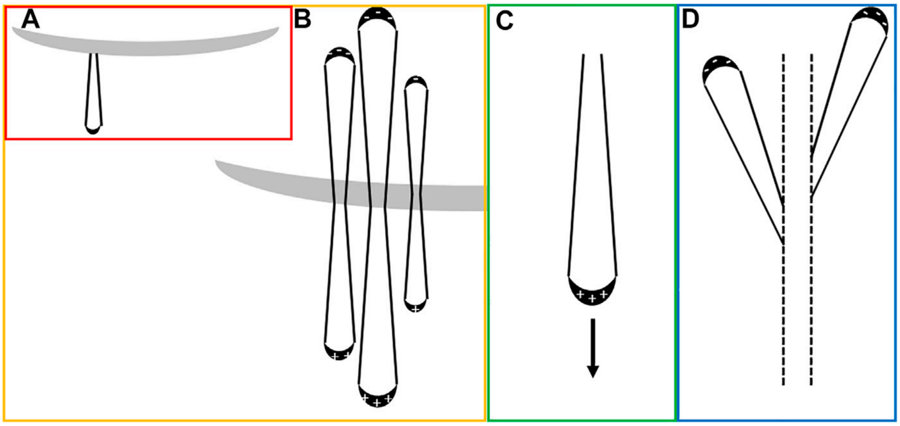

FIGURE 4 | To analyze the AP emission characteristics of each developed stage in ISUAL recorded sprites, we choose **(A)** sprite streamer inception, **(B)** upper branches of bi-directional streamers with negative polarity, **(C)** downward propagating streamers with positive polarity, and **(D)** reigniting of upward streamer in the sprite body for specific streamer process in **Figure 3** and later used to study the AP measured emission ratio.

lightning continuing current. Listed in **Table 1**, we selected sprite events from 2005 to 2011 to minimize possible uncertainty in emission ratios. Ten sprite events were excluded from twenty candidates. In six sprite events lightning was more powerful than the AP-measured blue/red emission. Difficulties were faced in another four sprite events in separating the sprite emission from the lightning emission. The final ten selections are included in **Table 1** which shows the characteristics of sprite halo and carrot sprite events in their inception altitudes, AP-measured ratios, and emission times.

In ISUAL recorded images (spatial resolution ~2 km), sprite halos events have narrow structures (likely column sprites) with a distinguished halo. In contrast, carrot sprites have compact structures with higher brightness and longer emission duration. For AP-measured emission altitudes, sprite halo events were accompanied by downwardly-propagating streamers, and were intercepted at altitudes 84.3 ± 3.8 km with an average emission time 0.9 ± 0.3 ms. Otherwise, the AP measured emission for carrot sprite events began at lower altitudes 67.4 ± 7.6 km and developed into upward and downward-propagating emissions with an average emission time 3.0 ± 0.5 ms. Besides, a mixed type was found that a sprite event at time 21:45:48.239 (UT) on Mach 16, 2006 initialized at 83.4 ± 6.8 km with an emission time 2.9 ms, not listed in **Table 1**. The sprite event has both characteristics of our categorized sprite halos and carrot sprites. We identified this event with the mixed type. The sprite may be accompanied by the halo emission at higher altitudes and finally developed into a whole carrot sprite with a more prolonged emission. The recorded images also show the cloud emission lasted more than 180 ms. We conjecture the sprite event may be affected by the lightning continuing current associated with cloud emissions.

Figure 5 compares two distinct categories of sprite events (sprite halo and carrot sprite events) distinguished by their inception altitudes and their AP-measured emission, listed in **Table 1**; **Figures 6**, **7** show their spatial and temporal diagrams of AP-measured blue-to-red ratios, respectively. For a sprite halo event (14:43:37.240 UT on October 3, 2005) **Figures 5A**, **6A** show AP-measured ratios in green cross symbols as referenced by curves to represent the simulated streamer ratios with 0.4–4.6 E_k. **Figure 6B** indicates the diagram of AP-measured ratios by colors in altitudes and times. In **Figure 6B**, a sprite halo is initialized at an altitude of 88.5 ± 6.3 km, which corresponds to the altitude range of the transition from a halo to the inception of sprite streamers in **Figure 5A**. The AP signals propagated down to a lower altitude of 62.6 ± 6.3 km. As shown in **Figure 6A**, AP-measured ratios (green cross symbols) are found between 0.9 E_k and 3.7–4.6 E_k in the streamer head. Although AP-measured ratios have lower values than predicted emission ratios (thick cyan and magenta lines), the statistical analysis in **Figure 8A** with more sprite halo events implies that the AP-measured ratios are consistent with predicted emission ratios.

Figure 5B shows a carrot sprite event without a distinguished halo observed at 04:36:16.235 (UT) on July 11, 2010. The AP-measured blue/red emission peaks are delayed about 0.4 ms after the recorded lightning signal by SP5 at 777.4 nm. The carrot sprite event initialized at an estimated altitude of 68.8 ± 6.8 km, and subsequently propagated downwardly and upwardly. **Figure 7A** compares AP-measured ratios with predicted emission ratios while **Figure 7B** shows their timing diagram in altitude. The carrot sprite initialized in an altitude range of 62–76 km at time −0.4 ms, and developed into lower altitude emission in the interval −0.4–0.05 ms. Unexpectedly, AP-measured ratios approach the red lines (0.9 E_k). After the time 0.05 ms, AP-measured ratios gradually decreased and reached to the blue lines (0.4 E_k). The gradual decrease of the emission ratios can be understood since the sprite streamer energy is finally dissipated in electron collisions with ambient molecules. In addition, the upper branches of sprite emission occurred after 0 ms where the AP-measured ratios have a maximum value 0.33. Similarly, the AP-measured ratios are slightly higher than red lines (0.9 E_k) and are lower than predicted emissions in cyan and magenta lines (3.7–4.6 E_k). Next, we collected

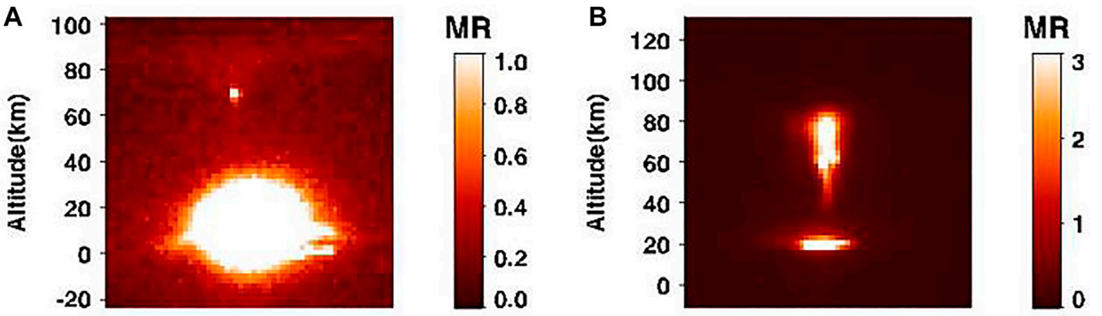

FIGURE 5 | Two distinct types of observed sprites determined by the AP where the color indicates the brightness in units of MR (mega Rayleigh): **(A)** the sprite halo event observed at 14:53:13.687–716 on October 3, 2005 where the upper part (70–90 km) was a funnel-shaped halo structure with a compact sprite emission at ~ 70 km, and the lower part (0–40 km) was a nut-shaped lightning emission filled with scattered photons (Luque et al., 2020), and **(B)** the carrot sprite event at 04:36: 16.235 (UT) on July 11, 2010. The carrot sprite emission extended widely at altitudes of 30–90 km over the cloud top emission at a projected altitude up to ~20 km.

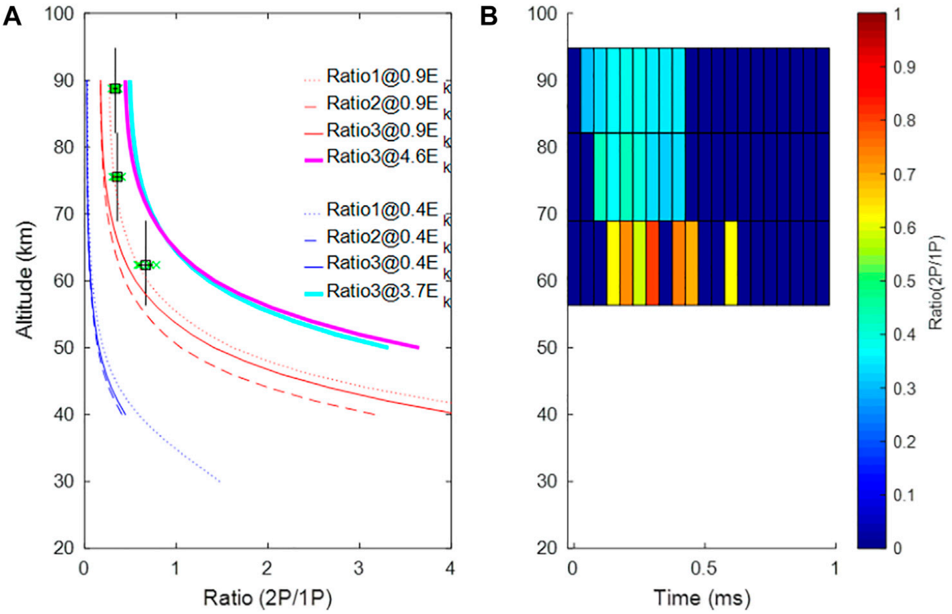

FIGURE 6 | The sprite halo event observed at 14:53:13.687–716 on October 3, 2005: **(A)** the AP-measured ratio 2P/1P with predicted emission ratios of Ratio 1 (r_{CB}), Ratio 2 (R_{CB}), and Ratio 3 (R^{*}_{CB}) at ambient electric fields of 0.4 E_k and 0.9 E_k. The thick cyan and magenta lines represent the predicted 2P/1P ratio in sprite streamer simulations with streamer head electric fields of 3.7 E_k and 4.6 E_k under ambient electric fields of 0.4 E_k and 0.9 E_k, respectively. The green crosses indicate the data points of AP-measured ratios, while the square symbols are the means of the AP-measured ratios, and the horizontal bars are their standard deviations. **(B)** the diagram of AP-measured ratios indicated by colors in altitudes and times.

additional sprite events to support more evidence on the higher emission ratios for sprite halos and lower values for carrot sprites.

Statistical Analysis of AP-Measured Emission Ratios

Figure 8 shows the selected sprite events where each event has 3-4 points measured in the corresponding altitude range by the AP vertically-stacked channels. The square symbol indicates the mean sprite ratio at a specified altitude, where the vertical error bars show the altitude range of the AP measurements. The horizontal error bars indicate the standard deviation of the AP-measured ratios in the same AP channels. In **Figure 8A**, the AP-measured ratios (2P/1P) in sprite halo events have data points scattered around the curves for predicted emission ratios from streamer head electric fields (3.7–4.6 E_k for cyan and magenta lines). The scatter in the distribution of AP measured ratios in sprite halos events of **Figure 8A** may is attributable to the variances of large-scale quasi-steady electric field magnitudes caused by charge transfer inside the clouds beneath or to uncertainty in the AP measurement with unknown reasons.

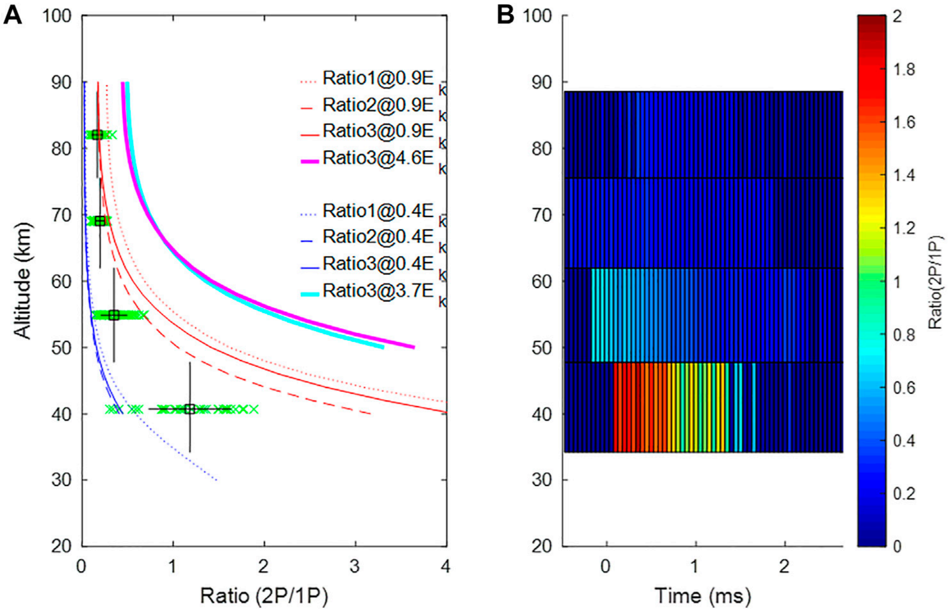

FIGURE 7 | The carrot sprite event at 04:36:16.235 (UT) on July 11, 2010: **(A)** the AP-measured ratio 2P/1P with predicted emission ratios of Ratio 1 (r_{CB}), Ratio 2 (R_{CB}), and Ratio 3 (R^{*}_{CB}) at ambient electric fields of 0.4 E_k and 0.9 E_k. The thick cyan and magenta lines represent the predicted 2P/1P ratio in sprite streamer simulations with streamer head electric fields of 3.7 E_k and 4.6 E_k under ambient electric fields of 0.4 E_k and 0.9 E_k, respectively. **(B)** the diagram of AP-measured ratios indicated by colors in altitude and time.

In **Figure 8B**, the carrot sprite events initialized at a lower altitude of 60–75 km, and have lower emission ratios than sprite halos events in **Figure 8A**. AP-measured ratios are slightly lower than the predicted ratios (streamer head electric fields of 3.7 E_k and 4.6 E_k in cyan and magenta lines) in higher altitudes of 65–90 km (sprite upper branches and central regions). The lower tendrils in carrot sprites at lower altitudes (50–65 km) have increased emission rates. The emission ratios reflect the quenching effect in *Analytical expressions for sprite emission ratios*. But these values are unexpected, ranging between blue lines (0.4 Ek) and red lines (0.9 E_k) in **Figure 8B**.

Figure 8B have a lower bound of data points near blue lines (0.4 E_k). Most of the estimated ambient electric fields were greater than 0.4 E_k. The ambient electric field threshold (0.4 E_k) is consistent with the results of remote electromagnetic field measurements for short-delayed or big/bright sprites (Hu et al., 2002; Li et al., 2008). The non-streamer head regions (such as sprite streamers' bodies and tails or the surroundings of sprite streamers) may contribute additional red (1P) emission, which may cause lower emission ratios (2P/1P). Stenbaek-Nielsen et al. (2020) compared the blue-to-red emission ratio and found that upper propagating streamer, sprite beads, and glow have lower emission ratios. For those non-streamer processes, a large percentage of 1P (red) emission makes lower AP-measured ratios, especially for the case of long emission time in the carrot sprites. Hence, for carrot sprites, our study shows that sprite inception at lower altitudes may favor development into the whole complex structures of sprites, which may be accompanied by non-streamer emission or sprite beads caused by attachment instability in streamer channels (Luque et al., 2016). The Possibly a pre-existing free ionized plasma patch in the early stage of sprites may provide more free energized electrons. More non-streamer processes with lower emission ratios could occur and co-exist with reigniting of upward streamers. Next, we provide an example case to show the effect of a favorable plasma environment.

The Effects of AP-Measured Ratios for a Pre-existing Sprite on a Later-Occurring Sprite

Figure 9 shows successive sprite events at 22:01:23.178 (UT) on August 3, 2007, which are also called dancing sprites (Lyons, 1994; Bór et al., 2018 and reference therein). The preceding sprite event in **Figure 9A** began ~85 ms before the second sprite event with lower brightness in **Figure 9B**. We also demonstrate the decrease in emission ratios for a pre-existing sprite on a later-occurring sprite in **Figures 10, 11**. The measured emission ratios for the pre-existing sprite and the later-occurring sprite are compared with predicted emission ratios Ratio 1 (r_{CB}), Ratio 2 (R_{CB}), and Ratio 3 (R^{*}_{CB}).

The comparison of **Figure 10A** with **Figure 11A** shows a slightly lower value of AP-measured emission ratio 2P/1P, which may imply that the plasma environment and the generation mechanism of the second sprite event may be different from that of the first sprite event. Successive sprite events have been reported in previous studies using a high-speed image-intensified camera (Stenbaek-Nielsen et al., 2000). A second sprite occurred in the fading region of the first sprite, gradually brightened, and developed branched tendrils towards lower altitudes. The

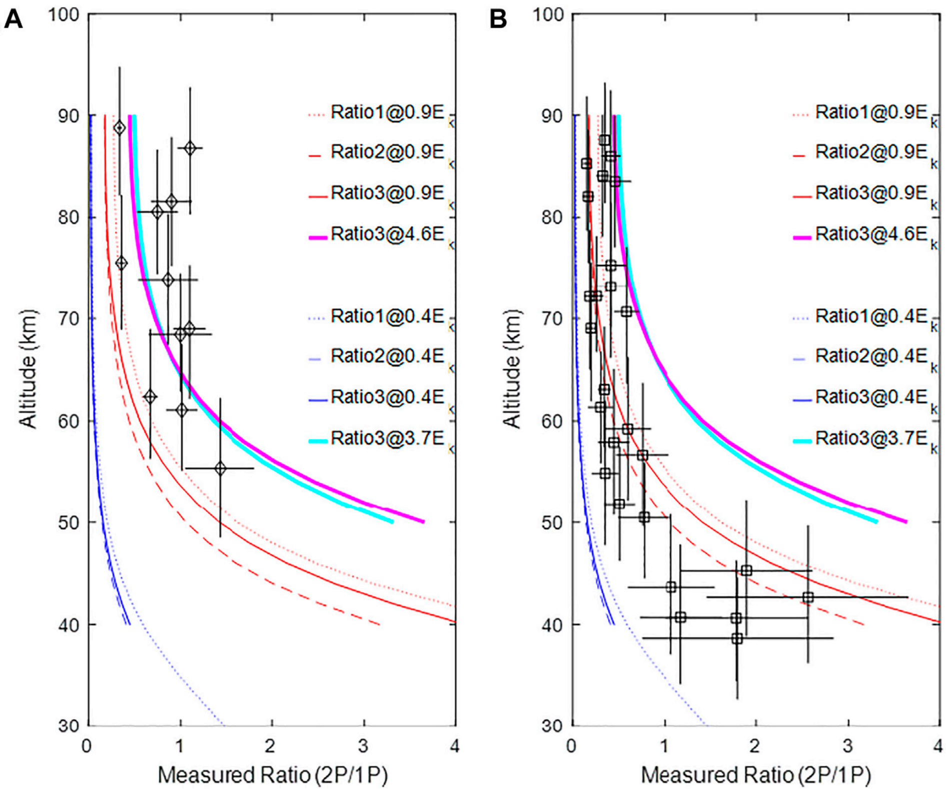

FIGURE 8 | AP-measured emission ratios of 2P to 1P for 10 selected sprite events without potential lightning contamination. Two categories of ISUAL sprite events are shown in AP-measured ratios: **(A)** sprite halo events with impulse AP emission time (0.9 ± 0.3 ms) and higher estimated electric fields, and **(B)** carrot sprite events with long AP emission time (3.0 ± 0.5 ms) and lower estimated electric fields.

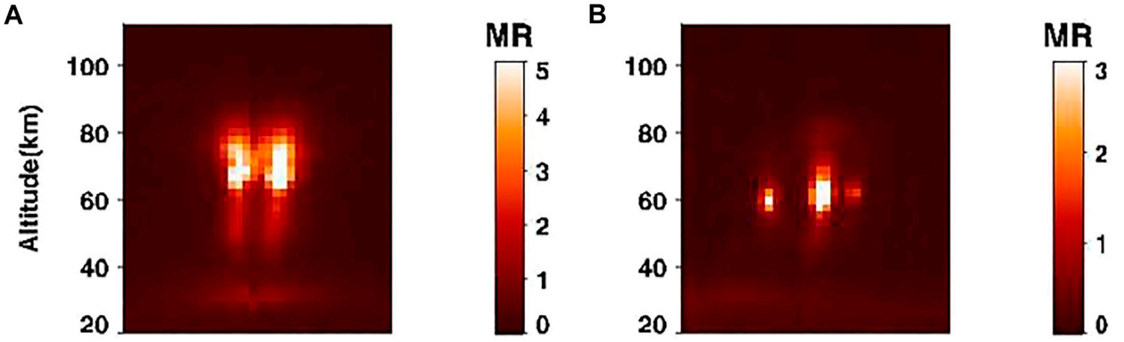

FIGURE 9 | Successive sprite events at 22:01:23.178 (UT) from August 3, 2007, demonstrating the effects of AP-measured emission ratios for **(A)** a pre-existing sprite and, **(B)** a later-occurring sprite, which are also called dancing sprites.

upwardly branched streamers may arise from previous older streamer channels (Stenbaek-Nielsen et al., 2000; Luque et al., 2016). The AP-measured emission ratio in **Figure 11B** provides direct evidence of the upper branches developing in pre-existing sprite structures where lower-altitude AP-measured ratios developed into the region at higher altitude. The AP-measured ratios in the later-occurring sprite are lower than that in the previous sprite event. That may support the idea that the change of the plasma environment may cause lower emission ratios in carrot sprite events.

SUMMARY

We verified experimentally the AP-measured emission ratio 2P/1P and compared it with the theoretically predicted sprite

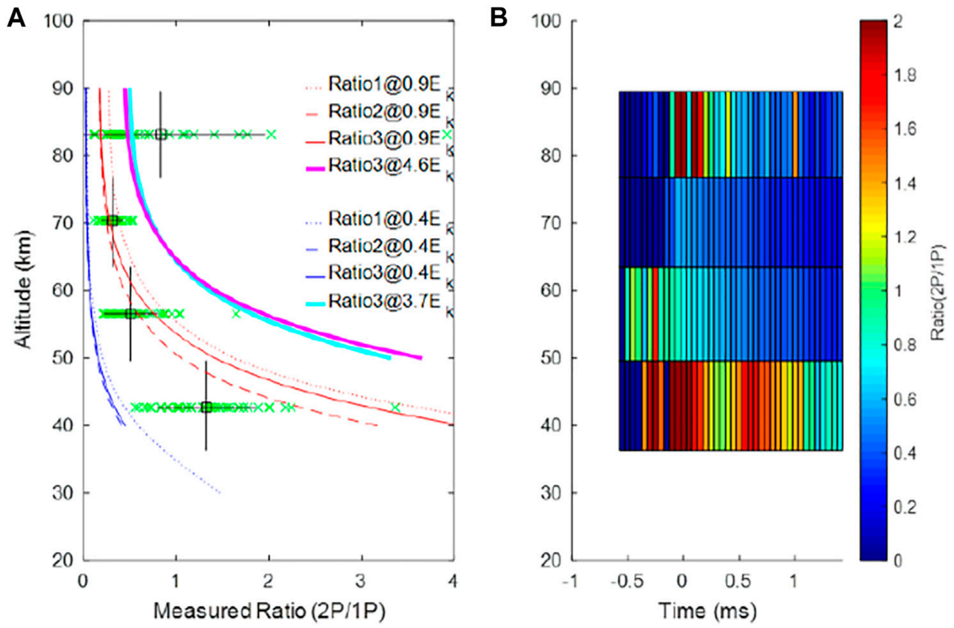

FIGURE 10 | The **(A)** AP-measured ratio 2P/1P with predicted emission ratios and **(B)** the diagram of AP-measured ratios indicated by colors in altitudes and times for the pre-existing sprite event at 22:01:23.178 (UT) from August 3, 2007.

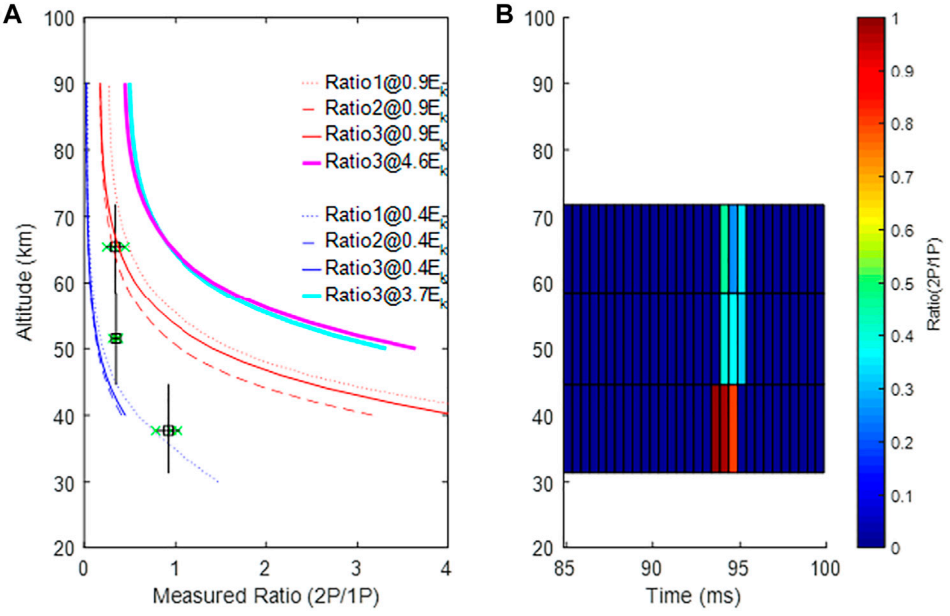

FIGURE 11 | The **(A)** the AP-measured ratio 2P/1P with predicted emission ratios and **(B)** the diagram of AP-measured ratios indicated by colors in altitude and time for the later-occurring sprite event at 22:01:23.178 (UT) from August 3, 2007.

emission ratio 2P/1P using numerical results on sprite streamers (Celestin and Pasko, 2010; Pérez-Invernón et al., 2018). AP-measured ratios in sprite halo events are consistent with predicted ratios for streamer head electric fields of 3.7 E_k and 4.6 E_k in **Figure 8A**. Most carrot sprite events initialized at altitudes 67.4 ± 7.6 km with lower estimated electric field 1~3 or 4 E_k. Below 60 km, surprisingly, AP-measured ratios fell below the predicted ratio 1 E_k. We conjectured that the lower emission ratios are contributed from those non-streamer regions (upper propagating streamer, sprite beads, and glow) by Stenbaek-Nielsen et al. (2020). In addition, the AP-measured ratios have a lower bound of predicted emission ratios associated with 0.4 E_k.

For space-based optical diagnostics in limb observation, as with the ISUAL mission, the main conclusions from our studies on the sprite emission ratio 2P/1P are the following:

1) For accurate analyses of ISUAL AP data, we selected sprite events from the first 7 years (2004–2011) of operation to avoid the degradation in instrument performance. After analyzing the ten selected sprite events, the AP-measured ratios scatter widely as previous results in sprites (Adachi et al., 2008), and estimated electric fields range between 0.4 E_k and greater than 4 E_k. The downward propagating streamers verified the streamer head electric fields in the range ~3.7–4.6 E_k. At lower altitudes, AP-measured ratios have a lower bound, corresponding to the predicted ratio for 0.4 E_k. The threshold of the estimated electric field (0.4 E_k) is consistent with the earlier results of remote electromagnetic field measurements for short-delayed or big/bright sprites (Hu et al., 2002; Li et al., 2008).
2) The AP-measured ratios of downward propagating streamers in sprite halo events scattered around the ratios predicted by numerical streamer head electric fields with 3.7–4.6 E_k (Ihaddadene and Celestin, 2017) where the estimated electric field was in the range 0.4–~0.9 E_k. However, for carrot sprite events, the AP-measured emission ratio 2P/1P showed lower values than predicted ratios. The extra 1P red emission may be contributed from non-streamer dominant emissions: sprite beads and glow or possibly by plasma environment changes in upper streamers in carrot sprites with lower inception altitude and longer emission time Qin et al., 2014.

DATA AVAILABILITY STATEMENT

The original contributions presented in the study are included in the article/Supplementary Material, and further inquiries can be directed to the corresponding author.

AUTHOR CONTRIBUTIONS

EW conceived the study to check AP data for sprite halos. C-LK analyzed AP data. KI and SC formulated the analytical equations for sprite emission ratios and conducted the simulation of sprite streamers. TA, YT, HF, and SM provided the AP calibration data. YT, HF, SM, R-RH, and L-CL were all part of the ISUAL science team. All authors contributed to the final interpretation and writing of the manuscript with major contribution by C-LK.

FUNDING

The work of C-LK was supported in part by grants MOST 110-2111-M-008-007, MOST 109-2111-M-008-006 and MOST 108-2111-M-008-005 from Ministry of Science and Technology of Taiwan.

ACKNOWLEDGMENTS

We benefitted from the preliminary studies by Master student Mr. Pei-Yu Chen, and appreciate the assistance and support from the staff at the Center for Astronautical Physics and Engineering of National Central University in Taiwan.

REFERENCES

Adachi, T., Fukunishi, H., Takahashi, Y., Hiraki, Y., Hsu, R.-R., Su, H.-T., et al. (2006). Electric Field Transition between the Diffuse and Streamer Regions of Sprites Estimated from ISUAL/array Photometer Measurements. *Geophys. Res. Lett.* 33, 17803. doi:10.1029/2006GL026495

Adachi, T., Hiraki, Y., Yamamoto, K., Takahashi, Y., Fukunishi, H., Hsu, R.-R., et al. (2008). Electric fields and Electron Energies in Sprites and Temporal Evolutions of Lightning Charge Moment. *J. Phys. D: Appl. Phys.* 41 (23), 234010. doi:10.1088/0022-3727/41/23/234010

Armstrong, R. A., Shorter, J. A., Taylor, M. J., Suszcynsky, D. M., Lyons, W. A., and Jeong, L. S. (1998). Photometric Measurements in the SPRITES '95 & '96 Campaigns of Nitrogen Second Positive (399.8 Nm) and First Negative (427.8 Nm) Emissions. *J. Atmos. Solar-Terrestrial Phys.* 60 (7–9), 787–799. doi:10.1016/S1364-6826(98)00026-1

Armstrong, R. A., Suszcynsky, D. M., Lyons, W. A., and Nelson, T. E. (2000). Multi-color Photometric Measurements of Ionization and Energies in Sprites. *Geophys. Res. Lett.* 27 (5), 653–656. doi:10.1029/1999GL003672

Babaeva, N. Y., and Naidis, G. V. (1997). Dynamics of Positive and Negative Streamers in Air in Weak Uniform Electric fields. *IEEE Trans. Plasma Sci.* 25, 375–379. doi:10.1109/27.602514

Barrington-Leigh, C. P., and Inan, U. S. (1999). Elves Triggered by Positive and Negative Lightning Discharges. *Geophys. Res. Lett.* 26, 683–686. doi:10.1029/1999gl900059

Bór, J., Zelkó, Z., Hegedüs, T., Jäger, Z., Mlynarczyk, J., Popek, M., et al. (2018). On the Series of +CG Lightning Strokes in Dancing Sprite Events. *J. Geophys. Res. Atmos.* 123, 11030–11047. doi:10.1029/2017JD028251

Celestin, S., and Pasko, V. P. (2010). Effects of Spatial Non-uniformity of Streamer Discharges on Spectroscopic Diagnostics of Peak Electric fields in Transient Luminous Events. *Geophys. Res. Lett.* 37 (7), a–n. doi:10.1029/2010GL042675

Chern, J. L., Hsu, R. R., Su, H. T., Mende, S. B., Fukunishi, H., Takahashi, Y., et al. (2003). Global Survey of Upper Atmospheric Transient Luminous Events on the ROCSAT-2 Satellite. *J. Atmos. Solar-Terrestrial Phys.* 65, 647–659. doi:10.1016/S1364-6826(02)00317-6

Cummer, S. A., Jaugey, N., Li, J., Lyons, W. A., Nelson, T. E., and Gerken, E. A. (2006). Submillisecond Imaging of Sprite Development and Structure. *Geophys. Res. Lett.* 33 (4). doi:10.1029/2005gl024969

Frey, H. U., Mende, S. B., Harris, S. E., Heetderks, H., Takahashi, Y., Su, H. T., et al. (2016). The Imager for Sprites and Upper Atmospheric Lightning (ISUAL). *J. Geophys. Res. Space Phys.* 121 (8), 8134–8145. doi:10.1002/2016JA022616

Gordillo-Vázquez, F. J., Luque, A., and Simek, M. (2012). Near Infrared and Ultraviolet Spectra of TLEs. *J. Geophys. Res.* 117, a–n. doi:10.1029/2012JA017516

Gordillo-Vázquez, F. J., and Pérez-Invernón, F. J. (2021). A Review of the Impact of Transient Luminous Events on the Atmospheric Chemistry: Past, Present, and Future. *Atmos. Res.* 252, 105432. doi:10.1016/j.atmosres.2020.105432

Green, B. D., Fraser, M. E., Rawlins, W. T., Jeong, L., Blumberg, W. A. M., Mende, S. B., et al. (1996). Molecular Excitation in Sprites. *Geophys. Res. Lett.* 23 (16), 2161–2164. doi:10.1029/96GL02071

Hampton, D. L., Heavner, M. J., Wescott, E. M., and Sentman, D. D. (1996). Optical Spectral Characteristics of Sprites. *Geophys. Res. Lett.* 23 (1), 89–92. doi:10.1029/95GL03587

Hu, W., Cummer, S. A., Lyons, W. A., and Nelson, T. E. (2002). Lightning Charge Moment Changes for the Initiation of Sprites. *Geophys. Res. Lett.* 29 (8), 120–124. doi:10.1029/2001gl014593

Ihaddadene, M. A., and Celestin, S. (2017). Determination of Sprite Streamers Altitude Based on N 2 Spectroscopic Analysis. *J. Geophys. Res. Space Phys.* 122 (1), 1000–1014. doi:10.1002/2016ja023111

Kanmae, T., Stenbaek-Nielsen, H. C., McHarg, M. G., and Haaland, R. K. (2010b). Observation of Blue Sprite Spectra at 10,000 Fps. *Geophys. Res. Lett.* 37, a–n. doi:10.1029/2010GL043739

Kanmae, T., Stenbaek-Nielsen, H. C., McHarg, M. G., and Haaland, R. K. (2010a). Observation of Sprite Streamer Head's Spectra at 10,000 Fps. *J. Geophys. Res.* 115, A00E48. doi:10.1029/2009JA014546

Kosar, B. C., Liu, N., and Rassoul, H. K. (2012). Luminosity and Propagation Characteristics of Sprite Streamers Initiated from Small Ionospheric Disturbances at Subbreakdown Conditions. *J. Geophys. Res.* 117 (A8), a–n. doi:10.1029/2012ja017632

Kuo, C.-L., Chou, J. K., Tsai, L. Y., Chen, A. B., Su, H. T., Hsu, R. R., et al. (2009). Discharge Processes, Electric Field, and Electron Energy in ISUAL-Recorded Gigantic Jets. *J. Geophys. Res.* 114 (A4), a–n. doi:10.1029/2008ja013791

Kuo, C.-L., Hsu, R. R., Chen, A. B., Su, H. T., Lee, L. C., Mende, S. B., et al. (2005). Electric fields and Electron Energies Inferred from the ISUAL Recorded Sprites. *Geophys. Res. Lett.* 32, a–n. doi:10.1029/2005GL023389

Kuo, C. L., Chen, A. B., Chou, J. K., Tsai, L. Y., Hsu, R. R., Su, H. T., et al. (2008). Radiative Emission and Energy Deposition in Transient Luminous Events. *J. Phys. D: Appl. Phys.* 41, 234014. doi:10.1088/0022-3727/41/23/234014

Li, J., Cummer, S. A., Lyons, W. A., and Nelson, T. E. (2008). Coordinated Analysis of Delayed Sprites with High-Speed Images and Remote Electromagnetic fields. *J. Geophys. Res.* 113 (D20), 77. doi:10.1029/2008jd010008

Liu, N., Pasko, V. P., Burkhardt, D. H., Frey, H. U., Mende, S. B., Su, H.-T., et al. (2006). Comparison of Results from Sprite Streamer Modeling with Spectrophotometric Measurements by ISUAL Instrument on FORMOSAT-2 Satellite. *Geophys. Res. Lett.* 33 (1), a–n. doi:10.1029/2005GL024243

Liu, N., and Pasko, V. P. (2004). Effects of Photoionization on Propagation and Branching of Positive and Negative Streamers in Sprites. *J. Geophys. Res.* 109, A04301. doi:10.1029/2003JA010064

Liu, N. Y., Pasko, V. P., Adams, K., Stenbaek-Nielsen, H. C., and McHarg, M. G. (2009). Comparison of Acceleration, Expansion, and Brightness of Sprite Streamers Obtained from Modeling and High-Speed Video Observations. *J. Geophys. Res.* 114 (A3), a–n. doi:10.1029/2008ja013720

Luque, A., Gordillo-Vázquez, F. J., Li, D., Malagón-Romero, A., Pérez-Invernón, F. J., Schmalzried, A., et al. (2020). Modeling Lightning Observations from Space-Based Platforms (CloudScat.Jl 1.0). *Geosci. Model. Dev.* 13 (11), 5549–5566. doi:10.5194/gmd-13-5549-2020

Luque, A., Stenbaek-Nielsen, H. C., McHarg, M. G., and Haaland, R. K. (2016). Sprite Beads and Glows Arising from the Attachment Instability in Streamer Channels. *J. Geophys. Res. Space Phys.* 121 (3), 2431–2449. doi:10.1002/2015ja022234

Lyons, W. A. (1994). Characteristics of Luminous Structures in the Stratosphere above Thunderstorms as Imaged by Low-Light Video. *Geophys. Res. Lett.* 21 (10), 875–878. doi:10.1029/94GL00560

Marshall, R. A., and Inan, U. S. (2005). High-speed Telescopic Imaging of Sprites. *Geophys. Res. Lett.* 32 (5). doi:10.1029/2004gl021988

McHarg, M. G., Stenbaek-Nielsen, H. C., and Kammae, T. (2007). Observations of Streamer Formation in Sprites. *Geophys. Res. Lett.* 34, 06804. doi:10.1029/2006GL027854

Mende, S. B., Frey, H. U., Hsu, R. R., Su, H. T., Chen, A. B., Lee, L. C., et al. (2005). Dregion Ionization by Lightning-Induced Electromagnetic Pulses. *J. Geophys. Res.* 110, 11312. doi:10.1029/2005JA011064

Mende, S. B., Rairden, R. L., Swenson, G. R., and Lyons, W. A. (1995). Sprite Spectra; N21 PG Band Identificationfication. *Geophys. Res. Lett.* 22 (19), 2633–2636. doi:10.1029/95GL02827

Miyasato, R., Fukunishi, H., Takahashi, Y., and Taylor, M. J. (2003). Energy Estimation of Electrons Producing Sprite Halos Using Array Photometer Data. *J. Atmos. Solar-Terrestrial Phys.* 65, 573–581. doi:10.1016/s1364-6826(02)00322-x

Miyasato, R., Taylor, M. J., Fukunishi, H., and Stenbaek-Nielsen, H. C. (2002). Statistical Characteristics of Sprite Halo Events Using Coincident Photometric and Imaging Data. *Geophys. Res. Lett.* 29 (21), 2033. doi:10.1029/2001GL014480

Morrill, J., Bucsela, E., Siefring, C., Heavner, M., Berg, S., Moudry, D., et al. (2002). Electron Energy and Electric Field Estimates in Sprites Derived from Ionized and neutralN2emissions. *Geophys. Res. Lett.* 29 (10), 100–104. doi:10.1029/2001gl014018

Moss, G. D., Pasko, V. P., Liu, N., and Veronis, G. (2006). Monte Carlo Model for Analysis of thermal Runaway Electrons in Streamer Tips in Transient Luminous Events and Streamer Zones of Lightning Leaders. *J. Geophys. Res.* 111 (A2). doi:10.1029/2005ja011350

Moudry, D., Stenbaek-Nielsen, H., Sentman, D., and Wescott, E. (2003). Imaging of Elves, Halos and Sprite Initiation at Time Resolution. *J. Atmos. Solar-Terrestrial Phys.* 65, 509–518. doi:10.1016/s1364-6826(02)00323-1

Pasko, V. P., Inan, U. S., and Bell, T. F. (1998). Spatial Structure of Sprites. *Geophys. Res. Lett.* 25 (12), 2123–2126. doi:10.1029/98gl01242

Pasko, V. P., Inan, U. S., Bell, T. F., and Taranenko, Y. N. (1997). Sprites Produced by Quasi-Electrostatic Heating and Ionization in the Lower Ionosphere. *J. Geophys. Res.* 102 (A3), 4529–4561. doi:10.1029/96ja03528

Pérez-Invernón, F. J., Luque, A., Gordillo-Vázquez, F. J., Sato, M., Ushio, T., Adachi, T., et al. (2018). Spectroscopic Diagnostic of Halos and Elves Detected from Space-Based Photometers. *J. Geophys. Res. Atmos.* 123 (22), 912917–912941. doi:10.1029/2018jd029053

Qin, J., Celestin, S., and Pasko, V. P. (2011). On the Inception of Streamers from Sprite Halo Events Produced by Lightning Discharges with Positive and Negative Polarity. *J. Geophys. Res.* 116, a–n. doi:10.1029/2010JA016366

Qin, J., Pasko, V. P., McHarg, M. G., and Stenbaek-Nielsen, H. C. (2014). Plasma Irregularities in the D-Region Ionosphere in Association with Sprite Streamer Initiation. *Nat. Commun.* 5, 3740. doi:10.1038/ncomms4740

Sentman, D. D., Wescott, E. M., Osborne, D. L., Hampton, D. L., and Heavner, M. J. (1995). Preliminary Results from the Sprites94 Aircraft Campaign: 1. Red Sprites. *Geophys. Res. Lett.* 22 (10), 1205–1208. doi:10.1029/95GL00583

Stanley, M., Krehbiel, P., Brook, M., Moore, C., Rison, W., and Abrahams, B. (1999). High Speed Video of Initial Sprite Development. *Geophys. Res. Lett.* 26 (20), 3201–3204. doi:10.1029/1999gl010673

Stenbaek-Nielsen, H. C., McHarg, M. G., Haaland, R., and Luque, A. (2020). Optical Spectra of Small-Scale Sprite Features Observed at 10,000 Fps. *J. Geophys. Res. Atmos.* 125, e2020JD033170. doi:10.1029/2020JD033170

Stenbaek-Nielsen, H. C., Kanmae, T., McHarg, M. G., and Haaland, R. (2013). High-Speed Observations of Sprite Streamers. *Surv. Geophys.* 34, 769–795. doi:10.1007/s10712-013-9224-4

Stenbaek-Nielsen, H. C., Moudry, D. R., Wescott, E. M., Sentman, D. D., and Sabbas, F. T. S. (2000). Sprites and Possible Mesospheric Effects. *Geophys. Res. Lett.* 27 (23), 3829–3832. doi:10.1029/2000gl003827

Wescott, E. M., Stenbaek-Nielsen, H. C., Sentman, D. D., Heavner, M. J., Moudry, D. R., and Sabbas, F. T. S. (2001). Triangulation of Sprites, Associated Halos and Their Possible Relation to Causative Lightning and Micrometeors. *J. Geophys. Res.* 106 (A6), 10467–10477. doi:10.1029/2000JA000182

Wu, Y. J., Williams, E., Chang, S. C., Chou, J. K., Hsu, R. R., Friedrich, M., et al. (2017). The Leading Role of Atomic Oxygen in the Collocation of Elves and Hydroxyl Nightglow in the Low-Latitude Mesosphere. *J. Geophys. Res. Space Phys.* 122 (5), 5550–5567. doi:10.1002/2016JA023681

Conflict of Interest: The authors declare that the research was conducted in the absence of any commercial or financial relationships that could be construed as a potential conflict of interest.

Advantages of publishing in Frontiers

OPEN ACCESS
Articles are free to read
for greatest visibility
and readership

FAST PUBLICATION
Around 90 days
from submission
to decision

HIGH QUALITY PEER-REVIEW
Rigorous, collaborative,
and constructive
peer-review

TRANSPARENT PEER-REVIEW
Editors and reviewers
acknowledged by name
on published articles

Frontiers
Avenue du Tribunal-Fédéral 34
1005 Lausanne | Switzerland

Visit us: www.frontiersin.org
Contact us: frontiersin.org/about/contact

REPRODUCIBILITY OF RESEARCH
Support open data
and methods to enhance
research reproducibility

DIGITAL PUBLISHING
Articles designed
for optimal readership
across devices

FOLLOW US
@frontiersin

IMPACT METRICS
Advanced article metrics
track visibility across
digital media

EXTENSIVE PROMOTION
Marketing
and promotion
of impactful research

LOOP RESEARCH NETWORK
Our network
increases your
article's readership